The Dissertation Committee for William Hamill Wilson
certifies that this is the approved version of the following dissertation:

Advancements in Radionuclide Monitoring Technologies

used to Detect Indications of Nuclear Explosions

Committee:

_____
Steven Biegalski, Supervisor

_____
Derek Haas

_____
Sheldon Landsberger

_____
Justin Lowrey

Advancements in Radionuclide Monitoring Technologies used to Detect Indications of Nuclear Explosions

by

William Hamill Wilson, B.S.M.E., M.S.E.

Dissertation

Presented to the Faculty of the Graduate School of
The University of Texas at Austin
in Partial Fulfillment
of the Requirements
for the Degree of
Doctor of Philosophy

The University of Texas at Austin
May 2017

Dedication

This dissertation is dedicated to my best friend and wife, Ashleigh Marie, to my two daughters, Sadie Claire and Ella Marie, and to my son, Lucas William.

Thank you, Ashleigh, for your constant encouragement, love, patience, and support, and thank you for all the sacrifices you made over the past five years that allowed me to make my dream of getting my Ph.D. a reality. You supported me whole-heartedly throughout this entire process and I could not have done this without you. You are my best friend and I love you with all my heart.

Thank you, Sadie, Ella, and Luke for your unconditional love and support and thank you for being sources of encouragement and happiness throughout the duration of my doctoral program. I want you guys to know that it was difficult for me to get through the work documented in this dissertation, but I always believed that I could do it, I trusted in God and His plan for my life, and your love and support encouraged me when I needed it the most. I hope that this note and this dissertation serve as reminders to you that you can do anything in this life if you set your mind to it and always trust in God. You guys are my pride and joy and I love you more than you will ever know.

Acknowledgments

The work documented in this dissertation was conducted over a period of about five years. While I, William H. Wilson, am listed as the sole author on the cover, this work could not have been undertaken, let alone completed, without the help and support of numerous organizations and individuals. While I will undoubtedly fail to acknowledge the contributions of all of those who helped me over the past five years, I would like to try to say "thank you" to as many of you as possible.

I would first like to thank the United States Department of Defense Defense Threat Reduction Agency for their generous financial support of this work through grant HDTRA1-12-1-0018. I hope that the work documented herein will provide meaningful and lasting support of the Defense Threat Reduction Agency's mission to safeguard the United States of America and its allies from threats posed by weapons of mass destruction. I would also like to thank XIA LLC (formerly X-Ray Instrumentation Associates) for their generous financial support of the Si-PIN diode spectrometer prototype characterization work documented herein.

Next I would like to thank my advisor, Dr. Steven Biegalski, for his guidance, patience, and support over the past five years. Thank you, Dr. Biegalski, for having me as a graduate student and for supporting me throughout the course of my doctoral program. Thank you for allowing me the freedom to explore many different curiosities and for giving me the opportunity to learn so much about so many different things.

I would also like to thank my committee members, Dr. Derek Haas, Dr. Sheldon Landsberger, and Dr. Justin Lowrey for their guidance, patience, and support over the past five years. Thank you, Dr. Haas and Dr. Lowrey for your guidance and patience and for the valuable insights you provided regarding various aspects of the Comprehensive Nuclear-Test-Ban Treaty. Thank you, Dr. Landsberger, for encouraging me to pursue nuclear engineering as an undergraduate student. You recommended that I apply for what turned out to be a wonderful undergraduate job at The University of Texas at Austin's Nuclear Engineering Teaching Laboratory, and you were instrumental in helping me to get into graduate school at The University of Texas at Austin. Thank you for all that you have done for me. I would also like to thank Dr. Erich Schneider, who effectively served as a fifth member on my committee for several years. Thank you, Dr. Schneider, for your inspired instruction and for introducing me to many of the computational methods and tools I used throughout the course of my doctoral program.

Next I would like to thank the staff of The University of Texas at Austin's Nuclear Engineering Teaching Laboratory for all they have done in support of my research efforts over the past five years. I would especially like to thank Mr. Paul (Mike) Whaley, Mr. Michael Krause, Mr. Larry Welch, Mr. Tracy Tipping, Mr. Greg Kline, and Ms. Dana Judson for the valuable direction, guidance, and support they provided so willingly over the past five years. Thank you all for your help.

I would also like to thank the undergraduate and graduate student employees of The University of Texas at Austin's Nuclear Engineering Teaching Laboratory for supporting the experiments documented herein along with many others that are not.

I would especially like to thank Mr. Nick Mohammed, Mr. Udit Chatterjee, and Mr. Hammad Afzal for their help and for their friendship.

I would like to thank Dr. Wolfgang Hennig and Dr. Christopher Cox of XIA LLC for their prolonged support of the Si-PIN diode spectrometer prototype characterization work documented herein. You were very generous in allowing me to work with your Si-PIN diode spectrometer prototype for an extended period and you willingly supported several complex troubleshooting efforts long after your obligation to do so had run out. Without your help the Si-PIN diode spectrometer prototype characterization work documented herein could not have been completed. Thank you both for all of your help.

Thank you to Dr. Forrest Brown and Dr. Albert (Skip) Kahler at Los Alamos National Laboratory for providing many valuable insights regarding the inner workings of the Monte Carlo N-Particle (MCNP) radiation transport code and the NJOY 2012 nuclear data processing code. Additionally, thank you to Dr. Cyrus Proctor, Mr. Chris Hempel, and Mr. Nathaniel Mendoza at the Texas Advanced Computing Center for helping to get the MCNP radiation transport code installed and running on the Texas Advanced Computing Center computational resources. Your contributions were crucial in supporting the development of the MCNP models used to support various aspects of the research efforts documented herein. Thank you all for your help.

I would like to thank Dr. Dimitri Rochman and his colleagues at The Paul Scherrer Institut in Switzerland for making available to me the evaluated nuclear data files which served as essential inputs to the MCNP models developed to conduct the detailed, site-specific Comprehensive Nuclear-Test-Ban Treaty-relevant radionuclide

background activity concentration characterization studies documented herein. Thank you for sharing your data and for many productive conversations.

I would like to thank my fellow graduate students and my friends within the Nuclear and Radiation Engineering Program at The University of Texas at Austin for their friendship and support over the past five years. I would especially like to thank Dr. Matt Paul, Dr. Joe Artnak, Dr. Franziska Klingberg, and Dr. Ken Dayman for sharing a number of offices and many hours of productive and enjoyable conversation with me over the past five years. I would like to thank Dr. Hirotatsu (James) Armstrong and Dr. Christine Johnson for their friendship and for their contributions to the background activity concentration characterization studies documented herein. Thank you to Mr. Will Gurecky for your help administering the Nukestar computing cluster and for many helpful MCNP- and NJOY 2012-themed conversations. I would also like to thank Mr. Matthew Montgomery, Mr. Michael Yoho, and Mr. Blake Copple for their friendship over the past five years. Thank you all for your help and for your friendship. I hope that we will remain close even as our time together at The University of Texas at Austin draws to a close.

I would like to conclude by thanking my family and my friends for all of the encouragement, love, and support they have provided not only throughout the past five years, but throughout my life. I want to thank my wife and my best friend, Ashleigh Marie, and my three wonderful children, Sadie Claire, Ella Marie, and Lucas William, for their encouragement, for their love, and for their unending support. I am so proud of you guys, I love you more than you will ever know, and this dissertation is dedicated to you.

Ashleigh and I would both like to thank our family and friends for their love and support over the past five years. We would like to thank my mother and father, Elba and Warren Wilson, for the encouragement, love, and support they have provided throughout our lives. You guys have done so much for us and for our family and we never could have undertaken this doctoral program without your love and support. We love you guys so much. We also want to thank my sister, Molly George, and my brother-in-law, Michael George, for all they have done for us and for our family. Thank you guys for loving and supporting us even as life dealt you your own challenges. We love you both. We want to thank my mother-in-law, Diana Jones, and my fathers-in-law, Jim Wilson and Mark Jones for their love and support as well. Thank you guys for believing in me and for supporting me, Ashleigh, and our family throughout the past five years. We could not have made it through the difficult times without you. We love you. We would also like to thank our extended family and all my friends for everything they have done for us over the past five years. There are too many of you to list here, but please know that we appreciate all you have done for us and that we love you.

And finally, Ashleigh and I want to thank our Lord and Savior, Jesus Christ, who sent us down this path and who sustained us throughout the course.

Advancements in Radionuclide Monitoring Technologies

used to Detect Indications of Nuclear Explosions

William Hamill Wilson, Ph.D.
The University of Texas at Austin, 2017

Supervisor: Steven Biegalski

The objective of the research documented in this dissertation was to advance the state-of-the-art radionuclide monitoring technologies used to detect indications of nuclear explosions, which are absolutely prohibited by the Comprehensive Nuclear-Test-Ban Treaty (CTBT). Advancements are made in two areas.

The first advancements are in the characterization and optimization of a Si-PIN diode-based radiation spectrometer prototype sensitive to both photons and conversion electrons. A novel peak-fitting algorithm referred to herein as the WiPFA algorithm was developed to support the Si-PIN diode spectrometer prototype characterization efforts. The absolute conversion electron detection efficiency of the prototype was found to be 5.2 ± 0.4 % at conversion electron energies near 150 keV, and the ^{131m}Xe, ^{133m}Xe, ^{133}Xe, and ^{135}Xe Minimum Detectable Concentrations (MDCs) were found to be 1.7, 2.0, 2.1, and 56 mBq-m^{-3}, respectively.

A series of Monte Carlo N-Particle (MCNP) radiation transport code models were then developed to evaluate the MDCs associated with a series of optimized Si-PIN diode-

based spectrometer designs. These optimization studies revealed that coupling Si-PIN diodes available today with thinner, cylindrical spectrometer designs could reduce the ^{131m}Xe, ^{133m}Xe, and ^{133}Xe, MDCs to 0.48, 0.57, and 0.58 mBq-m^{-3}, respectively. Subsequent studies utilizing larger, thicker Si-PIN diodes indicated that additional reductions down to 0.31, 0.37 and 0.37 mBq-m^{-3} might be possible. These small radioxenon MDCs coupled with other perceived advantages of Si-PIN diodes suggest that Si-PIN diode-based radiation spectrometers could serve as attractive alternatives to the high-resolution gamma-ray and beta-gamma coincidence spectrometers currently employed by the verification regime of the CTBT.

The second area in which advancements are made is the radionuclide background activity concentration characterization area. The focus here is on CTBT-relevant radioactive particulates and noble gases produced via spontaneous fission and via naturally occurring cosmic-ray induced fission and activation reactions.

A new application—the Terrestrial Xenon and Argon Simulator (TeXAS) application—was developed to streamline and automate the creation of high-fidelity MCNP models and dedicated nuclear data libraries required to support detailed, site-specific background activity concentration characterization studies. The capabilities of the TeXAS application are demonstrated and used to develop background activity concentration estimates specific to several layers of the Earth's atmosphere, several subsurface depths in six geologies prevalent in the Earth's upper crust, and seawater.

Table of Contents

List of Figures

List of Tables

Chapter 1: Introduction and Motivation

The objective of the research efforts documented in this dissertation was to advance the state-of-the-art radionuclide monitoring technologies used to detect indications of nuclear explosions, which are absolutely prohibited by the Comprehensive Nuclear-Test-Ban Treaty (CTBT). As will be seen, advancements are made in two areas.

The first advancement is in the characterization of a Si-PIN diode-based radiation spectrometer prototype. The results of the prototype characterization are used to develop an optimized Si-PIN diode spectrometer design, the performance characteristics of which are evaluated relative to the performance characteristics of the high-resolution gamma-ray and beta-gamma coincidence spectrometers currently employed by the verification regime of the CTBT.

The second advancement is in the development of a Terrestrial Xenon and Argon Simulator (TeXAS) application capable of estimating background activity concentrations resulting from natural processes for every radionuclide identified as relevant to the CTBT on a site-specific basis. Background activity concentrations resulting from natural processes must be well understood so that may be distinguished from radionuclide activity concentrations resulting from nuclear explosions.

The research efforts supporting these advancements are documented in Chapters 2 and 3, respectively. In order to provide context and motivate the work, this chapter opens with a brief historical account of the more than 2,050 nuclear explosions detonated since 1945, the effects of the explosions, and the political and technological efforts that have been expended to date in hopes of preventing the detonation of additional nuclear explosions in the future. The focus here is on the CTBT and the radioactive particulate and noble gas monitoring systems currently employed by the verification regime of the CTBT. Techniques used to distinguish radioactive particulate and noble gas detections indicative of nuclear explosions from detections characteristic of nuclear generating station and radiopharmaceutical facility releases are also discussed. The chapter concludes by building a case for next-generation radiation spectrometer development and advanced background activity concentration estimation methods as two areas for further development within the radionuclide monitoring technology area of the verification regime of the CTBT and by stating the objectives of the research efforts documented herein.

1.1 A Brief History of Nuclear Explosions

The world's first nuclear explosion was detonated on 16 July 1945 when the United States of America (USA) conducted its first test of a nuclear weapon at what was then known as Alamogordo Bombing Range about 55 mi (88.5 km) northwest of Alamogordo, New Mexico, USA [1, 2]. The objective of the test, which was christened *Trinity*, was to test a plutonium-fueled implosion-type nuclear weapon design developed

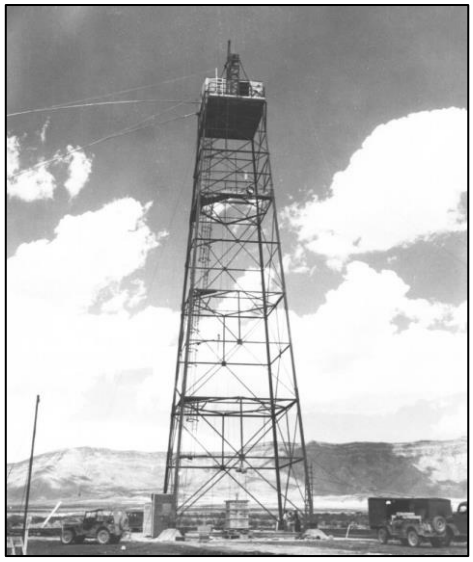

Figure 1.1: A photograph of the 100 ft tower atop which the world's first nuclear explosion was detonated on the morning of 16 July 1945 [4].

as a result of a secret World War II research and development project dubbed *The Manhattan Project* [2, 3]. The weapon, or "gadget" as it was referred to at the time, was detonated at the top of a 100 ft (30.5 m) tower (see Figure 1.1), and produced an explosive yield equivalent to 21 kt of TNT [3, 5].

Since the *Trinity* test, eight states (including the USA) have conducted more than 2,050 nuclear explosion tests of various kinds [6]. The vast majority of these tests (roughly 85 %) were conducted by the USA and the Russian Federation (Russia) (formerly the Union of Soviet Socialist Republics (USSR)); The USA has conducted 1,030 tests and Russia has conducted 715 tests [6]. The French Republic (France) has conducted 210 nuclear explosion tests and the People's Republic of China (China) and the United Kingdom (UK) have each conducted 45 tests [6]. More recently, the Republic

of India (India), the Islamic Republic of Pakistan (Pakistan), and the Democratic People's Republic of North Korea (North Korea), have conducted their own tests, with the most recent example being a North Korean test conducted on 9 September 2016 [7]. Table 1.1 presents a summary of the nuclear explosion tests conducted to date; the data in the table is organized by state, year, and test environment.

1.2 Effects of Nuclear Explosions

Nuclear explosions release tremendous amounts of energy when detonated; their explosive yields are typically expressed in thousands or millions of tons of TNT. The energy released during a nuclear explosion can affect humans and the environment in many different and complicated ways, many of which can be quite devastating.

To date, two nuclear explosions have been used as weapons against operational targets. Both explosions were detonated by the USA over Japanese targets at the end of World War II. The first was detonated over Hiroshima, Japan at 8:15 in the morning on 6 August 1945 and the second was detonated over Nagasaki, Japan at 11:02 in the morning on 9 August 1945 [8, 9]. The population of Hiroshima when it was bombed is estimated to have been about 350,000 [9, 10]. About 140,000 people, or about 40 % of the city's population, are believed to have been killed by the bomb by the end of 1945 [9, 10]. The loss of human life resulting from the Nagasaki attack was equally staggering: the population of Nagasaki when it was bombed is believed to have been roughly 280,000 and the bomb is believed to have killed about 74,000 people by the end of 1945 [9, 10].

Table 1.1: Nuclear explosion tests by state, year, and test environment [6].

Year	USA			USSR / Russia			UK [a]		France		China		India [b]	Pakistan [b]	North Korea [b]	Total
	Atm	UW	UG	Atm	UW	UG	Atm	UG	Atm	UG	Atm	UG				
1945	1	-	-	-	-	-	-	-	-	-	-	-	-	-	-	1
1946	1	1	-	-	-	-	-	-	-	-	-	-	-	-	-	2
1947	-	-	-	-	-	-	-	-	-	-	-	-	-	-	-	-
1948	3	-	-	-	-	-	-	-	-	-	-	-	-	-	-	3
1949	-	-	-	1	-	-	-	-	-	-	-	-	-	-	-	1
1950	-	-	-	-	-	-	-	-	-	-	-	-	-	-	-	-
1951	15	-	1	2	-	-	-	-	-	-	-	-	-	-	-	18
1952	10	-	-	-	-	-	1	-	-	-	-	-	-	-	-	11
1953	11	-	-	5	-	-	2	-	-	-	-	-	-	-	-	18
1954	6	-	-	10	-	-	-	-	-	-	-	-	-	-	-	16
1955	16	1	1	5	1	-	-	-	-	-	-	-	-	-	-	24
1956	18	-	-	9	-	-	6	-	-	-	-	-	-	-	-	33
1957	27	-	5	15	1	-	7	-	-	-	-	-	-	-	-	55
1958	60	2	15	34	-	-	5	-	-	-	-	-	-	-	-	116
1959	-	-	-	-	-	-	-	-	-	-	-	-	-	-	-	-
1960	-	-	-	-	-	-	-	-	3	-	-	-	-	-	-	3
1961	-	-	10	57	1	1	-	-	1	1	-	-	-	-	-	71
1962	38	1	57	78	-	1	-	2	-	1	-	-	-	-	-	178
1963	4	-	43	-	-	-	-	-	-	3	-	-	-	-	-	50
1964	-	-	45	-	-	9	-	2	-	3	1	-	-	-	-	60
1965	-	-	38	-	-	14	-	1	-	4	1	-	-	-	-	58
1966	-	-	48	-	-	18	-	-	6	1	3	-	-	-	-	76
1967	-	-	42	-	-	17	-	-	3	-	2	-	-	-	-	64
1968	-	-	56	-	-	17	-	-	5	-	1	-	-	-	-	79
1969	-	-	46	-	-	19	-	-	-	-	1	1	-	-	-	67
1970	-	-	39	-	-	16	-	-	8	-	1	-	-	-	-	64
1971	-	-	24	-	-	23	-	-	5	-	1	-	-	-	-	53
1972	-	-	27	-	-	24	-	-	4	-	2	-	-	-	-	57
1973	-	-	24	-	-	17	-	-	6	-	1	-	-	-	-	48
1974	-	-	22	-	-	21	-	1	9	-	1	-	1	-	-	55
1975	-	-	22	-	-	19	-	-	-	2	-	1	-	-	-	44
1976	-	-	20	-	-	21	-	1	-	5	3	1	-	-	-	51
1977	-	-	20	-	-	24	-	-	-	9	1	-	-	-	-	54
1978	-	-	19	-	-	31	-	2	-	11	2	1	-	-	-	66
1979	-	-	15	-	-	31	-	1	-	10	1	-	-	-	-	58
1980	-	-	14	-	-	24	-	3	-	12	1	-	-	-	-	54
1981	-	-	16	-	-	21	-	1	-	12	-	-	-	-	-	50
1982	-	-	18	-	-	19	-	1	-	10	-	1	-	-	-	49
1983	-	-	18	-	-	25	-	1	-	9	-	2	-	-	-	55
1984	-	-	18	-	-	27	-	2	-	8	-	2	-	-	-	57
1985	-	-	17	-	-	10	-	1	-	8	-	-	-	-	-	36
1986	-	-	14	-	-	-	-	1	-	8	-	-	-	-	-	23
1987	-	-	14	-	-	23	-	1	-	8	-	1	-	-	-	47
1988	-	-	15	-	-	16	-	-	-	8	-	1	-	-	-	40
1989	-	-	11	-	-	7	-	1	-	9	-	-	-	-	-	28
1990	-	-	8	-	-	1	-	1	-	6	-	2	-	-	-	18
1991	-	-	7	-	-	-	-	1	-	6	-	-	-	-	-	14

Table 1.1: Nuclear explosion tests by state, year, and test environment, continued [6].

Year	USA			USSR / Russia			UK [a]		France		China		India [b]	Pakistan [b]	North Korea [b]	Total
	Atm	UW	UG	Atm	UW	UG	Atm	UG	Atm	UG	Atm	UG				
1992	-	-	6	-	-	-	-	.	-	-	-	2	-	-	-	8
1993	-	-	-	-	-	-	-	.	-	-	-	1	-	-	-	1
1994	-	-	-	-	-	-	-	.	-	-	-	2	-	-	-	2
1995	-	-	-	-	-	-	-	.	-	5	-	2	-	-	-	7
1996	-	-	-	-	-	-	-	-	-	1	-	2	-	-	-	3
1997	-	-	-	-	-	-	-	-	-	-	-	-	-	-	-	-
1998	-	-	-	-	-	-	-	-	-	-	-	-	2 [c]	2 [d]	-	4
1999	-	-	-	-	-	-	-	-	-	-	-	-	-	-	-	-
2000	-	-	-	-	-	-	-	-	-	-	-	-	-	-	-	-
2001	-	-	-	-	-	-	-	-	-	-	-	-	-	-	-	-
2002	-	-	-	-	-	-	-	-	-	-	-	-	-	-	-	-
2003	-	-	-	-	-	-	-	-	-	-	-	-	-	-	-	-
2004	-	-	-	-	-	-	-	-	-	-	-	-	-	-	-	-
2005	-	-	-	-	-	-	-	-	-	-	-	-	-	-	-	-
2006	-	-	-	-	-	-	-	-	-	-	-	-	-	-	1	1
2007	-	-	-	-	-	-	-	-	-	-	-	-	-	-	-	-
2008	-	-	-	-	-	-	-	-	-	-	-	-	-	-	-	-
2009	-	-	-	-	-	-	-	-	-	-	-	-	-	-	1	1
2010	-	-	-	-	-	-	-	-	-	-	-	-	-	-	-	-
2011	-	-	-	-	-	-	-	-	-	-	-	-	-	-	-	-
2012	-	-	-	-	-	-	-	-	-	-	-	-	-	-	-	-
2013	-	-	-	-	-	-	-	-	-	-	-	-	-	-	1	1
2014	-	-	-	-	-	-	-	-	-	-	-	-	-	-	-	-
2015	-	-	-	-	-	-	-	-	-	-	-	-	-	-	-	-
2016	-	-	-	-	-	-	-	-	-	-	-	-	-	-	2	2
Totals	210	5	815	216	3	496	21	24	50	160	23	22	3	2	5	2,055
	1,030			715			45		210		45		3	2	5	2,055

Notes: Atm = atmospheric nuclear explosion test, UW = underwater nuclear explosion test, and UG = underground nuclear explosion test.

a: All of the nuclear explosion tests conducted by the UK since 1962 were conducted jointly with the USA at the Nevada Test Site, but these tests are listed only under the "UK" column in this table. Also note that safety tests conducted by the UK are not included in this table.

b: All of the nuclear explosion tests conducted by India, Pakistan, and North Korea have been detonated underground.

c: While multiple tests were conducted on each date, the nuclear explosion tests conducted by India on 11 and 13 May 1998 are listed as one test for each date in this table.

d: The five tests conducted by Pakistan on 28 May 1998 are also listed as one test in this table.

About one-half of the energy released by the nuclear weapons detonated over Hiroshima and Nagasaki was given off as blast energy and about one-third was given off as heat energy, and thus the majority of the people killed in Hiroshima and Nagasaki were either crushed in collapsed buildings or burned to death [9]. The majority of the remainder of the energy released by the bombs was released in the form of ionizing

radiation [9]. Victims exposed to ionizing radiation within 1 km of the hypocenters at Hiroshima and Nagasaki are believed to have received acute whole-body radiation doses of about 1,000 rads (10.00 Gy) [9]. In order to place this dose in perspective, note that virtually 100 % of people who receive an acute whole-body dose of 700 rads (7.00 Gy) die quickly as a result of the radiation exposure [9]. Furthermore, about 50 % of people who receive an acute whole-body dose of 450 rads (4.50 Gy) die within a month [9]. The victims at Hiroshima and Nagasaki who received these doses and were not killed quickly by the blast or fire undoubtedly suffered excruciatingly painful deaths.

Many of those who survived the Hiroshima and Nagasaki attacks have suffered from long-term health problems often attributed to ionizing radiation exposure. Some of the more common health problems include eye diseases, blood disorders, malignant tumors, and psychoneurological disturbances [9]. Survivors of the Hiroshima and Nagasaki attacks have been observed to contract Leukemia and solid cancers (*e.g.* stomach cancer, breast cancer, lung cancer, *etc.*) at elevated rates relative to other, non-exposed portions of the Japanese population [9, 11]. Increased Leukemia contraction rates were observed in Hiroshima and Nagasaki as early as 1947 [11]. Leukemia contraction rates in survivors peaked around 1953 and have since returned to baseline rates more representative of the Japanese population as a whole [11]. The Radiation Health Effects Foundation estimates that over the period from 1950 through 2010 an excess of 94 cases of Leukemia were observed in Hiroshima and Nagasaki [11]. This represents an excess of about 46 % [11]. Furthermore, the Radiation Health Effects Foundation estimates that over the same time period survivors of the nuclear explosions

at Hiroshima and Nagasaki have contracted an excess of 848 solid cancers [11]. This represents an excess of about 11 % [11]. The majority of the excess solid cancers have appeared as stomach cancer (150 excess cancers), breast cancer (147 excess cancers), lung cancer (117 excess cancers), and colon cancer (78 excess cancers) [11].

In contrast to the nuclear explosions detonated as weapons over Hiroshima and Nagasaki, nuclear explosions tests have typically been conducted so that human casualties have been avoided. That said, there have been a number of cases in which humans were exposed to fallout from nuclear explosion tests. Some well-documented examples are the crew of the Japanese fishing vessel *Lucky Dragon Number 5*, the American weathermen stationed on Rongerik Atoll, and several groups of Marshall Islanders, all of whom were exposed to radioactive fallout from nuclear explosion tests conducted by the USA in the Marshall Islands between 1946 and 1958 [12, 13]. The majority of the doses received by these individuals resulted from a 1 March 1954 test code-named *Bravo* [12]. The fallout from the test was supposed to drift north and to the

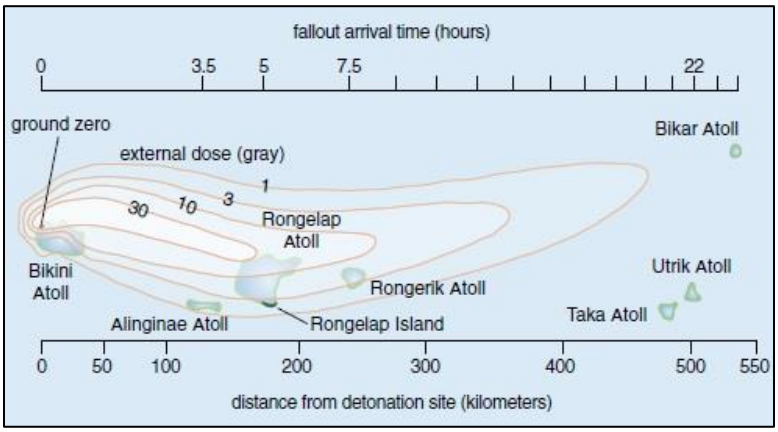

Figure 1.2: Fallout resulting from the 1 March 1954 American nuclear explosion test code-named *Bravo* [12].

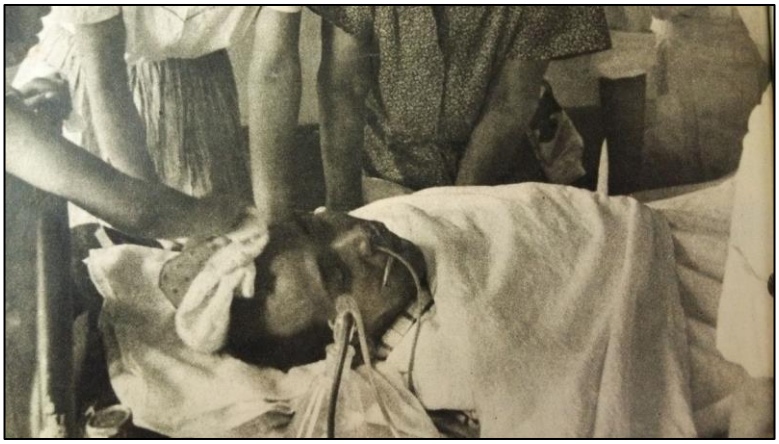

Figure 1.3: Caretakers attending to Aikichi Kuboyama, a crew member of the Japanese fishing boat *Lucky Dragon Number 5* that was exposed to fallout from an American nuclear explosion test on 1 March 1954 [12, 14].

west where it would have fallen over the open ocean, but a larger than expected explosive yield and wind shear apparently carried a large amount of fallout from the *Bravo* test east over several inhabited atolls as illustrated in Figure 1.2 [12]. Marshall Islanders on the Ailinginae, Rongelap, and Utrik Atolls are estimated to have received whole-body doses of about 1.4 Gy, 2 Gy, and 0.2 Gy, respectively [12]. The American weathermen stationed at Rongerik Atoll received whole-body doses of about 2.9 Gy, and the Japanese fishermen aboard *Lucky Dragon Number 5* received whole-body doses of about 1.7 to 6 Gy [12].

Several of the *Lucky Dragon Number 5* crew member became ill during their two week transit back to port and one crew member, Aikichi Kuboyama (see Figure 1.3), died five months later in September of 1954 [13]. While there is some debate as to the cause of Mr. Kuboyama's death, it must be noted that the physician who conducted his autopsy apparently noted "a remarkable deterioration in many of [Mr. Kuboyama's] organs,

especially his blood-producing organs," and that it was "evident, even by visual inspection, that the chief cause of death was radioactivity [15]."

Marshall Islanders on Rongelap Atoll also demonstrated symptoms of radiation sickness in the days following the *Bravo* test, including vomiting, skin damage, and hair loss [13]. Additionally, many Marshall Islanders have suffered long-term health problems as a result of their exposures. A study conducted by the National Cancer Institute found that about 500 excess cases of cancer may be contracted by Marshall Islanders as a result of radiation exposure attributed to the nuclear explosion tests conducted by the USA [16]. Most of these excess cancers are expected to be thyroid and colon cancers [16].

American citizens have also been exposed to fallout resulting from nuclear explosion tests conducted at various sites within the contiguous USA. According to a study conducted by the National Cancer Institute, Americans exposed to ^{131}I from tests conducted at the former Nevada Test Site are expected to contract an excess of about 49,000 cases of thyroid cancer (an excess of about 12 %) [12]. Most of these are expected to occur in adults aged 20 at any time over the period 1951 to 1957 [12]. Additionally, the National Cancer Institute expects that Americans may succumb to an excess of 1,800 Leukemia deaths as a result of exposure to fallout from the former Nevada Test Site [12]. This represents an excess of about 0.12 % relative to the number of Leukemia deaths that might be expected in a non-exposed American population.

The purpose of the nuclear explosion effects survey presented here is to illustrate the fact that all nuclear explosions, including nuclear explosion tests and so-called

"peaceful nuclear explosions," produce adverse human and environmental effects. This is why it is so important not only to prevent nuclear proliferation and promote nuclear disarmament but also to prevent the detonation of nuclear explosions. In the sections that follow the long and sometimes difficult path to an international agreement prohibiting nuclear explosions of all kinds is described.

1.3 Early Attempts to Ban Nuclear Explosions

The international community began engaging in discussions aimed at preventing nuclear proliferation, promoting nuclear disarmament, and prohibiting nuclear explosions almost immediately after the USA ushered in the nuclear age in 1945. From 1946 through 1952 the majority of these discussions were sanctioned by the United Nations Atomic Energy Commission (UNAEC) which was created on 24 January 1946 by United Nations General Assembly Resolution 1 [17, 18]. The objective of the UNAEC was "to deal with the problems raised by the discovery of atomic energy [18]." The entire international community, including both the USA and the USSR, unanimously agreed that the responsibility of overseeing atomic energy should be assumed by an international organization. However, there were many differing opinions regarding the policies that should be adopted by the organization and negotiations proved to be difficult.

In the USA, US Secretary of State Dean Acheson and Tennessee Valley Authority Chairman David Lilienthal were appointed co-chairs of a committee tasked with developing a US policy regarding atomic energy [19]. In March of 1946, the Acheson-Lilienthal committee presented what has come to be called the Acheson–Lilienthal

Report to the US State Department [17, 19]. The report suggested that any nuclear non-proliferation and disarmament agreement that relied on verification via inspections and policing would be unlikely to succeed. As an alternative, the report proposed that nuclear non-proliferation and disarmament could be achieved by placing the entirety of the nuclear fuel cycle under the control of an international agency [17, 19]. US President Harry S. Truman agreed with the findings of the Acheson–Lilienthal Report, in general, and appointed Bernard Baruch to carry an adaptation of the Acheson–Lilienthal Report, called the Baruch Plan, forward to the UNAEC [17, 19]. However, the USSR found the terms of the Baruch Plan to be unacceptable, largely because the plan insisted that the USSR agree not develop nuclear weapons and allowed for unrestricted inspections within the USSR while allowing the USA to temporarily retain their nuclear weapons [17, 19].

As a counter to the Baruch Plan presented by the USA, the USSR presented to the UNAEC an alternative nuclear non-proliferation and disarmament plan

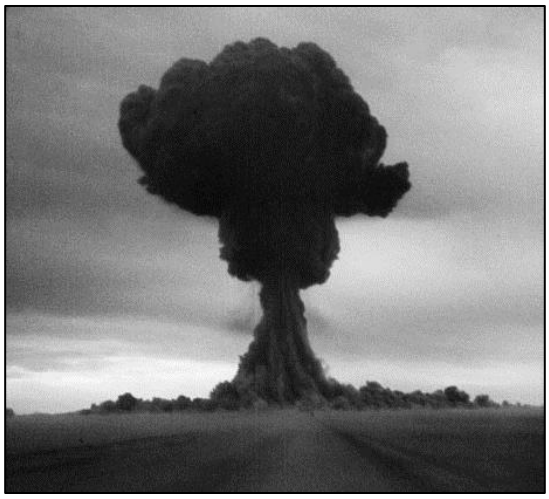

Figure 1.4: A photograph of *RDS-1*, the first Soviet nuclear explosion test conducted on 29 August 1949 [21].

on 19 June 1946 [17]. The USSR's plan, the Gromyko Plan, was similar to the Baruch Plan in that it called for the nuclear fuel cycle to be placed under international control [17]. However, the Gromyko Plan called for the USA to disband their nuclear weapons as a precursor to placing the nuclear fuel cycle under international control [17]. The USA rejected the terms of the Gromyko Plan.

After the USA and USSR failed to compromise on the terms of the Baruch and Gromyko plans, nuclear non-proliferation and disarmament discussions and negotiations continued at the UNAEC for about three more years, but finding a plan that was acceptable to all sides proved to be exceedingly difficult. In 1949 the United Nations issued a report noting that the UNAEC appeared to be at an impasse [20]. Later that same year, on 29 August 1949, the USSR detonated their first nuclear explosion (see Figure 1.4) [17]. Then, in 1950, the USSR withdrew from UNAEC sanctioned nuclear non-proliferation and disarmament discussions. Two years later, in 1952, the United Nations General Assembly dissolved the UNAEC [22].

Over the next ten years, from 1953 through 1963, the USA, the USSR, the UK, and France detonated more than 560 nuclear explosions [6]. During this time period international concerns regarding nuclear proliferation, the nuclear arms race, and the environmental effects associated with nuclear explosion testing continued to grow. In an attempt to curb these concerns both the USA and the USSR tabled several different proposals that would have banned nuclear explosion tests. However, the two sides were unable to come to terms on an agreement until 1963 when the US, the USSR, and the UK finally agreed to the terms of the Partial Test Ban Treaty (PTBT) [23]. The PTBT entered

Figure 1.5: A photograph of US President John F. Kennedy signing the Partial Test Ban Treaty on 10 October 1963 [23].

into force on 10 October 1963 (see Figure 1.5) and banned the US, the USSR, and the UK from conducting nuclear explosion tests underwater, in the Earth's atmosphere, and in space [23].

While the PTBT was historic in that it was the first multilateral agreement that placed limits and restrictions on nuclear explosion tests, it is important to note that the primary role of the PTBT was to address the environmental effects associated with atmospheric nuclear explosion testing [23]; the PTBT did nothing to address nuclear proliferation concerns, nuclear disarmament, or even the general rate at which nuclear explosion tests were conducted. In fact, in the years following the adoption of the PTBT the USA, the USSR and the UK actually conducted nuclear explosion tests at accelerated rates, the tests were just conducted underground as opposed to in the Earth's atmosphere [6, 23]. It is also important to note that neither France nor China were

members to the PTBT and both countries continued to conduct atmospheric nuclear explosion tests even after 1963 [6, 23].

About five years after the adoption of the PTBT a second international agreement was put into place specifically to address nuclear proliferation and disarmament concerns. On 1 July 1968 the USA, the USSR, the UK, and 58 other countries signed the Treaty on the Non-Proliferation of Nuclear Weapons, more commonly referred to as the Nuclear Non-Proliferation Treaty (NPT) [23]. The NPT is generally viewed as a three pillar treaty [23]. The first two pillars oblige Nuclear Weapon States (NWS) to eradicate their own nuclear armaments, prohibit NWS from transferring nuclear weapons and nuclear weapons technologies to Non-Nuclear Weapon States (NNWS), and forbid NNWS from pursuing their own nuclear weapons programs [23, 24]. The third pillar guarantees NNWS the inalienable right to pursue peaceful applications of nuclear power [23, 24].

Proponents of the NPT point to the fact that only four NNWS have acquired nuclear weapons since the NPT entered into force as an indication that the NPT has been a success [23]. Critics of the NPT on the other hand point to the fact that NWS are still believed to possess tens of thousands nuclear weapons as an indication that the disarmament pillar of the NPT has been a failure [23]. It should also be noted that the NPT did little to further the prevention of nuclear explosion tests. In fact, meaningful multilateral prohibitions on nuclear explosion tests beyond those specified by the PTBT would not be put into place until the subject of the next section, the CTBT, came into being in 1996.

1.4 The Comprehensive Nuclear-Test-Ban Treaty

From the later part of the 1970s through the early 1990s there arose a number of occasions on which the subject of a more comprehensive nuclear-test-ban agreement could be discussed. The most notable occasions include the 1985 NPT Review Conference, during which six PTBT Member States proposed expanding the scope of the PTBT to include all environments [25], and the 1991 PTBT Amendment Conference, during which 60 states supported initiating negotiations towards a comprehensive nuclear-test-ban agreement [25]. While these negotiations served to advance the cause towards a comprehensive nuclear-test-ban agreement the political climate at the time prevented meaningful results from being produced.

By the early 1990s, however, the situation had changed somewhat. The dissolution of the USSR in December of 1991 helped to curb cold war hostilities. Additionally, in the early 1990s the USA, the newly formed Russian Federation (internationally recognized as the successor to the USSR), and the UK all had their own nuclear testing moratoriums in place [6, 26]. The successful negotiation of the Chemical Weapons Convention at the 1992 Conference on Disarmament (CD) also served as an indication that the international community might be ready to make real progress towards a comprehensive nuclear-test-ban agreement [26].

On 10 August 1993 at the 659th CD plenary meeting member states adopted the decision to commence negotiations on a Comprehensive Nuclear-Test-Ban Treaty (CTBT) [26]. Formal treaty negotiations began on 3 February 1994, giving the CD a period of about 30 months to successfully negotiate a treaty before the 51st session of

the United Nations General Assembly and the CTBT negotiation deadline established later during the 1995 NPT Review and Extension Conference [26].

The CD member states had to work through a number of contentious issues throughout the duration of the negotiation period. The first issue was simply defining what constitutes a nuclear explosion. NWS suggested that they should be able to conduct low yield nuclear explosion tests to maintain the safety of their existing nuclear arsenals [27]. However, NNWS feared that allowing NWS to conduct low-yield tests would preserve the existence of nuclear weapons and perpetuate an imbalanced system and thus insisted that the CTBT must be a zero-yield treaty [27]. Indonesia even proposed that the word "explosion" be excluded from the treaty so that the treaty would effectively ban computer simulations of nuclear explosions, hydrodynamic experiments, and inertial confinement fusion experiments in addition to nuclear explosion tests [27]. In the end, the CTBT was established as a zero-yield treaty, but the word "explosion" was allowed to remain in the treaty text [27].

Another contentious issue was the formation of an Executive Council. The NWS felt that the CTBT should be overseen by an Executive Council and that the NWS should be permanent members of the council. The NNWS however were generally opposed to the idea of permanent Executive Council membership for NWS, and some NNWS were against the idea of an Executive Council altogether [28]. In the end it was decided that the CTBT would in fact be governed by an Executive Council and that the Executive Council would be comprised of 51 member states elected by the member states associated with six geographical regions [28]. Functionally, the CTBT Executive Council

serves to make decisions on procedural matters via a simple majority vote of council members. Matters of substance require a two-thirds majority [29].

While not as contentious as some of the other aspects of the treaty, the monitoring and inspection measures to verify member states compliance with the terms of the treaty were also discussed at length. It was clear from the beginning that the International Monitoring System (IMS) of the verification regime of the CTBT would employ a network of seismological monitoring stations to detect seismic signals indicative of nuclear explosions [30]. However, there were differing opinions as to which other monitoring technologies should be employed by the IMS and how the data should be collected, analyzed, and disseminated to CTBT member states. China and Pakistan expressed interest in incorporating an ElectroMagnetic Pulse (EMP) monitoring capability into the IMS element of the verification regime of the CTBT [30]. Russia suggested that space-based sensors and a dedicated fleet of aircraft could be used to constantly monitor the Earth's atmosphere for radioactive particulates indicative of nuclear explosions [30]. However, at an estimated annual cost of $3 billion USD these monitoring technologies were ultimately judged to be prohibitively expensive [30]. The CD member states ultimately decided that the IMS element of the verification regime of the CTBT would employ four monitoring technologies: (1) a seismic monitoring technology, (2) a hydroacoustic monitoring technology, (3) an infrasound monitoring technology, and (4) a radionuclide monitoring technology [30].

The subject of On-Site Inspections (OSIs) as part of a nuclear-test-ban agreement had been a sticking point between the USA and the Russian Federation dating back to the

late 1950s. The subject would prove to be divisive during CTBT negotiations as well. Most CD member states felt that provisions allowing for OSIs as a final verification measure had to be included in the CTBT [30]. Some CD member states however feared that their adversaries may try to use OSIs carried out in the name of the CTBT to gain foreign intelligence inside their borders and thus viewed OSIs as a threat to their national sovereignty [30]. In the end, provisions for OSIs were in fact written into the CTBT. CTBT member states may submit OSI requests to the CTBT Executive Council [30]. If at least 30 of the CTBT Executive Council member states vote in favor of the OSI then the accused state must allow a team of inspectors to conduct an OSI at the suspected nuclear explosion site [30].

One of the last issues requiring resolution as the 51st session of the United Nations General Assembly approached was the entry into force formula. The issue was determining which states should be required to sign and ratify the CTBT in order for the treaty to enter into force. A number of proposals had been considered dating back to 20 June 1994 when China proposed that the treaty should enter into force after all 65 CD member states and all states known by the International Atomic Energy Agency (IAEA) to possess nuclear generating stations or nuclear research reactors had deposited their instruments of ratification with the United Nations Depositary [31]. This proposal was rejected by many states because it would have allowed a single state to effectively veto the treaty [31]. Several other entry into force formulas were proposed and rejected until CD chairman Jaap Ramaker presented a list of 44 "Annex 2" states identified by the IAEA as having nuclear research and/or power reactors [31]. In the end it was decided

that the CTBT would enter into force 180 days after all 44 of the so-called Annex 2 states had deposited their instruments of ratification [31].

In August of 1996 it was clear that some CD member states disagreed with certain aspects of the CTBT [32]. Some of these states expressed their concerns but did not officially oppose the treaty. Others, however, felt that the treaty had issues they could not live with and, despite reassurances provided by other CD member states, India and Iran officially opposed the CTBT negotiated by the member states of the CD [32]. According to the rules of the CD, decisions adopted by the CD must be reached by consensus, and thus the official opposition of India and Iran initially made it impossible for the CD to include the CTBT in their report to the 51st session of the United Nations General Assembly [32]. As a work around, Belgium submitted the text of the CTBT to the CD as a national paper, making the text of the CTBT an official CD document and allowing the CD to submit the text of the treaty to the United Nations General Assembly [32].

A resolution containing the CTBT text was introduced to the CTBT General Assembly during the assembly's 51st session and on 10 September 1996 the General Assembly voted in favor of the CTBT with 158 votes in favor, three votes against (Bhutan, India, and the Libyan Arab Jamahiriya), and five abstentions (the Republic of Cuba, the Republic of Mauritius, the Syrian Arab Republic, the Lebanese Republic, and the United Republic of Tanzania) [32]. The CTBT opened for signature on 24 September 1996 in New York, NY, USA [32]. US President Bill Clinton signed first on behalf of the USA. Four other NWS—China, France, the Russian Federation, and the

United Kingdom—signed immediately thereafter, and by the end of the day 66 states had signed the CTBT [32].

As of 16 June 2016 the CTBT has been signed by 183 states and ratified by 164, including 36 of the 44 Annex 2 states [32]. Of the eight Annex 2 states that have not yet ratified the treaty, five have signed the treaty (China, the Arab Republic of Egypt, the Islamic Republic of Iran, the State of Israel, and the USA) and three have not (India, North Korea, and Pakistan) [32]. At this point it must be noted that while the CTBT has not yet entered into force, and will not enter into force until all 44 of the Annex 2 states ratify the treaty, the research efforts documented throughout the remainder of this dissertation are discussed within the context of the CTBT because the CTBT represents the most current effort to reach an international agreement prohibiting nuclear explosions.

1.5 The Verification Regime of the Comprehensive Nuclear-Test-Ban Treaty

When the CTBT ultimately enters into force, the responsibility of verifying that member States are in compliance with the terms of the treaty will fall primarily to the verification regime of the Comprehensive Nuclear-Test-Ban Treaty Organization (CTBTO) [33]. The verification regime of the CTBTO has been under development since 1997 and consists of six elements: (1) an IMS element, (2) an International Data Center (IDC) element, (3) a global communications infrastructure element, (4) a consultation and clarification element, (5) an OSI element, and (6) a confidence building measures element [33].

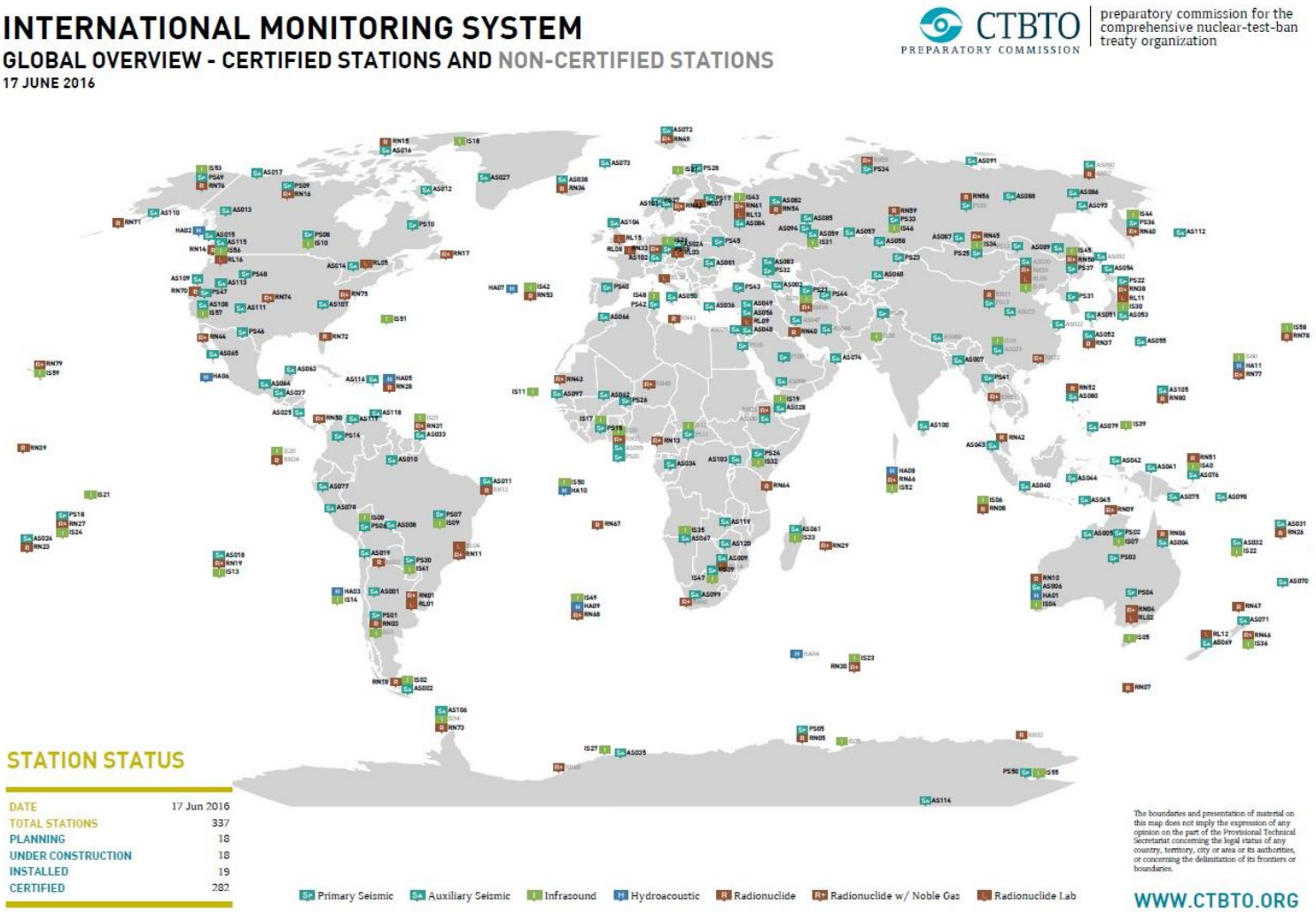

Figure 1.6: Locations of the 321 CTBT IMS monitoring stations and laboratories [34].

The first element of the verification regime of the CTBT, the IMS element, consists of 321 monitoring stations and 16 laboratories [33]. As illustrated in Figure 1.6, these monitoring stations and laboratories are located in 89 different countries [33]. Of the 321 CTBT IMS monitoring stations, 50 are primary seismic monitoring stations, 120 are auxiliary seismic monitoring stations, 11 are hydroacoustic monitoring stations, 60 are infrasound monitoring stations, and 80 are radionuclide monitoring stations [30]. The seismic monitoring stations and hydroacoustic monitoring stations are designed to detect waveforms indicative of nuclear explosions underground and underwater, respectively [33, 35, 36]. The infrasound monitoring stations are designed to detect waveforms indicative of nuclear explosions in the Earth's atmosphere [33, 37]. The radionuclide monitoring stations are designed to detect radioactive particulates and noble gases indicative of nuclear explosions detonated in any environment [33, 38]. The 16 CTBT laboratories are used to support follow-up analyses of radionuclide samples acquired at the CTBT radionuclide monitoring stations [33].

The IDC element of the verification regime of the CTBT is located at the CTBTO headquarters in Vienna, Austria and serves to support the IMS element of the verification regime by processing and analyzing data collected at IMS stations [33]. The IDC compiles collected and analyzed data into data bulletins that are distributed to CTBT Member States [33]. Data is transmitted from the CTBT IMS stations to the CTBT IDC via the third element of the verification regime, the global communications infrastructure element [33]. The global communications infrastructure element also serves to transmit raw CTBT IMS data and CTBT data bulletins to Member States [33].

In the event a CTBT Member State feels that data collected by the CTBT IMS suggests that a nuclear explosion may have been detonated by another CTBT Member State, the concerned State may request that additional information regarding the data be provided by the State in question. The concerned State may request the additional information directly, through the CTBT Executive Council or through the CTBTO Director-General [33]. Regardless of the path chosen by the concerned State, the objective of the consultation and clarification element of the CTBT is to serve as an avenue via which concerns may be addressed diplomatically. States under question have 48 hours to respond to requests for additional information [33].

Concerned States may also request that an OSI be conducted at the site of a suspicious event in order to gather additional data and facts needed to ascertain whether or not a nuclear explosion was detonated at the site [33]. OSI requests must be presented to the CTBT Executive Council and may only proceed if supported by at least 30 of the 51 Executive Council Member States [30]. A CTBT Member State may not refuse an OSI request authorized by the CTBT Executive Council [39].

Many of the most telling indications that a nuclear explosion was in fact detonated at a given site—seismic aftershocks and short-lived fission and activation products, for example—are only detectable for a short period after a nuclear explosion is detonated [39]. Therefore, the OSI element of the CTBT is developed to support rapid inspection team deployment after an OSI request is approved [39]. More specifically, inspection personnel and equipment must be at the border of the State to be inspected within six days after an OSI is requested [39]. The inspection team must then submit their

first report within 25 days [39]. By default, an OSI may last up to 60 days, but in exceptional cases an OSI may last as long as 130 days [39]. The CTBT also states that the area to be covered by an OSI shall not exceed 1,000 km^2 [39].

A number of inspection techniques may be utilized during an OSI. During the first 25 days of an OSI inspection personnel can conduct overflights, make visual observations of the site, make seismological aftershock measurements, and conduct air-borne and ground-based gamma radiation surveys [40]. These techniques help inspection personnel to acquaint themselves with the site and identify areas that might be of particular interest at the site. Additional inspection techniques may be utilized during the later phases of an OSI, as required [40]. The CTBT OSI Operation Manual is still under development, so detailed OSI procedures are not yet available. That being said, examples of radionuclide monitoring techniques that might be utilized during an OSI are discussed in Section 1.6.

The CTBT states that Member States must notify the CTBTO Technical Secretariat of plans to detonate chemical explosions of 0.3 kt or more [33]. These notifications, which constitute the primary component of the confidence building measures element of the verification regime, serve as advance warning of events that could otherwise be misconstrued as nuclear explosions [33]. The notifications also allow seismic, hydroacoustic, and infrasound monitoring station operators to use the explosions to test and fine-tune their equipment [33].

1.6 Detecting Radionuclides Indicative of Nuclear Explosions

The waveform monitoring technologies employed by the verification regime of the CTBT—the seismic, hydroacoustic, and infrasound monitoring technologies—are important to the verification regime of the CTBT in that they are capable of detecting very subtle indications of nuclear explosions in all Earth environments. They are also capable of very accurately determining the location at which a nuclear explosion was detonated [33, 35, 36, 37]. However, the radionuclide monitoring technology employed by the verification regime of the CTBT is particularly important in that it is the only monitoring technology capable of confirming the nuclear nature of a suspected nuclear explosion [33, 38]. The radionuclide monitoring technology is able to definitively determine that a nuclear explosion was detonated by detecting fission and activation products, which are literally residual elements or pieces of a detonated nuclear device. These fission and activation products thus provide the "smoking gun" that a suspected nuclear explosion was in fact a nuclear explosion.

In this section, the processes by which fission and activation products are generated during a nuclear explosion are described. The processes by which some of the fission and activation products might be able to migrate away from the site of a nuclear explosion to other locations where they may be detected remotely are also briefly discussed, as are the basic processes that may be used to collect, concentrate, and detect the presence of fission and activation products, both remotely and at the site of a nuclear explosion. The principal objective in discussing these subjects is to highlight the fact that the radionuclide monitoring technologies employed by the verification regime of the

CTBT must be capable of detecting very small concentrations of fission and activation products in order to have a chance at detecting small nuclear explosions.

When a nuclear explosion is detonated a tremendous amount of energy is released as the explosive's nuclear fuel—either ^{235}U or ^{239}Pu—fissions, or splits apart at the atomic level. A simplified illustration of the fission process is presented in Figure 1.7. The fission process begins when an incident neutron is absorbed by a fissionable target nucleus. In Figure 1.7 the fissionable target nucleus is a ^{235}U nucleus. After the ^{235}U nucleus absorbs the incident neutron it becomes unstable due to the addition of the surplus neutron and, according to the liquid drop fission model, it begins to oscillate [41]. As the unstable ^{235}U nucleus oscillates it elongates and contracts rapidly. As it elongates, the relatively long range repulsive forces between the protons in the ^{235}U nucleus overcome the very short range nuclear forces holding the ^{235}U nucleus together and the nucleus effectively splits into smaller nuclei called fission fragments or fission products [41]. Several stray neutrons are also released as a result of the fission process [41]. In Figure 1.7 the fission process is shown to release three stray neutrons. The neutrons released by one fission event can go on to cause other fissions and thus the fission process is referred to as a "chain reaction." The fission products released via the fission process have more binding energy than the original ^{235}U atom and thus the fission process results in a net release of energy equal to the difference in the binding energies. The energy released by a single ^{235}U fission is roughly 207 MeV (3.3×10^{-11} J) [41].

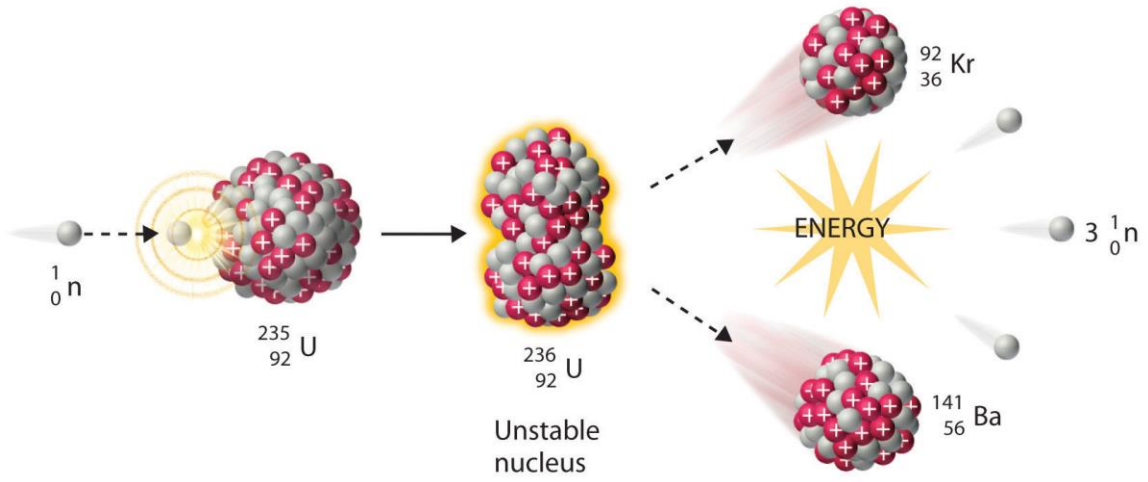

Figure 1.7: Illustration of the fission process [42].

In Figure 1.7 the fission products resulting from the ^{235}U fission are shown to be ^{92}Kr and ^{141}Ba, but many different combinations of fission products may be produced. The fission products resulting from the fission process are of great interest here for several reasons [43]. First, it is important to note that not all fission products are produced in equal amounts. In fact, as illustrated in Figure 1.8, fission product distributions have two humps so that fission products having mass numbers near 95 and 140 are significantly more likely to be produced than other fission products. This means that for a nuclear explosion of a given yield certain fission products will be produced in relatively large quantities while others will only be produced in very small quantities. From a CTBT verification perspective, fission products with larger fission yields are easier to detect.

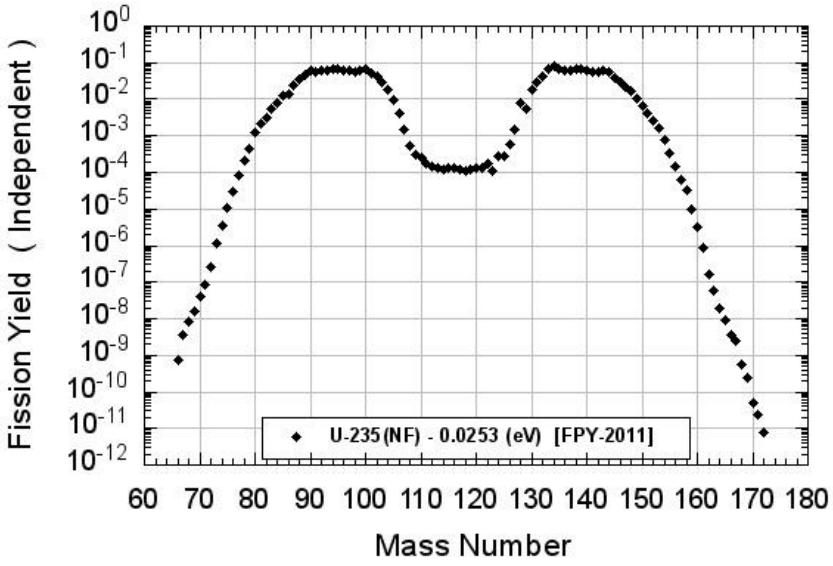

Figure 1.8: ^{235}U fission product yield distribution [44].

It is also important to note that different fission products have different nuclear and chemical characteristics and thus they behave differently after they are produced during an explosion. The nuclear characteristics that must be considered from a CTBT verification perspective are the half-lives and decay modes [43]. The half-life of a fission product establishes the time at which there is a 50 % chance the fission product will have decayed away [45]. As an example, if the half-life of a hypothetical fission product were 10 min then there would be a 50 % chance, or a one in two chance, that the fission product would decay away after existing for 10 min. In order for a fission product to be valuable from a CTBT verification perspective the fission product must have a half-life that is sufficiently long to allow it to survive until it may be detected, either remotely or at the nuclear explosion site [43].

The fission product decay modes establish the process or processes by which the fission products decay when they do decay. The fission product decay modes that have been of most interest from a CTBT verification perspective to date have been beta-particle and gamma-ray emission [43]. That being said, conversion electron and X-ray emission processes may also be of interest moving forward.

It is also important to note that different fission products behave differently, chemically speaking. Some fission products are strongly inclined to chemically bind themselves to other elements. These fission products often end up bound to dust and other particles and are referred to as "particulate" fission products [38]. Particulate fission products typically only escape from atmospheric and very shallow subsurface nuclear explosion sites. In these cases it is relatively easy for them to be swept up and carried away from the sites by prevailing winds [38]. Other fission products, most notably the noble gases, are less likely to chemically bind to other elements and are therefore much more likely to escape from subsurface nuclear explosion sites than particulate fission products are [38].

Activation products are produced during a nuclear explosion when some of the stray neutrons released by the fission process are absorbed by the nuclei of nonfuel materials, either in the nuclear explosive device itself or in the environment immediately surrounding the device [43, 46]. When these nuclei absorb the stray neutrons they become "activated," which is to say that they become unstable and radioactive.

Just as different fission products are produced to differing extents during a nuclear explosion, different activation products are also produced to differing extents during a nuclear explosion. The extent to which a particular activation product is produced is determined primarily by two factors. The first is the concentration of the activation target nuclei in the vicinity of the nuclear explosion, and the second is the magnitude of the cross-section associated with the activation reaction (the cross-section quantifies the probability that a neutron will cause the activation reaction to proceed in a given activation target nucleus). High activation target nucleus concentrations and large activation reaction cross-sections lead to large activation product concentrations at nuclear explosion sites. Conversely, low activation target nucleus concentrations and small activation reaction cross-sections lead to smaller activation product concentrations. From a CTBT-verification perspective, activation products produced in larger concentrations are easier to detect.

Fission and activation products specifically identified as relevant to the CTBT are listed in Tables 3.1 and 3.2, respectively, in Section 3.1. A total of 96 fission and activation products are listed in Tables 3.1 and 3.2; 92 of them are radioactive particulates and 4 of them are radioactive noble gases [45, 46]. All of the CTBT-relevant fission and activation products have half-lives ranging from 6 hours to 1,000 years [46]. Most of them decay via some combination of gamma-ray, beta-particle, conversion electron, and/or X-ray emission [46]. They also have chemical properties that make them such that they may be collected, concentrated, and then detected.

At this point, having described the processes by which fission and activation products are produced during nuclear explosions and having highlighted some of the criteria used to identify fission and activation products relevant to the CTBT, it is important to also consider the processes by which some of the fission and activation products might be able to escape from the site of a nuclear explosion and migrate to locations where they may be detected remotely by CTBT radionuclide monitoring stations.

Essentially all of the particulate and noble gas fission and activation products produced during atmospheric and shallow subsurface nuclear explosions are assumed to escape from their respective nuclear explosion sites [38]. This is because they are generated either directly in the atmosphere or on the Earth–atmosphere interface where they may be readily swept up and carried away by prevailing winds at the nuclear explosion site [38].

Conversely, the particulate fission and activation products generated during an underground nuclear explosion are assumed to be completely retained in the vicinity of the cavity created by the nuclear explosion (see Figure 1.9) and never escape the nuclear explosion site [38]. The fission and activation products generated during an underground nuclear explosion are retained in the vicinity of the explosion cavity simply because there is no driving force to push them towards the surface to be swept up and carried away.

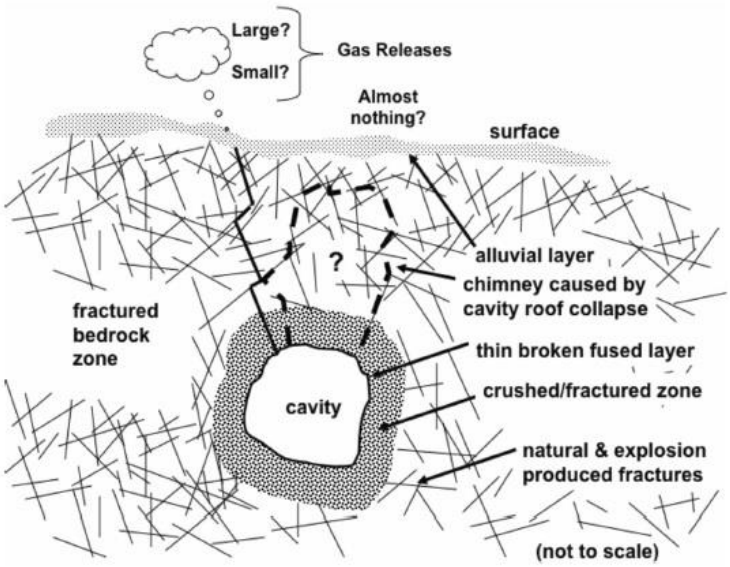

Figure 1.9: The situation following an underground nuclear explosion [47].

The extent to which radioactive noble gas fission and activation products escape from the site of an underground nuclear explosion is somewhat more complicated. The situation is as illustrated above in Figure 1.9 [47]. During an underground nuclear explosion a cavity is formed. The majority of the radioactive noble gas fission and activation products produced by the nuclear explosion are initially retained inside the cavity (that said some are immediately ejected into the surrounding geological media) [47]. Initially the cavity is very hot and the pressure inside the cavity is high, but as the cavity cools the pressure inside the cavity decreases [47]. As the cavity pressure decreases and the weight of the geological media above the cavity weighs down on the cavity the roof of the cavity may give in and collapse [47]. The geological media above the cavity, now unsupported, then tends to fracture and fall downward into the

cavity [47]. The opening in the top of the cavity and the fractured geological media extending from the cavity up at least a portion of the way to the surface provide a pathway for radioactive noble gases originally retained in the nuclear explosion cavity to migrate towards the surface [47].

A number of mechanisms may drive the radioactive noble gases from the cavity and towards the surface [47]. Initially the primary driving force is the high pressure differential between the cavity and the surface [47]. However, as time passes and the pressure differential between the cavity and the surface equalizes this driving force becomes less significant. Two other mechanisms then take over: the first is multiphase convection and the second is barometric pumping [47]. While the fundamentals associated with each of these mechanisms are different, the effect in all cases is to drive radioactive noble gases towards the surface where they may be swept up and carried away by trade winds at the nuclear explosion site [38, 47].

Studies conducted by Dubasov *et al.* [48] found that 43 % of the 340 nuclear explosion tests detonated at the Semipalatinsk Test Site vented radioactive noble gases to the atmosphere [47, 48]. Similarly, about 58 % of the nuclear explosion tests detonated at the Novaya Zemlya Test Site vented radioactive noble gases to the atmosphere [47, 48].

Radioactive fission products and noble gases that are swept up and carried away from a nuclear explosion site may be transported hundreds or thousands of miles and may be collected by CTBT radioactive noble gas monitoring systems as described in Sections 1.7.1 and 1.7.2 [38]. In this way, radioactive particulates and noble gases produced during nuclear explosions may be detected remotely. In the future, when the

CTBT enters into force, OSI procedures will also be in place to allow inspection teams to travel to suspected nuclear explosion sites to make local radioactive particulate and noble gas activity concentration measurements [30, 33, 39].

While the CTBT OSI Operation Manual is still under development and detailed OSI procedures are not yet available, several methods for collecting radioactive noble gases during on-site inspections have been proposed. One method, illustrated below in Figure 1.10 [47], would involve drilling a hole several meters down into the subsurface and using a pump to pull radioactive noble gases trapped just below the surface up out of the ground and into a collection tank [47]. The concentrations of the radioactive noble gases collected in the tanks would then be evaluated using systems comparable to the CTBT radioactive noble gas monitoring systems described in Sections 1.7.1 and 1.7.2.

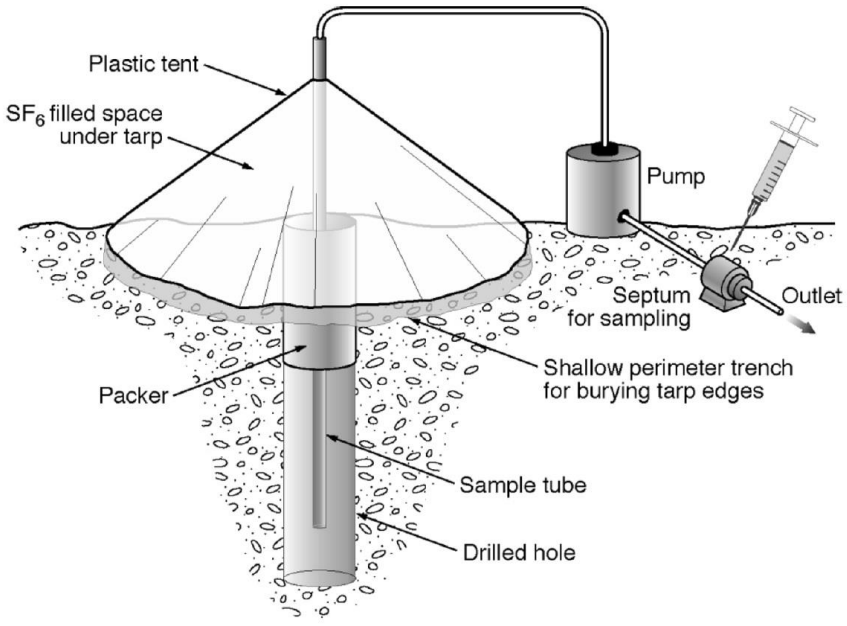

Figure 1.10: Soil gas sampling during an On-Site Inspection (OSI) [47].

1.7 The Current State of the Art

In the previous section the processes by which fission products are generated during a nuclear explosion, the processes by which some of the fission products might be able to migrate away from the site of the nuclear explosion, and the basic processes that may be used to detect the presence of the fission products, either remotely or at the site of a nuclear explosion, are described briefly. In this section more attention will be given to the state-of-the-art radionuclide monitoring systems currently employed by the verification regime of the CTBT. An example of a particulate monitoring system, the so-called Radionuclide Aerosol Sampler/ Analyzer [49], is described first in Section 1.7.1. Several radionuclide monitoring systems are then described in Section 1.7.2.

Figure 1.11: The particulate radionuclide monitoring system at CTBT IMS radionuclide station RN13 in Douala, Cameroon [38].

1.7.1 Particulate Radionuclide Monitoring Systems

As mentioned previously in Section 1.5, each of the 80 CTBT IMS radionuclide monitoring stations includes a particulate radionuclide monitoring system such as the system shown in Figure 1.11 [38]. These particulate radionuclide monitoring systems are designed to detect the presence of particulate radionuclides indicative of nuclear explosions. One of the CTBT IMS particulate radionuclide monitoring systems is known as the Radionuclide Aerosol Sampler/Analyzer (RASA) system [49]. The RASA system, shown in Figure 1.12, was developed at Pacific Northwest National Laboratory in Richland, WA, USA for the US Department of Energy specifically to support US particulate radionuclide monitoring obligations under the CTBT [49]. Brief descriptions of the RASA system design, its operating principles, and performance characteristics are presented below. While the designs associated with other CTBT IMS particulate radionuclide monitoring systems may vary somewhat from the RASA system design, the operating principles and performance characteristics of the other systems are comparable to the RASA system operating principles and operating characteristics described here.

The development of the RASA system presented several unique challenges that would not typically be encountered during the development of a more traditional laboratory-based particulate radionuclide monitoring system having comparable performance requirements. For example, the RASA system had to be designed to consume a minimal amount of power and to occupy a relatively small physical footprint while still satisfying sensitivity requirements set forth by the Preparatory Commission for the CTBT [49]. Additionally, because the CTBT IMS radionuclide monitoring stations

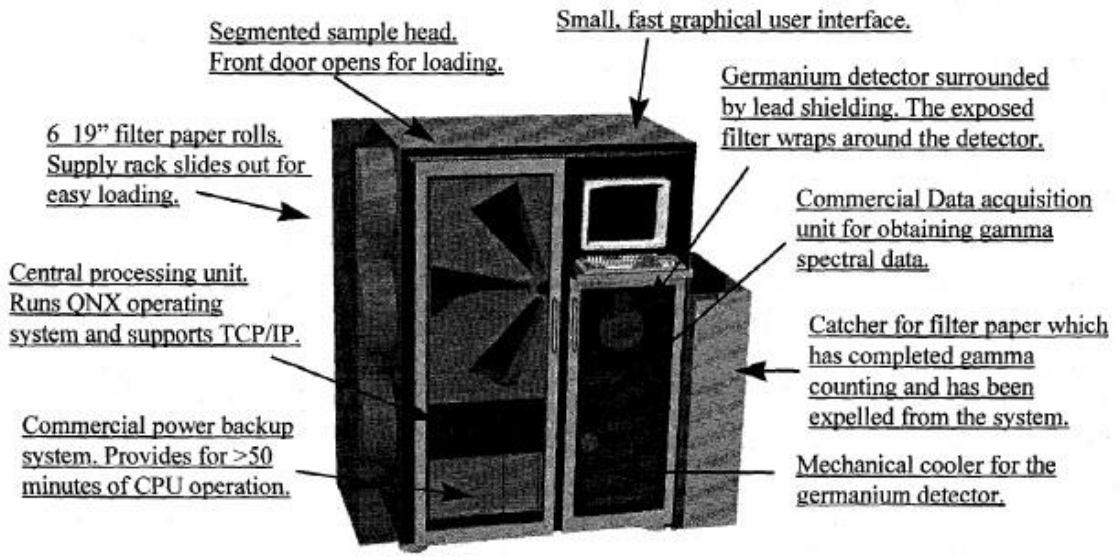

Figure 1.12: The Radionuclide Aerosol Sampler/Analyzer (RASA) system developed at Pacific Northwest National Laboratory [49].

are often located in remote areas, the RASA system had to be designed to operate in a fully automatic mode and to require only a minimal amount of maintenance [49].

At the most basic level, the RASA system serves to blow atmospheric air through an air filter capable of collecting particulates entrained in the air and then transfers the filter to a radiation spectrometer (or detector) where it may be "counted" to look for traces of particulate radionuclides indicative of nuclear explosions. In order to minimize power consumption, the RASA system employs a 1 hp industrial fan [49]. This fan blows about 20,000 standard cubic meters of atmospheric air through a segmented particulate filter every 24 hours [49]. The segmented particulate filter consists of six 10 cm by 40 cm high-efficiency filters having a cumulative area of about 0.25 m^2 [49]. The segmented particulate filter head and the high-efficiency filters (SBMF-40VF filters manufactured

by 3M) were designed and selected in order to minimize the pressure drop across the system and thus minimize the power consumed by the system's industrial fan [49, 50].

At the end of each 24 hour sampling period a motor pulls the six filters through a pair of rollers and seals them, one on top of the other, between two polyester strips as shown in Figure 1.13 [49]. The result of this process is a filter packet that measures roughly 10 cm wide by 40 cm long by 1 cm thick [49]. The filter packet is then allowed to decay for 24 hours before being wrapped around a High Purity Ge (HPGe) radiation spectrometer and counted [49]. The 24 hour decay period allows time for some of the shorter lived particulate daughters of naturally-occurring ^{220}Rn to decay and helps to reduce the background associated with the high-resolution gamma-ray spectrum acquired by the HPGe radiation spectrometer [49].

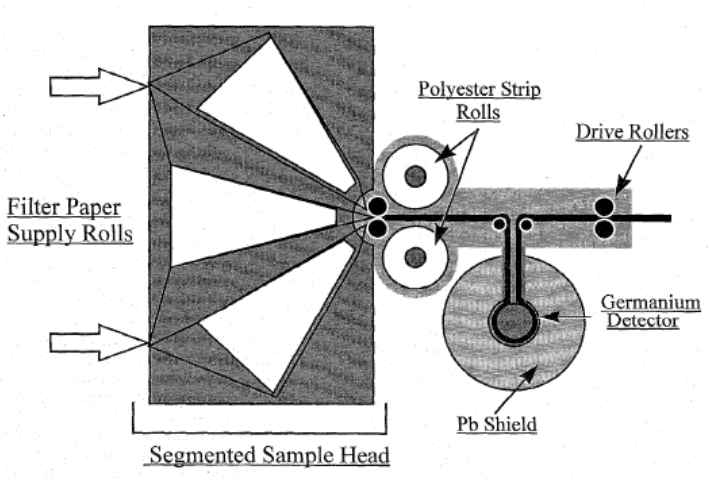

Figure 1.13: Filter paper path through the Radionuclide Aerosol Sampler/Analyzer (RASA) system [49].

The HPGe radiation spectrometer associated with the RASA system is mechanically cooled and consumes only about 1 kW of power [49]. An HPGe radiation spectrometer was incorporated into the RASA system as opposed to, say a NaI(Tl) radiation spectrometer, because it produces high resolution gamma-ray spectra with fewer spectral interferences [49]. The RASA system ^{140}Ba Minimum Detectable Concentration (MDC) is reportedly on the order of 10–30 Bq-m^{-3} [49, 51]. Additionally, 125 daily samples acquired and analyzed by an experimental RASA system in 1997 produced daily ^{99}Mo, ^{140}Ba, ^{140}La, and ^{141}Ce MDCs as illustrated below in Figure 1.14.

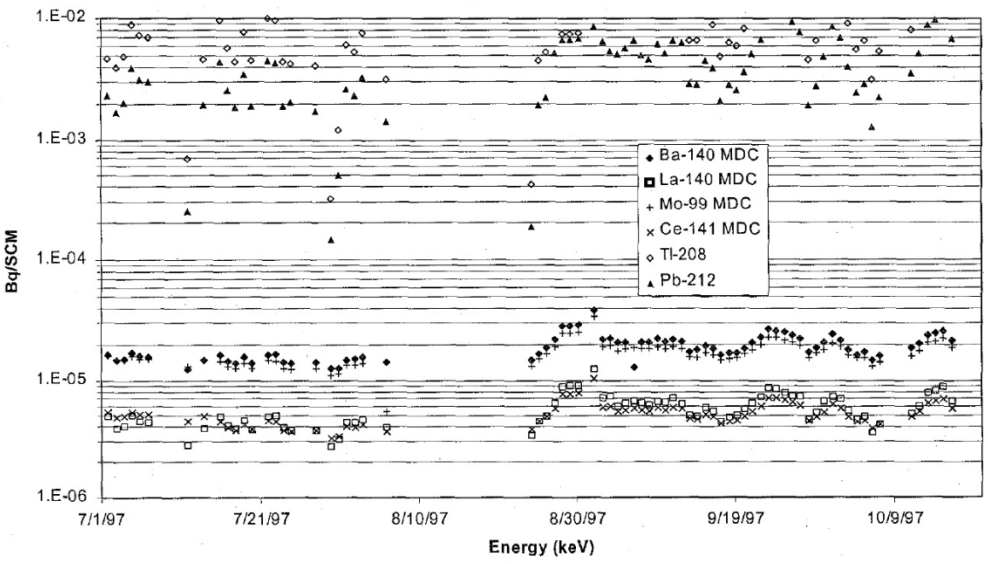

Figure 1.14: 125 daily RASA system ^{99}Mo, ^{140}Ba, ^{140}La, and ^{141}Ce Minimum Detectable Concentrations (MDCs) [51].

1.7.2 Radioactive Noble Gas Monitoring Systems

While all 80 of the CTBT IMS radionuclide monitoring stations will be equipped with radioactive particulate monitoring systems from the outset, only 40 of the stations will initially be equipped with radioactive noble gas monitoring systems [38]. The locations of CTBT IMS radionuclide monitoring stations equipped with both radioactive particulate and noble gas monitoring systems are highlighted on the CTBT IMS map in Figure 1.6 by the symbol "R+." It should be noted that the CTBT IMS radionuclide monitoring stations not initially equipped with radioactive noble gas monitoring systems may be fitted with radioactive noble gas monitoring systems at a later date.

While the deployment of radioactive noble gas monitoring systems will be limited initially, the importance of the radioactive noble gas monitoring technology in supporting the mission of the verification regime of the CTBT cannot be overstated. As mentioned previously, of the four monitoring technologies employed by the verification regime of the CTBT, the radionuclide monitoring technology is the only one capable of providing "the smoking gun," or the conclusive evidence that a suspected nuclear explosion was in fact of a nuclear nature [33, 38]. In the event of an atmospheric nuclear explosion, a large number of particulate radionuclides would be released directly to the atmosphere, would be transported away from the site of the explosion by prevailing winds, and would be readily detected by particulate monitoring systems at CTBT IMS radionuclide monitoring stations downwind of the site.

In the case of an underground nuclear explosion, however, the majority of the particulate radionuclides would likely remain trapped underground, making them unavailable for detection by CTBT IMS particulate radionuclide monitoring systems. Radioactive noble gases produced by the explosion would have a much better chance of migrating up through the subsurface to the atmosphere where they may be carried away from the site by prevailing winds [38]. Thus, the radioactive noble gas monitoring systems deployed at CTBT IMS radionuclide monitoring stations might provide the best chance of detecting a nuclear explosion detonated underground as part of a clandestine nuclear weapons program [38].

Four different radioactive noble gas monitoring systems have been deployed at CTBT IMS radionuclide monitoring stations: (1) the Automatic Radioanalyzer for Isotopic Xenon (ARIX) system (see Figure 1.15.(a)) developed at the Khlopin Radium Institute in St. Petersburg, Russia [52, 53], (2) the Automated Radioxenon Sampler/Analyzer (ARSA) system (see Figure 1.15.(b)) developed at Pacific Northwest National Laboratory in Richland, WA, USA [54, 55, 56], (3) the Swedish Automatic Unit for Noble gas Acquisition (SAUNA) system developed by the Swedish Defense Research Agency in Stockholm, Sweden [57], and (4) the Système de Prélèvement Automatique en Ligne avec l'Analyse du Xénon (SPALAX) system developed by the Commissariat à l'Energie Atomique in Bruyères-le-Châtel, France [58].

The radioactive noble gases that are most important to the verification regime of the CTBT are ^{131m}Xe, ^{133m}Xe, ^{133}Xe, and ^{135}Xe, and thus each of the radioactive noble gas monitoring systems mentioned above essentially serve to evaluate radioxenon activity

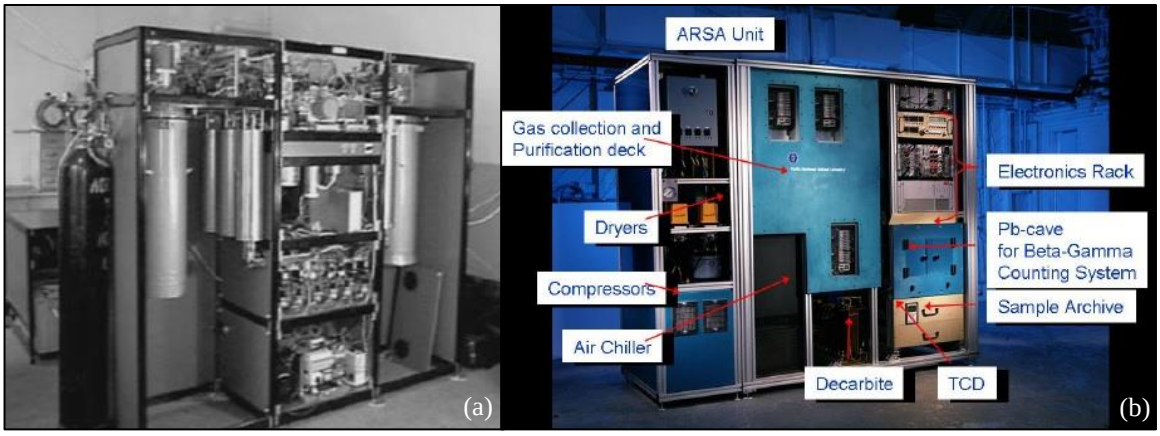

Figure 1.15: Photographs of (a) the Automatic Radioanalyzer for Isotopic Xenon (ARIX) system [52] and (b) the Automated Radioxenon Sampler/Analyzer (ARSA) system [56].

concentrations in atmospheric air. The process of evaluating radioxenon activity concentrations in atmospheric air involves four basic steps. These steps, and the means the ARIX, ARSA, SAUNA, and SPALAX systems employ to accomplish the steps, are discussed below.

The first step of the radioxenon activity concentration evaluation process involves sampling atmospheric air, removing moisture and carbon-dioxide (CO_2) from the sampled air, and then extracting elemental xenon from the dry, nearly CO_2-free air [59]. Moisture and CO_2 must be removed from the atmospheric air to the greatest extent possible because they significantly reduce the efficiency of the xenon extraction process if not removed [59].

In the ARIX system, a compressor is used to blow atmospheric air through a precooler, through two zeolite cartridges, and then through a cooled charcoal bed [52]. The precooler serves to remove moisture from the atmospheric air, the zeolite cartridges

remove CO_2 and residual moisture not removed by the precooler from the air, and the cooled activated charcoal bed adsorbs xenon [52]. Cooling the activated charcoal bed serves to improve the efficiency of the xenon adsorption process in the activated charcoal bed [52].

In the ARSA system, a compressor forces atmospheric air through an industrial air drying unit, a cryogenic air chiller, and then two activated charcoal traps, one after the other [54, 55]. The industrial air drying unit removes moisture and CO_2 from the atmospheric air and the cryogenic air chiller serves to cool the air and improve the efficiency of the xenon adsorption process in the activated charcoal filters [54, 55]. The first of the two activated charcoal filters serves as a radon pre-trap and the second is the main xenon trap [54, 55].

The SAUNA system uses a compressor to force atmospheric air through a heat exchanger, a molecular sieve, and then an activated charcoal bed [57]. The heat exchanger cools the air to remove moisture before the molecular sieve removes CO_2 and residual moisture from the air [57]. The activated charcoal beds, which are at ambient temperature in the SAUNA system, adsorb xenon from the dry, nearly CO_2-free air [57].

In the SPALAX system, an air compressor is used to blow atmospheric air through a polymeric permeation membrane composed of hundreds of hollow polyimide fibers [58]. The walls of the hollow polyimide fibers are more easily permeated by oxygen (O_2), CO_2, and moisture than by nitrogen (N_2) and xenon so that by the time the air reaches the end of the permeation membrane it is depleted in O_2, CO_2, and moisture and enriched in N_2 and xenon [58].

The second step of the radioxenon activity concentration evaluation process involves purifying the xenon samples collected in the first step [59]. In addition to removing residual moisture and CO_2 still present after the first step, this step primarily serves to remove radon from the xenon sample. Radon must be removed from the xenon samples because its activity concentration in atmospheric air can be several orders of magnitude greater than the activities of the radioxenons of interest [59]. In the ARIX system radon is removed by adsorbing and desorbing the xenon sample on a series of activated charcoal traps [52]. Helium is used as a carrier gas, the cycle time is 12 hours, and the ARIX system produces two 0.8 cm^3 xenon samples each day [52, 59]. In the ARSA system the xenon sample is run through a second radon trap (a radon trap was used in the first step as well) and an ascarite trap [54, 55]. A nitrogen carrier gas is used and the cycle time is 8 hours, meaning that the ARSA system produces three 1.5–2.0 cm^3 xenon samples each day [54, 55, 59]. The SAUNA system uses molecular sieves and a helium carrier gas to remove CO_2 and radon [57]. The SAUNA system is on a 12 hour cycle and produces two 0.5 cm^3 xenon samples each day [57, 59]. In the SPALAX system a series of activated charcoal columns and a nitrogen carrier gas are used to produce the final xenon sample [58]. The SPALAX system cycle time is 24 hours and the SPALAX system produces a single 7.5 cm^3 xenon sample each day [58, 59].

The third step of the radioxenon activity concentration evaluation process involves evaluating the volume of the collected xenon gas sample [59]. In the ARSA and SPALAX systems the volume of the collected sample is deduced from static thermal

conductivity measurements [54, 55, 58, 59]. The ARIX and SAUNA systems use gas chromatography to evaluate the xenon sample volumes [52, 57, 59].

The fourth and final step of the radioxenon activity concentration evaluation process involves quantifying the radioxenon activity concentrations associated with the xenon sample collected during the first three steps. In the ARIX, ARSA, and SAUNA systems the radioxenon activities are evaluated using beta-gamma coincidence spectrometers [52, 53, 54, 57, 59]. Plastic scintillators are used to detect the beta particles and NaI(Tl) detectors are used to detect the gamma-rays [52, 53, 54, 57, 59]. The geometric configurations of the NaI(Tl) gamma-ray detectors relative to the plastic scintillator beta particle detectors utilized by the beta-gamma coincidence spectrometers associated with the ARIX, ARSA, and SAUNA systems are shown in Figures 1.16.(a), 1.16.(b), and 1.16.(c), respectively. Note that in all three cases the NaI(Tl) gamma-ray detectors surround the plastic scintillators for maximum solid angle coverage [59].

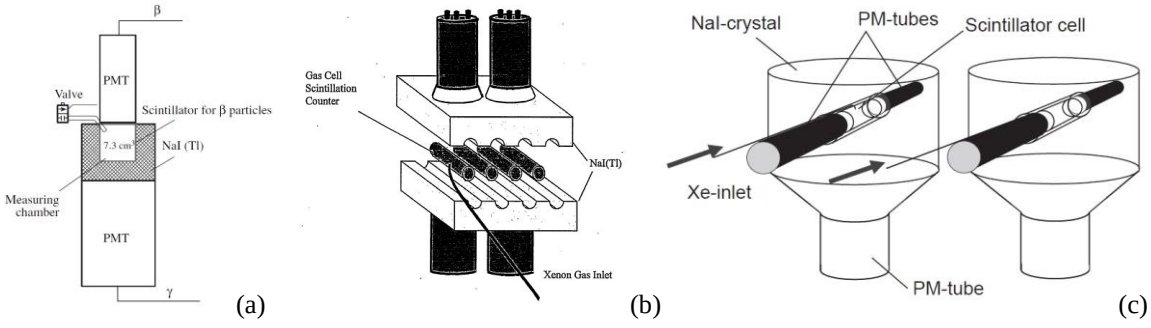

Figure 1.16: The geometric configurations of the NaI(Tl) gamma-ray detectors relative to the plastic scintillator beta particle detectors utilized by the beta-gamma coincidence spectrometers associated with (a) the ARIX system [53], (b) the ARSA system [54], and (c) the SAUNA system [58].

The SPALAX system is unique in that it uses a high-resolution gamma-ray spectrometer to evaluate the activity of the radioxenon collected in steps one through three [58, 59].

The primary metric used quantify the performance of the ARIX, ARSA, SAUNA, and SPALAX systems is the Minimum Detectable Concentration (MDC). A thorough description of the MDC is presented in Section 2.1.3.4. For now, however, suffice it to say that the MDC provides an *a priori* estimate as to the minimum activity concentration that a spectrometer should be expected to be capable of detecting to a given confidence or certainty. The ^{131m}Xe, ^{133m}Xe, ^{133}Xe, and ^{135}Xe MDCs associated with the ARIX, ARSA, SAUNA, and SPALAX systems are summarized below in Table 1.2.

Table 1.2: Minimum detectable concentrations associated with the radioactive noble gas monitoring systems currently employed by the verification regime of the CTBT.

Monitoring System	Radioxenon Minimum Detectable Concentrations (MDCs) [mBq-m^{-3}]			
	^{131m}Xe	^{133m}Xe	^{133}Xe	^{135}Xe
ARIX [1]	0.52	0.55	0.40	0.64
ARSA [2]	< 0.1	0.15	< 0.1	0.3
SAUNA [3]	0.71	0.57	0.93	0.90
SPALAX [4]	4.05	1.53	0.15	0.65

1. The ARIX system MDCs reported here were calculated from the minimum detectable activities reported by Popov *et al.* [53] and the 12 h cycle time reported by Dubasov *et al.* [52].
2. The ARSA system MDCs reported here were taken from Bowyer *et al.* [54]. Associated cycle time is 8 h.
3. The SAUNA system MDCs reported here were taken from Ringbom *et al.* [57]. Associated cycle time is 12 h.
4. The SPALAX system MDCs reported here were taken from Fontaine *et al.* [58]. Associated cycle time is 24 h.

1.8 Distinguishing Radionuclide Detections Indicative of Nuclear Explosions from Other Radionuclide Releases

If the radioactive particulates and noble gases of interest from a nuclear explosion monitoring perspective were only released by nuclear explosions then detecting indications of nuclear explosions would be relatively straightforward and easy. Unfortunately, this is not the case and radioactive particulates and noble gases having CTBT-relevance are produced via a number of other anthropogenic and natural processes. Anthropogenic sources of CTBT-relevant radionuclides include commercial nuclear generating stations, nuclear research reactors, and radiopharmaceutical facilities. Examples of natural processes that result in the production of CTBT-relevant radionuclides are the spontaneous fission of naturally occurring thorium and uranium and cosmic-ray induced fission and activation reactions. Radioactive particulates and noble gases resulting from each of these anthropogenic and natural processes have the potential to be misconstrued as indications of nuclear explosions. Therefore, a number of radioactive particulate and noble gas screening methods have been devised to distinguish radionuclide detections indicative of nuclear explosions from radionuclide detections characteristic of other types of releases.

One radioactive particulate screening method involves evaluating radioactive ^{134}Cs and ^{136}Cs activities [50]. Because ^{134}Cs and ^{136}Cs are both shielded on both sides of their decay chains (see Figure 1.17 [60]) neither ^{134}Cs nor ^{136}Cs may be produced as a decay product. Because ^{136}Cs has a relatively large fission yield it is present in both nuclear explosion debris and the debris released during nuclear generating station

Figure 1.17: A segment taken from the chart of the nuclides highlighting the fact that ^{134}Cs and ^{136}Cs are both shielded on both sides of their decay chains [60].

accidents. ^{134}Cs does not have a large fission yield and therefore is not present in nuclear weapons debris [50]. It does however buildup over time in nuclear generating stations as a result of radiative capture reactions with ^{133}Cs and therefore ^{134}Cs is present in debris released during nuclear generating station accidents [50]. Detecting the presence of ^{136}Cs without ^{134}Cs is thus a strong indication that the ^{136}Cs was produced by a nuclear explosion [50].

Another particulate screening method involves evaluating various ^{141}Ce, ^{143}Ce, ^{144}Ce, ^{95}Zr, and ^{97}Zr activity concentration ratios [50]. Nuclear explosions result in large ^{97}Zr to ^{95}Zr ratios, large ^{143}Ce to ^{144}Ce activity ratios, small ^{141}Ce to ^{143}Ce activity ratios, and small ^{144}Ce to ^{141}Ce activity ratios relative to nuclear reactor accidents [50]. This information may be used to attribute ^{141}Ce, ^{143}Ce, ^{144}Ce, ^{95}Zr, and ^{97}Zr activities accumulated on filter media at CTBT radionuclide monitoring stations to either nuclear explosions or nuclear reactor accidents [50].

Radionuclide activity concentration ratios may also be used to distinguish radioactive noble gas detections indicative of nuclear explosions from radioactive noble gas detections characteristic of commercial nuclear generating station, nuclear research reactor, and radiopharmaceutical facility releases. Kalinowski *et al.* [61] evaluated the suitability of numerous radioxenon activity concentration ratios and found that the best results are obtained when the ^{135}Xe to ^{133}Xe ratio is plotted against the ^{131m}Xe to ^{133m}Xe ratio as illustrated in Figure 1.18. Radioxenon activity concentration ratios appearing to the right and below the red screening line shown in Figure 1.18 are indicative of nuclear explosions while radioxenon activity concentration ratios appearing to the left and above the red screening line are characteristic of commercial nuclear generating station releases.

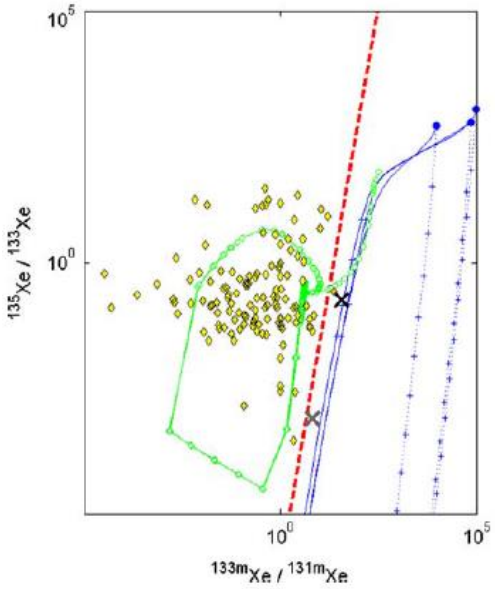

Figure 1.18: An illustration of a radioxenon activity concentration ratio screening method [61].

1.9 Areas for Further Development and Opportunities for Improvement

The introductory sections of this chapter present historical information regarding nuclear explosions detonated since 1945. The devastating human and environmental effects of the nuclear weapons detonated over Hiroshima and Nagaski and the effects of nuclear explosion tests detonated since are also discussed in order to specifically cite reasons why all forms of nuclear explosions, including so-called "peaceful nuclear explosions," must be absolutely prohibited moving forward. Subsequent sections of this chapter introduce the Comprehensive Nuclear Test-Ban-Treaty (CTBT), the verification regime of the CTBT [33], and the nuclear explosion monitoring technologies utilized by the verification regime of the CTBT [33, 35, 36, 37, 38].

The monitoring technologies of most interest herein are the radionuclide monitoring technologies [38]. These technologies have been shown to be very sensitive and capable of detecting radioactive particulates and noble gases indicative of nuclear explosions in very small concentrations, especially in laboratory settings [53, 54, 57, 58, 59, 62]. Operationally though, the radionuclide monitoring technologies employed by the verification regime of the CTBT have a mixed track record.

For example, since 2006, the Democratic People's Republic of Korea (North Korea) has claimed to have conducted four nuclear explosion tests [63]. In all four cases the waveform monitoring technologies employed by the verification regime of the CTBT have been used to confirm that large explosions were in fact detonated at the claimed North Korean nuclear test site [63]. The radioactive particulate and noble gas monitoring

stations deployed by the verification regime of the CTBT also successfully detected radioactive noble gases indicative of nuclear explosions following the 9 October 2006 and 12 February 2013 North Korean nuclear explosion tests [63, 64, 65]. However, no radioactive particulates or noble gases were ever detected following the claimed 25 May 2009 North Korean nuclear explosion test [63]. This failure provides strong evidence that the radionuclide monitoring technologies employed by the verification regime of the CTBT need to be developed further.

For one, next-generation radiation spectrometers must continue to be studied, developed, characterized, and optimized so that new radioactive particulate and noble gas monitoring systems with improved sensitivities may be deployed by the verification regime of the CTBT. With this in mind, one of the objectives of the research efforts documented herein was to characterize and optimize a prototype of a next-generation Si-PIN diode-based radiation spectrometer.

Si-PIN diode-based radiation spectrometers have a number of perceived advantages relative to the high-resolution gamma-ray and beta-gamma coincidence radiation spectrometers currently employed by the verification regime of the CTBT. These advantages are discussed in detail in Section 2.1.1. For now, suffice it to say that Si-PIN diode-based radiation spectrometers are known to have very low background levels and are expected to be capable of efficiently detecting conversion electrons emitted by radioactive xenon gases indicative of nuclear explosions. The objective of the Si-PIN diode spectrometer prototype characterization and optimization efforts documented herein was to evaluate the detection efficiencies associated with a Si-PIN diode

spectrometer prototype to determine if Si-PIN diode-based radiation spectrometers do in fact have the potential to outperform the high-resolution gamma-ray and beta-gamma coincidence radiation spectrometers currently employed by the verification regime of the CTBT.

In addition to more sensitive radioactive particulate and noble gas monitoring systems, more advanced radionuclide background activity concentration estimation methods are also needed. As mentioned in Section 1.8, radioactive particulates and noble gases of interest from a nuclear explosion monitoring perspective are not generated solely by nuclear explosions; they are generated through a number of anthropogenic and natural processes as well. The radioactive particulate and noble gas background activity concentrations resulting from natural processes must be well understood so that they may be distinguished from radioactive particulates and noble gases resulting from nuclear explosions.

The anthropogenic sources of these radioactive particulates and noble gases—nuclear generating stations, nuclear research reactors, radiopharmaceutical facilities, *etc.*—have been studied quite extensively and are relatively well understood. Natural processes responsible for generating radioactive particulates and noble gases have not been studied to the same extent to date, largely because the background activity concentrations resulting from natural processes are thought to be significantly lower than the background activity concentrations resulting from anthropogenic sources, generally speaking.

While background activity concentrations resulting from natural processes may in fact turn out to be quite low, it is still important that background activity concentrations resulting from natural processes be well understood so that they may not be used as a form of plausible deniability by a State accused of conducting a nuclear explosion test. In such a scenario it would not be enough to simply suggest that natural processes are not typically responsible for generating substantial radioactive particulate and noble gas background activity concentrations, but rather a scientific evaluation would have to be conducted to specifically discredit natural processes as a source of radioactive particles and noble gases. With this in mind, the Terrestrial Xenon and Argon Simulator (TeXAS) application described herein was developed to serve as a tool that may be used to rapidly develop background activity concentrations resulting from natural processes on a site-specific basis using the best available nuclear data.

Furthermore, in cases where radioactive particulate and noble gas background activity concentrations resulting from natural processes might be substantial, a strong understanding of the activity concentrations could make them useful as naturally-occurring operational check sources at remote CTBT radionuclide monitoring stations. While radioactive noble gas background activity concentrations resulting from natural processes are too low to be used as operational check sources in the high-resolution gamma-ray and beta-gamma coincidence spectrometers currently employed by the verification regime of the CTBT, the activity concentrations might be substantial enough to serve as operational check sources in next-generation radioactive noble gas monitoring systems that would presumably be more sensitive than the systems in use today.

For example, might it be possible to use ^{131m}Xe background activity concentrations resulting from cosmic-ray induced activation reactions as a means of verifying the proper operation of a CTBT radioactive noble gas monitoring station employing a Si-PIN diode spectrometer sensitive to the conversion electrons emitted by ^{131m}Xe? This dissertation documents a number of background activity concentration scoping studies conducted to answer these kinds of questions and also to generally develop our understanding of radioactive particulate and noble gas background activity concentrations resulting from natural processes.

1.10 Summary of Research Objectives

The objectives of the research efforts described throughout this chapter may be summarized as follows:

1. The first objective is to characterize a Si-PIN diode-based radiation spectrometer prototype developed by XIA LLC [66].
2. The second objective of the research efforts documented herein is to develop an optimized Si-PIN diode spectrometer design.
3. The third objective is to compare the performance characteristics of the XIA LLC Si-PIN diode-based radiation spectrometer prototype and the optimized Si-PIN diode spectrometer design to the performance characteristics associated with the ARIX [52], ARSA [54], SAUNA [57], and SPALAX [58] systems currently employed by the verification regime of the CTBT.

4. The fourth objective of the research efforts documented herein is to develop an application, referred to herein as the Terrestrial Xenon and Argon Simulator (TeXAS) application, capable of estimating background activity concentrations resulting from natural processes for every radionuclide identified as relevant to the CTBT on a site-specific basis.

5. The fifth and final objective of the research efforts documented herein is to demonstrate the capabilities of the TeXAS application by conducting a series of background activity concentration studies specific to several layers of the Earth's atmosphere, several subsurface depths in several different geologies prevalent in the Earth's upper crust, and seawater.

Chapter 2: Characterization and Optimization of a Si-PIN Diode Spectrometer Prototype

This chapter documents the characterization and optimization of a Si-PIN diode spectrometer prototype designed and assembled by XIA LLC [66, 67, 68]. The first section of this chapter, Section 2.1, presents introductory and background information relevant to both the characterization and optimization efforts. The second and third sections of this chapter, Sections 2.2 and 2.3, document the experimental methods and the analytical techniques supporting the Si-PIN diode spectrometer prototype characterization and optimization efforts, respectively. The final section of this chapter, Section 2.4 provides a review of the important results derived in Sections 2.2 and 2.3 and compares the performance characteristics of the XIA LLC Si-PIN diode spectrometer prototype and a number of optimized Si-PIN diode spectrometer designs to the performance characteristics of the spectrometers currently employed by the verification regime of the Comprehensive Nuclear-Test-Ban Treaty (CTBT) [33, 52, 54, 57, 58].

Section 2.1 begins with an introduction to Si-PIN diode spectrometers and their advantages relative to the high-resolution gamma-ray and beta-gamma coincidence spectrometers currently employed by the verification regime of the CTBT. Next, the Si-PIN diode spectrometer prototype designed and assembled by XIA LLC [67, 68] is

introduced. This is followed by an overview of spectrometer performance metrics including spectrometer linearity, resolution, detection efficiency, and the Minimum Detectable Concentration (MDC) [69, 70, 71]. In order to fully develop the afore-mentioned spectrometer performance metric concepts, a review of peak analysis methods, including relevant counting statistics and decision limit concepts [69, 70, 71, 72], is also provided. Additionally, a novel, totally-unconstrained peak-fitting algorithm, referred to herein as the WiPFA peak-fitting algorithm, developed specifically to support the Si-PIN diode spectrometer characterization efforts documented herein, is introduced. Section 2.1 then concludes with a review of simple linear and multiple linear regression methods used in Section 2.2 to develop spectrometer linearity, resolution, and detection efficiency curve fits [73].

Section 2.2 documents the characterization of the XIA LLC Si-PIN diode spectrometer prototype introduced in Section 2.1.2. The section begins with a description of the experimental methods used to produce radioxenon gas samples and acquire spectral data sets using the XIA LLC Si-PIN diode spectrometer prototype. The counting statistics and decision limit concepts developed in Section 2.1.4 and the WiPFA peak-fitting algorithm described in Section 2.1.5 and Appendix A are then applied to the spectral data sets in order to extract the peak mean, peak width, and peak area data required to characterize the linearity, the resolution, and the photon and conversion electron detection efficiencies of the Si-PIN diode spectrometer prototype. The conversion electron detection efficiencies are then used to develop MDCs for the four radioxenon gases most relevant to the verification regime of the CTBT: ^{131m}Xe,

^{133m}Xe, ^{133}Xe, and ^{135}Xe [46]. Section 2.2 concludes by comparing the performance characteristics of the Si-PIN diode spectrometer prototype to the performance characteristics of the spectrometers employed by the ARIX [52], ARSA [54], SAUNA [57], and SPALAX [58] systems currently employed by the verification regime of the CTBT [33].

Section 2.3 presents a series of studies conducted to optimize the performance of the Si-PIN diode spectrometer prototype. The section begins by introducing an MCNP [74, 75, 76, 77] model developed to generate simulated XIA LLC Si-PIN diode spectrometer prototype spectral data sets. The process of aligning the simulated spectral data sets generated by the MCNP model to the spectral data sets acquired experimentally using the XIA LLC Si-PIN diode spectrometer prototype is then discussed. The optimization process itself is then described in detail. The first set of optimization studies investigate performance gains that might be derived by making a series of changes to the spectrometer chamber dimensions while still using the Si-PIN diodes employed by the XIA LLC Si-PIN diode spectrometer prototype. Subsequent optimization studies investigate performance gains that might be made possible if improvements were made to the Si-PIN diodes themselves. Additionally, a series of optimization studies is conducted to gauge the performance of a Si-PIN diode spectrometer design adhering to applicable Xenon International requirements [78]. Section 2.3 concludes by comparing the performance characteristics of the optimized Si-PIN diode spectrometer designs to the performance characteristics of the XIA LLC

Si-PIN diode spectrometer prototype and the spectrometers currently employed by the verification regime of the CTBT.

Section 2.4 reviews and summarizes the important results derived in Sections 2.2 and 2.3 and draws some final conclusions regarding the performance characteristics of the XIA LLC Si-PIN diode spectrometer prototype and the optimized Si-PIN diode spectrometer designs relative to the performance characteristics of the spectrometers currently employed by the verification regime of the CTBT.

2.1 Introductory and Background Materials

This section presents introductory and background information relevant to both the XIA LLC Si-PIN diode spectrometer prototype characterization and optimization efforts. Topics of discussion include the design and assembly of the XIA LLC Si-PIN diode spectrometer prototype [67, 68], spectrometer performance metrics, a review of relevant counting statistics [69, 72] and decision limit concepts [69, 70, 71, 72], and simple linear and multiple linear regression methods [73]. A novel peak-fitting algorithm, referred to herein as the WiPFA peak-fitting algorithm is introduced in this section as well.

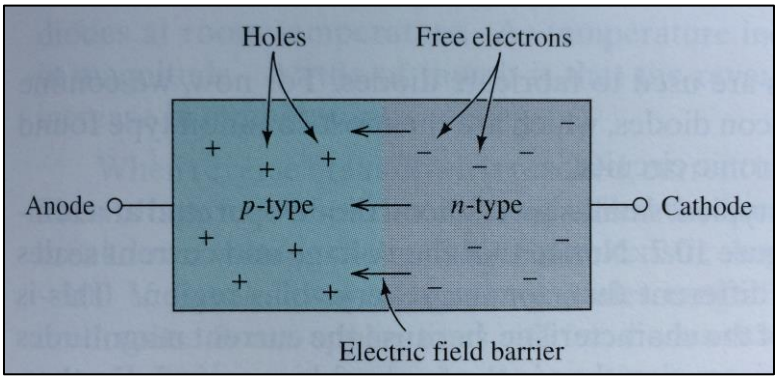

Figure 2.1: Simplified physical structure of a PN diode [79].

2.1.1 Si-PIN Diodes as Ionizing Radiation Spectrometers

In order to understand the advantages of Si-PIN diode radiation spectrometers relative to other radiation spectrometer types it is important to first develop an understanding of Si-PIN diode operating principles. At the most basic level, a diode is simply a two-terminal electronic component that presents very little resistance (ideally zero resistance) to current flow in one direction and very high resistance (ideally infinite resistance) to current flow in the other direction so that the diode essentially functions as an electronic check valve, allowing current to flow in one direction but not the other [80, 81]. There are many types of diodes, one of which is the so-called semiconductor p-n junction diode [80].

A semiconductor p-n junction diode, often referred to simply as a PN diode, consists of a semiconductor crystal with an abundance of holes on one side and an abundance of free electrons on the other side as illustrated above in Figure 2.1 [80].

The side of the semiconductor crystal that is doped with holes is said to be positively doped (and thus the “P” in the PN diode acronym) and the side of the semiconductor crystal that is doped with electrons is said to be negatively doped (and thus the “N” in the PN diode acronym) [80]. The region between the positively-doped and negatively-doped regions of the PN diode is referred to as the depleted region [81, 82, 83]. There are essentially no charge carriers in the depleted region of a PN diode [81, 82, 83]. The semiconductor material most commonly used to fabricate semiconductor PN diodes is silicon (Si), but germanium and selenium are also sometimes used [79, 23a]. Going forward, all references to semiconductor PN diodes, whether explicitly stated or not, will be to Si-PN diodes, unless specifically stated otherwise.

When a forward-biased electrical potential, or voltage, is applied to the anode (the positively-doped side) of a Si-PN diode electrons are allowed to flow from the negatively-doped side of the Si-PN diode, through the depleted region of the Si-PN diode, and to the positively-doped side of the Si-PN diode where they are collected at the anode [79, 80]. This is illustrated in Figure 2.2. In this mode of operation a Si-PN diode allows current to flow in one direction any time the forward-biased electrical potential across the diode is sufficiently high [79, 80].

However, when a reverse bias is applied to a Si-PN diode the voltage applied to the cathode is relatively high as compared to the voltage at the anode [79, 80]. This causes holes in the Si-PN diode to gravitate towards the cathode and electrons in the diode to gravitate towards the anode so that the width of the depleted region increases [79, 80, 81, 82]. As the width of the depleted region increases so too does the

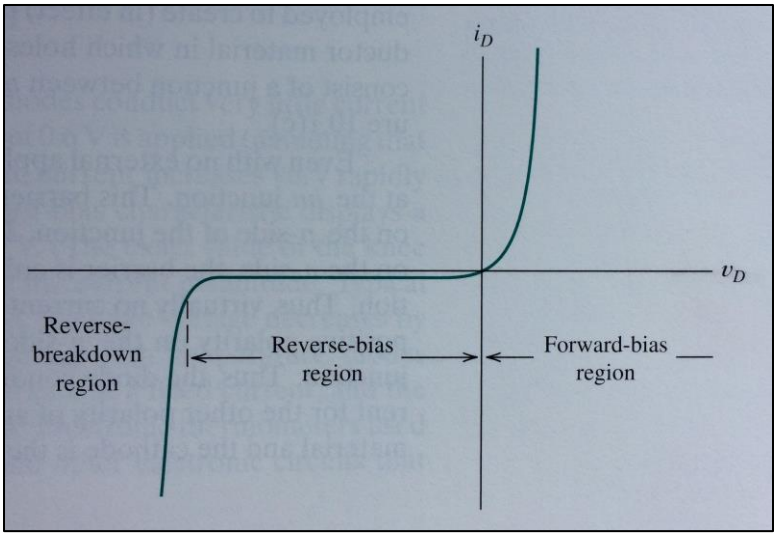

Figure 2.2: A diode voltage-current curve [79].

strength of the electric field across the Si-PN diode [81, 83]. Because the polarity of the electric field opposes charge carrier motion through the diode, current is not allowed to flow through a Si-PN diode to which a reverse bias is applied (see Figure 2.2) unless electron-hole pairs are created in the interior of the depleted region of the Si-PN diode [80, 82, 83]. Electron-hole pairs may be created in the depleted region of a Si-PN diode by photons entering the depleted region from the outside [80, 82, 83]. In this way, applying a reverse bias to a Si-PN diode allows it to function as a type of photodiode capable of detecting the presence of ionizing radiation [84].

Si-PIN diodes are, in many ways, similar to Si-PN diodes. They consist of silicon semiconductor crystals that are positively doped on one side and negatively doped on the other side [84, 85]. They are different than traditional Si-PN diodes, however, in that they feature an intrinsic, un-doped silicon region that is sandwiched between the positively-doped and negatively-doped regions of the diode as illustrated below in Figure 2. 3 [84,

85]. (It is this intrinsic layer that contributes the "I" to the PIN diode acronym.) The intrinsic region effectively serves to increase the width of the depleted region in a Si-PIN diode relative to the depleted region typically associated with a Si-PN diode [85]. The relatively wide depleted region associated with Si-PIN diodes makes them well suited to the task of detecting ionizing radiation because a larger depleted region means there is more volume available for photons to interact in.

As ionizing radiation spectrometers, Si-PIN diodes offer many advantages relative to the high-resolution gamma-ray and beta-gamma-coincidence spectrometers currently employed by the verification regime of the CTBT [52, 54, 57, 58]. First, the fundamental principles upon which Si-PIN diode spectrometer operations are based result in very low electronic noise levels, even at ambient temperatures (the leakage current associated with Si-PIN diodes is very low) [86]. This means that the number of background counts resulting from electronic noise is very low [67, 68], and, generally speaking, radiation spectrometers with lower background count rates are more sensitive to actual source

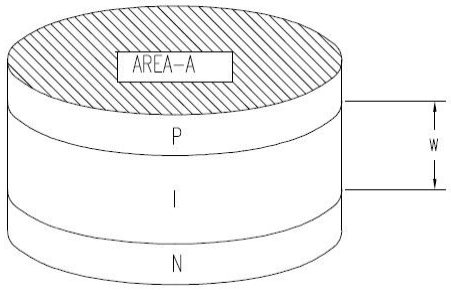

Figure 2.3: Simplified physical structure of a PIN diode [84].

detections than are radiation spectrometers with higher background count rates.

Another advantage of Si-PIN diode spectrometers is their excellent energy resolution, especially at low energies [67, 68]. As an example, consider the fact that one of the HPGe spectrometers currently in use at The University of Texas at Austin's Nuclear Engineering Teaching Laboratory [87] (an Ortec GMX series HPGe) reportedly has a photon energy resolution of 600 to 1,200 eV at 5.9 keV [88], while an 0.25 cm^2 Amptek model XR-100CR Si-PIN diode reportedly has a photon energy resolution in the 145 to 200 eV range at the same energy (5.9 keV) [86, 89, 90]. The photon energy resolution of the Si-PIN diode is more than twice as good as the energy resolution of the HPGe. In fact, the Si-PIN diode photon energy resolution is so good that peaks attributable to individual X-ray lines may be resolved in spectra acquired by Si-PIN diode-based radiation spectrometers.

Additionally, Si-PIN diodes have very thin dead layers. The thickness of the Amptek model XR-100CR Si-PIN diode dead layer is reportedly on the order of about 150 nm [90, 91]. This dead layer is so thin that it is easily penetrated by low-energy, monoenergetic conversion electrons, and thus Si-PIN diode spectrometers may be used to perform conversion electron spectroscopy.

Si-PIN diodes also have excellent photon detection efficiencies at low incident photon energies. In fact, as illustrated in Figure 2.4, Amptek reports that the intrinsic photon detection efficiency of their 500 μm thick Si-PIN diodes approaches 100 % in the 9 keV range [86]. That being said, Figure 2.4 also illustrates the fact that Si-PIN diode photon detection efficiencies fall off rapidly with increasing photon energy so that photon

detection efficiencies are very low above about 50 keV. This is typically viewed as a disadvantage of Si-PIN diodes. However, as will be seen shortly, the low photon detection efficiencies at higher photon energies may be advantageous when Si-PIN diodes are used to perform conversion electron spectroscopy (the low photon detection efficiencies help to keep background levels low).

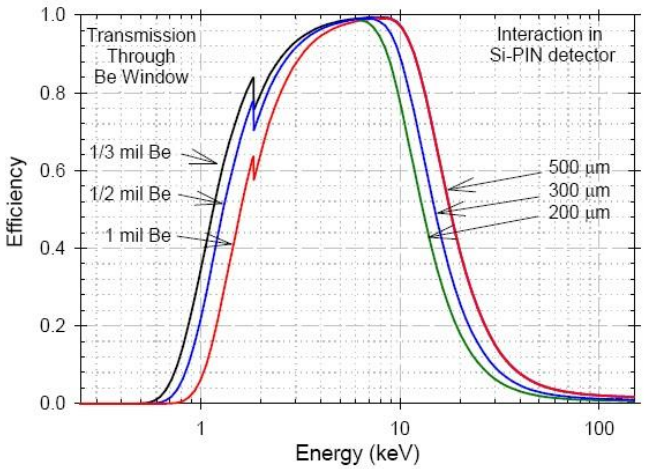

Figure 2.4: Amptek XR-100CR Si-PIN diode intrinsic photon detection efficiency curve [86].

2.1.2 The XIA LLC Si-PIN Diode Spectrometer Prototype

The Si-PIN diode spectrometer prototype characterized herein was designed and assembled by XIA LLC (formerly X-Ray Instrumentation Associates), a Hayward, CA, USA-based company that specializes in developing advanced digital data acquisition and processing systems for X-ray and gamma-ray detector applications [66]. The XIA LLC

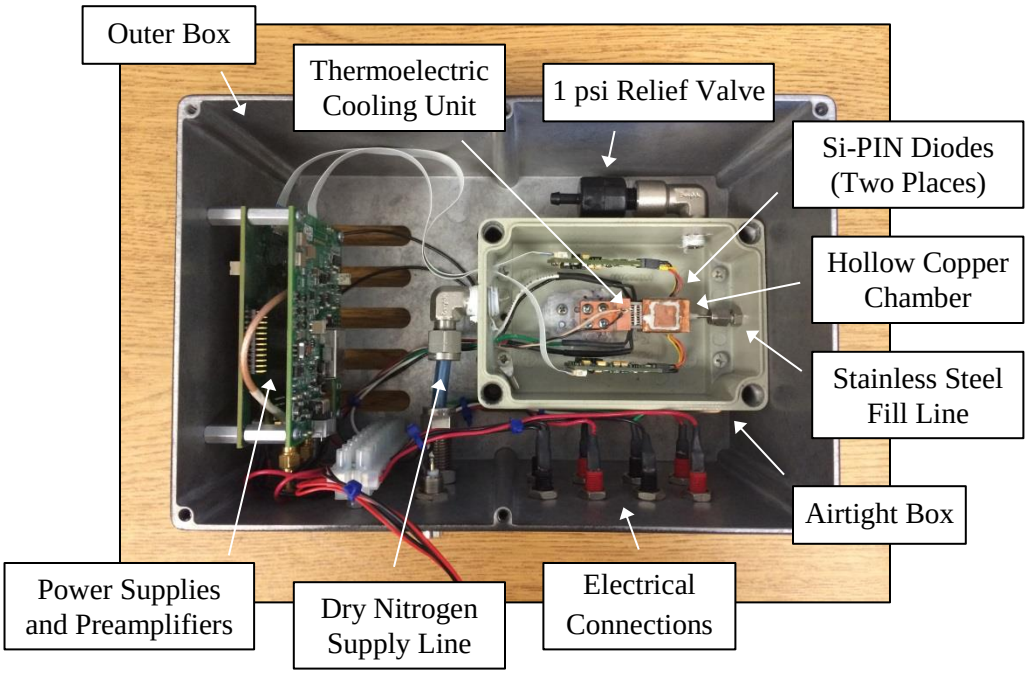

Figure 2.5: The XIA LLC Si-PIN diode spectrometer prototype.

Si-PIN diode spectrometer prototype was first assembled in early 2012, and Hennig *et al.* have published a number of papers describing the design, assembly, and initial testing of the prototype [67, 68].

A photograph of the Si-PIN diode spectrometer prototype assembly is presented above in Figure 2.5. The principal component of the Si-PIN diode spectrometer prototype is a small hollow copper chamber with one Si-PIN diode mounted on its front face and a second Si-PIN diode mounted on its back face. The Si-PIN diodes are actually mounted on thin silicon dioxide (SiO_2) substrates that are then affixed to recessed seating surfaces within the front and back faces of the copper chamber with glue. The silicon dioxide substrates are thin squares measuring 0.010 in (0.0254 cm) thick by 1.0 cm wide by 1.0 cm tall [67, 68, 92]. The interior of the hollow copper chamber is about 0.459 in (1.17

cm) thick by 0.382 in (0.97 cm) wide by 0.358 in (0.91 cm) tall [93] so that the space in the interior of the copper chamber between the two Si-PIN diodes ends up having a volume of about 1.02 cm^3. Gaseous samples may be introduced to the space in the interior of the copper chamber via a 1/16 in (0.16 cm) outer diameter stainless steel fill line that penetrates the right side of the copper chamber [67, 68].

The Si-PIN diodes employed by the XIA LLC Si-PIN diode spectrometer prototype are XR-100CR-type Si-PIN diodes manufactured by Amptek, Inc., a Bedford, MA, USA-based company that specializes in the design, development, and manufacture of radiation detection components [94]. The Si-PIN diodes are circular, are about 500 μm thick, and have surface areas of about 0.25 cm^2 [86]. Amptek reports that the dead layer associated with their XR-100CR-type Si-PIN diodes is only 150 nm thick [91].

The copper chamber and Si-PIN diodes may be cooled by a two-stage thermoelectric cooling unit mounted to a fourth side of the copper spectrometer chamber. The thermoelectric cooling unit is capable of cooling the copper spectrometer chamber and the Si-PIN diodes to an operating temperature of about 276 K (about 3 °C) [67, 68]. The Si-PIN diode spectrometer prototype assembly is housed in a 5 cm deep by 10 cm wide by 4 cm tall airtight box fitted with a dry nitrogen supply line and a 1 psi (6,900 Pa) relief valve [95]. The interior of the airtight box is purged with dry nitrogen gas prior to each use to prevent moisture from condensing on the sensitive, windowless faces of the Si-PIN diodes when the thermoelectric cooling unit is operating and the surfaces of the copper chamber and Si-PIN diodes are cold [67, 68]. The airtight box is mounted inside of an outer box that also houses the Si-PIN diode power supplies and preamplifiers and a

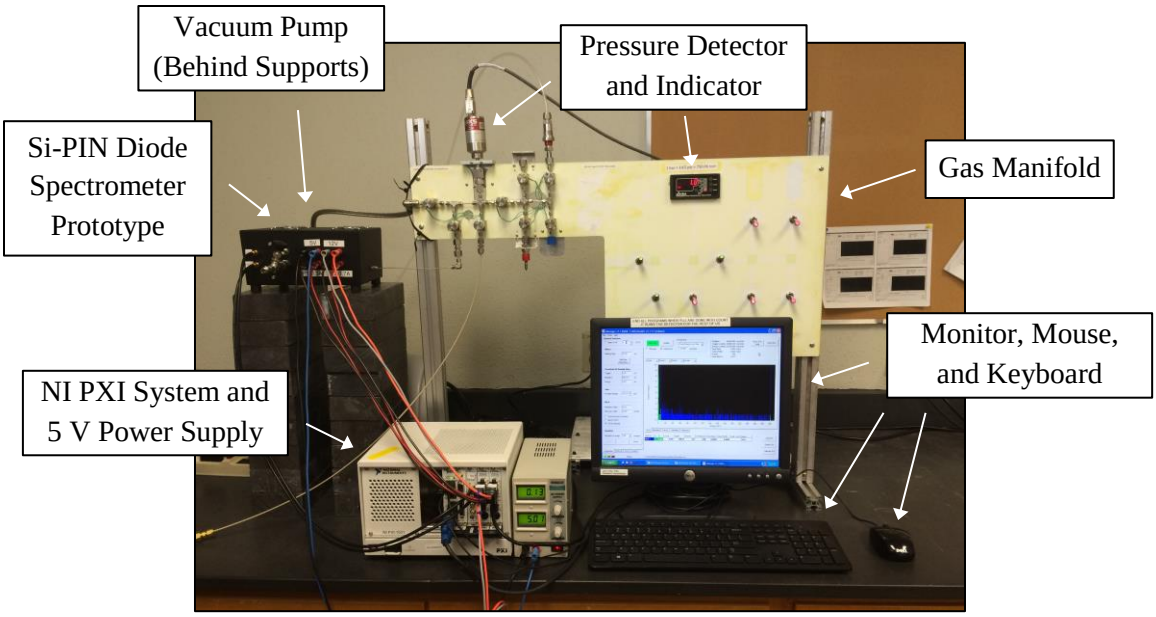

Figure 2.6: The XIA LLC Si-PIN diode spectrometer prototype connected to its support systems.

number of bulkhead electrical connections that provide an interface between the electronics inside the Si-PIN diode spectrometer prototype and its support systems.

An additional photograph showing the Si-PIN diode spectrometer prototype connected to its support systems is presented above in Figure 2.6. The main support systems include an external power supply and a National Instruments PXI system [96]. The power supply provides the Si-PIN diodes with a low noise, 5 V source of power [95]. The PXI system is essentially a small computer that hosts multiple applications used to interface with the Si-PIN diodes, the thermoelectric cooling unit, and cooling fans housed inside the outer Si-PIN diode spectrometer prototype box. The National Instruments NI-DCPower Soft Front Panel application is used to direct a 12.0 V, 0.3 A source of

power to the cooling fan and 6.0 V, 0.3 A and 6.0 V, 0.7 A sources of power to the two-stage thermoelectric cooling unit affixed to the copper chamber [95].

A gas manifold [97] is also visible in the background of Figure 2.6. The gas manifold is composed of several lengths of 1/16 in (0.16 cm) stainless steel tubing, several solenoid operated valves, a vacuum pump, a pressure indicating device, and several Swagelok quick-disconnect fittings. As discussed in Section 2.2.1.1, the gas manifold is used to support the production of radioactive gases at The University of Texas at Austin's Nuclear Engineering Teaching Laboratory [87] and, in this case, to support transferring the radioactive gases to the Si-PIN diode spectrometer prototype.

Two software applications may be used to interface with the Si-PIN diodes. The first is an XIA LLC application called xManager [96]. The xManager application may be used to start and stop spectral data set acquisitions and to interface with and export spectral data sets acquired by the Si-PIN diodes. It also provides the interface through which spectrometer configuration settings may be modified. A screenshot of the xManager application is presented in Figure 2.7, and a full list of the configuration settings used throughout the course of the Si-PIN diode spectrometer prototype characterization efforts documented herein are provided in Table 2.1. The majority of the spectrometer configuration settings listed in Table 2.1 were set based on recommendations provided by XIA LLC [95]. The xManager application also provides a means of saving spectrometer configuration settings to a configuration file so that spectrometer configuration settings may be imported by the other application used to interface with the Si-PIN diodes, an application called XeSDD [98].

Table 2.1: The XIA LLC Si-PIN diode spectrometer prototype configuration settings used throughout the course of the spectrometer characterization efforts documented herein.

Spectrometer Configuration Parameter	Setting
Peaking Time	16.00 μs
Baseline Threshold	4,980.47 eV
Dynamic Range	320.00 keV
Number of MCA Bins	8,192
MCA Bin Width	38.00 eV-bin^{-1}
Preamplifier Polarity	Negative
Preamplifier Reset Delay	100.00 μs
Preamplifier Gain (Channel 0)	0.8000 mV-keV^{-1}
Preamplifier Gain (Channel 1)	0.8254 mV-keV^{-1}

The XeSDD application was developed by XIA LLC specifically to interface with the Si-PIN diode spectrometer prototype. It is a simple application that allows users to load spectrometer configuration settings, specify spectral data set acquisition times, start spectral data set acquisitions, and save spectral data sets. While the functionality of the XeSDD application is somewhat limited, it is a useful application in that it allows users to acquire spectral data sets in a time-stamped list mode. The list mode data may be post-processed in a number of ways to produce one-dimensional singles spectra or two-dimensional coincidence spectra. A screenshot of the XeSDD application is presented below in Figure 2.7.

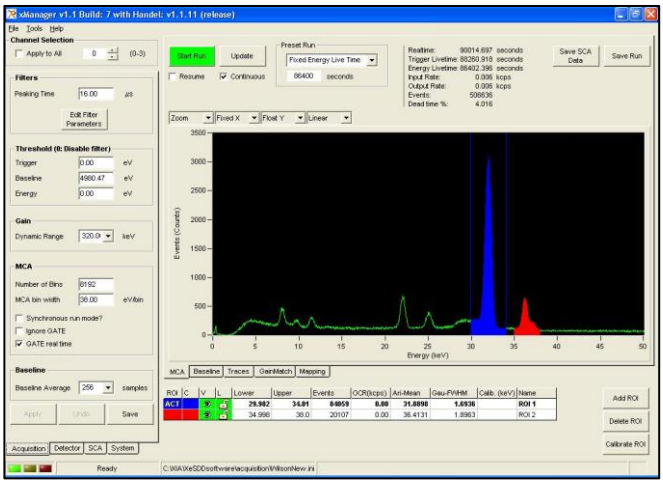

(a)

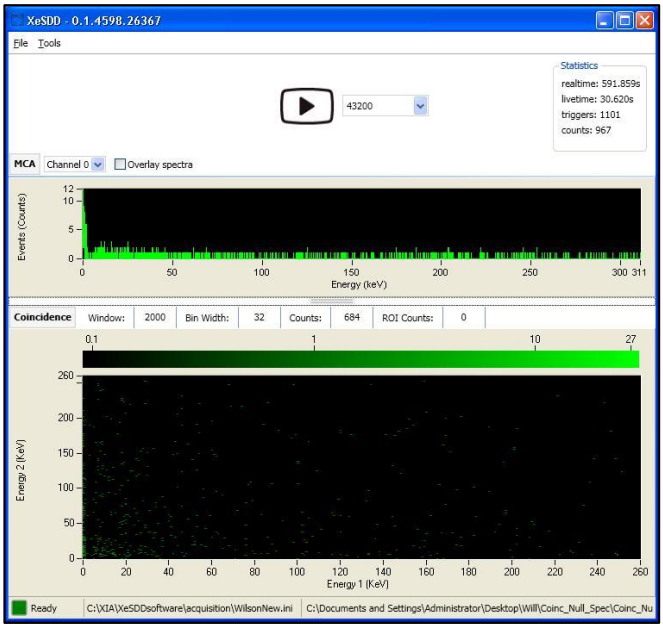

(b)

Figure 2.7: Screenshots of (a) the xManager and (b) the XeSDD applications used to interface with the XIA LLC Si-PIN diode spectrometer prototype.

2.1.3 Spectrometer Performance Metrics

As alluded to in several of the preceding sections, there are many different types of radiation spectrometers. Some of the more traditional spectrometer types include High-Purity Ge (HPGe), NaI(Tl), and plastic scintillation spectrometers [69, 72, 99]. Each of the aforementioned spectrometer types operate based on different physical principles, and thus each of the spectrometer types perform somewhat differently. For example, HPGe spectrometers are very good at identifying the energies of incident photons within tight tolerances, but they detect a relatively small fraction of the photons incident upon them. Because of this, HPGe spectrometers are sometimes said to be high-resolution, low-detection-efficiency spectrometers. Conversely, NaI(Tl) spectrometers detect a relatively large fraction of the photons incident upon them but they are not very good at identifying the energies of the incident photons. NaI(Tl) spectrometers are thus often said to be high-detection-efficiency, low-resolution spectrometers. In the sections that follow several performance metrics that are commonly used to evaluate spectrometer performance are introduced. The spectrometer performance metrics of most interest here are the spectrometer linearity, resolution, and detection efficiency metrics. The concept of a Minimum Detectable Concentration (MDC) is also introduced. These metrics will ultimately be used to evaluate the performance of the XIA LLC Si-PIN diode spectrometer prototype described in Section 2.1.2 relative to the spectrometers employed by the ARIX [52], ARSA [54], SAUNA [57], and SPALAX [58] systems of the verification regime of the CTBT [33].

2.1.3.1 Spectrometer Linearity

The first spectrometer performance metric of interest is the spectrometer linearity metric. As the name suggests, spectrometer linearity is a metric used to describe the linear relationship between spectrometer channel number and incident radiation energy [69]. Notice that the term "radiation" is used generically here to refer to photons, electrons, alpha particles, *etc.* because for a given spectrometer one linearity characterization may be applicable to one type of incident radiation (photons, for example) and another linearity characterization may be applicable to another type of incident radiation (conversion electrons, as another example). In other words, one cannot necessarily assume that a spectrometer linearity characterization generated using calibration sources emitting only photons will be applicable when analyzing a spectral data set that contains peaks resulting primarily from conversion electron detections.

The spectrometer linearity characterization process involves first acquiring one or more spectral data sets using one or more calibrated radiation sources emitting radiations whose energies are known to a high degree of precision. After the spectral data sets are acquired the means associated with the peaks in the spectral data sets are evaluated. Then, the incident radiation energies, which are known, are plotted against their respective peak means so that the relationship between incident radiation energy and spectrometer channel number may be evaluated. In most cases a simple linear regression method is used to fit a straight line to the data points so that the energy associated with any channel may be readily determined. The result of a spectrometer linearity characterization is typically referred to as a linearity calibration.

In order to generate consistent linearity calibrations a repeatable method of evaluating peak means must be established. There are at least two methods that can be used to evaluate the means associated with the peaks in spectral data sets. The first method involves simply identifying the channel number with the largest number of counts in a given peak and declaring that channel to be the peak mean as illustrated below in Figure 2.8 [69]. The second method involves fitting a curve to the peak and extracting the peak mean from the fit to the peak. This method is discussed in more detail in Section 2.1.5.

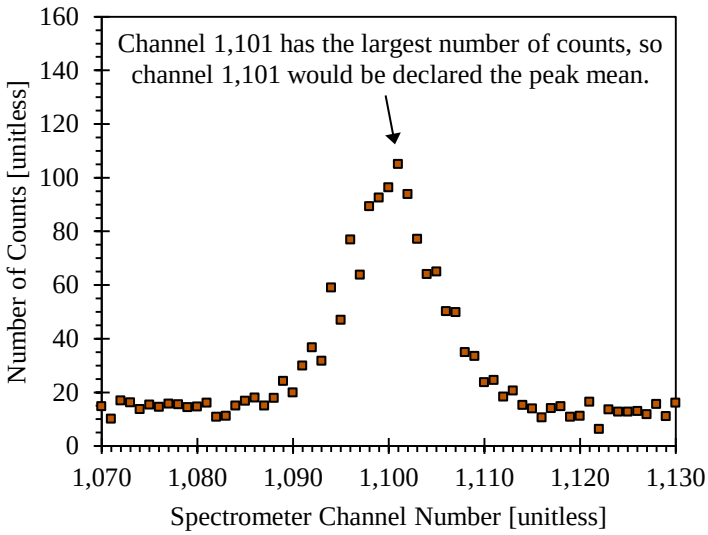

Figure 2.8: A simple method to identify the mean of a peak in a spectral data set.

An example of a spectrometer linearity calibration is presented below in Figure 2.9. The spectrometer linearity calibration presented in Figure 2.9 is an HPGe spectrometer linearity calibration that was generated at The University of Texas at Austin's Nuclear Engineering Teaching Laboratory [87] using the peak means associated with 30 different photon peaks generated by eight different calibration sources. The uncertainties associated with the peak means are very small so that the error bars associated with the peak mean data points are completed covered by the data points themselves. In this example the linear fit to the peak mean data points was generated using a simple linear regression technique [73]. A prediction interval with a

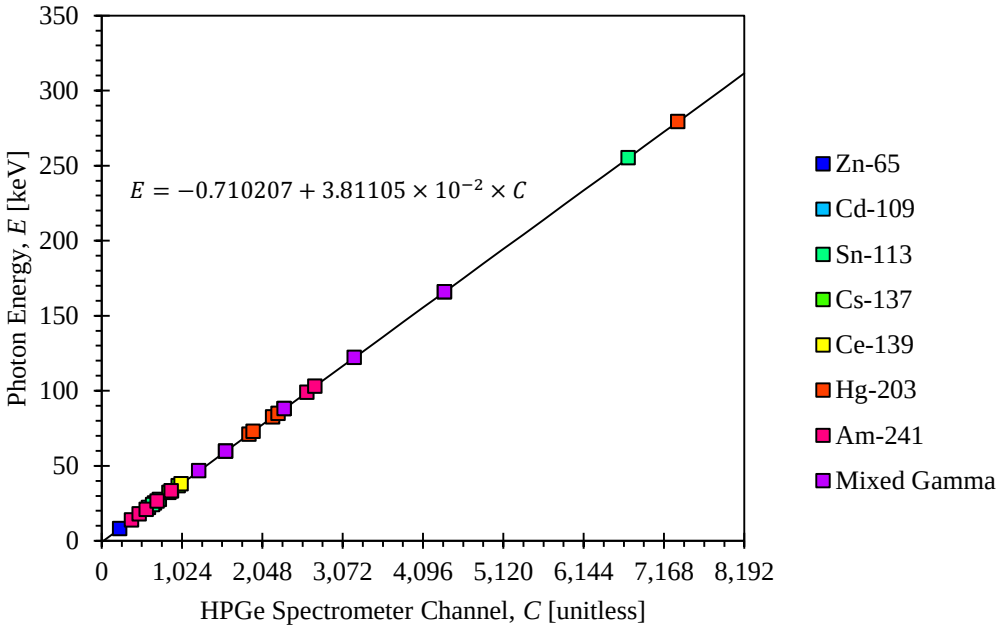

Figure 2.9: An HPGe spectrometer linearity calibration example (1·σ error bars).

95 % confidence level was generated to go along with the nominal fit to the data points, but the upper and lower bounds of the prediction interval essentially sit on top of the nominal linearity curve. As illustrated by Figure 2.9, the HPGe linearity calibration has an ordinate intercept that is very near to zero and the slope is in-fact very linear. This is typical of most modern spectrometers.

2.1.3.2 Spectrometer Resolution

Another important spectrometer performance metric is the spectrometer resolution metric. The spectrometer resolution metric describes the relationship between the widths of the peaks in spectral data sets and the energies of the incident radiations generating the peaks [69]. Again the term "radiation" is used generically here to refer to photons, electrons, alpha particles, *etc.* because for a given spectrometer one resolution characterization may be applicable to one type of incident radiation (photons, for example) and another resolution characterization may be applicable to another type of incident radiation (conversion electrons, as another example).

Two different peak parameters are used to gauge the widths of peaks. The first is the full width at half maximum, often abbreviated and reported simply as the FWHM. As the name suggests the peak FWHM quantifies the full width of a given peak at a height equal to half of the peak's maximum height [69, 99]. The second peak parameter used to gauge peak widths is the peak standard deviation. The peak standard deviation describes the degree to which the counts in a peak, which are assumed to be normally

distributed about a mean, are distributed or spread about the peak mean. The peak FWHM and standard deviation parameters are related as follows [99]:

$$FWHM = 2.355 \cdot \sigma. \qquad 2.1.3.2.1$$

Where: $FWHM$ is the peak full width at half maximum and

σ is the peak standard deviation.

It is important to have a general understanding of the widths associated with the peaks in spectral data sets generated by a given spectrometer because the peak widths will determine how easy or difficult it will be to resolve adjacent peaks within spectral data sets generated by the spectrometer. This point is easily made through the use of an exaggerated illustration such as the one provided in Figure 2.10. As illustrated by Figure 2.10.(a), when the widths of two adjacent peaks are narrow the two peaks are easily resolved and the number of counts in each peak may easily be evaluated. However, when the peak widths are increased (while the peak means and areas are held constant), as in Figure 2.10.(b), the two peaks become convoluted into a single multiplet and the task of determining the number of counts that should be attributed to each of the peaks constituting the multiplet becomes significantly more challenging. In some cases, large peak widths can make it difficult to even identify the presence of small peaks adjacent to larger peaks within a spectral data set.

The spectrometer resolution characterization process is very similar to the spectrometer linearity characterization process described in the preceding section. The process involves first acquiring one or more spectral data sets using one or more calibrated radiation sources emitting radiations whose energies are known. After the

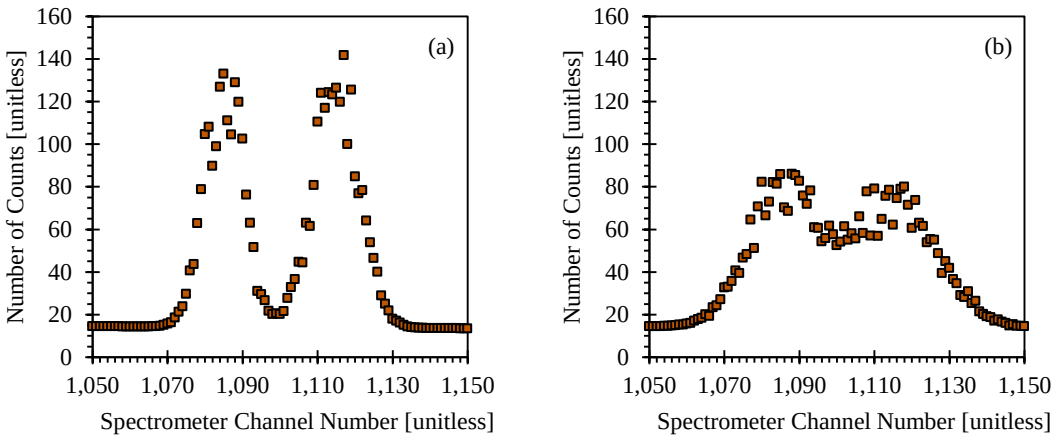

Figure 2.10: An illustration of peak convolution resulting from large peak widths.

spectral data sets are acquired the widths associated with the peaks generated by the radiations emitted by the calibration sources are evaluated. Then the peaks widths are plotted against their respective incident radiation energies so that the relationship between peak width and incident radiation energy may be evaluated. In most cases a linear regression method or a multiple regression method is used to fit a straight line or a polynomial to the data points so that the resolution associated with any incident radiation energy may readily be determined. The result of a spectrometer resolution characterization is typically referred to as a resolution calibration.

There are a number of methods that may be used to estimate peak widths in support of spectrometer resolution characterizations. One such method is the six step method prescribed by Gilmore and Hemingway [69]. The six steps are as follows:

(1) The first step is to estimate the peak height, C_T. The peak height estimate is simply the largest number of counts in the peak.

(2) The second step is to subtract a background estimate, C_0, from the peak height estimate, C_T. The peak background estimate is the average number of background counts to the left and right sides of the peak.

(3) Next subtract C_0 from C_T and divide the difference by two. Add the result back to C_0. This gives the expected number of counts at half of the peak height, C_H.

(4) Now, on the low-energy side of the peak, find the channels with the counts nearest below, A, and nearest above, B, the expected number of counts, C_H. If these are channels C_A and C_B, respectively, then the channel that corresponds to the half peak height on the low energy side of the peak may be calculated as follows:

$$H_L = A + \frac{C_H - C_A}{C_B - C_A} \qquad 2.1.3.2.2$$

(5) Now do the same thing on the high-energy side of the peak; find the channels with the counts nearest above, C, and nearest below, D, the expected number of counts, C_H. If these are channels C_C and C_D, respectively, then the channel that corresponds to the half peak height on the high energy side of the peak may be calculated as follows:

$$H_U = C + \frac{C_C - C_H}{C_C - C_D} \qquad 2.1.3.2.3$$

(6) The difference $H_U - H_L$ is the FWHM associated with the peak.

As an alternative to the method described above, a second peak width estimation method involves fitting a curve to the peak and extracting the peak width from the fit to the peak. This method is discussed more in Section 2.1.5.

An example of a spectrometer resolution calibration is presented in Figure 2.11. The spectrometer linearity calibration presented in Figure 2.11 is an HPGe spectrometer energy calibration that was generated at The University of Texas at Austin's Nuclear Engineering Teaching Laboratory [87] using the peak widths associated with 14 different gamma-rays emitted by six different calibration sources. The uncertainties associated with the peak widths are typically small (<1.0 %) so that the error bars associated with the peak width data points are completed covered by the data points themselves.

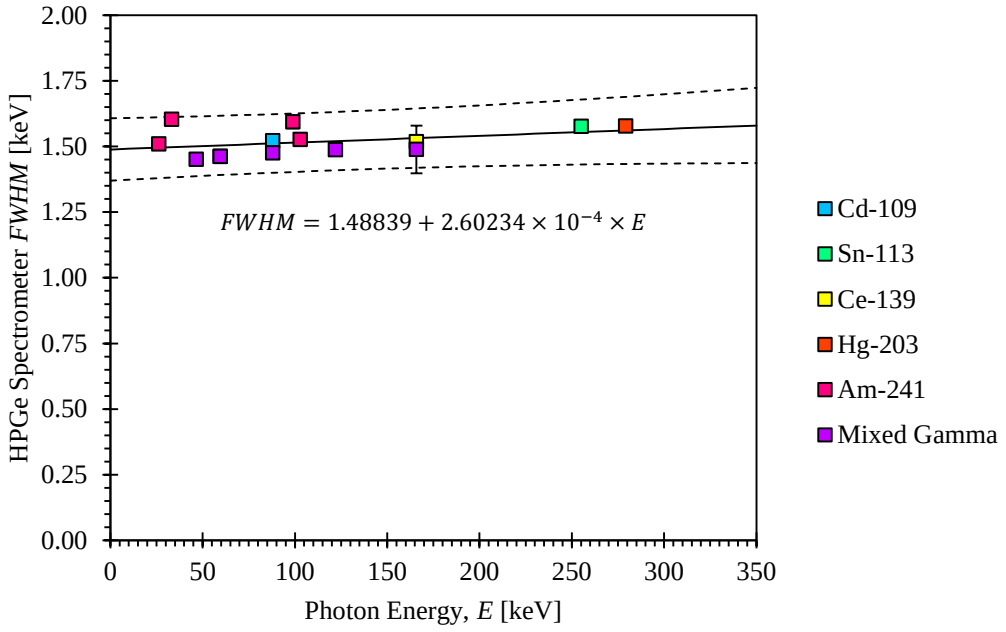

Figure 2.11: An HPGe spectrometer resolution calibration example (1·σ error bars).

That said, the uncertainty associated with the width of the ^{139}Ce 165.8575 keV gamma-ray peak is about 6.1 % and the error bars are visible in the figure. In this example the linear fit to the peak width data points was generated using a linear regression technique [73]. A prediction interval with a 95 % confidence level was generated to go along with the nominal fit to the data points. As illustrated by Figure 2.11, the HPGe linearity calibration has a vertical axis intercept that is very near to about 1.5 keV and a slope that is quite linear and very slightly positive. This is typical of most modern HPGe spectrometers.

2.1.3.3 Spectrometer Detection Efficiency

The third spectrometer performance metric of interest is the spectrometer detection efficiency metric. The spectrometer detection efficiency relates, in one manner or another, the number of radiation detections registered by a spectrometer to the number of radiations emitted by a radiation source [99]. Mathematically, the spectrometer detection efficiency is defined as follows [99]:

$$\varepsilon = \frac{N_{Reg}}{N_{Emi}} \qquad 2.1.3.3.1$$

Where: ε is the spectrometer detection efficiency,

N_{Reg} is the number of radiation detections registered by the spectrometer, and

N_{Emi} is the number of radiations emitted by the radiation source.

More specific spectrometer detection efficiency definitions may be developed by using more specific terms to describe how the number of radiation detections registered by the spectrometer will be quantified and how the number of source radiation emissions will be quantified. Depending on how each of these quantities is defined, a number of spectrometer detection efficiency metrics may be calculated and reported. A few of the more common spectrometer detection efficiency metrics are defined as follows:

Absolute detection efficiency metrics: If N_{Reg} is taken to be the number of detections registered anywhere in a spectrum (*i.e.* in any channel corresponding to any incident radiation energy) and N_{Emi} is taken to be the total number of source radiation emissions then the calculated detection efficiency is referred to as the absolute total detection efficiency [99]. If N_{Reg} is instead taken to be only the number of full-energy peak detections registered in the spectrum and N_{Emi} is again taken to be the total number of source radiation emissions then the calculated detection efficiency is referred to as the absolute full-energy peak detection efficiency [99]. The number of full-energy peak detections is typically smaller than the number of detections registered anywhere in the spectrum so that the absolute full-energy peak detection efficiency is typically smaller than the absolute total detection efficiency.

Intrinsic detection efficiency metrics: There are two intrinsic detection efficiency metrics; they are the intrinsic total detection efficiency and the intrinsic full-energy peak detection efficiency and they are analogous to the absolute total detection efficiency and the absolute full-energy peak detection efficiency described above with the difference being that for the intrinsic detection efficiency metrics N_{Emi} is taken to be the number of

source radiation emissions incident upon the spectrometer as opposed to total number of source radiation emissions [99]. The number of source radiation emissions incident upon the spectrometer is typically smaller than the total number of source radiation emissions so that the intrinsic detection efficiency metrics are typically larger than the absolute detection efficiency metrics.

Each of the aforementioned spectrometer detection efficiency metrics has its use. Spectrometer manufacturers typically report the intrinsic full-energy peak detection efficiencies associated with their spectrometers because the intrinsic full-energy peak detection efficiencies provide the best metric of spectrometer detection efficiency performance irrespective of the geometric arrangement between a given source and the spectrometer. Within the context of the XIA LLC Si-PIN diode spectrometer prototype characterization work documented herein, the principle purpose of the detection efficiency metric is to relate radiation detections registered in peaks attributable to specific radioisotopes to the total number of radioisotope atoms responsible for generating the detections, and thus the spectrometer detection efficiency metric that is of most interest here is the absolute full-energy peak detection efficiency. That said, the intrinsic full-energy peak detection efficiency metric will also be utilized during the prototype design optimization process.

The spectrometer detection efficiency characterization process is similar to the spectrometer linearity and resolution characterization processes described in the preceding sections. The process described here is specific to the development of an absolute full energy peak detection efficiency characterization, but only small changes to

this process would be required to develop, for example, an absolute total detection efficiency characterization. The process involves first acquiring one or more spectral data sets using one or more calibrated radiation sources. In the case of a spectrometer detection efficiency characterization it is important that not only the energies of the radiations emitted by the sources be precisely known, but also the activities, or decay rates, of the calibrated radiation sources. The activities of the calibrated radiation sources must be known precisely because they are used to evaluate the N_{Emi} term in the spectrometer detection efficiency expression, and large errors in calibration source activities lead to large errors in calculated spectrometer detection efficiencies.

After the spectral data sets are acquired, the number of detections registered in each of the peaks attributable to each of calibration sources is evaluated. As opposed to the simple peak mean and peak width estimation techniques discussed in previous sections, methods used to estimate the number of detections registered in the peaks of spectral data sets are somewhat more complicated. A full description of one method that is commonly used is described in Section 2.1.4. Suffice it to say here that the method essentially involves summing up the number of counts in each of the channels associated with a peak and then subtracting away a portion of the counts that are judged to be attributable to background sources. Peak fitting techniques may also be used to estimate the number of detections registered in peaks. In fact, in the case where multiple peaks overlap and form what are referred to as multiplets (see Figure 2.10 for examples of multiplets) peak fitting techniques may be the only way to estimate the number of detections registered in each of the peaks constituting the multiplets.

After the number of detections registered in the peaks of the spectral data sets have been evaluated, the next step associated with the spectrometer detection efficiency characterization process is to evaluate the number of radiation emissions expected for each of the calibration sources used. The number of radiation emissions expected during a spectrum acquisition may be calculated from the known source activities, the known source decay constants, and the known source decay mode branching ratios as follows:

$$N_{Emi} = \frac{A(t_{AS}) \cdot \left(1 - e^{-\lambda \cdot t}\right)}{\lambda}. \qquad 2.1.3.3.2$$

Where: N_{Emi} is the number of radiation emissions expected during a given spectral data set acquisition,

$A(t_{AS})$ is the activity of the radiation source at the time corresponding to the beginning of the spectral data set acquisition, t_{AS},

λ is the radiation source decay constant, and

t is the spectral data set acquisition time.

Plugging Equation 2.1.3.3.2 into Equation 2.1.3.3.1 produces the following expression relating the spectrometer detection efficiency to the number of detections registered in a spectral data set and the source-specific variables:

$$\varepsilon = \frac{N_{Reg} \cdot \lambda}{A(t_{AS}) \cdot (1 - e^{-\lambda \cdot t})}. \qquad 2.1.3.3.3$$

Spectrometer detection efficiencies calculated in accordance with Equation 2.1.3.3.3 are typically plotted against their respective incident radiation energies so that the relationship between spectrometer detection efficiency and incident radiation energy may be evaluated. In most cases a multiple regression method is used to fit a polynomial to the data points so that the detection efficiency associated with any incident radiation energy may be readily determined. The result of a spectrometer detection efficiency characterization is typically referred to as an efficiency calibration.

Figure 2.12 provides an example of an absolute full-energy peak detection efficiency calibration. The detection efficiency calibration presented in Figure 2.12 is an HPGe spectrometer detection efficiency calibration that was generated using the detection efficiencies associated with 24 different X- and gamma-rays emitted by six different calibration sources. The uncertainties associated with the detection efficiencies are typically on the order of about 4.2 % so that the error bars associated with most of the detection efficiency data points are visible in the figure.

In this example, the fit to the detection efficiency data points was generated using the multiple regression technique described in Section 2.1.6.2. A prediction interval with a 95 % confidence level was generated to go along with the nominal fit to the data points. As illustrated by Figure 2.12, the HPGe absolute detection efficiency calibration has an ordinate intercept that is very near to zero, it attains a maximum of about 0.0338 at incident photon energies of about 68.0 keV, and then decreases with increasing incident photon energy. This is fairly typical of most modern HPGe spectrometers.

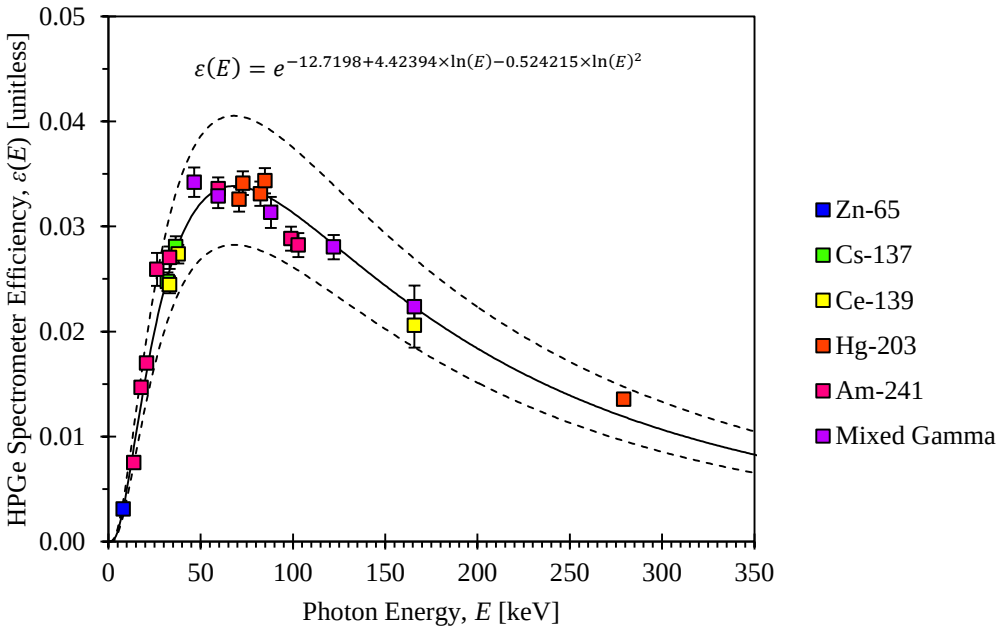

Figure 2.12: An HPGe spectrometer detection efficiency calibration example (1·σ error bars).

2.1.3.4 The Minimum Detectable Concentration

Of all the spectrometer performance metrics discussed herein, the Minimum Detectable Concentration (MDC) is probably the most important. It provides an *a priori* estimate as to the minimum activity concentration that a spectrometer should be expected to be capable of detecting to a given confidence or certainty. In order to illustrate what this means, say, for example, that a hypothetical spectrometer is known to have a ^{133}Xe MDC of 1.0 mBq-m^{-3}. Furthermore, assume that the confidence level or certainty associated with the ^{133}Xe MDC is known to be 95 %. This means that if the hypothetical spectrometer were used to count 100 gas samples where the ^{133}Xe activity concentration in each gas sample was known to be 1.0 mBq-m^{-3}, which is exactly equal to the

spectrometer's ^{133}Xe MDC, then the hypothetical spectrometer should be expected to detect the presence of the ^{133}Xe in 95 of the gas samples. Conversely, it should be expected to fail to detect the presence of the ^{133}Xe in five of the gas samples.

Throughout this dissertation, spectrometer MDCs will be evaluated using the MDC expression developed by McIntyre *et al.* [71]. This MDC expression, which was developed specifically to evaluate radioactive noble gas MDCs associated with CTBT radioactive noble gas monitoring systems, is as follows:

$$MDC_{I,G,M} = \frac{1{,}000 \cdot t_C \cdot \lambda_{I,G}^2 \cdot \left(k_\alpha^2 + 2 \cdot \sqrt{2} \cdot k_\alpha \cdot \sqrt{\sigma_{BG}^2 + \sigma_{Int}^2}\right)}{\beta_{M,I,G} \cdot \varepsilon_{M,I,G} \cdot V_{Air} \cdot (1 - e^{-\lambda_{I,G} \cdot t_C}) \cdot e^{-\lambda_{I,G} \cdot t_P} \cdot (1 - e^{-\lambda_{I,G} \cdot t_A})}. \qquad 2.1.3.4.1$$

Where: $MDC_{I,G,M}$ is the MDC of radioisotope I of gas G based on count data attributable to decay mode M of radioisotope I,

1,000 is a constant used to convert the decay-corrected activity of radioisotope I of gas G from units of Bq to units of mBq,

t_C is the gas collection time,

t_P is the gas processing time,

t_A is the spectral data set acquisition time,

$\lambda_{I,G}$ is the decay constant associated with radioisotope I of gas G,

k_α is a factor that establishes the confidence or certainty that may be ascribed to the calculated MDC,

σ_{BG}^2 is the variance associated with any background counts registered,

σ_{Int}^2 is the variance associated with any interfering counts registered,

$\beta_{M,I,G}$ is the branching ratio, or the intensity, associated with decay mode M of radioisotope I of gas G,

$\varepsilon_{M,I,G}$ is the spectrometer detection efficiency associated with decay mode M of radioisotope I of gas G, and

V_{Air} is the volume of gas G counted divided by the volumetric fraction of gas G in atmospheric air.

For a spectrometers that operates in a coincidence mode the expression for the MDC must be expanded to include two branching ratio terms—one for decay mode M_1 and one for decay mode M_2—and two detection efficiency terms—where again one is for decay mode M_1 and one is for decay mode M_2—so that the product $\beta_{M,I,G} \cdot \varepsilon_{M,I,G}$ that appears in Equation 2.1.3.4.1 becomes $\beta_{M_1,I,G} \cdot \varepsilon_{M_1,I,G} \cdot \beta_{M_2,I,G} \cdot \varepsilon_{M_2,I,G}$.

At this point it should be noted that the term that appears in parenthesis in the numerator of Equation 2.1.3.4.1 is the expression for the detection limit. The detection limit is one of several radiation counting statistics decision limit concepts that are developed in the next section.

Additionally, note that spectrometers with smaller MDCs are more sensitive, meaning they are able to detect smaller activity concentrations. It is therefore desirable for the spectrometers employed by the verification regime of the CTBT to have small MDCs because spectrometers that are capable of detecting smaller concentrations of radioactive noble gases are able to detect more subtle indications of nuclear explosions.

Reviewing Equation 2.1.3.4.1 reveals that there are several things that may practically be done to reduce a spectrometer's MDCs:

(1) The spectrometer should be designed and operated so that the number of background counts and the number of interference counts registered is minimized (*i.e.* minimize the σ_{BG}^2 and σ_{Int}^2 terms, which are proportional to the number of background and interference counts registered, respectively).

(2) Activity concentrations should be evaluated using count data attributable to radioisotope decay modes with large branching ratios (*i.e.* maximize the $\beta_{M,I,G}$ terms(s)).

(3) Activity concentrations should be evaluated using count data attributable to radioisotope decay modes for which the spectrometer detection efficiencies are high (*i.e.* maximize the $\varepsilon_{M,I,G}$ term(s)).

(4) Activity concentrations should be evaluated using large atmospheric air sample volumes (*i.e.* maximize the V_{Air} term).

Finally, note that a selection of radioxenon MDCs for the ARIX [52], ARSA [54], SAUNA [57], and SPALAX [58] systems currently employed by the verification regime of the CTBT are presented in Table 1.2 in Section 1.7.2. The MDCs for ^{133}Xe are all on the order of about 1.0 mBq-m^{-3}.

2.1.4 Radiation Counting Statistics and Decision Limits

As mentioned in Section 2.1.3.3, peak area estimation methods used to develop spectrometer detection efficiency calibrations are somewhat more complicated than the peak mean and peak width estimation methods commonly used to develop spectrometer linearity and resolution calibrations. The peak area estimation method described in this section is an expanded form of the peak area estimation method prescribed by Gilmore and Hemingway [69]. The expanded form of the peak area estimation method described here is more readily applicable to some of the X-ray peaks found in the spectral data sets acquired by the XIA LLC Si-PIN diode spectrometer prototype because it allows for different numbers of channels to be included in the background regions on the low-energy and high-energy sides of the X-ray peaks.

Consider the peak shown in Figure 2.13. Evaluating the area of this peak is a three step process. The first step involves evaluating the area of the background directly underneath the peak. This area is highlighted using the symbol B in Figure 2.13. Because the area directly underneath the peak cannot be evaluated directly, it must be estimated from the areas associated with the background regions on both the low-energy and high-energy sides of the peak [69]. These areas are highlighted using the symbols B_L and B_U in Figure 2.13. The area associated with the lower background region on the low-energy side of the peak may be calculated as

$$B_L = \sum_{i=L-m_L}^{L-1} C_i \qquad 2.1.4.1$$

and the area associated with the upper background region on the high-energy side of the peak may be calculated as

$$B_U = \sum_{i=U+1}^{U+m_U} C_i. \qquad 2.1.4.2$$

Where: C_i is the number of counts in channel i,

L is the channel that defines the low-energy boundary of the peak,

m_L is the number of channels associated with the lower background region on the low-energy side of the peak,

B_L is the area associated with the lower background region on the low-energy side of the peak,

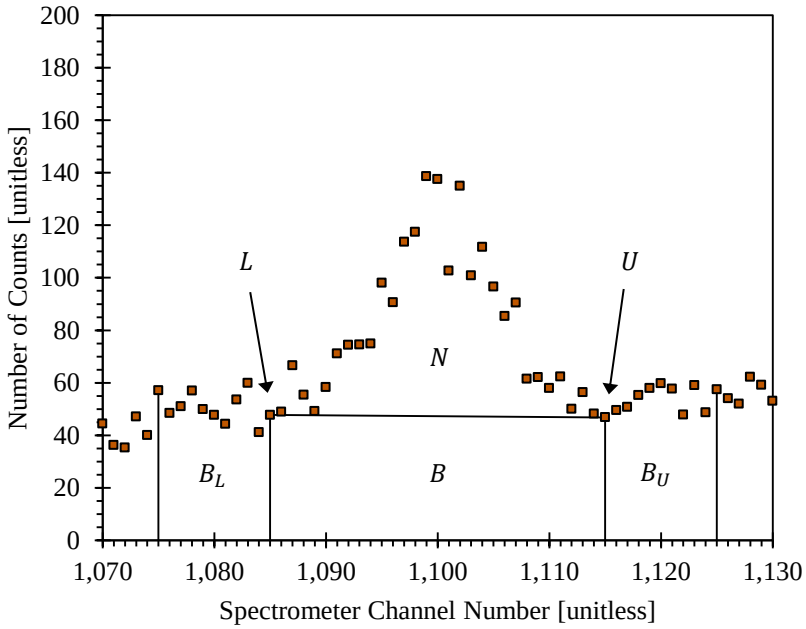

Figure 2.13: A peak from a hypothetical spectral data set.

U is the channel that defines the high-energy boundary of the peak,

m_U is the number of channels associated with the upper background region on the high-energy side of the peak, and

B_U is the area associated with the upper background region on the high-energy side of the peak.

The area of the background region directly underneath the peak is then estimated by calculating the number of counts per channel in the lower and upper background regions, calculating the average number of counts over both the lower and upper background regions, and then multiplying the average by the number of channels associated with the peak as follows:

$$B = \frac{(U - L + 1)}{2} \cdot \left(\frac{B_L}{m_L} + \frac{B_U}{m_U}\right). \qquad 2.1.4.3$$

Where:B is the area of the background region directly underneath the peak and

the quantity $U - L + 1$ represents the number of channels associated with the peak.

The variance associated with the background region directly underneath the peak, σ_B^2, may be calculated as follows:

$$\sigma_B^2 = \frac{B_L \cdot (U - L + 1)^2}{4 \cdot m_L^2} + \frac{B_U \cdot (U - L + 1)^2}{4 \cdot m_U^2}. \qquad 2.1.4.4$$

The next step is to calculate the gross area of the peak. This area, which is the union of the areas highlighted by the symbols B and N in Figure 2.13, may be calculated by simply adding up the number of counts in all of the channels associated with the peak:

$$G = \sum_{i=L}^{U} C_i. \qquad 2.1.4.5$$

Because radioactive decay is a binomial process and Poisson statistics are applicable in the realm of radiation counting statistics [69], the variance associated with the gross peak area is equal to the nominal gross peak area. That is:

$$\sigma_G^2 = G = \sum_{i=L}^{U} C_i. \qquad 2.1.4.6$$

Now, for the third step, the peak area of interest, the net peak area, N, may be evaluated by subtracting the area of the background directly underneath the peak, B, from the gross peak area, G, as follows:

$$N = G - B = G - \frac{(U - L + 1)}{2} \cdot \left(\frac{B_L}{m_L} + \frac{B_U}{m_U}\right). \qquad 2.1.4.7$$

Note that when the quantity $U - L + 1$ is denoted simply by the symbol n and when the number of channels associated with the lower background region is set equal to the number of channels associated with the upper background region and both quantities are denoted simply by the symbol m then Equation 2.1.4.7 reduces to the neat peak area equation developed by Gilmore and Hemingway [69]:

$$N = G - \frac{n \cdot (B_L + B_U)}{2 \cdot m}. \qquad 2.1.4.8$$

The variance associated with the net number of counts may be calculated as the sum of the variance associated with the gross peak area, σ_G^2, and the variance associated with the background directly underneath the peak, σ_B^2:

$$\sigma_N^2 = \sigma_G^2 + \sigma_B^2 = G + \frac{B_L \cdot (U - L + 1)^2}{4 \cdot m_L^2} + \frac{B_U \cdot (U - L + 1)^2}{4 \cdot m_U^2} \qquad 2.1.4.9$$

Note again that when the quantity $U - L + 1$ is denoted simply by the symbol n and when m_L and m_U are both denoted simply by the symbol m then Equation 2.1.4.9 reduces to the neat peak area variance equation developed by Gilmore and Hemingway [69]:

$$\sigma_N^2 = G + \frac{n^2 \cdot (B_L + B_U)}{4 \cdot m^2} \qquad 2.1.4.10$$

It should also be noted that rearranging Equation 2.1.4.7 for G and substituting into Equation 2.1.4.9 yields the following expression for σ_N^2:

$$\sigma_N^2 = N + \frac{(U - L + 1)}{2} \cdot \left(\frac{B_L}{m_L} + \frac{B_U}{m_U}\right) + \frac{B_L \cdot (U - L + 1)^2}{4 \cdot m_L^2} + \frac{B_U \cdot (U - L + 1)^2}{4 \cdot m_U^2}. \qquad 2.1.4.11$$

Simplifying Equation 2.1.4.11 produces the following expression for σ_N^2:

$$\sigma_N^2 = N + \frac{B_L \cdot (U - L + 1)}{2 \cdot m_L} \cdot \left(1 + \frac{U - L + 1}{2 \cdot m_L}\right) \ldots + \frac{B_U \cdot (U - L + 1)}{2 \cdot m_U} \cdot \left(1 + \frac{U - L + 1}{2 \cdot m_U}\right). \qquad 2.1.4.12$$

This form of the expression for σ_N^2 will be useful shortly when some of the decision limit concepts are developed.

Now, having developed a method of estimating the areas of the peaks in a spectral data set, it is also important to develop several decision limit concepts that may be used to answer the following questions regarding the number of counts in a peak: (1) Is the number of counts in a given peak statistically significant relative to the number of counts in the background region directly underneath the peak? (2) In the case where the number of counts in the peak is not statistically significant relative to the number of background counts, what is a reasonable estimate at the upper limit associated with the number of counts in the peak? (3) What is the minimum number of counts that can be detected by a spectrometer with a given confidence or certainty? Decision limits exist to support systematically answering each of these questions. The decision limits developed here are expanded forms of the decision limits developed by Gilmore and Hemingway [69].

The decision limit used to address the first question is known as the critical limit. Mathematically, the critical limit is defined as follows:

$$L_C = k_\alpha \cdot \sigma_0. \qquad 2.1.4.13$$

Where: L_C is the critical limit,

k_α is a factor selected so that a certain confidence or certainty may be ascribed to the calculated critical limit, and

σ_0 is the standard deviation associated with the distribution describing the net number of counts in a peak when there are zero net counts in the peak.

Having defined the critical limit mathematically, it is often easiest to develop a conceptual understanding of the critical limit using an illustration. So, with that in mind, imagine that a count is repeated many times. The number of counts recorded would vary

each time the count was repeated and would be normally distributed about some mean number of counts as illustrated below in Figure 2.14. If the net number of counts was known to be zero (*i.e.* if all the counts were known to be attributable only to background sources) then the mean number of net counts recorded would be zero, but half of the net counts recorded would be less than zero and half of the net counts recorded would be greater than zero. Recording a net number of counts greater than zero could be taken as an indication that there was a source present contributing counts above background, but again, in this hypothetical scenario the net number of counts is known to be zero. Thus it is clear that in order to be sure that the net number of counts recorded is truly greater than zero the net number of counts recorded must not only be greater than zero, but also greater than some non-zero threshold. This threshold, the so-called critical limit, is typically set to some number of standard deviations above the mean associated with the distribution describing the net number of counts recorded when the net number of counts is assumed to be equal to zero. The standard deviation associated with this distribution is equal to the square-root of Equation 2.1.4.12 with N set equal to zero, as follows:

$$\sigma_0 = \sqrt{\sigma^2_{N=0}} = \left[(N=0) + \frac{B_L \cdot (U-L+1)}{2 \cdot m_L} \cdot \left(1 + \frac{U-L+1}{2 \cdot m_L}\right) \ldots \right. \\ \left. + \frac{B_U \cdot (U-L+1)}{2 \cdot m_U} \cdot \left(1 + \frac{U-L+1}{2 \cdot m_U}\right)\right]^{1/2}. \qquad 2.1.4.14$$

Substituting this expression for σ_0 into Equation 2.1.4.13 produces the following expression for the critical limit:

$$L_C = k_\alpha \cdot \left[\frac{B_L \cdot (U - L + 1)}{2 \cdot m_L} \cdot \left(1 + \frac{U - L + 1}{2 \cdot m_L}\right) \ldots \right.$$
$$\left. + \frac{B_U \cdot (U - L + 1)}{2 \cdot m_U} \cdot \left(1 + \frac{U - L + 1}{2 \cdot m_U}\right)\right]^{1/2}. \qquad 2.1.4.15$$

The numerical value assigned to k_α establishes the confidence or certainty that may be ascribed to the critical limit. The confidence level associated with the critical limit becomes 90 % when k_α is set qual to 1.282, it becomes 95 % when k_α is set equal to 1.645, and it becomes 99 % when k_α is set equal to 2.326.

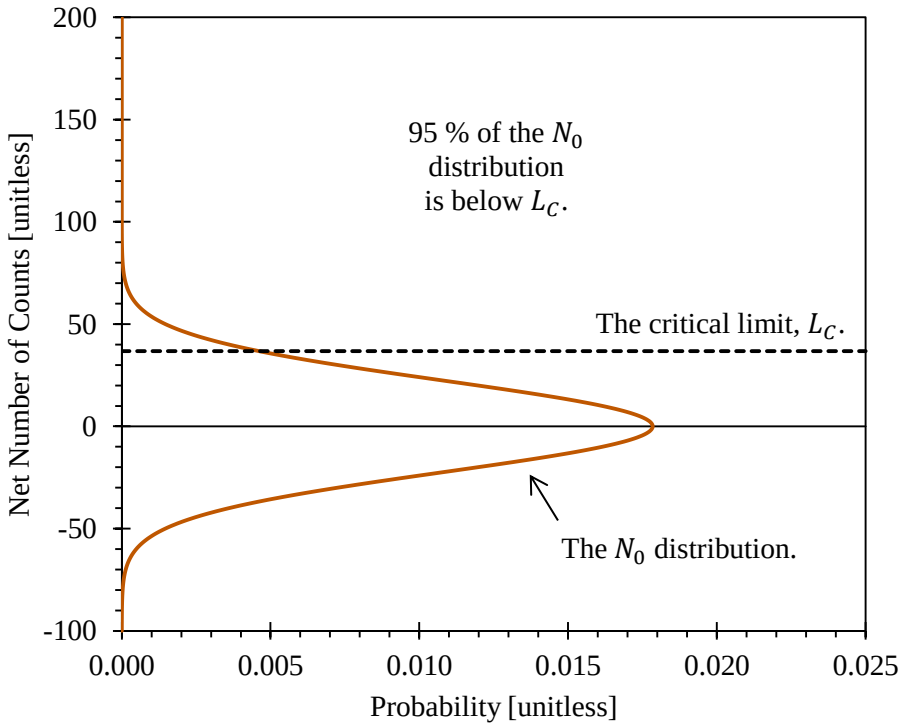

Figure 2.14: Illustration of the critical limit decision limit concept.

Imagine now that a count has been recorded, the number of counts recorded has been determined to be statistically insignificant relative to background based on the calculated critical limit, and thus it is assumed that there are no non-background sources present. Now, imagine that this assumption is wrong and that a non-background source is in fact present and contributing counts. Addressing the second decision limit question posed previously effectively allows an upper limit to be placed on the number of counts attributable to a source that is erroneously assumed to be not present. This decision limit is called the upper limit and is defined mathematically as follows:

$$L_U = N + k_\alpha \cdot \sigma_N. \qquad 2.1.4.16$$

Where:L_U is the upper limit and

σ_N is the standard deviation associated with the distribution describing the net number of counts in a peak.

As with the critical limit, a conceptual understanding of the upper limit is probably best developed using an illustration. So, with this in mind, imagine that a count is repeated many times. In this case, as stated previously, a non-background source is not only known to be present, but the source is known to contribute a mean number of counts that is exactly equal to the critical limit as illustrated in Figure 2.15. In half of the counts the number of counts contributed by the source would be less than the critical limit and thus the counts would be erroneously declared to be statistically insignificant relative to background. The upper limit effectively makes it such that even if the decision to declare the counts to be statistically insignificant is incorrect, the number of counts attributable to

the source is still known, to a certain confidence or certainty, to be less than some maximum number of counts equal to the upper limit.

The σ_N term that appears in Equation 2.1.4.16 is the square root of Equation 2.1.4.12, which is an expression for the variance associated with the distribution describing the net number of counts. Plugging the square-root of Equation 2.1.4.12 into Equation 2.1.4.16 produces the following expression for the upper limit:

$$L_U = N + k_\alpha \cdot \left[N + \frac{B_L \cdot (U - L + 1)}{2 \cdot m_L} \cdot \left(1 + \frac{U - L + 1}{2 \cdot m_L} \right) \ldots \right.$$

$$\left. + \frac{B_U \cdot (U - L + 1)}{2 \cdot m_U} \cdot \left(1 + \frac{U - L + 1}{2 \cdot m_U} \right) \right]^{1/2}. \qquad 2.1.4.17$$

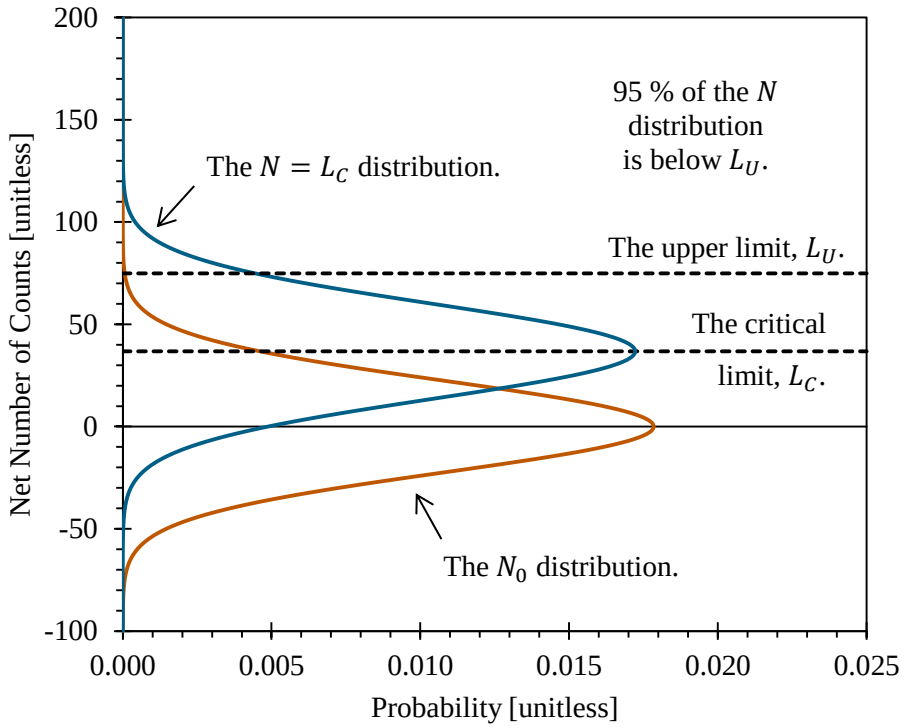

Figure 2.15: Illustration of the upper limit decision limit concept.

The third and final decision limit concept developed here is the detection limit. The detection limit varies from the critical limit and upper limit decision limit concepts developed above in that it is an *a priori* decision limit as opposed to an *a posteriori* decision limit. Recall that it is the detection limit that is referenced where the Minimum Detectable Concentration (MDC) spectrometer performance metric concept is developed in Section 2.1.3.4. The detection limit provides a means of estimating the minimum number of counts that a spectrometer should be expected to be capable of detecting. Mathematically, the detection limit is defined as follows:

$$L_D = k_\alpha \cdot \sigma_0 + k_\alpha \cdot \sigma_{N=L_D}. \qquad 2.1.4.18$$

Where: L_D is the detection limit,

σ_0 is the standard deviation associated with the distribution describing the net number of counts in a peak when there are zero net counts in the peak, and

$\sigma_{N=L_D}$ is the standard deviation associated with the distribution describing the net number of counts in a peak when the net number of counts in the peak is equal to the detection limit.

In order to further develop the expression for the detection limit, a better expression for $\sigma_{N=L_D}$ is needed. A better expression for $\sigma_{N=L_D}$ may be developed by first recalling that Equation 2.1.4.9 states that the variance associated with the net number of counts in a peak, σ_N^2, may be calculated as follows:

$$\sigma_N^2 = \sigma_G^2 + \sigma_B^2. \qquad 2.1.4.19$$

Now also recall that Equation 2.1.4.6 states that the variance associated with the gross number of counts in a peak, σ_G^2, is simply equal to the gross number of counts in the peak, G:

$$\sigma_G^2 = G. \qquad 2.1.4.20$$

Furthermore, rearranging Equation 2.1.4.7 reveals that G is equal to the sum of B and N:

$$G = B + N. \qquad 2.1.4.21$$

Substituting Equation 2.1.4.21 into Equation 2.1.4.20 produces the following expression for σ_G^2:

$$\sigma_G^2 = B + N. \qquad 2.1.4.22$$

In the case of a simple count the variance associated with the background, σ_B^2, is simply equal to the number of background counts (Poisson statistics are applicable [69]):

$$\sigma_B^2 = B. \qquad 2.1.4.23$$

Substituting Equations 2.1.4.22 and 2.1.4.23 into Equation 2.1.4.19 produces the following expression for σ_N^2:

$$\sigma_N^2 = (B + N) + (B) = 2 \cdot B + N. \qquad 2.1.4.24$$

In this case the net number of counts, N, is known to be equal to the detection limit, L_D, and Equation 2.1.4.24 becomes:

$$\sigma_{N=L_D}^2 = 2 \cdot B + L_D. \qquad 2.1.4.25$$

Recognizing that for a simple count the product $2 \cdot B$ is equal to σ_0^2 [69] and by substituting this identity into Equation 2.1.4.25 and taking the square root the following expression for $\sigma_{N=L_D}$ may be produced:

$$\sigma_{N=L_D} = \sqrt{\sigma_0^2 + L_D}. \qquad 2.1.4.26$$

Substituting the above expression for $\sigma_{N=L_D}$ into Equation 2.1.4.18 and simplifying produces the following expression for the detection limit:

$$L_D = k_\alpha^2 + 2 \cdot k_\alpha \cdot \sigma_0. \qquad 2.1.4.27$$

This basic expression for the detection limit may be developed one step further by substituting in an appropriate expression for σ_0. As stated previously, σ_0 takes the following form if the detection limit is developed using count data from a simple count:

$$\sigma_0 = \sqrt{2 \cdot B}. \qquad 2.1.4.28$$

Substituting this expression for σ_0 into Equation 2.1.4.27 produces the following expression for the detection limit:

$$L_D = k_\alpha^2 + 2 \cdot \sqrt{2} \cdot k_\alpha \cdot \sqrt{B}. \qquad 2.1.4.29$$

When the detection limit is developed using count data from a peak in a spectral data set the expression for σ_0 is given by Equation 2.1.4.14 and the expression for the detection limit is as follows:

$$L_D = k_\alpha^2 + 2 \cdot k_\alpha \cdot \left[\frac{B_L \cdot (U - L + 1)}{2 \cdot m_L} \cdot \left(1 + \frac{U - L + 1}{2 \cdot m_L}\right) \ldots + \frac{B_U \cdot (U - L + 1)}{2 \cdot m_U} \cdot \left(1 + \frac{U - L + 1}{2 \cdot m_U}\right)\right]^{1/2}. \qquad 2.1.4.30$$

The detection limit decision limit concept developed above is illustrated in Figure 2.16.

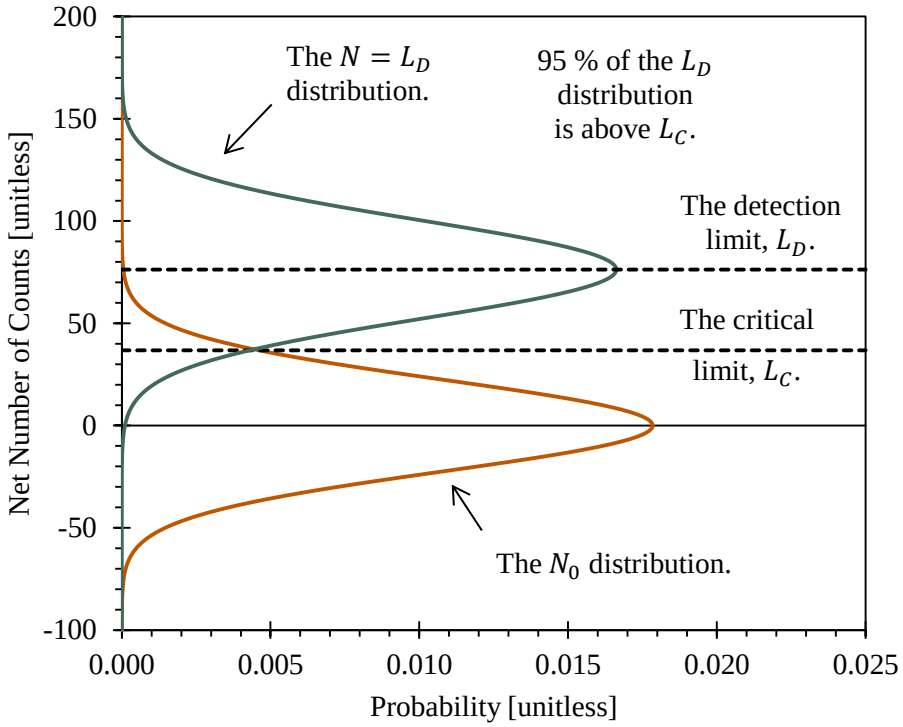

Figure 2.16: Illustration of the detection limit decision limit concept.

2.1.5 The WiPFA Peak-Fitting Algorithm

In order to develop good spectrometer linearity, resolution, and detection efficiency characterizations it is first necessary to extract good peak mean, peak width, and peak area estimates from spectral data sets acquired by the spectrometer to be characterized. Sections 2.1.3.1, 2.1.3.2, and 2.1.4 describe some simple methods that may be used to develop the required peak mean, peak width, and peak area estimates. These methods may be used to produce satisfactory results in many cases. However, a number of issues were encountered when these methods were applied to the spectral data sets acquired by the XIA LLC Si-PIN diode spectrometer prototype.

First, the peak mean estimation method prescribed by Gilmore and Hemingway [69] provides only a crude estimate of the true peak mean and is very sensitive to statistical aberrations. Furthermore, while the method may be readily applied to strong peaks it was somewhat difficult to apply to some of the subtle peaks in the spectral data sets acquired by the XIA LLC Si-PIN diode spectrometer prototype.

As for the peak width estimation method, it produced relatively good results when applied to Regions Of Interest (ROIs) containing only a single peak. However, it was not possible to apply it to the peaks of multiplets because the required C_H, C_A, C_B, C_C, and C_D estimates (see Equations 2.1.3.2.2 and 2.1.3.2.3) could not be developed for peaks in multiplets. Another issue associated with the peak mean and peak width estimation methods prescribed by Gilmore and Hemingway is there is not a straight forward way to quantify the uncertainties associated with the peak mean or peak width estimates.

The peak area estimation method prescribed by Gilmore and Hemingway [69] produced good peak area estimates and peak area uncertainty estimates and the method was thus used a number of times to estimate the area of singlets in support the XIA LLC Si-PIN diode spectrometer prototype detection efficiency characterization effort. However, like the peak width estimation method, the peak area estimation method prescribed by Gilmore and Hemingway can only be applied to ROIs containing a single peak. This was an issue because the majority of the low-energy photon peaks of interest in the spectral data sets acquired by the XIA LLC Si-PIN diode spectrometer prototype were components of multiplets.

Given the issues associated with the peak mean, peak width, and peak area estimation methods described in Section 2.1.3.1, 2.1.3.2, and 2.1.4, a novel peak-fitting algorithm was developed specifically to support the XIA LLC Si-PIN diode spectrometer prototype characterization efforts documented herein. The algorithm, which is referred to herein as Wilson's Peak-Fitting Algorithm, or the WiPFA peak-fitting algorithm, is a robust, easy-to-use peak-fitting algorithm capable of fitting expressions to spectral data set regions of interest composed of any number of Gaussian-shaped peaks in a totally unconstrained manner. The WiPFA peak-fitting algorithm develops uncertainty estimates for each of its peak parameter estimates using a Monte Carlo method that utilizes the fact that radioactive decay is viewed as a binomial process to which the rules of Poisson statistics are applicable [69]. Additionally, the WiPFA peak-fitting algorithm develops decision limits applicable to each of the individual peaks in a given ROI in a manner consistent with the methodology prescribed by Currie [70].

The details associated with the workings of the WiPFA peak fitting algorithm are presented in Appendix A. Only an example of a curve fit to a ^{133}Ba multiplet containing two peaks is described here. The peaks in the ^{133}Ba multiplet shown in Figure 2.17 are the 79.6142 and 80.9979 keV ^{133}Ba gamma-ray peaks [60]. The multiplet was extracted from a spectral data set acquired by the XIA LLC Si-PIN diode spectrometer prototype. As illustrated by the figure, the curve fits appear to fit the data points associated with the ROI quite well, qualitatively speaking. Quantitatively speaking, the peak means are estimated to be 2,093.3 ± 0.6 (0.03 %) and 2,128.7 ± 0.1 (0.005 %), respectively. Note that the fitted peak means are channel numbers and are unitless. The ratio of the

larger peak mean to the smaller peak mean is 1.017. This ratio is in excellent agreement with the ratio of the larger ^{133}Ba gamma-ray energy to the smaller ^{133}Ba gamma-ray energy—80.9979 keV / 79.6142 keV = 1.017.

The ^{133}Ba gamma-ray peak widths are estimated to be about 8.87 ± 0.62 (6.9 %) and 8.13 ± 0.09 (1.1 %), respectively. The peak widths differ from one another by about 9 %. Adjacent peaks should have comparable peak widths, so the fact that the peak width estimates generated by the WiPFA peak-fitting algorithm are in relatively good agreement with one another provides some assurance that the peak width estimates generated by the WiPFA algorithm are reasonable.

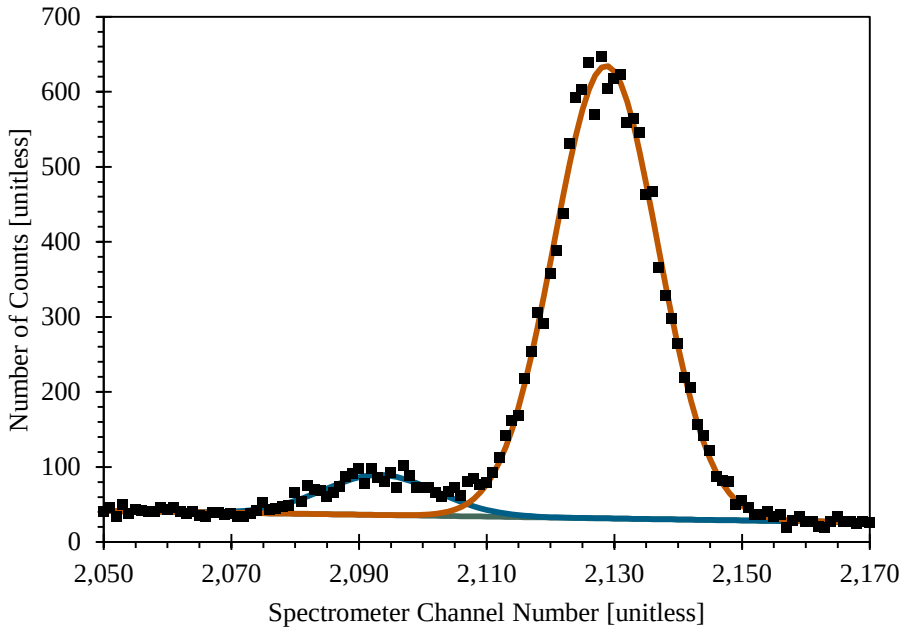

Figure 2.17: The WiPFA peak-fitting algorithm was used to generate curve fits to the 79.6142 and 80.9979 keV gamma-ray peaks in a ^{133}Ba spectral data set.

As for the peak areas, they are estimated to be about 1,184 ± 89 (7.5 %) and 12,300 ± 132 (1.1 %), respectively. The ratio of the number of counts registered in the larger peak to the number of counts registered in the smaller peak is about 10.4, which is about 16.4 % lower than might have been expected based on the branching ratios associated with the 79.6142 and 80.9979 keV ^{133}Ba gamma-rays. However, the peak area estimates generated by the WiPFA algorithm seem to be reasonably good.

2.1.6 Simple Linear and Multiple Linear Regression Methods

This section provides the mathematical framework associated with the simple linear and multiple linear regression methods used throughout this dissertation to fit curves to peak mean, peak width, and spectrometer detection efficiency data sets. The simple linear and multiple linear regression methods described herein are the methods described by Hayter [73].

2.1.6.1 The Simple Linear Regression Method

Spectrometer peak mean and peak width data sets may be viewed as sets of n paired observations of the form $(x_1, y_1), (x_2, y_2), \ldots, (x_{n-1}, y_{n-1}), (x_n, y_n)$. In the case of a peak mean data set, the x_i terms represent the channel numbers associated with the peak means and the y_i terms represent the energies associated with the radionuclide decay modes responsible for generating the peaks in the spectral data sets. In the case of a peak width data set, the x_i terms represent the energies associated with the radionuclide decay

modes and the y_i terms represent the peak widths. As illustrated in Figures 2.9 and 2.11, the energies associated with the radionuclide decay modes and the peak widths tend to increase in a fairly linear manner as their respective explanatory variables increase. When this is the case, a simple linear regression model may be used to describe the relationship between the dependent variables (*i.e.* the energies associated with the radionuclide decay modes and the peak widths) and the explanatory variables [73]. The simple linear regression model is as follows [73]:

$$y_i = \beta_0 + \beta_1 \cdot x_i + \epsilon_i. \qquad 2.1.6.1.1$$

Where: y_i is an observed value of the dependent variable,

β_0 is referred to as the intercept parameter,

β_1 is referred to as the slope parameter,

x_i is an observed value of the explanatory variable, and

ϵ_i is an error term that describes the vertical deviation between the regression line and paired observation i.

The regression line described by Equation 2.1.6.1.1 may be thought of as the line that is "closest" to the paired observations $(x_1, y_1), (x_2, y_2), \dots, (x_{n-1}, y_{n-1}), (x_n, y_n)$. Here, the line that is "closest" to the paired observations will be defined as the one that minimizes the sum of squares of the error terms, ϵ_i [73]. This may be expressed mathematically as follows:

$$\underset{\beta_0,\beta_1}{\operatorname{argmin}} \sum_{i=1}^{n} \epsilon_i^2 \,(x_i, y_i, \beta_0, \beta_1) = \underset{\beta_0,\beta_1}{\operatorname{argmin}} \sum_{i=1}^{n} \big(y_i - (\beta_0 + \beta_1 \cdot x_i)\big)^2. \qquad 2.1.6.1.2$$

The sum of the squares of the error terms is often given the symbol Q, and, as indicated by Equation 2.1.6.1.2, it is the β_0 and β_1 values that minimize Q that are sought here. Estimates of the β_0 and β_1 values, $\hat{\beta}_0$ and $\hat{\beta}_1$, may be evaluated by taking the partial derivatives of Q with respect to β_0 and β_1 and setting the resulting expressions equal to zero. Doing this reveals that the estimate at the slope parameter, $\hat{\beta}_1$, is

$$\hat{\beta}_1 = \frac{n \cdot \sum_{i=1}^{n} x_i \cdot y_i - \sum_{i=1}^{n} x_i \cdot \sum_{i=1}^{n} y_i}{n \cdot \sum_{i=1}^{n} x_i^2 - (\sum_{i=1}^{n} x_i)^2} \qquad 2.1.6.1.3$$

and the estimate at the intercept parameter, $\hat{\beta}_0$, is

$$\hat{\beta}_0 = \frac{\sum_{i=1}^{n} y_i}{n} - \hat{\beta}_1 \cdot \frac{\sum_{i=1}^{n} x_i}{n} = \bar{y} - \hat{\beta}_1 \cdot \bar{x}. \qquad 2.1.6.1.4$$

Where: $\bar{x}$ is the mean value taken by the explanatory variable associated with the paired observations and

$\bar{y}$ is the mean value taken by the dependent variable associated with the paried observations.

Note that the numerator of Equation 2.1.6.1.3 is often simplified as follows

$$n \cdot \sum_{i=1}^{n} x_i \cdot y_i - \sum_{i=1}^{n} x_i \cdot \sum_{i=1}^{n} y_i = \sum_{i=1}^{n} x_i \cdot y_i - n \cdot \bar{x} \cdot \bar{y} = \sum_{i=1}^{n} (x_i - \bar{x}) \cdot (y_i - \bar{y}) \qquad 2.1.6.1.5$$

and given the symbol S_{XY} [73]. Similarly, the denominator of Equation 2.1.6.1.3 is often rewritten as

$$n \cdot \sum_{i=1}^{n} x_i^2 - \left(\sum_{i=1}^{n} x_i\right)^2 = \sum_{i=1}^{n} x_i^2 - n \cdot \bar{x}^2 = \sum_{i=1}^{n} (x_i - \bar{x})^2 \qquad 2.1.6.1.6$$

and given the symbol S_{XX} [73].

An estimate of the error variance, $\hat{\sigma}^2$, associated with the fitted regression line defined by $\hat{\beta}_0$ and $\hat{\beta}_1$ may be evaluated as follows [73]:

$$\hat{\sigma}^2 = \frac{\sum_{i=1}^{n}\left(y_i - \left(\hat{\beta}_0 + \hat{\beta}_1 \cdot x_i\right)\right)^2}{n-2} = \frac{\sum_{i=1}^{n} y_i^2 - \hat{\beta}_0 \cdot \sum_{i=1}^{n} y_i - \hat{\beta}_1 \cdot \sum_{i=1}^{n} x_i \cdot y_i}{n-2}. \quad 2.1.6.1.7$$

This error variance estimate may be used to develop a $1-\alpha$ confidence level two-sided confidence interval specific to an expected value of the dependent variable evaluated at a particular value of the explanatory variable, x^*, as follows [73]:

$$y|_{x^*} \in \left(\hat{\beta}_0 + \hat{\beta}_1 \cdot x^* - t_{\alpha/2,n-2} \cdot \hat{\sigma} \cdot \sqrt{\frac{1}{n} + \frac{(x^* - \bar{x})^2}{S_{XX}}}, \ldots \right. \quad 2.1.6.1.8$$

$$\left. \hat{\beta}_0 + \hat{\beta}_1 \cdot x^* + t_{\alpha/2,n-2} \cdot \hat{\sigma} \cdot \sqrt{\frac{1}{n} + \frac{(x^* - \bar{x})^2}{S_{XX}}} \right).$$

Where: $1-\alpha$ denotes the desired confidence level (usually 95 %) and

$t_{\alpha/2,n-2}$ is a critical point of the t-Distribution corresponding to the desired confidence level and $n-2$ degrees of freedom.

Notice that as the number of paired observations, n, used to develop the fitted regression line tends towards infinity the error variance estimate associated with the fitted regression line tends towards zero and the upper and lower bounds of the confidence interval associated with the fitted regression line converge so that the fitted regression line becomes an increasingly accurate estimate of the true regression line [73].

The error variance may also be used to develop a $1-\alpha$ confidence level two-sided prediction interval as follows [73]:

$$y|_{x^*} \in \left(\hat{\beta}_0 + \hat{\beta}_1 \cdot x^* - t_{\alpha/2,n-2} \cdot \hat{\sigma} \cdot \sqrt{\frac{n+1}{n} + \frac{(x^* - \bar{x})^2}{S_{XX}}}, \ldots \right.$$

$$\left. \hat{\beta}_0 + \hat{\beta}_1 \cdot x^* + t_{\alpha/2,n-2} \cdot \hat{\sigma} \cdot \sqrt{\frac{n+1}{n} + \frac{(x^* - \bar{x})^2}{S_{XX}}} \right). \quad 2.1.6.1.9$$

Note that the upper and lower bounds associated with a predication interval are always outside of the upper and lower bounds associated with a confidence interval. This is because the prediction interval accounts for both the uncertainty in the regression line at x^* and the variability associated with the error variance, $\hat{\sigma}^2$, while the confidence interval only accounts for the uncertainty in the value of the regression line at x^*.

2.1.6.2 The Multiple Linear Regression Method

At first glance, detection efficiency data sets also appear to be sets of n paired observations of the form $(x_1, y_1), (x_2, y_2), \ldots, (x_{n-1}, y_{n-1}), (x_n, y_n)$. In this case the x_i terms represent the energies associated with the radionuclide decay modes generating the peaks in the spectral data sets and the y_i values represent the detection efficiencies. However, a review of Figure 2.12 reveals that the relationship between detection efficiency and radionuclide decay mode energy is obviously not linear and suggests that a somewhat more complicated model than the simple linear regression model described in the preceding section is needed to model the relationship between detection efficiency

and radionuclide decay mode energy. When this is the case, a multiple linear regression model may be used. The multiple linear regression model is as follows [73]:

$$y_i = \beta_0 + \beta_1 \cdot x_{1,i} + \beta_2 \cdot x_{2,i} + \cdots + \beta_k \cdot x_{k,i} + \epsilon_i. \quad 2.1.6.2.1$$

Where: y_i is an observed value of the dependent variable,

β_0 is again referred to as the intercept parameter,

β_1, β_2, and β_k are the slope parameters associated with dimensions one, two, and k, respectively,

$x_{1,i}$, $x_{2,i}$, and $x_{k,i}$ are observed values of the explanatory variables associated with dimensions one, two, and k, respectively, and

ϵ_i is an error term that describes the vertical deviation between the regression line and observation i.

The regression line described by Equation 2.1.6.2.1 may be thought of as the line that is "closest" to the observations $(x_{1,1}, x_{2,1}, \dots, x_{k,1}, y_1), (x_{1,2}, x_{2,2}, \dots, x_{k,2}, y_2), \dots (x_{1,n-1}, x_{2,n-1}, \dots, x_{k,n-1}, y_k), (x_{1,n}, x_{2,n}, \dots, x_{k,n}, y_n)$. Here, the line that is "closest" to the observations will be defined as the one that minimizes the sum of squares of the error terms, ϵ_i [73]. This may be expressed mathematically as follows:

$$\underset{\beta_0,\beta_1,\beta_2,\dots,\beta_k}{\operatorname{argmin}} \sum_{i=1}^{n} \epsilon_i^2 (x_{1,i}, x_{2,i}, \dots, x_{k,i}, y_i, \beta_0, \beta_1, \beta_2, \dots, \beta_k) \dots$$

$$= \underset{\beta_0,\beta_1,\beta_2,\dots,\beta_k}{\operatorname{argmin}} \sum_{i=1}^{n} \left(y_i - (\beta_0 + \beta_1 \cdot x_{1,i} + \beta_2 \cdot x_{2,i} + \cdots + \beta_k \cdot x_{k,i})\right)^2. \quad 2.1.6.2.2$$

The sum of the squares of the error terms is often given the symbol Q, and, as indicated by Equation 2.1.6.2.2, it is the β_0 and β_1 through β_k values that minimize Q that are sought here. As was done with the simple linear regression method described in the previous section, estimates of the β_0 and β_1 through β_k values, $\hat{\beta}_0$ and $\hat{\beta}_1$ through $\hat{\beta}_k$, may be evaluated by taking the partial derivatives of Q with respect to β_0 and β_1 through β_k and setting the resulting expressions equal to zero. Doing this produces a set of $k+1$ simultaneous equations which have the following forms:

Form one (where the partial derivative of Q was evaluated with respect to β_0) [73]:

$$\sum_{i=1}^{n} x_{1,i} \cdot y_i = \beta_0 \cdot \sum_{i=1}^{n} x_{1,i} + \beta_1 \cdot \sum_{i=1}^{n} x_{1,i}^2 + \beta_2 \cdot \sum_{i=1}^{n} x_{1,i} \cdot x_{2,i} \ldots + \cdots + \beta_k \cdot \sum_{i=1}^{n} x_{1,i} \cdot x_{k,i}. \quad 2.1.6.2.3$$

Form two (where the partial derivative of Q was evaluated with respect to β_1) [73]:

$$\sum_{i=1}^{n} x_{2,i} \cdot y_i = \beta_0 \cdot \sum_{i=1}^{n} x_{2,i} + \beta_1 \cdot \sum_{i=1}^{n} x_{2,i} \cdot x_{1,i} + \beta_2 \cdot \sum_{i=1}^{n} x_{2,i}^2 \ldots + \cdots + \beta_k \cdot \sum_{i=1}^{n} x_{2,i} \cdot x_{k,i}. \quad 2.1.6.2.4$$

Form $k+1$ (where the partial derivative of Q was evaluated with respct to β_{k+1}) [73]:

$$\sum_{i=1}^{n} x_{k,i} \cdot y_i = \beta_0 \cdot \sum_{i=1}^{n} x_{k,i} + \beta_1 \cdot \sum_{i=1}^{n} x_{k,i} \cdot x_{1,i} + \beta_2 \cdot \sum_{i=1}^{n} x_{k,i} \cdot x_{2,i} \ldots + \cdots + \beta_k \cdot \sum_{i=1}^{n} x_{k,i}^2. \quad 2.1.6.2.5$$

The expressions of the forms given by Equations 2.1.6.2.3 through 2.1.6.2.5 may be solved to obtain the intercept parameter estimate, $\hat{\beta}_0$, and the estimates of each of the slope parameters $\hat{\beta}_1$ through $\hat{\beta}_k$. However, becaue the process of solving the above equations by hand is quite tedious, Equation 2.1.6.2.1 is often rewritten as a matrix algebra problem as follows:

$$\boldsymbol{Y} = \boldsymbol{X} \cdot \boldsymbol{\beta} + \boldsymbol{\epsilon}. \qquad 2.1.6.2.6$$

Where: $\boldsymbol{Y}$ is an $n \times 1$ vector containing the observed dependent variables values y_1 through y_n,

$\boldsymbol{X}$ is an $n \times (k+1)$ matrix containing the observed explanatory variable values x_1 through x_n,

$\boldsymbol{\beta}$ is a $(k+1) \times 1$ vector containing the estimates of the intercept parameter, $\hat{\beta}_0$, and each of the slope parameters $\hat{\beta}_1$ through $\hat{\beta}_k$, and

$\boldsymbol{\epsilon}$ is an $n \times 1$ vector containing the error terms ϵ_1 through ϵ_n.

Equation 2.1.6.2.2 is often rewritten as

$$\underset{\boldsymbol{\beta}}{\operatorname{argmin}} \sum_{i=1}^{n} \epsilon_i^2(\boldsymbol{X}, \boldsymbol{Y}, \boldsymbol{\beta}) = \underset{\boldsymbol{\beta}}{\operatorname{argmin}} (\boldsymbol{Y} - \boldsymbol{X} \cdot \boldsymbol{\beta})' \cdot (\boldsymbol{Y} - \boldsymbol{X} \cdot \boldsymbol{\beta}) \qquad 2.1.6.2.7$$

and the set of $k+1$ simultaneous equations defined by Equations 2.1.6.2.3 through 2.1.6.2.5 may be rewritten simply as

$$\boldsymbol{X}' \cdot \boldsymbol{Y} = \boldsymbol{X}' \cdot \boldsymbol{X} \cdot \widehat{\boldsymbol{\beta}}. \qquad 2.1.6.2.8$$

Equation 2.1.6.2.8 may be rearranged and solved as follows [73]:

$$\widehat{\boldsymbol{\beta}} = (\boldsymbol{X}' \cdot \boldsymbol{X})^{-1} \cdot \boldsymbol{X}' \cdot \boldsymbol{Y}. \qquad 2.1.6.2.9$$

An estimate of the error variance, $\hat{\sigma}^2$, associated with the fitted regression line defined by the intercept and slope parameter estimates may be evaluated as follows [73]:

$$\hat{\sigma} = \frac{\sum_{i=1}^{n}(y_i - \hat{y}_i)^2}{n - k - 1}. \qquad 2.1.6.2.10$$

This estimate of the error variance may be used to develop $1 - \alpha$ confidence level two-sided confidence intervals and prediction intervals specific to an expected value of the dependent variable evaluated at a particular value of the explanatory variable, x^*. The confidence interval may be developed as follows [73]:

$$y|_{\boldsymbol{x}^*} \in \left(y|_{\boldsymbol{x}^*} - t_{\alpha/2,n-k-1} \cdot \hat{\sigma} \cdot \sqrt{\boldsymbol{x}^{*\prime} \cdot (\boldsymbol{X}' \cdot \boldsymbol{X})^{-1} \cdot \boldsymbol{x}^*}, \ldots \right. \qquad 2.1.6.2.11$$
$$\left. y|_{\boldsymbol{x}^*} + t_{\alpha/2,n-k-1} \cdot \hat{\sigma} \cdot \sqrt{\boldsymbol{x}^{*\prime} \cdot (\boldsymbol{X}' \cdot \boldsymbol{X})^{-1} \cdot \boldsymbol{x}^*}\right).$$

Similarly, the prediction interval may be developed as follows [73]:

$$y|_{\boldsymbol{x}^*} \in \left(y|_{\boldsymbol{x}^*} - t_{\alpha/2,n-k-1} \cdot \hat{\sigma} \cdot \sqrt{1 + \boldsymbol{x}^{*\prime} \cdot (\boldsymbol{X}' \cdot \boldsymbol{X})^{-1} \cdot \boldsymbol{x}^*}, \ldots \right. \qquad 2.1.6.2.12$$
$$\left. y|_{\boldsymbol{x}^*} + t_{\alpha/2,n-k-1} \cdot \hat{\sigma} \cdot \sqrt{1 + \boldsymbol{x}^{*\prime} \cdot (\boldsymbol{X}' \cdot \boldsymbol{X})^{-1} \cdot \boldsymbol{x}^*}\right).$$

These confidence and prediction intervals are analogous to the confidence and prediction intervals developed in the previous section.

2.2 Characterization of the XIA LLC Si-PIN Diode Spectrometer Prototype

This section documents the characterization of the XIA LLC Si-PIN diode spectrometer prototype [67, 68] introduced in Section 2.1.2. The section begins with a description of the experimental methods used to produce radioxenon gas samples and acquire spectral data sets (spectra) using the XIA LLC Si-PIN diode spectrometer prototype. The counting statistics and decision limit concepts developed in Section 2.1.4 and the WiPFA peak-fitting algorithm described in Section 2.1.5 are then applied to the spectra in order to extract the peak mean, peak width, and peak area data required to characterize the linearity, the resolution, and the photon and conversion electron detection efficiencies of the XIA LLC Si-PIN diode spectrometer prototype. The conversion electron detection efficiencies are then used to develop Minimum Detectable Concentrations (MDCs) for each of the four radioxenon gases that are most relevant to the verification regime of the CTBT: ^{131m}Xe, ^{133m}Xe, ^{133}Xe, and ^{135}Xe [46]. This section concludes by comparing the performance characteristics of the XIA LLC Si-PIN diode spectrometer prototype to the performance characteristics of the ARIX [52], ASRA [54], SAUNA [57], and SPALAX [58] systems currently employed by the verification regime of the CTBT [33].

2.2.1 Experimental Methods

In order to characterize the performance of the XIA LLC Si-PIN diode spectrometer prototype it was first necessary to acquire several spectra using the prototype and several different radiation sources. Given that the ultimate objective of the Si-PIN diode spectrometer prototype characterization efforts documented herein was to evaluate the performance of the Si-PIN diode spectrometer prototype relative to the ARIX [52], ARSA [54], SAUNA [57], and SPALAX [58] systems currently employed by the verification regime of the CTBT [33], it was obvious that several spectra would need to be acquired using the four radioxenon gases most relevant to the verification regime of the CTBT: ^{131m}Xe, ^{133m}Xe, ^{133}Xe, and ^{135}Xe [46]. These radioxenon gases were produced in-house at The University of Texas at Austin's Nuclear Engineering Teaching Laboratory [87]. As will be seen, the radioxenon gas spectra only generated a few peak mean, peak width, and peak area data points so additional data points were needed to adequately characterize the linearity, resolution, and photon and conversion electron detection efficiencies of the XIA LLC Si-PIN diode spectrometer prototype. These additional data points were generated by acquiring eight additional spectra using eight calibration sources. This section begins with a description of the experimental methods used to produce the radioxenon gas samples and acquire the radioxenon spectra; the experimental methods used to acquire the calibration source spectra are discussed towards the end of the section in Section 2.2.1.3.

2.2.1.1 Production of Radioxenon Gas Samples

Three radioxenon gas samples were produced to support the XIA LLC Si-PIN diode spectrometer prototype linearity, resolution, and detection efficiency calibrations. The radioxenon gas samples were produced by irradiating stable xenon gases in the three element (3L) irradiation facility [100] of the TRIGA Mark II nuclear research reactor at The University of Texas at Austin's Nuclear Engineering Teaching Laboratory [87]. A gas manifold [97], was used to prepare the stable xenon gas samples for irradiation and to transfer the radioxenon gases to the XIA LLC Si-PIN diode spectrometer prototype. A photograph of the gas manifold is presented below in Figure 2.18.

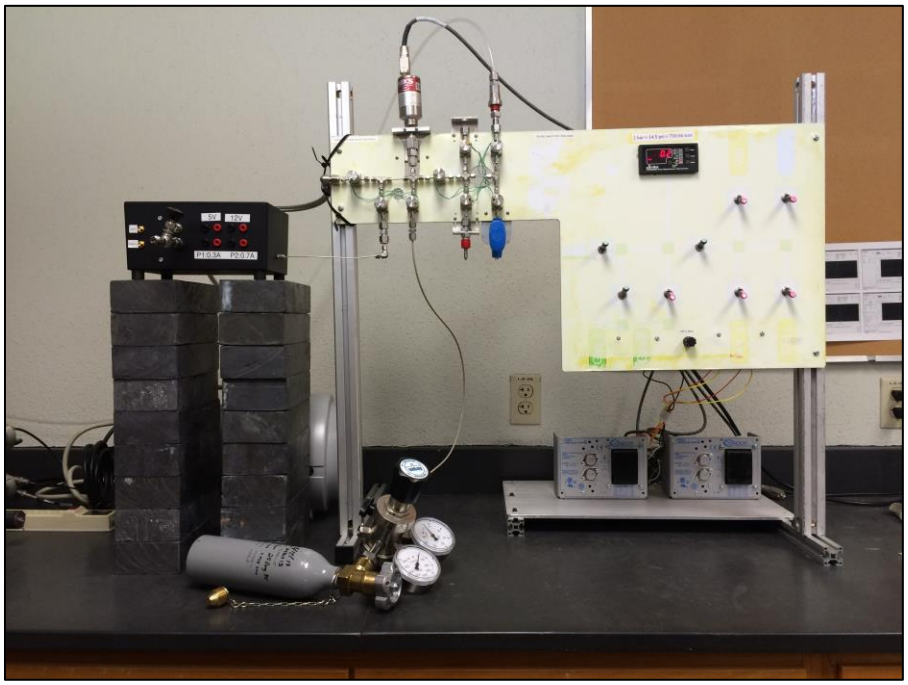

Figure 2.18: A photograph of the gas manifold used to prepare stable xenon gas samples for irradiation.

The four-step procedure used to (1) trap stable xenon gas samples in capped ¼ in Swagelok quarter-turn PFA plug valves, (2) irradiate the stable xenon gases, (3) quantify the activities of the radioxenon gases produced, and then (4) expand the radioxenon gases into the XIA LLC Si-PIN diode spectrometer prototype was executed as described in the next four sections.

2.2.1.1.1 Capturing Stable Xenon Gas Samples

The first step of the radioxenon gas sample production procedure involved capturing three stable xenon gas samples in three capped ¼ in Swagelok quarter-turn PFA plug valves [101]. A photograph of a capped ¼ in Swagelok quarter-turn PFA plug valve is presented in Figure 2.19.

Capturing a stable xenon gas sample in a capped ¼ in Swagelok quarter-turn PFA plug valve involved first flushing the combined Swagelok PFA plug valve - gas manifold - spectrometer system with dry nitrogen gas to remove contaminants from the system, connecting a canister of high-purity, stable xenon gas to the gas manifold, and then performing a series of valve manipulations to expand the stable xenon gas out of the gas canister, through the gas manifold, and into a capped ¼ in Swagelok quarter-turn PFA plug valve.

Three stable xenon gases were used to produce the four radioxenon gases most relevant to the verification regime of the CTBT [33]: ^{131m}Xe was produced by capturing and irradiating stable ^{130}Xe, ^{133m}Xe and ^{133}Xe were produced by capturing and irradiating stable ^{132}Xe, and ^{135}Xe was produced by capturing and irradiating stable ^{134}Xe.

The isotopic enrichments associated with each of the stable xenon gases, all of which were procured from Isoflex USA [102, 103, 104], are reported in Table 2.2.

Each time a stable xenon gas sample was expanded into a Swagelok PFA plug valve the pressure of the gas expanded into the PFA plug valve, P_{PFA}, was recorded before the plug valve was shut, capturing the stable xenon gas in the two volumes highlighted below in Figure 2.19. After a stable xenon gas sample was captured in a Swagelok PFA plug valve the valve was removed from the gas manifold and transferred to University of Texas at Austin Nuclear Engineering Teaching Laboratory [87] reactor operations personnel to be loaded into the 3L irradiation facility [100] and irradiated. Latex gloves were worn when handling the Swagelok PFA plug valves to prevent the transfer of skin oils to the valves; skin oils contain sodium (^{23}Na) which can pose an activation problem if transferred to a Swagelok PFA plug valve and irradiated.

Figure 2.19: A capped ¼ in Swagelok quarter-turn PFA plug valve.

Table 2.2: Information pertaining to the stable ^{130}Xe, ^{132}Xe, and ^{134}Xe gases used to produce ^{131m}Xe, ^{133m}Xe, ^{133}Xe, and ^{135}Xe gas samples.

Stable Xe Isotope	Isotopic Enrichment [%] [102, 103, 104]	Isoflex USA Cert. No. [102, 103, 104]	P_{PFA} [Torr]
^{130}Xe	99.949	54-01-130-4008	582.6 ± 0.2
^{132}Xe	99.892	5085	758.4 ± 0.2
^{134}Xe	99.941	5086	320.8 ± 0.2

2.2.1.1.2 Irradiation of Stable Xenon Gas Samples

The stable xenon gas samples captured in the ¼ in Swagelok quarter-turn PFA plug valves [101] as described in the previous section were irradiated in a 1.1 MW TRIGA nuclear research reactor housed at The University of Texas at Austin's Nuclear Engineering Teaching Laboratory [87]. The stable xenon gases were irradiated in the reactor's three element (3L) irradiation facility [100] which is so-named because it takes the place of three fuel elements in the TRIGA nuclear research reactor core. The 3L irradiation facility is basically a lead-lined aluminum canister with an inner diameter of 3.88 cm [100]. The process of loading the Swagelok PFA plug valves into the 3L irradiation facility involved first placing the 3L irradiation facility in a rack at the reactor pool surface and removing the cap from the top of the 3L irradiation facility as illustrated in Figure 2.20. The blue handles on the tops of the Swagelok PFA plug valves were then removed from the tops of the plug valves (the plug valves do not fit in the 3L irradiation facility with the handles on) and the plug valves were lowered to the bottom of the 3L irradiation facility with a special tool. The 3L irradiation facility cap was then placed

back on the 3L irradiation facility and tightened and the interior of the 3L irradiation facility was purged with dry carbon dioxide gas (to remove argon gas, which presents an activation problem). The 3L irradiation facility was then lowered into the reactor core and the reactor was brought up to the desired power level. Table 2.3 lists the parameters pertaining to each of the stable xenon gas irradiations. At the end of each irradiation the 3L irradiation facility was removed from the reactor core and stowed temporarily to allow activation products produced in the 3L irradiation facility to decay. The 3L irradiation facility was then placed in the rack at the reactor pool surface so that the Swagelok PFA plug valves could be removed from the 3L irradiation facility, frisked, checked for external contamination, and released for counting.

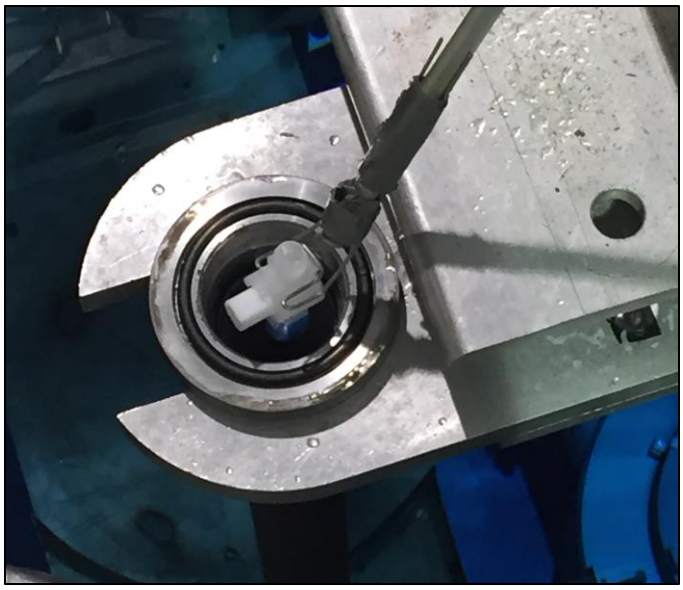

Figure 2.20: A Swagelok PFA plug valve being loaded into the three element (3L) irradiation facility prior to irradiation in the TRIGA Mark II nuclear research reactor at The University of Texas at Austin's Nuclear Engineering Teaching Laboratory.

Table 2.3: Parameters pertaining to each of the stable xenon gas irradiations.

Stable Xe Gas Irradiated	Radioxenon(s) Produced	Reactor Power Level [kW]	Irradiation Start Date and Time [dd mm yyyy, hh:mm]	Irradiation Duration [min]
^{130}Xe	^{131m}Xe	100	5 Feb 2016, 10:59	40
^{132}Xe	^{133m}Xe and ^{133}Xe	100	4 Feb 2016, 16:12	30
^{134}Xe	^{135}Xe	100	2 Feb 2016, 12:01	30

2.2.1.1.3 Radioxenon Gas Sample Activity Quantification

In order to use the radioxenon gas samples produced as described in the preceding sections to support the XIA LLC Si-PIN diode spectrometer prototype detection efficiency characterizations, the activities of the radioxenon gases expanded into the Si-PIN diode spectrometer prototype had to be quantified. Thus, the radioxenon gas activities trapped in the Swagelok PFA plug valves [101] were quantified both before and after the radioxenon gases were expanded into the Si-PIN diode spectrometer prototype using a High-Purity Ge (HPGe) spectrometer. The radioxenon gas activities were quantified both before and after the expansions because, as will be seen, some of the radioxenon gases were retained in the plug valves following the gas expansions.

Quantifying the activities of the radioxenon gases trapped in the Swagelok PFA plug valves involved acquiring radioxenon spectra for each of the radioxenon gas samples, evaluating the peak areas associated with each of the prominent X-ray and gamma-ray peaks in each of the radioxenon spectra, and then relating the radioxenon peak areas to radioxenon activities via Equations 2.2.1.1.3.1 through 2.2.1.1.3.4.

The radioxenon spectra were acquired with the Swagelok PFA plug valves sitting on top of a source holder which positioned the bottom surfaces of the plug valves 50 cm above the top face of the HPGe spectrometer as illustrated in Figure 2.21. Ortec's GammaVision application [105] was used to acquire the radioxenon spectra.

Each of the radioxenon spectra acquired contained a number of radioxenon X-ray and gamma-ray peaks. The energies of the X-rays and gamma-rays producing these peaks and the areas associated with each of the peaks are tabulated in Table 2.4. The peak areas were evaluated using the WiPFA peak-fitting algorithm described in Section 2.1.5 and in Appendix A. Note that two peak areas, a pre-expansion peak area and a post-expansion peak area, are reported for each of the radioxenon isotopes and decay modes. The pre-expansion peak areas are the areas of the peaks in the spectra acquired before the radioxenon gases were expanded out of the Swagelok PFA plug valves and into the XIA LLC Si-PIN diode spectrometer prototype and the post-expansion peak areas are the areas of the peaks in the spectra acquired after the radioxenon gases were expanded out of the Swagelok PFA plug valves and into the Si-PIN diode spectrometer prototype.

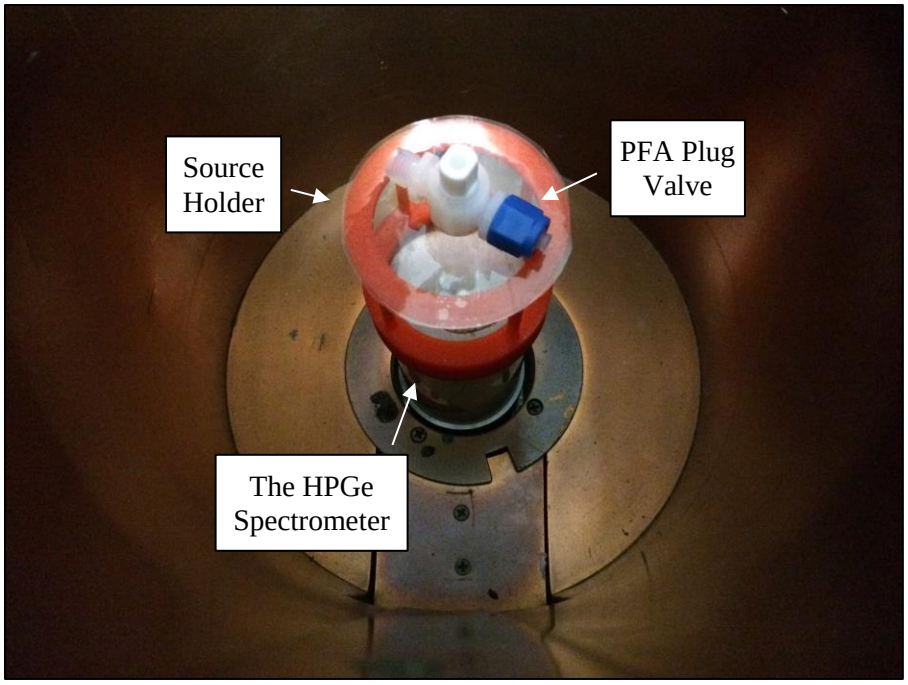

Figure 2.21: A photograph of a Swagelok PFA plug valve sitting on a source holder 50 cm above an HPGe spectrometer.

Table 2.4: Radioxenon X-ray and gamma-ray energies and peak areas from the HPGe spectra.

Radioxenon Isotope and Decay Mode	Nominal Decay Mode Energy [keV]	Peak Areas (Pre-Expansion) [unitless]	Peak Areas (Post-Expansion) [unitless]
^{131m}Xe Kα X-Rays	29.669	339,898 ± 957 (0.28 %)	156,801 ± 827 (0.53 %)
^{131m}Xe Kβ X-Rays	33.738	79,031 ± 696 (0.88 %)	35,492 ± 644 (1.8 %)
^{131m}Xe γ-Ray	163.930	14,211 ± 566 (4.0 %)	7,610 ± 564 (7.4 %)
^{133m}Xe γ-Ray	233.221	20,403 ± 562 (2.8 %)	7,720 ± 515 (6.7 %)
^{133}Xe γ-Rays	80.9816	583,749 ± 975 (0.17 %)	229,096 ± 673 (0.29 %)
^{135}Xe Kα X-Rays	30.850	6,886 ± 169 (2.5 %)	635 ± 83 (13 %)
^{135}Xe Kβ X-Rays	35.109	1,582 ± 145 (9.2 %)	Not Stat. Sig.
^{135}Xe γ-Ray	249.794	117,326 ± 378 (0.32 %)	9,698 ± 120 (1.2 %)

The areas associated with the radioxenon peaks in the HPGe spectra (see Table 2.4) were used to calculate the ^{131m}Xe, ^{133m}Xe, and ^{135}Xe activities at the times the ^{131m}Xe, ^{133m}Xe, and ^{135}Xe HPGe spectra acquisitions started. The ^{131m}Xe, ^{133m}Xe, and ^{135}Xe activities were calculated from their respective HPGe spectra peak areas in accordance with the following expression:

$$A_x(t_{AS}) = \frac{\lambda_x \cdot C_{y,x}}{\beta_{y,x} \cdot \varepsilon_{E,y,x} \cdot (1 - e^{-\lambda_x \cdot t_{Live}})}. \qquad 2.2.1.1.3.1$$

Where: $A_x(t_{AS})$ is the activity of radioxenon isotope x (where x may be 131m, 133m, or 135) at the spectral data set acquisition start time, t_{AS},

λ_x is the decay constant associated with radioxenon isotope x,

$C_{y,x}$ is the area of the peak attributable to decay mode y of radioxenon isotope x,

$\beta_{y,x}$ is the branching ratio associated with decay mode y of radioxenon isotope x,

$\varepsilon_{E,y,x}$ is the absolute full-energy peak detection efficiency of the HPGe spectrometer at the energy E associated with decay mode y of radioxenon isotope x, and

t_{Live} is the spectral data set acquisition live time.

Note that Equation 2.2.1.1.3.1 assumes that radioxenon is only lost due to radioactive decay during a given spectral data set acquisition. This is in fact the case for ^{131m}Xe, ^{133m}Xe, and ^{135}Xe. However, ^{133}Xe is not only lost to radioactive decay during a spectral data set acquisition, but is also produced from the decay of ^{133m}Xe. When this is the case Equation 2.2.1.1.3.1 is not valid. The ^{133}Xe activities were thus calculated in accordance with the following somewhat more complicated expression:

$$A_{133}(t_{AS}) = \frac{\lambda_{133} \cdot C_{y,133}}{\beta_{y,133} \cdot \varepsilon_{E_y,y,133} \cdot (1 - e^{-\lambda_{133} \cdot t_{Live}})} \ldots$$

2.2.1.1.3.2

$$+ \frac{\lambda_{133} \cdot \lambda_{133m} \cdot C_{z,133m} \cdot \left(e^{-\lambda_{133m} \cdot t_{Live}} - e^{-\lambda_{133} \cdot t_{Live}}\right)}{\beta_{z,133m} \cdot \varepsilon_{E_z,z,133m} \cdot (\lambda_{133} - \lambda_{133m}) \cdot (1 - e^{-\lambda_{133m} \cdot t_{Live}}) \cdot (1 - e^{-\lambda_{133} \cdot t_{Live}})}.$$

Where: $A_{133}(t_{AS})$ is the ^{133}Xe activity at the spectral data set acquisition start time, t_{AS},

λ_{133} and λ_{133m} are the ^{133}Xe and ^{133m}Xe decay constants, respectively,

$C_{y,133}$ and $C_{z,133m}$ are the areas of the peaks attributable to ^{133}Xe decay mode y and ^{133m}Xe decay mode z, respectively,

$\beta_{y,133}$ and $\beta_{z,133m}$ are the branching ratios associated with ^{133}Xe decay mode y and ^{133m}Xe decay mode z, respectively,

$\varepsilon_{E_y,y,133}$ and $\varepsilon_{E_z,z,133m}$ are the absolute full-energy peak detection efficiencies of the HPGe spectrometer at the energies E_y and E_z associated with ^{133}Xe decay mode y and ^{133m}Xe decay mode z, respectively, and

t_{Live} is the spectral data set acquisition live time.

The radioxenon activities calculated in accordance with Equations 2.2.1.1.3.1 and 2.2.1.1.3.2 were decay corrected to the times at which the XIA LLC Si-PIN diode spectrometer prototype spectra acquisitions were started. The ^{131m}Xe, ^{133m}Xe, and ^{135}Xe activities were decay corrected to the appropriate time, t_{Ref}, as follows:

$$A_x(t_{Ref}) = A_x(t_{AS}) \cdot e^{-\lambda_x \cdot t_{Live}}. \qquad 2.2.1.1.3.3$$

The ^{133}Xe activities were decay corrected to the appropriate time, t_{Ref}, using a slightly more complicated equation:

$$A_{133}(t_{Ref}) = \frac{\lambda_{133} \cdot A_{133m}(t_{AS}) \cdot \left(e^{-\lambda_{133m} \cdot t_{Live}} - e^{-\lambda_{133} \cdot t_{Live}}\right)}{\lambda_{133} - \lambda_{133m}} \ldots$$
$$+ A_{133}(t_{AS}) \cdot e^{-\lambda_{133} \cdot t_{Live}}. \qquad 2.2.1.1.3.4$$

The radioxenon gas activities calculated in accordance with Equations 2.2.1.1.3.1 through 2.2.1.1.3.4 are tabulated in Table 2.5. The $A_{Pre}(t_{Ref})$ and $A_{Post}(t_{Ref})$ radioxenon gas activities represent the radioxenon gas activities present in the Swagelok PFA plug valves before and after the radioxenon gas expansions, respectively, decay-corrected to the XIA LLC Si-PIN diode spectrometer prototype spectra acquisition start times. The radioxenon gas activities $A_{Exp}(t_{Ref})$ are the differences in the activities $A_{Pre}(t_{Ref})$ and $A_{Post}(t_{Ref})$ and represent the radioxenon gas activities available for expansion into the XIA LLC Si-PIN diode spectrometer prototype at the Si-PIN diode spectrometer prototype spectra acquisition start times. Note that the radioxenon gas activities reported in Table 2.5 are, in most cases, the averages of multiple radioxenon activities calculated from peak areas associated with multiple radioxenon decay modes (see Table 2.4). It is interesting to note that about 6.2 ± 1.1 % of the ^{131m}Xe, about 8.3 ± 2.7 % of the ^{133m}Xe, about 7.6 ± 0.6 % of the ^{133}Xe, and about 8.5 ± 1.8 % of the ^{135}Xe remained absorbed in the body of the Swagelok PFA plug valve or adsorbed onto the inner surfaces of the open Swagelok PFA plug valves after the radioxenon gas expansions.

Table 2.5: Radioxenon gas activities derived from radioxenon HPGe spectra.

Radioxenon Isotope	$A_{Pre}(t_{Ref})$ [Bq]	$A_{Post}(t_{Ref})$ [Bq]	$A_{Exp}(t_{Ref})$ [Bq]
^{131m}Xe	6,000 ± 700 (12 %)	370 ± 40 (12 %)	5,600 ± 710 (13 %)
^{133m}Xe	3,600 ± 80 (23 %)	300 ± 70 (24 %)	3,300 ± 820 (25 %)
^{133}Xe	17,000 ± 940 (5.7 %)	1,300 ± 79 (6.3 %)	15,000 ± 1,000 (6.7 %)
^{135}Xe	22,000 ± 3,000 (13 %)	1,800 ± 300 (17 %)	20,000 ± 2,800 (14 %)

2.2.1.1.4 Radioxenon Gas Sample Expansions

As alluded to in the previous section, after the radioxenon gas activities trapped in the Swagelok PFA plug valves were quantified the plug valves were connected to the gas manifold [97] and the radioxenon gases were allowed to expand out of the plug valves, through the gas manifold, and into the interior of the XIA LLC Si-PIN diode spectrometer prototype [67, 68] where they could occupy the volume between the two Si-PIN diodes. However, it is important to note that, during a given radioxenon expansion, not all of the radioxenon gas expanded all the way into the interior of the XIA LLC Si-PIN diode spectrometer prototype; some of the radioxenon gas remained in the Swagelok PFA plug valve, some occupied the volume of the gas manifold, and some expanded into the interior of the XIA LLC Si-PIN diode spectrometer prototype. It is important that the fractions of the radioxenon gas activities that expanded all the way into the interior of the Si-PIN diode spectrometer prototype be well understood, because these are the radioxenon gas activities that should be thought of as being available for detection

in the context of spectrometer detection efficiency calculations. The fractions of the radioxenon gas activities available for detection were calculated as follows:

$$A_{Int}(t_{Ref}) = A_{Exp}(t_{Ref}) \cdot \frac{V_{Int}}{V_{Sys}} \qquad 2.2.1.1.4.1$$

Where: $A_{Int}(t_{Ref})$ is the radioxenon gas activity assumed to occupy the volume between the two Si-PIN diodes in the interior of the XIA LLC Si-PIN diode spectrometer prototype at the beginning of a given radioxenon spectrum acquisition,

$A_{Exp}(t_{Ref})$ is the radioxenon gas activity assumed to be available for expansion into the XIA LLC Si-PIN diode spectrometer prototype at the beginning of a given radioxenon spectrum acquisition,

V_{Int} is the volume associated with the interior of the XIA LLC Si-PIN diode spectrometer prototype, and

V_{Sys} is the volume of the combined Swagelok PFA plug valve - gas manifold - spectrometer system.

The volume of the interior of the Si-PIN diode spectrometer prototype, V_{Int}, was calculated from dimensions reported in mechanical drawings provided by XIA LLC [106] and was found to be 1.02 ± 0.02 cm^3. This volume accounts for the fact that the Si-PIN diodes occupy a small portion of the volume in the interior of the XIA LLC Si-PIN diode spectrometer prototype. The volume of the combined Swagelok PFA plug valve–gas manifold–spectrometer system, V_{Sys}, was evaluated through a series of dedicated experiments and was found to be 9.2 ± 0.2 cm^3.

The $A_{Exp}(t_{Ref})$ values reported in Table 2.5 and the V_{Int} and V_{Sys} values were plugged into Equation 2.2.1.1.4.1 to calculate the radioxenon gas activities transferred to the interior of the Si-PIN diode spectrometer prototype at the radioxenon spectra acquisition start times. The results of these calculations are presented below in Table 2.6.

Table 2.6: Radioxenon gas activities transferred to the interior of the XIA LLC Si-PIN diode spectrometer prototype.

Radioxenon Isotope	$A_{IC}(t_{Ref})$ [Bq]
^{131m}Xe	620 ± 80 (13 %)
^{133m}Xe	370 ± 90 (25 %)
^{133}Xe	1,700 ± 100 (6.8 %)
^{135}Xe	2,200 ± 300 (15 %)

2.2.1.2 Acquisition of Prototype Radioxenon Spectra

The XeSDD application introduced in Section 2.1.2 was used to acquire XIA LLC Si-PIN diode spectrometer prototype radioxenon spectra in a time-stamped list mode. The dates and times at which each of the spectrum acquisitions started are reported in Table 2.7. The real times associated with each of the acquisitions are also reported. Note that there was an issue with the acquisition live times reported by the XeSDD application and thus the acquisition live times were assumed to be equal to the acquisition real times. Because the count rates during the radioxenon spectrum acquisitions were low the dead times are assumed to have been small, and thus the error introduced to the radioxenon

spectra analyses as a result of the aforementioned live time assumption is assumed to be small.

As indicated in Table 2.7 each of the radioxenon gases was counted three times and each count was one hour in duration. Three separate spectra were acquired for each of the radioxenon gases because the XIA LLC Si-PIN diode spectrometer prototype was known to leak and there were concerns that the leak would introduce uncertainty into the radioxenon spectra analyses in two ways. For one, the leak introduces some uncertainty into the amount of radioxenon gas assumed to be present in the interior of the Si-PIN diode spectrometer prototype. Additionally, the leak caused the pressure in the interior of the XIA LLC Si-PIN diode spectrometer prototype to increase by roughly 1 Torr (133 Pa) every five minutes as nitrogen gas was allowed to leak into the interior of the XIA LLC Si-PIN diode spectrometer prototype. There were concerns that the conversion electrons emitted by the radioxenon gases might be attenuated to a greater extent as time passed and the total amount of gas present in the interior of the XIA LLC Si-PIN diode spectrometer prototype increased. Three spectra were acquired for each of the radioxenon gases so that count data acquired at later times could simply be discarded if it was found to be suspect. Note that only two ^{135}Xe spectra are listed in Table 2.7 because the XeSDD application crashed during the first of the three ^{135}Xe spectrum acquisitions and the data associated with that first acquisition was found to be invalid.

A selection of radioxenon spectra acquired by the XIA LLC Si-PIN diode spectrometer prototype are presented in Figures 2.22 through 2.30. Figures 2.22 through 2.24 present three different views the ^{131m}Xe spectrum acquired at 18:50:00 on 5

February 2016: Figure 2.22 effectively shows all of the interesting features of the ^{131m}Xe spectrum up through roughly 170 keV, Figure 2.23 presents a detailed view of the ^{131m}Xe X-ray peaks at the low energy end of the spectrum, and Figure 2.24 presents a detailed view of the ^{131m}Xe conversion electron peaks at the high energy end of the spectrum.

Figures 2.25 through 2.27 present three similar views of the mixed ^{133m}Xe and ^{133}Xe spectrum acquired at 23:55:00 on 4 February 2016, and Figures 2.28 through 2.30 present the three similar views of the ^{135}Xe spectrum acquired at 22:58:00 on 2 February 2016. The means, widths, and areas associated with some of the peaks in Figures 2.22 through 2.30 are reported in Tables B.1, B.2, and B.3 of Appendix B.

Table 2.7: Radioxenon spectrum acquisition information.

Radioxenon Isotopes in Spectrum	Acquisition Start Date and Time [dd mmm yyyy, hh:mm]	Acquisition Real Time [s]
^{131m}Xe	5 Feb 2016, 18:50	3,600
	5 Feb 2016, 19:51	3,600
	5 Feb 2016, 20:52	3,600
^{133m}Xe and ^{133}Xe	4 Feb 2016, 23:55	3,600
	5 Feb 2016, 00:56	3,600
	5 Feb 2016, 01:57	3,600
^{135}Xe	2 Feb 2016, 22:58	3,600
	3 Feb 2016, 00:00	3,600

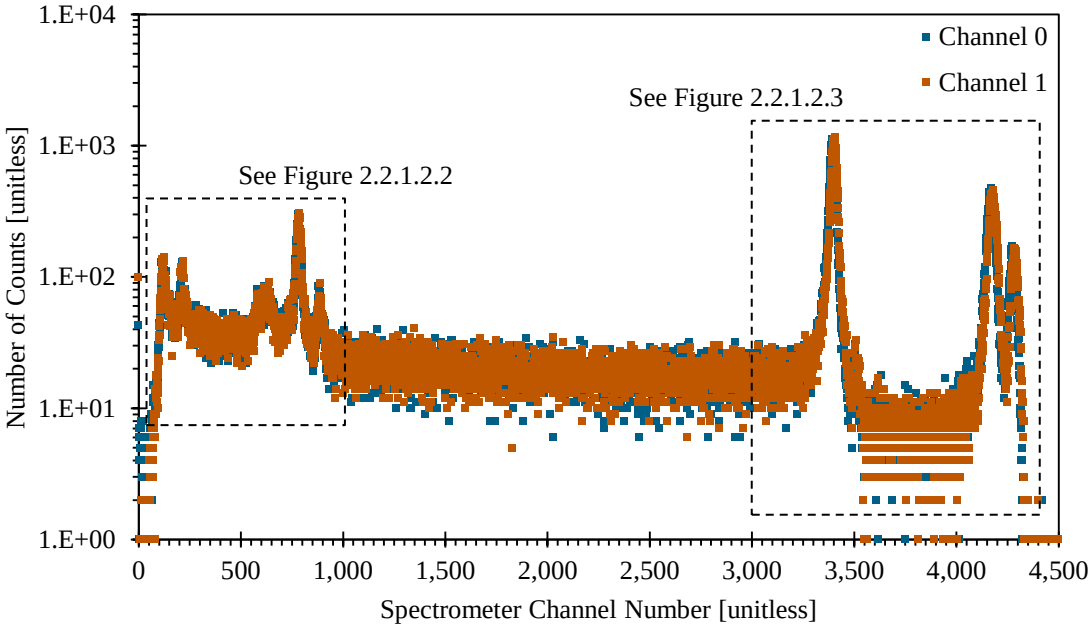

Figure 2.22: The ^{131m}Xe spectrum acquired by the XIA LLC Si-PIN diode spectrometer prototype at 18:50:00 on 5 February 2016.

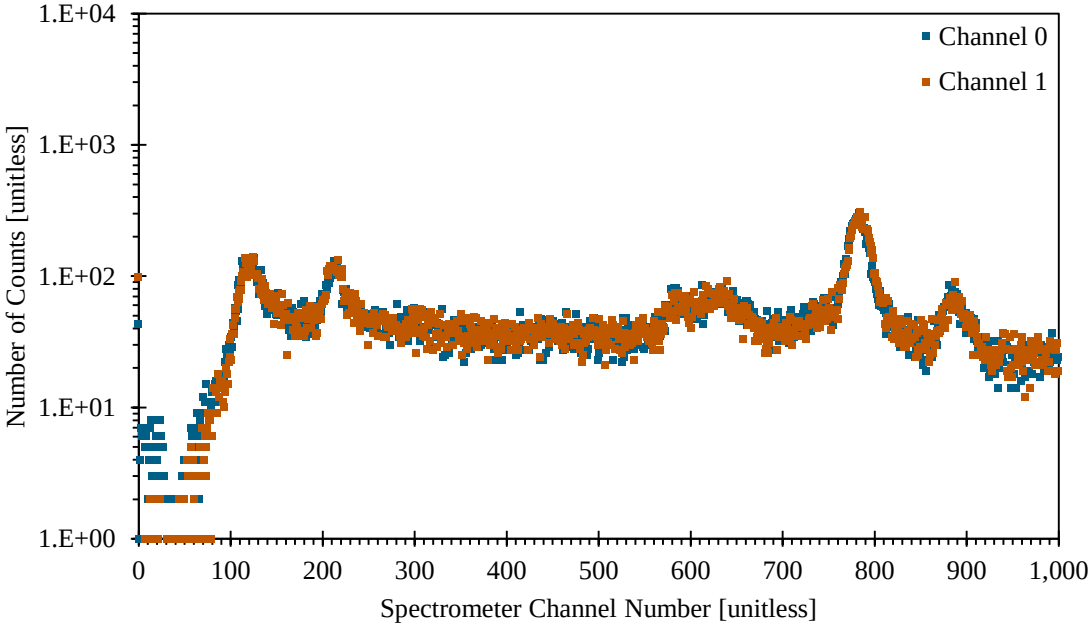

Figure 2.23: Detailed view of the ^{131m}Xe X-ray peaks in the ^{131m}Xe spectrum acquired by the XIA LLC Si-PIN diode spectrometer prototype.

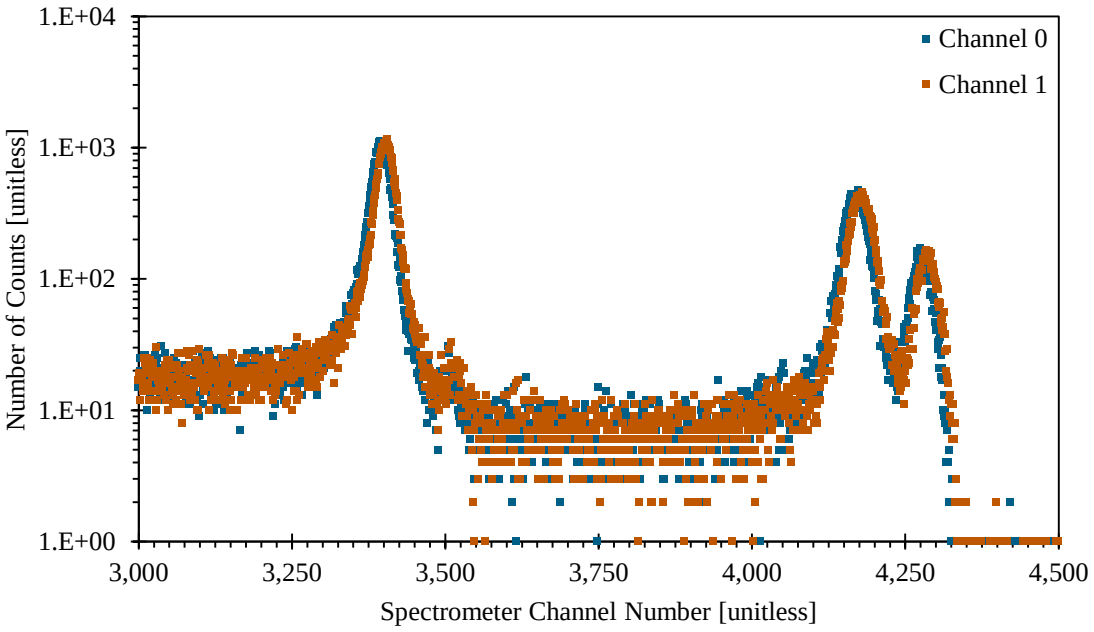

Figure 2.24: Detailed view of the ^{131m}Xe conversion electron peaks in the ^{131m}Xe spectrum acquired by the XIA LLC Si-PIN diode spectrometer prototype.

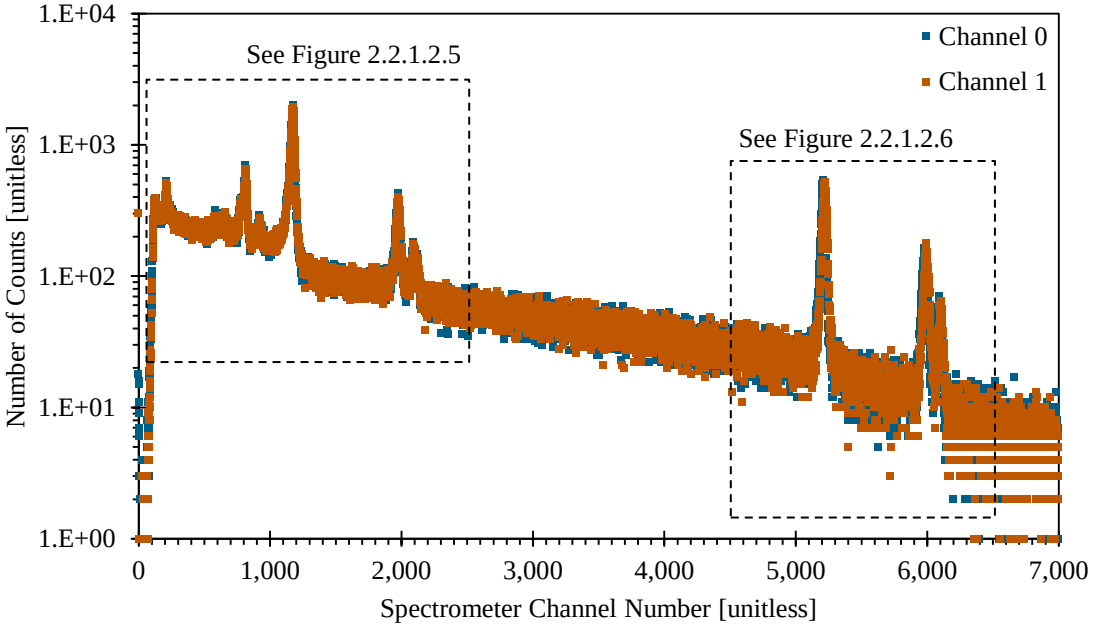

Figure 2.25: The mixed ^{133m}Xe and ^{133}Xe spectrum acquired by the XIA LLC Si-PIN diode spectrometer prototype at 23:55:00 on 4 February 2016.

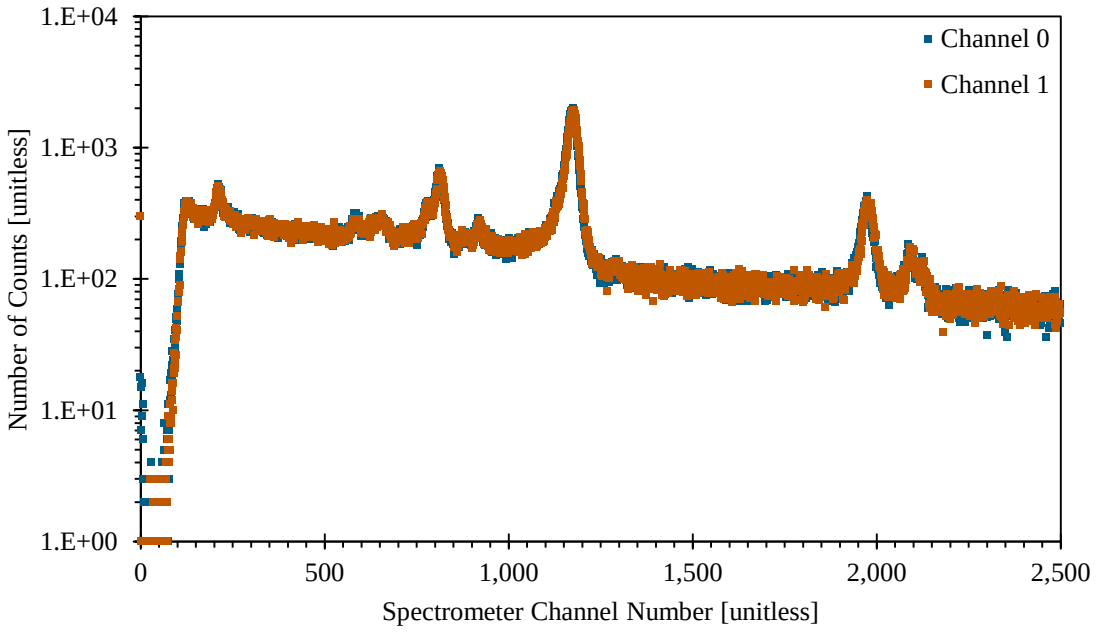

Figure 2.26: Detailed view of the ^{133m}Xe and ^{133}Xe X-ray peaks in the mixed ^{133m}Xe and ^{133}Xe spectrum acquired by the XIA LLC Si-PIN diode spectrometer prototype.

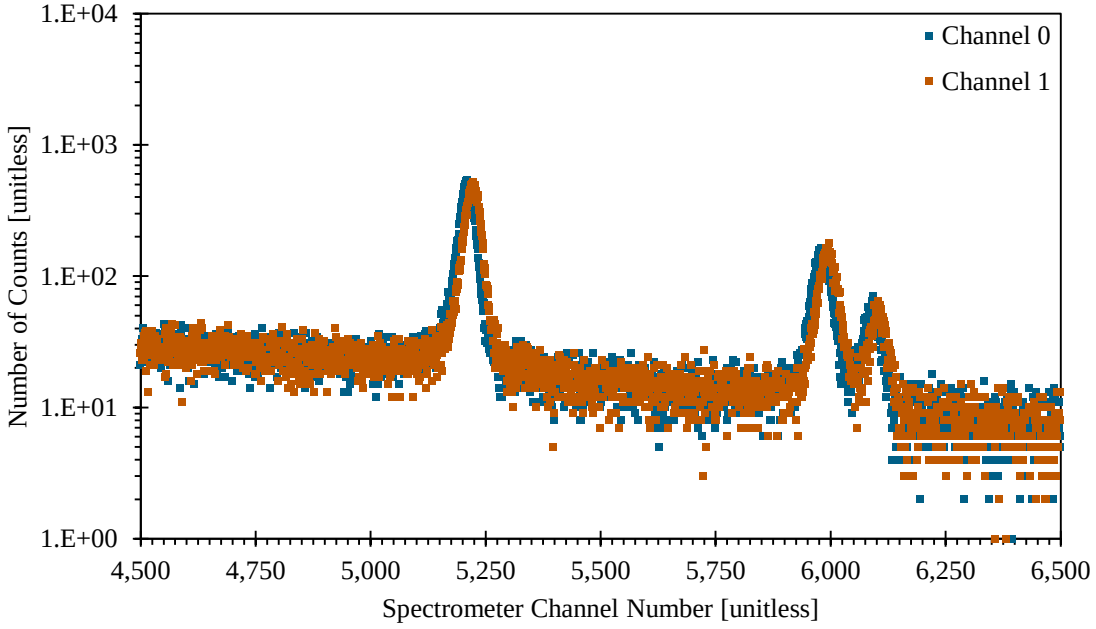

Figure 2.27: Detailed view of the ^{133m}Xe and ^{133}Xe conv. elec. peaks in the mixed ^{133m}Xe and ^{133}Xe spectrum acquired by the XIA LLC Si-PIN diode spec. prototype.

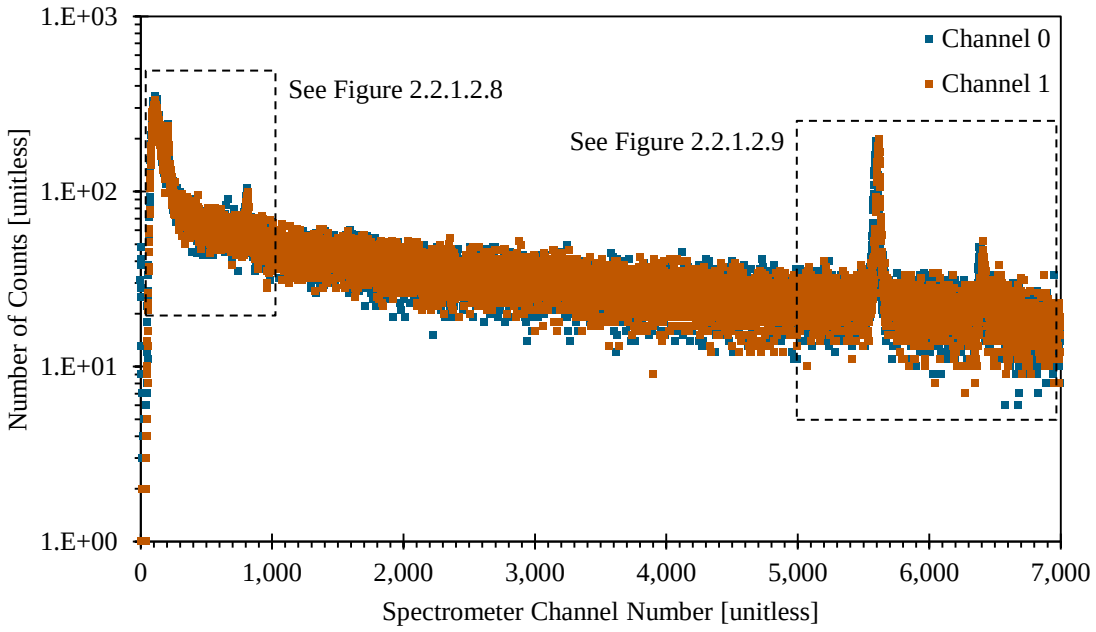

Figure 2.28: The ^{135}Xe spectrum acquired by the XIA LLC Si-PIN diode spectrometer prototype at 22:58:00 on 2 February 2016.

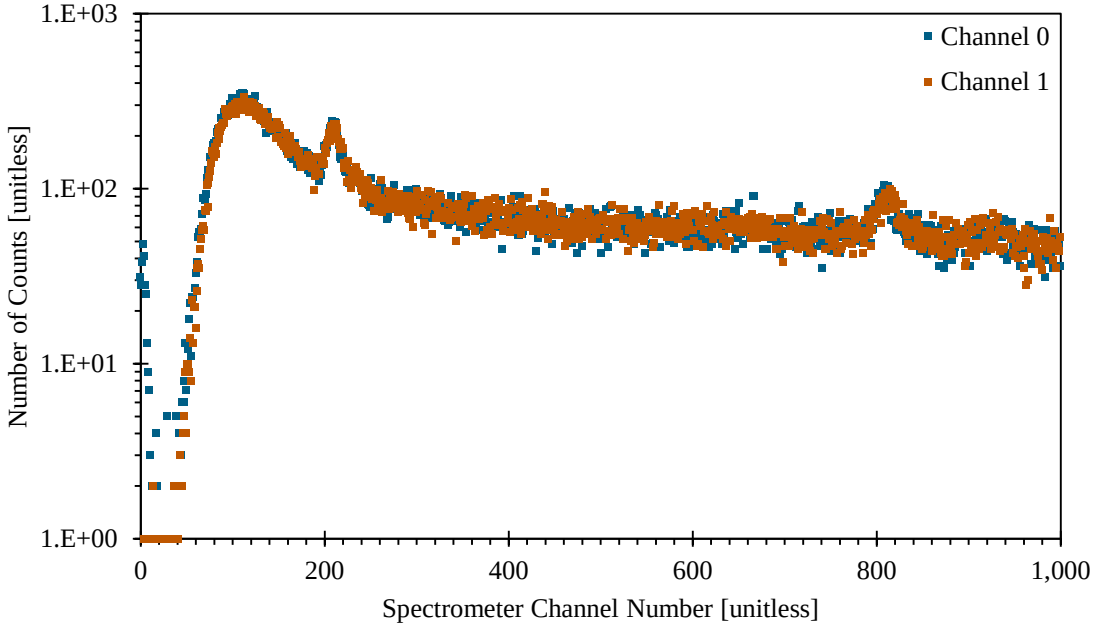

Figure 2.29: Detailed view of the ^{135}Xe X-ray peaks in the ^{135}Xe spectrum acquired by the XIA LLC Si-PIN diode spectrometer prototype.

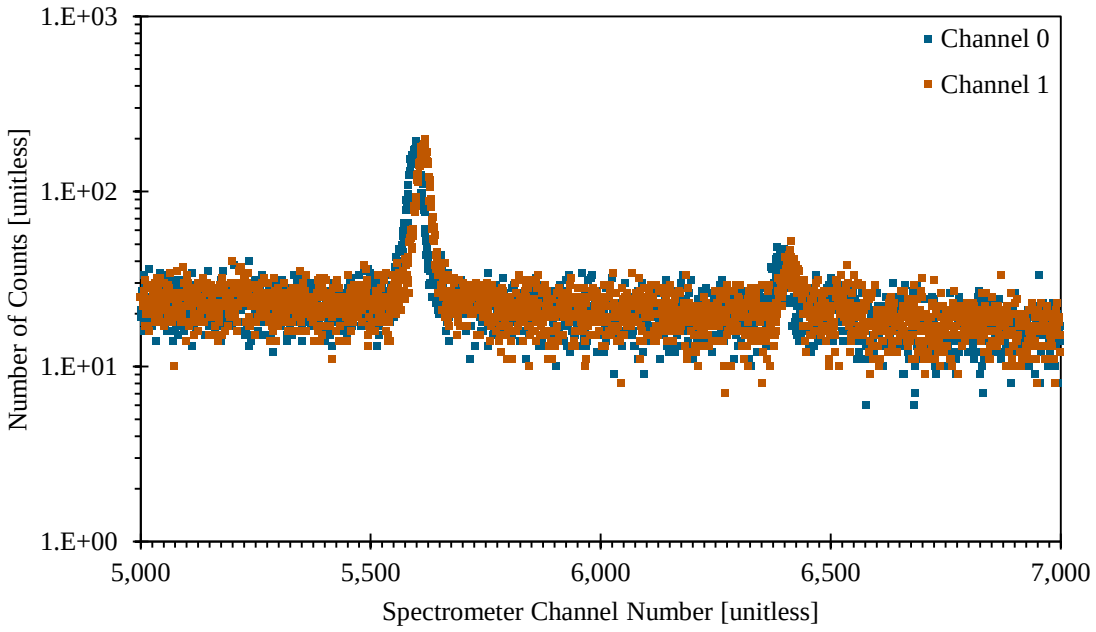

Figure 2.30: Detailed view of the ^{135}Xe conversion electron peaks in the ^{135}Xe spectrum acquired by the XIA LLC Si-PIN diode spectrometer prototype.

2.2.1.3 Acquisition of Prototype Calibration Source Spectra

In addition the radioxenon spectra acquired as described in the previous section, eight additional spectra were acquired using eight calibration sources. Seven of the calibration sources were type-D calibration sources produced by Eckert and Ziegler Isotope Products [107]. The eighth source was a ^{133}Ba check source that was calibrated using an HPGe spectrometer at The University of Texas at Austin's Nuclear Engineering Teaching Laboratory [87]. The information associated with each of the aforementioned calibration sources is presented below in Table 2.8.

Table 2.8: Information associated with the calibration sources used to support the XIA LLC Si-PIN diode spectrometer prototype characterization.

Source Radioisotope	Source Serial Number	Source Activity [Bq]	Calibration Date and Time [dd mmm yyyy, hh:mm:ss]
^{65}Zn	1835-8-4	$3.56\times10^{4} \pm 9\times10^{2}$	1 Oct 2015, 12:00:00
^{109}Cd	1835-8-1	$3.57\times10^{4} \pm 9\times10^{2}$	1 Oct 2015, 12:00:00
^{113}Sn	1835-8-6	$3.70\times10^{4} \pm 9\times10^{2}$	1 Oct 2015, 12:00:00
^{133}Ba	N/A	$6.2\times10^{3} \pm 5\times10^{2}$	26 Dec 2015, 11:49:43
^{137}Cs	1835-8-2	$3.40\times10^{4} \pm 8\times10^{2}$	1 Oct 2015, 12:00:00
^{139}Ce	1835-8-5	$3.86\times10^{4} \pm 9\times10^{2}$	1 Oct 2015, 12:00:00
^{203}Hg	1823-67-2	$3.79\times10^{4} \pm 9\times10^{2}$	15 Oct 2015, 12:00:00
^{241}Am	1823-67-1	$3.63\times10^{4} \pm 1.1\times10^{3}$	1 Oct 2015, 12:00:00

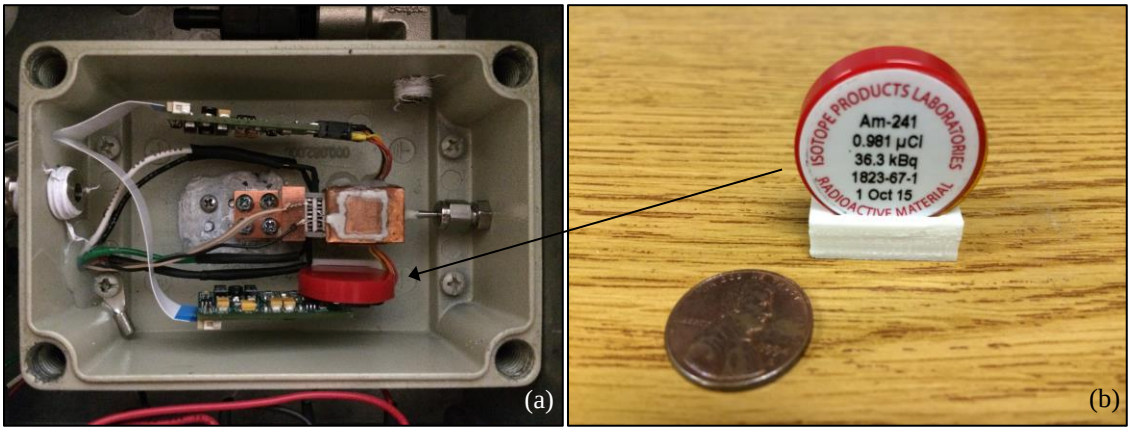

Figure 2.31: The positioning of a calibration source inside the XIA LLC Si-PIN diode spectrometer prototype.

The calibration sources listed in Table 2.8 were placed inside the airtight box in the XIA LLC Si-PIN diode spectrometer prototype (see Figure 2.5) as illustrated in Figure 2.31.(a) and used to acquire eight spectra. The calibration sources were positioned as close to the front (Channel 0) Si-PIN diode as possible, but because of the arrangement of the electronics and other components inside the airtight box the sources ended up being placed about 1.0 cm from the front face of the front Si-PIN diode and about 0.25 cm to the left of the vertical centerline of the front Si-PIN diode. Vertically, the sources were aligned with the horizontal center of the front Si-PIN diode. In order to ensure that the calibration sources were positioned as repeatably as possible inside the airtight box, a simple source holder was manufactured using a MakerBot desktop 3-D printer [108]. A photograph of a calibration source sitting in the source holder is presented in Figure 2.31.(b).

The xManager application [96] was used to acquire the calibration source spectra. The dates and times at which each of the calibration source spectra were acquired are reported in Table 2.9. The real and live times associated with each of the acquisitions are reported in Table 2.9 as well. As indicated by the table, most of the calibration sources were counted for long periods of time to ensure that plenty of detections would be registered in the peaks, particularly the peaks associated with some of the less intense calibration source photons. The goal was to register at least 10,000 detections in each of the peaks of interest so that the uncertainties associated with the peak areas would be less than about 1 %.

The calibration source spectra acquired by the XIA LLC Si-PIN diode spectrometer prototype are presented in Figures 2.32 through 2.39. Note that the spectra acquired by the back Si-PIN diode (Channel 1) are all shifted downward with respect to the spectra acquired by the front Si-PIN diode (Channel 0). This is because the back Si-PIN diode was significantly further away from the calibration sources than the front Si-PIN diode was (see Figure 2.31.(a)) and the photons emitted by the calibration sources were attenuated more as they travelled through the additional space.

The means, widths, and areas associated with some of the peaks in Figures 2.32 through 2.39 were evaluated using the WiPFA peak-fitting algorithm introduced in Section 2.1.5. The results of the peak mean, peak width, and peak area evaluations are presented in Tables B1., B.2, and B.3 in Appendix B.

Table 2.9: Calibration source spectral data set acquisition information.

Source Radioisotope	Acquisition Start Date and Time [dd mmm yyyy, hh:mm:ss]	Acquisition Real Time [s]	Acquisition Live Time [s]
^{65}Zn	15 Jan 2016, 12:28:04	89,735.48	88,650.99
^{109}Cd	6 Feb 2016, 23:27:00	176,165.88	173,959.07
^{113}Sn	28 Jan 2016, 10:30:00	176,000.18	173,979.58
^{133}Ba	19 Jan 2016, 19:11:00	176,992.25	174,565.66
^{137}Cs	31 Jan 2016, 00:01:00	90,014.70	88,260.92
^{139}Ce	9 Feb 2016, 14:41:00	176,058.17	173,937.34
^{203}Hg	25 Jan 2016, 10:58:00	177,539.58	175,173.85
^{241}Am	21 Jan 2016, 22:24:01	176,910.72	174,488.11

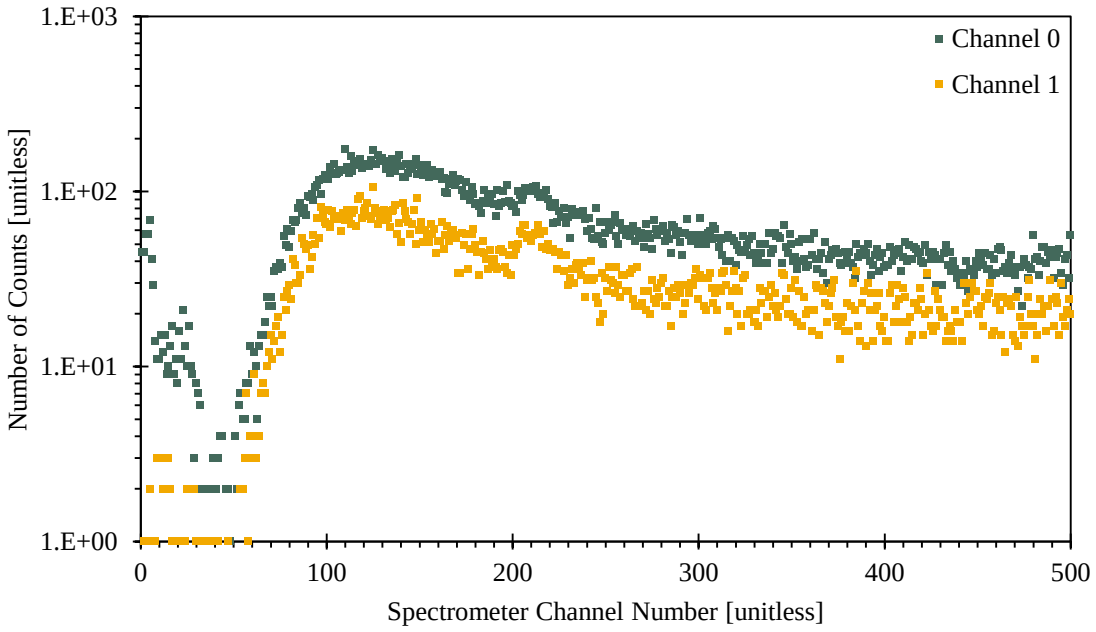

Figure 2.32: The ^{65}Zn spectrum acquired by the XIA LLC Si-PIN diode spectrometer prototype at 12:28:04 on 15 January 2016.

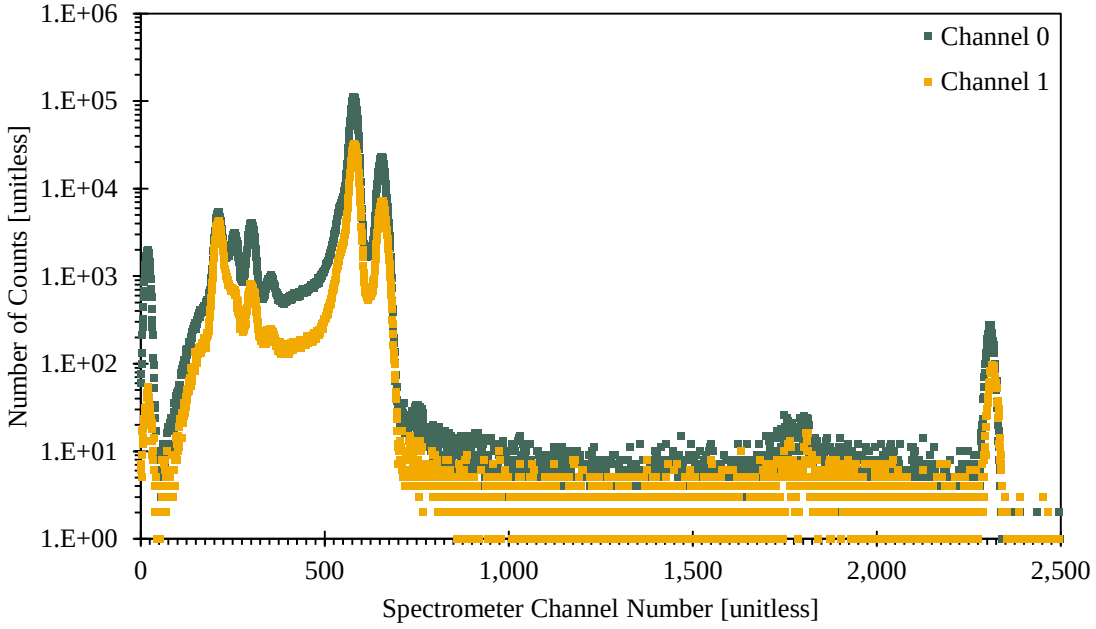

Figure 2.33: The ^{109}Cd spectrum acquired by the XIA LLC Si-PIN diode spectrometer prototype at 23:27:00 on 6 February 2016.

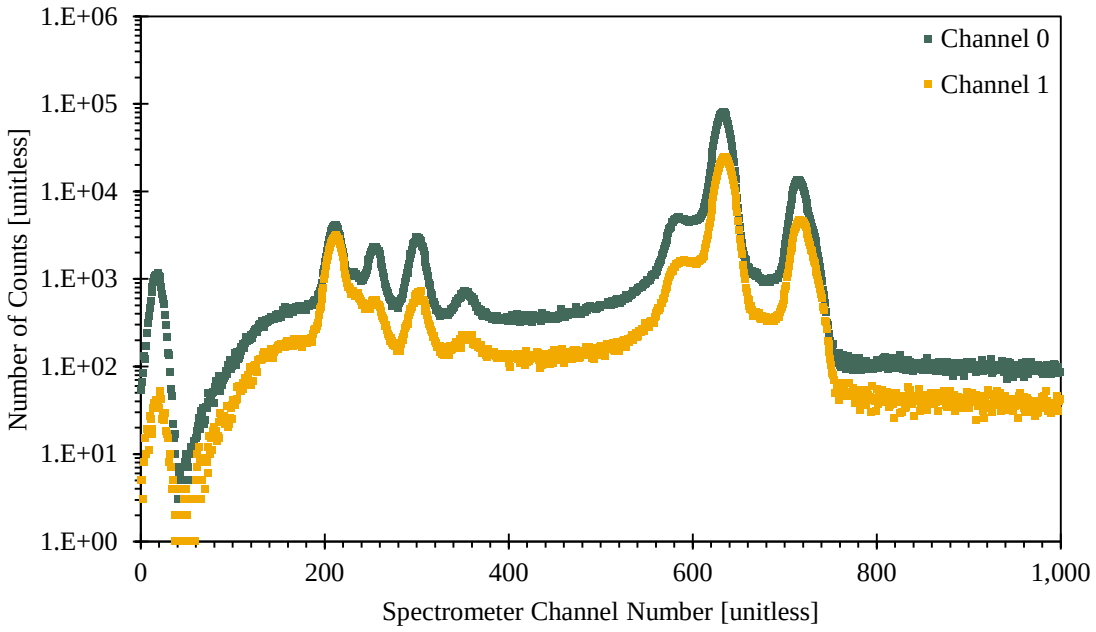

Figure 2.34: The ^{113}Sn spectrum acquired by the XIA LLC Si-PIN diode spectrometer prototype at 10:30:00 on 28 January 2016.

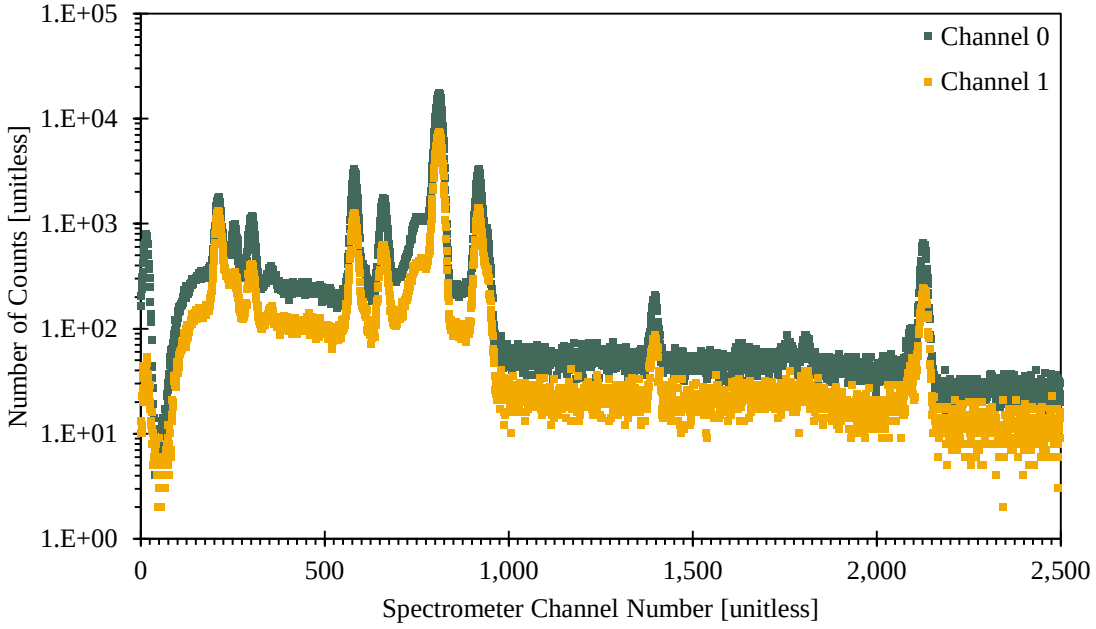

Figure 2.35: The ^{133}Ba spectrum acquired by the XIA LLC Si-PIN diode spectrometer prototype at 19:11:00 on 19 January 2016.

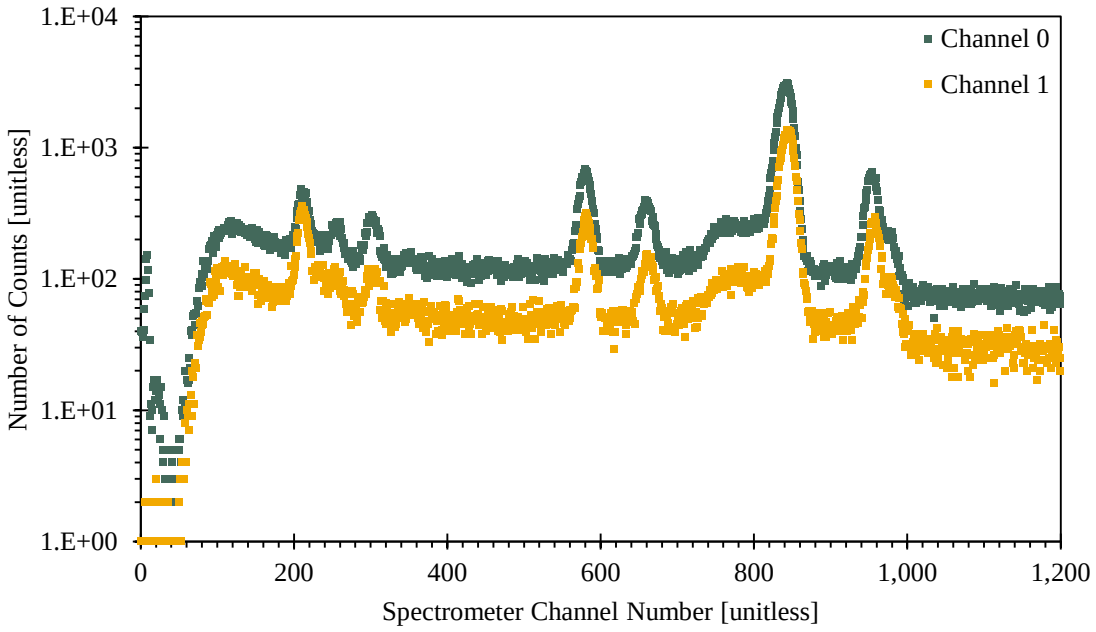

Figure 2.36: The ^{137}Cs spectrum acquired by the XIA LLC Si-PIN diode spectrometer prototype at 00:01:00 on 31 January 2016.

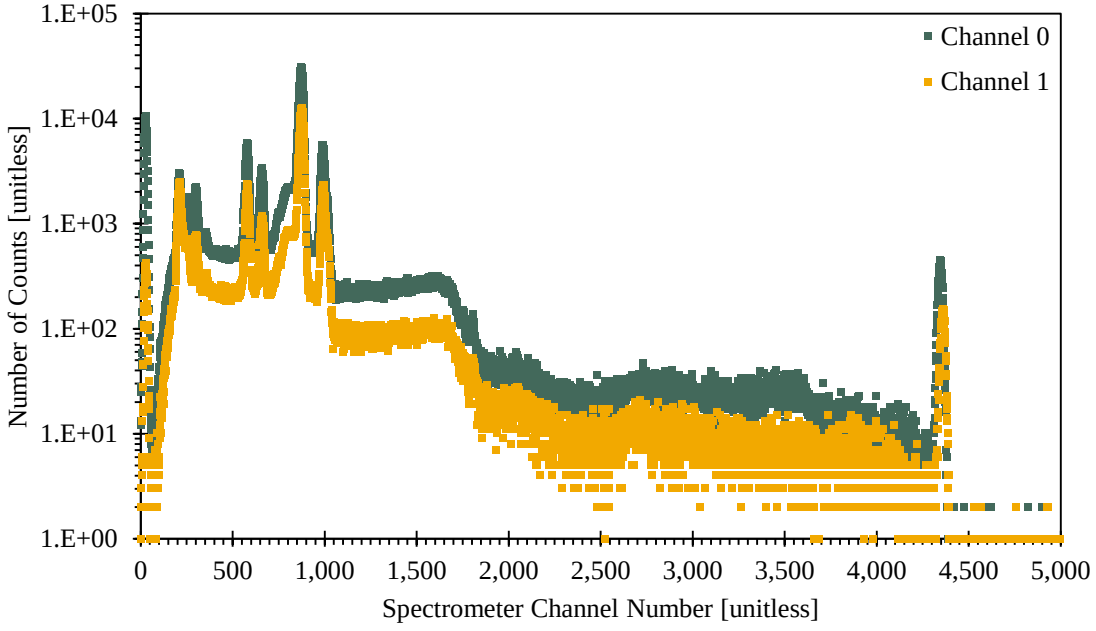

Figure 2.37: The ^{139}Ce spectrum acquired by the XIA LLC Si-PIN diode spectrometer prototype at 14:41:00 on 9 February 2016.

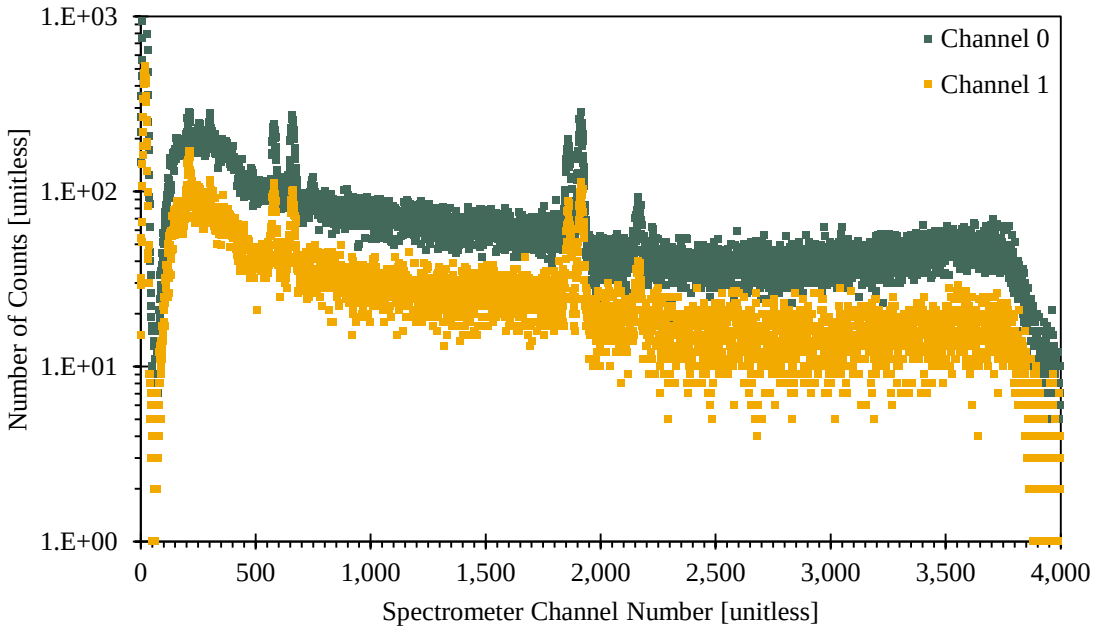

Figure 2.38: The ^{203}Hg spectrum acquired by the XIA LLC Si-PIN diode spectrometer prototype at 10:58:00 on 25 January 2016.

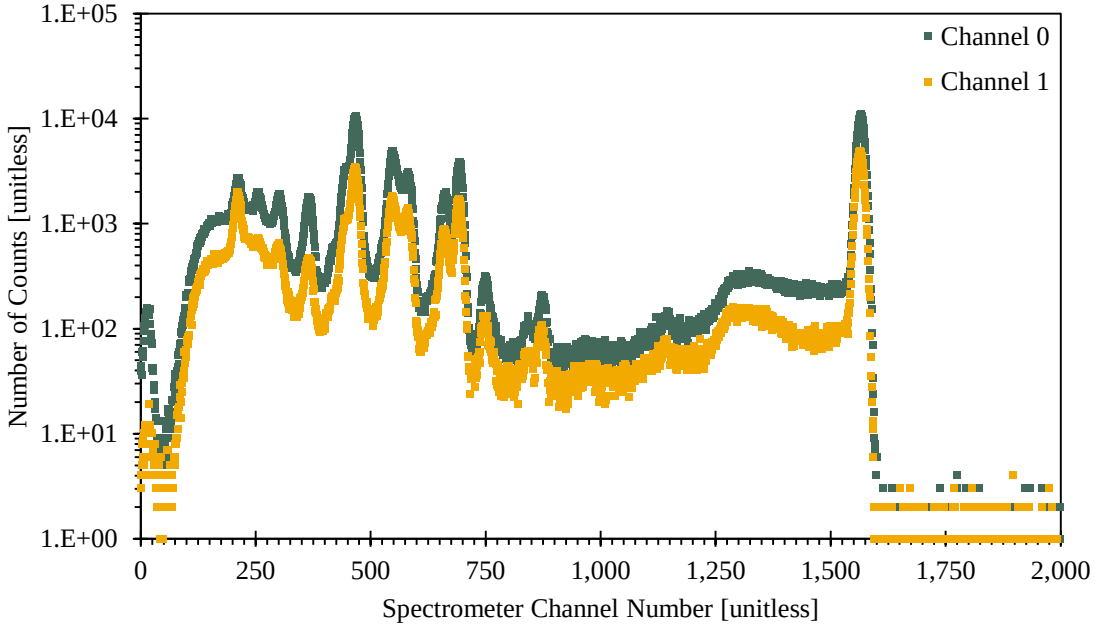

Figure 2.39: The ^{241}Am spectrum acquired by the XIA LLC Si-PIN diode spectrometer prototype at 22:24:01 on 21 January 2016.

2.2.2 Prototype Linearity Characterization

The peak means associated with the prominent photon and conversion electron peaks in the radioxenon and calibration source spectra acquired using the XIA LLC Si-PIN diode spectrometer prototype [67, 68] as described in Sections 2.2.1.2 and 2.2.1.3 were evaluated using the WiPFA peak-fitting algorithm described in Section 2.1.5 and Appendix A. In total, the peak means associated with 36 photon peaks and twelve conversion electron peaks were evaluated. The results of all the peak mean evaluations are reported in Table B.1 in Appendix B. As indicated by the peak mean data in Table B.1, the uncertainties associated with the peak means are, on average, well less than 0.1 %.

The radioxenon and calibration source photon and conversion electron energies are plotted against their respective peak means in Figures 2.40 and 2.41, respectively. Because the uncertainties associated with the peak means are so small, the error bars associated with the peak mean data points are completely covered by the data points themselves. The Si-PIN diode spectrometer prototype photon and conversion electron linearity expressions shown in Figures 2.40 and 2.41 were fit to the photon and conversion electron peak mean data points using the simple linear regression method described in Section 2.1.6.1. 95 % confidence limit prediction intervals were generated to go along with the nominal linearity curves but the widths of the prediction intervals are so narrow that the upper and lower bounds associated with the predication intervals are not visible outside of the nominal linearity curves shown in Figures 2.40 and 2.41.

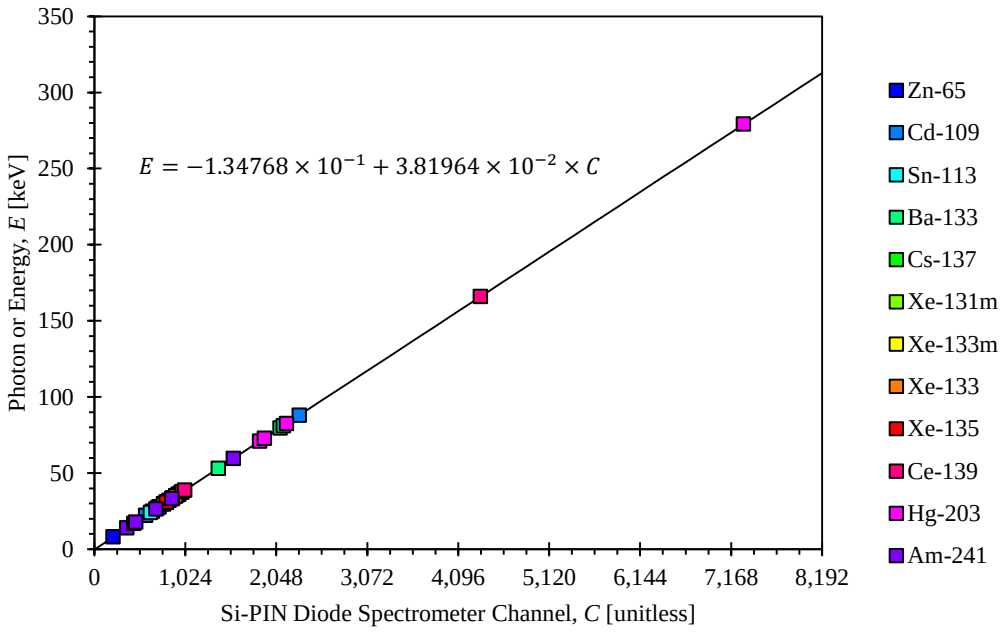

Figure 2.40: XIA LLC Si-PIN diode spectrometer prototype photon linearity calibration (1·σ error bars).

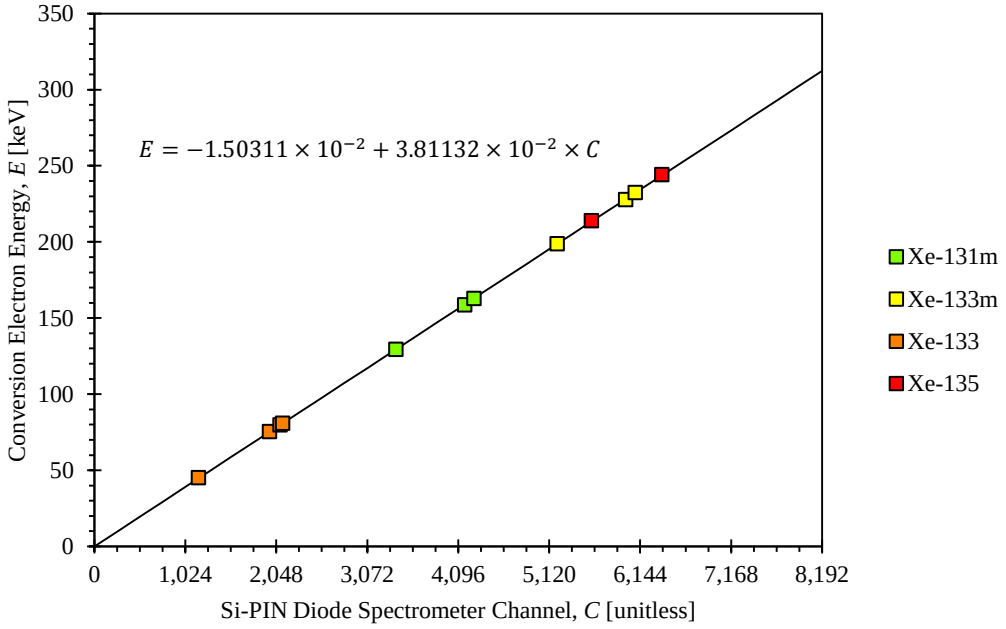

Figure 2.41: XIA LLC Si-PIN diode spectrometer prototype conversion electron linearity calibration (1·σ error bars).

The XIA LLC Si-PIN diode spectrometer prototype photon and conversion electron linearity calibrations were initially treated separately, as illustrated in Figures 2.40 and 2.41, because going into the linearity characterizations there was no reason to assume that the photon and conversion electron peak mean data points would all fall on a single line. However, it turned out that the photon and conversion electron peak mean data points did all fall nicely onto one line and thus it was found that a single, combined photon and conversion electron linearity calibration could be generated for the XIA LLC Si-PIN diode spectrometer prototype.

The combined photon and conversion electron linearity calibration associated with the XIA LLC Si-PIN diode spectrometer prototype is presented in Figure 2.42. The combined photon and conversion electron linearity expression shown in Figure 2.42 was fit to the photon and conversion electron peak mean data points using the simple linear regression method described in Section 2.1.6.1 in the same way the method was applied individually to the photon and conversion electron data points. The vertical axis intercept associated with the linearity expression is very close to zero, as expected, and the peak mean data points all fit along the line quite nicely.

The fact that a single linearity calibration can be applied to both the photon and conversion electron peaks in spectra acquired be the XIA LLC Si-PIN diode spectrometer prototype is important simply because it makes the spectral analysis process much more straight forward than it would be if two separate linearity calibrations had to be applied to the photon and conversion electron peaks.

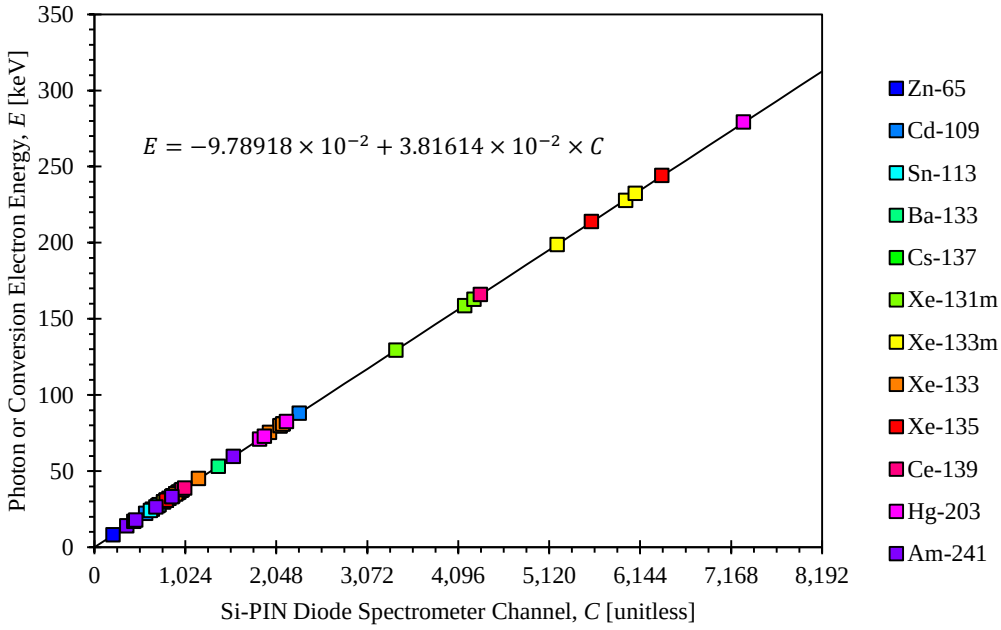

Figure 2.42: XIA LLC Si-PIN diode spectrometer prototype combined photon and conversion electron linearity calibration (1·σ error bars).

2.2.3 Prototype Resolution Characterization

The peak widths associated with the prominent photon and conversion electron peaks in the radioxenon and calibration source spectra acquired by the XIA LLC Si-PIN diode spectrometer prototype [67, 68] were evaluated using the WiPFA peak-fitting algorithm described in Section 2.1.5 and Appendix A. In total, the peak widths associated with 36 photon peaks and twelve conversion electron peaks were evaluated. The results of the peak width evaluations are reported in Table B.2 in Appendix B. As indicated by the peak width data in Table B.2, the uncertainties associated with the photon peak widths are on the order of about 7.0 %, on average, and the uncertainties associated with the conversion electron peak widths are on the order of about 5.0 %, on average.

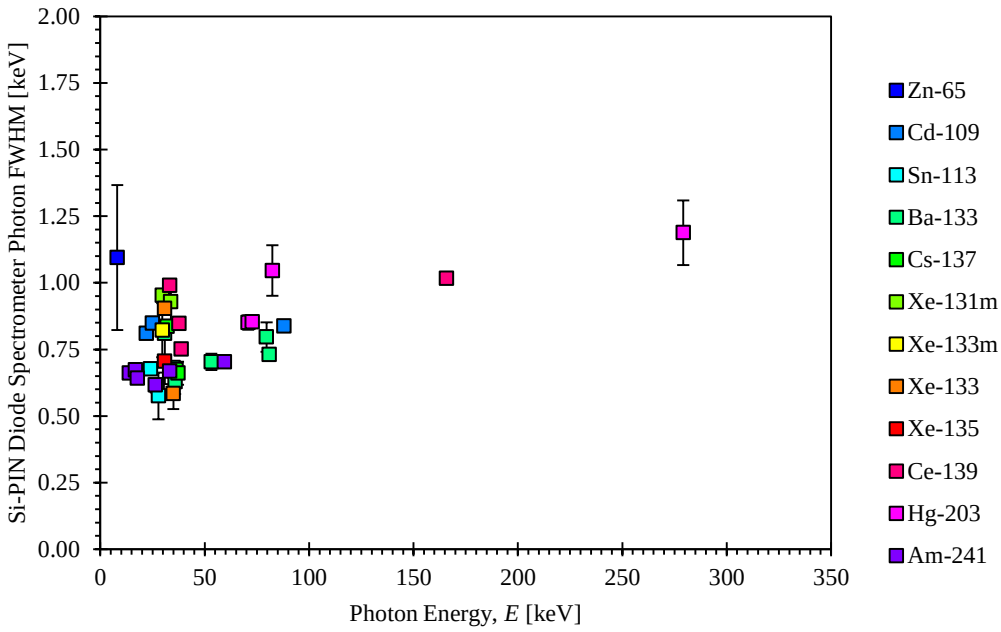

Figure 2.43: XIA LLC Si-PIN diode spectrometer prototype photon peak widths plotted as a function of photon energy (1·σ error bars).

The radioxenon and calibration source photon peak widths are plotted against their respective energies in Figure 2.43. Note that the radioxenon and calibration source X-ray peak widths from Table B.2 are plotted in Figure 2.43 alongside the radioxenon and calibration source gamma-ray peak widths. Unfortunately, however, the X-ray peak widths included in Figure 2.43 are included primarily for completeness; the X-ray peak width data points were of little use in developing a resolution calibration because, as illustrated in Figure 2.43, there is a great deal of variability in the radioxenon and calibration source X-ray peak widths, even over short energy intervals.

The variability in the X-ray peak widths results from the fact that the X-ray peaks used to support the X-ray peak width evaluations are almost all components of multiplets.

These X-ray multiplets are composed of multiple X-ray peaks that are spaced so close together that they typically cannot be resolved from one another. As an example, consider the barium-133 (^{133}Ba) K_β X-ray multiplet shown in Figure 2.44. The ^{133}Ba K_β X-ray multiplet is composed of three X-ray peaks; the three peaks are attributable to the ^{133}Ba $K_{\beta1}$, $K_{\beta2}$, and $K_{\beta3}$ X-rays. The nominal energies associated with the ^{133}Ba $K_{\beta1}$, $K_{\beta2}$, and $K_{\beta3}$ X-rays are 34.987, 35.818, and 34.92 keV, respectively [60]. The nominal energy of the ^{133}Ba $K_{\beta2}$ X-ray differs from the nominal energies associated with the ^{133}Ba $K_{\beta1}$ and $K_{\beta3}$ X-rays enough that the $K_{\beta2}$ X-ray peak may be resolved from the $K_{\beta1}$ and $K_{\beta3}$ X-ray peaks in the ^{133}Ba K_β X-ray multiplet. However, the nominal energies of the ^{133}Ba $K_{\beta1}$ and $K_{\beta3}$ X-rays are so similar that they effectively produce one wide peak in the ^{133}Ba K_β X-ray multiplet. The width of this wide, combined $K_{\beta1}$ and $K_{\beta3}$ X-ray peak is really not representative of any particular photon energy and thus is not useful in terms of generating a photon resolution calibration.

Given that the X-ray peak widths were not useful in terms of generating a photon resolution calibration, an XIA LLC Si-PIN diode spectrometer prototype photon resolution calibration was produced using only gamma-ray peak width data. The XIA LLC Si-PIN diode spectrometer prototype gamma-ray resolution calibration presented in Figure 2.45 was developed from nine gamma-ray peak width data points. It worked out nicely that the nine gamma-ray peaks for which peak width data was available spanned the majority of the 0 to 310 keV energy range covered by the XIA LLC Si-PIN diode spectrometer prototype.

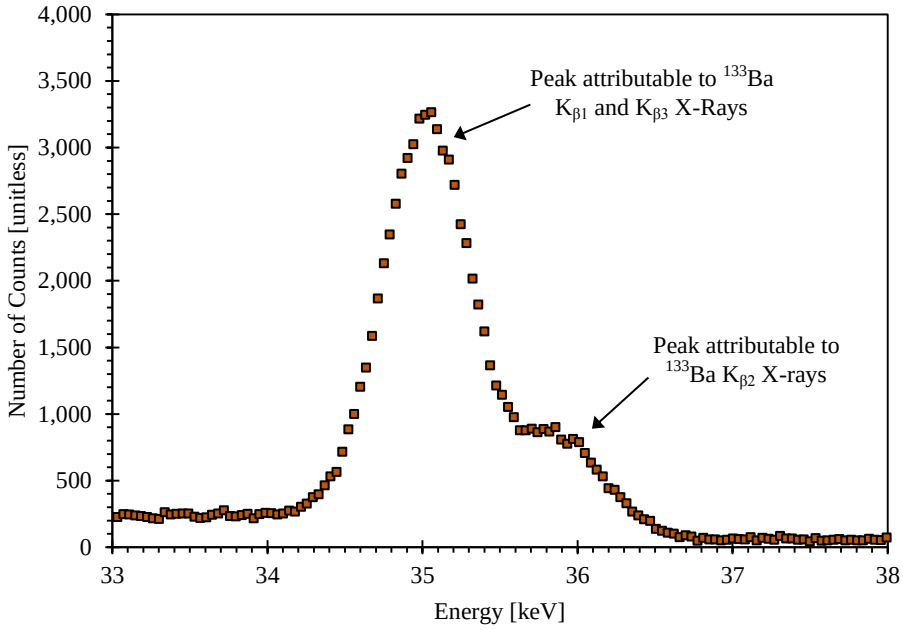

Figure 2.44: The ^{133}Ba K_β X-ray multiplet.

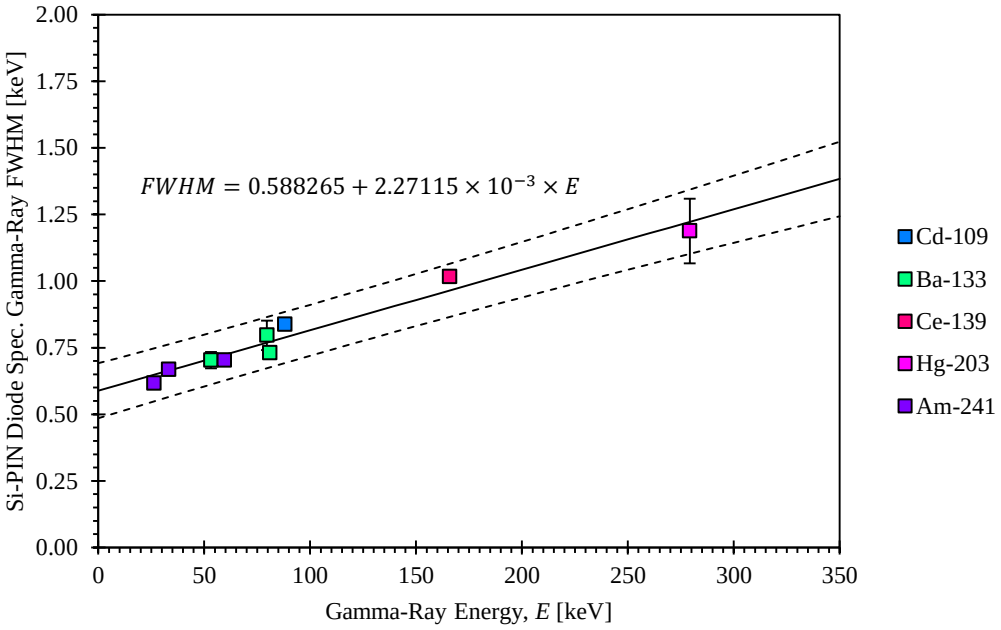

Figure 2.45: XIA LLC Si-PIN diode spectrometer prototype gamma-ray resolution calibration (1·σ error bars).

The expression describing the XIA LLC Si-PIN diode spectrometer prototype gamma-ray resolution as a function of energy was fit to the gamma-ray peak width data points shown in Figure 2.45 using the simple linear regression method described in Section 2.1.6.1. The dashed lines on either side of the nominal gamma-ray resolution fit represent the upper and lower bounds of a 95 % confidence limit prediction interval. Note that the fit has a vertical axis intercept of about 0.59 keV and a positive slope. Additionally, the fit predicts that the widths of photon peaks produced by 5.89, 25.27, and 59.54 keV photons should be about 0.60 keV ± 0.10 keV (17 %), 0.65 keV ± 0.10 keV (15 %), and 0.72 keV ± 0.10 keV (13 %), respectively.

These photon peak widths are somewhat wider than even the largest widths predicted by Amptek, Inc. (the manufacturer of the Si-PIN diodes employed by the XIA LLC Si-PIN diode spectrometer prototype) [94]. The largest 5.89, 25.27, and 59.54 keV photon peak width predictions reported by Amptek, Inc. are 0.250 keV, 0.331 keV, and 0.440 keV, respectively [86]. The discrepancies between the peak widths evaluated herein and the peak widths predicted by Amptek, Inc. likely result largely from the fact that the Amptek, Inc. peak width evaluations were made with the Si-PIN diodes cooled to -55 °C (218.2 K), [86] which is considerably cooler than the temperature the Si-PIN diodes were cooled to for the characterization studies documented herein (276 K (3 °C)) [67, 68].

While the gamma-ray peak widths evaluated herein are somewhat larger than the photon peak width predictions reported by Amptek, Inc., they are in relatively close agreement with the photon peak widths reported by Hennig *et al.* [67, 68]. Table 2.10

presents a summary of the X-ray, gamma-ray, and conversion electron peak widths reported by Hennig *et al.* [67, 68]. Comparing the gamma-ray peak widths evaluated herein to the photon peak widths reported by Hennig *et al.* reveals that the peak widths are in fact in close agreement with one another. It should be noted, however, that the peak widths reported by Hennig *et al.* were developed from spectra acquired with the Si-PIN diodes at room temperature, so the conditions were somewhat different than the conditions during the experiments documented herein.

In addition to the gamma-ray peak width calibration shown in Figure 2.45, a second gamma-ray peak width resolution calibration was generated in accordance with the theoretical resolution function prescribed by Amptek, Inc. [86]. This theoretical resolution function relates the width of the 5.9 keV photon peak to the widths of peaks produced by photons of other energies as follows [86]:

$$FWHM_{E_x} = \sqrt{FWHM_{E=5.9\ keV}^2 - 120^2 + 2{,}440 \cdot E_x}. \qquad 2.2.3.1$$

Where: $FWHM_{E_x}$ is the FWHM of a peak produced by photons of energy E_x and

$FWHM_{E=5.9\ keV}$ is the FWHM of the 5.9 keV photon peak.

The gamma-ray peak width data used to generate the gamma-ray calibration shown in Figure 2.45 was plugged into Equation 2.2.3.1 to produce the three gamma-ray resolution calibration curves shown in Figure 2.46. In order to generate the three gamma-ray resolution calibration curves shown in Figure 2.46 the nine gamma-ray peak widths shown in Figure 2.45 were first adjusted to 5.9 keV via Equation 2.2.3.1. The solid gamma-ray resolution calibration curve shown in Figure 2.46 is the gamma-ray resolution

calibration developed using Equation 2.2.3.1 and the average of the nine gamma-ray resolutions adjusted 5.9 keV. The dashed lines shown in Figure 2.46 are gamma-ray resolution calibrations developed using Equation 2.2.3.1 and the smallest and largest of the nine gamma-ray resolutions adjusted to 5.9 keV. The gamma-ray resolution calibrations represented by the dashed lines in Figure 2.46 serve to illustrate the uncertainty that may be associated with the nominal gamma-ray resolution calibration curve given by the solid line.

Table 2.10: X-ray, gamma-ray, and conversion electron peak widths reported by Hennig *et al.* [67].

Source	Decay Mode	Energy [keV]	Peak Width * [keV]
^{133m}Xe	X-Ray	30	0.564
^{133}Xe	X-Ray	31	0.618
^{133}Ba	X-Ray	35	0.450
^{133}Xe	Gamma-Ray	81	1.456
^{133}Ba	Gamma-Ray	81	0.584
^{133m}Xe	Conv. Elec.	199	1.098
^{133m}Xe	Conv. Elec.	229	1.319
^{133}Xe	Conv. Elec.	45	0.852
^{137}Cs	Conv. Elec.	656	1.538
^{133}Ba	Conv. Elec.	348	7.651

* Note that these peak widths were developed from spectra acquired with the Si-PIN diodes at room temperature.

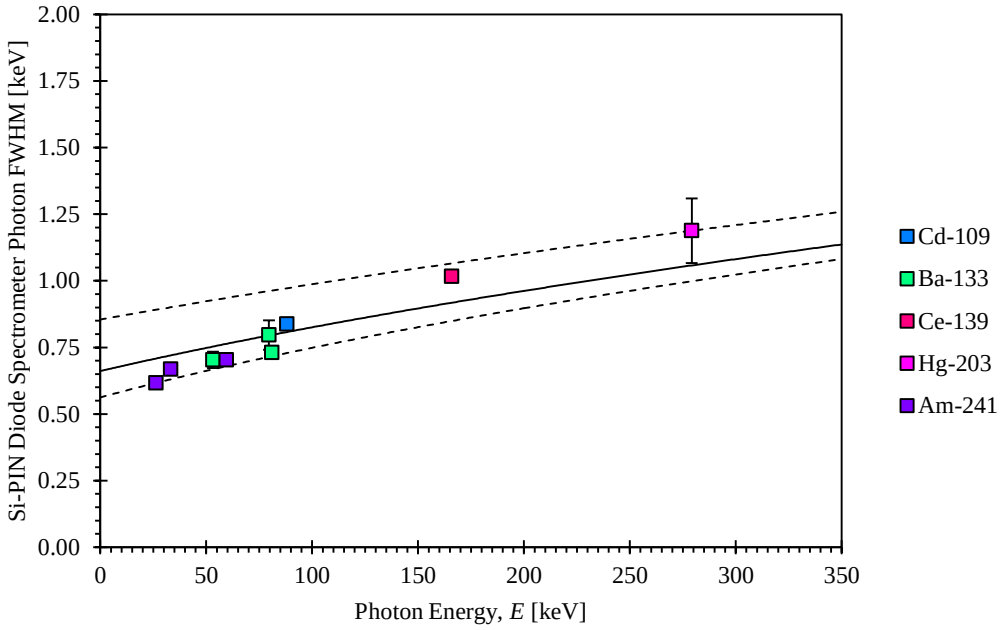

Figure 2.46: XIA LLC Si-PIN diode spectrometer prototype gamma-ray resolution calibration generated in accordance with the theoretical resolution function prescribed by Amptek, Inc. (1·σ error bars).

A separate XIA LLC Si-PIN diode spectrometer prototype conversion electron resolution calibration was also developed by plotting the radioxenon conversion electron peak widths reported in Table B.2 of Appendix B against their respective conversion electron energies as shown in Figure 2.47. The expression describing the conversion electron resolution as a function of conversion electron energy was fit to the twelve conversion electron peak width data points using the simple linear regression method described in Section 2.1.6.1. The fit predicts that the widths of the conversion electron peaks produced by 50, 150, and 250 keV conversion electrons should be about 1.29 keV ± 0.42 keV (32 %), 1.37 keV ± 0.37 keV (27 %), and 1.45 keV ± 0.39 keV (27 %), respectively. The dashed lines on either side of the nominal conversion electron

resolution fit represent the upper and lower bounds of a 95 % confidence limit prediction interval. The prediction interval is fairly wide in this case simply because there is a significant amount of scatter in the conversion electron peak width data points.

The most important result that may be derived from the XIA LLC Si-PIN diode spectrometer prototype conversion electron resolution calibration is the fact that the twelve radioxenon conversion electron peaks most relevant to the verification regime of the CTBT are all separated from one another by several FWHMs. This is a significant and important result because it means that the radioxenon conversion electron peaks do not overlap or interfere with each other, which makes the peaks easier to analyze.

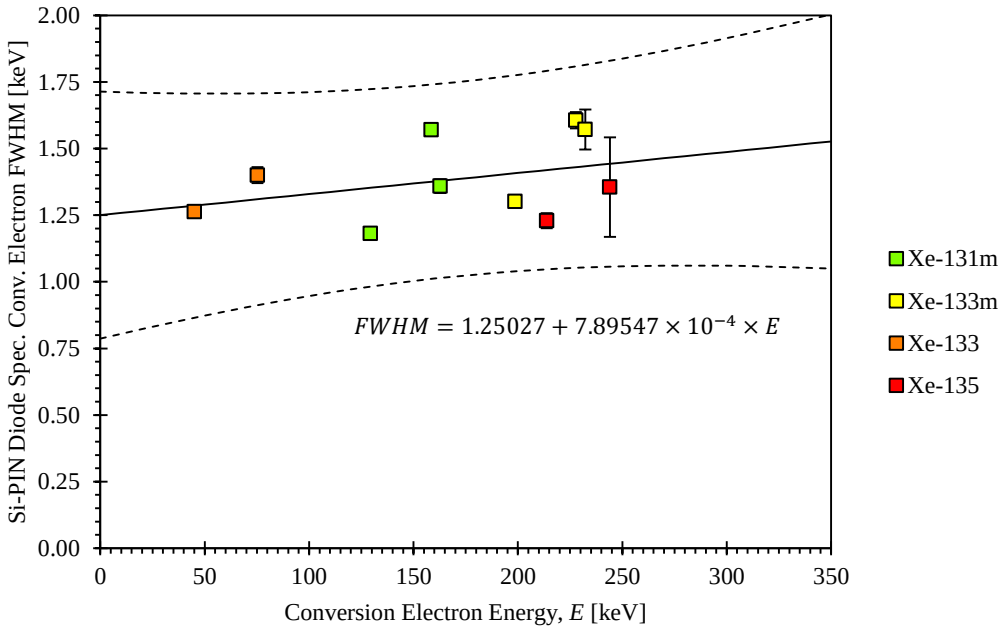

Figure 2.47: XIA LLC Si-PIN diode spectrometer prototype conversion electron resolution calibration (1·σ error bars).

2.2.4 Prototype Detection Efficiency Characterization

The areas associated with each of the prominent peaks in the radioxenon and calibration source spectra were evaluated using the WiPFA peak-fitting algorithm described in Section 2.1.5 and Appendix A. In total, the peak areas associated with 48 peaks (36 photon peaks and twelve conversion electron peaks) were evaluated. The results of all of the peak area evaluations are presented in Table B.3 in Appendix B. As indicated by the peak area data in Table B.3, the uncertainties associated with the radioxenon photon peak areas are on the order of about 8.2 %, on average, the uncertainties associated with the calibration source photon peak areas are on the order of about 4.9 %, on average, and the uncertainties associated with the conversion electron peak areas are on the order of about 5.1 %, on average.

The radioxenon and calibration source photon and conversion electron peak areas presented in Table B.3 were used to calculate absolute photon and conversion electron detection efficiencies for the XIA LLC Si-PIN diode spectrometer prototype. The absolute photon and conversion electron detection efficiencies were calculated in accordance with Equation 2.1.3.3.1. For each of the absolute detection efficiency calculations the expected number of photon or conversion electron emissions was calculated using Equation 2.1.3.3.2. The radioxenon and calibration source activities and the spectral data set acquisition times supporting the expected photon and conversion electron emission calculations are in Tables 2.6, 2.7, 2.8, and 2.9.

The results of the radioxenon and calibration source absolute photon and conversion electron detection efficiency calculations are shown in Figure 2.48. All of the absolute photon and conversion electron detection efficiencies are plotted in the same figure for context, but comparisons should only be made amongst absolute detection efficiency data points of a given category. Also, note that the absolute detection efficiencies plotted in Figure 2.48 are the absolute detection efficiencies specific to the front Si-PIN diode. The absolute detection efficiencies associated with the Si-PIN diode spectrometer prototype are equal to about two times the plotted values.

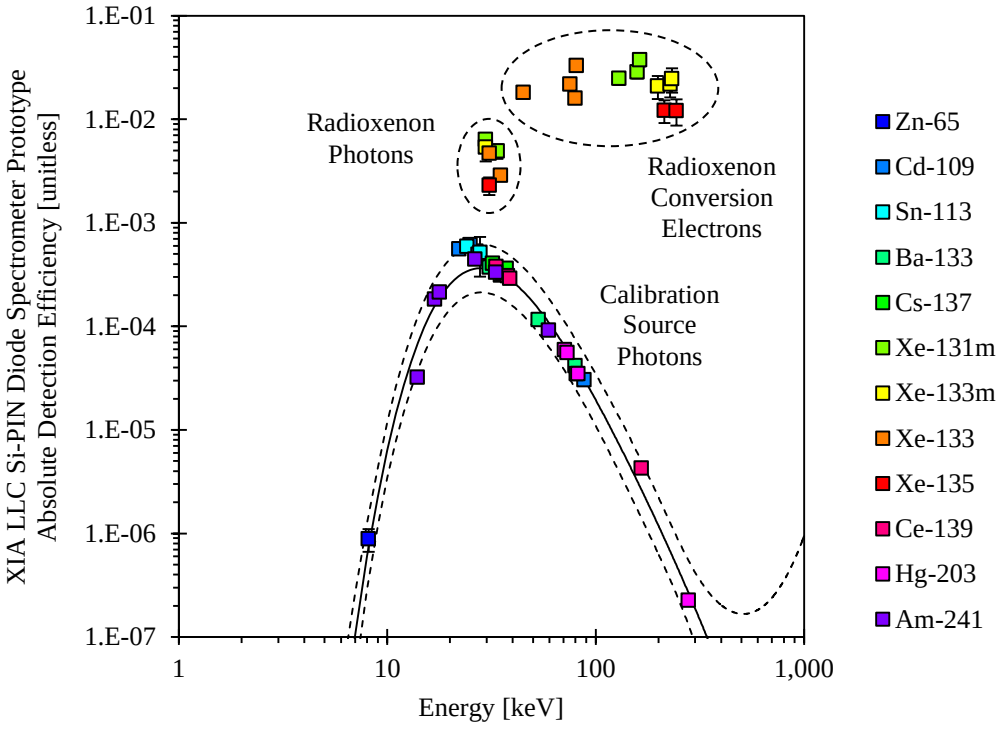

Figure 2.48: XIA LLC Si-PIN diode spectrometer prototype absolute photon and conversion electron detection efficiency calibration (1·σ error bars).

A curve was fit to the absolute photon detection efficiency data points attributable to the calibration source using the multiple regression method described in Section 2.1.6.2. The dashed lines on either side of the absolute photon detection efficiency curve fit represent the upper and lower bounds of a 95 % confidence limit prediction interval. The curve fit predicts that the maximum absolute photon detection efficiency of the XIA LLC Si-PIN diode spectrometer prototype is about 0.036 % and is achieved at photon energies near 28 keV. It is also interesting to note that the shape of the absolute photon detection efficiency curve fit is consistent with both the HPGe absolute photon detection efficiency curve fit shown in Figure 2.12 and the XR-100CR Si PIN diode intrinsic photon detection efficiency curve shown in Figure 2.4 [86].

As illustrated by Figure 2.48, all of the radioxenon absolute photon detection efficiency data points are above the absolute photon detection efficiency data points attributable to calibration source photons. This seems reasonable given that the radioxenon source to Si-PIN diode geometric configuration is more favorable than the calibration source to Si-PIN diode geometric configuration.

In total six radioxenon photon absolute detection efficiency data points were available for analysis over an energy range extending from about 29.669 keV to 34.964 keV. However, because the ^{133}Xe absolute detection efficiency uncertainties are very large the ^{133}Xe data points are not considered here. Given that only a limited number of data points were available over a narrow energy range it did not make sense to fit a curve to the radioxenon absolute photon detection efficiency data. Instead, an average

radioxenon photon absolute detection efficiency was calculated and found to be about 0.48 ± 0.05 % at photon energies near 30 keV.

In order to support more direct comparisons to the theoretical XR-100CR Si-PIN diode intrinsic photon detection efficiencies reported by Amptek (see Figure 2.4) the radioxenon absolute detection efficiencies were divided by the geometric efficiency associated with the XIA LLC Si-PIN diode spectrometer prototype. The geometric efficiency associated with the XIA LLC Si-PIN diode spectrometer prototype was evaluated as described in Appendix C. Suffice it to say here that the geometric efficiency associated with the prototype (both Si-PIN diodes) was found to be 9.6 %. The geometric efficiency associated with one of the Si-PIN diodes should then be about 4.8 %. Dividing the absolute photon detection efficiency of one Si-PIN diode by the geometric efficiency associated with one Si-PIN diode produced an intrinsic XR-100CR Si-PIN diode detection efficiency estimate of about 9.9 % for photon energies near 30 keV. This intrinsic photon detection efficiency is in relatively close agreement with the intrinsic 30 keV photon detection efficiency reported by Amptek (about 15 %) [86].

The absolute conversion electron detection efficiencies associated with the XIA LLC Si-PIN diode spectrometer prototype are also plotted in Figure 2.48. As expected, the absolute conversion electron detection efficiencies are higher than the photon detection efficiencies. As was the case with the radioxenon absolute photon detection efficiency data, only a limited number of radioxenon absolute conversion electron detection efficiency data points were available and so it did make sense to fit a curve to the radioxenon absolute conversion electron detection efficiency data. Instead an average

absolute conversion electron detection efficiency was calculated and found to be about 2.6 ± 0.2 %. Given that the average energy associated with the conversion electron data points used to evaluate the average conversion electron absolute detection efficiency was about 150 keV, the average absolute conversion electron detection efficiency is attributed to conversion electron energies near 150 keV.

Dividing the average absolute conversion electron detection efficiency associated with one Si-PIN diode by the geometric efficiency associated with one Si-PIN diode reveals that the intrinsic conversion electron detection efficiency associated with the Amptek XR-100CR Si-PIN diodes is about 55 %.

Note that the large disparity between the absolute and intrinsic photon and conversion electron detection efficiencies associated with the XIA LLC Si-PIN diode spectrometer prototype indicate that modifying the geometric configuration of the prototype could produce significant absolute detection efficiency performance improvements. The performance improvements associated with some basic geometric configuration modifications are studied in the Si-PIN diode spectrometer prototype optimization section (Section 2.3).

2.2.5 Prototype Minimum Detectable Concentrations

XIA LLC Si-PIN diode spectrometer prototype radioxenon Minimum Detectable Concentrations (MDCs) were evaluated using the absolute conversion electron detection efficiencies evaluated in the previous section and the MDC expression given by Equation 2.1.3.4.1 [71]. An eight hour cycle time was assumed in support of the

XIA LLC Si-PIN diode spectrometer prototype MDC evaluations. Furthermore, the radioxenon half-life and conversion electron branching ratio data needed to support the MDC evaluations was taken from the nuclear decay database maintained by the National Nuclear Data Center [60]. The results of the XIA LLC Si-PIN diode spectrometer prototype radioxenon MDC evaluations are presented in Figure 2.49.

Comparisons will be made to the radioxenon MDCs associated with the ARIX, ARSA, SAUNA, and SPALAX systems in the next section. For now, note that the smallest XIA LLC Si-PIN diode spectrometer prototype ^{131m}Xe, ^{133m}Xe, and ^{133}Xe MDCs are all on the order of about 1.9 mBq-m^{-3}. For each of the radioxenons, the smallest MDC is the one attributable to the radioxenon conversion electron with the largest branching ratio. The ^{135}Xe MDC is fairly large compared to the ^{131m}Xe, ^{133m}Xe, and ^{133}Xe MDCs because the branching ratio associated with the most intense ^{135}Xe conversion electron is fairly small (about 5.61 % [60]) compared to the branching ratios associated with the most intense ^{131m}Xe, ^{133m}Xe, and ^{133}Xe conversion electron branching ratios. A review of Equation 2.1.3.4.1 reveals that the MDC is inversely related to the branching ratio, so it makes sense that the radioxenon with the smallest branching ratio has the largest MDC.

Unfortunately, there are no alternate ^{135}Xe gamma-rays that may be used to produce a smaller ^{135}Xe MDC result using the XIA LLC Si-PIN diode spectrometer prototype. The most intense ^{135}Xe gamma-ray has an energy of 249.794 keV [60] and at those energies the XIA LLC Si-PIN diode absolute photon detection efficiencies are very low (about 4.4×10^{-5} %).

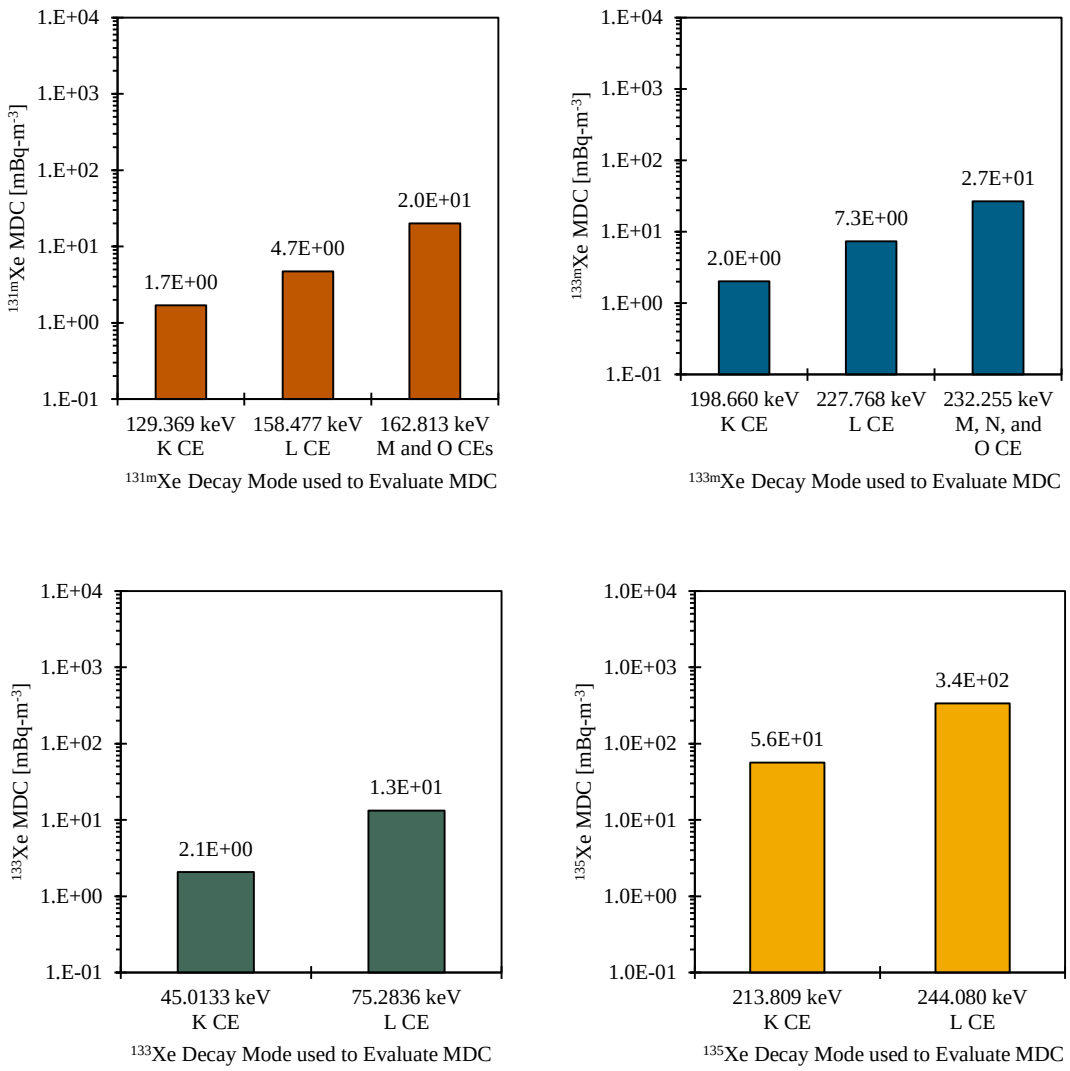

Figure 2.49: XIA LLC Si-PIN diode spectrometer prototype Minimum Detectable Concentrations (MDCs).

2.2.6 Prototype Performance Comparisons

The radioxenon MDCs associated with the XIA LLC Si-PIN diode spectrometer prototype are reproduced in Table 2.11. In addition to the 8 hour cycle time MDCs reported in the previous section, Table 2.11 also reports the radioxenon MDCs associated with 12 and 24 hour cycle times. The MDCs associated with these additional cycle times are reported here to make for more meaningful comparisons with the ARIX [52], SAUNA [57], and SPALAX [58] systems, which utilize 12 and 24 hour cycle times. The ARSA system [54] uses an 8 hour cycle time.

The XIA LLC Si-PIN diode spectrometer prototype radioxenon MDCs reported in Table 2.11 are, generally speaking, comparable to the radioxenon MDCs associated with the ARIX, ARSA, SAUNA, and SPALAX systems. The one exception is the XIA LLC Si-PIN diode spectrometer prototype ^{135}Xe MDC, which is about two orders of magnitude larger than the ^{135}Xe MDCs associated with the other systems. Recall from Section 2.2.5 that the large ^{135}Xe MDC comes as a result of the small ^{135}Xe branching ratio.

While a smaller ^{135}Xe MDC would obviously be preferred, note that because ^{135}Xe has a relatively short half-life (only about 9.14 hours [60]) it is the radioxenon that is least likely to be detected following a nuclear explosion. Additionally, studies conducted by Kalinowki *et al.* [61] indicate that, of the four radioxenons, ^{135}Xe is the least useful in terms of discriminating radioxenon detections indicative of nuclear explosions from radioxenon detections characteristic of commercial nuclear generating station, nuclear research reactor, and radiopharmaceutical facility releases.

An additional set of MDCs were calculated using the intrinsic full-energy peak detection efficiencies associated with the XIA LLC Si-PIN diode spectrometer prototype. These calculations indicate that the absolute lowest ^{131m}Xe, ^{133m}Xe, ^{133}Xe, and ^{135}Xe MDCs achievable using Si-PIN diode-based spectrometers are probably about 0.081, 0.097, 0.099, and 2.7 mBq-m^{-3}, respectively. The fact that these radioxenon MDCs are considerable lower than the radioxenon MDCs associated with the ARIX, ARSA, SAUNA, and SPALAX system suggests that optimized Si-PIN diode-based radiation spectrometers could outperform the aforementioned systems.

Table 2.11: XIA LLC Si-PIN diode spectrometer prototype MDC comparisons.

Monitoring System	Radioxenon Minimum Detectable Concentrations (MDCs) [mBq-m^{-3}]			
	^{131m}Xe	^{133m}Xe	^{133}Xe	^{135}Xe
ARIX [1]	0.52	0.55	0.40	0.64
ARSA [2]	< 0.1	0.15	< 0.1	0.3
SAUNA [3]	0.71	0.57	0.93	0.90
SPALAX [4]	4.05	1.53	0.15	0.65
XIA LLC Si-PIN Diode Spec. Prototype	1.7 (8 h)	2.0 (8 h)	2.1 (8 h)	56 (8 h)
	1.4 (12 h)	1.8 (12 h)	1.7 (12 h)	79 (12 h)
	0.99 (24 h)	1.7 (24 h)	1.3 (24 h)	270 (24 h)

1. The ARIX system MDCs reported here were calculated from the minimum detectable activities reported by Popov *et al.* [53] and the 12 h cycle time reported by Dubasov *et al.* [52].
2. The ARSA system MDCs reported here were taken from Bowyer *et al.* [54]. Associated cycle time is 8 h.
3. The SAUNA system MDCs reported here were taken from Ringbom *et al.* [57]. Associated cycle time is 12 h.
4. The SPALAX system MDCs reported here were taken from Fontaine *et al.* [58]. Associated cycle time is 24 h.

2.3 Si-PIN Diode Spectrometer Prototype Optimization

As discussed in Sections 2.2.5 and 2.2.6, the Si-PIN diode spectrometer prototype developed and assembled by XIA LLC [67, 68] has ^{131m}Xe, ^{133m}Xe, and ^{133}Xe Minimum Detectable Concentrations (MDCs) that are comparable to the MDCs associated with the ARIX [52], ARSA [54], SAUNA [57], and SPALAX [58] systems currently employed by the verification regime of the CTBT [33]. The fact that the XIA LLC Si-PIN diode spectrometer prototype has radioxenon MDCs that are comparable to those of the ARIX, ARSA, SAUNA, and SPALAX systems suggests that Si-PIN diode-based spectrometers could serve as viable alternatives to the high-resolution gamma-ray and beta-gamma coincidence spectrometers currently employed by the aforementioned systems. That said, additional Si-PIN diode spectrometer radioxenon MDC reductions could strengthen the case for Si-PIN diode based systems further.

The large disparity between the absolute and intrinsic photon and conversion electron detection efficiencies associated with the XIA LLC Si-PIN diode spectrometer prototype (see Section 2.2.4) suggests that a Si-PIN diode-based spectrometer with an optimized source to Si-PIN diode geometric configuration might have significantly better absolute photon and conversion electron detection efficiencies and thus reduced MDCs.

The objective of the optimization studies documented in this section was to evaluate the absolute detection efficiency and MDC performance gains that might be achievable through a variety of Si-PIN diode spectrometer prototype design modifications. The first round of optimization studies evaluate the performance gains that might be achievable utilizing thinner, cylindrical spectrometer chambers coupled with

Si-PIN diodes identical to the Si-PIN diodes employed by the XIA LLC Si-PIN diode spectrometer prototype. These studies provide valuable insights regarding Si-PIN diode-based spectrometer performance capabilities that should be achievable utilizing Si-PIN diodes available today.

Subsequent studies evaluate absolute detection efficiency and MDC performance gains that might be achievable if larger, thicker Si-PIN diodes were to become available. While the performance estimates generated by these studies might not be achievable using Si-PIN diodes available today, the results are still interesting in that they provide an indication as to what might be achievable in the future if larger, thicker Si-PIN diodes become available.

2.3.1 Development of an MCNP Model of the XIA LLC Si-PIN Diode Spectrometer Prototype

The Si-PIN diode spectrometer optimization studies discussed in this section were conducted using the Monte Carlo N-Particle (MCNP) radiation transport code developed and maintained by Los Alamos National Laboratory [74, 75, 76, 77]. More specifically, these studies utilized MCNP version 6.1.1beta [75], which was the most current version of MCNP available at the time the studies documented here were initiated.

At the most basic level, the MCNP radiation transport code serves to introduce a simulated radiation source to a simulated physical system. The code then uses tabulated data describing radiation interaction probabilities specific to the materials the simulated physical system is composed of to simulate the movement of the simulated radiations

through the simulated physical system. The code monitors the behavior of the simulated radiations as they move through the simulated system and is capable of tabulating and returning various pieces of useful information regarding the movement and interactions of the simulated radiations in the simulated system.

The MCNP radiation transport code has been in existence for more than 50 years [76] and has been used quite extensively in the radiation spectrometer design and characterization fields, particularly in recent years. There are an abundance of papers describing the use of MCNP as a radiation spectrometer characterization tool readily available in the literature [109, 110, 111].

In the Si-PIN diode optimization studies documented herein, the MCNP radiation transport code is used to introduce photons and conversion electrons representative of ^{131m}Xe, ^{133m}Xe, ^{133}Xe, and ^{135}Xe decay modes to simulated Si-PIN diode spectrometer systems, to track the movement of the photons and conversion electrons through the simulated systems, and to tabulate the energy deposited in the Si-PIN diodes associated with the simulated Si-PIN diode spectrometer systems. In this way, simulated radioxenon photon and conversion electron spectra are generated and subsequently used to develop absolute photon and conversion electron detection efficiency estimates for a number of Si-PIN diode-based spectrometer designs. The absolute conversion electron detection efficiency estimates are used to develop radioxenon MDC estimates for each of the designs. The performance characteristics associated with several of the optimized Si-PIN diode spectrometer designs are then compared to the performance characteristics associated with the XIA LLC Si-PIN diode spectrometer prototype [67, 68] and the high-

resolution and beta-gamma coincidence spectrometers currently utilized by the ARIX [52], ARSA [54], SAUNA [57], and SPALAX [58] systems.

The next four sections describe the methods used to develop several Si-PIN diode spectrometer MCNP models in general terms. Sections 2.3.1.1 and 2.3.1.2 begin by describing the methods used to define the geometric configurations of the Si-PIN diode spectrometers and the methods used to define the spectrometer material properties. Sections 2.3.1.3 and 2.3.1.4 then describe the methods used to define the photon and conversion electron sources introduced to the models and the development of the tally cards used to extract simulated photon and conversion electron spectra from the MCNP models. Additionally, an input deck associated with one of the XIA LLC Si-PIN diode spectrometer prototype MCNP models is presented in Appendix D. The input deck has an abundance of comments that explain all the details associated with the model.

2.3.1.1 MCNP Model Development: Geometry

In MCNP, the geometry of a system being modelled must be defined using two types of "cards:" surface cards and cell cards. Surface cards are simply lines of code used to define surfaces that describe the features of the system being modelled. Cell cards are used to define the volumes of the system being modelled. Cells are defined in terms of surfaces. The following example may help to illustrate the MCNP surface and cell card concepts.

Assume that some feature of a given system may be modelled as a cube. Six surface cards would be required to define the six surfaces of the cube: two surfaces would be needed to describe the front and back faces, two surfaces would be needed to describe the left and right faces, and two surfaces would be needed to describe the top and bottom faces. A single cell would then be used to define the volume of the cube. The cell would be defined as occupying the region in space behind the front surface, in front of the back surface, to the right of the left surface, to the left of the right surface, below the top surface, and above the bottom surface. While this is a very basic example, more complicated geometries may defined by simply extending this basic concept.

In fact, only 47 surface cards and 13 cell cards were required to model the most important features of the XIA LLC Si-PIN diode spectrometer prototype [67, 68]. These features include the copper spectrometer chamber, each of the two Si-PIN diodes, the stainless steel evacuate and fill line, the radioxenon gas inside the spectrometer chamber and fill line, the air-tight inner box, and the nitrogen gas inside the air-tight inner box. With regards to the Si-PIN diodes, each Si-PIN diode was modelled in two pieces, an inner sensitive volume and an outer dead layer. The locations of the surfaces used to define these features were developed primarily from dimensions extracted from mechanical drawings provided by XIA LLC [106]. These dimensions were supplemented, as required, by measurements made at The University of Texas at Austin.

Figure 2.50 presents a top-down view of the inside of the XIA LLC Si-PIN diode spectrometer prototype air-tight inner box and a graphical top-down representation of the MCNP model of the XIA LLC Si-PIN diode spectrometer prototype.

The geometries of the optimized Si-PIN diode spectrometer designs studied in Sections 2.3.3.2 through 2.3.3.5 were developed in the manner described here. However, for the optimized spectrometer designs only 45 surface cards were required, as opposed to the 47 surface cards required to define the geometry of the XIA LLC Si-PIN diodes spectrometer prototype.

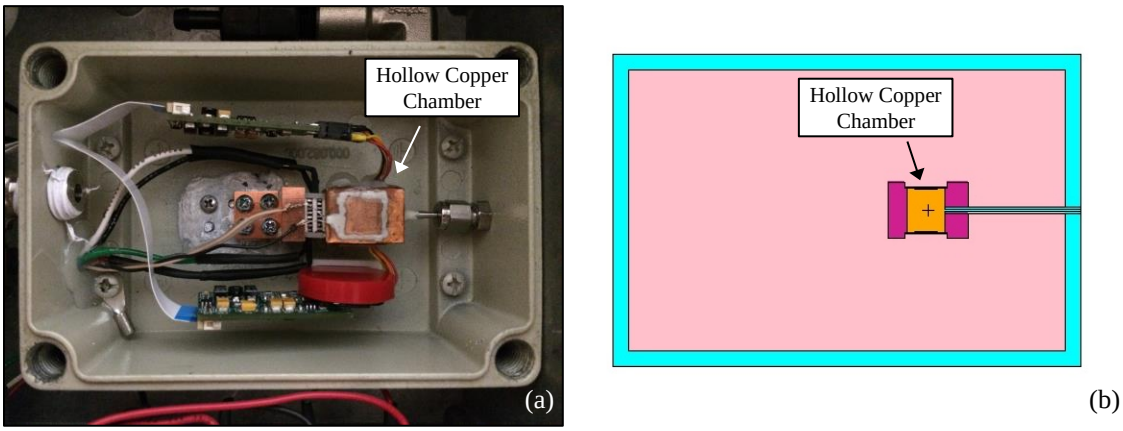

Figure 2.50: Top-down views of (a) the inside of the XIA LLC Si-PIN diode spectrometer prototype and (b) the MCNP model of the prototype.

2.3.1.2 MCNP Model Development: Materials

Six different material data cards were required to assign material properties to the modelled features of the XIA LLC Si-PIN diode spectrometer prototype and the optimized Si-PIN diode spectrometer designs. The hollow copper spectrometer is assumed to be composed of natural copper having the isotopic composition prescribed by the National Institute of Standards and Technology (NIST) [112]. The evacuate and fill line and the air-tight inner box are both assumed to be composed of stainless steel, the isotopic composition of which was extracted from a Pacific Northwest National Laboratory compendium of material properties compiled specifically to support MCNP modelling efforts [113].

The Si-PIN diodes are assumed to be composed of natural silicon having the isotopic composition prescribed by NIST [112]. The isotopic composition of the silicon dioxide substrates the Si-PIN diodes sit on was developed assuming a basic SiO_2 composition, and the isotopic compositions of natural silicon and oxygen were taken from NIST [112].

The radioxenon gas inside the copper spectrometer chamber was assumed to be pure ^{130}Xe, ^{132}Xe, or ^{134}Xe depending on which radioxenon decay modes were being modelled during a given MCNP run. When ^{131m}Xe decay modes were being modelled the gas was assumed to be pure ^{130}Xe because it was ^{130}Xe that was irradiated to produce the ^{131m}Xe and ^{130}Xe still accounted for the majority of the gas in the samples even after the irradiations. When ^{133m}Xe and ^{133}Xe decay modes were being modelled the gas in the copper spectrometer chamber was assumed to be pure ^{132}Xe, and when ^{135}Xe decay

modes were being modelled the gas in the copper spectrometer chamber was assumed to be pure ^{134}Xe for the same reason described above. The nitrogen gas inside the air-tight inner box was modelled as natural diatomic nitrogen gas having the isotopic composition prescribed by the NIST [112]. The MCNP "GAS" card was used to calculate electron stopping power density effect correction factors appropriate for the radioxenon and nitrogen gas phases (MCNP calculates factors appropriate for the condensed phase by default) [75].

2.3.1.3 MCNP Model Development: Source Terms

Before the MCNP radiation transport code [75] can transport radiation in support of a given study, radiation must be introduced to the modelled system using an MCNP radiation source definition (SDEF) card [75]. The MCNP SDEF card is used to define all the characteristics of an MCNP radiation source.

Because Si-PIN diode spectrometers are sensitive to both photons and electrons, the MCNP models used to support the Si-PIN diode spectrometer optimization studies documented here utilize both photon and electron sources. The type of source utilized during a given MCNP run varied as the radioxenon decay mode of interest varied. For example, seven different photon source terms and four different electron source terms were used to support the ^{131m}Xe studies described in Section 2.3.2. These source terms were adequate to account for all the ^{131m}Xe decay modes having branching ratios of 0.1 % or greater. For the ^{133m}Xe and ^{133}Xe studies sixteen different photon source terms were used to account for the ^{133m}Xe and ^{133}Xe photon decay modes, while twelve

different electron source terms were used to account for the ^{133m}Xe and ^{133}Xe conversion electron and beta particle decay modes. Similarly, the ^{135}Xe studies utilized eleven different photon source terms and six different electron terms. Again, these source terms were sufficient to account for all ^{135}Xe photon, conversion electron, and beta particle decay modes with branching ratios greater than 0.1 %.

The decay energies and branching ratios associated with the monoenergetic radioxenon photons and conversion electrons were taken from the nuclear decay database maintained by the National Nuclear Data Center (NNDC) [60]. Because the radioxenon beta particles of interest are not monoenergetic, but rather are emitted with an array of energies, the energies of the ^{133}Xe and ^{135}Xe beta particles introduced to the MCNP models had to be sampled from distributions representative of the actual ^{133}Xe and ^{135}Xe beta particle energy distributions. These distributions, which are shown in Figure 2.51, were developed from ^{133}Xe and ^{135}Xe beta particle energy distribution data taken from ICRP 107 [114]. More specifically, the distributions shown in Figure 2.51 are ^{133}Xe and ^{135}Xe beta particle energy Cumulative Density Functions (CDFs) with 97 and 109 different energy bins covering the energy ranges associated with the ^{133}Xe and ^{135}Xe beta particles, respectively. The energy structures associated with the CDFs shown in Figure 2.51 are consistent with the energy structures associated with the original ICRP 107 beta particle energy distribution data.

In order to account for the spatial distribution of the radioxenon gases inside the copper spectrometer chamber three pairs of MCNP source information (SI) and source probability (SP) cards were used [75]. These SI and SP cards were used to define a spatial source distribution that was uniform throughout the interior of the hollow copper spectrometer chamber. Additionally, the MCNP cookie-cutter keyword (CCC) was used to verify that each of the sampled locations was in fact inside the MCNP cell used to model the radioxenon gas in the hollow copper spectrometer chamber.

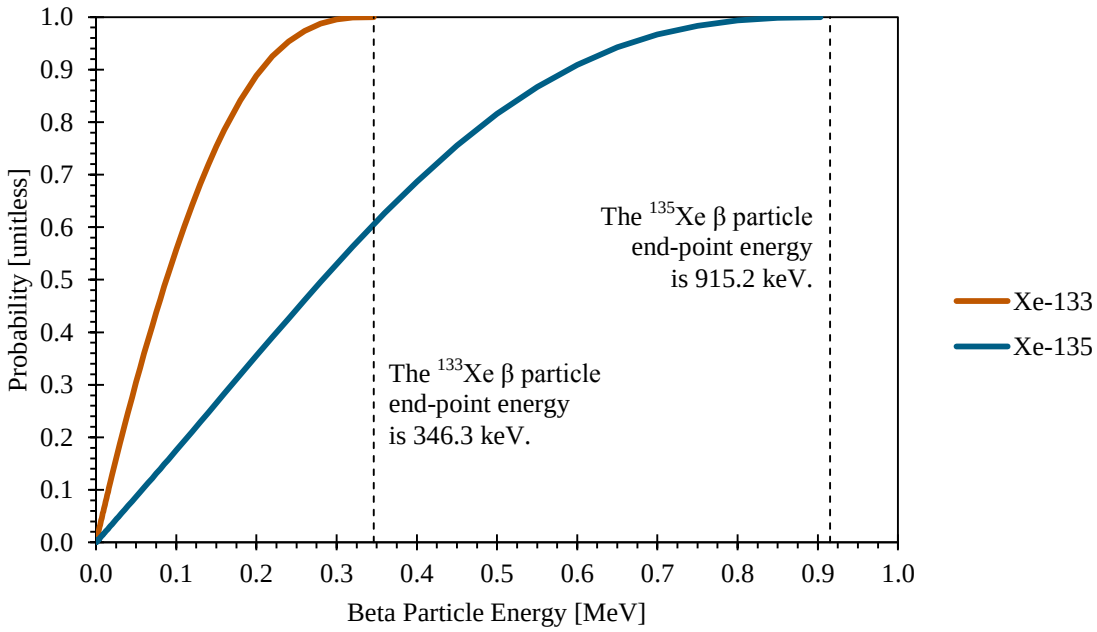

Figure 2.51: The Cumulative Density Functions (CDFs) from which the ^{133}Xe and ^{135}Xe beta particle energies were sampled.

2.3.1.4 MCNP Model Development: Tallies

Each of the Si-PIN diode spectrometer MCNP models include two F8 pulse-height tallies, one in the sensitive volume of the front Si-PIN diode and one in the sensitive volume of the back Si-PIN diode. These tallies are used to generate pulses in simulated photon and conversion electron spectra.

MCNP tally energy (E) cards are used to establish default energy-bin structures for each of the pulse-height tallies. The E cards specify that the energy-bin structure of the simulated spectra should have 8,192 bins and should cover an energy range extending from 0 keV up through 311.296 keV. This energy-bin structure is equivalent to the energy-bin structure associated with the spectra acquired by the XIA LLC Si-PIN diode spectrometer prototype.

MCNP Gaussian Energy Broadening (GEB) cards are also used so that the peaks in the simulated spectra have widths representative of those in the spectra acquired by the XIA LLC Si-PIN diode spectrometer prototype. MCNP uses the following expression to establish the mean FWHM as a function of energy:

$$FWHM = a + b \cdot \sqrt{E + c \cdot E^2}. \qquad 2.3.1.4.1$$

Where: $FWHM$ is the mean peak FWHM at the energy E and

a, b, and c are coefficients used to estblish the relationship between the FWHM and the energy, E.

The values assigned to the a, b, and c coefficients were established by fitting the MCNP FWHM expression defined by Equation 2.3.1.4.1 to the photon and conversion

electron data acquired by the Si-PIN diode spectrometer prototype. For photon spectra, the values assigned to the a, b, and c coefficients were 3.95350×10^{-4}, 1.32538×10^{-3}, and 1.13750, respectively. For conversion electron spectra, the values assigned to the a, b, and c coefficients were 1.05556×10^{-3}, 8.05653×10^{-4}, and 0, respectively.

2.3.2 Validation and Alignment of the Si-PIN Diode Spectrometer MCNP Models

The XIA LLC Si-PIN diode spectrometer prototype MCNP model developed as described in the previous section was used to generate a series of simulated ^{131m}Xe, mixed ^{133m}Xe and ^{133}Xe, and ^{135}Xe spectra. These simulated spectra were then compared to the radioxenon spectra acquired experimentally using the XIA LLC Si-PIN diode spectrometer prototype (see Section 2.2.1.2). The objective of these comparisons was to validate the outputs generated by the XIA LLC Si-PIN diode spectrometer prototype MCNP model and also the outputs generated by the optimized Si-PIN diode spectrometer MCNP models.

The simulated ^{131m}Xe, mixed ^{133m}Xe and ^{133}Xe, and ^{135}Xe spectra generated by the XIA LLC Si-PIN diode spectrometer prototype are shown in Figures 2.52 through 2.60. The simulated ^{131m}Xe spectrum represents the summation of seven simulated photon spectra and four simulated conversion electron spectra. The simulated mixed ^{133m}Xe and ^{133}Xe spectrum represents the summation of 16 photon spectra, 12 conversion electron spectra, and one beta particle spectrum. And finally, the simulated ^{135}Xe spectrum represents the summation of eleven photon spectra, six conversion electron spectra, and

one beta particle spectrum. The individual spectra were generated by running 10^7 MCNP source particle histories. This was sufficient to reduce the variances in the peaks of the simulated spectra to less than 1 % in all cases.

The simulated radioxenon spectra generated by MCNP were normalized in two ways. First, the individual photon and conversion electron spectra were normalized to the number of ^{131m}Xe, ^{133m}Xe, ^{133}Xe, and ^{135}Xe photon and conversion electron emissions expected during the XIA LLC Si-PIN diode spectrometer prototype radioxenon spectrum acquisitions. For example, the simulated ^{131m}Xe 129.369 keV conversion electron spectrum was normalized to the number of ^{131m}Xe 129.369 keV conversion electron emissions expected during the ^{131m}Xe spectrum acquisition. The expected number of 129.369 keV conversion electron emissions was evaluated by multiplying the expected number of ^{131m}Xe decays by the ^{131m}Xe 129.369 keV conversion electron branching ratio [60]. The simulated radioxenon spectra normalized in this way are represented by the green data points in Figures 2.52 through 2.60.

A review of Figures 2.52 through 2.60 reveals that, in most cases, the simulated radioxenon spectra normalized as described above were in relatively good agreement with the radioxenon spectra acquired experimentally (the orange data points in Figures 2.52 through 2.60). The background levels and the areas of the simulated photon and conversion electron peaks are in good agreement with the background levels and the areas of the peaks in the experimentally acquired radioxenon spectra. The widths of the simulated photon and conversion electron peaks also appear to align well with the widths of the photon and conversion electron peaks in the experimentally acquired radioxenon

spectra. The agreement amongst the conversion electron peaks appears to be particularly good (see Figures 2.54 and 2.57). The simulated and experimentally acquired spectra even appear to be in good agreement at energies as low as about 10 keV (see the Kα and Kβ copper X-ray peaks in Figures 2.53, 2.56, and 2.59).

Note that the simulated ^{135}Xe spectrum does not appear to be in good agreement with the ^{135}Xe spectrum acquired experimentally using the XIA LLC Si-PIN diode spectrometer prototype. As illustrated in Figure 2.58, there are significantly more counts in all channels of the simulated ^{135}Xe spectrum than in the experimentally acquired ^{135}Xe spectrum. This is an indication that the number of ^{135}Xe atoms expected to decay during the experimental ^{135}Xe spectrum acquisition was too large. This is an interesting revelation because the XIA LLC Si-PIN diode spectrometer prototype detection efficiencies evaluated using peak areas from the experimentally acquired ^{135}Xe spectrum were low relative to the detection efficiencies developed using the other radioxenon peak areas. Lower than expected detection efficiencies also suggest that the expected number of ^{135}Xe decays may have been too high. Taken together, these results suggest that the number of ^{135}Xe decays expected during the ^{135}Xe spectrum acquisition was in fact too high and that the experimentally evaluated XIA LLC Si-PIN diode spectrometer prototype absolute detection efficiencies are biased to the low side.

Forced normalizations were also applied to the simulated radioxenon spectra. For the forced normalizations the average number of counts over regions of the experimentally acquired radioxenon spectra were evaluated and then the counts in the same regions of the simulated spectra were forced to be the same. This normalization

method removes the uncertainty associated with the radioxenon samples from the normalization process and produces better agreement between the simulated and experimentally acquired spectra. This is particularly true in the case of the ^{135}Xe spectra where the agreement between the experimentally acquired spectrum and the simulated spectrum normalized using the first method was found to be quite poor. The simulated ^{135}Xe spectrum to which the forced normalization was applied is in good agreement with the experimentally acquired ^{135}Xe spectrum.

The comparisons between the simulated and experimentally acquired radioxenon spectra provided an opportunity to validate the alignment of certain aspects of the Si-PIN diode spectrometer MCNP models. Two aspects of the models that were of particular interest here were the Si-PIN diode dead layer thicknesses and the values assigned to the MCNP GEB equation coefficients (see Equation 2.3.1.4.1). Nine different dead layer thicknesses ranging from 1.0 μm through 10,000 μm were evaluated. There were really no differences in any of the spectra until the dead layer thickness was increased to 4,200 μm. Therefore, the nominal dead layer thickness reported by Amptek (150 μm) [91] was retained in the MCNP model as were the initial estimates at the MCNP GEB equation coefficients.

In terms of the Si-PIN diode spectrometer optimization studies, the fact that the simulated radioxenon spectra generated using the MCNP model of the XIA LLC Si-PIN diode spectrometer prototype are generally in good agreement with the radioxenon spectra acquired experimentally using the XIA LLC Si-PIN diode spectrometer prototype suggests that simulated radioxenon spectra generated using MCNP models of optimized

Si-PIN diode-based spectrometer designs should also be representative of the radioxenon spectra that might be acquired by optimized Si-PIN diode-based spectrometers. In other words, the strong agreement between the simulated radioxenon spectra and the experimentally acquired spectra serves to validate the use of MCNP as a tool to develop optimized Si-PIN diode-based spectrometer designs.

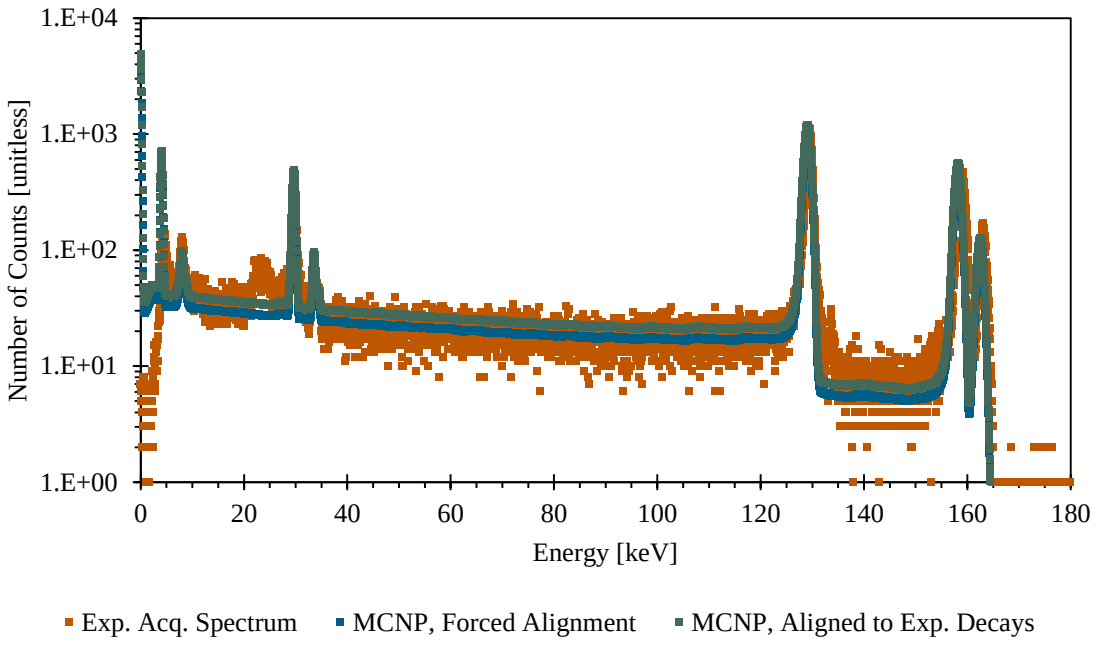

Figure 2.52: Simulated and experimentally acquired ^{131m}Xe spectra.

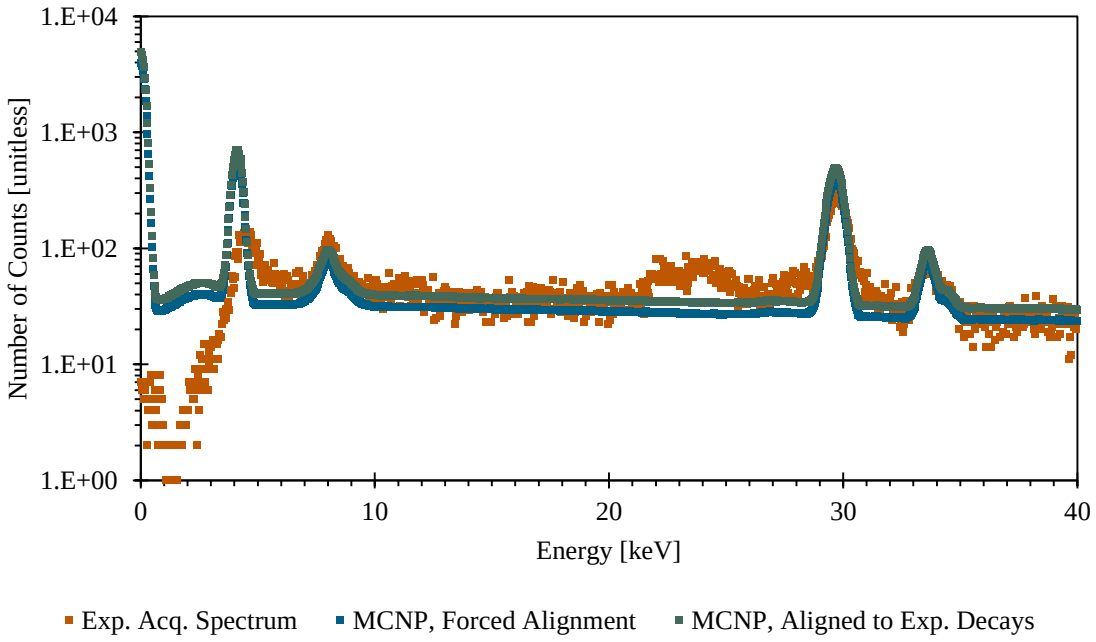

Figure 2.53: Detailed view of the ^{131m}Xe X-ray peaks in the simulated and experimentally acquired ^{131m}Xe spectra.

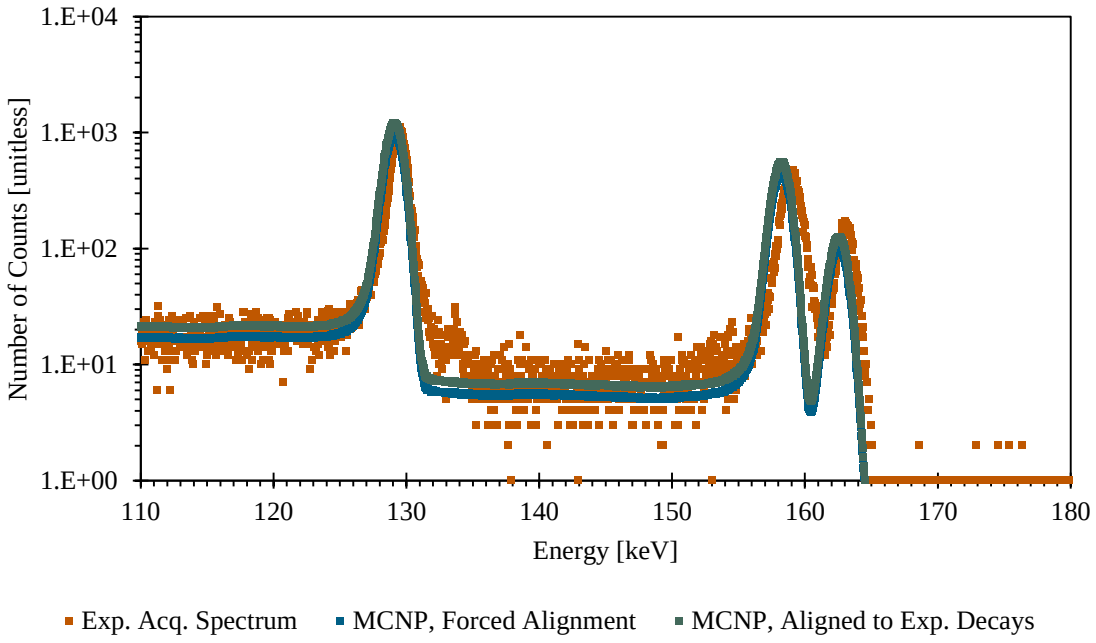

Figure 2.54: Detailed view of the ^{131m}Xe conversion electron peaks in the simulated and experimentally acquired ^{131m}Xe spectra.

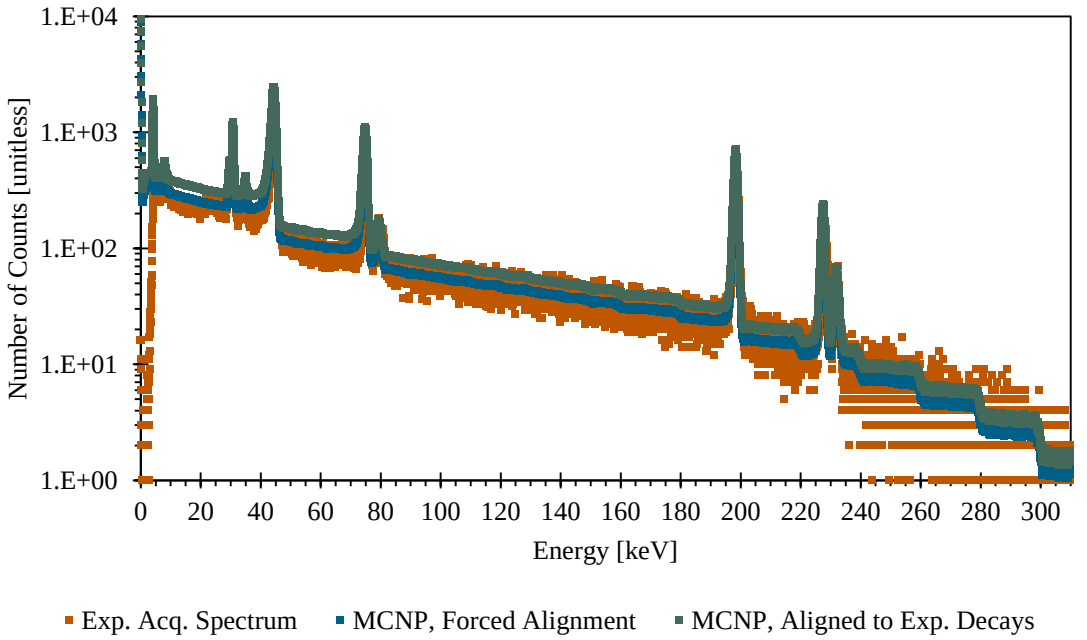

Figure 2.55: Simulated and experimentally acquired mixed ^{133m}Xe and ^{133}Xe spectra.

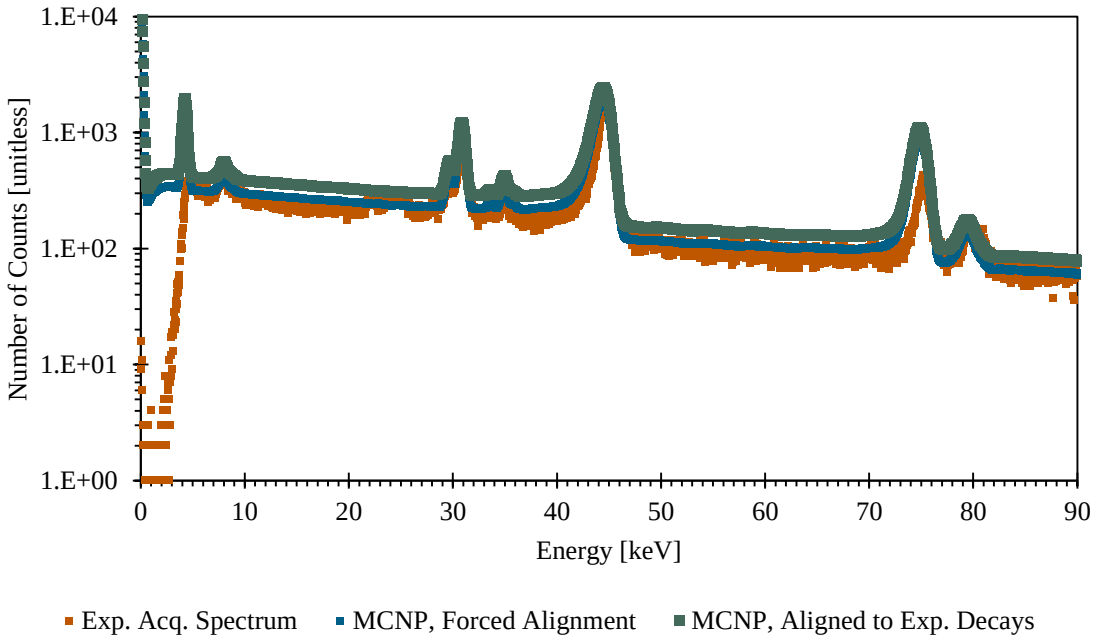

Figure 2.56: Detailed view of the ^{133m}Xe and ^{133}Xe X-ray peaks in the simulated and experimentally acquired mixed ^{133m}Xe and ^{133}Xe spectra.

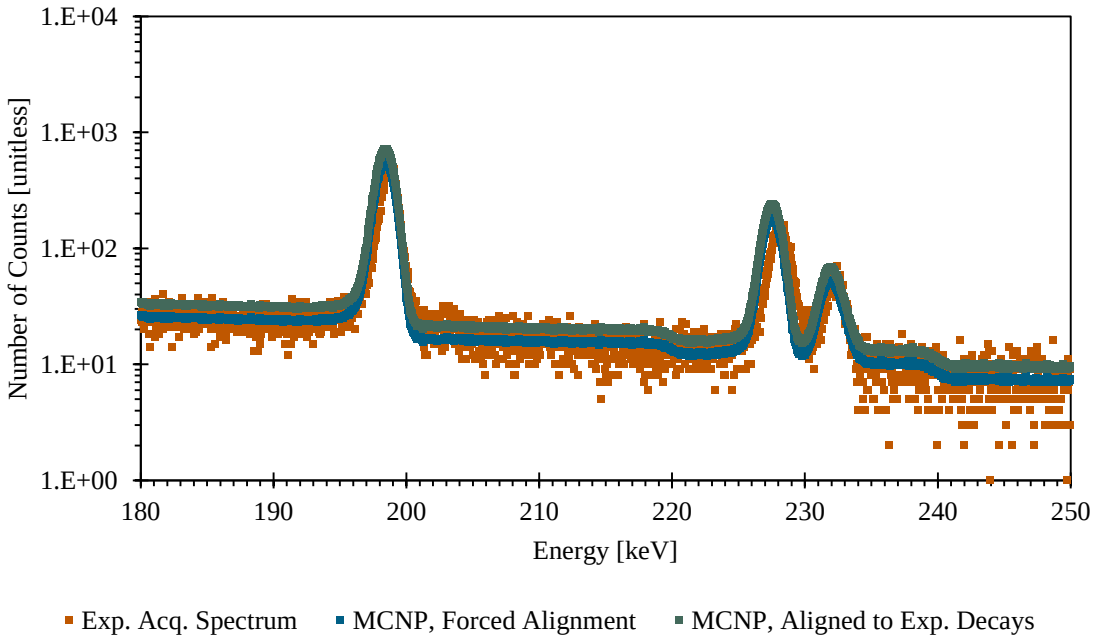

Figure 2.57: Detailed view of the ^{133m}Xe and ^{133}Xe conversion electron peaks in the simulated and experimentally acquired mixed ^{133m}Xe and ^{133}Xe spectra.

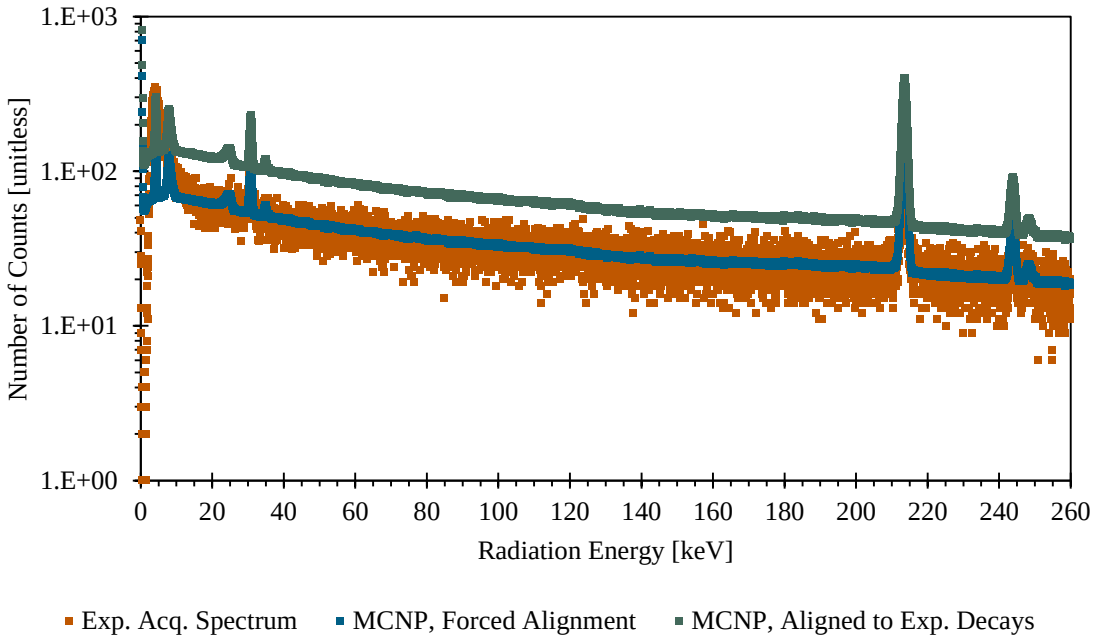

Figure 2.58: Simulated and experimentally acquired ^{135}Xe spectra.

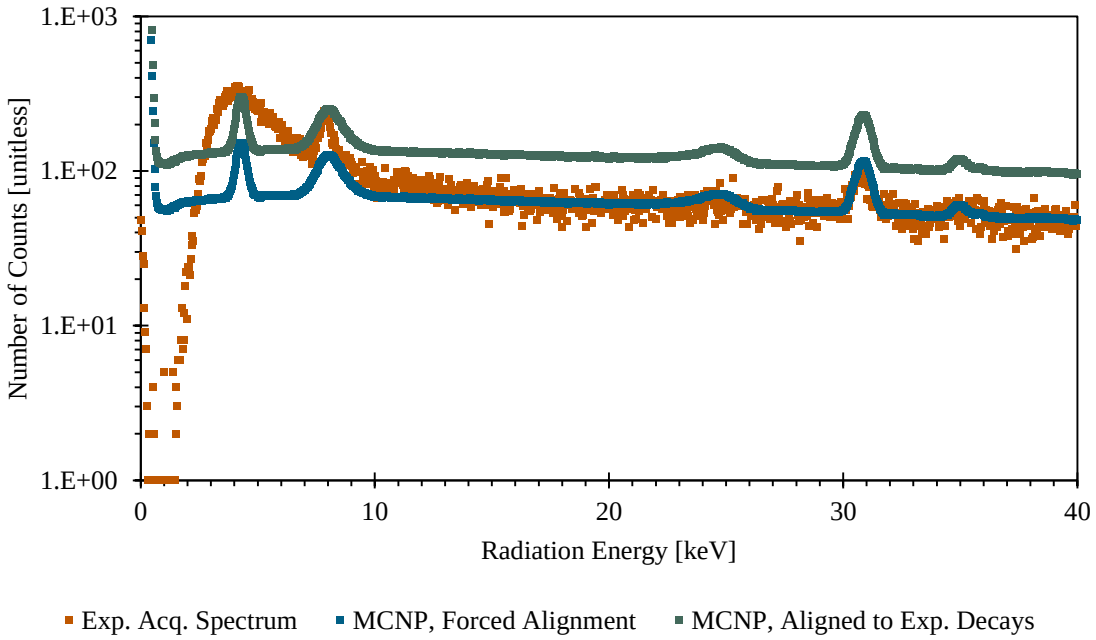

Figure 2.59: Detailed view of the ^{135}Xe X-ray peaks in the simulated and experimentally acquired ^{135}Xe spectra.

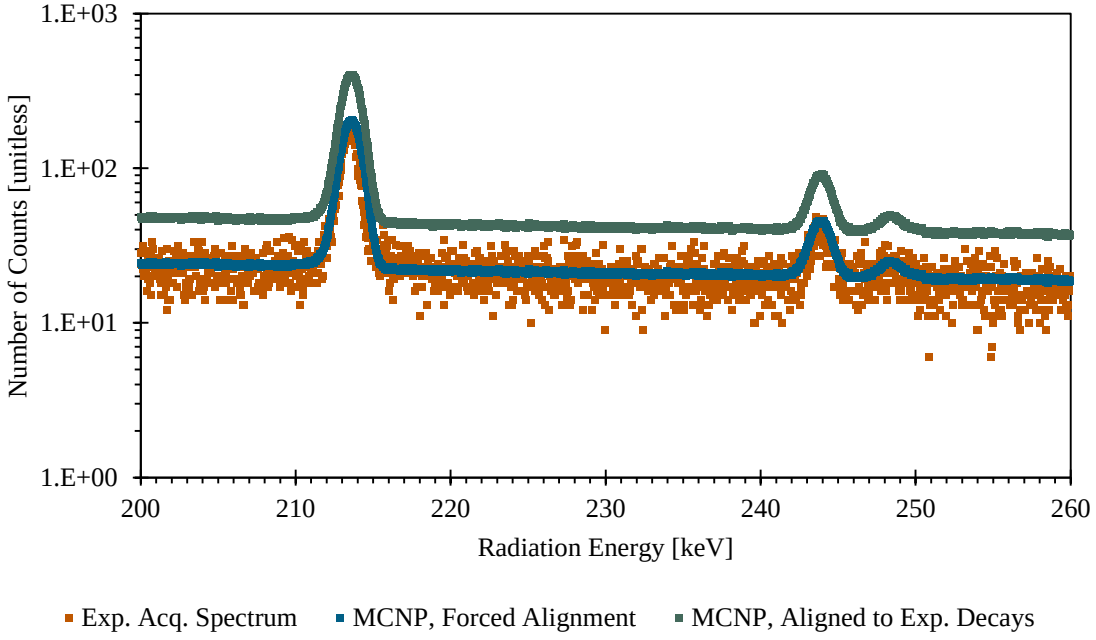

Figure 2.60: Detailed view of the ^{135}Xe conversion electron peaks in the simulated and experimentally acquired ^{135}Xe spectra.

2.3.3 Si-PIN Diode Spectrometer Prototype Optimization Studies

This section presents the results of several Si-PIN diode spectrometer optimization studies. These studies were conducted using a number of Si-PIN diode spectrometer MCNP models developed as described in the previous section. The first optimization studies investigate Si-PIN diode spectrometer performance improvements that might be achieved by making a few simple changes to the geometry of the XIA LLC Si-PIN diode spectrometer prototype. For these studies only the dimensions of the copper spectrometer chamber are altered; the Si-PIN diode dimensions are left unchanged. The performance improvements associated with these studies should be viewed as being achievable today with existing Si-PIN diode technology.

Subsequent studies investigate performance improvements that might be achieved if larger, thicker Si-PIN diodes are made available. The results of these studies might not be achievable using Si-PIN diodes available today, but should be viewed as possible when Si-PIN diode manufacturers begin producing larger Si-PIN diodes. Additional studies are conducted to evaluate the sensitivity of Si-PIN diode spectrometer performance to changes in radioxenon fill pressure.

2.3.3.1 Optimization Studies: Various Rectangular Spectrometer Chamber Thicknesses

The optimization studies documented in this section serve to evaluate the absolute detection efficiency and MDC performance gains that might be achieved by a Si-PIN diode-based spectrometer with a thinner rectangular spectrometer chamber. In the MCNP models used to support these optimization studies the dimensions of the Si-PIN diodes associated with the modelled spectrometer are assumed to be identical to the dimensions of the 0.25 cm^2 Si-PIN diodes employed by the XIA LLC Si-PIN diode spectrometer prototype. The rectangular shape and the cross-sectional area of the XIA LLC Si-PIN diode spectrometer prototype are retained for these studies as well. Only the thickness of the copper spectrometer chamber is allowed to vary. Nine different spectrometer chamber thicknesses are evaluated ranging from a maximum of 1.06 cm (the thickness of the XIA LLC Si-PIN diode spectrometer prototype chamber) down through a minimum of 0.3 cm.

Simulated 30 keV photon and 150 keV conversion electron spectra were generated using each of the modelled spectrometer chamber thicknesses. The areas of the photon and conversion electron peaks in the simulated spectra were evaluated using the peak area estimation technique prescribed by Gilmore and Hemingway [69] (see Section 2.1.4). In this case, because the number of counts registered in the channels of the simulated spectra are normalized to the number of source particle histories run, the evaluated peak areas are numerically equal to the absolute detection efficiencies of interest.

The results of the rectangular spectrometer chamber thickness optimization studies are presented in Figure 2.61. The first thing to note in Figure 2.61 is that the absolute photon and conversion electron detection efficiencies associated with the 1.06 cm thick spectrometer chamber are estimated to be about 0.9 % and 3.6 %, respectively. These absolute photon and conversion electron detection efficiency estimates are about 93 % and 27 % higher than the absolute photon and conversion electron detection efficiencies determined experimentally (see Section 2.2.4).

Given that the dimensions in the MCNP model with the 1.06 cm thick spectrometer chamber are basically equivalent to the dimensions of the XIA LLC Si-PIN

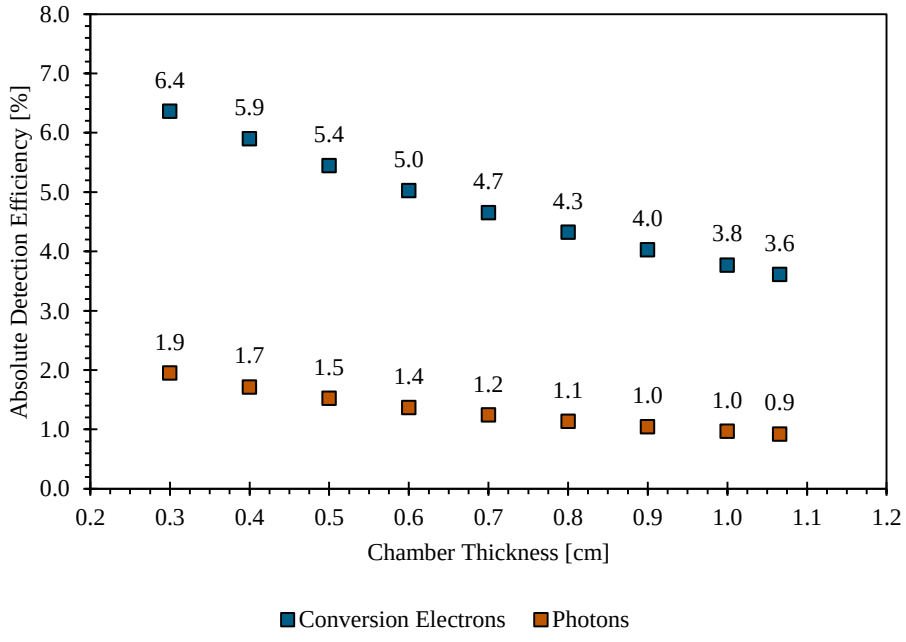

Figure 2.61: Results of the rectangular Si-PIN diode spectrometer chamber thickness optimization studies.

diode spectrometer prototype, the absolute detection efficiency estimates generated by the MCNP model with the 1.06 cm thick spectrometer chamber were expected to line up well with the experimentally determined absolute detection efficiencies. While the exact cause of the discrepancy is not clear, it is apparent that something about the way the Si-PIN diode spectrometer is modelled here results in larger than expected peak areas and higher than expected absolute detection efficiency estimates.

This discrepancy is presumably present not only in the results generated by the MCNP model with the 1.06 cm thick spectrometer chamber, but in the results generated by all the Si-PIN diode spectrometer MCNP models used throughout these optimization studies. With this in mind, the absolute detection efficiency performance gains achieved by the optimized Si-PIN diode spectrometer designs described in this section and subsequent sections will be normalized to the absolute detection efficiency estimates generated here by the MCNP model with the 1.06 cm thick spectrometer chamber before they are applied to the experimentally determined absolute detection efficiencies.

Returning to Figure 2.61, the results of the rectangular spectrometer chamber thickness optimization studies show that reducing the thickness of the spectrometer chamber while maintaining the cross-sectional area of the chamber constant increases the absolute 150 keV conversion electron detection efficiency of the Si-PIN diode spectrometer from about 3.6 % to a maximum of about 6.4 %. This represents an increase of a factor of about 1.76 in the absolute 150 keV conversion electron detection efficiency. Applying this factor to the experimentally determined XIA LLC Si-PIN diode spectrometer prototype 150 keV conversion electron detection efficiency and plugging

the adjusted detection efficiency into the spectrometer MDC equation indicates that the ^{131m}Xe, ^{133m}Xe, ^{133}Xe, and ^{135}Xe MDCs associated with a Si-PIN diode spectrometer with a thin rectangular chamber would be about 0.96, 1.2, 1.2, and 32 mBq-m^{-3}, respectively.

2.3.3.2 Optimization Studies: Various Cylindrical Spectrometer Chamber Thicknesses

The optimization studies documented in this section serve to evaluate the absolute detection efficiency and MDC performance gains that might be achieved using a cylindrical Si-PIN diode spectrometer chamber design as opposed to the rectangular spectrometer chamber design employed by the XIA LLC Si-PIN diode spectrometer prototype. In the MCNP models used to support these optimization studies the Si-PIN diodes associated with the modelled spectrometers are again assumed to be identical to the 0.25 cm^2 Si-PIN diodes employed by the XIA LLC Si-PIN diode spectrometer prototype. However, the rectangular spectrometer chamber is replaced with a cylindrical chamber with an inner diameter just large enough to accommodate the 0.25 cm^2 Si-PIN diodes. As with the rectangular spectrometer chamber thickness studies, nine different cylindrical spectrometer chamber thicknesses are evaluated ranging from a maximum of 1.06 cm (the thickness of the XIA LLC Si-PIN diode spectrometer prototype chamber) down through a minimum of 0.3 cm.

The areas of the 30 keV photon and 150 keV conversion electron peaks in the simulated spectra were evaluated using the peak area estimation technique prescribed by Gilmore and Hemingway [69] (see Section 2.1.4). Here again, because the number of

counts registered in each of the channels of the simulated spectra are normalized to the number of source particle histories run the evaluated peak areas are numerically equal to the absolute detection efficiencies of interest.

The results of the cylindrical spectrometer chamber thickness optimization studies presented in Figure 2.62 show that using a cylindrical Si-PIN diode spectrometer chamber design as opposed to a rectangular spectrometer chamber design provides an immediate boost in absolute detection efficiency performance. The absolute 150 keV conversion electron detection efficiency associated with the 1.06 cm thick cylindrical spectrometer chamber design is about 6.0 % while the absolute 150 keV conversion

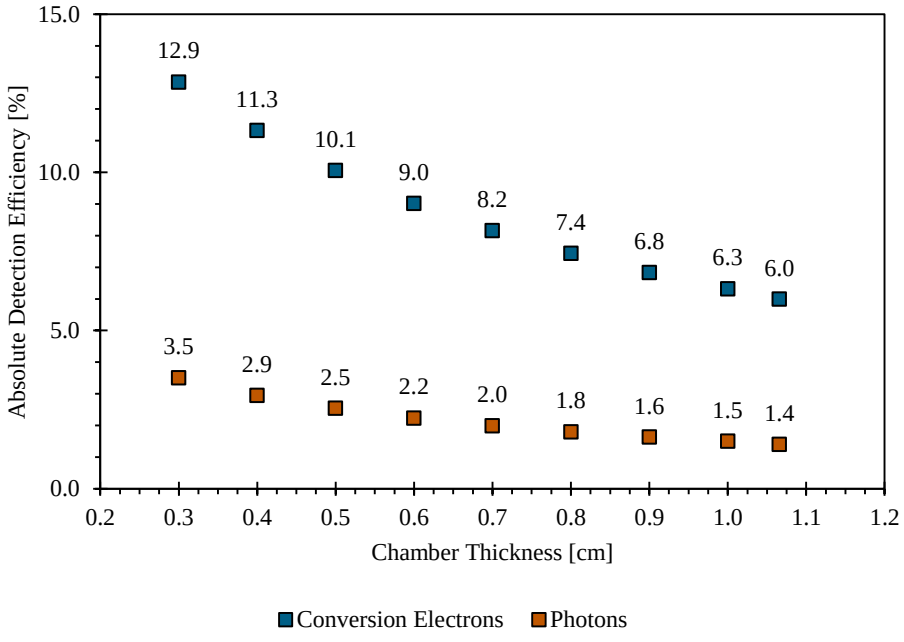

Figure 2.62: Results of the cylindrical Si-PIN diode spectrometer chamber thickness optimization studies.

electron detection efficiency associated with the 1.06 cm thick rectangular spectrometer chamber design was about 3.6 %. Switching to a cylindrical spectrometer chamber design therefore improves the absolute detection efficiency by a factor of about 1.66.

Reducing the thickness of the cylindrical spectrometer chamber produced additional absolute detection efficiency performance improvements. As was the case with the rectangular spectrometer chamber thickness studies, the 150 keV conversion electron absolute detection efficiencies increased as the Si-PIN diode spectrometer chamber thickness was reduced. The optimal absolute detection efficiency was found to be about 12.9 % when the cylindrical spectrometer chamber was 0.3 cm thick. This represents an increase of a factor of about 3.56 in the 150 keV absolute conversion electron detection efficiency associated with the rectangular XIA LLC Si-PIN diode spectrometer design.

Applying this factor to the experimentally determined XIA LLC Si-PIN diode spectrometer prototype 150 keV conversion electron detection efficiency and plugging the adjusted detection efficiency into the spectrometer MDC equation indicates that the ^{131m}Xe, ^{133m}Xe, ^{133}Xe, and ^{135}Xe MDCs associated with a Si-PIN diode spectrometer with a thin cylindrical chamber would be about 0.48, 0.57, 0.58, and 16 mBq-m^{-3}, respectively.

2.3.3.3 Optimization Studies: Various Si-PIN Diode Areas

In this section, the performance characteristics of a number of Si-PIN diode spectrometers designed to analyze 1 cm^3 of xenon gas are evaluated. The Si-PIN diode spectrometer designs utilize Si-PIN diodes having ten different cross-sectional areas ranging from 25 mm^2 (the area associated with the Si-PIN diodes employed by the XIA LLC Si-PIN diode spectrometer prototype) up through 250 mm^2. In order to maintain the volume of the xenon gas samples analyzed constant at 1 cm^3, the thickness of the spectrometer chamber is reduced as the area of the Si-PIN diodes is increased. The xenon gas volume is maintained constant at 1 cm^3 for consistency with the xenon sample volume requirement prescribed by the Xenon International project [78].

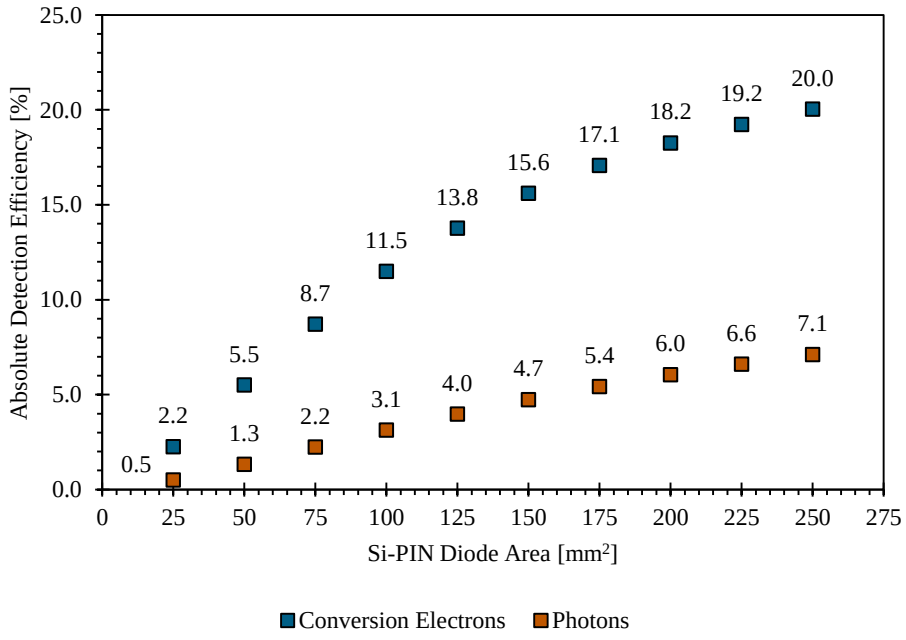

Figure 2.63: Results of the Si-PIN diode area optimization studies.

The results of these studies are presented in Figure 2.63. The results illustrate that the absolute photon and conversion electron detection efficiencies both increase considerably as the area of the Si-PIN diodes increases and as the spectrometer chamber thickness is reduced. The optimal absolute conversion electron detection efficiency was found to be about 20.0 % when the Si-PIN diode area was increased to 250 mm^2 and the cylindrical spectrometer chamber thickness was reduced to 0.37 cm. This represents an increase of a factor of about 5.54 in the 150 keV absolute conversion electron detection efficiency associated with the rectangular 1.06 cm thick XIA LLC Si-PIN diode spectrometer prototype design.

Applying this factor to the experimentally determined XIA LLC Si-PIN diode spectrometer prototype 150 keV conversion electron detection efficiency and plugging the adjusted detection efficiency into the spectrometer MDC equation indicates that the ^{131m}Xe, ^{133m}Xe, ^{133}Xe, and ^{135}Xe MDCs of a Si-PIN diode spectrometer with large area Si-PIN diodes and a thin cylindrical chamber would be about 0.31, 0.37, 0.37, and 10 $mBq\text{-}m^{-3}$, respectively.

Also note that the photon and conversion electron absolute detection efficiencies associated with the spectrometer design utilizing the 25 mm^2 Si-PIN diodes are actually smaller than the photon and conversion electron detection efficiencies associated with the XIA LLC Si-PIN diode spectrometer prototype, which also utilizes 25 mm^2 Si-PIN diodes. This is because the spectrometer chamber associated with the 25 mm^2 Si-PIN diode system studied here has a thickness of 3.36 cm so that the volume of the gas in the spectrometer chamber to support maintaining the chamber volume constant at 1 cm^3.

This is a considerable increase relative to the 1.06 cm spectrometer chamber thickness associated with the XIA LLC Si-PIN diode spectrometer prototype. The increased chamber thickness obviously has a negative impact on the photon and conversion electron absolute detection efficiencies.

2.3.3.4 Optimization Studies: Various Radioxenon Fill Pressures

As mentioned previously, one of the requirements associated with the Xenon International project is that evaluated xenon samples must have a volume of 1 cm^3 [78]. Another Xenon International project requirement states that xenon samples must be evaluated at standard temperature and pressure (T = 273.15 K, P = 100 kPa) [78]. The xenon samples used to support the XIA LLC Si-PIN diode spectrometer prototype characterization efforts documented in Section 2.2 were at pressures around 50 Torr (6.7 kPa), considerably less than the 100 kPa requirement associated with the Xenon International project.

Therefore, the optimization studies documented here serve to evaluate the absolute detection efficiency and MDC performance changes that might be associated with different radioxenon fill pressures. Eleven different radioxenon fill pressures are considered. The lowest radioxenon fill pressure considered is 50 Torr (6.7 kPa) and the highest radioxenon fill pressure considered is 760 Torr (101 kPa). The geometric configuration of the Si-PIN diode spectrometer is assumed to be the optimal geometric configuration associated with the Si-PIN diode area studies documented in the previous

section: The Si-PIN diodes are assumed to have areas of 250 mm^2 and the spectrometer chamber is assumed to be cylindrical with a thickness of 0.37 cm.

The results of the radioxenon fill pressure studies are presented below in Figure 2.64. As illustrated by the figure, increasing the radioxenon fill pressure from 50 Torr (6.7 kPa) to 380 Torr (50.7 kPa) increases the absolute conversion electron detection efficiency from 20.8 % to 22.1 %. This represents an increase of about 6.25 %. The ^{131m}Xe, ^{133m}Xe, ^{133}Xe, and ^{135}Xe MDCs associated a 380 Torr (50.7 kPa) radioxenon fill pressure would be about 0.28, 0.33, 0.34, and 9.2 $mBq\text{-}m^{-3}$, respectively.

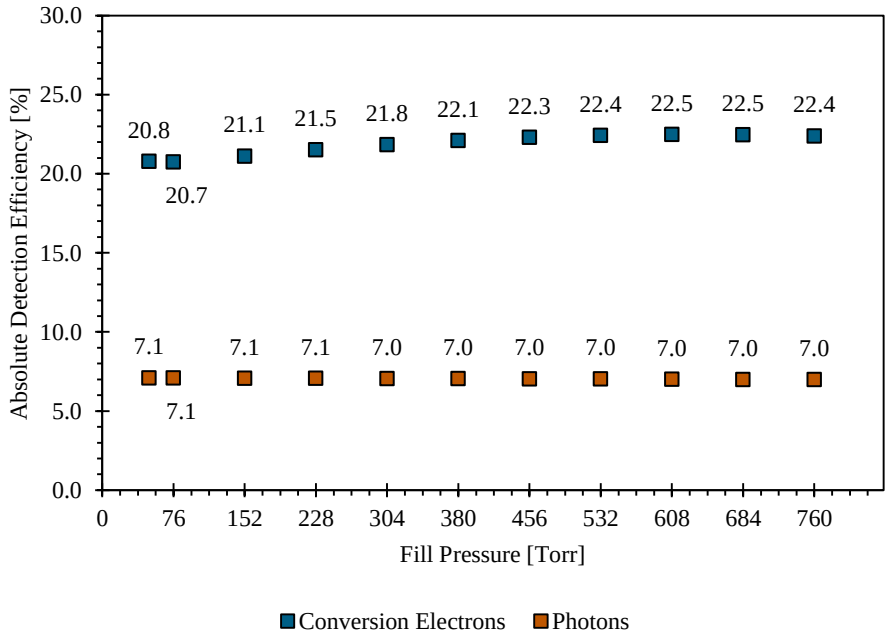

Figure 2.64: Results of the fill gas pressure optimization studies.

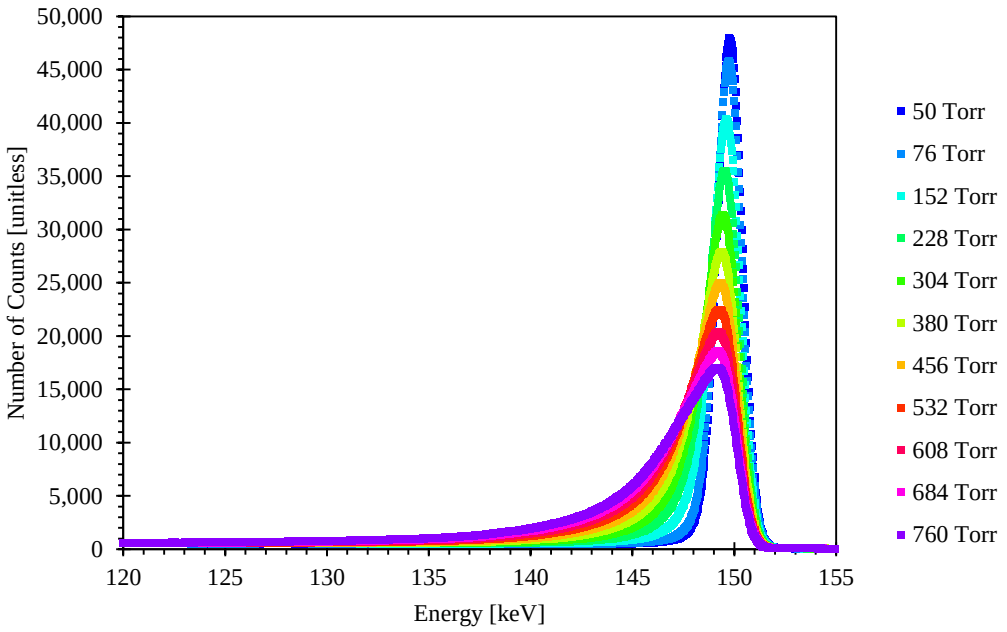

Figure 2.65: 150 keV conversion electron peak widths associated with various radioxenon fill pressures.

Returning to Figure 2.64, note that increasing the radioxenon fill pressure above 380 Torr (50.7 kPa) actually produces additional increases in absolute conversion electron detection efficiency. However, as illustrated in Figure 2.65, increasing the radioxenon fill pressure above 380 Torr (50.7 kPa) also leads to increases in conversion electron peak widths. Larger peak widths are generally undesirable because they cause peaks to overlap and complicate the spectral analysis process. In this case, the additional increase in absolute conversion electron detection efficiency associated with increasing the radioxenon fill pressure beyond 380 Torr (50.7 kPa) does not appear to be worth the complications introduced by the larger peak widths.

2.3.3.5 Optimization Studies: Various Si-PIN Diode Thicknesses

The objective of the Si-PIN diode thickness studies was to evaluate the absolute photon and conversion electron detection efficiency improvements that might be achievable if thicker Si-PIN diodes are made available in the future. The idea was that thicker Si-PIN diodes might have higher intrinsic detection efficiencies and thus higher absolute detection efficiencies and reduced MDCs, resulting in improved Si-PIN diode spectrometer performance.

The Si-PIN diode thickness studies documented here evaluated the absolute photon and conversion electron detection efficiencies associated with eleven Si-PIN diode thicknesses ranging from a minimum of 500 μm (the thickness of the Si-PIN diodes employed by the XIA LLC Si-PIN diode spectrometer prototype) up through a maximum of 1,000 μm. It should be noted that the 500 μm thick Si-PIN diodes employed by the XIA LLC Si-PIN diode spectrometer prototype were the thickest available from Amptek, Inc. at the time these studies were conducted. As mentioned previously, the Si-PIN diode thickness studies documented here were conducted to evaluate the Si-PIN diode spectrometer performance improvements that might be achievable if thicker Si-PIN diodes are made available in the future.

The optimal Si-PIN diode spectrometer configuration produced during the large area Si-PIN diode studies described in Section 2.3.3.3 served as the base Si-PIN diode spectrometer configuration for the Si-PIN diode thickness studies documented here. The Si-PIN diodes were assumed to have an area of 2.5 cm^2, the thickness of the Si-PIN diode spectrometer chamber was assumed to be 0.37 cm, and the volume of the

spectrometer chamber was assumed to be 1 cm^3. The radioxenon pressure in the spectrometer chamber was assumed to be 50 Torr.

The results of the Si-PIN diode thickness studies are presented in Figure 2.66. The results indicate that there is nothing to be gained in the way of improved conversion electron detection efficiencies by transitioning to thicker Si-PIN diodes. That said, the thicker Si-PIN diodes demonstrate absolute photon detection efficiency improvements of more than 50 %.

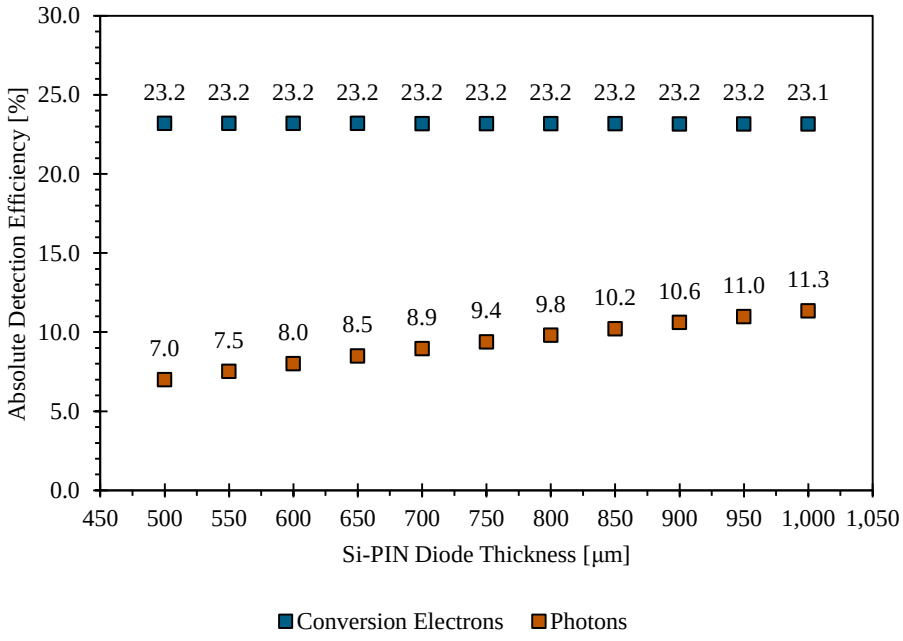

Figure 2.66: Results of the Si-PIN diode thickness studies.

2.3.4 Optimized Prototype Performance Comparisons

Table 2.3.4.1 summarizes the results of the Si-PIN diode spectrometer optimization studies documented in Sections 2.3.3.1 through 2.3.3.5. The optimization studies were carried out so that absolute detection efficiency and Minimum Detectable Concentration (MDC) performance gains achieved at each step of the optimization process added to the absolute detection efficiency and MDC gains achieved during the previous steps of the optimization process. Therefore, each step of the optimization process produced larger absolute detection efficiencies and smaller radioxenon MDCs.

As illustrated by Table 2.12, the radioxenon MDCs associated with the Si-PIN diode spectrometer design with the thin, 0.3 cm thick rectangular spectrometer chamber are roughly 43 % smaller than the radioxenon MDCs associated with the XIA LLC Si-PIN diode spectrometer prototype. Switching to a thin, 0.3 cm thick cylindrical spectrometer chamber reduces the radioxenon MDCs by an additional 51 % relative to the MDCs associated with the thin rectangular Si-PIN diode spectrometer design.

The absolute detection efficiency and MDC gains achieved using the thin rectangular and cylindrical spectrometer chamber designs utilized Si-PIN diodes that were equivalent to the Si-PIN diodes utilized by the XIA LLC Si-PIN diode spectrometer prototype. Additional radioxenon MDC reductions were achieved using larger Si-PIN diodes. The largest Si-PIN diodes modelled here had a surface area of 250 mm^2 (10 times larger than the surface area associated with the Si-PIN diodes employed by the XIA LLC Si-PIN diode spectrometer prototype). These large Si-PIN diodes were paired with a spectrometer chamber that was 0.37 cm thick. The spectrometer chamber thickness was

set so that the volume of the radioxenon gas evaluated would be 1 cm^3, consistent with the radioxenon gas volume requirement set forth by the Xenon International project [78]. As illustrated by Table 2.12, coupling the large area Si-PIN diodes with a thin cylindrical spectrometer chamber reduced the radioxenon MDCs by about 36 % relative to the MDCs associated with the Si-PIN diode spectrometer design with the thin cylindrical spectrometer chamber and the smaller 0.25 mm^2 Si-PIN diodes.

Table 2.12: Optimized Si-PIN diode spectrometer design performance comparisons.

Monitoring System	Radioxenon Minimum Detectable Concentrations (MDCs) [$mBq\text{-}m^{-3}$]			
	^{131m}Xe	^{133m}Xe	^{133}Xe	^{135}Xe
XIA LLC Si-PIN Diode Spec. Prototype	1.7	2.0	2.1	56
Thin Rectangular Spec. Chamber	0.96	1.2	1.2	32
Thin Cylindrical Spec. Chamber	0.48	0.57	0.58	16
Large Area Si-PIN Diodes	0.31	0.37	0.37	10
"High" Radioxenon Fill Pressure	0.28	0.33	0.34	9.2
Thick Si-PIN Diodes	0.26	0.32	0.32	8.7
Best Possible using Si-PIN Diodes	0.081	0.097	0.099	2.7

The sensitivity of the radioxenon MDCs to changes in radioxenon fill pressure and Si-PIN diode thickness were also evaluated. As discussed in Section 2.3.3.4, increasing the radioxenon fill pressure from 50 Torr (6.7 kPa) to 380 Torr (50.7 kPa) reduced the radioxenon MDCs by about 9.4 %. Increasing the radioxenon fill pressure above 380 Torr (50.7 kPa) resulted in significant widening of the conversion electron peaks and only very small MDC reductions. These results indicate that in order to operate a Si-PIN diode-based spectrometer with radioxenon samples at standard temperature and pressure a thinner spectrometer chamber would be highly desirable.

The sensitivity of the radioxenon MDCs to changes in Si-PIN diode thickness were evaluated as well. As described in Section 2.3.3.5, increasing the thickness of the Si-PIN diodes by a factor of two produced fairly significant increases in absolute photon detection efficiency (about 62 %), but essentially no changes in absolute conversion electron detection efficiency. These small changes in absolute conversion electron detection efficiency produced only very slight radioxenon MDC reductions, as illustrated in Table 2.12. This indicates that, in terms of Si-PIN diodes intended to support conversion electron spectroscopy, there is little to be gained by developing thicker Si-PIN diodes.

The Si-PIN diode spectrometer optimization studies documented herein produced a Si-PIN diode spectrometer design utilizing large area Si-PIN diodes and a thin cylindrical spectrometer chamber. The absolute 150 keV conversion electron detection efficiencies associated with this design are expected to be about 450 % larger than the absolute 150 keV conversion electron detection efficiencies associated with the XIA

LLC Si-PIN diode spectrometer prototype. The absolute 150 keV conversion electron detection efficiency gains result in radioxenon MDCs that are about 82 % lower than the radioxenon MDCs associated with the XIA LLC Si-PIN diode spectrometer prototype. These are significant performance improvements. However, the fact that the best possible radioxenon MDCs are still about 73 % smaller than the radioxenon MDCs associated with the large area Si-PIN diode spectrometer design produced here indicates that additional design modifications could lead to additional performance improvements.

2.4 Final Conclusions Regarding the Si-PIN Diode Spectrometer Prototype Characterization and Optimization Studies

This chapter documents the characterization and optimization of a Si-PIN diode spectrometer prototype developed by XIA LLC [66, 67, 68]. Section 2.2.1.2 documents the acquisition of three radioxenon spectra acquired using four radioxenon gas samples prepared as described in Sections 2.2.1.1.1 through 2.2.1.1.4. Section 2.2.1.3, describes the acquisition of eight additional calibration source spectra. Sections 2.2.2, 2.2.3, and 2.2.4 document the process of extracting peak mean, peak width, and peak area data from the spectra to support the development of prototype linearity, resolution, and absolute detection efficiency characterizations.

The most significant finding associated with the XIA LLC Si-PIN diode spectrometer prototype linearity characterization is the fact that a single linearity calibration curve may be used for both photons and conversion electrons (see Section 2.2.2). The photon resolution of the XIA LLC Si-PIN diode spectrometer

prototype was found to be quite good (0.66 ± 0.10 keV FWHM at photon energies near 30 keV) relative to the photon resolution typical of High-Purity Ge (HPGe) spectrometers (about 1.50 ± 0.12 keV FWHM at photon energies near 30 keV) (See Section 2.2.3). Conversion electron peak widths were found to be about 1.37 ± 0.37 keV at conversion electron energies near 150 keV. The radioxenon conversion electron peaks most important in the context of the CTBT are all separated by several FWHM so that there are no interferences amongst the peaks. Absolute photon and conversion electron detection efficiencies were found to be about 0.48 ± 0.05 % and 2.6 ± 0.2 %, respectively at photon and conversion electron energies near 30 keV and 150 keV (see Section 2.2.4).

In section 2.2.5 the absolute conversion electron detection efficiency characterization developed in Section 2.2.4 is used to evaluate the ^{131m}Xe, ^{133m}Xe, ^{133}Xe, and ^{135}Xe Minimum Detectable Concentrations (MDCs) associated with the XIA LLC Si-PIN diode spectrometer prototype. The ^{131m}Xe, ^{133m}Xe, ^{133}Xe, and ^{135}Xe MDCs associated with the XIA LLC Si-PIN diode spectrometer prototype were found to be 1.7, 2.0, 2.1, and 56 mBq-m^{-3}, respectively. As illustrated in Figure 2.67, with the exception of the ^{135}Xe MDC, these MDCs are all fairly comparable to the radioxenon MDCs associated with the ARIX [52], ARSA [54], SAUNA [57], and SPALAX [58] systems. Note that the ^{135}Xe MDC is large compared to the ^{131m}Xe, ^{133m}Xe, and ^{133}Xe MDCs because the branching ratio associated with the most intense ^{135}Xe conversion electron is small (about 5.61 % [60]) compared to the branching ratios associated with the most intense ^{131m}Xe, ^{133m}Xe, and ^{133}Xe conversion electron branching ratios.

Section 2.3 presents a series of studies conducted to optimize the performance of the Si-PIN diode spectrometer prototype. The results of these optimization studies are summarized in Figure 2.67. The first set of optimization studies investigated performance gains that might be achieved by making a series of changes to the spectrometer chamber dimensions while still using the Si-PIN diodes employed by the XIA LLC Si-PIN diode

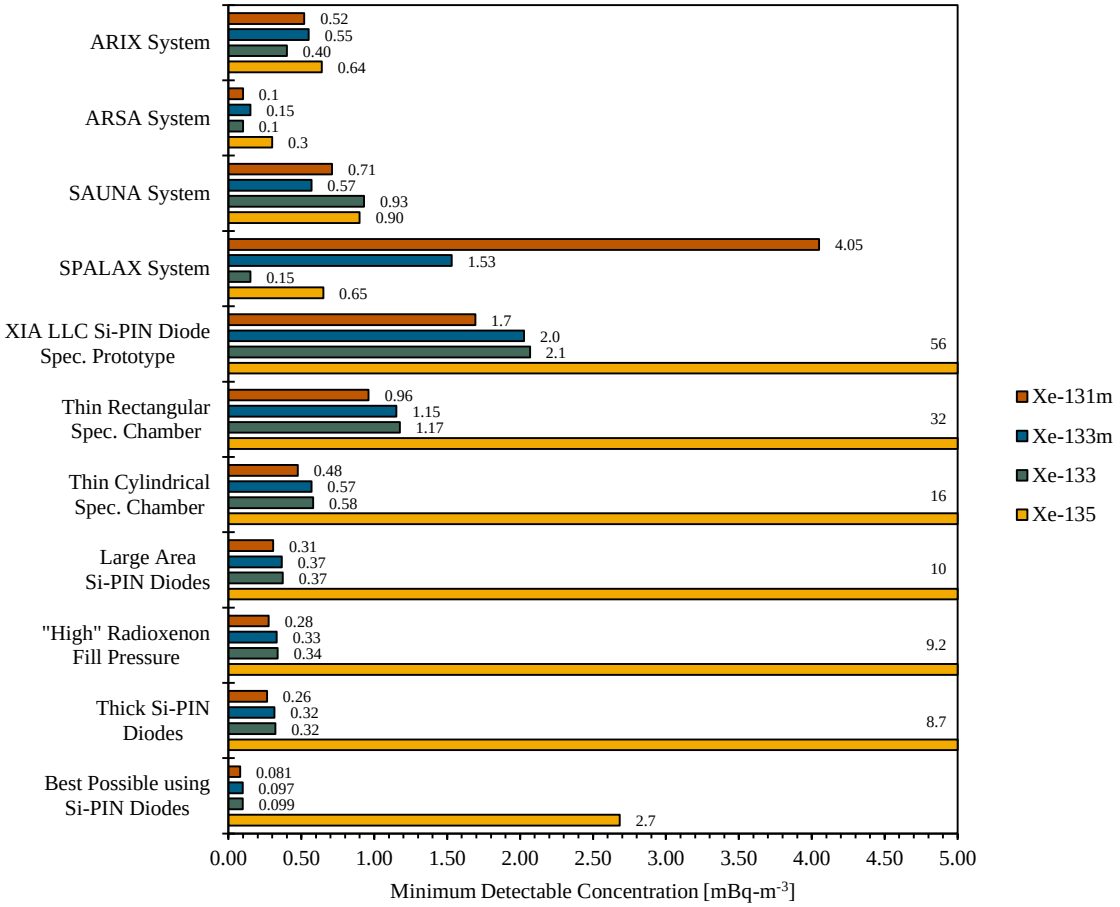

Figure 2.67: Si-PIN diode spectrometer Minimum Detectable Concentration (MDC) comparisons.

spectrometer prototype. As illustrated by Figure 2.67, the radioxenon MDCs associated with a Si-PIN diode spectrometer design with a thin, 0.3 cm thick rectangular spectrometer chamber were roughly 43 % smaller than the radioxenon MDCs associated with the XIA LLC Si-PIN diode spectrometer prototype. Switching to a thin, 0.3 cm thick cylindrical spectrometer chamber reduced the radioxenon MDCs by an additional 51 % relative to the MDCs associated with the thin rectangular Si-PIN diode spectrometer design.

Additional radioxenon MDC reductions were achieved using larger Si-PIN diodes. The largest Si-PIN diodes modelled here had a surface area 10 times larger than the surface area of the Si-PIN diodes employed by the XIA LLC Si-PIN diode spectrometer prototype–of 250 mm^2. These large Si-PIN diodes were paired with a spectrometer chamber that was 0.37 cm thick. The spectrometer chamber thickness was set so that the volume of the radioxenon gas evaluated would be 1 cm^3, consistent with the radioxenon gas volume requirement set forth by the Xenon International project [78]. As illustrated by Figure 2.67, coupling the large area Si-PIN diodes with a thin cylindrical spectrometer chamber reduced the ^{131m}Xe, ^{133m}Xe, ^{133}Xe, and ^{135}Xe MDCs to 0.31, 0.37, 0.37, and 10 $mBq\text{-}m^{-3}$, respectively. These MDCs are about 36 % lower than the ^{131m}Xe, ^{133m}Xe, ^{133}Xe, and ^{135}Xe MDCs associated with the Si-PIN diode spectrometer design with the thin cylindrical spectrometer chamber and the smaller 0.25 mm^2 Si-PIN diodes.

The sensitivity of the radioxenon MDCs to changes in radioxenon fill pressure and Si-PIN diode thickness were also evaluated. Increasing the radioxenon fill pressure

from 50 Torr (6.7 kPa) to 380 Torr (50.7 kPa) reduced the radioxenon MDCs by about 9.4 %. Increasing the radioxenon fill pressure above 380 Torr (50.7 kPa) resulted in significant widening of the conversion electron peaks and only very small MDC reductions. As described in Section 2.3.3.5, increasing the thickness of the Si-PIN diodes by a factor of two produced fairly significant increases in absolute photon detection efficiency (about 62 %), but essentially no changes in absolute conversion electron detection efficiency. As illustrated in Figure 2.67, these small changes in absolute conversion electron detection efficiency produced only very slight radioxenon MDC reductions. This indicates that, in terms of Si-PIN diodes intended to support conversion electron spectroscopy, there is little to be gained by developing thicker Si-PIN diodes.

Ultimately, the Si-PIN diode spectrometer optimization studies documented herein produced a Si-PIN diode spectrometer design utilizing large area Si-PIN diodes and a thin cylindrical spectrometer chamber. The absolute 150 keV conversion electron detection efficiency associated with this design is expected to be about 14 %, which is 450 % larger than the absolute 150 keV conversion electron detection efficiency associated with the XIA LLC Si-PIN diode spectrometer prototype. As illustrated in Figure 2.67, the absolute 150 keV conversion electron detection efficiency gains result in radioxenon MDCs that are about 82 % lower than the radioxenon MDCs associated with the XIA LLC Si-PIN diode spectrometer prototype and very competitive with the radioxenon MDCs associated with the ARIX [52], ARSA [54], SAUNA [57], and SPALAX [58] systems. However, the fact that the best possible radioxenon MDCs are still about 73 % smaller than the radioxenon MDCs associated with the large area Si-PIN

diode spectrometer design produced here indicates that additional design modifications could lead to additional performance improvements.

Chapter 3: CTBT-Relevant Radionuclide Background Activity Concentrations Resulting from Natural Processes

This chapter documents a series of studies conducted to evaluate background activity concentrations associated with 100 Comprehensive Nuclear-Test-Ban Treaty (CTBT)-relevant radioactive particulates and noble gases in the Earth's atmosphere, in several different geologies, and in seawater. The first section of this chapter introduces the radioactive particulates and noble gases relevant to the CTBT and the processes by which they are produced during nuclear explosions. The next section (Section 3.2) then describes background sources (*i.e.* non-explosion sources) of the same CTBT-relevant radioactive particulates and noble gases. Anthropogenic sources, which have already been studied somewhat extensively by others, are discussed briefly, and then the primary focus is on natural processes by which the CTBT-relevant radionuclides may be produced. The natural processes of most interest here are spontaneous fission, cosmic neutron-induced fission, and cosmic neutron-induced activation. Note that the so-called "cosmic neutrons" are not, strictly speaking, of cosmic origin, but rather are produced via cosmic ray-induced spallation reactions in the Earth's atmosphere (as described in Section 3.2.2) [115].

Section 3.4 describes the methods used to evaluate the CTBT-relevant radioactive particulate and noble gas background activity concentrations of interest. The background activity concentrations resulting from spontaneous fission, cosmic neutron-induced fission, and cosmic neutron-induced activation are all evaluated using an application developed specifically to support CTBT-relevant radioactive particulate and noble gas background activity concentration studies. The application, referred to herein as the TeXAS application, supports the generation of CTBT-relevant radioactive particulate and noble gas background activity concentration estimates by: (1) automating and streamlining the process of developing high-fidelity material composition and temperature data, (2) incorporating the data into Monte Carlo N-Particle (MCNP) radiation transport code [74, 75, 76, 77] models, (3) collecting and processing the best-available nuclear data required to support the MCNP models, and (4) post-processing the outputs generated by the MCNP models and evaluating the radioactive particulate and noble gas background activity concentration estimates of interest.

The remainder of this chapter describes several studies conducted to evaluate background activity concentrations associated with 100 CTBT-relevant radioactive particulates and noble gases in the Earth's atmosphere, in several different geologies, and in seawater. The atmospheric studies, documented in Section 3.5.1, describe the CTBT-relevant radioactive noble gas background activity concentrations resulting from cosmic neutron-induced activation of various constituents of the Earth's atmosphere at geometric heights of 50,000 m, 15,000 m, and 1 m. The cosmic neutron flux profiles and the

atmospheric constituents most responsible for attenuating the cosmic neutron flux at each of the aforementioned geometric heights are also discussed.

The geological studies, documented in Section 3.5.2, describe the CTBT-relevant radioactive particulate and noble gas background activity concentrations resulting from spontaneous fission, cosmic neutron-induced fission, and cosmic neutron-induced activation of various geological constituents as a function of depth in three different igneous geologies and three different sedimentary geologies. The igneous geologies considered are a granite geology, a basalt geology, and a granodiorite geology. The sedimentary geologies considered are a shale geology, a sandstone geology, and a limestone geology. These geologies were selected based on their prevalence in the Earth's upper crust. As with the atmospheric studies, the cosmic neutron flux profiles and the geological constituents most responsible for attenuating the cosmic neutron flux in each of the aforementioned geologies are also discussed.

The seawater studies, documented in Section 3.5.3, describe the CTBT-relevant radioactive noble gas background activity concentrations resulting from spontaneous fission, cosmic neutron-induced fission, and cosmic neutron-induced activation as a function of depth in seawater. The primary focus of the seawater studies is on the background activity concentrations associated with the radioactive noble gases of most interest to the verification regime of the CTBT—^{37}Ar, ^{131m}Xe, ^{133m}Xe, ^{133}Xe, and ^{135}Xe.

The last set of studies, documented in Section 3.5.4, is a set of sensitivity studies conducted to evaluate the sensitivity of the CTBT-relevant radioactive particulate and noble gas background activity concentration estimates generated by the TeXAS

application to changes in various inputs. Sensitivity studies are carried out by applying a number of geological composition perturbations to a granite geology, by filling the porosity voids in the granite geology to water, and by removing the study-specific nuclear data and replacing it with basic nuclear data packaged with MCNP.

3.1 CTBT-Relevant Radionuclides

Originally, the software employed at the CTBT International Data Center flagged every CTBT International Monitoring System (IMS)-acquired radionuclide spectrum found to contain a non-naturally occurring radionuclide as "interesting" [116]. This was problematic in that a large number of spectra were found to contain non-naturally occurring radionuclides, a large number of spectra were flagged as interesting, and each spectrum flagged as interesting required further evaluation by a CTBT analyst. The end result was that a large portion of available CTBT analyst resources were directed towards evaluating spectra that were not truly interesting from a CTBT verification perspective. In order to minimize the CTBT analyst resources directed towards irrelevant spectra and free more analyst resources to evaluate spectra of a truly CTBT-relevant nature, a list of CTBT-relevant radionuclides was developed. This list is reproduced in Tables 3.1 and 3.2. Table 3.1 lists all of the CTBT-relevant radionuclides resulting from spontaneous and neutron-induced fission, while Table 3.2 lists all of the CTBT-relevant radionuclides resulting from neutron-induced activation.

Table 3.1: CTBT-relevant fission products.

Fission Product	Half-Life	Fission Yield
Strontium-91	9.65 h	4.81 %
Yttrium-91	58.51 d	4.82 %
Yttrium-93	10.18 h	5.19 %
Zirconium-95	64.032 d	5.17 %
Niobium-95	34.991 d	5.17 %
Zirconium-97	16.749 h	5.14 %
Molybdenum-99	65.976 h	5.14 %
Technetium-99m	6.0067 h	4.52 %
Ruthenium-103	39.247 d	3.20 %
Rhodium-105	35.36 h	1.87 %
Ruthenium-106	371.8 d	1.61 %
Palladium-109	13.7012 h	1.17 %
Silver-111	7.45 d	1.08 %
Palladium-112	21.04 h	1.08 %
Cadmium-115m	44.56 d	0.46 %
Cadmium-115	53.46 h	0.64 %
Tin-123	129.2 d	0.06 %
Tin-125	9.64 d	0.92 %
Antimony-125	2.75856 y	1.46 %
Tellurium-125m	57.40 d	0.33 %
Antimony-126	12.35 d	0.34 %
Antimony-127	3.85 d	2.16 %
Tellurium-127m	106.1 d	2.17 %
Tellurium-127	9.35 h	0.36 %

Fission Product	Half-Life	Fission Yield
Antimony-128	9.05 h	0.48 %
Tellurium-129m	33.6 d	0.71 %
Iodine-130	12.36 h	0.03 %
Tellurium-131m	33.25 h	1.34 %
Iodine-131	8.0252 d	2.88 %
Tellurium-132	3.204 d	4.09 %
Iodine-133	20.83 h	5.36 %
Iodine-135	6.58 h	4.22 %
Cesium-136	13.16 d	0.23 %
Cesium-137	30.08 y	4.93 %
Barium-140	12.7527 d	4.49 %
Lanthanum-140	1.67855 d	4.53 %
Cerium-141	32.511 d	4.49 %
Cerium-143	33.039 h	3.81 %
Cerium-144	284.91 d	3.17 %
Neodymium-147	10.98 d	1.62 %
Promethium-149	53.08 h	0.81 %
Promethium-151	28.40 h	0.36 %
Samarium-153	46.50h	0.20 %
Europium-155	4.753 y	0.08 %
Samarium-156	9.4 h	0.05 %
Europium-156	15.19 d	0.06 %
Europium-157	15.18 h	0.04 %
-	-	-

The list of CTBT-relevant fission products reproduced above was taken from De Geer [116]. The CTBT-relevant fission product half-lives reproduced above are the half-lives reported by the NNDC [60]. The fission yields reproduced above are the 14.0 MeV neutron induced fission yields specific to ^{235}U and and were taken from version B-VII.1of the Evaluated Nuclear Data File (ENDF/B-VII.1) [117, 118].

Table 3.2: CTBT-relevant activation products.

Activation Product	Half-Life	Nuclear Device				Environment
		(n,γ)	(n,p)	(n,α)	(n,2n)	(n,γ)
Sodium-24	14.997 h	-	-	✓	-	✓
Potassium-42	12.360 h	-	-	-	-	✓
Scandium-46	83.79 d	-	✓	-	-	-
Scandium-47	3.3492 d	-	✓	-	-	-
Chromium-51	27.7010 d	✓	-	-	✓	-
Manganese-54	312.20 d	-	✓	-	✓	-
Cobalt-57	271.74 d	-	-	-	-	-
Cobalt-58	70.86 d	-	✓	-	✓	-
Iron-59	44.495 d	✓	-	-	-	✓
Cobalt-60	1,925.28 d	✓	✓	-	-	-
Copper-64	12.701 h	✓	✓	-	✓	-
Zinc-65	243.93 d	✓	-	-	✓	-
Zinc-69m	13.756 h	✓	-	-	✓	-
Gallium-72	14.10 h	✓	-	-	-	-
Arsenic-74	17.77 d	-	-	-	-	-
Arsenic-76	26.24 h	-	-	-	-	-
Rubidium-84	32.82 d	-	-	-	-	-
Rubidium-86	18.642 d	-	-	-	-	-
Yttrium-88	106.627 d	-	-	-	-	-
Zirconium-89	78.41 h	-	-	-	-	-
Rhodium-102	207.3 d	-	-	-	-	-
Silver-106m	8.28 d	-	-	-	✓	-
Silver-108m	438 y	✓	-	-	-	-
Silver-110m	249.83 d	✓	-	-	-	-
Antimony-120	5.76 d	-	-	-	✓	-
Antimony-122	2.7238 d	✓	-	-	✓	-
Antimony-124	60.20 d	✓	-	-	-	-
Cesium-132	6.479 d	-	-	-	✓	-
Barium-133	10.551 y	-	-	-	-	-
Cesium-134	2.0652 y	✓	-	-	-	-
Europium-152m	9.3116 h	-	-	-	-	✓
Europium-152	13.517 y	-	-	-	-	✓
Thulium-170	128.6 d	-	-	-	-	-
Tungsten-187	24.000 h	✓	-	-	-	-
Iridium-190	11.78 d	-	-	-	-	-
Iridium-192	73.829 d	-	-	-	-	-
Gold-196	6.1669 d	-	-	-	✓	-
Gold-196m	9.6 h	-	-	-	✓	-
Gold-198	2.6941 d	✓	-	-	-	-
Lead-203	51.92 h	-	-	-	✓	-
Radium-224	3.66 d	-	-	-	-	-
Uranium-237	6.75 d	-	-	-	-	-
Neptunium-239	2.356 d	-	-	-	-	-
Americium-241	432.6 y	-	-	-	-	-

The CTBT-relevant activation product half-lives reproduced above are the half-lives reported by the NNDC [60]. Columns three through six of the table highlight activation products produced via various activation reactions involving nuclear device materials while column seven highlights activation products produced via (n,γ) reactions with environmental materials [116].

As illustrated by the division of Tables 3.1 and 3.2, there are two broad classes of CTBT-relevant radionuclides. The first class consists of CTBT-relevant fission products. The CTBT-relevant fission products are radionuclides that are produced via neutron-induced fission in the fissionable material that constitutes the fuel of a nuclear device (usually ^{235}U or ^{239}Pu). The fission yields reproduced in Table 3.1 are the 14.0 MeV ^{235}U fission yields from version B-VII.1 of the Evaluated Nuclear Data File (ENDF/B-VII.1) [117, 118]. The fission yields provide an indication as to how much each of the CTBT-relevant fission products is produced during a nuclear explosion.

The second class of CTBT-relevant radionuclides consists of CTBT-relevant activation products. As illustrated by Table 3.2, the CTBT-relevant activation products may be produced via a wide range of neutron-induced activation reactions. The (n,γ) reaction nomenclature used in Table 3.2 is used to denote a neutron-induced activation reaction where an incident neutron is absorbed by a target atom, the target atom is activated, meaning it is made radioactive, and then a gamma-ray is ejected from the nucleus of the activated atom. Note that some of the (n,γ) activation reactions listed in Table 3.2 involve the activation of materials associated with the nuclear device while others involve the activation of materials in the environment surrounding the device. The (n,p), (n,α), and (n,2n) reactions listed in Table 3.2 are other neutron-induced activation reactions that involve the absorption of a neutron by a target atom and the subsequent emission of either a proton (in the case of an (n,p) reaction), an alpha-particle (in the case of an (n,α) reaction), or two neutrons (in the case of an (n,2n) reaction). Note that while Table 3.2 highlights the fact that the (n,p), (n,α), and (n,2n) activation

reactions occur primarily in nuclear device materials, many of them also occur in the environment surrounding the device. Also note that activation reactions for which none of the columns in Table 3.2 are checked occur primarily via other activation processes described by De Geer [116] that are not discussed here.

3.2 Background Sources of CTBT-Relevant Radionuclides

If the CTBT-relevant radionuclides identified in Tables 3.1 and 3.2 were only produced via processes exclusive to nuclear explosions then the radionuclide monitoring technology element of the verification regime of the CTBT would provide a very straight forward means of detecting nuclear explosions. In fact, if this were the case, detecting the presence of any CTBT-relevant radionuclide in a spectral data set would be a clear indication that a nuclear explosion was detonated. However, in reality this is not the case and CTBT-relevant radionuclides are constantly being produced via many different processes. Some of these processes are associated with human activities (the operation of commercial nuclear generating stations, for example) and some are completely natural processes.

It is important that the CTBT-relevant radionuclide background activity concentrations resulting from these anthropogenic sources and natural processes be well understood so that CTBT-relevant radionuclide detections in CTBT IMS-acquired spectra that are indicative of these processes may be distinguished from CTBT-relevant radionuclide detections indicative of nuclear explosions. Thus, the remainder of this

section presents an overview of the anthropogenic sources and natural processes that produce CTBT-relevant radioactive particulate and noble gas background activities.

3.2.1 Anthropogenic Sources of CTBT-Relevant Radioactive Noble Gas Background Activity Concentrations

CTBT-relevant radionuclides are produced via several anthropogenic sources. The most important anthropogenic sources are believed to be commercial nuclear generating stations, spent nuclear fuel reprocessing facilities, nuclear research reactors, and radiopharmaceutical facilities [119]. A number of studies conducted to assess the CTBT-relevant radioactive noble gas background activity concentrations released by commercial nuclear generating stations and radiopharmaceutical facilities are reviewed here briefly in order to provide context for the CTBT-relevant radioactive particulate and noble gas background activity concentrations documented in Section 3.5.

In commercial nuclear generating stations, the CTBT-relevant radioactive particulates and noble gases identified in Tables 3.1 and 3.2 are produced primarily as fission products inside the nuclear reactor fuel elements. The majority of the radioactive particulates and noble gases are retained inside the fuel elements. However, some of the fuel elements fail periodically and allow some of the radioactive particulates and noble gases to leak to the reactor coolant. The CTBT-relevant radioactive particulates are removed from the reactor coolant by reactor coolant filtration systems and thus the CTBT-relevant radioactive particulates are unable to escape from commercial nuclear generating stations to the environment in meaningful quantities. The CTBT-relevant

radioactive noble gases on the other hand are released to the environment in substantial quantities when dissolved gases are vented from the reactor coolant.

According to Kalinowksi and Tuma [120], a generic commercial nuclear generating station releases about 1.09×10^{11} Bq of ^{131m}Xe, about 1.24×10^{12} Bq of ^{133m}Xe, about 3.42×10^{10} Bq of ^{133}Xe, and about 8.97×10^{11} Bq of ^{135}Xe via continuous releases in a given year [120]. Kalinowksi and Tuma [120] also found that a generic commercial nuclear generating station releases an additional 3.82×10^{9} Bq of ^{131m}Xe, an additional 4.64×10^{11} Bq of ^{133m}Xe, an additional 2.84×10^{9} Bq of ^{133}Xe, and an additional 3.62×10^{10} Bq of ^{135}Xe via batch releases in a given year [120].

At radiopharmaceutical facilities, small uranium targets, typically encapsulated in aluminum, are bombarded by a thermal neutron flux [121]. The radioisotopes having pharmaceutical value are generated as fission products inside the aluminum-encapsulated uranium targets, as are the CTBT-relevant radioactive particulates and noble gases. The uranium targets are typically irradiated for 3 to 10 days [121]. After they are irradiated the targets are allowed to decay, typically for about 24 hours [121]. After the brief decay period the uranium targets are dissolved and the radioisotopes having pharmaceutical value are separated from the other fission products via chemical processes [121].While the CTBT-relevant radioactive particulates tend to remain in the chemical solution, the ^{131m}Xe, ^{133m}Xe, ^{133}Xe, and ^{135}Xe gases escape from the solution and are typically vented to the atmosphere.

Simulations conducted by Saey, Bowyer, and Ringbom [121] indicate that the ^{131m}Xe, ^{133m}Xe, ^{133}Xe, and ^{135}Xe activities five days after the dissolution of a uranium

target in which the ^{133}Xe activity reached its maximum value should be on the order of about 7.9×10^{13} Bq, 2.7×10^{11} Bq, 3.3×10^{12} Bq, and 8.9×10^{10} Bq, respectively [121]. Additionally, an atmospheric ^{133}Xe activity concentration measurement campaign conducted by Saey *et al.* over a three week period in the summer of 2008 at distances between 0.5 and 100 km from the emission stack of the National Institute for Radioelements radiopharmaceutical facility in Fleurus, Belgium found that atmospheric ^{133}Xe activity concentrations were in the range 0.7 to 4×10^5 mBq-m^{-3} [122]. A second ^{133}Xe activity concentration measurement campaign conducted by Saey *et al.* in 2008 in Mafikeng, South Africa 250 km from the NTP Radioisotopes Ltd. radiopharmaceutical facility found that atmospheric ^{133}Xe activity concentrations varied from 0 to 27 mBq-m^{-3} over a 42 day period with a mean value of about 3.24 mBq-m^{-3} [122].

3.2.2 Natural Sources of CTBT-Relevant Radioactive Particulate and Noble Gas Background Activities

In addition to nuclear explosions and the human activities described in the previous section, CTBT-relevant radio-nuclides may also be produced via natural processes. The natural processes of most interest here are (1) the spontaneous fission of thorium, uranium, and plutonium, (2) cosmic neutron-induced fission of thorium, uranium, and plutonium, (3) cosmic neutron-induced activation of various elements that occur naturally in the Earth's upper crust.

Spontaneous Fission of Thorium, Uranium, and Plutonium

Spontaneous fission is a natural process by which heavy radioactive nuclei decay from a relatively high energy nuclear configuration to a lower energy nuclear configuration by fissioning, or splitting into two smaller nuclei. The process by which a heavy radioactive nucleus having atomic number Z_1 and mass number A_1 fissions spontaneously, producing two smaller nuclei having atomic numbers Z_2 and $Z_3 = Z_1 - Z_2$ and mass numbers A_2 and $A_3 = A_1 - A_2 - x \cdot n$, respectively, where $x \cdot n$ is some number of stray neutrons, may be expressed as follows:

$$ {}^{A_1}_{Z_1}X_1^* \rightarrow {}^{A_2}_{Z_2}X_2 + {}^{A_3=A_1-A_2-x\cdot n}_{Z_3=Z_1-Z_2}X_3 + x \cdot n \qquad 3.2.2.1$$

The factors of most importance in establishing CTBT-relevant radionuclide background activity concentrations resulting from spontaneous fission of thorium, uranium, and plutonium are (1) the atom concentrations, (2) the half-lives, (3) the spontaneous fission branching ratios, and (4) the CTBT-relevant radionuclide spontaneous fission yields associated with the thorium, uranium, and plutonium isotopes that decay via spontaneous fission.

The average concentration of thorium in the Earth's upper crust is about 1.05×10^{-3} wt. % [123, 124, 125], and natural thorium consists of a single radioactive isotope, ^{232}Th [112]. ^{232}Th has a relatively long half-life of 1.40×10^{10} years and a spontaneous fission branching ratio of 1.4×10^{-9} % [117]. The ^{232}Th half-life describes the rate at which it is expected to decay. In this case, about half of it is expected to decay in 14.0×10^9 years. The spontaneous fission branching ratio describes the fraction of ^{232}Th decays which proceed via spontaneous fission as opposed to some other decay

process, such as alpha-particle emission. In this case, one in about 10^{11} ^{232}Th decays proceeds via spontaneous fission. The CTBT-relevant radionuclide spontaneous fission yields associated with ^{232}Th are presented in Table 3.3.

The average concentration of uranium in the Earth's upper crust is about 2.7×10^{-4} wt. % [123, 124, 125]. At this point, it is somewhat interesting to note that the average thorium and uranium concentrations associated with the Earth' upper crust are both comparable to the average copper concentration associated with the Earth's upper crust (2.2×10^{-3} wt. % [123, 124, 125]) and several orders of magnitude larger than the average gold and silver concentrations associated with the Earth's upper crust (1.6×10^{-7} and 5.3×10^{-6} wt. %, respectively [123, 124, 125]). Unlike thorium, which has only one naturally occurring isotope, natural uranium is composed of three isotopes, all of which are radioactive. The vast majority of natural uranium is ^{238}U, which accounts for over 99 % of natural uranium [112]. The remainder is composed of ^{235}U and ^{234}U which account for about 0.7 % and 0.005 % of natural uranium, respectively [112]. The half-lives and spontaneous fission branching ratios associated with the aforementioned uranium isotopes are presented in Table 3.4. The ^{234}U, ^{235}U, and ^{238}U spontaneous fission yields are presented in Table 3.3.

Table 3.3: CTBT-relevant fission product spontaneous fission yields associated with thorium, uranium, and plutonium isotopes [117].

CTBT-Relevant Fission Product	Spontaneous Fission Yield (unitless) associated with Parent Radionuclide:						
	^{232}Th	^{234}U	^{235}U	^{238}U	^{238}Pu	^{239}Pu	^{240}Pu
Strontium-91	7.0×10^{-2}	6.4×10^{-2}	6.5×10^{-2}	6.2×10^{-2}	4.5×10^{-2}	3.8×10^{-2}	3.1×10^{-2}
Yttrium-91	7.0×10^{-2}	6.4×10^{-2}	6.5×10^{-2}	6.2×10^{-2}	4.5×10^{-2}	3.8×10^{-2}	3.1×10^{-2}
Yttrium-93	6.6×10^{-2}	7.2×10^{-2}	7.0×10^{-2}	6.4×10^{-2}	6.2×10^{-2}	5.5×10^{-2}	4.7×10^{-2}
Zirconium-95	7.2×10^{-2}	7.1×10^{-2}	7.2×10^{-2}	7.1×10^{-2}	6.3×10^{-2}	6.0×10^{-2}	5.6×10^{-2}
Niobium-95	7.2×10^{-2}	7.1×10^{-2}	7.2×10^{-2}	7.1×10^{-2}	6.3×10^{-2}	6.0×10^{-2}	5.6×10^{-2}
Zirconium-97	4.6×10^{-2}	6.4×10^{-2}	6.4×10^{-2}	6.8×10^{-2}	6.5×10^{-2}	6.1×10^{-2}	5.7×10^{-2}
Molybdenum-99	1.6×10^{-2}	4.7×10^{-2}	5.8×10^{-2}	6.8×10^{-2}	6.9×10^{-2}	6.8×10^{-2}	6.4×10^{-2}
Technetium-99m	1.4×10^{-2}	4.2×10^{-2}	5.1×10^{-2}	6.0×10^{-2}	6.1×10^{-2}	6.0×10^{-2}	5.6×10^{-2}
Ruthenium-103	2.8×10^{-4}	1.6×10^{-3}	4.1×10^{-3}	2.8×10^{-2}	4.4×10^{-2}	5.8×10^{-2}	6.7×10^{-2}
Rhodium-105	6.2×10^{-5}	1.1×10^{-4}	3.6×10^{-4}	6.4×10^{-3}	1.8×10^{-2}	3.3×10^{-2}	4.9×10^{-2}
Ruthenium-106	6.8×10^{-5}	4.7×10^{-5}	1.4×10^{-4}	2.4×10^{-3}	9.1×10^{-3}	1.9×10^{-2}	3.5×10^{-2}
Palladium-109	4.9×10^{-5}	2.4×10^{-5}	4.5×10^{-5}	7.9×10^{-5}	4.9×10^{-4}	1.7×10^{-3}	5.0×10^{-3}
Silver-111	6.2×10^{-5}	2.7×10^{-5}	5.1×10^{-5}	2.0×10^{-5}	7.0×10^{-5}	1.9×10^{-4}	6.9×10^{-4}
Palladium-112	7.7×10^{-5}	2.7×10^{-5}	5.3×10^{-5}	2.4×10^{-5}	4.8×10^{-5}	7.2×10^{-5}	2.3×10^{-4}
Cadmium-115m	3.0×10^{-6}	1.6×10^{-6}	3.3×10^{-6}	8.5×10^{-7}	2.7×10^{-6}	1.6×10^{-6}	1.3×10^{-6}
Cadmium-115	5.5×10^{-5}	2.8×10^{-5}	5.5×10^{-5}	1.5×10^{-5}	4.0×10^{-5}	2.7×10^{-5}	2.2×10^{-5}
Tin-123	2.7×10^{-6}	4.3×10^{-6}	6.1×10^{-6}	9.6×10^{-7}	1.0×10^{-5}	5.4×10^{-6}	2.6×10^{-6}
Tin-125	9.6×10^{-6}	1.0×10^{-5}	1.6×10^{-5}	3.0×10^{-6}	2.4×10^{-5}	1.6×10^{-5}	1.5×10^{-5}
Antimony-125	3.4×10^{-5}	2.3×10^{-5}	3.7×10^{-5}	1.4×10^{-5}	4.8×10^{-5}	3.5×10^{-5}	3.2×10^{-5}
Tellurium-125m	7.5×10^{-6}	5.1×10^{-6}	8.3×10^{-6}	3.0×10^{-6}	1.1×10^{-5}	8.0×10^{-6}	7.2×10^{-6}
Antimony-126	6.2×10^{-5}	1.8×10^{-5}	3.2×10^{-5}	1.4×10^{-5}	7.0×10^{-5}	6.3×10^{-5}	6.8×10^{-5}
Antimony-127	3.1×10^{-5}	3.9×10^{-5}	5.7×10^{-5}	3.5×10^{-5}	3.1×10^{-4}	2.6×10^{-4}	2.9×10^{-4}
Tellurium-127m	5.1×10^{-6}	6.7×10^{-6}	9.8×10^{-6}	5.7×10^{-6}	5.2×10^{-5}	4.4×10^{-5}	4.9×10^{-5}
Tellurium-127	3.1×10^{-5}	3.9×10^{-5}	5.8×10^{-5}	3.5×10^{-5}	3.1×10^{-4}	2.6×10^{-4}	2.9×10^{-4}
Antimony-128	5.6×10^{-4}	1.2×10^{-4}	1.3×10^{-4}	1.0×10^{-4}	9.1×10^{-4}	9.3×10^{-4}	1.1×10^{-3}
Tellurium-129m	7.0×10^{-6}	8.2×10^{-5}	6.5×10^{-5}	3.2×10^{-5}	5.7×10^{-4}	4.1×10^{-4}	4.5×10^{-4}
Iodine-130	0	1.8×10^{-6}	3.8×10^{-7}	0	3.0×10^{-5}	5.6×10^{-6}	1.2×10^{-6}
Tellurium-131m	3.5×10^{-4}	2.1×10^{-3}	1.0×10^{-3}	3.6×10^{-4}	6.4×10^{-3}	3.8×10^{-3}	3.0×10^{-3}
Iodine-131	4.0×10^{-3}	8.9×10^{-3}	6.5×10^{-3}	4.0×10^{-3}	1.8×10^{-2}	1.6×10^{-2}	1.6×10^{-2}
Tellurium-132	2.4×10^{-2}	2.3×10^{-2}	2.0×10^{-2}	1.4×10^{-2}	3.0×10^{-2}	3.3×10^{-2}	3.1×10^{-2}
Iodine-133	3.1×10^{-2}	4.4×10^{-2}	3.9×10^{-2}	2.9×10^{-2}	4.6×10^{-2}	4.9×10^{-2}	5.3×10^{-2}
Iodine-135	6.8×10^{-2}	6.1×10^{-2}	6.3×10^{-2}	7.6×10^{-2}	5.1×10^{-2}	6.3×10^{-2}	7.1×10^{-2}
Cesium-136	1.2×10^{-6}	1.8×10^{-4}	3.6×10^{-5}	8.0×10^{-7}	1.1×10^{-3}	3.2×10^{-4}	1.3×10^{-4}
Cesium-137	6.6×10^{-2}	8.3×10^{-2}	6.9×10^{-2}	6.9×10^{-2}	7.8×10^{-2}	7.6×10^{-2}	7.8×10^{-2}

Table 3.3: CTBT-relevant fission product spontaneous fission yields associated with thorium, uranium, and plutonium isotopes, continued [117].

CTBT-Relevant Fission Product	Spontaneous Fission Yield (unitless) associated with Parent Radionuclide:						
	^{232}Th	^{234}U	^{235}U	^{238}U	^{238}Pu	^{239}Pu	^{240}Pu
Lanthanum-140	7.0×10^{-2}	6.1×10^{-2}	6.8×10^{-2}	6.6×10^{-2}	6.1×10^{-2}	5.6×10^{-2}	5.4×10^{-2}
Cerium-141	6.5×10^{-2}	6.2×10^{-2}	5.8×10^{-5}	7.1×10^{-2}	5.8×10^{-2}	5.5×10^{-2}	5.1×10^{-2}
Cerium-143	6.3×10^{-2}	7.4×10^{-2}	6.1×10^{-5}	6.2×10^{-2}	5.9×10^{-2}	5.4×10^{-2}	5.6×10^{-2}
Cerium-144	6.3×10^{-2}	6.2×10^{-2}	7.5×10^{-5}	6.5×10^{-2}	5.1×10^{-2}	5.5×10^{-2}	5.2×10^{-2}
Neodymium-147	3.2×10^{-2}	3.2×10^{-2}	3.1×10^{-2}	4.0×10^{-2}	3.2×10^{-2}	2.9×10^{-2}	3.0×10^{-2}
Promethium-149	1.4×10^{-2}	1.1×10^{-2}	1.2×10^{-2}	1.8×10^{-2}	1.5×10^{-2}	1.5×10^{-2}	1.7×10^{-2}
Promethium-151	2.3×10^{-3}	1.8×10^{-3}	2.2×10^{-3}	4.5×10^{-3}	5.9×10^{-3}	5.6×10^{-3}	5.8×10^{-3}
Samarium-153	1.8×10^{-4}	2.1×10^{-4}	2.3×10^{-4}	4.2×10^{-4}	1.7×10^{-3}	1.5×10^{-3}	1.9×10^{-3}
Europium-155	7.8×10^{-6}	7.3×10^{-6}	1.3×10^{-5}	4.0×10^{-5}	3.0×10^{-4}	2.8×10^{-4}	3.6×10^{-4}
Samarium-156	1.5×10^{-6}	1.8×10^{-6}	2.1×10^{-6}	1.0×10^{-5}	1.3×10^{-4}	1.1×10^{-4}	1.4×10^{-4}
Europium-156	1.5×10^{-6}	1.8×10^{-6}	2.1×10^{-6}	1.0×10^{-5}	1.3×10^{-4}	1.1×10^{-4}	1.4×10^{-4}
Europium-157	2.0×10^{-7}	4.0×10^{-7}	2.0×10^{-7}	2.5×10^{-6}	4.8×10^{-5}	4.2×10^{-5}	5.9×10^{-5}

Table: 3.4: Half-lives and spontaneous fission yields associated with naturally occurring uranium isotopes [117].

Uranium Isotope	Half-Life	S.F. Branching Ratio
Uranium-234	2.45×10^{5} y	1.7×10^{-9} %
Uranium-235	7.04×10^{8} y	7.2×10^{-9} %
Uranium-238	4.47×10^{9} y	5.46×10^{-5} %

Plutonium is somewhat unique relative to thorium and uranium in that it is not a naturally occurring element but it does exist in nature, largely as a result of fallout from historic nuclear explosions and nuclear accidents. According to data reported by Efurd *et al.* [126], mean subsurface ^{239}Pu and ^{240}Pu atom concentrations representative of fallout in the northern hemisphere are 3.39×10^{8} and 1.50×10^{7} cm^{-3}, respectively [126].

The ^{239}Pu and ^{240}Pu concentrations are, of course, typically higher in locations directly downwind of historic nuclear explosion sites. Additionally, ^{238}Pu is often found downwind of historic nuclear safety test sites [126]. The half-lives and spontaneous fission branching ratios associated with the aforementioned plutonium isotopes are presented in Table 3.5. The ^{238}Pu, ^{239}Pu, and ^{240}Pu spontaneous fission yields are presented in Table 3.3.

Table: 3.5: Half-lives and spontaneous fission yields associated with plutonium fallout isotopes [117].

Plutonium Isotope	Half-Life	S.F. Branching Ratio
Plutonium -238	87.7 y	1.86×10^{-7} %
Plutonium -239	2.41×10^{4} y	3.1×10^{-10} %
Plutonium -240	6.56×10^{3} y	5.7×10^{-6} %

Cosmic Neutron-Induced Fission and Activation

Cosmic neutron-induced fission and activation reactions are fission and activation reactions induced by "cosmic" neutrons. Note that the so-called "cosmic" neutrons are not actually of cosmic origin, but rather are produced as secondary cosmic rays in the Earth's atmosphere. Figure 3.1 illustrates the processes by which cosmic neutrons are produced. Most primary cosmic rays, which are of cosmic origin, are protons (about 92 %) and alpha particles (about 6 %); the remainder (about 2 %) are heavier nuclei [127]. The majority of the primary cosmic rays originate in deep space, typically outside of the Solar System, and sometimes outside of the Milky Way galaxy [128].

The primary cosmic ray flux incident upon the Earth's atmosphere varies with time and is a function of the Sun's solar cycle which has a period of about 11 years as illustrated in Figure 3.2 [127, 129]. As primary cosmic rays penetrate the Earth's atmosphere they participate in spallation reactions with various constituents of the Earth's atmosphere, mostly nitrogen and oxygen. These spallation reactions produce an array of secondary cosmic rays including neutrons, pions, and kaons. The pions decay to muons. All of the aforementioned primary and secondary cosmic rays make their way down through the Earth's atmosphere to various extents. The secondary cosmic rays of most interest here are the cosmic neutrons. The cosmic neutrons induce an array of fission and activation reactions in both the Earth's atmosphere and in the Earth's subsurface. For more information on the fission process itself, refer to Section 1.6.

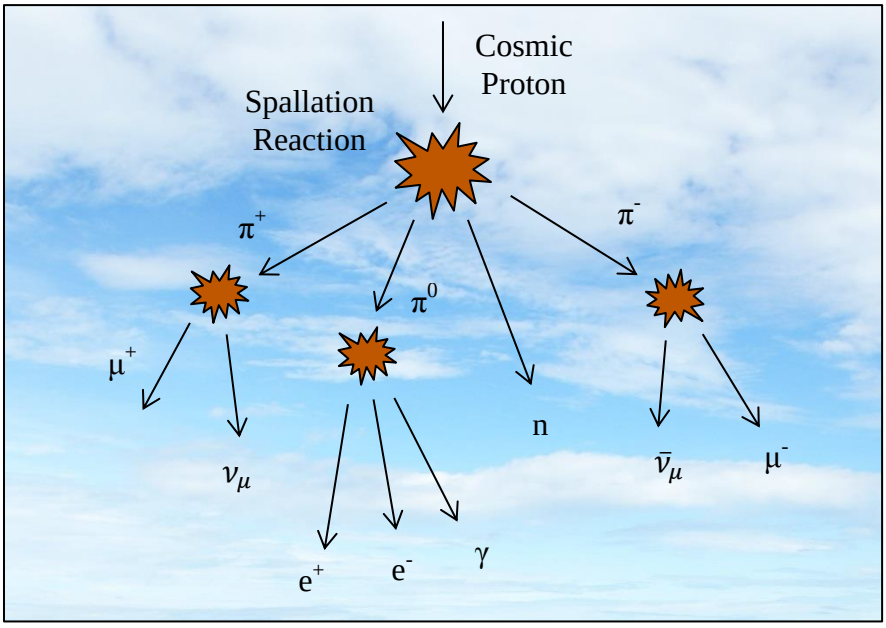

Figure 3.1: Production of secondary cosmic rays in the Earth's atmosphere.

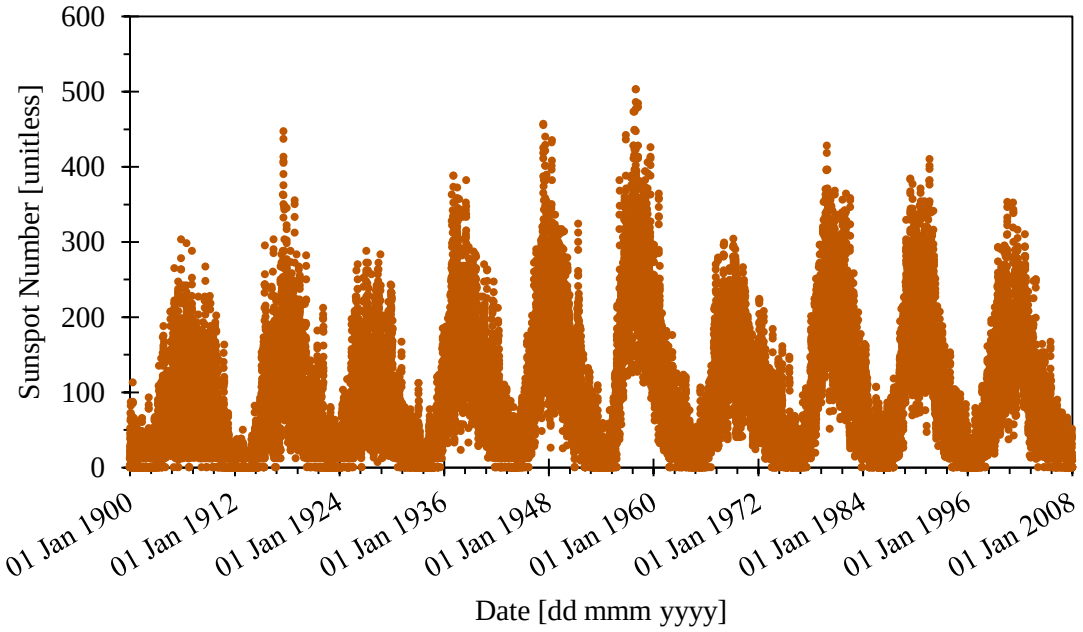

Figure 3.2: The solar cycle over the period 1 Jan 1900 through 1 Jan 2008 [127, 129].

The factors of most importance in establishing CTBT-relevant radionuclide background activity concentrations resulting from cosmic neutron-induced fission of thorium, uranium, and plutonium are (1) the atom concentrations, (2) the cosmic neutron flux profile, (3) the incident neutron fission cross-sections, and (4) the incident neutron fission yields associated with each of the CTBT-relevant radionuclides identified in Table 3.1. Uranium, thorium, and plutonium concentrations representative of the Earth's upper crust are discussed above. The primary difference between the method used to support the CTBT-relevant radionuclide background activity concentration studies documented herein and the methods used to support other studies conducted to date (see the next section for more information on studies conducted to date) is the method

employed here utilizes cosmic neutron flux profiles and incident neutron fission cross-sections generated using the Monte Carlo N-Particle (MCNP) radiation transport code [74, 75, 76, 77] on a study-specific basis. Additional information regarding the development of the study-specific cosmic neutron flux profiles and incident neutron fission cross-sections is presented in Section 3.4.1. The incident neutron fission yields used to generate the CTBT-relevant radionuclide background activity concentration estimates reported herein are one-group fission yields developed from pointwise incident neutron fission yield data and interpolation scheme data extracted from ENDF/B-VII.1 [117].

The factors of most importance in establishing CTBT-relevant radionuclide background activity concentrations resulting from cosmic neutron-induced activation of thorium, uranium, and plutonium are (1) the atom concentrations, (2) the cosmic neutron flux profile, (3) the incident neutron activation cross-sections, and (4) the multiplicities associated with each of the CTBT-relevant radionuclides identified in Table 3.1. Uranium, thorium, and plutonium concentrations representative of the Earth's upper crust and the methods used to develop the study-specific cosmic neutron flux profiles and incident neutron activation cross-sections are discussed above. The CTBT-relevant radionuclide multiplicities used to generate the CTBT-relevant radionuclide background activity concentration estimates reported herein are one-group multiplicities developed from pointwise incident neutron activation reaction data and interpolation scheme data extracted from ENDF/B-VII.1 [117].For more information on the activation process itself, refer to Section 1.6.

3.3 CTBT-Relevant Radionuclide Background Activity Concentration Studies Conducted To Date

The CTBT-relevant radionuclide background activity concentration studies documented herein are not the first of their kind. Several studies have been conducted to date, most in the past few years. This section attempts to identify some of the most pertinent studies conducted to date, to summarize the results generated by these studies, and to highlight how the CTBT-relevant radionuclide background activity concentration studies documented herein attempt to improve upon the studies conducted to date.

Some of the earliest CTBT-relevant radionuclide background activity concentration studies were conducted by Hebel [130, 131]. Hebel identified various processes by which the radioactive noble gases most relevant to the CTBT—^{131m}Xe, ^{133m}Xe, ^{133}Xe, and ^{135}Xe—are produced in nature and calculated the activity concentrations resulting from some of the more important processes by which they are generated. The processes considered by Hebel include spontaneous fission of ^{238}U and the cosmic-neutron-induced fission of ^{232}Th, ^{235}U, and ^{238}U. Hebel's theoretical radioxenon background activity concentration calculations were an extension of the work of Fabryka-Martin [132] and relied on a postulated cosmic neutron flux profile and geological composition data, reaction cross-section data, and fission yield data taken from various places in the literature. The ^{133}Xe background activity concentration estimates generated by Hebel at a depth of 1 m in granite and limestone are reproduced in Table 3.6 It should be noted that Hebel's activity concentrations account for the emanation of the radioactive noble gases out of the rock matrix and into the geological

porosity volumes, but diffusion of the radioactive noble gases out of the geological porosity volumes to the atmosphere is not accounted for [130, 131].

Table 3.6: Overview of CTBT-relevant radionuclide background activity concentration studies conducted to date.

Reference	Geology	Depth [m]	^{133}Xe [mBq-m^{-3}]	^{37}Ar [mBq-m^{-3}]	Theoretical Measured	Production Mechanisms
Hebel [130, 131]	Granite	1.0	152.2	-	Theoretical	(1) and (2)
	Sandstone	1.0	1.5	-	Theoretical	(1) and (2)
Riedmann And Purschert [133]	Unspecified 65% Ca Geology	2.1	-	77.9 ± 9.0	Measured	(3)
	Unspecified 65% Ca Geology	4.1	-	59.9 ± 13.6	Measured	(3)
Lowrey [134]	Hi-Ca Granite	1.0	2.83	243.67	Theoretical	(1), (2), (3) and (4)
	Sandstone	1.0	0.361	64.02	Theoretical	(1), (2), (3) and (4)
Johnson and Johnson *et al.* [135, 136]	Carbonate	1.0	1.98	4,012	Theoretical	(1), (3), and (5)
	Igneous	1.0	0.561	174.5	Theoretical	(1), (3), and (5)

Production mechanisms considered: (1) spontaneous fission of ^{238}U; (2) cosmic-neutron-induced fission of ^{232}Th, ^{235}U, and ^{238}U; (3) cosmic-neutron-induced activation of ^{40}Ca via the ^{40}Ca(n,α)^{37}Ar reaction; (4) cosmic-μ-induced activation of K via the following reactions: ^{39}K(μ,2n)^{37}Ar, ^{40}K(μ,3n)^{37}Ar, and ^{41}K(μ,4n)^{37}Ar; and (5) cosmic-neutron-induced activation of ^{39}K via the ^{39}K(n,2n+p)^{37}Ar reaction.

Additional radioactive noble gas background activity concentration studies were conducted by Riedmann and Purtschert [133]. While Hebel focused on studying the radioxenon activity concentrations resulting from various natural processes, Riedmann and Purtschert focused on the ^{37}Ar activity concentrations resulting from cosmic neutron-induced activation of calcium-40. In their work, Riedmann and Purtschert developed theoretical ^{37}Ar activity concentration profiles for a number of sampling locations and geologies. They also measured the ^{37}Ar activity concentrations at several of the same locations and geologies and found that their measurements were in close agreement with their theoretical activity concentration profiles [133]. The measured ^{37}Ar activity concentrations reported by Riedmann and Purtschert for a geology high in Ca are presented in Table 3.6.

More recently, Lowrey [134] studied radioxenon background activity concentrations resulting from spontaneous fission and cosmic neutron-induced reactions and radioargon background activity concentrations resulting cosmic neutron- and cosmic muon-induced reactions as part of a larger study investigating the subsurface transport of CTBT-relevant radioactive noble gases. As was the case with the studies conducted by Hebel [130, 131] and Riedmann and Purtschert [133], Lowrey's CTBT-relevant radioactive noble gas background activity concentration calculations relied on geological composition data, cosmic neutron flux profiles, reaction cross-section data, fission yield data, and radioactive decay constants taken from the literature. The ^{133}Xe and ^{37}Ar background activity concentrations reported by Lowrey at a depth of 1 m in a hi-Ca granite as well as a sandstone are presented in Table 3.6.

The most detailed radioactive noble gas background concentration studies conducted to date were carried out by Johnson [135] and Johnson *et al.* [136]. The studies conducted by Johnson [135] and Johnson *et al.* [136] used a Monte Carlo N-Particle (MCNP) radiation transport code [74, 75, 76, 77] model to generate cosmic neutron flux profiles specific to several different points in the solar cycle, several different locations, and several different geologies. The remainder of the inputs to the calculations of Johnson and Johnson *et al.* were taken from the literature. The ^{133}Xe and ^{37}Ar background activity concentrations reported by Johnson *et al.* at a depth of 1 m in carbonate rock and limestone are presented in Table 3.6.

A review of the radioactive noble gas background activity concentrations reproduced in Table 3.6 reveals that the ^{133}Xe and ^{37}Ar background activity concentrations resulting from natural processes in different locations and geologies may span several orders of magnitude. Furthermore, given that the detection limits associated with the CTBT ^{133}Xe and ^{37}Ar field detection systems [137, 138] are about 1.0 and 20 mBq-m^{-3}, respectively [139], in some cases the radioxenon and radioargon activity concentrations resulting from natural processes may be high enough to be detected during a CTBT On-Site Inspection. Table 3.6 also reveals that while the various studies conducted to date have produced results that are in good general agreement with one another, in some cases there are order-of-magnitude differences between predictions, even within a given geology.

The primary difference between the CTBT-relevant radionuclide background activity concentration studies documented herein and the CTBT-relevant radionuclide

background activity concentration studies conducted by Hebel [130, 131], Riedmann and Purtschert [133], Lowrey [134], Johnson [135], and Johnson *et al.* [136] is the studies documented here utilize study-specific, high-fidelity cosmic neutron flux profiles and incident neutron fission and activation cross-section data generated using Monte Carlo N-Particle (MCNP) radiation transport code [74, 75, 76, 77] models created by an application referred to herein as the Terrestrial Xenon and Argon Simulator (TeXAS) application.

3.4 Evaluation of CTBT-Relevant Radionuclide Background Activity Concentrations resulting from Natural Processes

This section describes the methods used to calculate the CTBT-relevant radionuclide background activity concentrations resulting from spontaneous fission, cosmic neutron-induced fission, and cosmic neutron-induced activation. The CTBT-relevant radionuclide background activity concentrations resulting from spontaneous fission, cosmic neutron-induced fission, and cosmic neutron-induced activation are all evaluated using an application referred to herein as the TeXAS application. The most important aspects of the TeXAS application are described in Section 3.4.1; a more complete description of the TeXAS application is presented in Appendix E.

3.4.1 The TeXAS Application

In this dissertation, CTBT-relevant radionuclide background activity concentrations resulting from spontaneous fission, cosmic neutron-induced fission, and

cosmic neutron-induced activation are evaluated using the TeXAS application. The TeXAS application is a set of MATLAB [140] code modules capable of generating of high-fidelity, site-specific background activity concentration estimates for 100 radioactive particulates and noble gases identified as relevant to the verification regime of the CTBT [116]. Some of the most important aspects of the TeXAS application are summarized here; a more complete description of the TeXAS application is presented in Appendix E.

Note first that the CTBT-relevant radionuclide background activity concentration estimates generated by the TeXAS application should be viewed as nominal upper limits; they account for production via three natural processes—(1) spontaneous fission, (2) cosmic neutron-induced fission, and (3) cosmic neutron-induced activation—and for loses via radioactive decay. It is important to note that the TeXAS application does not make any attempt to account for the physical movement or loss of radioactive particulates or noble gases resulting from transport processes. Also note that the so-called "cosmic neutrons" are not, strictly speaking, of cosmic origin, but are produced from primary cosmic rays as described in Section 3.2.2 [128].

The TeXAS application supports the generation of CTBT-relevant radioactive particulate and noble gas background activity concentration estimates by: (1) automating and streamlining the process of developing high-fidelity material composition and temperature data, (2) incorporating the data into Monte Carlo N-Particle (MCNP) radiation transport code [74, 75, 76, 77] models, (3) collecting and processing the best-available nuclear data required to support the MCNP models, and (4) post-processing the

outputs generated by the MCNP models and evaluating the radioactive particulate and noble gas background activity concentration estimates. An example of the general form of the MCNP models generated by the TeXAS application is presented in Figure 3.3. Additionally, the basic equation the TeXAS application uses to generate CTBT-relevant radionuclide background activity concentration estimates is as follows (this equation is derived in Section E.4 of Appendix E):

$$A_{CTBT_i} = \sum_{j=1}^{n_{SFP}} N_{SFP_j} \cdot \lambda_{SFP_j} \cdot \beta_{SF,SFP_j} \cdot \chi_{CTBT_i,SFP_j} \cdots$$
$$+ \sum_{k=1}^{n_{FT}} \sum_{E=1}^{n_E} N_{FT_k} \cdot \sigma_{Fiss,FT_k,E} \cdot \Phi_E(t) \cdot \chi_{CTBT_i} \cdots \quad 3.4.1.1$$
$$+ \sum_{l=1}^{n_{AT}} \sum_{E=1}^{n_E} N_{AT_l} \cdot \sigma_{Act,AT_l,E} \cdot \Phi_E \cdot m_{CTBT_i,AT_l}.$$

Where: A_{CTBT_i} is the nominal upper limit of the activity concentration associated with CTBT relevant radionuclide $CTBT_i$,

N_{SFP_j} is the parent radionuclide SFP_j number density,

β_{SF,SFP_j} is the spontaneous fission branching ratio associated with parent radionuclide SFP_j,

χ_{CTBT_i,SFP_j} is the CTBT-relevant radionuclide $CTBT_i$ yield resulting from the spontaneous fission of parent radionuclide SFP_j,

N_{FT_k} is the fissionable target FT_k number density,

$\sigma_{Fiss,FT_k,E}$ is the neutron-induced fission cross-section associated with fissionable target FT_k and energy bin E,

$\Phi_E(t)$ is the neutron-flux associated with energy bin E,

χ_{CTBT_i} is the CTBT-relevant radionuclide $CTBT_i$ yield resulting from neutron-induced fissions of fissionable target FT_k,

N_{AT_l} is the activation target AT_l number density,

$\sigma_{Act,AT_l,E}$ is the neutron-induced activation cross-section associated with activation target AT_l and energy bin E, and

m_{CTBT_i,AT_l} is the multiplicity by which CTBT-relevant radionuclide $CTBT_i$ is produced via neutron induced activation of activation target AT_l

Perhaps the most important thing about the TeXAS application is it was designed to be easy to use. Users of the TeXAS application need to have working MATLAB, MCNP, and NJOY 2012 nuclear data processing system [141] installations, but they do not need have any experience working with any of the aforementioned codes. The TeXAS application was created to make it possible for anyone to develop high-fidelity, site-specific CTBT-relevant radioactive particulate and noble gas background activity concentration estimates by handling all the details associated with the material data processing, the development of the MCNP models, and the nuclear data processing so that TeXAS application users are not encumbered with the details of these processes,

but rather are left free to focus on the basic inputs associated with the studies they wish to conduct. Again, for more information on the TeXAS application, refer to Appendix E.

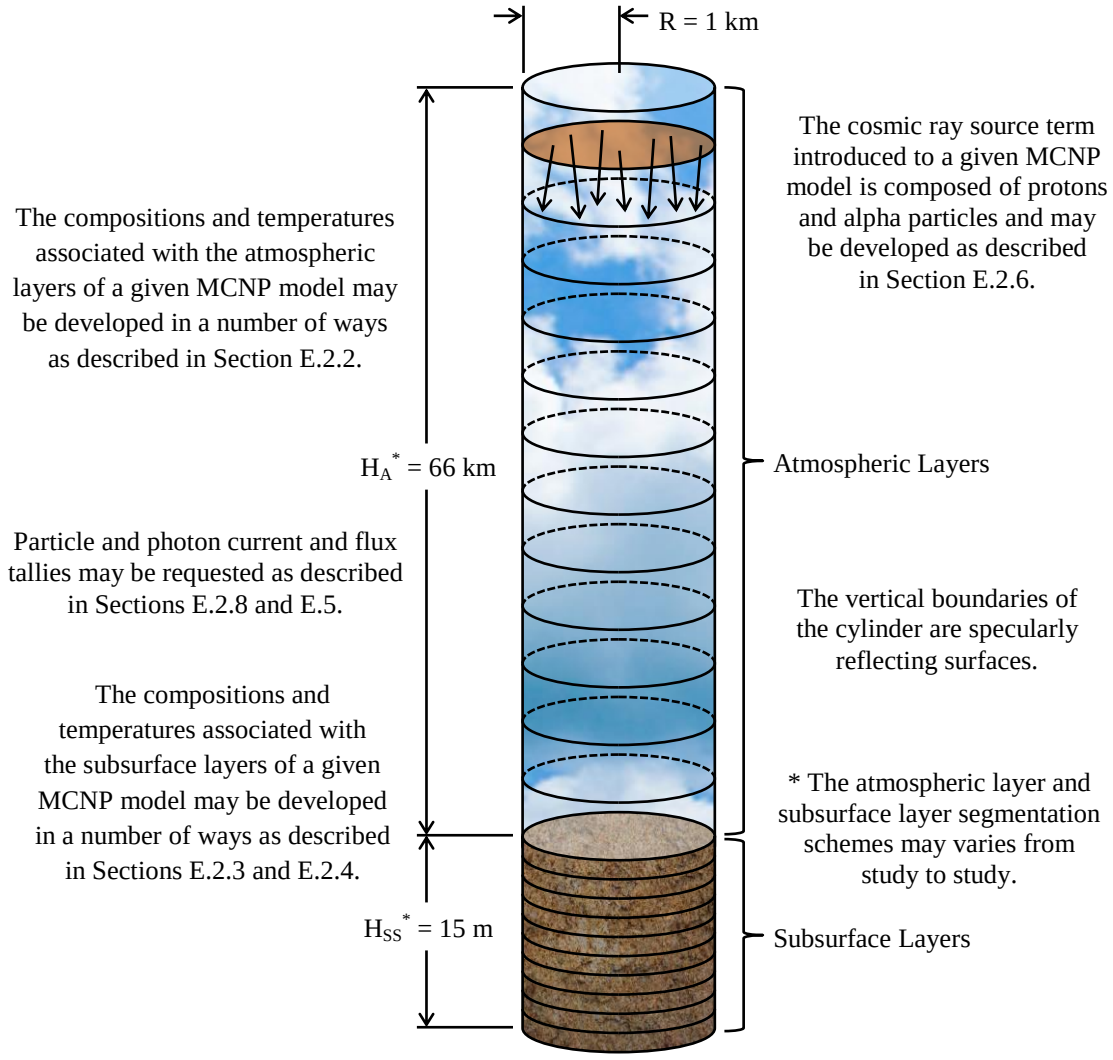

Figure 3.3: The geometric configuration of the MCNP models created by the TeXAS application.

3.5 CTBT-Relevant Radionuclide Background Activity Concentration Studies

This section presents several studies conducted to evaluate the background activity concentrations associated with 100 CTBT-relevant radionuclides resulting from natural processes in the Earth's atmosphere, in several different geologies, and in seawater. The atmospheric studies, documented in Section 3.5.1, describe the CTBT-relevant radioactive noble gas background activity concentrations resulting from spontaneous fission, cosmic neutron-induced fission, and cosmic neutron-induced activation at geometric heights of 50,000 m, 15,000 m, and 1 m in the Earth's atmosphere. The cosmic neutron flux profiles and the atmospheric constituents most responsible for attenuating the cosmic neutron flux at each of the aforementioned geometric heights are also discussed.

The geological studies, documented in Section 3.5.2, describe the CTBT-relevant radioactive particulate and noble gas background activity concentrations resulting from spontaneous fission, cosmic neutron-induced fission, and cosmic neutron-induced activation as a function of depth in three different igneous geologies and three different sedimentary geologies. The igneous geologies evaluated are a granite geology, a basalt geology, and a granodiorite geology. The sedimentary geologies considered are a shale geology, a sandstone geology, and a limestone geology. These geologies were selected based on their prevalence in the Earth's upper crust. As with the atmospheric studies, the cosmic neutron flux profiles and the geological constituents most responsible for

attenuating the cosmic neutron flux in each of the aforementioned geologies are also discussed.

The seawater studies, documented in Section 3.5.3, describe the CTBT-relevant radionuclide background activity concentrations resulting from spontaneous fission, cosmic neutron-induced fission, and cosmic neutron-induced activation as a function of depth in seawater. The primary focus of the seawater studies is on the radioactive noble gas background activity concentrations of most interest to the verification regime of the CTBT—^{37}Ar, ^{131m}Xe, ^{133m}Xe, ^{133}Xe, and ^{135}Xe.

3.5.1 Atmospheric Studies

The objectives of the atmospheric studies documented in this section were (1) to evaluate the cosmic neutron flux profile as a function of geometric height in the Earth's atmosphere, (2) to identify the atmospheric constituents that are most important in terms of attenuating the cosmic neutron flux at different geometric heights, and (3) to evaluate the CTBT-relevant radioactive noble gas background activity concentrations associated with several layers of the Earth's atmosphere. A single Monte Carlo N-Particle (MNCP) model developed by the TeXAS application (see Appendix E) was used to evaluate and identify the aforementioned cosmic neutron flux profiles, the neutron-flux-attenuating atmospheric constituents, and the CTBT-relevant radioactive noble gas background activity concentrations in seven different one-meter-thick atmospheric layers centered at seven different geometric heights. The first two atmospheric layers were located at geometric heights of 50,000 m and 15,000 m in two constant-temperature atmospheric

layers known the stratopause and the tropopause, respectively. The other atmospheric layers were centered at 1, 2, 3, 4, and 5 m above the Earth's surface.

3.5.1.1 Atmospheric Study Inputs

The TeXAS application (see Appendix E) was used to develop the MCNP model used to support the atmospheric studies documented here. While it would have been possible to develop temperature, pressure, and number density profiles describing the dry portion of the Earth's atmosphere manually and then supply them as inputs to the TeXAS application, in this case it was easier to allow the TeXAS application to develop atmospheric temperature, pressure, and number density profiles for the dry portion of the Earth's atmosphere automatically as described in Section E.2.2 of Appendix E. The atmospheric temperature and number density profiles developed specifically to support the studies documented here are presented below in Figure 3.4.

The atmospheric segmentation scheme used to develop the atmospheric temperature and number density profiles presented in Figure 3.4 consists of 79 atmospheric layers, most of which are 1 km thick with upper and lower boundaries placed at even 1 km intervals. That said, seven 1 m thick layers were centered at geometric heights of 50,000 km, 15,000 km, 69 m, 68 m, 67 m, 66 m, and 65 m to support evaluating tallies at those geometric heights. Note that the Earth's surface is assumed to be at a geometric height of 64 m above sea level, so the atmospheric layers centered at 69, 68, 67, 66, and 65 m are effectively, 5 m, 4 m, 3 m, 2 m, and 1 m above sea level, respectively.

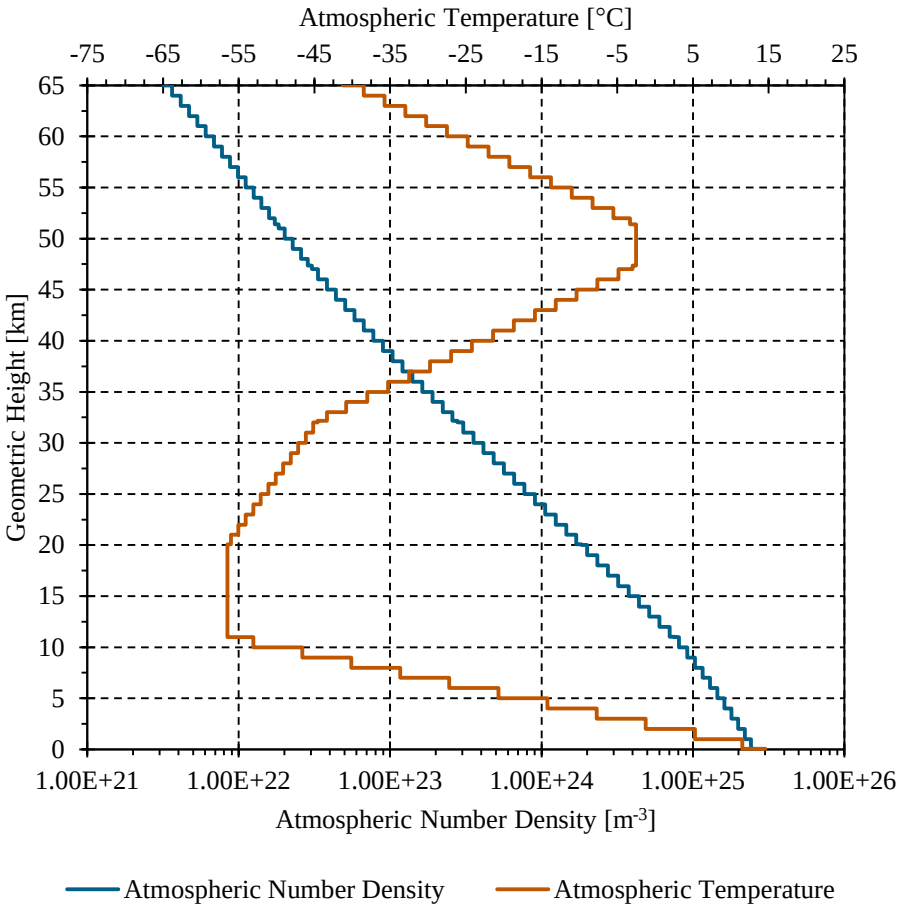

Figure 3.4: Atmospheric temperature and number density profiles developed to support the atmospheric studies.

The composition of the dry portion of the Earth's atmosphere was set equal to the atmospheric composition defined by the *U.S. Standard Atmosphere, 1976* [142] (see Table E.3). Additionally, H_2O resulting from water vapor was incorporated into the atmospheric layers having geometric heights less than about 15,960 m. The water vapor profile, shown in Figures 3.5 and 3.6, was developed using the TeXAS application water vapor profile development tool described in Section E.2.2.1 of

Appendix E. Table 3.7 presents the volume fractions associated with each of the atmospheric constituents present in (1) a generic dry atmospheric layer and (2) the wet atmospheric layer centered at a geometric height of 65 m (1 m above the Earth's surface). The atmospheric compositions presented in Table 3.7 are expanded to the isotopic forms used in the MCNP input decks supporting the atmospheric studies documented here in Appendix F.

Several subsurface layers simulating a granite geology were incorporated into the MCNP model supporting the atmospheric studies documented here to account for the effects of neutrons scattering from the Earth's subsurface back up into the atmospheric layers centered at geometric heights just above the Earth's surface. A granite geology was chosen because granite is one of the most common geology in the Earth's upper crust [143]. More information regarding the density, porosity, and composition of the granite geology is presented in Section 3.5.2.1.

The subsurface temperature profile incorporated into the MCNP model supporting the atmospheric studies documented here was developed using the subsurface temperature profile development tool described in Section E.2.3.1 of Appendix E. Note that the subsurface temperature profile, which is shown in Figures 3.11 and 3.12, was developed specifically for a date of 1 July. For more information regarding the development of the subsurface temperature profile described here, refer to Sections 3.5.2.1 and E.2.3.1.

In order to incorporate a cosmic-ray source term representative of the average cosmic-ray flux incident upon the Earth's upper atmosphere into the MCNP model

generated by the TeXAS application, the date assigned to the MCNP source definition (SDEF) card was 1 Nov 2003. This date was selected (1) because it is an example of a recent date on which the sunspot number was approximately equal to the average sunspot number associated with the period 1 January 1990 through 31 December 2015 [129], and (2) because it is a date for which actual solar modulation data (as opposed to projected solar modulation data) is available in MCNP [74, 75, 76, 77].

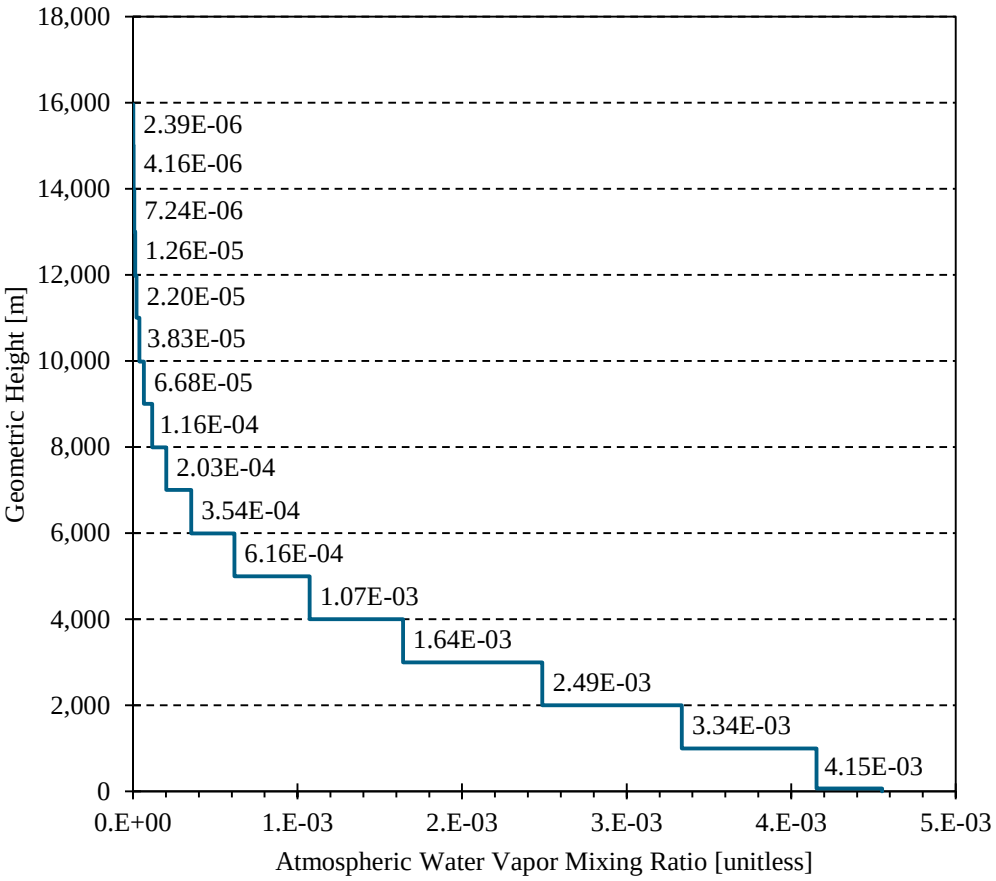

Figure 3.5: Atmospheric water vapor mixing ratio profile (geometric heights between 64 m and 18,000 m).

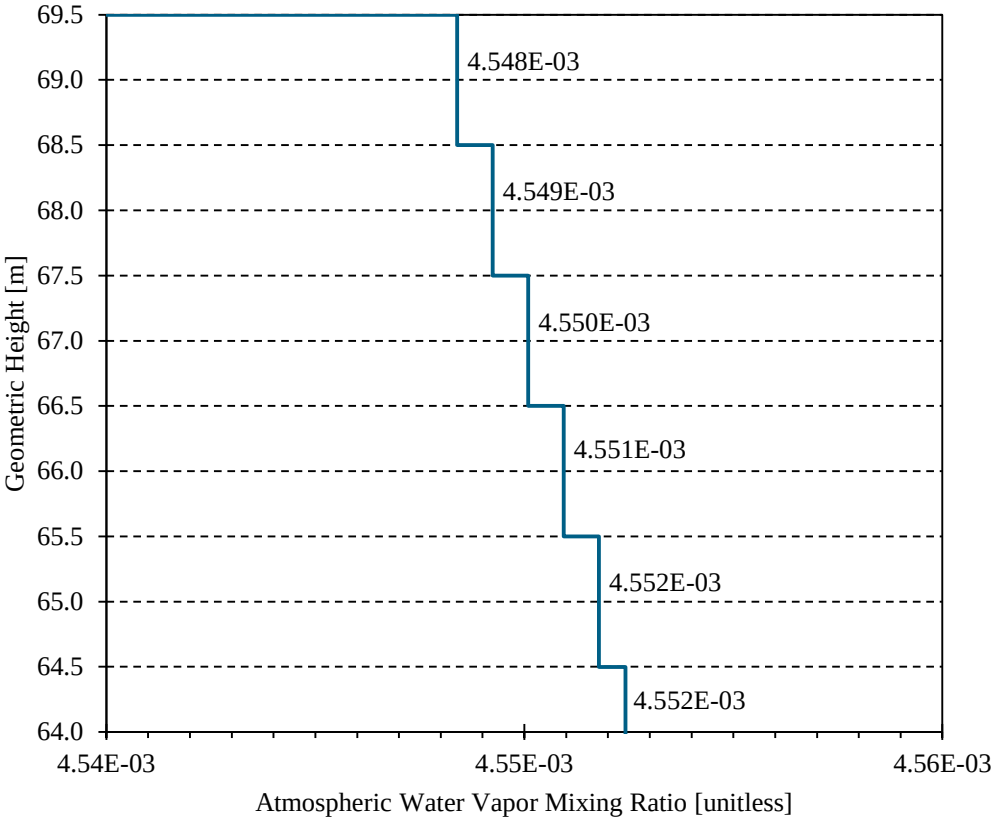

Figure 3.6: Atmospheric water vapor mixing ratio profile (geometric heights between 64 m and 69.5 m).

Table 3.7: The composition of the Earth's atmosphere.

Atmospheric Constituent	Volume Fraction [unitless]	
	Dry Atmosphere	Wet Atmosphere (at H= 65 m)
N_2	7.808×10^{-1}	7.752×10^{-1}
O_2	2.095×10^{-1}	2.080×10^{-1}
Ar	9.340×10^{-3}	9.272×10^{-3}
H_2O	N/A	7.232×10^{-3}
CO_2	3.220×10^{-4}	3.197×10^{-4}
Ne	1.818×10^{-5}	1.805×10^{-5}
He	5.240×10^{-6}	5.202×10^{-6}
CH_4	1.500×10^{-6}	1.489×10^{-6}
Kr	1.140×10^{-6}	1.132×10^{-6}
H2	5.000×10^{-7}	4.964×10^{-7}
N_2O	2.700×10^{-7}	2.680×10^{-7}
CO	1.900×10^{-7}	1.886×10^{-7}
Xe	8.700×10^{-8}	8.637×10^{-8}
O_3	4.000×10^{-8}	3.971×10^{-8}
NH_3	4.000×10^{-9}	3.971×10^{-9}
NO_2	1.000×10^{-9}	9.928×10^{-10}
SO_2	1.000×10^{-9}	9.928×10^{-10}
NO	5.000×10^{-10}	4.964×10^{-10}
H_2S	5.000×10^{-11}	4.964×10^{-11}

3.5.1.2 Atmospheric Neutron Flux Profiles

The outputs generated by the Monte Carlo N-Particle (MCNP) model created by the TeXAS application using the inputs described in Section 3.5.1.1 were post-processed by the TeXAS application. The cosmic neutron flux profiles specific to the atmospheric layers centered at 50,000 m, 15,000 m, and 65 m are presented in Figure 3.7. The cosmic neutron flux profiles shown in Figure 3.7 are 63-energy group neutron flux profiles. The 63 energy group structure is equivalent to the CINDER '90 63 energy group structure [144]. The 63-energy group cosmic neutron flux profiles shown in Figure 3.7 were also collapsed to generate one-group fluxes. The one group fluxes at 50,000 m, 15,000 m, and 65 m were found to be $9.43 \pm 0.02 \times 10^{-1}$ cm^{-2}-s^{-1}, 5.41 ± 0.01 cm^{-2}-s^{-1}, and $2.76 \pm 0.04 \times 10^{-2}$ cm^{-2}-s^{-1}, respectively. Note that the reported one-group flux uncertainties are the statistical variances reported by MCNP and that all are on the order of 1.5 % of their nominal values or less. The uncertainties associated with the cosmic neutron fluxes are quite small given that the tallies were evaluated in MCNP cells located 15,000 m, 50,000 m, and roughly 65,000 m away from the surface where the cosmic-ray source term was introduced to the MCNP model.

The general trend in the 63-energy group cosmic neutron flux profiles shown in Figure 3.7 and the one-group cosmic neutron fluxes reported above indicate that the cosmic neutron flux is relatively small in the upper portions of the Earth's atmosphere, that it then initially increases with decreasing geometric height, peaks somewhere around 15,000 m, and then ultimately decreases as geometric height continues to decrease. These trends in the cosmic neutron flux profile are as expected.

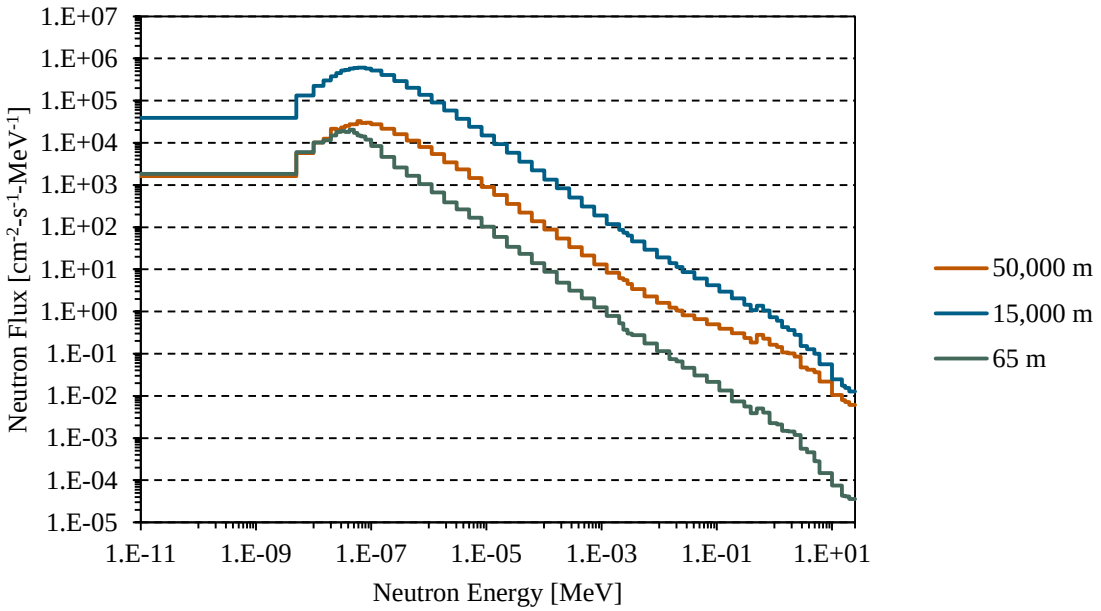

Figure 3.7: Cosmic neutron flux profiles applicable to atmospheric layers centered at geometric heights of 50,000 m, 15,000 m, and 65 m (1 m above Earth's surface).

3.5.1.3 Atmospheric Neutron Flux Attenuation Studies

In addition to providing information regarding the cosmic neutron fluxes associated with the atmospheric layers of interest, the Monte Carlo N-Particle (MCNP) model generated by the TeXAS application also provides valuable information regarding the constituents that are most important in attenuating the cosmic neutron flux as it approaches the Earth's surface. The TeXAS application provides this information by requesting that MCNP evaluate neutron removal cross-sections for every isotopic constituent in every MCNP cell in which tallies are evaluated. For the atmospheric studies documented here neutron removal cross-sections were evaluated for each of the isotopic constituents associated with each of the atmospheric layers of interest (for the

full atmospheric isotopic compositions, refer to Table F.1 in Appendix F). The total neutron removal cross-section associated with each of the atmospheric layers of interest was also evaluated. The relative importance of each isotopic constituent in each of the atmospheric layers of interest was then evaluated as a fraction of the total neutron removal cross section associated with each atmospheric layer. Isotopic constituents for which this fraction is larger are deemed to be more important from a cosmic neutron flux attenuation perspective and isotopic constituents for which this fraction is smaller are deemed to be less important from a cosmic neutron flux attenuation perspective.

The results of the atmospheric neutron flux attenuation studies are summarized in Figure 3.8, which illustrates the fraction of the total neutron removal cross-section attributable to each of the atmospheric constituents at geometric heights of 50,000 m, 15,000 m, and 65 m (1 m above the Earth's surface), respectively. Note that ^{14}N accounts for 92 % or more of the total neutron removal cross-section at all three of the geometric heights considered. The remainder of the total neutron removal cross-section is attributable almost entirely to ^{16}O at all three geometric heights. These results appear to be reasonable given that the ^{14}N and ^{16}O number fractions in all three atmospheric layers are roughly 77 % and 21 %, respectively.

It is also interesting to note that ^{14}N appears to take on an increasingly important role in attenuating the cosmic neutron flux at lower geometric heights. It appears that ^{14}N becomes more important in this role at lower geometric heights because the cosmic neutron flux becomes more thermalized at lower geometric heights, effectively shifting more of the flux to lower energies where the ^{14}N neutron removal cross-section is larger.

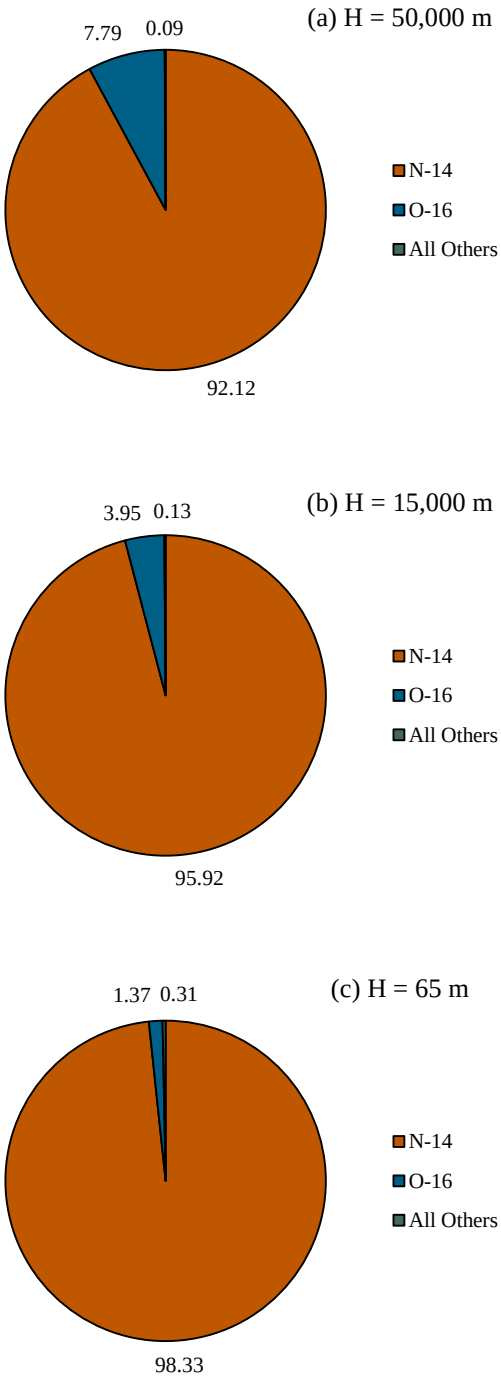

Figure 3.8: Neutron flux attenuation by constituent in three atmospheric layers centered at (a) 50,000 m, (b) 15,000 m, and (c) 65 m (1 m above the Earth's surface).

3.5.1.4 Atmospheric CTBT-Relevant Radioactive Noble Gas Background Activity Concentration Estimates

The outputs generated by the Monte Carlo N-Particle (MCNP) model created by the TeXAS application in support of the atmospheric studies also provide an abundance of information regarding CTBT-relevant radioactive noble gas background activity concentrations produced via neutron activation in each of the atmospheric layers of interest here. The CTBT-relevant radioactive noble gases of most interest here are ^{37}Ar, ^{131m}Xe, ^{133}Xe, and ^{135}Xe. In the Earth's atmosphere, these radioactive noble gases are produced via neutron activation as described in Section 3.2.2. The TeXAS application evaluates the background activity concentrations resulting from cosmic neutron induced reactions as described in Section E.4 of Appendix E.

Figure 3.9 shows the CTBT-relevant radioactive noble gas background activity concentrations associated with each of the atmospheric layers of interest here. As illustrated by Figure 3.9, all five of the radioactive noble gas background activity concentrations are lowest in the atmospheric layer centered at a geometric height of 50,000 m, all five concentrations increase and are highest in the atmospheric layer centered at 15,000 m, and then all five concentrations decrease from their 15,000 m concentrations to concentrations that are still an order of magnitude to two orders of magnitude above their respective 50,000 m concentrations. These changes seem reasonable given the relationships between the cosmic neutron flux profiles at the given geometric heights and the general increase in target atom concentration at lower heights.

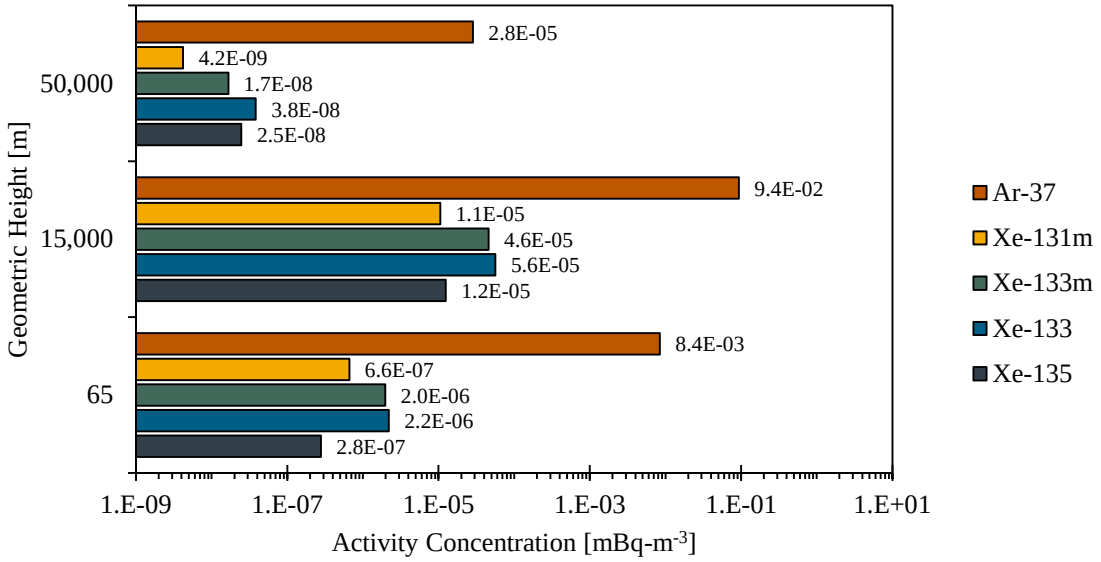

Figure 3.9: CTBT-relevant radioactive noble gas background activity concentrations at various geometric heights in the Earth's atmosphere.

The ^{131m}Xe, ^{133m}Xe, ^{133}Xe, and ^{135}Xe background activity concentrations are all several orders of magnitude below their respective CTBT monitoring station field and laboratory detection limits (the detection limits are reported in Table 1.2) in each of the atmospheric layers of interest here. The ^{37}Ar background activity concentrations are also several orders of magnitude below the detection limit associated with the ^{37}Ar field measurement system [137, 139]. That said, the ^{37}Ar background activity concentration 1 m above the Earth's surface is within an order of magnitude of the detection limit associated with the ^{37}Ar laboratory measurement system. These results indicate that it should be nearly impossible to detect CTBT-relevant radioxenon gases resulting from natural processes in the Earth's atmosphere, but it might be possible to detect ^{37}Ar resulting from natural process in the Earth's atmosphere.

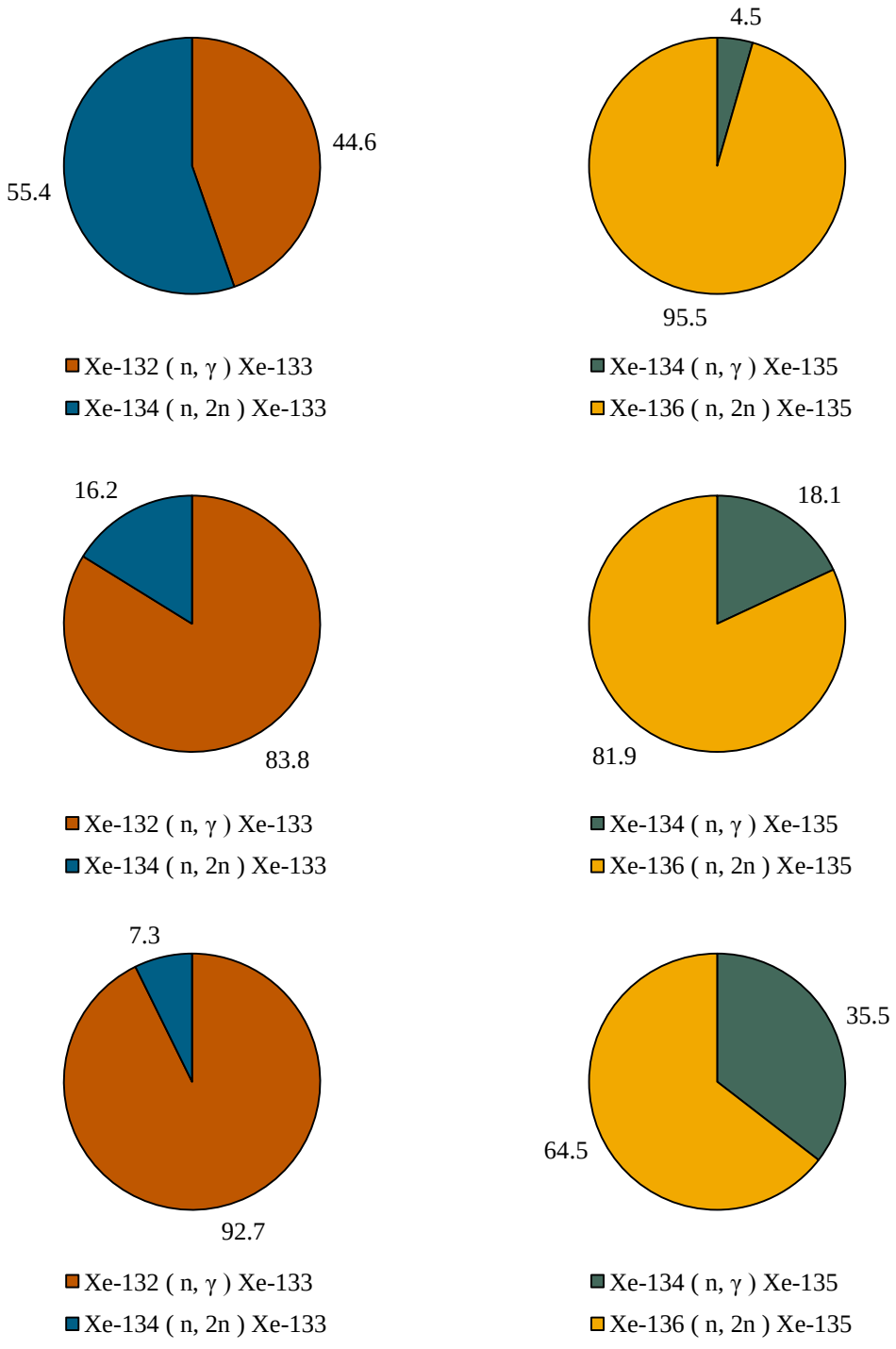

Figure 3.10: Predominant ^{133}Xe and ^{135}Xe production mechanisms at (a) 50,000 m, (b) 15,000 m, and (c) 65 m (1 m above the Earth's surface) in the Earth's atmosphere.

In addition to providing the radioactive noble gas background activity concentrations themselves, the TeXAS application also provides valuable information regarding the processes most responsible for generating the radioactive noble gas background activity concentrations. This is illustrated in Figure 3.10, which shows how the predominant ^{133}Xe and ^{135}Xe production mechanisms change significantly as a function of geometric height in the Earth's atmosphere. In the Earth's upper atmosphere the cosmic neutron flux profile is relatively hard (see Figure 3.7). This means that there are a relatively large number of high energy neutrons with sufficient energy to induce (n,2n) reactions in ^{134}Xe and ^{136}Xe target atoms high in the Earth's atmosphere. At lower geometric heights the neutron flux profile is thermalized, or softened (again, see Figure 3.7). This means that there are fewer high energy neutrons available to induce (n,2n) reactions at lower geometric heights. As a result, the (n,2n) reactions become less significant contributors to the ^{133}Xe and ^{135}Xe radioactive noble gas background activity concentrations at lower atmospheric heights.

3.5.2 Geological Studies

The objectives of the geological studies documented in this section were (1) to evaluate the cosmic neutron flux profile as a function of depth in several different geologies, (2) to identify the constituents that are most important in terms of attenuating the cosmic neutron flux at different depths in several different geologies, and (3) to evaluate the CTBT-relevant radioactive particulate and noble gas background activity concentrations resulting from natural processes as a function of depth in several different

geologies. The TeXAS application was used to develop six Monte Carlo N-Particle (MNCP) models to evaluate and identify the aforementioned cosmic neutron flux profiles, the neutron-flux-attenuating geological constituents, and the CTBT-relevant radioactive particulate and noble gas background activity concentrations in six geologies representative of the Earth's upper crust. Of the six geologies considered here, three were igneous geologies (granite, basalt, and granodiorite), and three of were sedimentary geologies (shale, limestone, and sandstone). The studies documented here focused on igneous and sedimentary rock geologies because they account for 95 % and 5 %, respectively, of the Earth's upper crust [143]. In fact, granite, basalt, and granodiorite alone account for about 22.9 %, 19.2 %, and 12.2 %, respectively, of the Earth's upper crust [143]. Shale, limestone, and sandstone account for 4.00 %, 0.75 %, and 0.25 %, respectively, of the Earth's upper crust [143].

3.5.2.1 Geological Study Inputs

This section describes the inputs supplied to the TeXAS application in order to develop six Monte Carlo N-Particle (MNCP) models used to evaluate the cosmic neutron flux profiles, the most important cosmic neutron-flux-attenuating geological constituents, and the CTBT-relevant radioactive particulate and noble gas background activity concentrations in six geologies representative of the Earth's upper crust. Again, the six geologies of interest here are a granite geology, a basalt geology, a granodiorite geology, a shale geology, a sandstone geology, and a limestone geology.

For each of the geologies of interest, the TeXAS application had to be given several inputs. First, the TeXAS application had to be given the mass density of each geology. The mass densities associated with each of the geologies of interest are presented in Table 3.8. These mass densities were developed as averages of several geological mass densities reported by Rudd [145]. Second, the TeXAS application had to be given the porosities associated with each of the geologies of interest. The porosities associated with each of the geologies of interest are reported in Table 3.8 alongside their respective mass densities. As with the mass densities, the porosities reported in Table 3.8 are the averages of several porosity values taken from the literature [146].

In addition to the mass densities and the porosities associated with each of the geologies of interest, the TeXAS application also had to be given information regarding the composition of each geology. The compositions assumed in support of the geological studies documented here are presented in Table 3.9. These geological compositions represent averages of several granite, basalt, granodiorite, shale, sandstone, and limestone compositions compiled by Potts, Tindle, and Webb [147].

Table 3.8: Geological mass densities, number densities, and porosities.

Geology	Mass Density [g-cm^{-3}]	Number Density [cm^{-3}]	Porosity [vol %]
Granite	2.63	7.75×10^{22}	1.0
Basalt	2.33	6.65×10^{22}	11.0
Granodiorite	2.64	6.74×10^{22}	9.7
Shale	1.99	7.56×10^{22}	17.4
Sandstone	1.99	7.13×10^{22}	16.4
Limestone	2.48	6.65×10^{22}	7.5

Table 3.9: Granite, basalt, granodiorite, shale, sandstone, and limestone compositions used as inputs to the TeXAS application.

Geological Constituent	Geological Constituent Mass Fraction [unitless] in each of Six Geologies					
	Granite	Basalt	Granodiorite	Shale	Sandstone	Limestone
SiO_2	7.18E-01	4.63E-01	7.00E-01	5.19E-01	7.59E-01	3.40E-02
Al_2O_3	1.43E-01	1.34E-01	1.48E-01	1.33E-01	1.11E-01	8.57E-03
K_2O	4.48E-02	1.08E-02	4.04E-02	3.11E-02	2.34E-02	1.58E-03
Na_2O	3.83E-02	3.09E-02	3.42E-02	1.20E-02	2.68E-03	5.68E-04
CaO	1.64E-02	1.07E-01	2.54E-02	3.29E-02	5.81E-03	5.17E-01
FeO	1.15E-02	7.76E-02	1.83E-02	1.28E-02	1.48E-02	2.19E-03
Fe_2O_3	9.23E-03	3.71E-02	1.05E-02	5.48E-02	3.12E-02	3.56E-03
MgO	6.17E-03	8.92E-02	1.06E-02	2.79E-02	1.18E-02	1.04E-02
H2O	5.77E-03	1.73E-02	5.69E-03	1.28E-01	2.88E-02	8.34E-03
TiO_2	2.80E-03	2.10E-02	4.13E-03	5.87E-03	4.85E-03	5.96E-04
P_2O_5	2.13E-03	5.50E-03	1.45E-03	2.09E-03	1.06E-03	5.30E-04
CO_2	1.42E-03	4.61E-03	9.35E-04	3.93E-02	5.24E-03	4.12E-01
MnO	4.99E-04	1.77E-03	5.89E-04	3.87E-04	6.07E-04	4.67E-04
Th	3.71E-05	5.47E-06	3.48E-05	9.83E-06	1.29E-05	9.65E-07
U	9.62E-06	1.38E-06	3.06E-06	1.53E-05	1.52E-06	1.51E-06
Gd	6.49E-06	6.87E-06	5.74E-06	5.39E-06	6.77E-06	-

In addition to the mass densities, the porosities, and the geological compositions described above, a subsurface temperature profile was developed for each of the geologies of interest. The subsurface temperature profiles developed for the granite, basalt, granodiorite, shale, sandstone, and limestone geologies are presented in Figures 3.11 and 3.12. These subsurface temperature profiles were developed using the subsurface temperature profile development tool described in Section E.2.3.1 of Appendix E. Note that the subsurface temperature profiles were developed specifically

for a date of 1 July. For more information regarding the development of the subsurface temperature profiles described here, refer to Section E.2.3.1 of Appendix E.

The atmospheric layers above the granite, basalt, granodiorite, shale, sandstone, and limestone geologies were defined in the same manner as the atmospheric layers incorporated into the MCNP model used to conduct the atmospheric studies documented in the previous section. Refer to Section 3.5.1.1 for more information.

The date assigned to the MCNP source definition (SDEF) card was set equal to 1 Nov 2003 in order to support incorporating a cosmic-ray source term representative of the average cosmic-ray flux incident upon the Earth's upper atmosphere into the MCNP models supporting the geological studies. This is the same date that was used to support the atmospheric studies documented in Section 3.5.1.

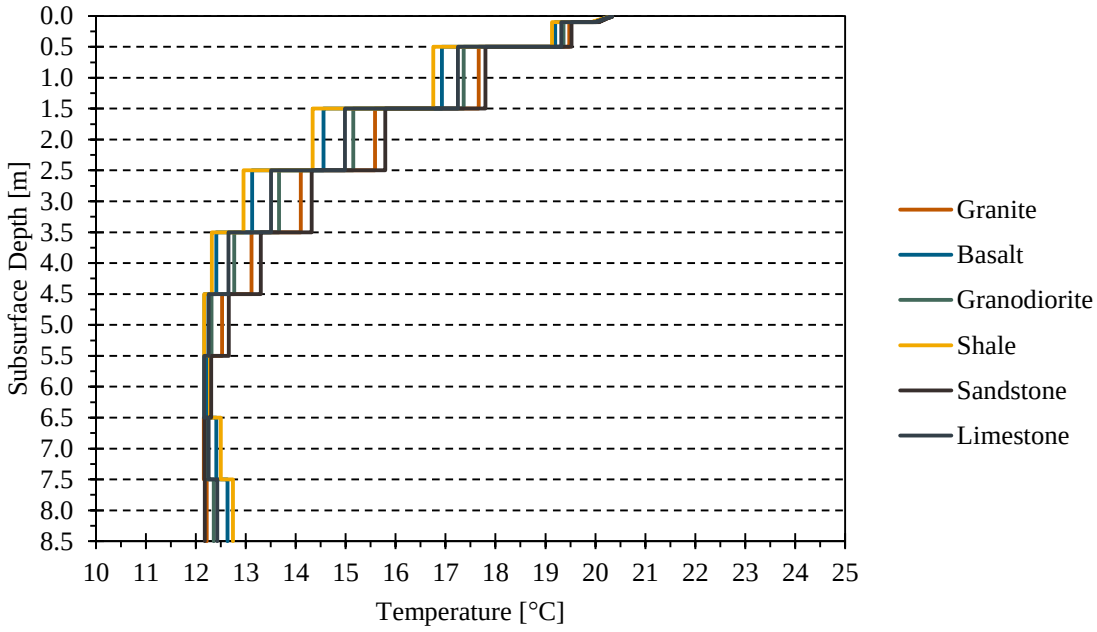

Figure 3.11: Geological subsurface temperature profiles (subsurface depths between 0 and 8.5 m).

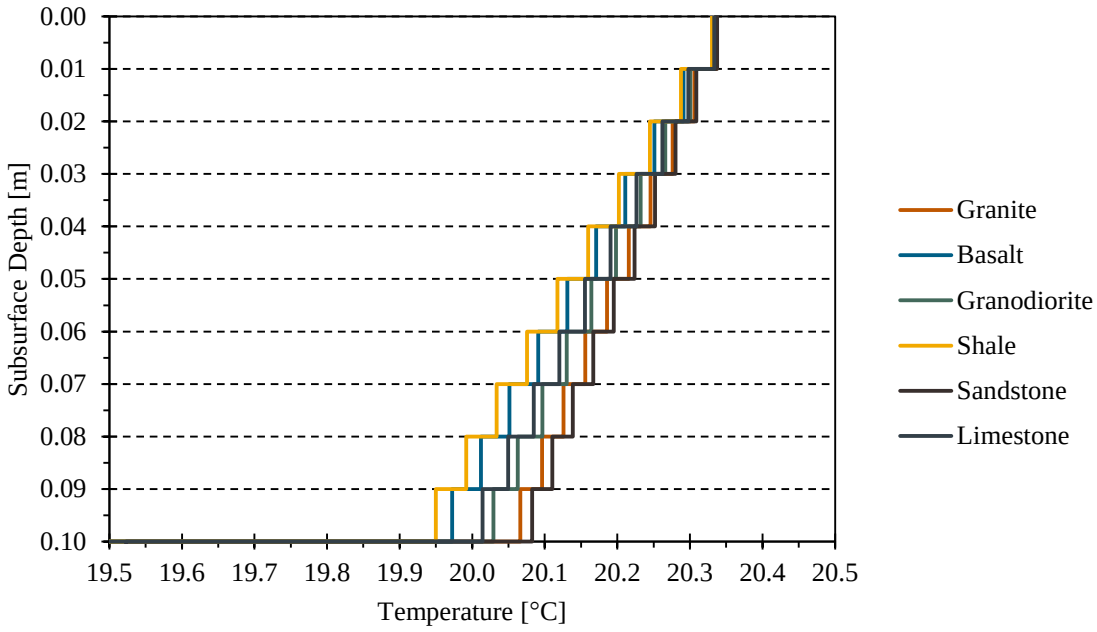

Figure 3.12: Geological subsurface temperature profiles (subsurface depths between 0 and 8.5 m).

3.5.2.2 Geological Cosmic Neutron Flux Profiles

The outputs generated by the Monte Carlo N-Particle (MCNP) models created by the TeXAS application using the inputs described in Section 3.5.2.1 were post-processed by the TeXAS application. The cosmic neutron flux profiles at depths of 1, 2, 3, 4, and 5 m in the granite, basalt, granodiorite, shale, sandstone, and limestone geologies are presented in Figures 3.13 through 3.24, respectively. The cosmic neutron flux profiles shown in Figures 3.13 through 3.24 are 63-energy group neutron flux profiles and the 63-energy group structure is equivalent to the CINDER ‘90 63-energy group structure [144]. Note that two figures are presented for each geology. The first presents the cosmic neutron flux profile at each of the aforementioned subsurface depths in units

of cm^{-2}-s^{-1}-MeV^{-1}. The second figure illustrates the change in the cosmic neutron flux profile at each of the five subsurface depths considered relative to the cosmic neutron flux profile at a subsurface depth of 1 m.

As illustrated by Figures 3.13 through 3.24 the general trend across all six geologies of interest here is a decrease in the cosmic neutron flux profile with increasing subsurface depth. For example, the one-group cosmic neutron flux at a subsurface depth of 1 m in the granite geology is $1.29 \pm 0.02 \times 10^{-2}$ cm^{-2}-s^{-1}; this value is reduced by 77 % to $3.01 \pm 0.09 \times 10^{-3}$ cm^{-2}-s^{-1} as the subsurface depth is increased to 2 m. The one-group neutron flux at a subsurface depth of 3 m in the granite geology is further reduced to $1.17 \pm 0.04 \times 10^{-3}$ cm^{-2}-s^{-1} (a 91 % reduction relative to the one-group neutron flux at a subsurface depth of 1 m). And finally, at a subsurface depth of 5 m in the granite geology the one-group cosmic neutron flux is reduced to less than 5 % of the one-group cosmic neutron flux at 1 m in the granite geology.

Similarly, the one-group cosmic neutron flux at a subsurface depth of 1 m in the shale geology is $4.35 \pm 0.10 \times 10^{-3}$ cm^{-2}-s^{-1}; this value is reduced by 73 % to $1.20 \pm 0.05 \times 10^{-3}$ cm^{-2}-s^{-1} as the subsurface depth is increased to 2 m. The one-group neutron flux at a subsurface depth of 3 m in the shale geology is further reduced to $4.44 \pm 0.22 \times 10^{-4}$ cm^{-2}-s^{-1} (a 90 % reduction relative to the one-group neutron flux at a subsurface depth of 1 m). And finally, at a subsurface depth of 5 m in the granite geology the one-group cosmic neutron flux is reduced to less than 5 % of the one-group cosmic neutron flux at 1 m in the granite geology. These trends in the cosmic neutron flux profiles are as expected.

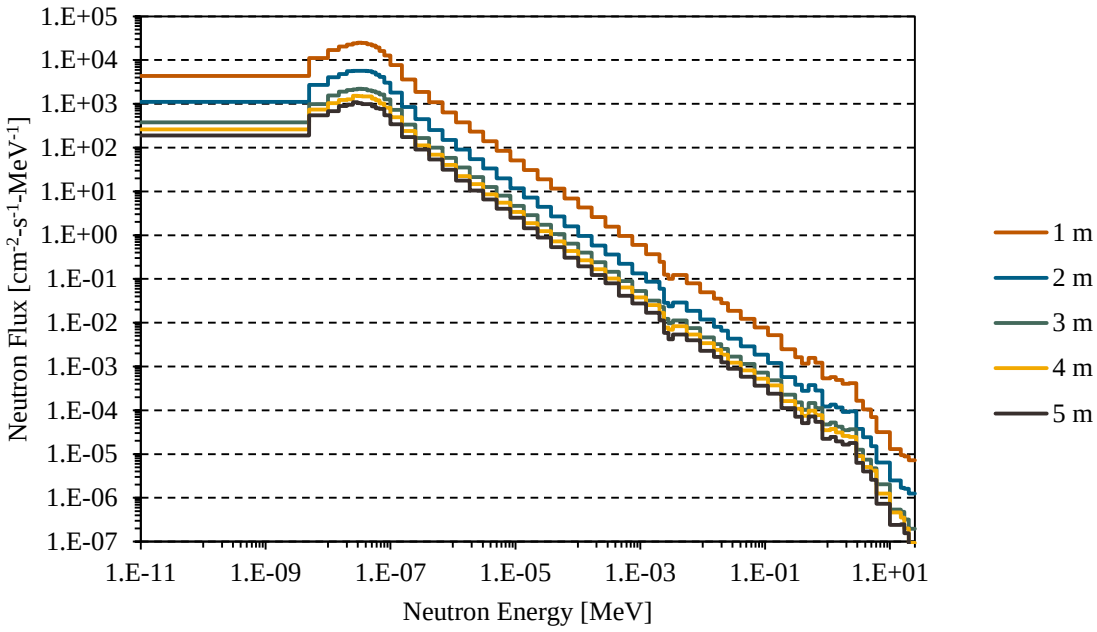

Figure 3.13: 63-energy group neutron flux profiles
at various depths in a granite geology.

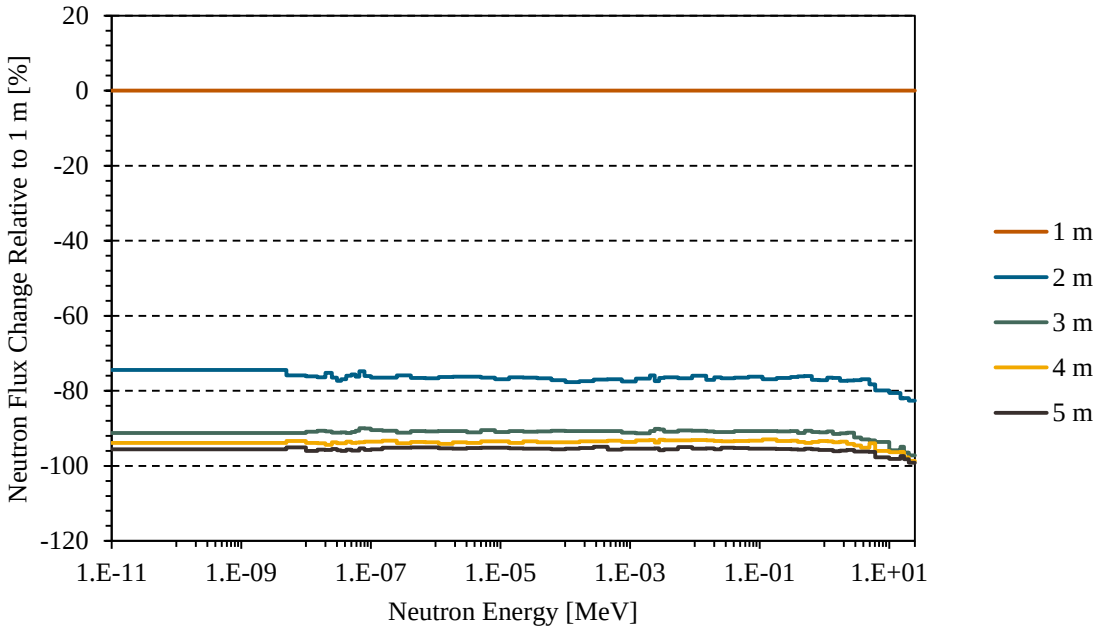

Figure 3.14: 63-energy group neutron flux profiles at various depths
in a granite geology relative to the neutron flux profile at
a subsurface depth of 1 m in the same geology.

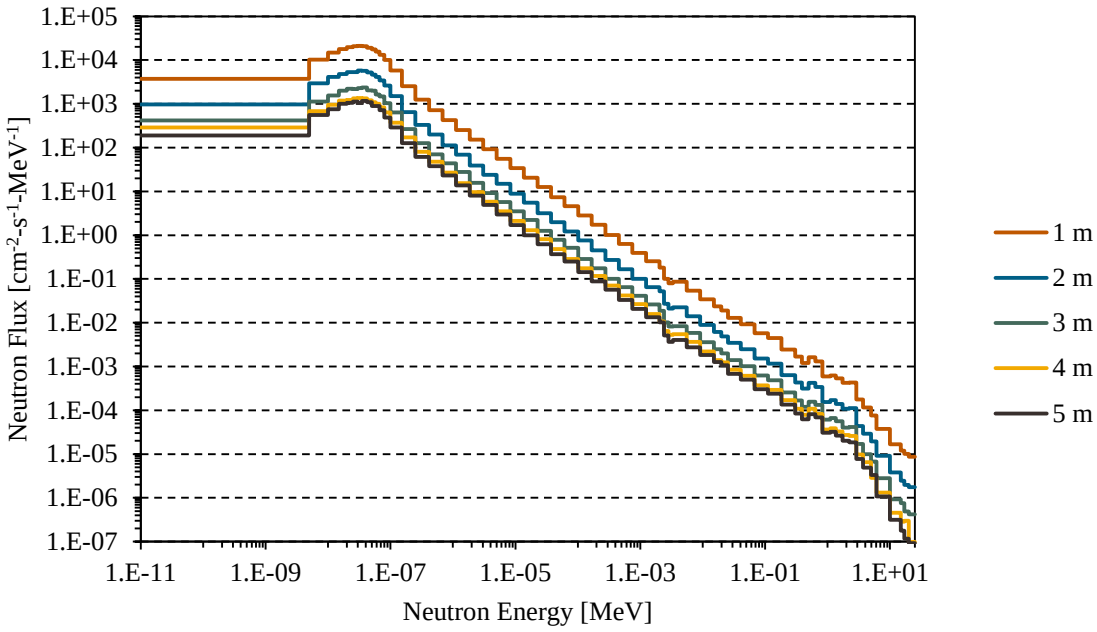

Figure 3.15: 63-energy group neutron flux profiles
at various depths in a basalt geology.

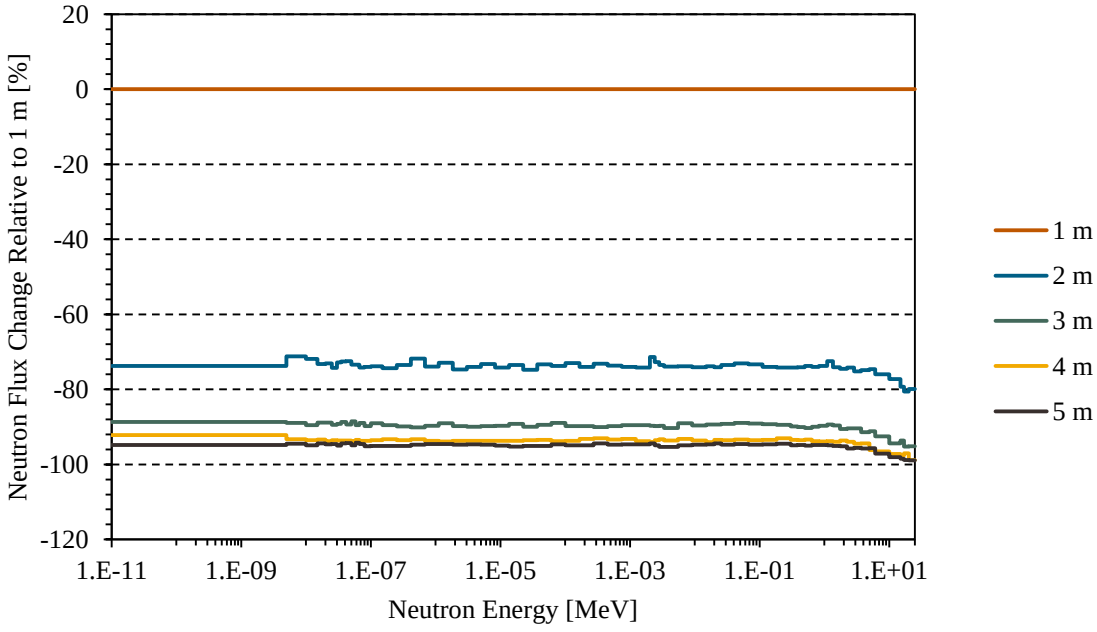

Figure 3.16: 63-energy group neutron flux profiles at various depths
in a basalt geology relative to the neutron flux profile at
a subsurface depth of 1 m in the same geology.

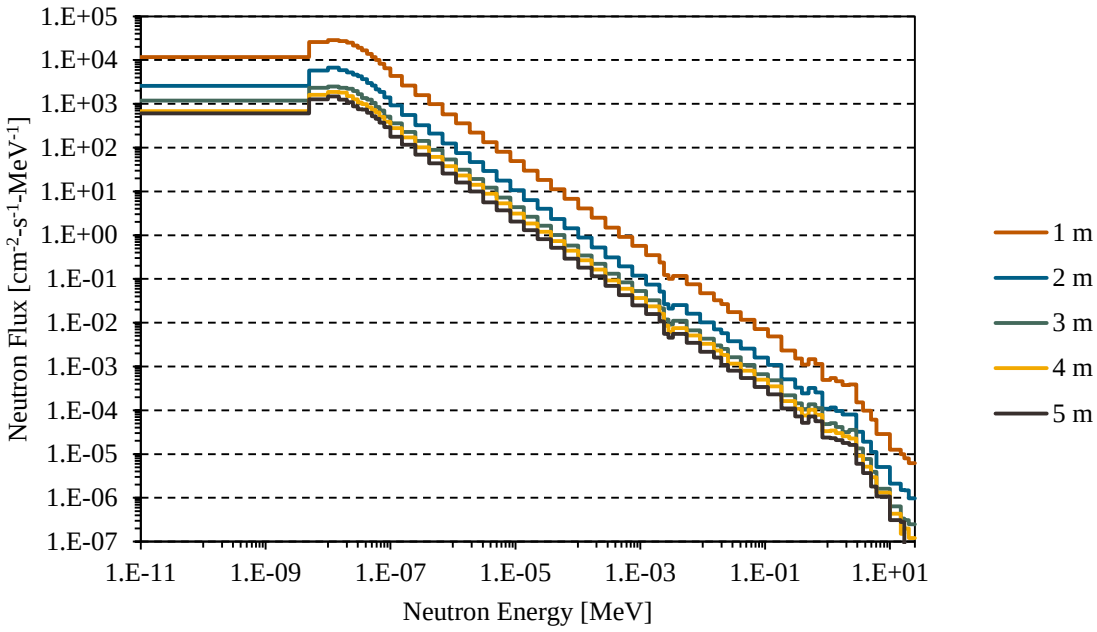

Figure 3.17: 63-energy group neutron flux profiles at various depths in a granodiorite geology.

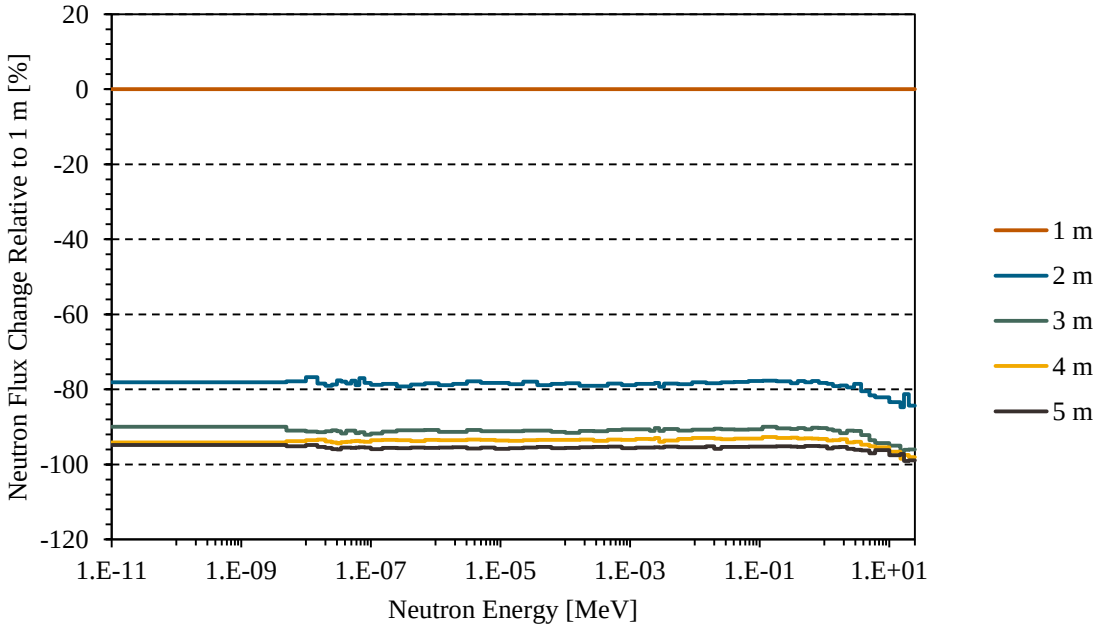

Figure 3.18: 63-energy group neutron flux profiles at various depths in a granodiorite geology relative to the neutron flux profile at subsurface depth of 1 m in the same geology.

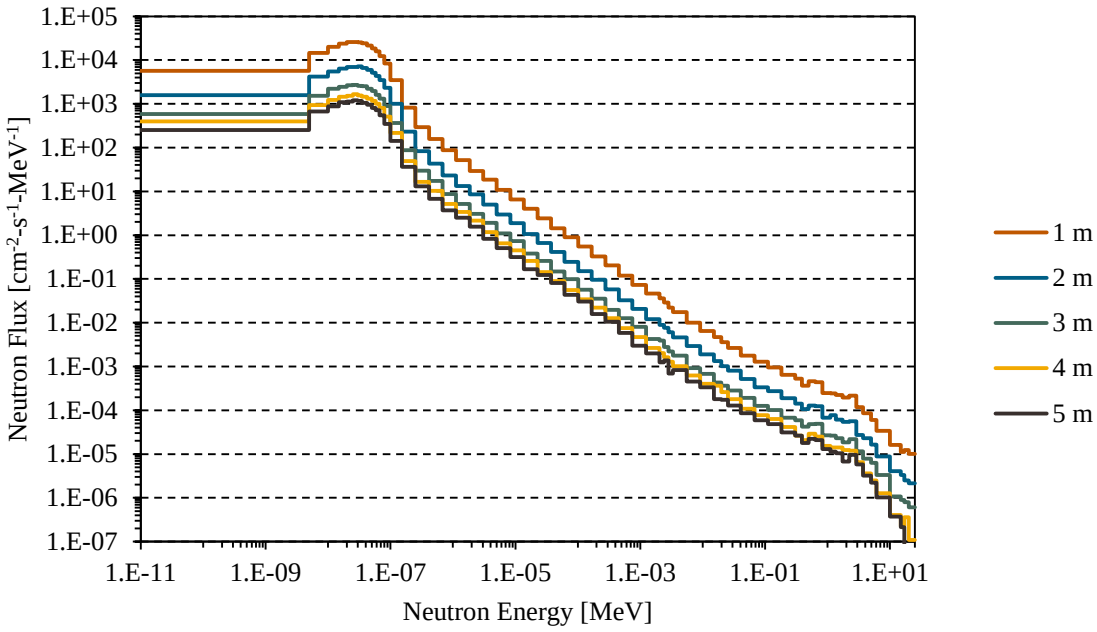

Figure 3.19: 63-energy group neutron flux profiles at various depths in a shale geology.

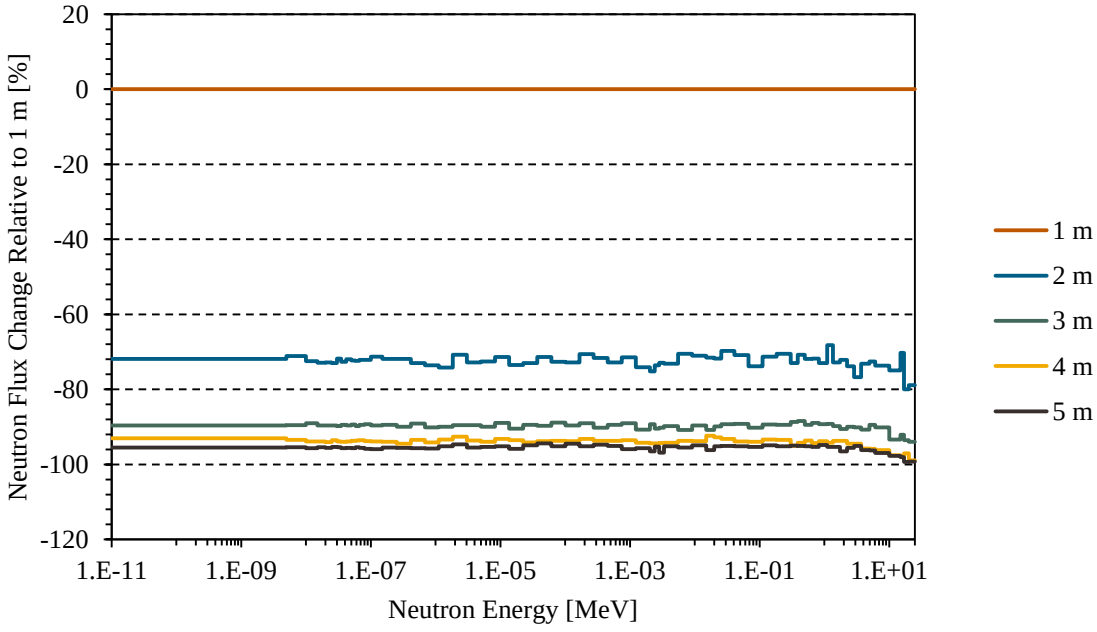

Figure 3.20: 63-energy group neutron flux profiles at various depths in a shale geology relative to the neutron flux profile at subsurface depth of 1 m in the same geology.

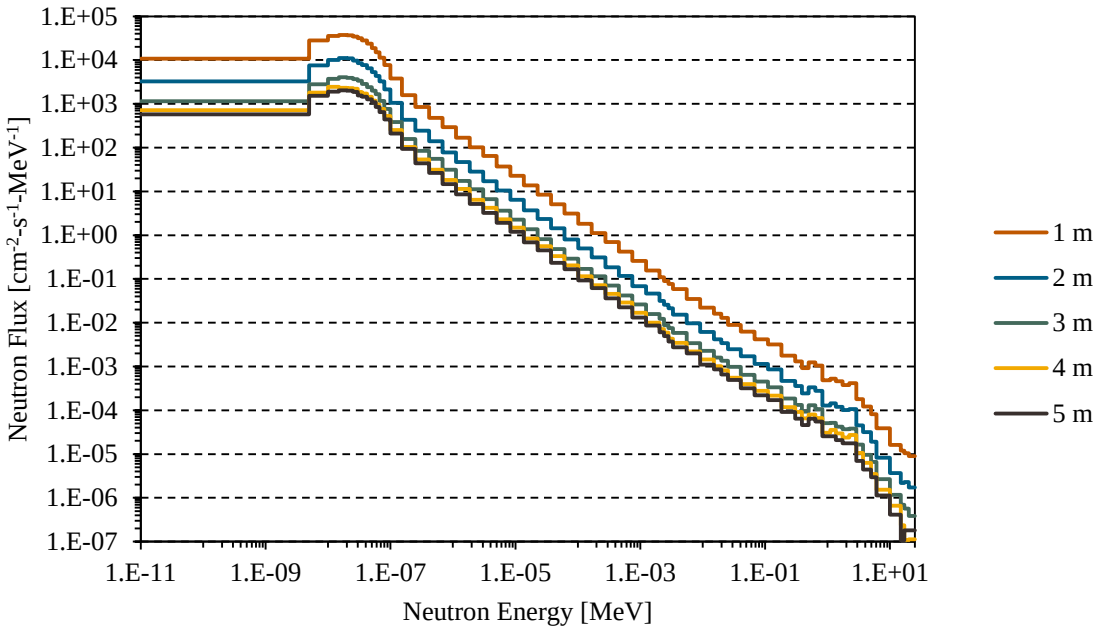

Figure 3.21: 63-energy group neutron flux profiles at various depths in a sandstone geology.

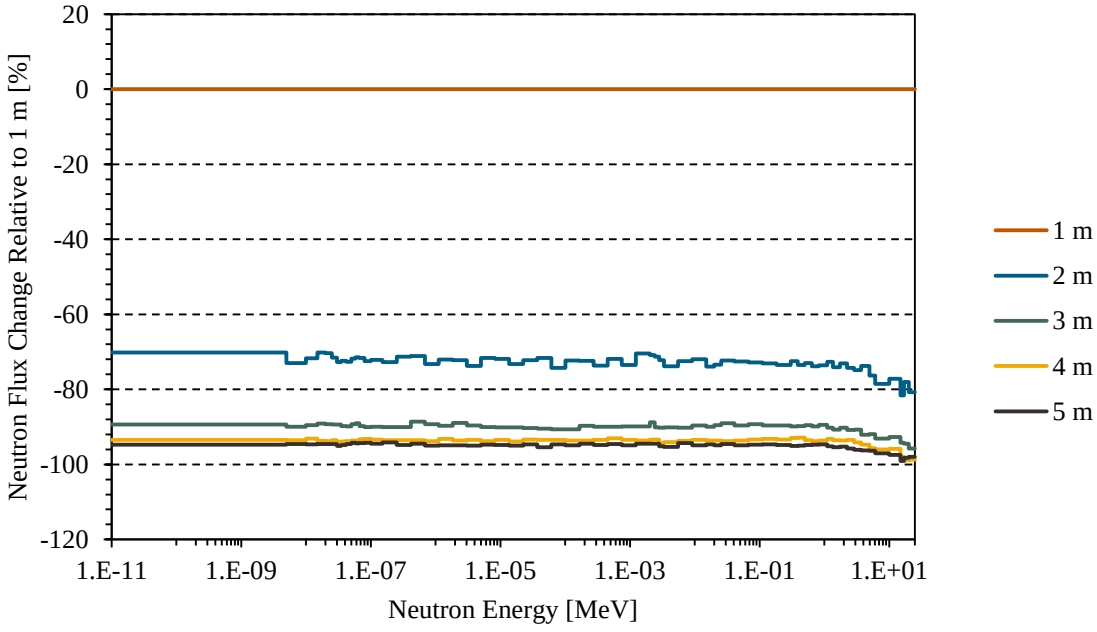

Figure 3.22: 63-energy group neutron flux profiles at various depths in a sandstone geology relative to the neutron flux profile at subsurface depth of 1 m in the same geology.

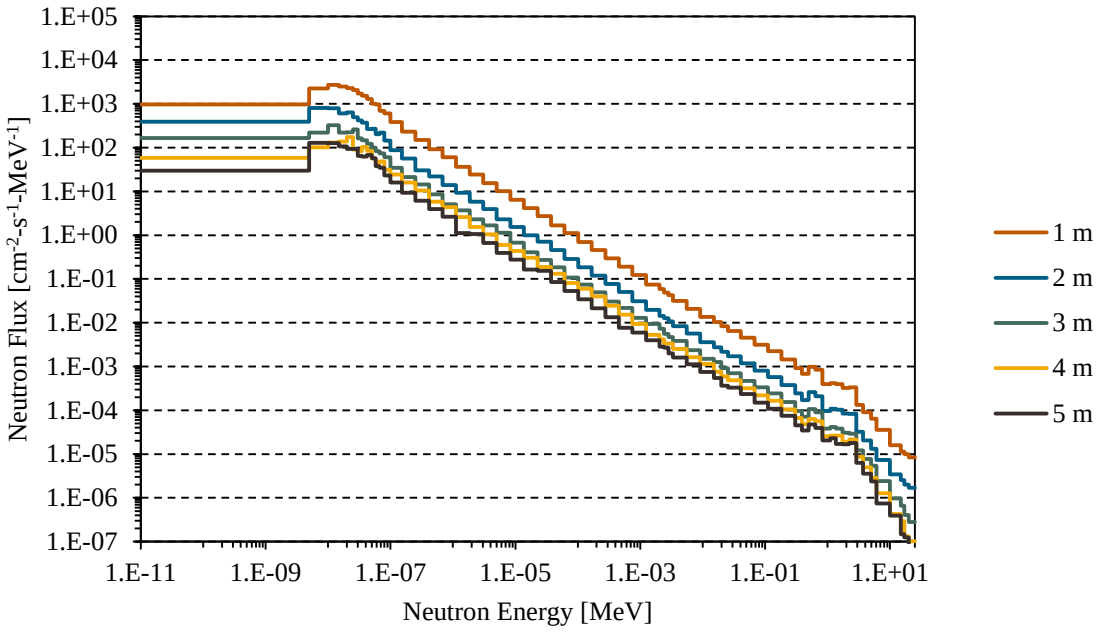

Figure 3.23: 63-energy group neutron flux profiles at various depths in a limestone geology.

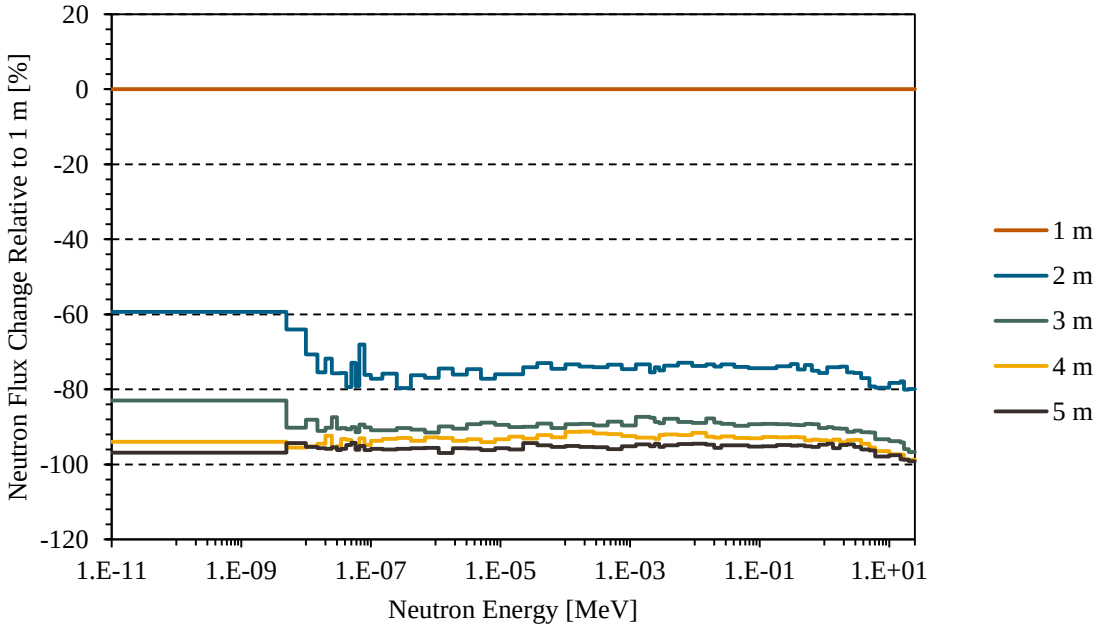

Figure 3.24: 63-energy group neutron flux profiles at various depths in a limestone geology relative to the neutron flux profile at subsurface depth of 1 m in the same geology.

3.5.2.3 Geological Cosmic Neutron Flux Attenuation Studies

In addition to providing information regarding the cosmic neutron fluxes at various depths in each of the geologies of interest, the output produced by the Monte Carlo N-Particle (MCNP) models generated by the TeXAS application also provide valuable information regarding the constituents that are most important in attenuating the cosmic neutron flux as it penetrates down into the Earth's subsurface. The relative importance of each isotopic constituent in each of the geologies was evaluated as a fraction of the total neutron removal cross-section associated with the given geology. Isotopic constituents for which this fraction is larger are deemed to be more important from a cosmic neutron flux attenuation perspective and isotopic constituents for which this fraction is smaller are deemed to be less important from a cosmic neutron flux attenuation perspective.

The results of the cosmic neutron flux attenuation studies are presented in Figures 3.25 through 3.30, which illustrate the fraction of the total neutron removal cross-section attributable to the various constituents of each geology at a subsurface depth of 1 m. Perhaps the most interesting aspect of the cosmic neutron flux attenuation results presented in Figures 3.25 through 3.30 is the fact that in all six of the geologies studied here 50 % or more of the total neutron removal cross-section is attributable to only three isotopes. Furthermore, the same isotopes appear to account for the majority of the neutron removal cross-section in five of the six geologies (the most important constituents associated with the shale geology are somewhat different than the others).

It is also interesting to note that the gadolinium isotopes are also relatively important in terms of attenuating the neutron flux in each of the geologies that contain gadolinium. This is an interesting result because, while the gadolinium neutron removal cross-section is known to be very large, gadolinium is only present in the geologies studied here at trace concentrations; the elemental gadolinium concentrations in granite, basalt, granodiorite, shale, and sandstone are about 6.49 ppm, 6.87 ppm, 5.74 ppm, 5.39 ppm, and 6.77 ppm, respectively (limestone does not appear to contain gadolinium). This result indicates that while gadolinium may only be present in a geology at trace concentrations, it should still be accounted for in MCNP models developed to study CTBT-relevant radioactive particulate and noble gas background activity concentrations.

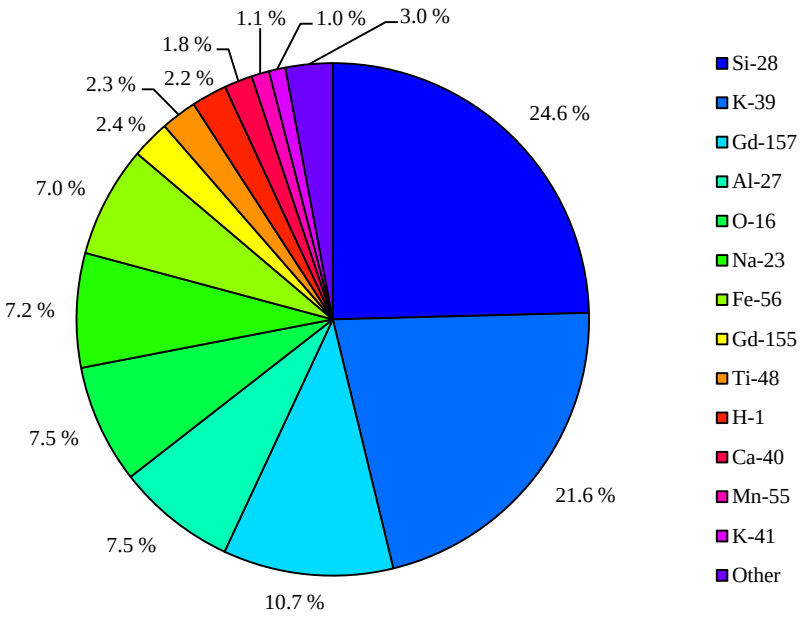

Figure 3.25: Cosmic neutron flux attenuation by the isotopic constituents of granite at a subsurface depth of 1 m.

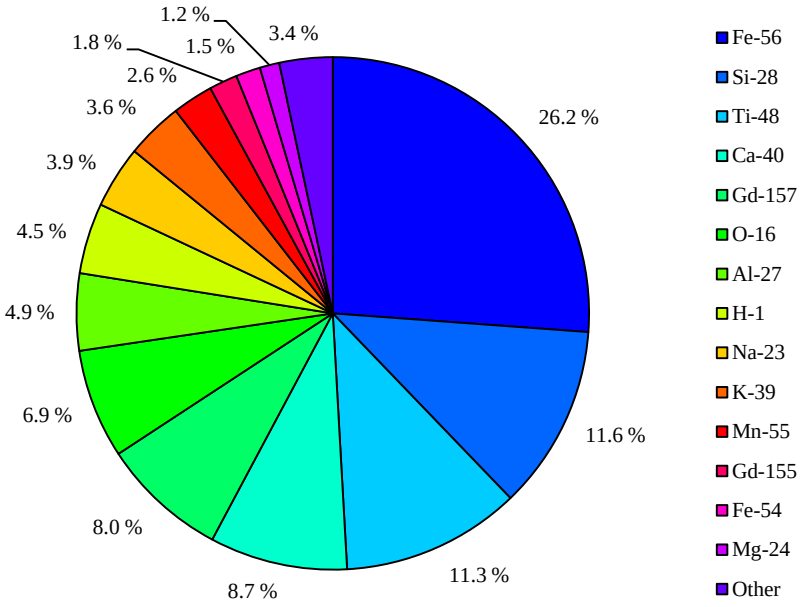

Figure 3.26: Cosmic neutron flux attenuation by the isotopic constituents of basalt at a subsurface depth of 1 m.

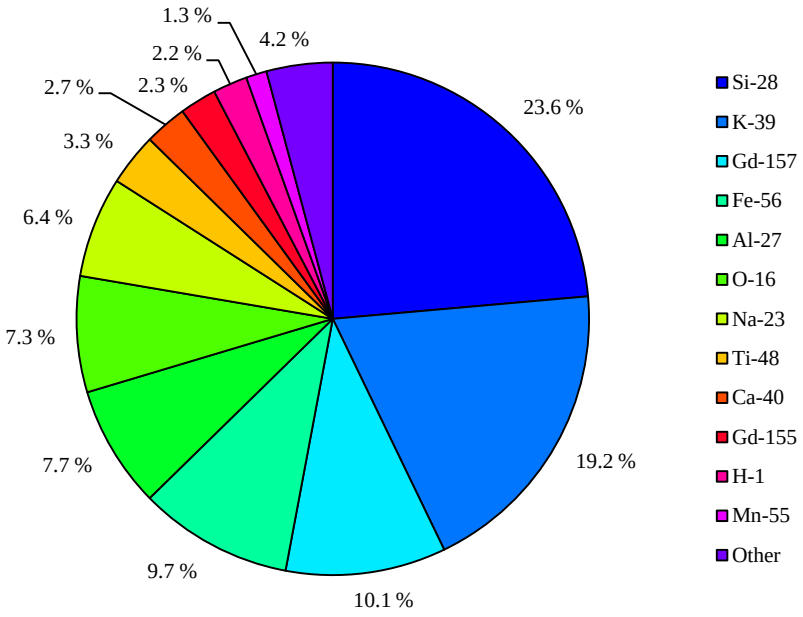

Figure 3.27: Cosmic neutron flux attenuation by the isotopic constituents of granodiorite at a subsurface depth of 1 m.

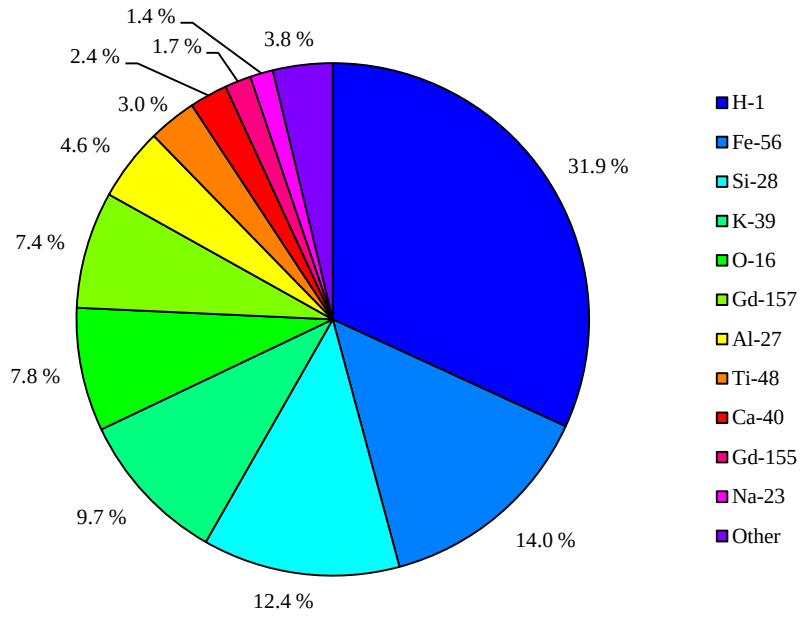

Figure 3.28: Cosmic neutron flux attenuation by the isotopic constituents of shale at a subsurface depth of 1 m.

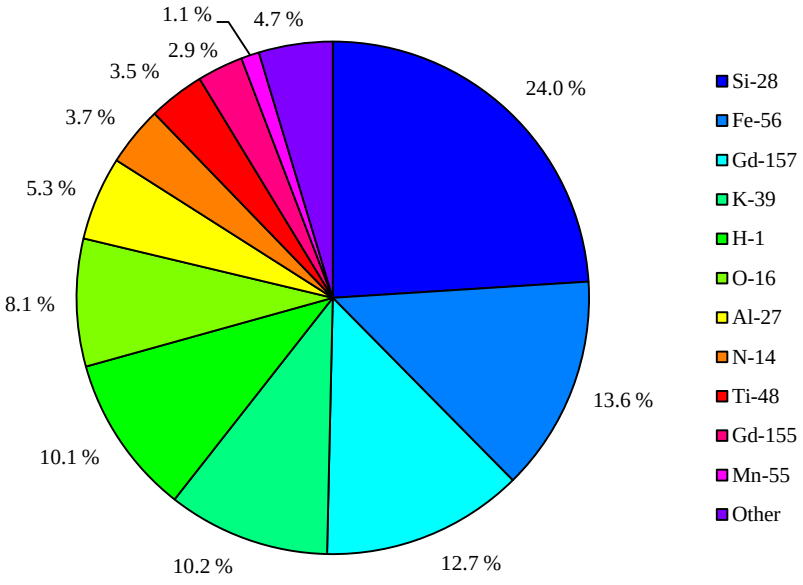

Figure 3.29: Cosmic neutron flux attenuation by the isotopic constituents of sandstone at a subsurface depth of 1 m.

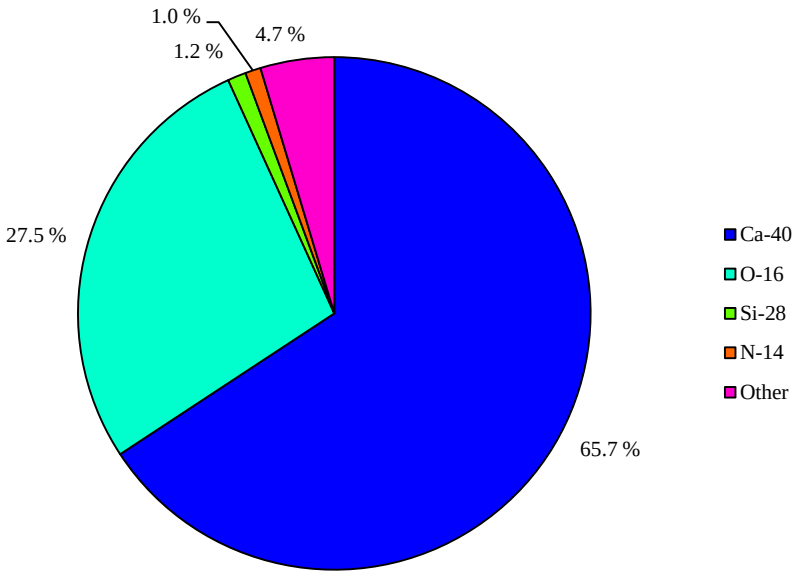

Figure 3.30: Cosmic neutron flux attenuation by the isotopic constituents of limestone at a subsurface depth of 1 m.

3.5.2.4 Geological CTBT-Relevant Radioactive Particulate and Noble Gas Background Activity Concentration Estimates

In addition to the cosmic neutron flux and the cosmic neutron flux attenuation results reported in the previous sections, the TeXAS application also generated a great deal of information regarding CTBT-relevant radioactive particulate and noble gas background activity concentrations resulting from natural processes in each of the geologies of interest. The CTBT-relevant radioactive particulate and noble gas background activity concentrations associated with the granite, basalt, granodiorite, shale, sandstone, and limestone geologies of interest here are presented in Figures 3.31 through 3.42. A pair of figures is presented for each of the six geologies. The first figure

of each pair presents the CTBT-relevant radioactive particulate and noble gas background activity concentrations resulting from natural processes in the given geology at a subsurface depth of 1 m; the second figure of each pair presents the same information at a subsurface depth of 3 m in the same geology.

Note that the radioactive particulate and noble gas background activity concentrations reported in Figures 3.31 through 3.42 account for radioactive particulate and noble gas background activity concentrations resulting from (1) spontaneous fission of naturally occurring thorium (^{232}Th) and uranium (^{234}U, ^{235}U, and ^{238}U), (2) cosmic neutron-induced fission of naturally occurring ^{232}Th, ^{234}U, ^{235}U, and ^{238}U, and (3) cosmic neutron-induced activation of various geological constituents. Loses due to radioactive decay are accounted for, but loses due to transport processes are not. Therefore, the radioactive particulate and noble gas background activity concentrations reported here should be viewed as nominal upper limits. For more information regarding the evaluation of the radioactive particulate and noble gas background activity concentrations, refer to Section E.4 of Appendix E.

Comparing the CTBT-relevant radioactive noble gas background activity concentrations reported in Figures 3.31 through 3.42 to the radioactive noble gas background activity concentrations taken from the literature (see in Table 3.6) reveals that the CTBT-relevant radioactive noble gas background activity concentration estimates generated by the TeXAS application are in relatively close agreement with the CTBT-relevant radioactive noble gas background activity concentration estimates reported by other studies conducted to date.

Comparing the radioactive particulate and noble gas background activity concentrations for a given geology at subsurface depths of 1 m and 3 m reveals that both the radioactive particulate and noble gas background activity concentrations decrease slightly with increasing subsurface depth. This is as expected given that the cosmic neutron-induced fission and activation components of the background activity concentrations are functions of the cosmic neutron flux, and the magnitude of the cosmic neutron flux is shown to decrease with increasing subsurface depth in all geologies in Section 3.5.2.2. However, because spontaneous fission is the dominant radionuclide production mechanism the decrease in the activity concentrations with depth is not very drastic.

Additional information regarding the most predominant production mechanisms associated with each of the CTBT-relevant radioxenons—^{131m}Xe, ^{133m}Xe, ^{133}Xe, and ^{135}Xe—is presented in Figures 3.43 through 3.46. It is interesting to note the large fractions of the ^{131m}Xe, ^{133m}Xe, ^{133}Xe, and ^{135}Xe background activity concentrations attributed to spontaneous fission. This result is consistent with the results produced by other studies conducted to date.

It is also interesting to consider the CTBT-relevant radioactive noble gas background activity concentrations, highlighted by the blue bars in Figures 3.31 through 3.42, in the context of the MDCs associated with the radioactive noble gas monitoring systems currently employed by the verification regime of the CTBT. In Figures 3.47 through 3.50 the ^{131m}Xe, ^{133m}Xe, ^{133}Xe, and ^{135}Xe background concentrations at 1 m in each of the geologies considered here are plotted relative to the

SAUNA system [57] MDC. These figures illustrate that, for most of the geologies considered here, the CTBT-relevant radioxenon background concentrations resulting from natural processes are actually comparable to the radioxenon MDCs associated with the SUANA system. The one exception to this is ^{131m}Xe, the background activity concentrations for which are roughly two orders of magnitude lower than the SAUNA system ^{131m}Xe MDC. This indicates that radioxenon background activity concentrations resulting from natural process may be significant enough to be detected by CTBT radionuclide monitoring systems. However, it is important to note that the radioxenon background activity concentrations considered here are to be viewed as nominal upper limits. Loses due to gas transport might reduce the background activity concentrations significantly so that they would be less likely to be detected.

The ^{37}Ar background activity concentrations, which are also highlighted by blue bars in Figures 3.31 through 3.42, are considered in the context of (1) the MDC associated with the Movable ^{37}Ar Rapid Detection System (MARDS), which is reportedly less than 1 mBq-m^{-3} [137, 138], and (2) the MDC associated with a laboratory based ^{37}Ar detection system, which is reportedly on the order of about 0.02 mBq-m^{-3} [139]. As indicated by Figures 3.31 through 3.42 the ^{37}Ar background concentration estimates are quite high, particularly at a subsurface depth of 1 m in the basalt and limestone geologies where the concentrations reach 3.21×10^2 and 1.29×10^3 mBq-m^{-3}, respectively. These ^{37}Ar concentrations are well in excess of the reported MARDS ^{37}Ar MDC and should be readily detected by such a system.

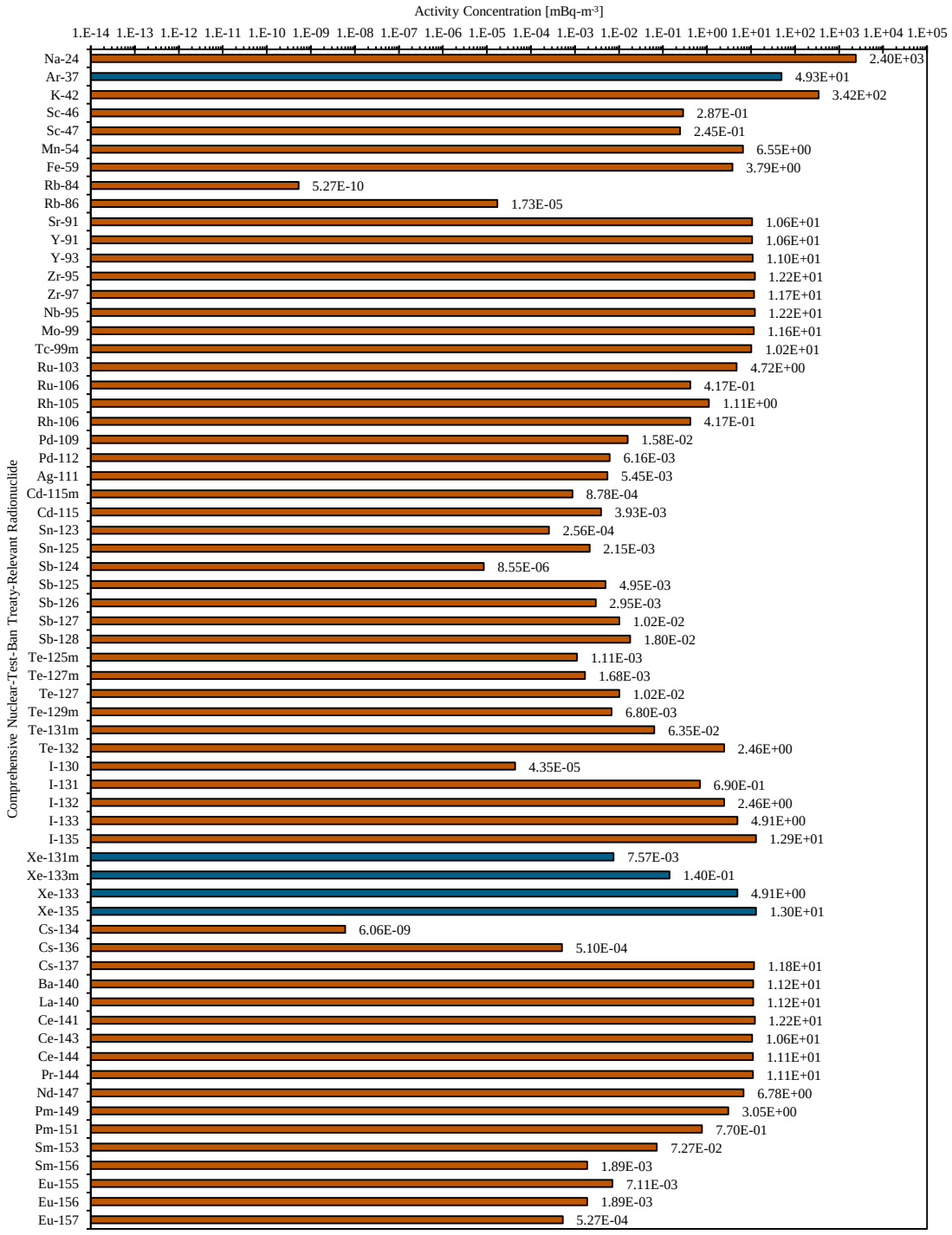

Figure 3.31: CTBT-relevant radioactive particulate and noble gas background activity concentration estimates at a depth of 1 m in a granite geology.

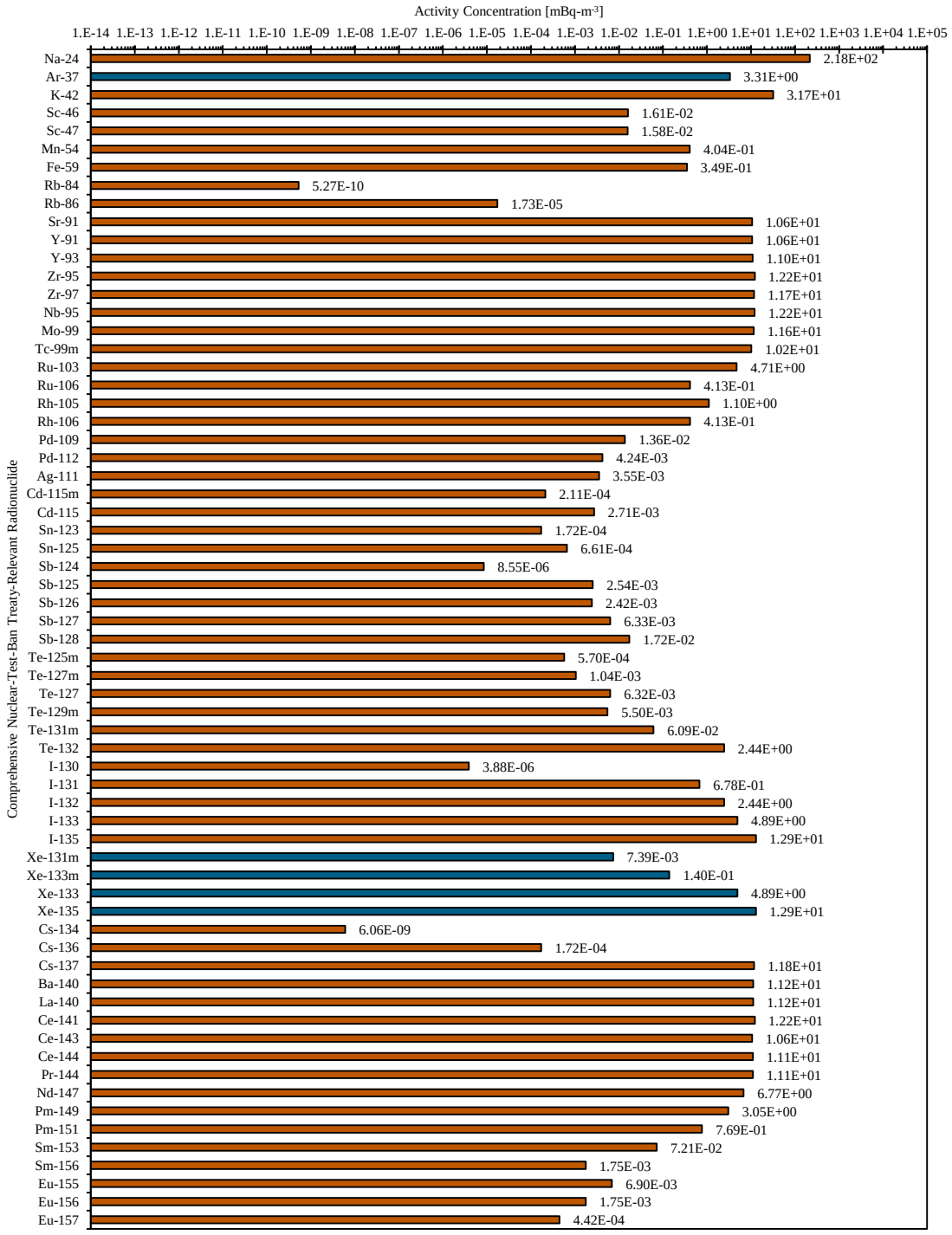

Figure 3.32: CTBT-relevant radioactive particulate and noble gas background activity concentration Estimates at a depth of 3 m in a granite geology.

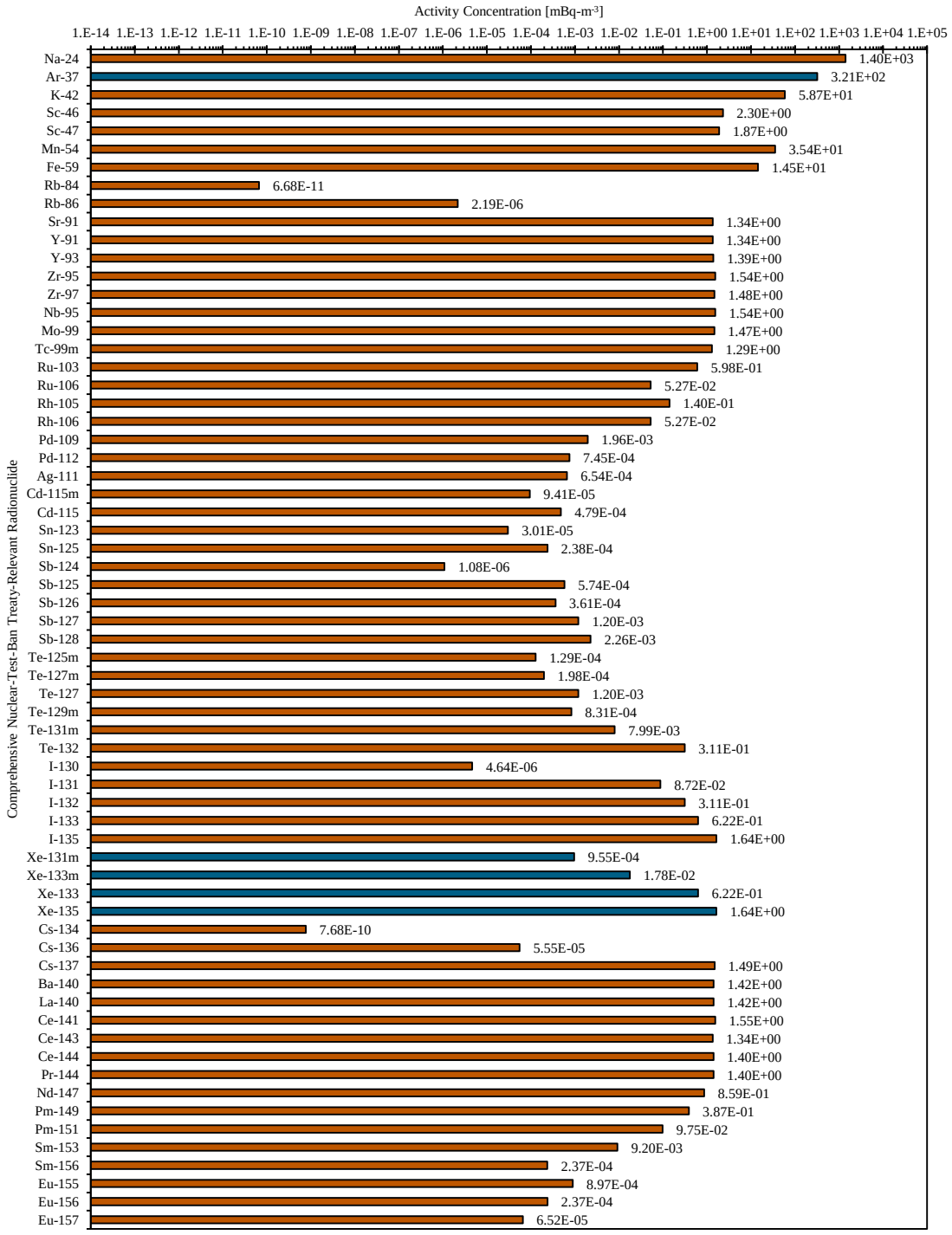

Figure 3.33: CTBT-relevant radioactive particulate and noble gas background activity concentration estimates at a depth of 1 m in a basalt geology.

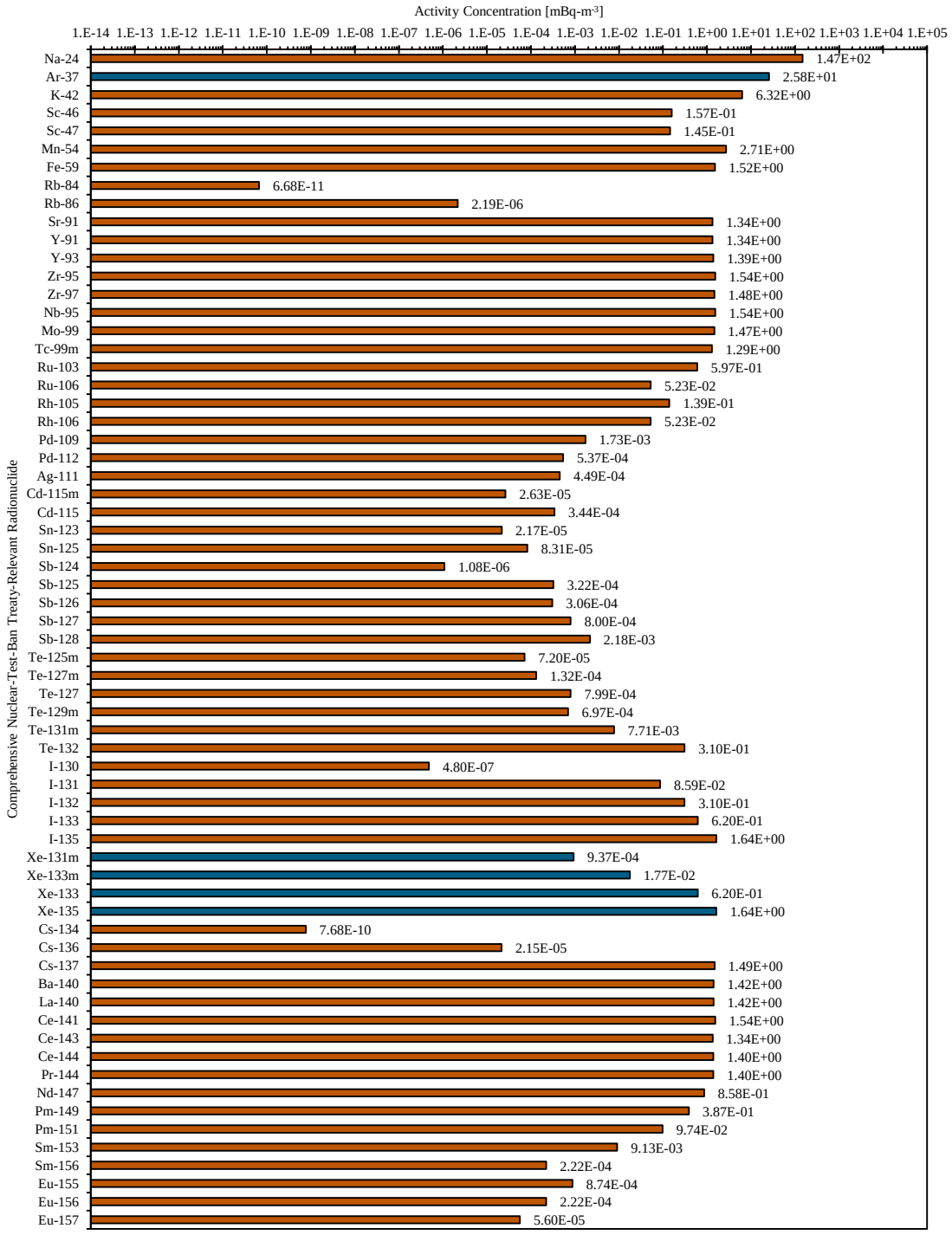

Figure 3.34: CTBT-relevant radioactive particulate and noble gas background activity concentration estimates at a depth of 3 m in a basalt geology.

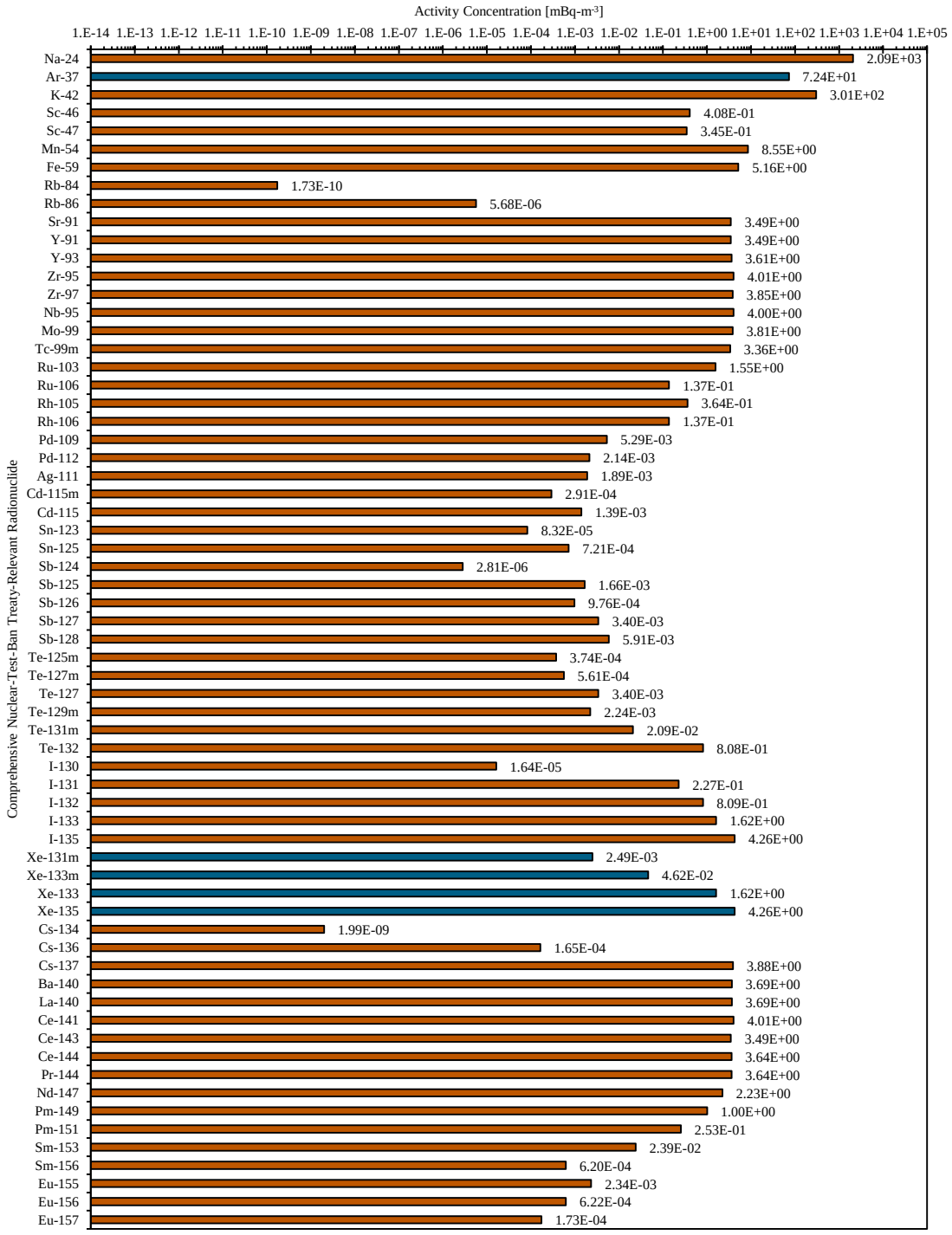

Figure 3.35: CTBT-relevant radioactive particulate and noble gas background activity concentration estimates at a depth of 1 m in a granodiorite geology.

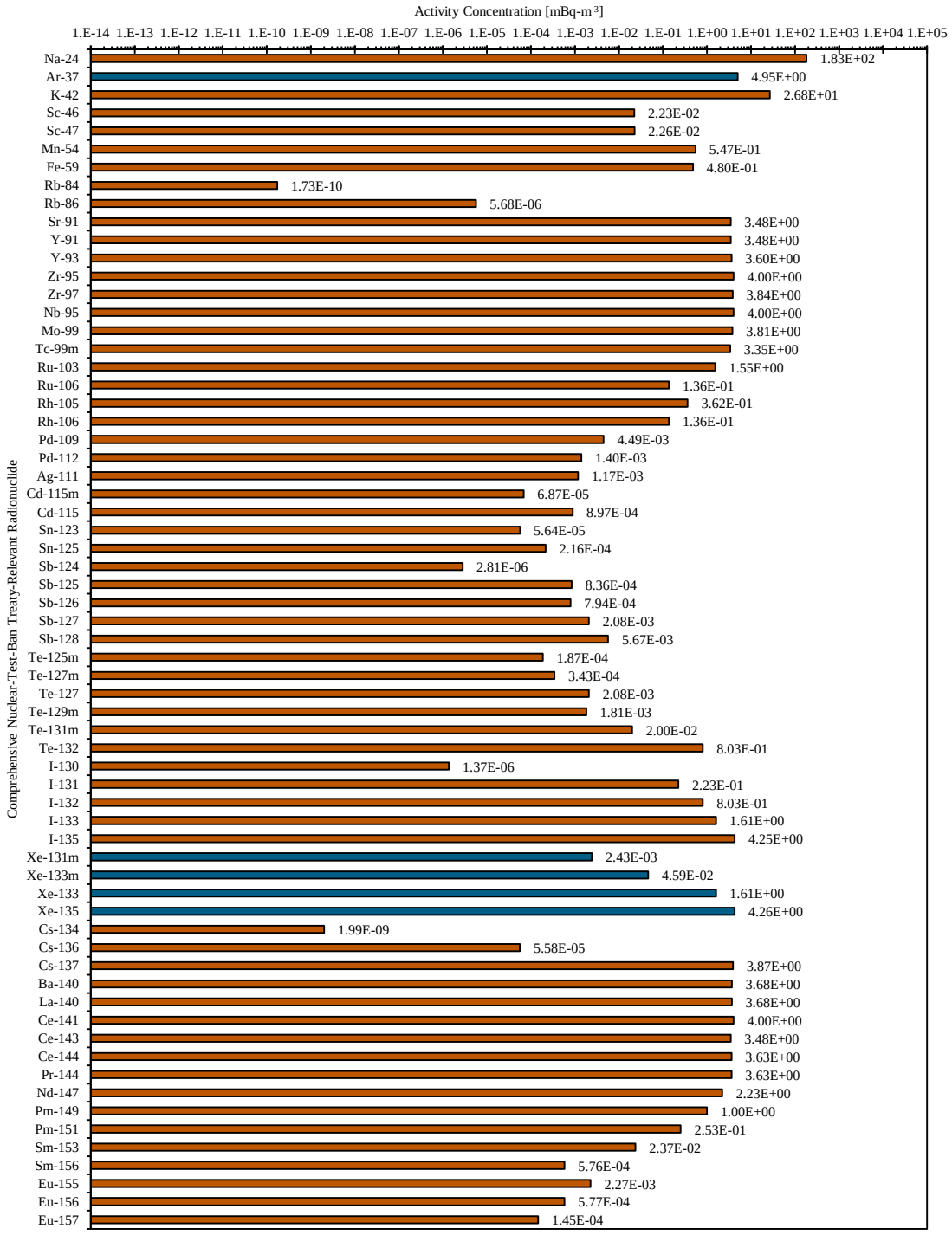

Figure 3.36: CTBT-relevant radioactive particulate and noble gas background activity concentration estimates at a depth of 3 m in a granodiorite geology.

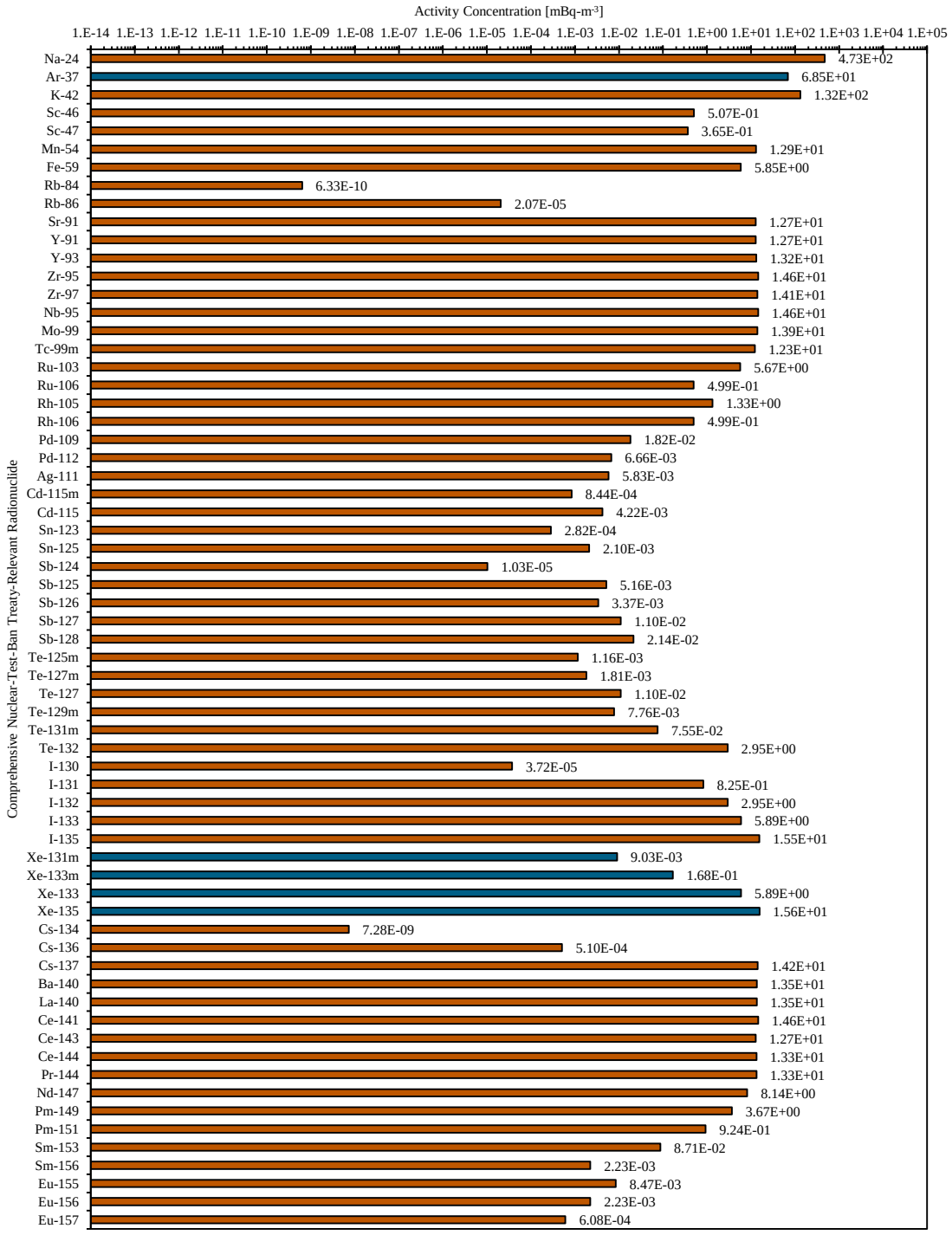

Figure 3.37: CTBT-relevant radioactive particulate and noble gas background activity concentration estimates at a depth of 1 m in a shale geology.

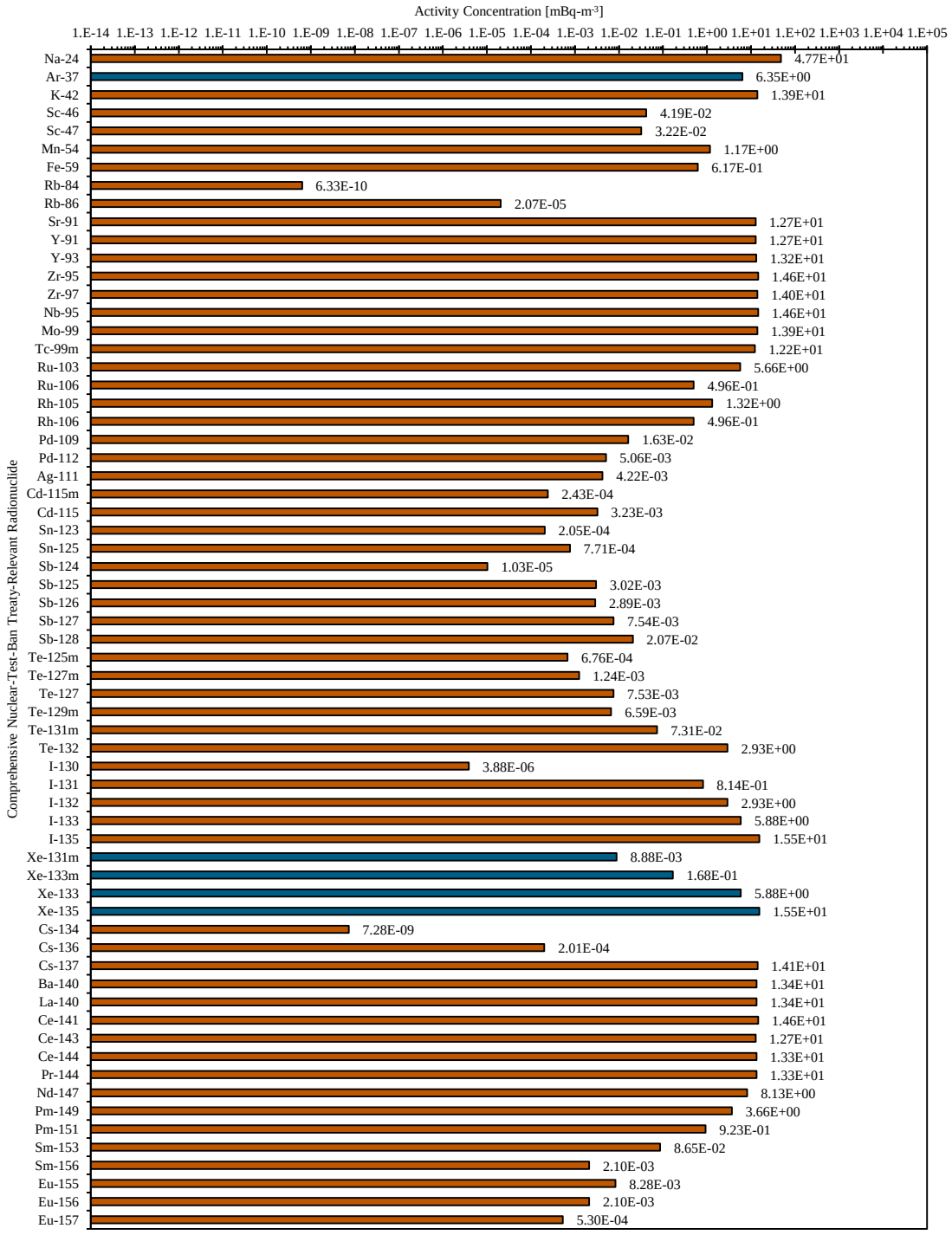

Figure 3.38: CTBT-relevant radioactive particulate and noble gas background activity concentration estimates at a depth of 3 m in a shale geology.

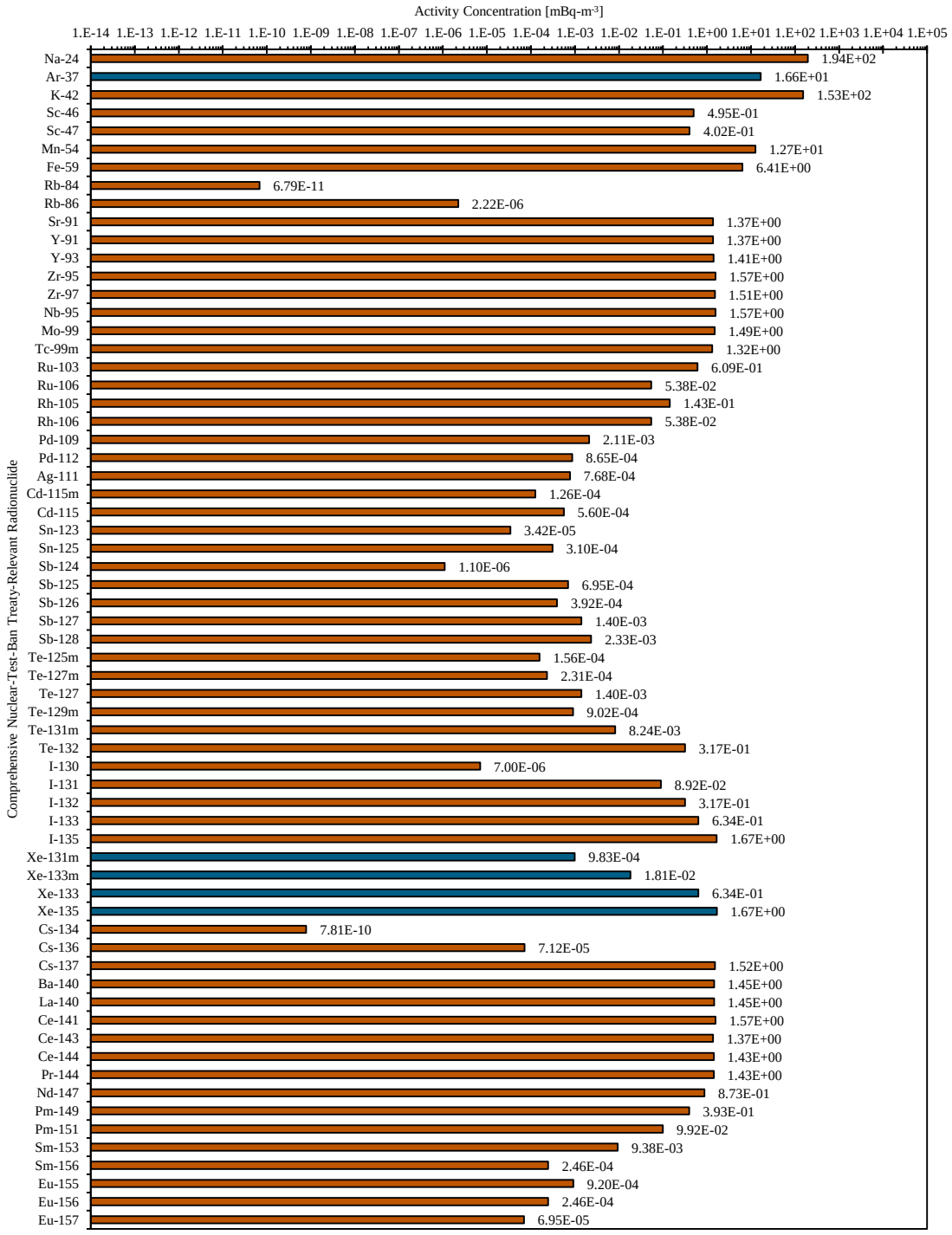

Figure 3.39: CTBT-relevant radioactive particulate and noble gas background activity concentration estimates at a depth of 1 m in a sandstone geology.

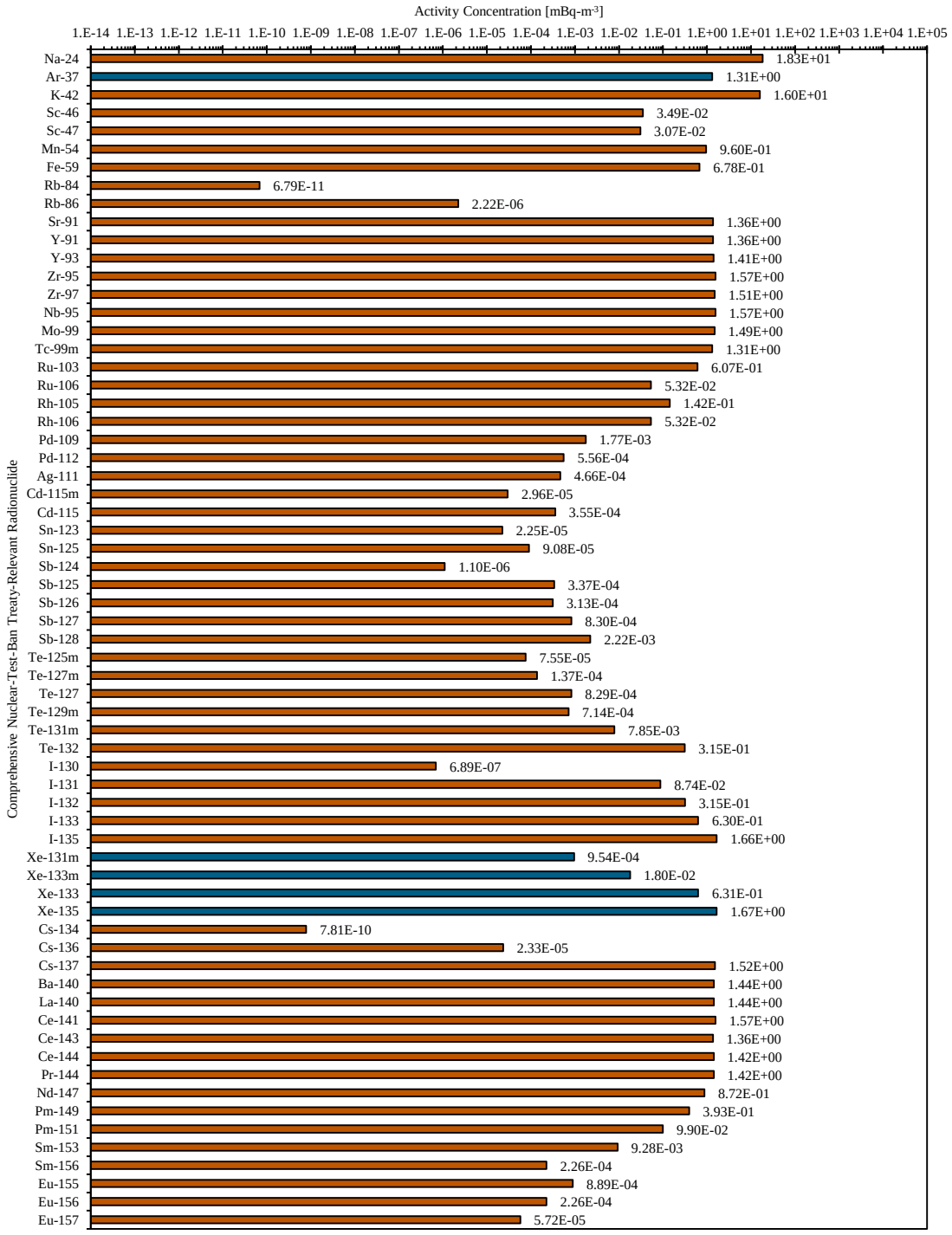

Figure 3.40: CTBT-relevant radioactive particulate and noble gas background activity concentration estimates at a depth of 3 m in a sandstone geology.

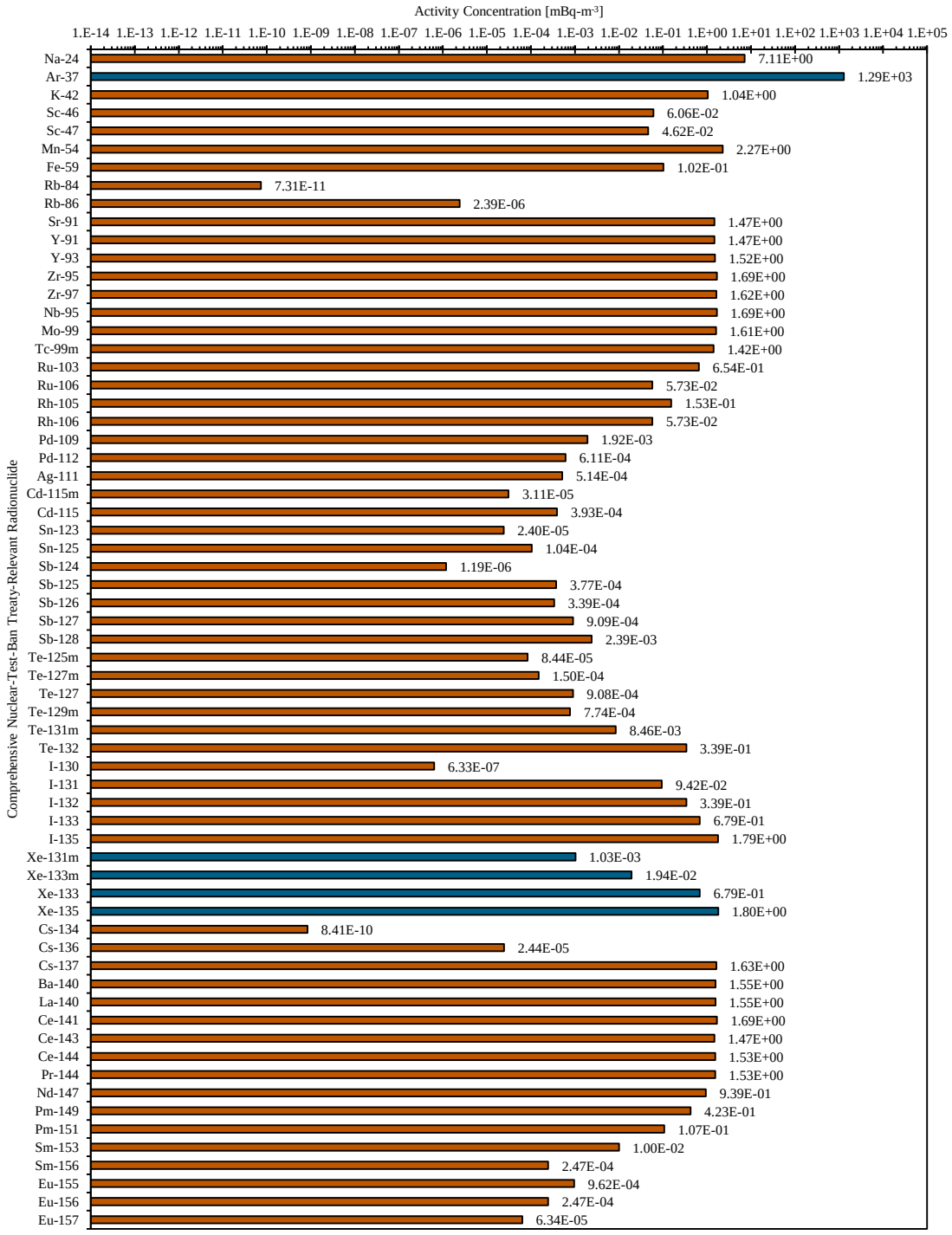

Figure 3.41: CTBT-relevant radioactive particulate and noble gas background activity concentration estimates at a depth of 1 m in a limestone geology.

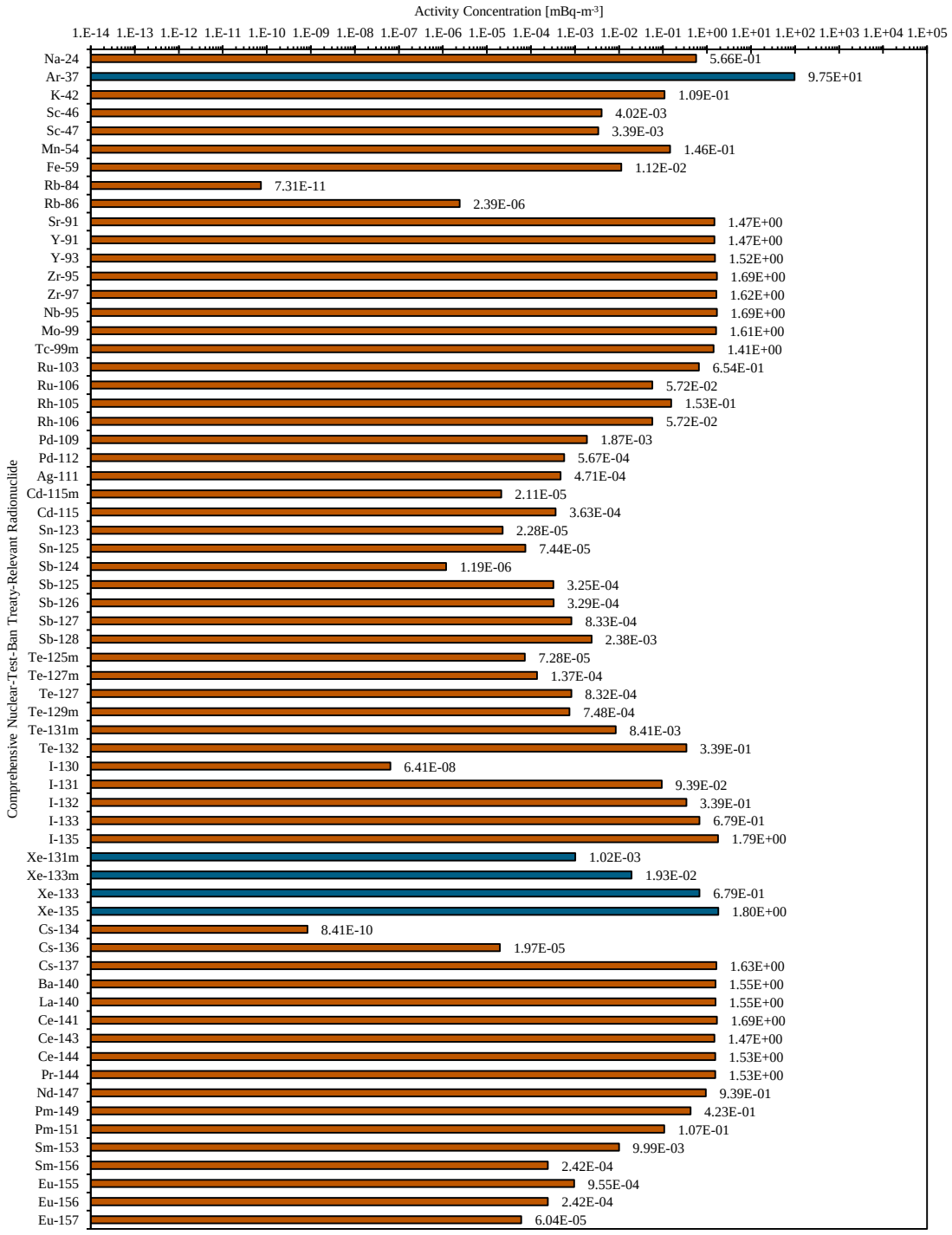

Figure 3.42: CTBT-relevant radioactive particulate and noble gas background activity concentration estimates at a depth of 3 m in a limestone geology.

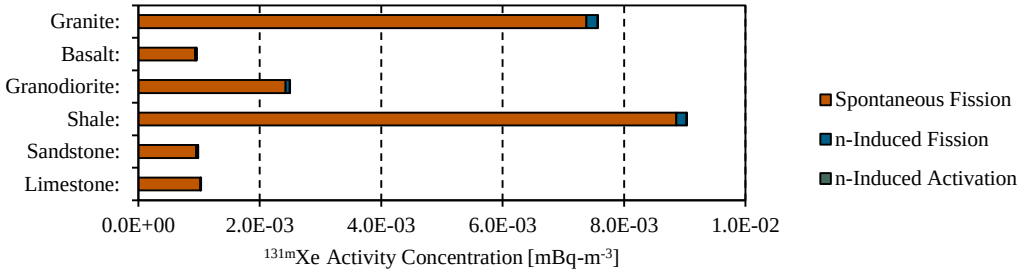

Figure 3.43: ^{131m}Xe background activity concentrations in various geologies.

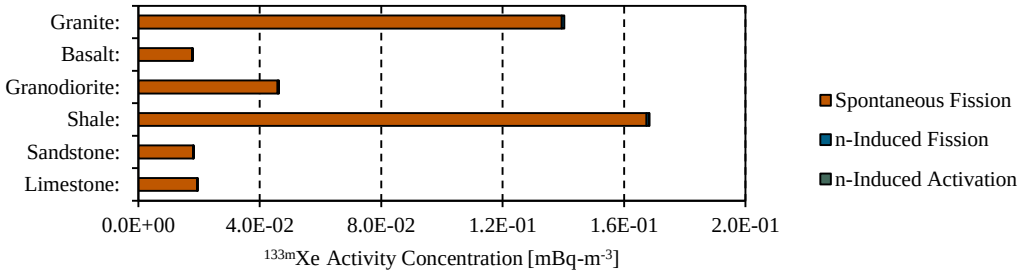

Figure 3.44: ^{133m}Xe background activity concentrations in various geologies.

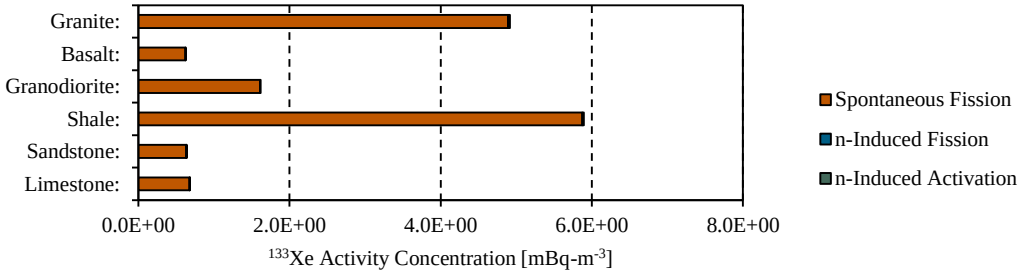

Figure 3.45: ^{133}Xe background activity concentrations in various geologies.

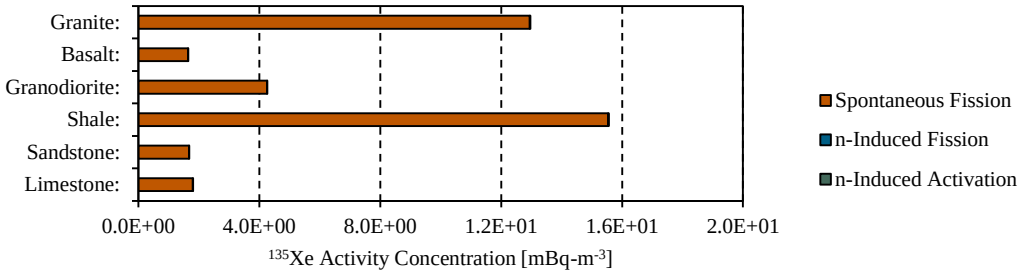

Figure 3.46: ^{135}Xe background activity concentrations in various geologies.

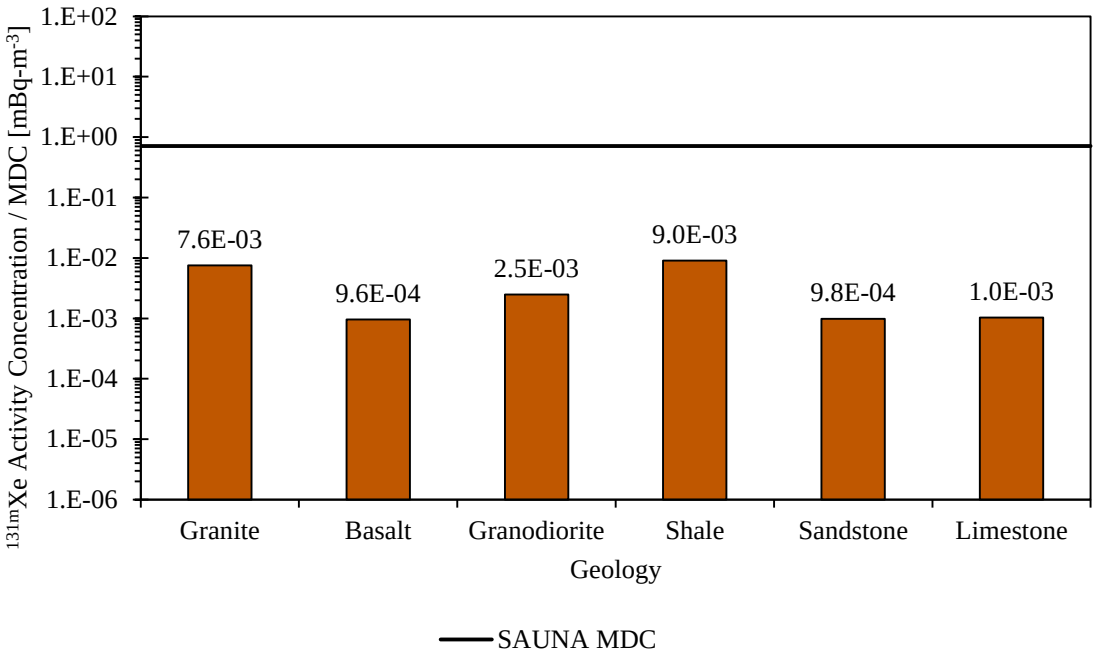

Figure 3.47: ^{131m}Xe background activity concentrations resulting from natural processes in six geologies relative to SAUNA system MDCs.

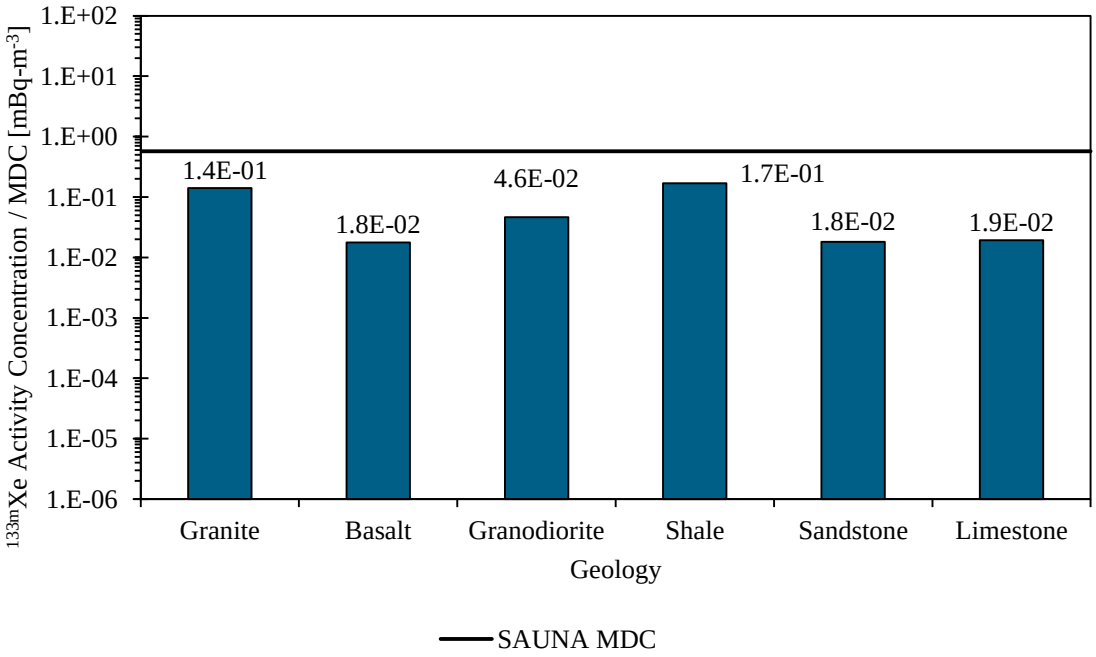

Figure 3.48: ^{133m}Xe background activity concentrations resulting from natural processes in six geologies relative to SAUNA system MDCs.

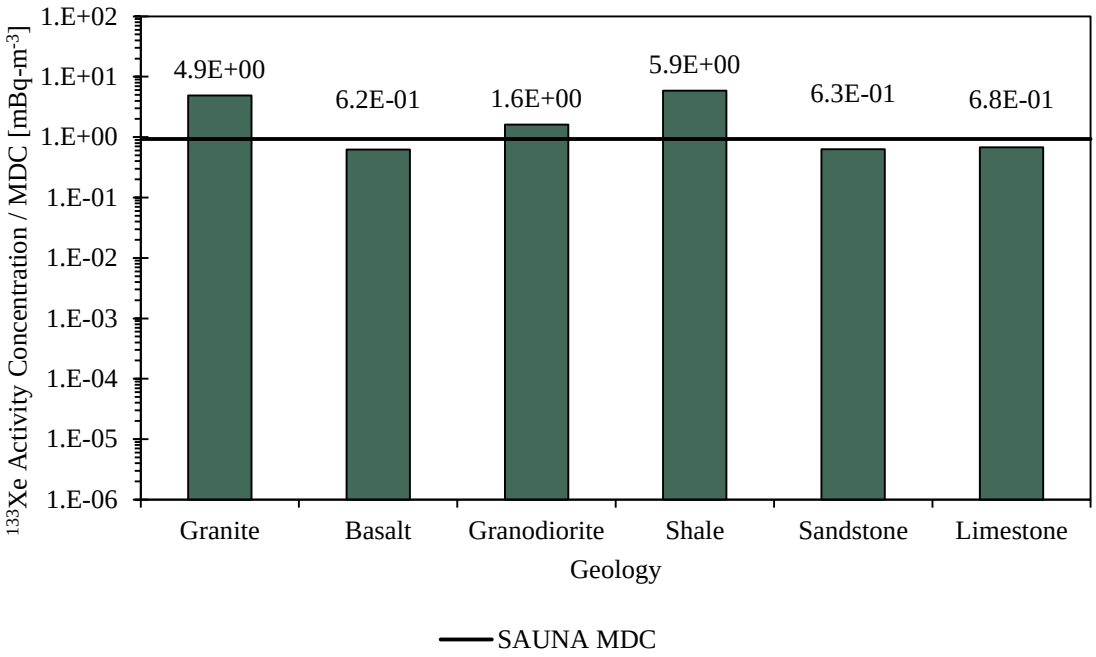

Figure 3.49: ^{133}Xe background activity concentrations resulting from natural processes in six geologies relative to SAUNA system MDCs.

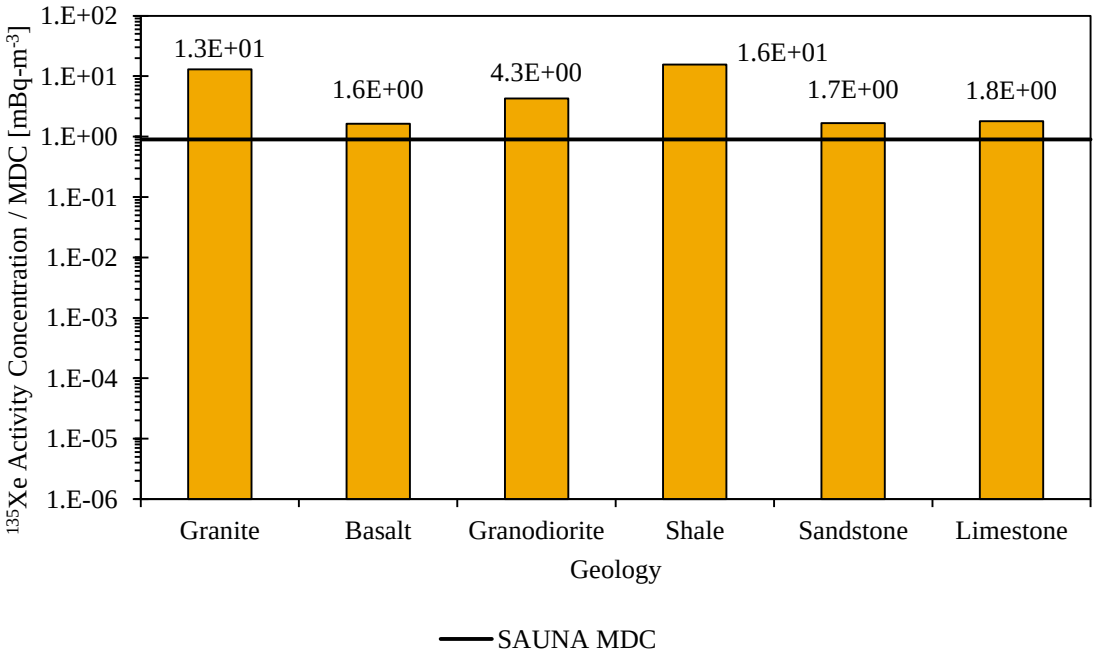

Figure 3.50: ^{135}Xe background activity concentrations resulting from natural processes in six geologies relative to SAUNA system MDCs.

3.5.3 Seawater Studies

The objectives of the seawater studies documented in this section were (1) to evaluate the cosmic neutron flux profile at a depth of 5 m in seawater and (2) to evaluate the CTBT-relevant radioactive noble gas background activity concentrations at a depth of 5 m in seawater. A single Monte Carlo N-Particle (MNCP) model developed by the TeXAS application (see Appendix E) was used to evaluate and identify the aforementioned cosmic neutron flux profiles and the CTBT-relevant radioactive noble gas background activity concentrations in a 5 m thick seawater layer centered at a depth of 5 m.

Note that the cosmic neutron flux profile and CTBT-relevant radioactive noble gas background activity concentrations are not evaluated in additional seawater layers closer to the surface because the temperature, pressure, and salinity data taken from the World Ocean Database [148] in support of the seawater studies documented here is in short supply very near to the seawater surface. In order to evaluate meaningful seawater temperature, pressure, and salinity averages the data near the seawater surface had to be averaged over 5 m thick seawater layers.

3.5.3.1 Seawater Study Inputs

This section describes the inputs supplied to the TeXAS application in order to develop the Monte Carlo N-Particle (MNCP) model used to evaluate the cosmic neutron flux profile and the CTBT-relevant radioactive noble gas background activity

concentrations at a depth of 5 m in seawater. In order to develop the seawater MCNP model the TeXAS application needed information regarding the temperature, pressure, and salinity associated with each of the seawater layers of interest. It would have been possible specify the seawater temperature, pressure, and salinity profiles manually and provide them as inputs to the TeXAS application. However, in this case the TeXAS application was directed to seawater temperature, pressure, and salinity data taken from the World Ocean Database (WOD) [148]. The temperature, pressure, and salinity data are passed to the Equation of State for Seawater [149, 150, 151, 152] and used to evaluate the mass density of the seawater. The seawater density, salinity, and temperature profiles generated for the seawater studies documented here are shown below in Figure 3.51. Refer to Section E.2.4 of Appendix E for more information regarding the methods used to develop these density, temperature, pressure, and salinity profiles.

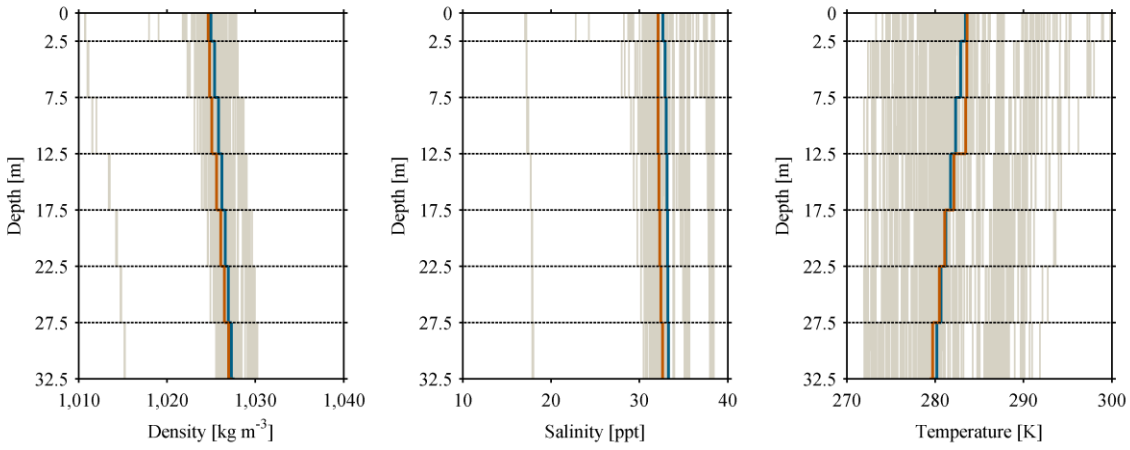

Figure 3.51: Density, salinity, and temperature of the seawater layers in the MCNP model developed to support the seawater studies.

After the TeXAS application generated the seawater mass density profile shown in Figure 3.51 it evaluated the seawater salt constituent atom concentrations for each of the seawater layers by evaluating the product of the seawater layer mass density, the seawater layer salinity, and the mass fraction associated with each of the seawater salt constituents. The seawater salt mass fractions used by the TeXAS application were taken from Castro and Huber [153]. The seawater Th and U atom concentrations were set to 1.6×10^{-7} and 3.3×10^{-3} ppm, respectively [154, 155]. The remainder of the seawater is assumed to be H_2O. The TeXAS application expanded the seawater compositions to an isotopic basis before incorporating them into the MCNP input deck. The expanded, isotopic seawater composition used to support the seawater studies documented here is shown in Table F.3 in Appendix F.

Table 3.10: Seawater salt constituent concentrations [153].

Seawater Salt Constituent	Constituent Concentrations [unitless]
Cl	5.5034E-01
Na	3.0588E-01
SO_4	7.684E-02
Mg	3.684E-02
Ca	1.18E-02
K	1.11E-02
HCO_3	4.13E-03
Br	1.9E-03
BO_3	7.7E-04
Sr	3.7E-04
F	3.E-05

The atmospheric layers above the seawater layers of the MCNP model were defined in the same manner as the atmospheric layers incorporated into the MCNP model used to conduct the atmospheric studies documented in Section 3.5.1 as well as the geological studies documented in Section 3.5.2. Refer to Section 3.5.1.1 for more information regarding the atmospheric layers of the model.

The date assigned to the MCNP source definition (SDEF) card was set equal to 1 Nov 2003 in order to support incorporating a cosmic-ray source term representative of the average cosmic-ray flux incident upon the Earth's upper atmosphere into the MCNP models supporting the geological studies. This is the same date that was used to support the atmospheric studies documented in Section 3.5.1 and the geological studies documented in Section 3.5.2.

3.5.3.2 Seawater CTBT-Relevant Radioactive Noble Gas Background Activity Concentration Estimates

The CTBT-relevant radioactive noble gas background activity concentration estimates generated by the TeXAS application as presented in Table 3.11. The ^{131m}Xe, ^{133m}Xe, ^{133}Xe, and ^{135}Xe background activity concentrations account for production via (1) spontaneous fission of ^{232}Th, ^{235}U, and ^{238}U, (2) cosmic neutron-induced activation of ^{232}Th, ^{234}U, and ^{238}U, and (3) cosmic neutron-induced activation of various seawater constituents. ^{37}Ar is assumed to be produced solely via cosmic neutron induced-activation of calcium-40 (^{40}Ca). Loses due to radioactive decay are accounted for, but loses due to transport processes are not accounted for. Given this, the CTBT-relevant radioactive

noble gas background activity concentrations reported here should be interpreted as nominal upper limits.

The ^{131m}Xe, ^{133m}Xe, ^{133}Xe, and ^{135}Xe background activity concentrations reported in Table 3.11 are all several orders of magnitude less than their respective SAUNA system [57] Minimum Detectable Concentrations (MDCs). The background activity concentrations are so low that they would not contribute meaningfully to radioxenon measurements made in the vicinity of the sea. The ^{37}Ar background activity concentration on the other hand is of the same order of magnitude as the MDC associated with the MARDS system (less than 0.1 mBq-m^{-3}) [137, 139]. It does seem entirely possible that ^{37}Ar resulting from cosmic neutron-induced activation of ^{40}Ca in seawater could contribute meaningful counts to radioargon measurements made near the sea.

Table 3.11: CTBT-relevant radioactive noble gas background activity concentrations at a depth of 5 m in seawater.

CTBT-Relevant Radionuclide	Background Activity Concentration [mBq-m^{-3}]
^{37}Ar	3.02×10^{-1}
^{131m}Xe	5.35×10^{-9}
^{133m}Xe	2.48×10^{-8}
^{133}Xe	8.49×10^{-7}
^{135}Xe	8.32×10^{-7}

3.5.4 Sensitivity Studies

The objective of the sensitivity studies documented in this section was to evaluate the sensitivity of the CTBT-relevant radioactive particulate and noble gas background activity concentration estimates generated by the TeXAS application to changes in various inputs. All of the sensitivity studies documented here are evaluated as perturbations to the granite CTBT-relevant radioactive particulate and noble gas background activity concentration studies documented in Section 3.5.2. The results of several studies are presented.

The first study illustrates the sensitivity of the CTBT-relevant radioactive particulate and noble gas background activity concentration estimates to changes in the assumed granite composition. The constituents considered here were thorium, uranium, SiO_2, and K_2O. Thorium and uranium were selected for the study because they spontaneously fission and they may be made to fission by cosmic neutrons; and thus modifying their concentrations should be expected to produced noticeable changes in the CTBT-relevant radioactive particulate and noble gas background activity concentration estimates generated by the TeXAS application.SiO_2 and K_2O were selected for the study because they represent two major constituents of granite, as illustrated in Table 3.9.

The second sensitivity study investigates the sensitivity of the granite CTBT-relevant radioactive particulate and noble gas background concentration estimates to the material used to fill the porosity voids in the granite. The granite study conducted in Section 3.5.2 assume the granite porosity voids are filled with atmospheric air; the sensitivity study documented here replaces the atmospheric air with water.

An additional sensitivity study is conducted to gauge the sensitivity of the CTBT-relevant radioactive noble gas and background activity concentration estimates to the nuclear data utilized by the Monte Carlo N-Particle (MCNP) radiation transport code. Recall that the studies documented in Section 3.5.2 use temperature-corrected, study-specific nuclear data processed by the TeXAS application and passed to MCNP as described in Section E.3 of Appendix E. The study conducted here does not use study-specific nuclear data; instead, it relies solely on the nuclear data packaged with MCNP.

The results of the granite composition sensitivity studies are presented in Figures 3.52 through 3.59. The first pair of figures illustrates the sensitivity of the CTBT-relevant radioactive particulate and noble gas background activity concentrations to changes in thorium content. Figures 3.52 and 3.53 illustrate that the CTBT-relevant radioactive particulate and noble gas background activity concentrations in granite are relatively unaffected by a 20 % change in the assumed thorium content in either direction. Technically, both Figures 3.52 and 3.53 do show slight changes in the CTBT-relevant radioactive particulate and noble gas background activity concentrations, but most of the changes are 2-3 %; given that the variances associated with the MCNP tallies used to evaluate the background activity concentrations are also in the 2-3 % range, the changes in the background activity concentrations cannot be considered significant.

Figures 3.54 and 3.55 on the other hand show that the CTBT-relevant radioactive particulate and noble gas background activity concentrations in granite are strongly affected by changes in uranium content. Figure 3.54 indicates that increasing the uranium content of granite by 20 % increases the CTBT-relevant radioactive particulates and

noble gas background activity concentrations associated with the radioactive particulates and noble gases of interest by roughly 16-18 %. Given that the variances associated with the tallies used to support these evaluations were all on the order of 1-2 %, a 16-18 % increase in the radioactive particulates and noble gas background activity concentrations is significant.

Similarly, Figure 3.55 indicates that decreasing the uranium content of granite by 20 % decreases the CTBT-relevant radioactive particulates and noble gas background activity concentrations associated with the radioactive particulates and noble gases of interest by more than 30 % in many cases. Given that the variances associated with the tallies used to support these evaluations were all on the order of 1-2 %, a 30 % decrease in the radioactive particulates and noble gas background activity concentrations is significant.

The results of the sensitivity study for which the porosity voids were filled with water as opposed to atmospheric air are presented in Figure 3.56. The results of this study indicate that the CTBT-relevant radioactive particulate and noble gas background activity concentrations increase slightly when the porosity voids are filled with water as opposed to atmospheric air. However, as is the case with many of the sensitivity studies reported above, the changes in the background activity concentrations are of the same order as the variances associated with the MCNP tallies used to evaluate the background activity concentrations, so changes may not be viewed as statistically significant.

The results generated by the final sensitivity study, the nuclear data sensitivity study, are presented in Figure 3.57. These studies indicate that using the nuclear data that

comes packaged with MCNP as opposed to the temperature-corrected, study-specific nuclear data processed by the TeXAS application causes the CTBT-relevant radioactive particulate and noble gas background activity concentration estimates to decrease by 2-4 %. The variances associated with the MCNP tallies used to evaluate were in the range of 1-2 %, again, so the decreases in the CTBT-relevant radioactive noble gases resulting from the use of basic nuclear data appear to be significant.

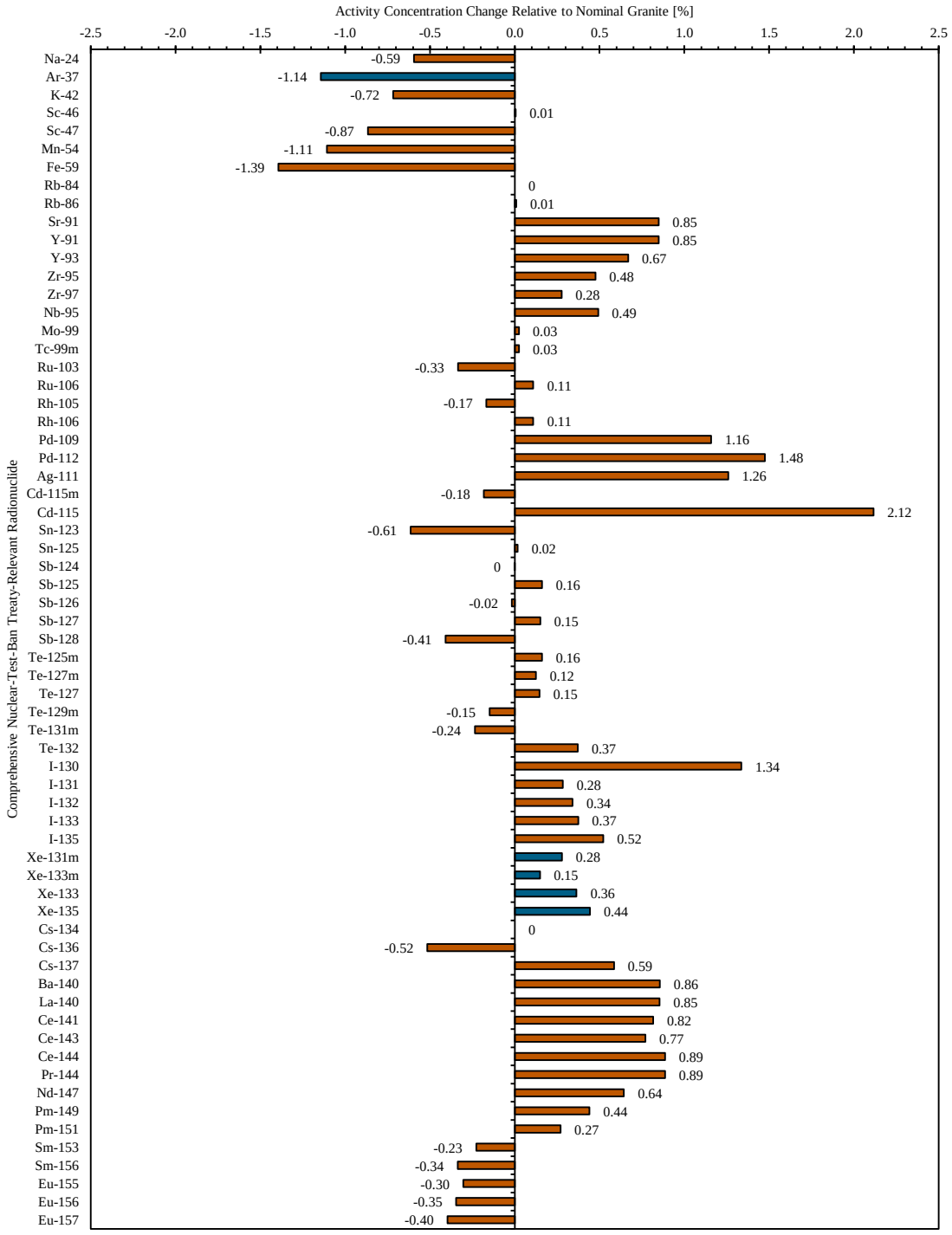

Figure 3.52: CTBT-relevant radioactive particulate and noble gas background activity concentration estimates in granite with a 20 % thorium surplus.

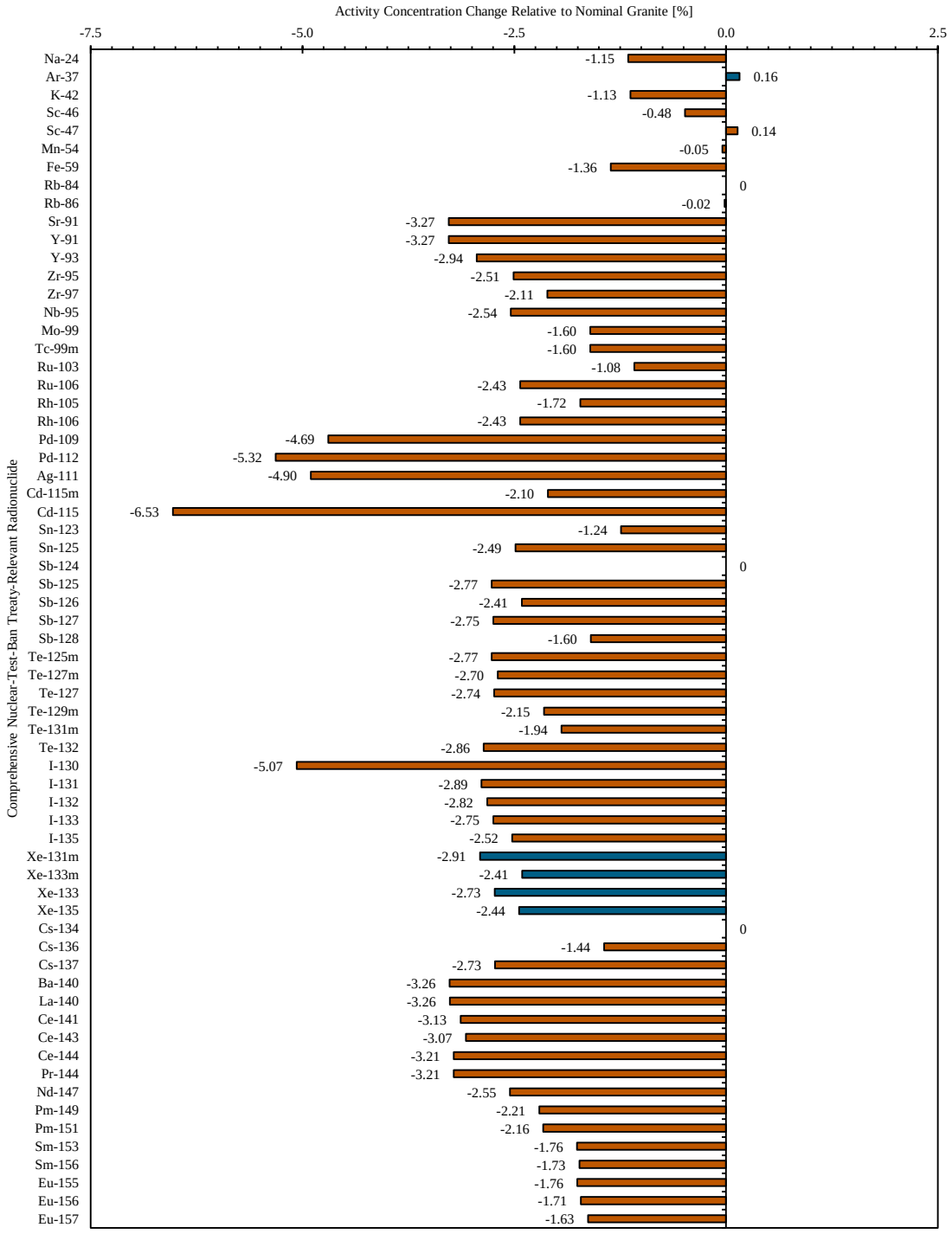

Figure 3.53: CTBT-relevant radioactive particulate and noble gas background activity concentration estimates in granite with a 20 % thorium deficiency.

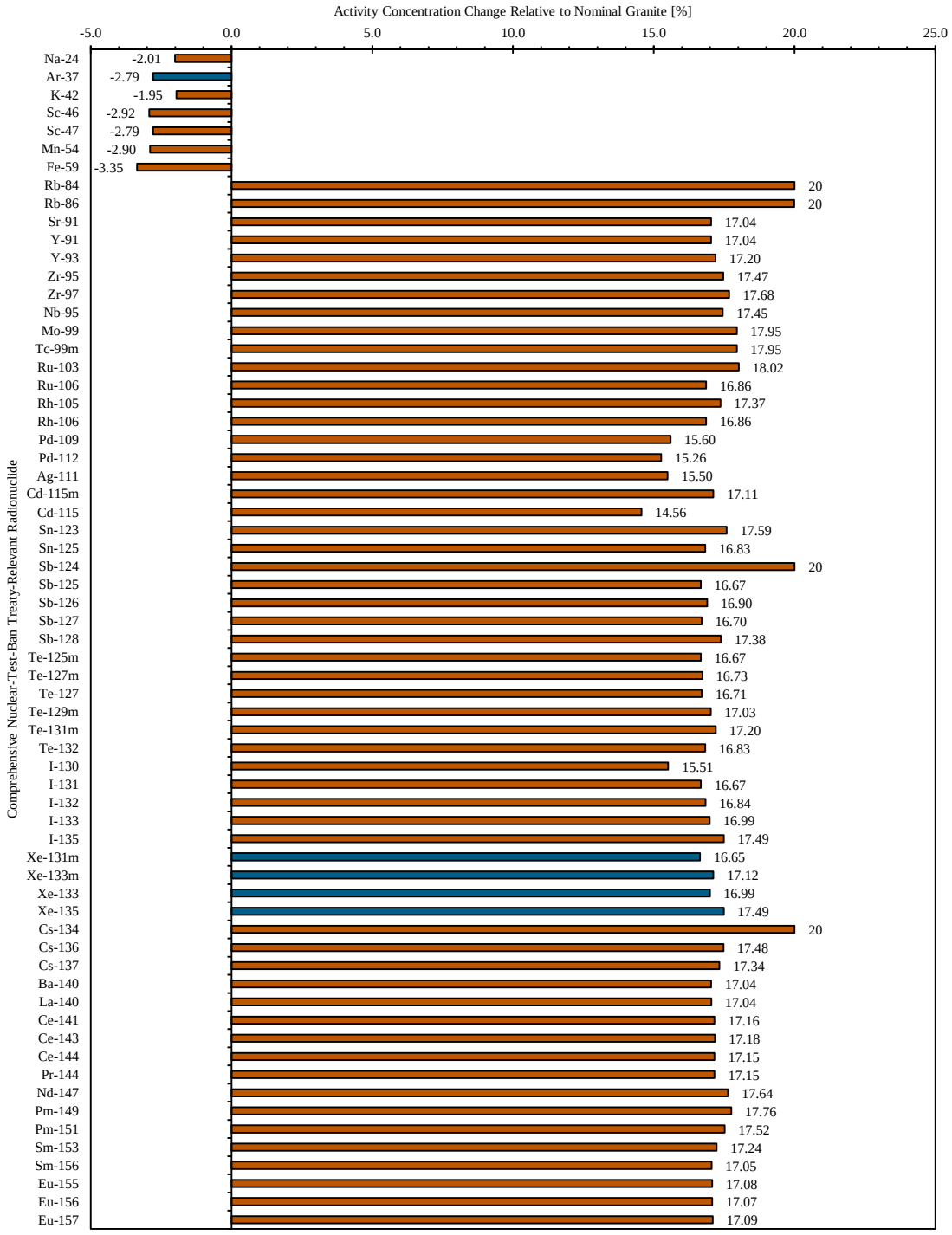

Figure 3.54: CTBT-relevant radioactive particulate and noble gas background activity concentration estimates in granite with a 20 % uranium surplus.

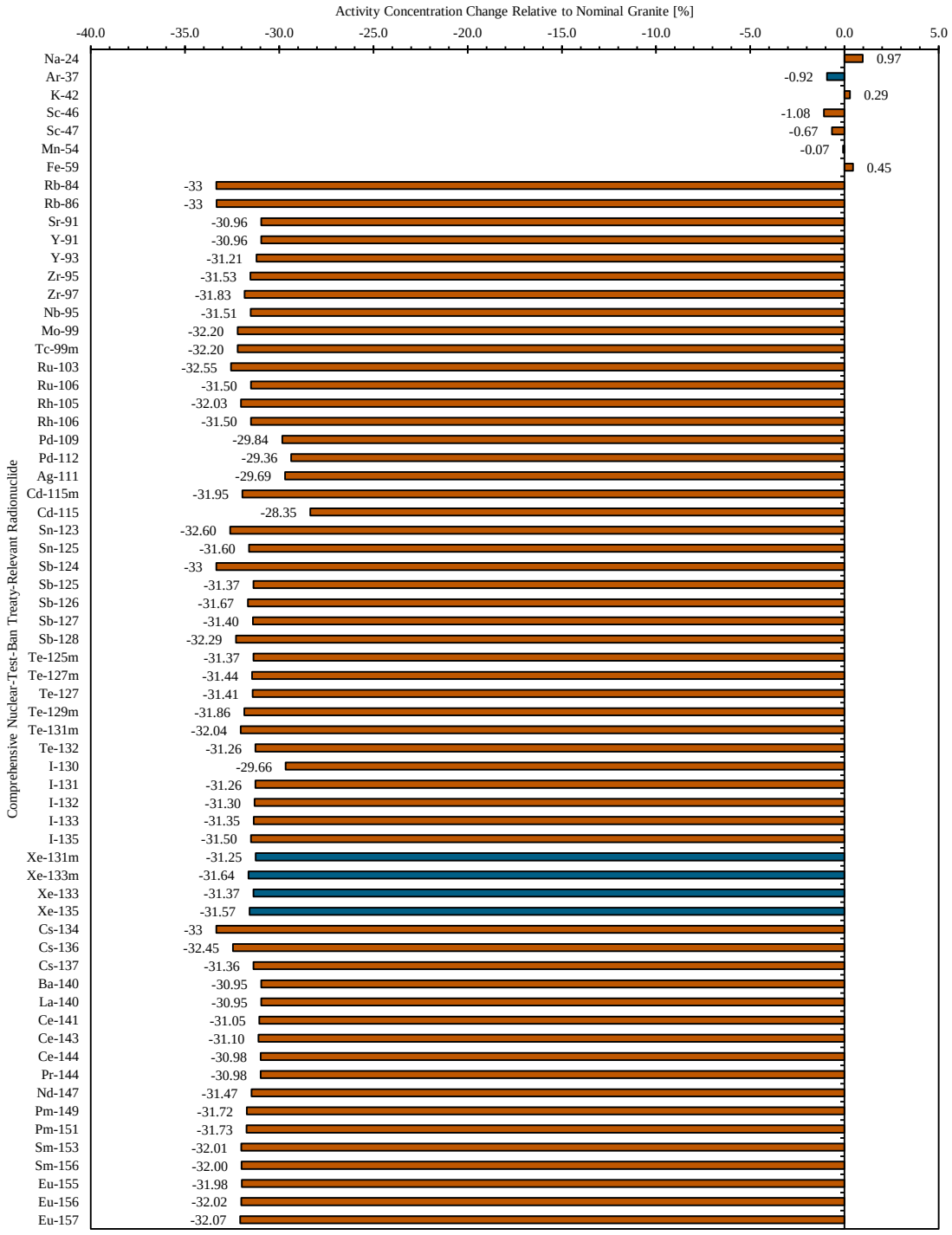

Figure 3.55: CTBT-relevant radioactive particulate and noble gas background activity concentration estimates in granite with a 20 % uranium deficiency.

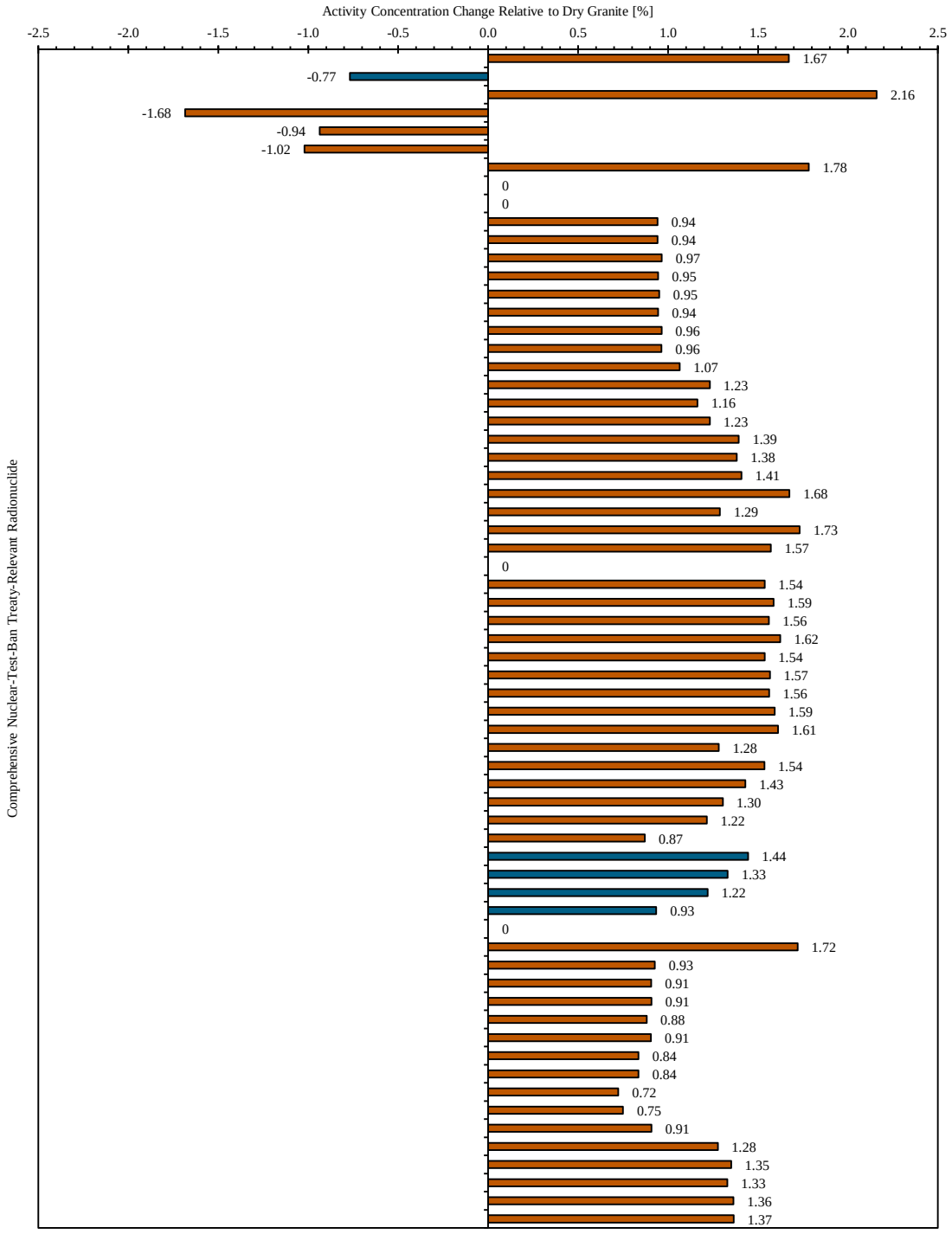

Figure 3.56: CTBT-relevant radioactive particulate and noble gas background activity concentration estimates in granite with water-filled porosity voids.

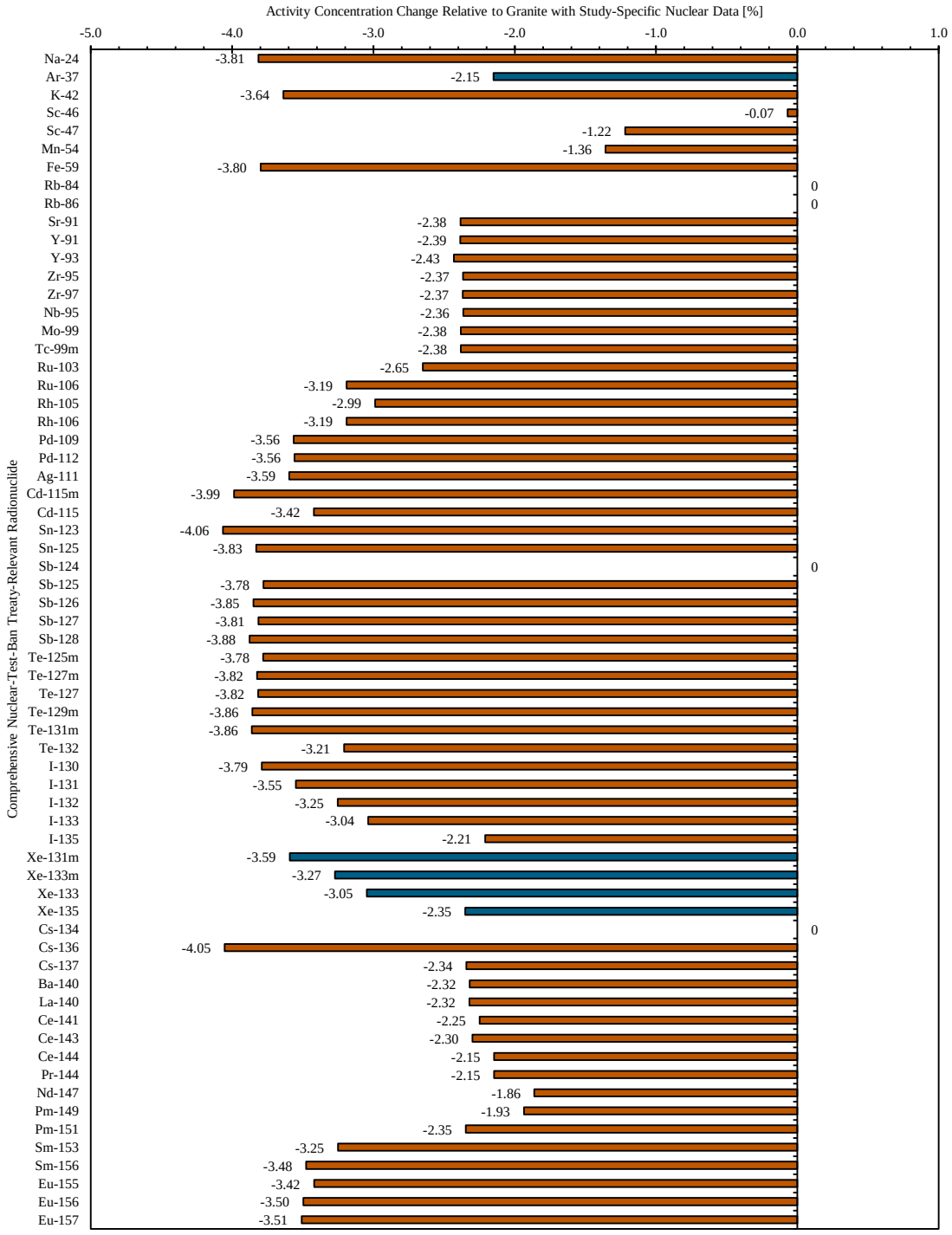

Figure 3.57: CTBT-relevant radioactive particulate and noble gas background activity concentration estimates in granite with basic nuclear data.

3.6 Final Conclusions Regarding CTBT-Relevant Radionuclide Background Activity Concentrations Resulting from Natural Processes

This chapter documents a series of studies conducted to evaluate background activity concentrations associated with 100 CTBT-relevant radioactive particulates and noble gases in the Earth's atmosphere, in several different geologies, and in seawater. The CTBT-relevant radioactive particulates and noble gases of interest are identified in Tables 3.1 and 3.2.

In order to develop the CTBT-relevant radioactive particulate and noble gas background activity concentration estimates documented herein, a set of MATLAB code modules, referred to herein as the Terrestrial Xenon and Argon Simulator (TeXAS) application, was developed. The CTBT-relevant radioactive particulate and noble gas background activity concentration estimates developed by the TeXAS application account for production via three natural processes: (1) spontaneous fission, (2) cosmic neutron induced fission, and (3) cosmic neutron induced activation. The TeXAS application accounts for the loss of radioactive particulates and noble gases via radioactive decay. Note that the TeXAS application does not make any attempt to account for the physical movement or loss of radioactive particulates or noble gases resulting from transport processes, and thus the CTBT-relevant radioactive particulate and noble gas background activity concentration estimates reported herein should be viewed as nominal upper limits.

In this chapter, the TeXAS application was used to generate CTBT-relevant radioactive particulate and noble gas background activity concentration estimates for three layers of the Earth's atmosphere, six different geologies, and seawater. The first set of studies, the atmospheric studies, generated CTBT-relevant radioactive noble gas background activity concentrations resulting from cosmic neutron-induced activation of various constituents of the Earth's atmosphere at geometric heights of 50,000 m, 15,000 m, and 1 m above the Earth's surface. The results of these studies are presented in Figure 3.9. Of the three geometric heights considered here, the radioactive noble gas background activity concentrations were highest in the atmospheric layer centered at a geometric height of 15,000 m. However, even at 15,000 m the CTBT-relevant background activity concentrations are only expected to be on the order of 10^{-5} mBq-m^{-3}, which is well short of the 0.1 mBq-m^{-3} Minimum Detectable Concentration associated with the CTBT monitoring stations. Section 3.5.1.4, which presents the CTBT-relevant radioactive noble gas background activity concentrations for each of the atmospheric layers also provides some information regarding the production mechanisms that are most important in terms of generating the radioactive noble gases of interest in the atmosphere. For ^{133}Xe and ^{135}Xe the processes of most important were found to be radiative capture and (n,2n) reactions, with radiative capture becoming increasingly more important with decreasing geometric height.

The cosmic neutron flux profiles and the atmospheric constituents most responsible for attenuating the cosmic neutron flux at each of the aforementioned geometric heights were also discussed. The cosmic neutron flux was found to peak at a

geometric height of 15,000, and the most important atmospheric constituents in terms of attenuating the cosmic neutron flux were found to be ^{14}N and ^{16}O.

The geological studies, documented in Section 3.5.2, describe the CTBT-relevant radioactive particulate and noble gas background activity concentrations resulting from spontaneous fission, cosmic neutron-induced fission, and cosmic neutron-induced activation of various geological constituents as a function of depth in three different igneous geologies and three different sedimentary geologies. The igneous geologies considered are a granite geology, a basalt geology, and a granodiorite geology. The sedimentary geologies considered are a shale geology, a sandstone geology, and a limestone geology. These geologies were selected based on their prevalence in the Earth's upper crust.

For each of the aforementioned geologies, background activity concentrations were evaluated for each of the 100 radionuclides identified as relevant to the CTBT [116]. The CTBT-relevant radioactive particulates and noble gases for which the activities were found to be nonzero are presented in Figures 3.31 through 3.42. The ^{133m}Xe, ^{133}Xe, and ^{135}Xe background activity concentrations were found to be comparable to their respective SAUNA system MDCs. The 131mXe background activity concentration was found to be roughly an order of magnitude lower than the SAUAN system ^{131m}Xe MDC. These results indicate that when radioxenon background activity concentrations resulting from natural processes are near their nominal upper limits, perhaps in situations where loses due to gas transport processes are minimal) it might be possible to detect them with CTBT radionuclide monitoring systems.

As with the atmospheric studies, the cosmic neutron flux profiles and the geological constituents most responsible for attenuating the cosmic neutron flux in each of the aforementioned geologies were also studied. Interestingly, in all six of the geologies considered here, 50 % or more of the cosmic neutron flux was found to be attenuated by just three nuclides. furthermore, the nuclides were mostly the same across all six geologies. This is somewhat remarkable given the geologies are composed of more than 70 nuclides.

The seawater studies, documented in Section 3.5.3, describe the CTBT-relevant radioactive noble gas background activity concentrations resulting from spontaneous fission, cosmic neutron-induced fission, and cosmic neutron-induced activation at a depth of 5 m in seawater. The primary focus of the seawater studies is on the background activity concentrations associated with the radioactive noble gases of most interest to the verification regime of the CTBT—^{37}Ar, ^{131m}Xe, ^{133m}Xe, ^{133}Xe, and ^{135}Xe. The radioxenon background activity concentrations at a depth of 5 m in seawater were found to be several orders of magnitude less than their respective SAUNA system [157] MDCs.

Chapter 4: Conclusions and Closing Remarks

The objective of the research efforts documented in this dissertation was to advance the state-of-the-art radionuclide monitoring technologies used to detect indications of nuclear explosions, which are absolutely prohibited by the Comprehensive Nuclear-Test-Ban Treaty (CTBT). The research efforts documented herein have produced advancements in two areas. The first advancement is in the characterization and optimization of a Si-PIN diode-based radiation spectrometer prototype. The second advancement is in the development of a Terrestrial Xenon and Argon Simulator (TeXAS) application capable of estimating background activity concentrations resulting from natural processes for every radionuclide identified as relevant to the CTBT on a site-specific basis. The details associated with the efforts supporting these advancements are documented in Chapters 2 and 3 and in Appendix E.

This chapter serves to review and summarize the results and significance of the aforementioned advancements. Section 4.1 discusses the results and significance of the Si-PIN diode-based radiation spectrometer prototype characterization and optimization advancements and Section 4.2 reviews the results and significance of the CTBT-relevant radionuclide background activity concentration studies conducted using the TeXAS

application. And finally, the last section of this chapter, Section 4.3, places the results of the CTBT-relevant radionuclide background activity concentration studies in the context of the Si-PIN diode-based spectrometer advancements.

4.1 Review of Si-PIN Diode Spectrometer Prototype Characterization and Optimization Study Results

The Si-PIN diode spectrometer prototype characterization and optimization studies were carried out using a Si-PIN diode spectrometer prototype developed by XIA LLC [66, 67, 68]. As discussed in Section 2.1.2, the XIA LLC Si-PIN diode spectrometer prototype is essentially a small, thermoelectrically cooled copper chamber with one small 0.25 cm^2 Si-PIN diode affixed to its front face and a second small 0.25 cm^2 Si-PIN diode affixed to its back face. The Si-PIN diodes are sensitive to both photons and conversion electrons. The interior of the copper chamber between the two Si-PIN diodes has a volume of about 1.02 cm^3. Gaseous samples may be introduced to this volume via a 1/16 in (0.16 cm) outer diameter stainless steel fill line that penetrates the right side of the copper chamber.

Four radioxenon gas sample spectra and eight calibration source spectra were acquired and analyzed in support of the XIA LLC Si-PIN diode spectrometer prototype characterization effort, which generated linearity, resolution, and detection efficiency calibration curves specific to the XIA LLC Si-PIN diode spectrometer prototype. A single linearity calibration curve was found to be sufficient to define both the photon and conversion electron energy calibrations. The photon resolution of the XIA LLC

Si-PIN diode spectrometer prototype was found to be about 0.66 ± 0.10 keV Full Width Half Maximum (FWHM) at photon energies near 30 keV. This is a significant reduction relative to the photon resolutions typically associated with High-Purity Ge (HPGe) spectrometers which tend to have FWHM on the order of about 1.50 ± 0.12 keV at photon energies near 30 keV. Conversion electron peak widths were found to be about 1.37 ± 0.37 keV at conversion electron energies near 150 keV. It is also important to note that the radioxenon conversion electron peaks most important in the context of the CTBT are all separated by several FWHM so that there are no interferences amongst the peaks. Absolute photon and conversion electron detection efficiencies were found to be about 0.48 ± 0.05 % and 2.6 ± 0.2 %, respectively at photon and conversion electron energies near 30 keV and 150 keV.

The absolute conversion electron detection efficiency characterization was used to evaluate the ^{131m}Xe, ^{133m}Xe, ^{133}Xe, and ^{135}Xe Minimum Detectable Concentrations (MDCs) associated with the XIA LLC Si-PIN diode spectrometer prototype. The ^{131m}Xe, ^{133m}Xe, ^{133}Xe, and ^{135}Xe MDCs associated with the XIA LLC Si-PIN diode spectrometer prototype were found to be 1.7, 2.0, 2.1, and 56 mBq-m^{-3}, respectively. With the exception of the ^{135}Xe MDC, these MDCs are all fairly comparable to the radioxenon MDCs associated with the ARIX [52], ARSA [54], SAUNA [57], and SPALAX [58] systems currently employed by the verification regime of the CTBT.

Upon completion of the XIA LLC Si-PIN diode spectrometer characterization effort, a number of Si-PIN diode spectrometer optimization studies were conducted. These studies were carried out using a number of Si-PIN diode spectrometer Monte Carlo

N-Particle (MCNP) [74, 75, 76, 77] models developed as described in Section 2.3. The first optimization studies investigated Si-PIN diode spectrometer performance improvements that might be achieved by making simple changes to the geometry of the XIA LLC Si-PIN diode spectrometer prototype. For these studies only the dimensions of the copper spectrometer chamber were altered; the Si-PIN diode dimensions were left unchanged. Subsequent studies investigated performance improvements that might be achieved if larger, thicker Si-PIN diodes are made available. Additional studies were conducted to evaluate the sensitivity of Si-PIN diode spectrometer performance to changes in radioxenon fill pressure. The results of the Si-PIN diode spectrometer optimization studies are summarized in Figure 4.1.

As illustrated by Figure 4.1, the radioxenon MDCs associated with a Si-PIN diode spectrometer design with a thin, 0.3 cm thick rectangular spectrometer chamber were roughly 43 % smaller than the radioxenon MDCs associated with the XIA LLC Si-PIN diode spectrometer prototype. Switching to a thin, 0.3 cm thick cylindrical spectrometer chamber reduced the radioxenon MDCs by an additional 51 % relative to the MDCs associated with the thin rectangular Si-PIN diode spectrometer design.

Additional radioxenon MDC reductions were achieved using larger Si-PIN diodes. Coupling the large area Si-PIN diodes with a thin cylindrical spectrometer chamber reduced the ^{131m}Xe, ^{133m}Xe, ^{133}Xe, and ^{135}Xe MDCs to 0.31, 0.37, 0.37, and 10 mBq-m^{-3}, respectively. Increasing the thickness of the Si-PIN diodes by a factor of two produced fairly significant increases in absolute photon detection efficiency (about 62 %), but essentially no changes in absolute conversion electron detection efficiency.

These small changes in absolute conversion electron detection efficiency produced only very slight radioxenon MDC reductions. This indicates that there is little to be gained by developing thicker Si-PIN diodes.

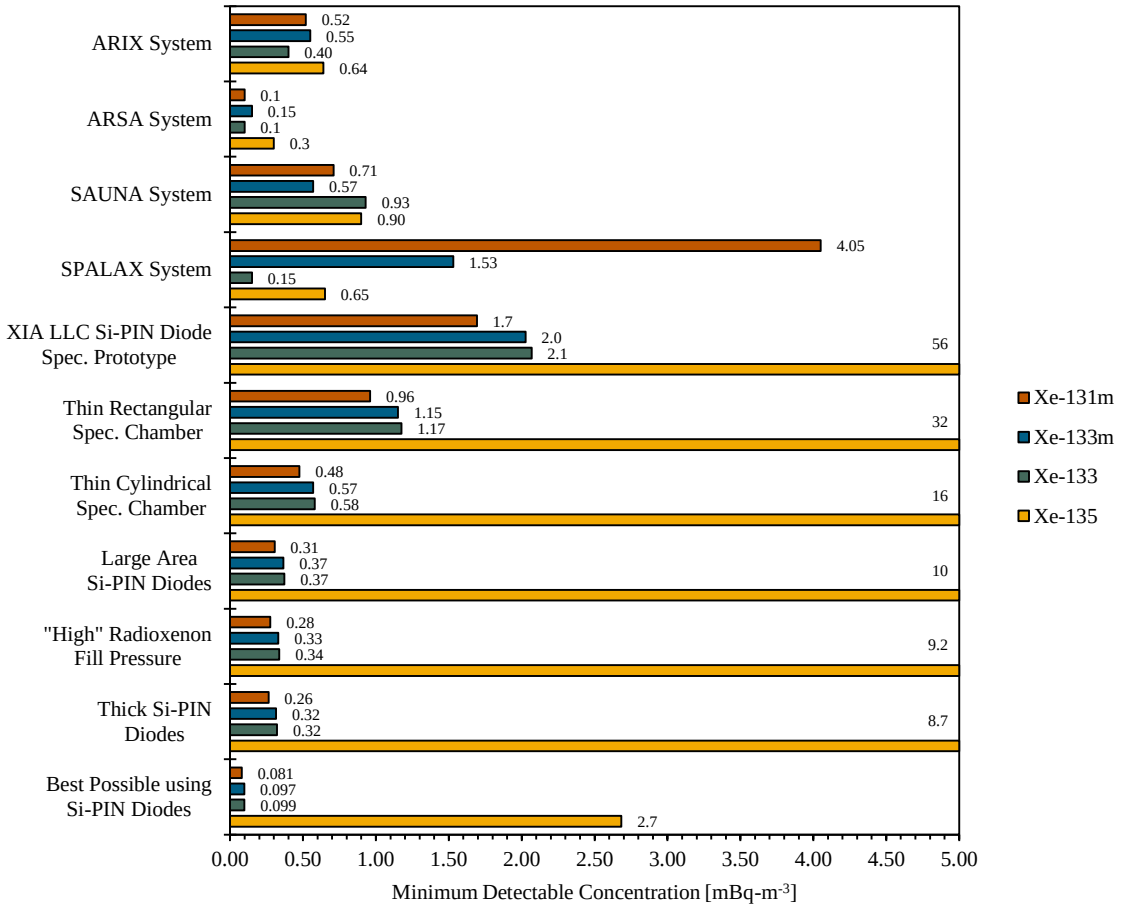

Figure 4.1: Si-PIN diode spectrometer Minimum Detectable Concentration (MDC) comparisons.

Ultimately, the Si-PIN diode spectrometer optimization studies produced a Si-PIN diode spectrometer design utilizing large area Si-PIN diodes and a thin cylindrical spectrometer chamber. The absolute 150 keV conversion electron detection efficiency associated with this design is expected to be about 14 %, which is roughly 450 % larger than the absolute 150 keV conversion electron detection efficiency associated with the XIA LLC Si-PIN diode spectrometer prototype. The radioxenon MDCs associated with this optimized Si-PIN diode spectrometer design are expected to be about 82 % lower than the radioxenon MDCs associated with the XIA LLC Si-PIN diode spectrometer prototype and very competitive with the radioxenon MDCs associated with the ARIX [52], ARSA [54], SAUNA [57], and SPALAX [58] systems currently employed by the verification regime of the CTBT. However, the fact that the best possible radioxenon MDCs are still about 73 % smaller than the radioxenon MDCs associated with the large area Si-PIN diode spectrometer design produced here indicates that additional design modifications could lead to additional performance improvements.

4.2 Review of the TeXAS Application and the CTBT-Relevant Radionuclide Background Activity Concentration Study Results

A set of MATLAB [140] code modules, referred to herein as the Terrestrial Xenon and Argon Simulator (TeXAS) application, was developed to support the generation of high-fidelity, site-specific background activity concentration estimates for 100 radioactive particulates and noble gases identified as relevant to the verification regime of the CTBT. The background activity concentration estimates generated by the

TeXAS application account for production via three natural processes—(1) spontaneous fission, (2) cosmic neutron induced fission, and (3) cosmic neutron induced activation—and for loses via radioactive decay. Note that the TeXAS application does not make any attempt to account for the physical movement or loss of radioactive particulates or noble gases resulting from transport processes, and thus the background activity concentration estimates generated by the TeXAS application should be viewed as nominal upper limits.

As described in Appendix E, the TeXAS application supports the generation of CTBT-relevant radioactive particulate and noble gas background activity concentration estimates by: (1) automating and streamlining the process of developing high-fidelity material composition and temperature data, (2) incorporating the data into MCNP radiation transport code [74, 75, 76, 77] models, (3) collecting and processing the best-available nuclear data required to support the MCNP models, and (4) post-processing the outputs generated by the MCNP models and evaluating the radioactive particulate and noble gas background activity concentration estimates. Perhaps most importantly, the TeXAS application was designed to do all of these things automatically so that users of the TeXAS application are not encumbered with the details of these processes, but rather are left free to focus on the development of the inputs to and the interpretation of the results produced by the studies they conduct.

The TeXAS application was used to conduct several CTBT-relevant radionuclide background activity concentration studies. The atmospheric studies evaluated the CTBT relevant radioactive noble gas background activity concentrations specific to three different layers of the Earth's atmosphere. Of the three atmospheric layers studied, the

^{131m}Xe, ^{133m}Xe, ^{133}Xe, and ^{135}Xe background concentrations were found to be the highest in the layer at 15,000 m. That said, the background activity concentrations in this layer—1.1×10^{-5}, 4.6×10^{-5}, 5.6×10^{-5}, and 1.2×10^{-5} mBq-m^{-3}—were all still well below their respective SAUNA system MDCs.

The cosmic neutron flux profiles and the atmospheric constituents most responsible for attenuating the cosmic neutron flux at each of the aforementioned geometric heights in the Earth's atmosphere were also evaluated in Chapter 3. The cosmic neutron flux was found to peak at a geometric height of 15,000 m and the most important atmospheric constituents in terms of attenuating the cosmic neutron flux were found to be ^{14}N and ^{16}O.

The geological studies, documented in Section 3.5.2, describe the CTBT-relevant radioactive particulate and noble gas background activity concentrations resulting from spontaneous fission, cosmic neutron-induced fission, and cosmic neutron-induced activation of various geological constituents as a function of depth in three different igneous geologies and three different sedimentary geologies. The igneous geologies considered are a granite geology, a basalt geology, and a granodiorite geology. The sedimentary geologies considered are a shale geology, a sandstone geology, and a limestone geology. For each of the aforementioned geologies, background activity concentrations were evaluated for each of the 100 radionuclides identified as relevant to the CTBT. The nominal upper limit on the ^{131m}Xe background activity concentration was found to be roughly two orders of magnitude lower than the SAUNA system ^{131m}Xe MDC. The nominal upper limits on the ^{133m}Xe, ^{133}Xe, and ^{135}Xe background

activity concentrations however found to be comparable to the SAUNA system ^{133m}Xe, ^{133}Xe, and ^{135}Xe MDCs. While loses due to transport would reduce radioxenon background activity concentrations somewhat, these results indicate that it might be possible to detect radioxenon resulting from natural processes using CTBT radionuclide monitoring systems.

As with the atmospheric studies, the cosmic neutron flux profiles and the geological constituents most responsible for attenuating the cosmic neutron flux in each of the aforementioned geologies were also studied. Interestingly, in all six of the geologies considered here, 50 % or more of the cosmic neutron flux was found to be attenuated by just three nuclides. Furthermore, the nuclides were mostly the same across all six geologies. This is somewhat remarkable given the geologies are composed of more than 70 nuclides.

The seawater studies, documented in Section 3.5.3, describe the CTBT-relevant radioactive noble gas background activity concentrations resulting from spontaneous fission, cosmic neutron-induced fission, and cosmic neutron-induced activation at a depth of 5 m in seawater. The primary focus of the seawater studies is on the background activity concentrations associated with the radioactive noble gases of most interest to the verification regime of the CTBT—^{37}Ar, ^{131m}Xe, ^{133m}Xe, ^{133}Xe, and ^{135}Xe. The radioxenon background activity concentrations at a depth of 5 m in seawater were found to be several orders of magnitude less than their respective SAUNA system [57] MDCs.

4.3 Closing Remarks

We will close by tying together the results generated by each of the two halves of this dissertation. As noted in the introductory section to this dissertation, the objective of the research efforts documented here was to advance the state-of-the-art radionuclide monitoring technologies used to detect indications of nuclear explosions, which are absolutely prohibited by the CTBT. Advancements have been made in two areas. One advancement is in the characterization and optimization of a Si-PIN diode-based radiation spectrometer prototype. The second advancement is in the development of the TeXAS application, which may be used to develop background activity concentration estimates for all 100 radionuclides identified as relevant to the CTBT.

The question now becomes whether the CTBT-relevant radioactive noble gas background activity concentration estimates developed using the TeXAS application in Chapter 3, which are below the MDCs associated with the ARIX [52], ARSA [54], SAUNA [57], and SPALAX [58] systems, might be detected using an optimized Si-PIN diode-based spectrometer, which are shown to have the potential to outperform the monitoring systems currently employed by the verification regime of the CTBT.

The ^{131m}Xe, ^{133m}Xe, ^{133}Xe, and ^{135}Xe background activity concentration estimates developed for granite, basalt, granodiorite, shale, sandstone, and limestone are plotted in Figures 4.2 through 4.5 along with the MDCs of the SAUNA system, the XIA LLC Si-PIN diode-based spectrometer prototype, and an optimized XIA LLC Si-PIN diode-based spectrometer. These figures reiterate the fact that the ^{131m}Xe, ^{133m}Xe, and ^{133}Xe MDCs associated with the XIA LLC Si-PIN diode-based spectrometer prototype are all

slightly larger than the MDCs associated with the SAUNA system [57]. However, the ^{131m}Xe, ^{133m}Xe, and ^{133}Xe MDCs associated with the optimized Si-PIN diode-based spectrometer design are roughly an order of magnitude lower than the MDCs associated with the SAUNA system. This indicates that optimized Si-PIN diode-based spectrometers have the potential to outperform the monitoring systems currently employed by the verification regime of the CTBT. And finally, Figures 4.2 through 4.5 also highlight the fact that the radioxenon background activity concentrations resulting from natural processes might be detectable by CTBT radionuclide monitoring systems under certain circumstances where the background activity concentrations approach the nominal upper limits reported here.

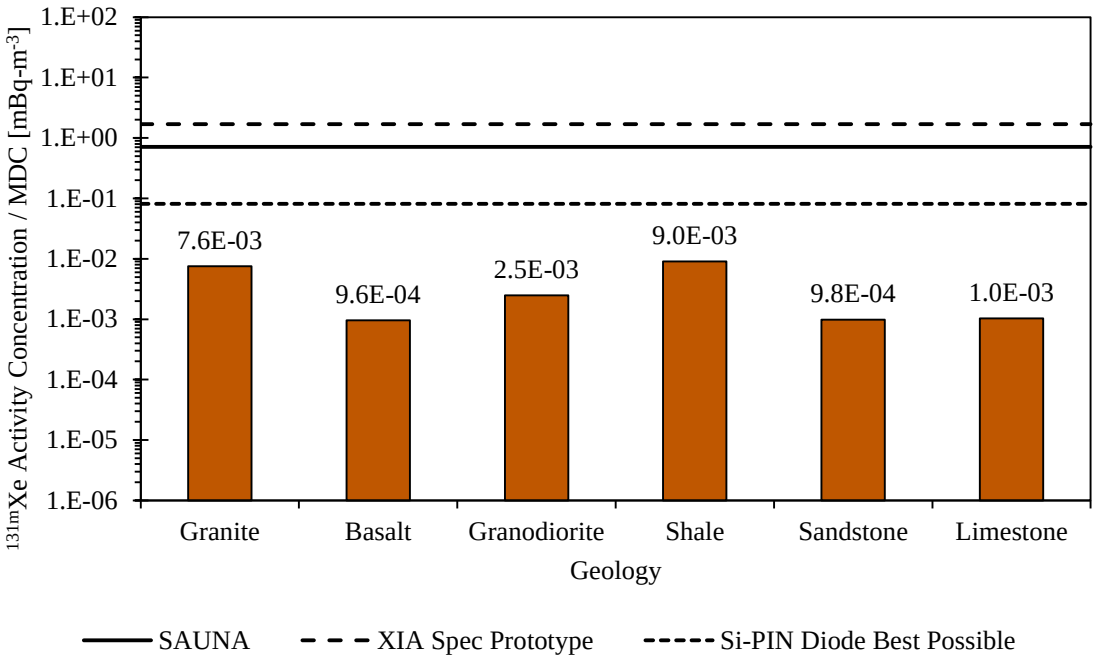

Figure 4.2: ^{131m}Xe background activity conc. resulting from natural processes in six geologies relative to SAUNA system and Si-PIN diode-based spectrometer MDCs.

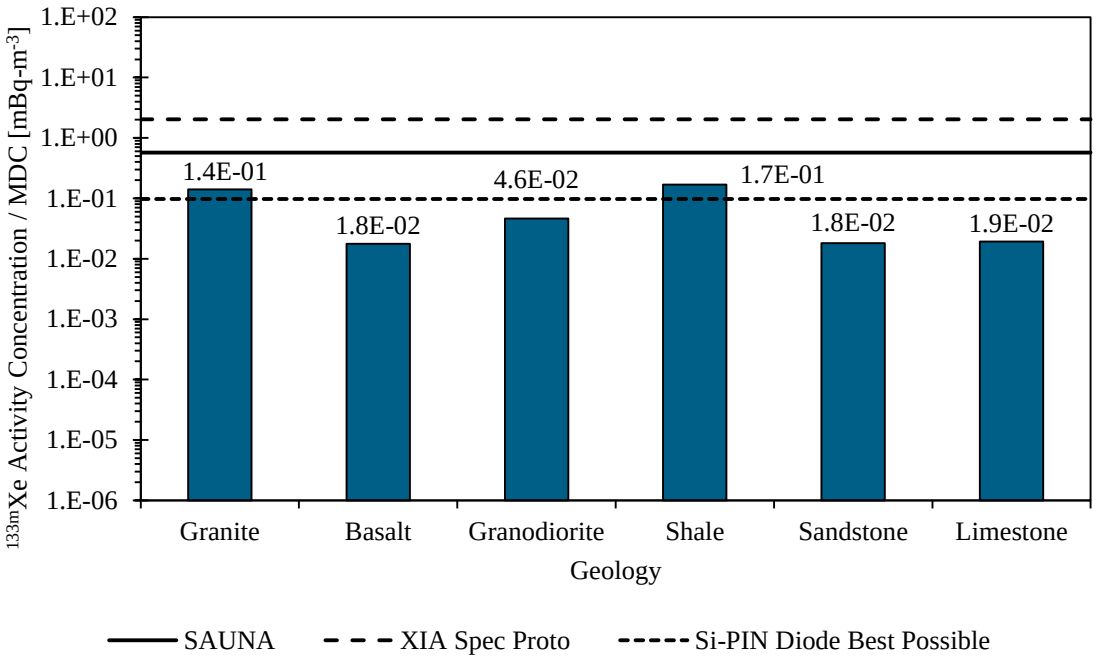

Figure 4.3: ^{133m}Xe background activity conc. resulting from natural processes in six geologies relative to SAUNA system and Si-PIN diode-based spectrometer MDCs.

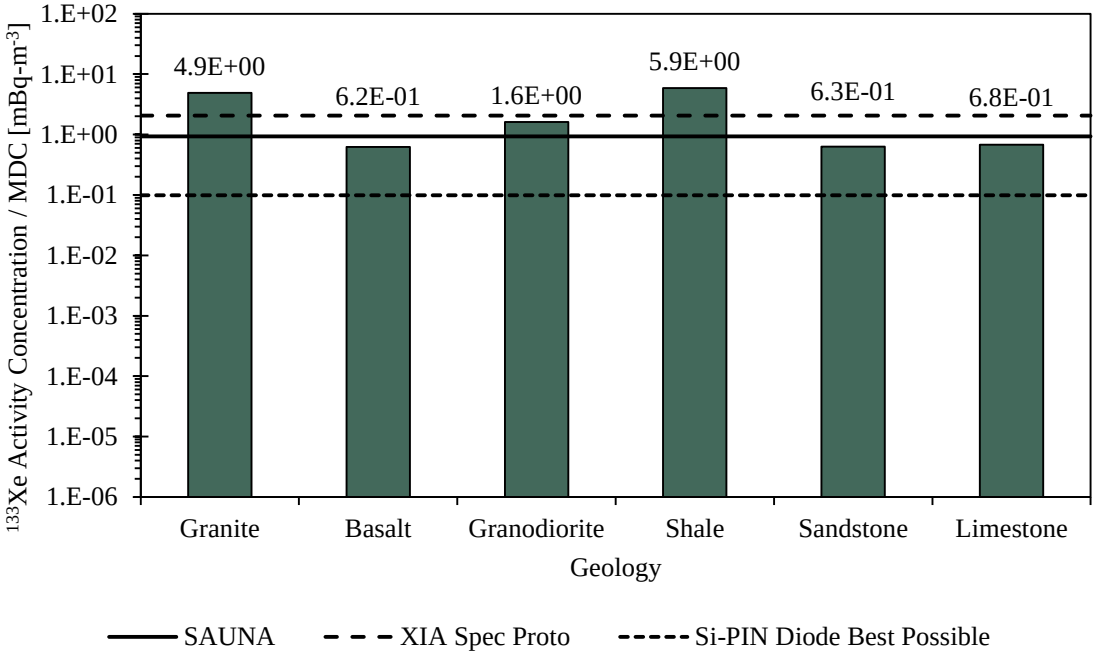

Figure 4.4: ^{133}Xe background activity conc. resulting from natural processes in six geologies relative to SAUNA system and Si-PIN diode-based spectrometer MDCs.

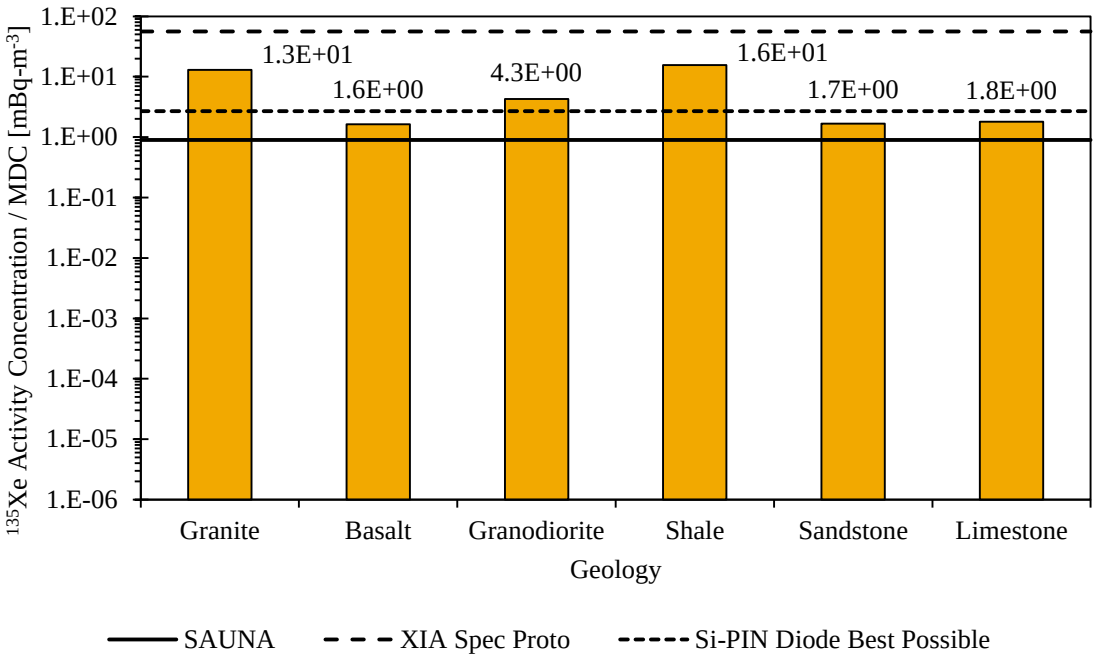

Figure 4.5: ^{135}Xe background activity conc. resulting from natural processes in six geologies relative to SAUNA system and Si-PIN diode based-spectrometer MDCs.

4.4 Future Work

There are a number of ways in which the research efforts documented in this dissertation should be continued in the future. First, a pair of 0.25 cm^2 Si-PIN diodes should be affixed to a prototype utilizing a thin cylindrical copper chamber having dimensions comparable to the thin cylindrical Si-PIN diode spectrometer design described in Section 2.3.3.2. This prototype should then be characterized in the same way the XIA LLC Si-PIN diode spectrometer was characterized in Section 2.2. Doing this would serve as a check against the theoretical detection efficiencies and MDCs reported for the thin cylindrical spectrometer design described in Section 2.3.3.2. Additionally, Si-PIN diodes having larger areas should be procured and affixed to thin cylindrical

copper chambers having dimensions comparable to the Si-PIN diode spectrometer designs described in Section 2.3.3.3. Again, doing this would serve as a check against the theoretical detection efficiencies and MDCs reported for the large area Si-PIN diode spectrometer design described in Section 2.3.3.3.

There are a number of ways in which the TeXAS application should be further improved, tested, and used to conduct additional background activity concentration studies as well. A graphical user interface should be developed to replace the formatted input files which are currently used to provide inputs to the TeXAS application. Replacing the formatted input files with a graphical user interface would make the TeXAS application easier to use. Additionally, the TeXAS application would probably be accessible to more users if it was written in an open source language such as Python. Rewriting the TeXAS application in another language would be a fairly significant undertaking and the effort to rewrite the code should only be expended if there is enough interest from a large enough pool of potential users.

The most interesting path forward in terms of conducting additional background characterization studies would probably involve a series of studies conducted in parallel with an experimental field measurement campaign. The idea here would be to develop detailed atmospheric and geological characterizations for a given site, to make radioxenon measurements at the site, and then develop MCNP models of the site to see how well the background activity concentration estimates generated by the TeXAS application align with the measured radioxenon concentrations.

Appendix A: The WiPFA Peak-Fitting Algorithm

This appendix documents the development of Wilson's Peak-Fitting Algorithm, referred to herein as the WiPFA peak-fitting algorithm. The WiPFA peak-fitting algorithm was originally developed to fit X-ray, gamma-ray, and conversion electron peaks in spectra acquired by a Si-PIN diode spectrometer prototype [67, 68] developed by XIA LLC [66]. In that particular application the objective was to use peak mean, peak width, and peak area estimates developed by fitting peaks in spectra acquired by the XIA LLC Si-PIN diode spectrometer prototype to support linearity, resolution, and detection efficiency characterizations applicable to the prototype.

However, the WiPFA peak-fitting algorithm was more-generally developed to be a robust, easy-to-use peak-fitting algorithm capable of fitting expressions to spectral data set Regions of Interest (ROIs) composed of any number of Gaussian-shaped peaks in a totally unconstrained manner. The WiPFA peak-fitting algorithm develops uncertainty estimates for each of its peak mean, width, and area estimates using an iterative Monte Carlo approach that utilizes the fact that the counts registered in the individual channels of spectra are all samples from Poisson distributions (radioactive decay is a binomial process to which the rules of Poisson statistics are applicable [69]). Additionally, the

WiPFA peak-fitting algorithm develops critical limits for each of the individual peaks in a given ROI in a manner consistent with the classic method originally prescribed by Currie [70].

A.1 Advantages of the WiPFA Peak-Fitting Algorithm

The WiPFA peak-fitting algorithm is a robust, easy-to-use peak-fitting algorithm with several advantages relative to other, existing peak-fitting algorithms. The first advantage of the WiPFA peak-fitting algorithm is that it develops peak mean, width, and area estimates for each of the peaks in a ROI in a totally unconstrained manner. Initial estimates at the peak mean, width, and area parameters associated with each of the peaks in an ROI are provided as inputs and then the WiPFA algorithm is free to vary all of the parameters simultaneously until an optimal set of peak parameters is identified. This is an advantage relative to other, existing peak-fitting algorithms that require the user to identify peak means manually and rely on existing resolution calibration information to determine the widths of peaks. These types of peak-fitting algorithms really only generate peak area estimates.

The second advantage of the WiPFA peak-fitting algorithm is that it develops uncertainty estimates for each of its peak mean, width, and area estimates. The uncertainty estimates are developed using an iterative Monte Carlo method that utilizes optimized peak parameter estimates generated not only for the nominal spectrum but also for thousands of supplemental spectra produced by sampling from the nominal spectrum. This method of evaluating the peak mean, width, and area estimate

uncertainties is powerful in that it accounts for the underlying uncertainty in the spectral data used to generate the peak parameter estimates—the uncertainty in the counts registered in each of the channels of the ROI.

Another advantage of the WiPFA peak-fitting algorithm is that it develops critical limits applicable to each of the individual peaks in an ROI in a manner consistent with the classic method originally prescribed by Currie [70]. The critical limits developed by Currie provide a means of determining if the counts accumulated in peaks in spectra are statistically distinguishable from background count levels. Procedurally speaking, a critical regarding the statistical significance of a peak is made by evaluating the mean background count level under the peak and its associated standard deviation and then determining if the number of counts accumulated in the peak exceeds the mean background count level by some predetermined number of background count level standard deviations. The WiPFA peak-fitting algorithm utilizes not only background count level standard deviation data but also interference peak standard deviation data produced to support peak area uncertainty evaluations to generate critical limits for each of the peaks in an ROI in a manner comparable to the classic method prescribed by Currie.

A.2 The Peak-Fitting Problem as an Optimization Problem

Spectra acquired by radiation spectrometers may be thought of as sets of paired observations of the form $(1, C_1), (2, C_2), (3, C_3), \ldots, (n-1, C_{n-1}), (n, C_n)$. The integer values 1 through n represent the channel numbers associated with a given spectrum, and

the C_1 through C_n values represent the number of counts registered in channels 1 through n of the spectrum. A portion of a ^{139}Ce spectrum is presented in Figure A.1. The portion of the spectrum presented in Figure A.1 represents a ROI in the spectrum in that it contains an obvious peak where registered ^{139}Ce Kα X-ray detections have produced counts in certain channels of the spectrum that exceed the background count levels on either side of the peak.

Notice that the shape of the ^{139}Ce peak shown in Figure A.1 strongly resembles a Gaussian distribution. Gaussian distributions typically describe the shapes of gamma-ray peaks in spectra acquired by modern radiation spectrometers quite well [99]. However, in some cases a Gaussian distribution may not, strictly speaking, be the most appropriate

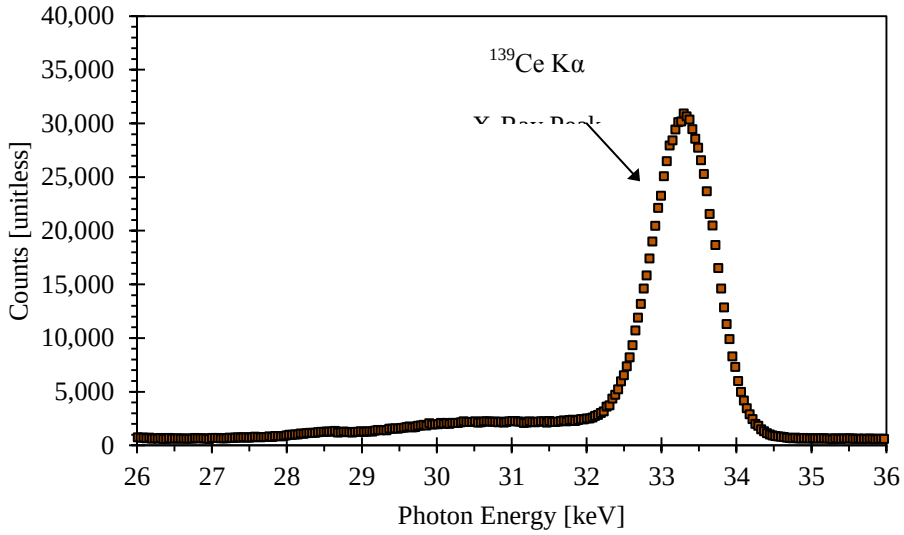

Figure A.1: A Region Of Interest (ROI) from a ^{139}Ce spectrum.

distribution to describe a peak. For example, peaks produced by low-energy X-rays are sometimes better described by Lorentz distributions [99]. In other cases a combination function might be the best choice to describe a peak in a spectral data set. The Voigt function, which is a convolution of a Gaussian distribution and a Lorentz distribution, is one example of a combination function sometimes used to describe peaks in spectral data sets [99]. In many cases, however, a Gaussian distribution may be used to describe a peak that would, strictly speaking, be better described by some other distribution without introducing an excessive amount of error into the peak analysis.

With this in mind, it must be noted that the WiPFA peak-fitting algorithm currently only supports fitting peaks that may be well described by Gaussian distributions. This limitation is based solely on time constraints encountered to date. The methodology employed by the WiPFA peak-fitting algorithm could be expanded to support fitting peaks described by other distributions as well in the near future. That being said, the remainder of the discussion presented here focuses on fitting peaks that may be well described by Gaussian distributions.

A Gaussian distribution is fully defined by three parameters: (1) The first of these parameters is a peak mean parameter, typically given the symbol μ. The peak mean parameter establishes the mean value, or the center of the peak, along the horizontal axis. (2) The second parameter that defines a Gaussian distribution is a standard deviation parameter, typically given the symbol σ. The standard deviation establishes the width of the peak. (3) The third and final parameter that defines a Gaussian distribution is an area

parameter, typically given the symbol A. The area parameter establishes the area underneath the peak.

All three of these Gaussian peak parameters are of interest when calibrating and operating radiation spectrometers: peak means extracted from spectral data sets are used to develop spectrometer linearity characterizations; peak standard deviations are used to develop spectrometer resolution calibration data; and, finally, peak areas are used to develop spectrometer detection efficiency calibration data. The linearity, resolution, and detection efficiency of a radiation spectrometer must all be well understood so that useful information may be extracted from spectra acquired by the spectrometer.

For ROIs such as the one presented in Figure A.1 that contain only a single, isolated peak, simple algorithms may be used to estimate the mean, the width, and the area associated with the isolated peak. Examples of simple peak mean, peak width, and peak area estimation algorithms are prescribed by Gilmore and Hemingway [69]. Unfortunately, these simple algorithms tend to fail when applied to ROIs that contain multiple overlapping peaks called multiplets. An example of a ^{139}Ce Kβ X-ray multiplet composed of three peaks is shown in Figure A.2. More advanced peak-fitting methods are required to extract peak mean, peak width, and peak area information from multiplets.

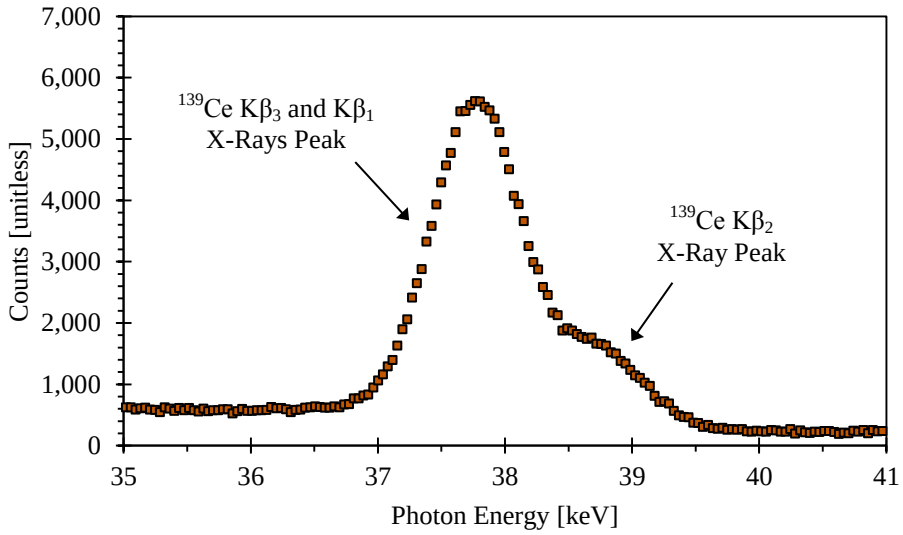

Figure A.2: An example of a ^{139}Ce Kβ X-ray multiplet.

Peak-fitting methods provide a means of fitting functions to peaks in ROIs in spectral data sets. In the simple case of an ROI containing only a single Gaussian-shaped peak (see Figure A.1) the fitted function would be a Gaussian distribution defined by three peak parameters: μ, σ, and A. In the case of an ROI containing three Gaussian-shaped peaks (see Figure A.2) the fitted function would be a summation of three Gaussian distributions defined by nine peak parameters: μ_1, σ_1, and A_1 would be used to define the first peak; μ_2, σ_2, and A_2 would be used to define the second peak; and μ_3, σ_3, and A_3 would be used to define the third peak (assuming all three peaks may be resolved). More generically, in the case of an ROI containing n peaks the fitted function would be a summation of n Gaussian distributions defined by $3 \cdot n$ peak parameters.

Peak-fitting methods provide structured processes that aim to identify the μ, σ, and A parameters associated with each of the peaks in an ROI so that the fitted function defined by the parameters fits the peak, or peaks, associated with the ROI as closely as possible. The "closeness" of a fitted function to an ROI in a spectral data set may be quantified in a number of different ways. Here, the closeness will be defined as the sum of the squared vertical deviations between (1) the values attained by the fitted function at each of the channels associated with the ROI and (2) the number of counts registered in each of the same channels. In this case the peak-fitting problem becomes a least-squares problem which may be defined mathematically as follows:

$$\underset{\substack{\mu_1,\sigma_1,A_1,\\ \dots \\ \mu_n,\sigma_n,A_n}}{\operatorname{argmin}} R_n^2(\mu_1,\sigma_1,A_1,\dots,\mu_n,\sigma_n,A_n,i,C_i)\dots$$

$$= \underset{\substack{\mu_1,\sigma_1,A_1,\\ \dots \\ \mu_n,\sigma_n,A_n}}{\operatorname{argmin}} \sum_{i=L-m_L}^{U+m_U} (f_G(\mu_1,\sigma_1,A_1,i)+\dots+f_G(\mu_n,\sigma_n,A_n,i)-C_i)^2. \qquad \text{A.2.1}$$

Where: μ_1 through μ_n are the means associated with peaks 1 through n,

σ_1 through σ_n are the standard deviations associated with peaks 1 through n,

A_1 through A_n are the areas associated with peaks 1 through n,

$f_G(\mu_1,\sigma_1,A_1,i)$ through $f_G(\mu_n,\sigma_n,A_n,i)$ represent the values attained by the Gaussian distributions describing peaks 1 through n at channel i,

C_i is the number of counts registered in channel i of the spectrum,

L is the lower boundary of the peak(s) within the ROI,

m_L is the number of channnels associated with the lower background region of the ROI,

U is the upper boundary of the peak(s) within the ROI, and

m_U is the number of channnels associated with the upper background region of the ROI.

Note that the "argmin" notation used in Equation A.2.1 denotes that it is the arguments μ_1, σ_1, A_1 through μ_n, σ_n, A_n that minimize the function R_n^2 that are sought.

The WiPFA peak-fitting algorithm approaches the least-squares peak-fitting problem defined by Equation A.2.1 as an optimization problem, the solutions to which are generated using Newton's method in optimization [156]. Newton's method in optimization is an iterative optimization method. An initial set of argument estimates must be provided as inputs to the method. The Hessian matrix and gradient vector associated with the function to be minimized are then developed and used to generate a new set of argument estimates. These new argument estimates are then used to develop a second Hessian matrix and a second gradient vector which are used to generate a second set of new argument estimates. This process is repeated until the arguments estimates converge to a final argument estimate set or until a certain number of argument estimate sets has been evaluated.

Mathematically, The general form of Newton's method in optimization applied to a generic function $f(\boldsymbol{x})$ is as follows [156]:

$$\boldsymbol{x}_{r+1} = \boldsymbol{x}_r - \gamma \cdot \boldsymbol{H}f(\boldsymbol{x}_r)^{-1} \cdot \boldsymbol{\nabla} f(\boldsymbol{x}_r). \qquad \text{A.2.2}$$

Where: $\boldsymbol{x}_r$ and $\boldsymbol{x}_{r+1}$ are vectors containing estimates at each of the x arguments associated with the generic function $f(\boldsymbol{x})$ after estimate evaluation rounds r and $r+1$, respectively,

γ is a scalar that may be used to control the size of the steps taken between argument estimate evaluation rounds,

$\boldsymbol{H}f(\boldsymbol{x}_r)$ is the Hessian matrix of $f(\boldsymbol{x}_r)$, and

$\boldsymbol{\nabla}f(\boldsymbol{x}_r)$ is the gradient vector of $f(\boldsymbol{x}_r)$.

Applying Newton's method in optimization and Equation A.2.2 to the least-squares peak-fitting problem defined by Equation A.2.1 produces the least-squares peak-fitting optimization problem of interest here:

$$\boldsymbol{P}_{r+1} = \boldsymbol{P}_r - \gamma \cdot \boldsymbol{H}R_n^2(\boldsymbol{P}_r, i, C_i)^{-1} \cdot \boldsymbol{\nabla}R_n^2(\boldsymbol{P}_r, i, C_i). \quad \text{A.2.3}$$

Where: $\boldsymbol{P}_r$ and $\boldsymbol{P}_{r+1}$ are vectors containing estimates at the peak parameters μ, σ, and A associated with each of the peaks in an ROI after peak parameter estimate evaluation rounds r and $r+1$, respectively,

$\boldsymbol{H}R_n^2(\boldsymbol{P}_r, i, C_i)$ is the Hessian matrix of $R_n^2(\boldsymbol{P}_r, i, C_i)$, and

$\boldsymbol{\nabla}R_n^2(\boldsymbol{P}_r, i, C_i)$ is the gradient vector of $R_n^2(\boldsymbol{P}_r, i, C_i)$.

For the specific case of an ROI containing only a single peak, Equation A.2.3 may be rewritten as follows:

$$\begin{bmatrix}\mu_{r+1}\\ \sigma_{r+1}\\ A_{r+1}\end{bmatrix} = \begin{bmatrix}\mu_r\\ \sigma_r\\ A_r\end{bmatrix} - \gamma \cdot \boldsymbol{H}R_{n=1}^2(\mu_r, \sigma_r, A_r, i, C_i)^{-1} \cdot \boldsymbol{\nabla}R_{n=1}^2(\mu_r, \sigma_r, A_r, i, C_i). \quad \text{A.2.4}$$

Similarly, for the specific case of an ROI containing two peaks, Equation A.2.3 may be rewritten as follows:

$$\begin{bmatrix}\mu_{1,r+1}\\ \sigma_{1,r+1}\\ A_{1,r+1}\\ \mu_{2,r+1}\\ \sigma_{2,r+1}\\ A_{2,r+1}\end{bmatrix} = \begin{bmatrix}\mu_{1,r}\\ \sigma_{1,r}\\ A_{1,r}\\ \mu_{2,r}\\ \sigma_{2,r}\\ A_{2,r}\end{bmatrix} - \gamma \cdot \boldsymbol{H} R_{n=2}^{2}\left(\mu_{1,r}, \sigma_{1,r}, A_{1,r}, \mu_{2,r}, \sigma_{2,r}, A_{2,r}, i, C_i\right)^{-1} \ldots \quad \text{A.2.5}$$

$$\cdot \boldsymbol{\nabla} R_{n=2}^{2}\left(\mu_{1,r}, \sigma_{1,r}, A_{1,r}, \mu_{2,r}, \sigma_{2,r}, A_{2,r}, i, C_i\right).$$

Now, having framed the peak-fitting problem as a least-squares optimization problem, the challenge becomes developing the Hessian matrices and gradient vectors of the R_n^2 expression required to solve for the peak parameters of interest. In the next section, a general method for reconstructing R_n^2 expressions is described. Then, in Section A.4, this method is extended to support the development of the required R_n^2 Hessian matrices and gradient vectors.

A.3 A General Method to Reconstruct Expressions for R_n^2

In order to make the WiPFA peak-fitting algorithm generally applicable to Regions of Interest (ROIs) containing any number of peaks (as opposed to ROIs containing only one peak, only two peaks, only three peaks, *etc*.) the WiPFA peak-fitting algorithm employs a general method to reconstruct expressions for R_n^2, where R_n^2 represents the squared vertical deviations expression applicable to a generic ROI containing an arbitrary number of peaks, n (see Equation A.2.1). In order to explain how this general method to reconstruct expressions for R_n^2 works, a number of cases are

considered here in sequence. Consider first the simple case of an ROI that contains only a single peak. In this case the expression for $R^2_{n=1}$ is as follows:

$$R^2_{n=1}(\mu, \sigma, A, i, C_i) = \sum_{i=L-m_L}^{U+m_U} (f_G(\mu, \sigma, A, i) - C_i)^2. \quad \text{A.3.1}$$

Where: μ is the peak mean,

σ is the peak standard deviation,

A is the peak area,

$f_G(\mu, \sigma, A, i)$ represents the value attained by the Gaussian distribution describing the peak at channel i, and

C_i is the number of counts registered in channel i of the spectrum.

Note that the sigma notation associated with the summation in Equation A.3.1 denotes that the summation is evaluated over channels $L - m_L$ through $U + m_U$, which constitutes the entirety of the ROI. If the squared term in the summation is expanded, Equation A.3.1 becomes:

$$R^2_{n=1}(\mu, \sigma, A, i, C_i) = \sum_{i=L-m_L}^{U+m_U} (f_G^2(\mu, \sigma, A, i) - 2 \cdot C_i \cdot f_G(\mu, \sigma, A, i) + C_i^2). \quad \text{A.3.2}$$

Having developed the above expression for R^2_n applicable to an ROI containing only a single peak, consider now the slightly more complicated case of an ROI containing a multiplet composed of two overlapping peaks. In this case the expression for $R^2_{n=2}$ becomes:

$$R^2_{n=2}(\mu_1, \sigma_1, A_1, \mu_2, \sigma_2, A_2, i, C_i)$$

$$= \sum_{i=L-m_L}^{U+m_U} (f_G(\mu_1, \sigma_1, A_1, i) + f_G(\mu_2, \sigma_2, A_2, i) - C_i)^2. \quad \text{A.3.3}$$

Where: μ_1 and μ_2 are the means associated with peaks 1 and 2,

σ_1 and σ_2 are the standard deviations associated with peaks 1 and 2,

A_1 and A_2 are the areas associated with peaks 1 and 2, and

$f_G(\mu_1, \sigma_1, A_1, i)$ and $f_G(\mu_2, \sigma_2, A_2, i)$ represent the values attained by the Gaussian distributions describing peaks 1 and 2 at channel i.

If the squared term in the summation is expanded, Equation A.3.3 becomes:

$$R^2_{n=2}(\mu_1, \sigma_1, A_1, \mu_2, \sigma_2, A_2, i, C_i) = \sum_{i=L-m_L}^{U+m_U} (f_G^2(\mu_1, \sigma_1, A_1, i) + f_G^2(\mu_2, \sigma_2, A_2, i) \ldots$$

$$+C_i^2 + 2 \cdot f_G(\mu_1, \sigma_1, A_1, i) \cdot f_G(\mu_2, \sigma_2, A_2, i) \ldots \quad \text{A.3.4}$$

$$-2 \cdot C_i \cdot f_G(\mu_1, \sigma_1, A_1, i) - 2 \cdot C_i \cdot f_G(\mu_2, \sigma_2, A_2, i)\big).$$

Now consider a third, considerably more complicated case of an ROI containing a multiplet composed of not two, but three overlapping peaks. In this case the expression for $R^2_{n=3}$ becomes:

$$R^2_{n=3}(\mu_1, \sigma_1, A_1, \mu_2, \sigma_2, A_2, \mu_3, \sigma_3, A_3, i, C_i) = \sum_{i=L-m_L}^{U+m_U} (f_G(\mu_1, \sigma_1, A_1, i) \ldots \quad \text{A.3.5}$$

$$+f_G(\mu_2, \sigma_2, A_2, i) + f_G(\mu_3, \sigma_3, A_3, i) - C_i)^2.$$

Where: μ_1, μ_2, and μ_3 are the means associated with peaks 1, 2, and 3,

σ_1, σ_2, and σ_3 are the standard deviations associated with peaks 1, 2 and 3,

A_1, A_2, and A_3 are the areas associated with peaks 1, 2, and 3, and

$f_G(\mu_1, \sigma_1, A_1, i)$, $f_G(\mu_2, \sigma_2, A_2, i)$, and $f_G(\mu_3, \sigma_3, A_3, i)$ represent the values attained by the Gaussian distributions describing peaks 1, 2, and 3 at channel i.

If the squared term in the summation is expanded, Equation A.3.5 becomes:

$$R^2_{n=3}(\mu_1, \sigma_1, A_1, \mu_2, \sigma_2, A_2, \mu_3, \sigma_3, A_3, i, C_i) = \sum_{i=L-m_L}^{U+m_U} (f_G^2(\mu_1, \sigma_1, A_1, i) \ldots$$

$$+f_G^2(\mu_2, \sigma_2, A_2, i) + f_G^2(\mu_3, \sigma_3, A_3, i) + C_i^2 \ldots$$

$$+2 \cdot f_G(\mu_1, \sigma_1, A_1, i) \cdot f_G(\mu_2, \sigma_2, A_2, i) \ldots \qquad \text{A.3.6}$$

$$+2 \cdot f_G(\mu_1, \sigma_1, A_1, i) \cdot f_G(\mu_3, \sigma_3, A_3, i) \ldots$$

$$+2 \cdot f_G(\mu_2, \sigma_2, A_2, i) \cdot f_G(\mu_3, \sigma_3, A_3, i) - 2 \cdot C_i \cdot f_G(\mu_1, \sigma_1, A_1, i) \ldots$$

$$-2 \cdot C_i \cdot f_G(\mu_2, \sigma_2, A_2, i) - 2 \cdot C_i \cdot f_G(\mu_3, \sigma_3, A_3, i)\big).$$

At this point, having developed expressions for R_n^2 for ROIs containing one, two, and three peaks, it should be fairly apparent that the expression for R_n^2 becomes increasingly more complicated as the number of peaks in the ROI increases. If additional R_n^2 expressions are developed for ROIs containing more and more peaks, three interesting properties of the general form of the expression for R_n^2 become apparent:

I. The first interesting property of the general form of the expression for R_n^2 is that the expanded summation term in the expression for R_n^2 always contains $\sum_{i=1}^{n+1} i$ terms.

II. The second interesting property of the general form of the expression for R_n^2 is that the term in the summation is always composed of terms having at most four different forms. The four term forms are as follows:

1. Term form 1 is the square of the value attained by a Gaussian distribution describing one of the peaks in the ROI, say peak j, at channel i:

$$f_G^2(\mu_j, \sigma_j, A_j, i). \quad \text{A.3.7}$$

2. Term form 2 is the number of counts registered in channel i of the spectral data set squared:

$$C_i^2. \quad \text{A.3.8}$$

3. Term form 3 is 2 times the product of the values attained by Gaussian distributions describing two of the peaks in the ROI, say peaks j and k, at channel i:

$$2 \cdot f_G(\mu_j, \sigma_j, A_j, i) \cdot f_G(\mu_k, \sigma_k, A_k, i). \quad \text{A.3.9}$$

4. Term form 4 is -2 times the product of the number of counts registered in channel i of the spectral data set and the value attained by a Gaussian distribution describing one of the peaks in the ROI, say peak j, at channel i:

$$-2 \cdot C_i \cdot f_G(\mu_j, \sigma_j, A_j, i). \quad \text{A.3.10}$$

For ROIs containing two or more peaks the expression for R_n^2 will always contain terms having each of these four forms. For ROIs containing only a single peak the expression for R_n^2 will contain terms having forms 1, 2, and 4, but not form 3.

III. The third property of the expression for R_n^2 is that the number of times each of the term forms identified above appear in an expression for R_n^2 is always known based solely on the number of peaks in the ROI, n. More specifically, an expression for R_n^2 always contains: (1) n instances of term form 1, (2) one instance of term form 2, (3) $\sum_{i=1}^{n-1} i$ instances of term form 3, and (4) n instances of term form 4.

These properties of the general form of the expression for R_n^2 make it such that the squared term in the summation of an R_n^2 expression for an ROI containing an arbitrary number of peaks, n, may always be reconstructed by properly populating the elements of an $n+1$ by $n+1$ matrix, $\boldsymbol{M}$. The expression for R_n^2 can then be evaluated by summing over all i, over all j, and over all k as follows:

$$R_n^2 = \sum_{i=L-m_L}^{U+m_U} \sum_{j=1}^{n+1} \sum_{k=1}^{n+1} \boldsymbol{M}_{j,k} \qquad \text{A.3.11}$$

Where: $\boldsymbol{M}$ is an $n+1$ by $n+1$ matrix (and n is the number of peaks in the ROI),

j denotes the row index of the matrix $\boldsymbol{M}$, and

k denotes the column index of the matrix $\boldsymbol{M}$.

In order to explain how to properly populate an $\boldsymbol{M}$ matrix, the one, two, and three peak ROI cases considered previously are considered again here. The $\boldsymbol{M}$ matrix applicable to the one peak ROI case is as follows:

$$\boldsymbol{M} = \begin{bmatrix} f_{G,1}^2 & -2 \cdot C_i \cdot f_{G,1} \\ 0 & C_i^2 \end{bmatrix}. \qquad \text{A.3.12}$$

Where: $f_{G,1}$ is shorthand for $f_G(\mu_1, \sigma_1, A_1, i)$.

The $\boldsymbol{M}$ matrix applicable to the two peak ROI case is as follows:

$$\boldsymbol{M} = \begin{bmatrix} f_{G,1}^2 & 2 \cdot f_{G,1} \cdot f_{G,2} & -2 \cdot C_i \cdot f_{G,1} \\ 0 & f_{G,2}^2 & -2 \cdot C_i \cdot f_{G,2} \\ 0 & 0 & C_i^2 \end{bmatrix}. \quad \text{A.3.13}$$

Where: $f_{G,1}$ is shorthand for $f_G(\mu_1, \sigma_1, A_1, i)$ and

$f_{G,2}$ is shorthand for $f_G(\mu_2, \sigma_2, A_2, i)$.

And finally, the $\boldsymbol{M}$ matrix applicable to the three peak ROI case is as follows:

$$\boldsymbol{M} = \begin{bmatrix} f_{G,1}^2 & 2 \cdot f_{G,1} \cdot f_{G,2} & 2 \cdot f_{G,1} \cdot f_{G,3} & -2 \cdot C_i \cdot f_{G,1} \\ 0 & f_{G,2}^2 & 2 \cdot f_{G,2} \cdot f_{G,3} & -2 \cdot C_i \cdot f_{G,2} \\ 0 & 0 & f_{G,3}^2 & -2 \cdot C_i \cdot f_{G,3} \\ 0 & 0 & 0 & C_i^2 \end{bmatrix}. \quad \text{A.3.14}$$

Where: $f_{G,1}$ is shorthand for $f_G(\mu_1, \sigma_1, A_1, i)$,

$f_{G,2}$ is shorthand for $f_G(\mu_2, \sigma_2, A_2, i)$, and

$f_{G,3}$ is shorthand for $f_G(\mu_3, \sigma_3, A_3, i)$.

Substituting Equations A.3.12, A.3.13, and A.3.14 into Equation A.3.11 and comparing the results to Equations A.3.2, A.3.4, and A.3.6, respectively, reveals that the R_1^2, R_2^2, and R_3^2 expressions developed above using the matrix $\boldsymbol{M}$ formulation are in fact equivalent to the R_1^2, R_2^2, and R_3^2 expressions developed previously.

With populated $\boldsymbol{M}$ matrices applicable to the one, two, and three peak ROI cases now available for reference, the general logic used to populate an $\boldsymbol{M}$ matrix applicable to an ROI containing n peaks may be described as follows. Note again that the $\boldsymbol{M}$ matrix is an $n + 1$ by $n + 1$ matrix, j is the matrix row index, and k is the matrix column index:

(1) Elements of the $\boldsymbol{M}$ matrix for which the matrix column index, k, is less than the matrix row index, j, should be filled with zeros.

(2) Elements of the $\boldsymbol{M}$ matrix for which (a) the matrix column index, k, is equal to the matrix row index, j, and (b) the matrix row index is not equal to $n+1$ should be filled with terms having the form given by Equation A.3.7 (R_n^2 expression term form 1).

(3) Elements of the $\boldsymbol{M}$ matrix for which (a) the matrix column index, k, is equal to $n+1$, and (b) the matrix row index, j, is not equal to $n+1$ should be filled with terms having the form given by Equation A.3.10 (R_n^2 expression term form 4).

(4) The bottom right element of the $\boldsymbol{M}$ matrix, matrix element $\boldsymbol{M}_{j=n+1,k=n+1}$, should be filled with a term having the form given by Equation A.3.8 (R_n^2 expression term form 2).

(5) The remainder of the elements of the $\boldsymbol{M}$ matrix should all be filled with terms having the form given by Equation A.3.9 (R_n^2 expression term form 3).

This logic may be used to populate $\boldsymbol{M}$ matrices supporting the reconstruction of R_n^2 expressions applicable to ROIs containing any number of peaks. In the next section this same logic will be extended so that the Hessian matrices and gradient vectors needed to solve the peak-fitting optimization problem defined by Equation A.2.3 may be developed as well.

A.4 Hessian Matrix and Gradient Vector Development

In the previous section a general method to reconstruct expressions for R_n^2 was developed. However, it is the Hessian matrix of R_n^2 and the gradient vector of R_n^2 that are needed to solve the peak-fitting optimization problem defined by Equation A.2.3. Recall that the general forms of the Hessian matrix and gradient vector of a generic function of n variables, $f(x_1, x_2, \dots, x_n)$, are as follows.

The Hessian matrix of the generic $f(x_1, x_2, \dots, x_n)$ is given by:

$$\boldsymbol{H}f(x_1, x_2, x_3) = \begin{bmatrix} \frac{\partial^2 f(x_1, x_2, \dots, x_n)}{\partial x_1^2} & \frac{\partial^2 f(x_1, x_2, \dots, x_n)}{\partial x_1 \cdot \partial x_2} & \cdots & \frac{\partial^2 f(x_1, x_2, \dots, x_n)}{\partial x_1 \cdot \partial x_n} \\ \frac{\partial^2 f(x_1, x_2, \dots, x_n)}{\partial x_2 \cdot \partial x_1} & \frac{\partial^2 f(x_1, x_2, \dots, x_n)}{\partial x_2^2} & \cdots & \frac{\partial^2 f(x_1, x_2, \dots, x_n)}{\partial x_2 \cdot \partial x_n} \\ \vdots & \vdots & \ddots & \vdots \\ \frac{\partial^2 f(x_1, x_2, \dots, x_n)}{\partial x_n \cdot \partial x_1} & \frac{\partial^2 f(x_1, x_2, \dots, x_n)}{\partial x_n \cdot \partial x_2} & \cdots & \frac{\partial^2 f(x_1, x_2, \dots, x_n)}{\partial x_n^2} \end{bmatrix}. \qquad \text{A.4.1}$$

The gradient vector of the generic function $f(x_1, x_2, \dots, x_n)$ is given by:

$$\boldsymbol{\nabla} f(x_1, x_2, x_3) = \begin{bmatrix} \frac{\partial f(x_1, x_2, \dots, x_n)}{\partial x_1} \\ \frac{\partial f(x_1, x_2, \dots, x_n)}{\partial x_2} \\ \vdots \\ \frac{\partial f(x_1, x_2, \dots, x_n)}{\partial x_n} \end{bmatrix}. \qquad \text{A.4.2}$$

A quick review of Equation A.4.1 serves to remind that the Hessian matrix of a generic function $f(x_1, x_2, \dots, x_n)$ of n variables is an n by n matrix containing n^2 second-order partial derivatives of the function. Similarly, the gradient vector of a generic function $f(x_1, x_2, \dots, x_n)$ of n variables is an n by 1 matrix containing n first-order partial derivatives of the function. Also note that the arguments with respect to which the

function is to be differentiated correspond to the indices of the elements of the Hessian matrix and the gradient vector. For example, the element of the Hessian matrix having a row index, j, equal to 2 and a column index, k, equal to 1 is differentiated with respect to the second argument of the function, x_2, first and then with respect to the first argument of the function, x_1, second. Similarly, the element of the gradient having a row index, j, equal to 2 is differentiated with respect to the second argument of the function, x_2.

This structure within the Hessian matrix and gradient vector make it such that an algorithm may be used to create a Hessian matrix or gradient vector having the appropriate dimensions and then step through the elements of the Hessian matrix or gradient vector and determine which arguments the function should be differentiated with respect to. This structure within the Hessian matrix and gradient vector makes it such that an algorithm may be used to step through and populate the elements of Hessian matrices and gradient vectors with functions differentiated with the respect to the appropriate arguments based on the indices of the Hessian matrix or gradient vector.

This is the method the WiPFA peak-fitting algorithm uses to develop the Hessian matrices and gradient vectors required to solve the peak-fitting optimization problem defined by Equation A.2.3. A detailed description of the algorithm used to develop Hessian matrices is presented here. A similar but somewhat simpler algorithm is used to develop gradient vectors.

Hessian Matrix Development, Step 1:

First, the dimensions of the Hessian matrix are evaluated and the matrix is initialized. For the peak-fitting optimization problems of interest here, the number of arguments to Equation A.2.3 is typically equal to 3 times the number of peaks associated with the ROI, n, so the dimensions of the Hessian matrix are typically $3 \cdot n$ by $3 \cdot n$. If peak parameters are to be constrained (see Section A.7) then the dimensions of the Hessian matrix are reduced by the number of constrained peak parameters.

Hessian Matrix Development, Step 2:

Having initialized the Hessian matrix as described in Step 1, the next steps involve populating the elements of the Hessian matrix. Two nested loops are used to step through the elements of the Hessian matrix and populate them one at a time. The arguments with respect to which a particular second-order partial derivative should be evaluated are determined based on the row and column indices, j and k, respectively, associated with the element of the Hessian matrix.

Hessian Matrix Development, Step 3:

The second-order partial derivative required to populate a particular element of the Hessian matrix is evaluated using an extension of the $\boldsymbol{M}$ matrix method described in Section A.3. While the $\boldsymbol{M}$ matrix method is used in Section A.3 to reconstruct the basic form of the R_n^2 expression required to solve the peak-fitting optimization problem defined by Equation A.2.3, the same method may be extended to reconstruct second-order partial derivatives of the R_n^2 expression.

This extension of the $\boldsymbol{M}$ matrix method is possible because the $\boldsymbol{M}$ matrix method is basically just used to store the individual terms required to reconstruct the R_n^2 expression. As described in Section A.3, the terms that appear in the R_n^2 expression all take one of four forms. These forms are defined by Equations A.3.7 through A.3.10. A review of these term forms reveals the following: (1) Term form 1 is a function of three arguments that are relevant in the context of the peak-fitting optimization problem:μ_j, σ_j, and A_j. This means that term form 1 has nine second-order partial derivative forms that are relevant in the context of the peak-fitting optimization problem of interest here. (2) Term form 2 is a constant and thus the second-order partial derivative of term form 2 is always zero. (3) Term form 3 is a function of six arguments that are relevant in the context of the peak-fitting optimization problem: μ_j, σ_j, A_j, μ_k, σ_k, and A_k. This means that term form 3 has 36 second-order partial derivative forms that are relevant in the context of the peak-fitting optimization problem of interest here. (4) Term form 4 is a function of three arguments that are relevant in the context of the peak-fitting optimization problem: μ_j, σ_j, and A_j. This means that term form 4 has nine second-order partial derivative forms that are relevant in the context of the peak-fitting optimization problem of interest here.

The forms of these second order partial derivatives may be evaluated and substituted into an $\boldsymbol{M}$ matrix as needed in the same way that the basic forms of term forms 1 through 4 are evaluated and substituted into an $\boldsymbol{M}$ matrix in Section A.3. The second-order partial derivative of the R_n^2 expression may then be evalauted by

summing the second order partial derivative term forms populating the elements of the $\boldsymbol{M}$ matrix in accordance with Equation A.3.11.

Hessian Matrix Development, Step 4:

After all of the second-order partial derivatives required to populate the Hessian matrix have been evaluated and substituted into the Hessian matrix the Hessian matrix is passed to the peak-fitting optimization problem defined by Equation A.2.3 and used to support the development of a new set of peak parameter estimates. This constitutes the last step of the Hessian matrix development algorithm.

As mentioned previously, a similar but somewhat simpler algorithm is used to develop the gradient vectors required to solve the peak-fitting optimization problem defined by Equation A.2.3. The algorithm used to develop the gradient vectors is simpler in that (1) the gradient vectors are one-dimensional column vectors as opposed to n-dimensional matrices and (2) the gradient vectors contain only first-order partial derivatives as opposed to second-order partial derivatives. Hessian matrices and gradient vectors required to solve the peak-fitting optimization problem may be developed as described here and passed to Equation A.2.3 as needed in an iterative fashion until the optimal peak parameters representing the solution to the peak-fitting optimization problem are attained or a predetermined number of peak parameter guess sets has been evaluated.

A.5 Estimating the Uncertainty associated with the Fitted Parameters

One of the unique aspects of the WiPFA peak-fitting algorithm is it reports the uncertainty associated with each of the peak parameter estimates it generates. The peak parameter estimate uncertainties are developed using an iterative Monte Carlo method that utilizes the fact that the counts registered in the individual channels of spectra are all samples from Poisson distributions (radioactive decay is a binomial process to which the rules of Poisson statistics are applicable [69]). The peak parameter uncertainty estimation method employed by The WiPFA peak-fitting algorithm is described as a Monte Carlo method because it involves using the nominal spectrum for which optimal peak parameter estimates are to be generated to produce a large number of supplemental spectra (usually on the order of ten thousand of them) and generates optimal peak parameter estimates for all of the supplemental spectra as well as the nominal spectra. The optimal peak parameter estimates associated with the nominal and supplemental spectra are tabulated as they are evaluated and then, after a sufficient number of optimal peak parameter estimates have been generated, the mean value and the standard deviation associated with each peak parameter is evaluated. The WiPFA peak-fitting algorithm reports the mean peak parameter estimates produced at the end of this process as the optimal peak parameters representing the solutions to the peak-fitting optimization problem and the peak parameter estimate standard deviations as the optimal peak parameter estimate uncertainties.

The supplemental spectra required to support this Monte Carlo uncertainty estimation method are produced by sampling from the nominal spectrum for which

optimal peak parameter estimates are to be generated. In a given supplemental spectrum, the number of counts placed in channel i is determined by sampling from a Possion distribution having a mean and a variance equal to the number of counts registered in channel i of the nominal spectrum for which optimal peak parameter estimates are to be generated. The supplemental spectra may be generated by sampling from the nominal spectrum in this way because radioactive decay is a fundamentally a binomial process (in a given time interval a radioactive atom may either (1) decay or (2) not decay) and because Poisson statistics are applicable to the field of radiation counting statistics [69]. Figure A.3 presents a number of data points associated with three supplemental spectra generated in accordance with the method described above plotted on top of a number of data points associated with a nominal ^{139}Ce Kβ X-ray multiplet.

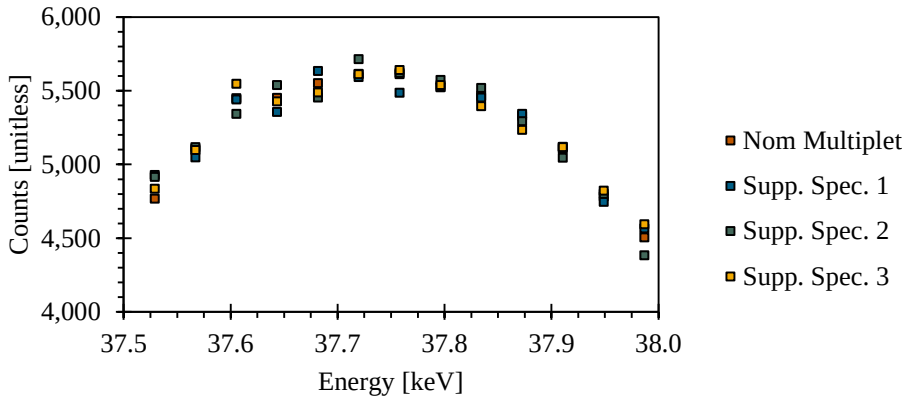

Figure A.3: Data points associated with three supplemental spectra plotted on top of points associated with a nominal ^{139}Ce Kβ X-ray multiplet.

A.6 Decision Limits

Another unique aspect of the WiPFA peak-fitting algorithm is it reports critical limits applicable to each of the individual peaks in a given ROI in a manner consistent with the classic method originally prescribed by Currie [70]. The classic method originally prescribed by Currie effectively states that a peak p may be declared statistically significant if the net number of counts in the peak is some number of standard deviations above the mean associated with a distribution describing the total number of background and interference counts underneath the peak p [70]. This concept, which is illustrated below in Figure A.4, may be expressed mathematically in the form given by Equation A.6.1.

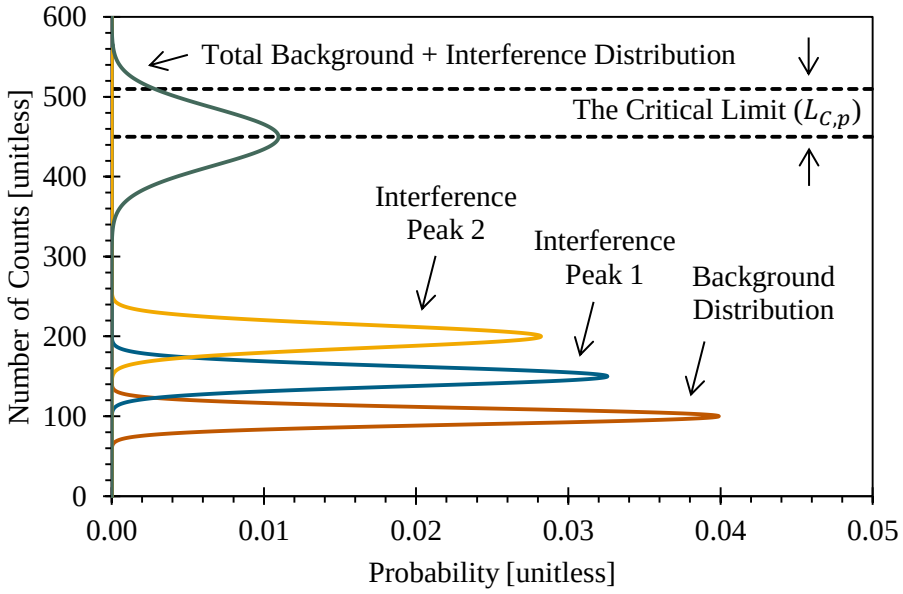

Figure A.4: Illustration of the critical limit decision limit concept.

$$L_{C,p} = k_\alpha \cdot \sigma_{BG+Int,p}. \quad \text{A.6.1}$$

Where: L_C, p is the critical limit associated with the peak p,

k_α is a factor selected so that a certain confidence or certainty may be ascribed to the calculated critical limit, and

$\sigma_{BG+Int,p}$ is the standard deviation associated with the distribution describing the total number of background and interference counts underneath the peak p.

The standard deviation associated with the distribution describing the total number of background and interference counts underneath the peak p may be evaluated as follows:

$$\sigma_{BG+Int,p} = \left[var(N_{BG}) + \sum_{\substack{i=1 \\ i \neq p}}^{n} cov(N_{BG}, N_i) \ldots + \sum_{\substack{i=1 \\ i \neq p}}^{n} cov(N_i, N_{BG}) + \sum_{\substack{i=1 \\ i \neq p}}^{n} \sum_{\substack{j=1 \\ j \neq p}}^{n} cov(N_i, N_j) \right]^{1/2}. \quad \text{A.6.2}$$

Where: $var(N_{BG})$ is the variance associated with the number of background counts (N_{BG}) underneath the peak p,

$cov(N_{BG}, N_i)$ is the covariance associated with the background counts and the counts in interference peak i (N_i) underneath peak p,

$cov(N_i, N_{BG})$ is the covariance associated with the counts in interference peak i and the background counts underneath peak p, and

$cov(N_i, N_j)$ is the covariance associated with the counts in interference peaks i and j underneath peak p.

As an example, consider the case of a multiplet composed of three overlapping peaks; the standard deviation associated with the total number of background and interference counts underneath peak 1 of the multiplet may be calculated as follows:

$$\sigma_{BG+Int,1} = \left[var(N_{BG}) + \sum_{\substack{i=1 \\ i\neq 1}}^{3} cov(N_{BG}, N_i) \ldots + \sum_{\substack{i=1 \\ i\neq 1}}^{3} cov(N_i, N_{BG}) + \sum_{\substack{i=1 \\ i\neq 1}}^{3}\sum_{j=1}^{3} cov(N_i, N_j) \right]^{1/2}. \quad \text{A.6.3}$$

Expanding the summations in Equation A.6.3 produces the following expression:

$$\sigma_{BG+Int,1} = [var(N_{BG}) + cov(N_{BG}, N_2) + cov(N_{BG}, N_3) + cov(N_2, N_{BG}) \ldots + cov(N_3, N_{BG}) + cov(N_2, N_2) + cov(N_2, N_3) \ldots + cov(N_3, N_2) + cov(N_3, N_3)]^{1/2}. \quad \text{A.6.4}$$

Recognizing that $cov(N_2, N_2) = var(N_2)$, $cov(N_3, N_3) = var(N_3)$, $cov(N_{BG}, N_2) + cov(N_2, N_{BG}) = 2 \cdot cov(N_{BG}, N_2)$, *etc.* allows Equation A.6.4 to be rewritten as follows:

$$\sigma_{BG+Int,1} = [var(N_{BG}) + var(N_2) + var(N_3) + 2 \cdot cov(N_{BG}, N_2) \ldots + 2 \cdot cov(N_{BG}, N_3) + 2 \cdot cov(N_2, N_3)]^{1/2}. \quad \text{A.6.5}$$

Substituting Equation A.6.5 into Equation A.6.1 ultimately produces the following expression for the critical limit associated with peak 1 of the three peak multiplet:

$$L_{C,1} = k_\alpha \cdot [var(N_{BG}) + var(N_2) + var(N_3) + 2 \cdot cov(N_{BG}, N_2) \ldots + 2 \cdot cov(N_{BG}, N_3) + 2 \cdot cov(N_2, N_3)]^{1/2}. \quad \text{A.6.6}$$

A.7 Using the WiPFA Peak-Fitting Algorithm

In its current form the WiPFA peak-fitting algorithm receives inputs in the form of two formatted text files. The first formatted text file should contain a spectral data set in a space- or tab-delimited two-column format. The values in the first column should be the channels associated with the spectral data set and the values in the second column should be the number of counts registered in each of the channels. The spectral data set is read from the formatted text file and stored in a two-column cell array.

The WiPFA peak-fitting algorithm indexes within the columns of this cell array assuming that the row indices correspond to the spectral data set channel numbers. Therefore, the first channel in a spectral data set passed to the WiPFA peak-fitting algorithm must be either zero or one. If the first channel of a spectral data set is found to be zero only the spectral data associated with channels 1 and up is retained; the channel data and the count data for channel zero is expunged.

Note that the first two lines of a formatted text file containing a spectral data set are assumed to be header lines. These lines may be used to record notes pertinent to the spectral data set stored in the formatted text file. The WiPFA peak-fitting algorithm ignores these header lines and assumes that the spectral data set starts on line three of a given formatted text file.

The second formatted text file contains the inputs to the WiPFA peak-fitting algorithm. The first two lines of the WiPFA inputs file are assumed to be header lines and are ignored by the WiPFA peak-fitting algorithm. The inputs to the WiPFA peak-fitting

algorithm are then assumed to begin on line three of the WiPFA inputs file as illustrated below in Figure A.5.

```
1  Created by: William H. Wilson
2  Inputs for 28 Sept 2015 radioxenon study.
3  0.1 0.01 0.05 1000 10000
4  1000 10
5  1075 10
6  1025 U 10 C 12000 U
7  1050 C 11 U 15000 U
```

Figure A.5: An example of a formatted text file containing inputs to the WiPFA peak-fitting algorithm.

The five input parameters on the third line of the WiPFA inputs file control the implementation of Newton's method in optimization. The first input parameter on the third line of the WiPFA inputs file is used to assign a value to the γ parameter that appears in Equation A.2.3. The γ parameter is used to control the size of the steps taken between peak parameter estimate evaluation rounds. Experience suggests that it is typically best to use a step size of around 0.1 as illustrated in Figure A.5.

The second and third input parameters on the third line of the WiPFA inputs file specify the peak parameter estimate convergence criteria and the R_n^2 convergence criteria, respectively. These convergence criteria should be specified as percentages. Assigning a value of 0.01 % to the peak parameter estimate convergence criteria and a value of

0.05 % to the R_n^2 convergence criteria, as illustrated in Figure A.5, will force the WiPFA peak-fitting algorithm to continue to evaluate new peak parameter estimate sets until the peak parameter estimates all change by less than 0.01 % and R_n^2 changes by less than 0.05 %.

The fourth input parameter on the third line of the WiPFA inputs file specifies the maximum number of peak parameter estimate sets to be evaluated, n_{Eval}. Assigning a value of 1,000 to n_{Eval}, as illustrated in Figure A.5, will force the WiPFA peak-fitting algorithm to stop evaluating new peak parameter estimate sets if 1,000 peak parameter estimate sets are evaluated before the peak parameter estimate convergence criteria and R_n^2 convergence criteria are satisfied. To this point, experience has shown that if the initial estimates at each of the peak parameters passed to the WiPFA peak-fitting algorithm are relatively good and if the peak parameter estimate convergence criteria and R_n^2 convergence criteria are both set equal to 0.01 % the WiPFA peak-fitting algorithm typically converges after evaluating between 10 and 100 peak parameter estimate sets.

The fifth input parameter on the third line of the WiPFA inputs file specifies the number of supplemental spectra to be generated and evaluated in support of the peak parameter estimate uncertainty evaluations, n_{Supp}. Assigning a value of 10,000 to n_{Supp}, as illustrated in Figure A.5, will force the WiPFA peak-fitting algorithm to generate and evaluate 10,000 supplemental spectra. Experience suggests that generating and evaluating 10,000 supplemental spectra is typically more than sufficient to allow all the mean peak parameter estimates to converge to their expected values.

The input parameters on line four of the WiPFA inputs file specify the lower boundary of the peak within the ROI and the number of channels to include in the lower background region of the ROI. These input parameters represent the L and m_L parameters that appear in Equation A.3.11. The input parameters on line five of the WiPFA inputs file specify the upper boundary of the peak within the ROI and the number of channels to include in the upper background region of the ROI. These input parameters represent the U and m_U parameters that appear in Equation A.3.11. In the example presented in Figure A.5 values of 1,000 and 10 are assigned to the input parameters L and m_L, respectively, and values of 1,075 and 10 are assigned to the input parameters U and m_U, respectively.

The input parameters on the last line(s) of the WiPFA inputs file are the initial peak parameter estimates. One line of initial peak parameter estimates should be provided for each of the peaks in an ROI. The first peak parameter estimate associated with a given line of peak parameter estimates is an initial peak mean estimate, μ. This estimate is immediately followed by a flag indicating whether or not the initial peak mean estimate is to be constrained. If the WiPFA peak-fitting algorithm is allowed to vary the peak mean as it attempts to generate a better fit to the spectral data set then the peak mean flag should be set equal to "U." However, if the peak mean is to be constrained the peak mean flag should be set equal to "C."

The second peak parameter estimate associated with a given line of peak parameter estimates is an initial peak standard deviation estimate, σ. This estimate is immediately followed by another flag indicating whether or not the initial peak standard

deviation estimate is to be constrained. The third peak parameter estimate associated with a given line of peak parameter estimates is an initial peak area estimate, A. This estimate is immediately followed by yet another flag indicating whether or not the initial peak area estimate is to be constrained.

In the example presented in Figure A.5 the ROI is assumed to contain two peaks. This may be inferred from the fact that two lines of initial peak parameter estimates are provided on lines 6 and 7 of the WiPFA inputs file. For the first peak, the initial mean, standard deviation, and area estimates are 1,025, 10, and 12,000, respectively. The "U" parameters that follow the initial peak mean and area estimates specify that the initial peak mean and area estimates are unconstrained estimates; the "C" that follows the initial peak standard deviation estimate specifies that it is a constrained estimate. The initial estimates at the mean, the standard deviation, and the area associated with the second peak in the ROI are 1,050, 11, and 15,000, respectively. The initial peak standard deviation and peak area estimates associated with the second peak are unconstrained estimates, while the initial peak mean estimate associated with the second peak is a constrained estimate.

A.8 Validation of the WiPFA Peak-Fitting Algorithm

In order to validate the results generated by the WiPFA peak-fitting algorithm, several validation data sets were generated and used as inputs to the algorithm. The validation data sets represent hypothetical spectra containing Regions of Interest (ROIs) composed of various numbers of peaks. The peak parameters associated

with each of the peaks in each of the ROIs are, of course, all known. The validation data sets were supplied as inputs to the WiPFA peak-fitting algorithm via formatted text files in the same way any other spectral data set would be supplied to the algorithm. The methodology employed by the WiPFA peak-fitting algorithm and the results generated by the WiPFA peak-fitting algorithm were then validated by evaluating the ability of the algorithm to converge to the known peak parameters.

The first, most-basic validation data set tested contained an ROI composed of a single peak. The peak mean, the peak standard deviation, and the peak area associated with the peak were known to be 1,124, 7.5, and 12,192, respectively, as illustrated below in Table A.1. In addition to the validation data set, the WiPFA peak-fitting algorithm was given initial peak mean, peak standard deviation, and peak area estimates of 1,120, 7.8, and 11,460, respectively. Note that these initial peak parameter estimates deviate from the known peak parameters used to generate the validation data set by -0.4 %, 4.0 %, and -6.0 %, respectively. The other inputs to the WiPFA peak-fitting algorithm were set as specified in the notes to Table A.1.

As illustrated by Table A.1 and Figure A.6, the $R^2_{n=1}$ value associated with the initial peak parameter estimates was about 718,614. However, after evaluating 115 peak parameter estimate sets the $R^2_{n=1}$ value was reduced to 5.21×10^{-2} and the peak mean, peak standard deviation, and peak area estimates had converged to within 7.81×10^{-6} %, 7.36×10^{-3} %, and 1.10×10^{-2} % of their known values. Figure A.7 illustrates how the peak parameter estimates were modified by the WiPFA peak-fitting algorithm during the

evaluation and eventually converged to their known values. It took the WiPFA peak-fitting algorithm less than 6.7 s to evaluate validation data set 1.

Table A.1: WiPFA peak-fitting algorithm evaluation of validation data set 1.

While evaluating validation data set 1, the step size parameter, γ, was set equal to 0.1, the peak parameter and $R^2_{n=1}$ convergence criteria were set equal to 0.01 %, and the n_{Eval} parameter was set equal to 1,000. The boundaries of the ROI were set as follows: $L = 1{,}095$, $m_L = 10$, $U = 1{,}155$, and $m_U = 10$. All of the initial peak parameter estimates tabulated below were provided as unconstrained estimates.

Peak Parameters	Known Values	Initial Estimates		Converged Values	
		Nominal	Percent Dev. from Known	Nominal	Percent Dev. from Known
Peak 1 Mean, μ_1	1,124	1,120	-0.4	1,124.000	7.81×10^{-6}
Peak 1 Std. Dev., σ_1	7.5	7.8	4.0	7.499	-7.36×10^{-3}
Peak 1 Area, A_1	12,192	11,460	-6.0	12,190.657	-1.10×10^{-2}
Associated R^2 Value	-	718,614		5.21×10^{-2}	

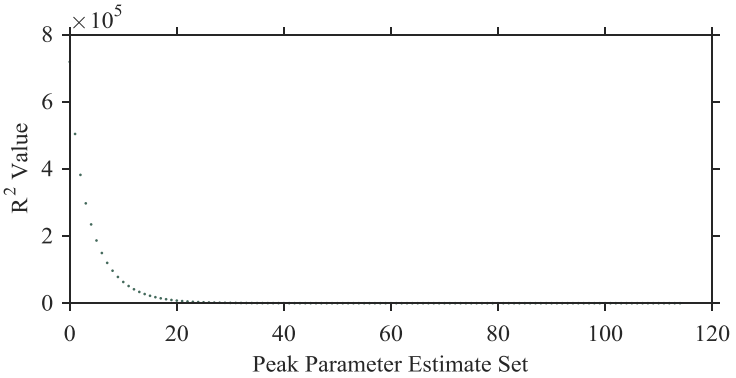

Figure A.6: Evolution of the $R^2_{n=1}$ value during the evaluation of validation data set 1.

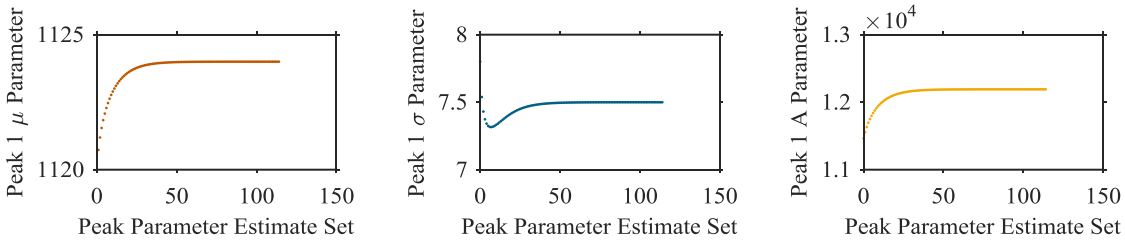

Figure A.7: Evolution of the peak parameter estimates during the evaluation of validation data set 1.

The second validation data set contained an ROI composed of two peaks. The mean, the standard deviation, and the area associated with each of the peaks were known to take the values tabulated in Table A.2. In addition to the validation data set, the WiPFA peak-fitting algorithm was given the initial peak mean, peak standard deviation, and peak area estimates tabulated in Table A.2. The other inputs to the WiPFA peak-fitting algorithm were set as specified in the notes to Table A.2.

As illustrated by Table A.2 and Figure A.8, the $R^2_{n=2}$ value associated with the initial peak parameter estimates was 3,171,410. However, after evaluating 118 peak parameter estimate sets the $R^2_{n=2}$ value was reduced to 1.80×10^{-1} and the peak mean, peak standard deviation, and peak area estimates had converged to their known values. Figure A.9 illustrates how the peak parameter estimates were modified by the WiPFA peak-fitting algorithm during the evaluation and eventually converged to their known values. It took the WiPFA peak-fitting algorithm about 5.0 s to evaluate validation data set 2.

Table A.2: WiPFA peak-fitting algorithm evaluation of validation data set 2.

While evaluating validation data set 2, the step size parameter, γ, was set equal to 0.1, the peak parameter and $R^2_{n=2}$ convergence criteria were set equal to 0.01 %, and the n_{Eval} parameter was set equal to 1,000. The boundaries of the ROI were set as follows: $L = 1{,}085$, $m_L = 10$, $U = 1{,}165$, and $m_U = 10$. All of the initial peak parameter estimates tabulated below were provided as unconstrained estimates.

Peak Parameters	Known Values	Initial Estimates		Converged Values	
		Nominal	Percent Dev. from Known	Nominal	Percent Dev. from Known
Peak 1 Mean, μ_1	1,112	1,106	-0.5	1,112.000	2.02×10^{-5}
Peak 1 Std. Dev., σ_1	7.3	7.9	8.0	7.299	-1.35×10^{-2}
Peak 1 Area, A_1	12,311	14,404	17.0	12,308.429	-2.09×10^{-2}
Peak 2 Mean, μ_2	1,134	1,137	0.3	1,134.000	-3.00×10^{-5}
Peak 2 Std. Dev., σ_2	7.4	8.1	9.0	7.400	-1.76×10^{-3}
Peak 2 Area, A_2	15,427	18,204	18.0	15,426.075	-6.00×10^{-3}
Associated R^2 Value	-	3,171,410		1.80×10^{-1}	

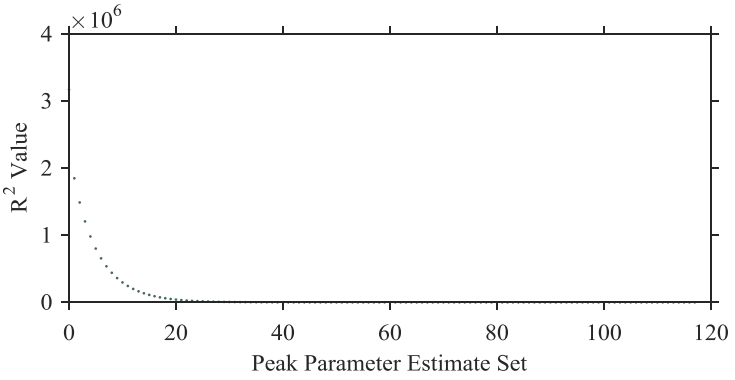

Figure A.8: Evolution of the $R^2_{n=2}$ value during the evaluation of validation data set 2.

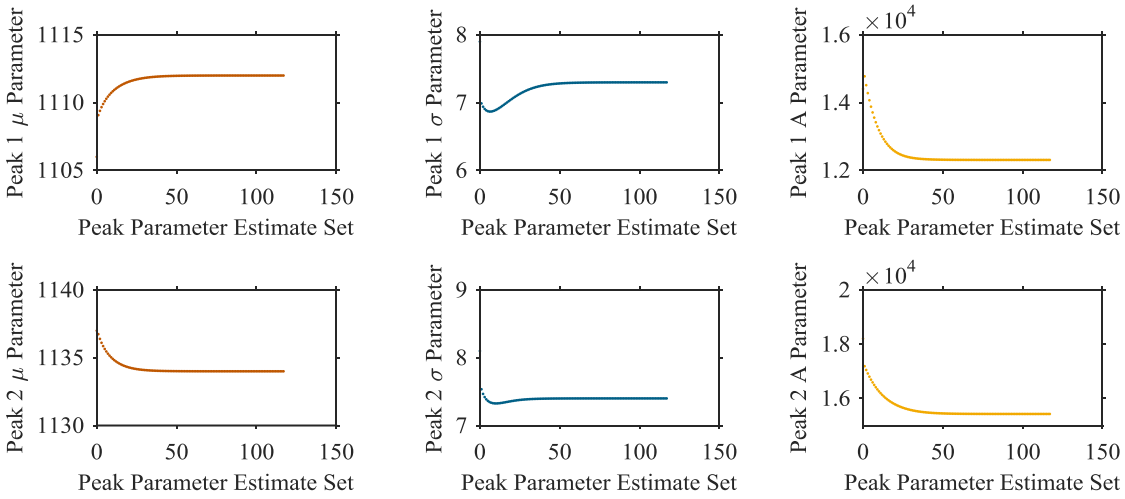

Figure A.9: Evolution of the peak parameter estimates
during the evaluation of validation data set 2.

The third validation data set contained an ROI composed of three peaks. The mean, the standard deviation, and the area associated with each of the peaks were known to take the values listed in Table A.3. In addition to the validation data set, the WiPFA peak-fitting algorithm was given the initial peak mean, peak standard deviation, and peak area estimates tabulated in Table A.3. The other inputs to the algorithm were set as specified in the notes to Table A.3.

As illustrated by Table A.3 and Figure A.10, the $R^2_{n=3}$ value associated with the initial peak parameter estimates was about 911,236. However, after evaluating 144 peak parameter estimate sets the $R^2_{n=3}$ value was reduced to 2.47×10^{-4} and the peak mean, peak standard deviation, and peak area estimates had converged to their known values. Figure A.11 illustrates how the peak parameter estimates were modified by the WiPFA peak-fitting algorithm during the evaluation and eventually converged to their

known values. It took the WiPFA peak-fitting algorithm about 13.2 s to evaluate validation data set 3.

Table A.3: WiPFA peak-fitting algorithm evaluation of validation data set 3.

While evaluating validation data set 3, the step size parameter, γ, was set equal to 0.1, the peak parameter and $R^2_{n=3}$ convergence criteria were set equal to 0.01 %, and the n_{Eval} parameter was set equal to 1,000. The boundaries of the ROI were set as follows: $L = 1{,}075$, $m_L = 10$, $U = 1{,}175$, and $m_U = 10$. All of the initial peak parameter estimates tabulated below were provided as unconstrained estimates.

Peak Parameter	Known Value	Initial Estimate		Converged Value	
		Nominal	Percent Dev. from Known	Nominal	Percent Dev. from Known
Peak 1 Mean, μ_1	1,106	1,102	-0.4	1,106.000	-4.16×10^{-6}
Peak 1 Std. Dev., σ_1	6.8	6.7	-2.0	6.800	-7.95×10^{-4}
Peak 1 Area, A_1	9,985	9,486	-5.0	9,984.861	-1.40×10^{-3}
Peak 2 Mean, μ_2	1,124	1,125	0.1	1,124.000	-3.26×10^{-8}
Peak 2 Std. Dev., σ_2	7.0	7.2	3.0	7.000	7.92×10^{-4}
Peak 2 Area, A_2	15,067	15,971	6.0	15,067.121	8.01×10^{-4}
Peak 3 Mean, μ_3	1,143	1,145	0.2	1,143.000	3.36×10^{-6}
Peak 3 Std. Dev., σ_3	7.1	6.9	-3.0	7.100	-7.97×10^{-4}
Peak 3 Area, A_3	11,899	11,185	-6.0	11,898.848	-1.28×10^{-3}
Associated R^2 Value	-	911,236		2.47×10^{-4}	

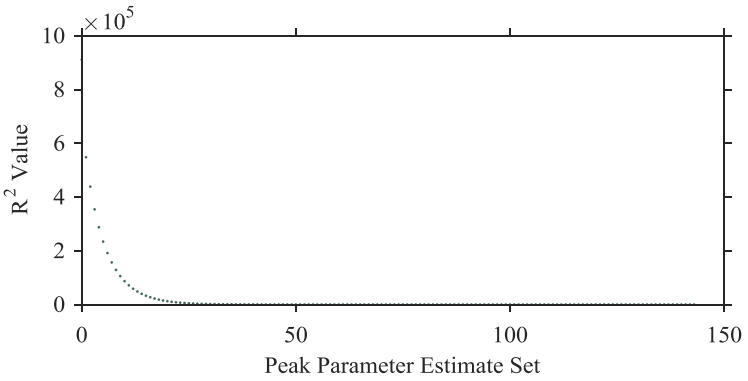

Figure A.10: Evolution of the $R^2_{n=3}$ value during the evaluation of validation data set 3.

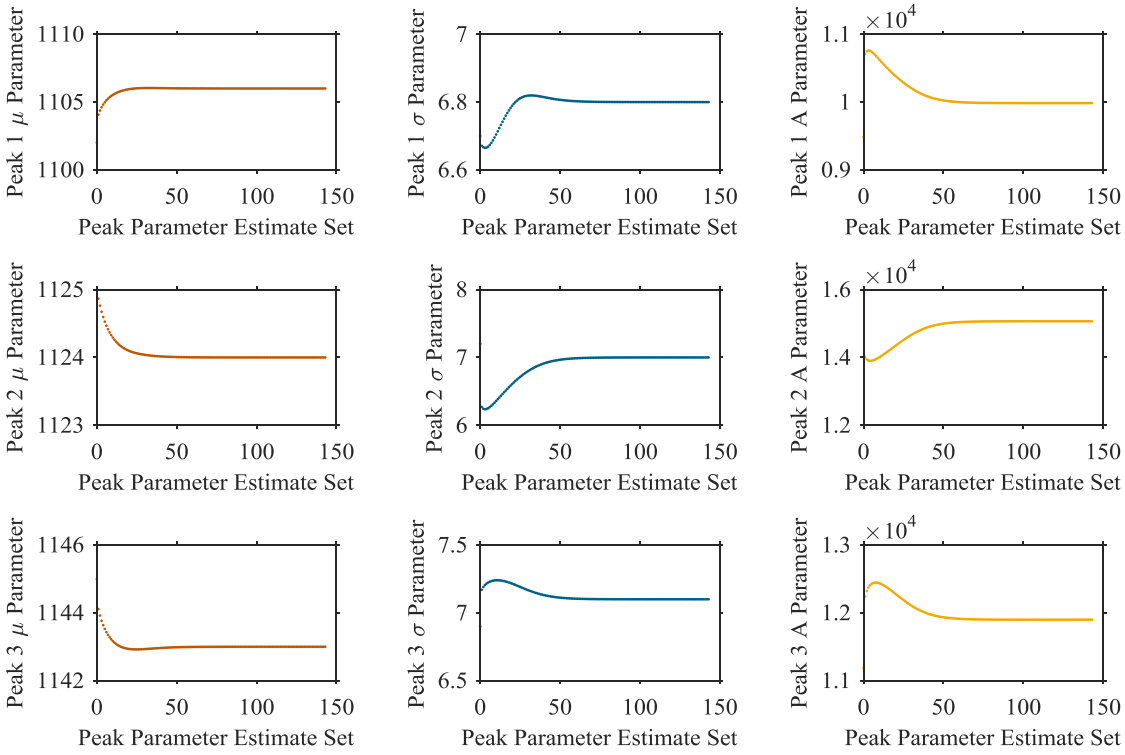

Figure A.11: Evolution of the peak parameter estimates during the evaluation of validation data set 3.

Appendix B: Peak Mean, Width, and Area Data from Spectra acquired using an XIA LLC Si-PIN Diode Spectrometer Prototype

This appendix contains peak mean, peak width, and peak area data extracted from radioxenon and calibration source spectra acquired using an XIA LLC Si-PIN diode spectrometer prototype [67, 68]. The peak mean data is reported in Table B.1, the peak width data is reported in Table B.2, and the peak area data is reported in Table B.3. The peak means are reported as spectrum channel numbers and are unitless. The peak widths are standard deviations and are reported in units of keV. The peak areas are unitless. All of the peak means, widths, and areas were evaluated using the WiPFA peak-fitting algorithm described in Section 2.1.5 and Appendix A.

The radioxenon and calibration source spectra were acquired as described in Sections 2.2.1.2 and 2.2.1.3, respectively. The radioisotope decay mode and energy data reproduced in Tables B.1 through B.3 was taken from the nuclear decay scheme database maintained by the National Nuclear Data Center [60]. In cases where multiple radioisotope decay modes contributed counts to a single peak, the reported decay mode energy is the branching-ratio-weighted average decay mode energy.

Table B.1: Peak mean data extracted from XIA LLC Si-PIN diode spectrometer prototype radioxenon and calibration source spectra.

Radioisotope and Decay Mode	Decay Mode Energy				Peak Mean			
	[keV]		[keV]	[%]	[unitless]		[unitless]	[%]
^{65}Zn Kα and Kβ X-Rays	8.133	±	N/R	N/R	211.2661	±	1.9363	0.92
^{109}Cd Kα X-Rays	22.103	±	N/R	N/R	580.1047	±	0.0071	0.0012
^{109}Cd Kβ X-Rays	25.006	±	N/R	N/R	655.7271	±	0.0173	0.0026
^{109}Cd 88.0336 keV γ-Ray	88.0336	±	0.0001	0.00011	2,309.0340	±	0.1521	0.0066
^{113}Sn Kα X-Rays	24.137	±	N/R	N/R	632.9766	±	0.0078	0.0012
^{113}Sn $K\beta_3$ and $K\beta_1$ X-Rays	27.263	±	N/R	N/R	715.1161	±	0.2509	0.035
^{113}Sn $K\beta_2$ X-Ray	27.863	±	N/R	N/R	730.2926	±	2.1281	0.29
^{113}Sn 255.134 keV γ-Ray	255.134	±	0.010	0.0039	N.S.S.	±	N.S.S.	N.S.S.
^{133}Ba Kα X-Rays	30.850	±	N/R	N/R	811.0641	±	0.0184	0.0023
^{133}Ba $K\beta_3$ and $K\beta_1$ X-Rays	34.964	±	N/R	N/R	919.2323	±	0.0762	0.0083
^{133}Ba $K\beta_2$ X-Ray	35.818	±	N/R	N/R	942.0310	±	1.0629	0.11
^{133}Ba 53.1622 keV γ-Ray	53.1622	±	0.0006	0.0011	1,397.0470	±	0.2780	0.020
^{133}Ba 79.6142 keV γ-Ray	79.6142	±	0.0012	0.0015	2,093.3207	±	0.6241	0.030
^{133}Ba 80.9979 keV γ-Ray	80.9979	±	0.0011	0.0014	2,128.7056	±	0.1006	0.0047
^{137}Cs Kα X-Rays	32.061	±	N/R	N/R	841.3056	±	0.0459	0.0055
^{137}Cs $K\beta_3$ and $K\beta_1$ X-Rays	36.353	±	N/R	N/R	953.9239	±	0.1531	0.016
^{137}Cs $K\beta_2$ X-Ray	37.255	±	N/R	N/R	977.7125	±	0.5331	0.055
^{131m}Xe Kα X-Rays	29.669	±	N/R	N/R	782.4721	±	0.1862	0.024
^{131m}Xe Kβ X-Rays	33.738	±	N/R	N/R	886.4703	±	0.7690	0.087
^{131m}Xe 129.369 keV K CE	129.369	±	0.008	0.0062	3,395.4256	±	0.0906	0.0027
^{131m}Xe 158.477 keV L CE	158.477	±	0.008	0.0050	4,169.1829	±	0.1649	0.0040
^{131m}Xe M and O CEs	162.813	±	0.008	0.0049	4,276.2449	±	0.2494	0.0058
^{133m}Xe Kα X-Rays	29.669	±	N/R	N/R	780.2283	±	1.1751	0.15
^{133m}Xe $K\beta_3$ and $K\beta_1$ X-Rays	33.603	±	N/R	N/R	D.N.E.	±	D.N.E.	D.N.E.
^{133m}Xe $K\beta_2$ X-Ray	34.419	±	N/R	N/R	D.N.E.	±	D.N.E.	D.N.E.
^{133m}Xe 198.660 keV K CE	198.660	±	0.015	0.0076	5,210.5764	±	0.1432	0.0027
^{133m}Xe 227.768 keV L CE	227.768	±	0.015	0.0066	5,981.3328	±	0.3150	0.0053
^{133m}Xe M, N, and O CE	232.255	±	0.015	0.0065	6,089.5711	±	0.6201	0.010
^{133m}Xe 233.221 keV γ-Ray	233.221	±	0.015	0.0064	D.N.E.	±	D.N.E.	D.N.E.

Notes: "N/R" = Not Reported; "D.N.E." = Did Not Evaluate; and "N.S.S." = Not Statistically Significant.

Table B.1: Peak mean data extracted from XIA LLC Si-PIN diode spectrometer prototype radioxenon and calibration source spectra, continued.

Radioisotope and Decay Mode	Decay Mode Energy				Peak Mean			
	[keV]		[keV]	[%]	[unitless]		[unitless]	[%]
^{133}Xe Kα X-Rays	30.850	±	N/R	N/R	812.9651	±	0.2301	0.028
^{133}Xe Kβ$_3$ and Kβ$_1$ X-Rays	34.964	±	N/R	N/R	919.6803	±	0.6207	0.067
^{133}Xe Kβ$_2$ X-Ray	35.818	±	N/R	N/R	D.N.E.	±	D.N.E.	D.N.E.
^{133}Xe 45.0133 keV K CE	45.0133	±	0.0012	0.0027	1,172.5249	±	0.0811	0.0069
^{133}Xe 75.2836 keV L CE	75.2836	±	0.0012	0.0016	1,973.3387	±	0.2340	0.012
^{133}Xe M, N, O, and M CE	79.7632	±	0.0067	0.0084	2,090.5392	±	0.9712	0.046
^{133}Xe 79.6142 keV γ-Ray	79.6142	±	0.0012	0.0015	D.N.E.	±	D.N.E.	D.N.E.
^{133}Xe N and O CE	80.7928	±	0.0043	0.0054	2,121.6090	±	1.8309	0.086
^{133}Xe 80.9979 keV γ-Ray	80.9979	±	0.0011	0.0014	D.N.E.	±	D.N.E.	D.N.E.
^{135}Xe Kα X-Rays	30.850	±	N/R	N/R	808.6016	±	0.7821	0.10
^{135}Xe 213.809 keV K CE	213.809	±	0.015	0.0070	5,597.3135	±	0.2734	0.0049
^{135}Xe 244.080 keV L CE	244.080	±	0.015	0.0061	6,390.9919	±	1.2664	0.020
^{135}Xe M, N, and O CEs	248.770	±	0.043	0.0173	D.N.E.	±	D.N.E.	D.N.E.
^{139}Ce Kα X-Rays	33.297	±	N/R	N/R	873.5403	±	0.0154	0.0018
^{139}Ce Kβ$_3$ and Kβ$_1$ X-Rays	37.773	±	N/R	N/R	991.2969	±	0.0615	0.0062
^{139}Ce Kβ$_2$ X-Ray	38.726	±	N/R	N/R	1,017.2470	±	0.2051	0.020
^{139}Ce 165.8575 keV γ-Ray	165.8575	±	0.0011	0.00066	4,347.3986	±	0.1296	0.0030
^{203}Hg Kα$_2$ X-Ray	70.832	±	N/R	N/R	1,860.6099	±	0.2816	0.015
^{203}Hg Kα$_1$ X-Ray	72.873	±	N/R	N/R	1,914.2004	±	0.2016	0.011
^{203}Hg Kβ$_3$ and Kβ$_1$ X-Rays	82.416	±	N/R	N/R	2,165.6481	±	0.7952	0.037
^{203}Hg Kβ$_2$ X-Ray	84.865	±	N/R	N/R	2,226.9375	±	7.2791	0.33
^{203}Hg 279.1952 keV γ-Ray	279.1952	±	0.0010	0.00036	7,306.2797	±	1.6113	0.022
^{241}Am Lα X-Rays	13.9269	±	N/R	N/R	366.4628	±	0.0691	0.019
^{241}Am Lβ$_2$ and Lβ$_4$ X-Rays	16.91	±	N/R	N/R	446.1528	±	0.1110	0.025
^{241}Am Lβ$_5$ X-Ray	17.39	±	N/R	N/R	D.N.E.	±	D.N.E.	D.N.E.
^{241}Am Lβ$_1$ and Lβ$_3$ X-Rays	17.774	±	N/R	N/R	467.6864	±	0.0374	0.0080
^{241}Am Lγ$_1$ and Lγ$_2$ X-Rays	20.83	±	N/R	N/R	D.N.E.	±	D.N.E.	D.N.E.
^{241}Am Lγ$_3$, Lγ$_6$, & Lγ$_8$ X-Rays	21.38	±	N/R	N/R	D.N.E.	±	D.N.E.	D.N.E.
^{241}Am Lγ$_4$ X-Ray	22.20	±	N/R	N/R	D.N.E.	±	D.N.E.	D.N.E.
^{241}Am 26.3446 keV γ-Ray	26.3446	±	0.0002	0.00076	693.4098	±	0.0376	0.0054
^{241}Am 33.196 keV γ-Ray	33.196	±	0.001	0.0030	873.9776	±	0.2744	0.031
^{241}Am 59.5409 keV γ-Ray	59.5409	±	0.0001	0.00017	1,566.1877	±	0.0213	0.0014
^{241}Am 98.97 keV γ-Ray	98.97	±	0.02	0.020	N.S.S.	±	N.S.S.	N.S.S.
^{241}Am 102.98 keV γ-Ray	102.98	±	0.02	0.019	N.S.S.	±	N.S.S.	N.S.S.

Notes: “N/R” = Not Reported; “D.N.E.” = Did Not Evaluate; and “N.S.S.” = Not Statistically Significant.

Table B.2: Peak width data extracted from XIA LLC Si-PIN diode spectrometer prototype radioxenon and calibration source spectra.

Radioisotope and Decay Mode	Decay Mode Energy				Peak Width (Standard Deviation)			
	[keV]		[keV]	[%]	[keV]		[keV]	[%]
^{65}Zn Kα and Kβ X-Rays	8.133	±	N/R	N/R	1.0947	±	0.2722	25
^{109}Cd Kα X-Rays	22.103	±	N/R	N/R	0.8096	±	0.0006	0.074
^{109}Cd Kβ X-Rays	25.006	±	N/R	N/R	0.8487	±	0.0014	0.17
^{109}Cd 88.0336 keV γ-Ray	88.0336	±	0.0001	0.00011	0.8377	±	0.0121	1.4
^{113}Sn Kα X-Rays	24.137	±	N/R	N/R	0.6762	±	0.0007	0.097
^{113}Sn $K\beta_3$ and $K\beta_1$ X-Rays	27.263	±	N/R	N/R	0.6128	±	0.0141	2.3
^{113}Sn $K\beta_2$ X-Ray	27.863	±	N/R	N/R	0.5754	±	0.0881	15
^{113}Sn 255.134 keV γ-Ray	255.134	±	0.010	0.0039	N.S.S.	±	N.S.S.	N.S.S.
^{133}Ba Kα X-Rays	30.850	±	N/R	N/R	0.8099	±	0.0015	0.19
^{133}Ba $K\beta_3$ and $K\beta_1$ X-Rays	34.964	±	N/R	N/R	0.6818	±	0.0083	1.2
^{133}Ba $K\beta_2$ X-Ray	35.818	±	N/R	N/R	0.6290	±	0.0463	7.4
^{133}Ba 53.1622 keV γ-Ray	53.1622	±	0.0006	0.0011	0.7028	±	0.0307	4.4
^{133}Ba 79.6142 keV γ-Ray	79.6142	±	0.0012	0.0015	0.7966	±	0.0553	6.9
^{133}Ba 80.9979 keV γ-Ray	80.9979	±	0.0011	0.0014	0.7309	±	0.0084	1.1
^{137}Cs Kα X-Rays	32.061	±	N/R	N/R	0.8369	±	0.0039	0.47
^{137}Cs $K\beta_3$ and $K\beta_1$ X-Rays	36.353	±	N/R	N/R	0.6743	±	0.0132	2.0
^{137}Cs $K\beta_2$ X-Ray	37.255	±	N/R	N/R	0.6610	±	0.0432	6.5
^{131m}Xe Kα X-Rays	29.669	±	N/R	N/R	0.9530	±	0.0199	2.1
^{131m}Xe Kβ X-Rays	33.738	±	N/R	N/R	0.9293	±	0.0770	8.3
^{131m}Xe 129.369 keV K CE	129.369	±	0.008	0.0062	1.1806	±	0.0084	0.71
^{131m}Xe 158.477 keV L CE	158.477	±	0.008	0.0050	1.5701	±	0.0142	0.91
^{131m}Xe M and O CEs	162.813	±	0.008	0.0049	1.3590	±	0.0253	1.9
^{133m}Xe Kα X-Rays	29.669	±	N/R	N/R	0.8222	±	0.1012	0.10
^{133m}Xe $K\beta_3$ and $K\beta_1$ X-Rays	33.603	±	N/R	N/R	D.N.E.	±	D.N.E.	D.N.E.
^{133m}Xe $K\beta_2$ X-Ray	34.419	±	N/R	N/R	D.N.E.	±	D.N.E.	D.N.E.
^{133m}Xe 198.660 keV K CE	198.660	±	0.015	0.0076	1.3008	±	0.0137	1.1
^{133m}Xe 227.768 keV L CE	227.768	±	0.015	0.0066	1.6058	±	0.0306	1.9
^{133m}Xe M, N, and O CE	232.255	±	0.015	0.0065	1.5717	±	0.0750	4.8
^{133m}Xe 233.221 keV γ-Ray	233.221	±	0.015	0.0064	D.N.E.	±	D.N.E.	D.N.E.

Notes: "N/R" = Not Reported; "D.N.E." = Did Not Evaluate; and "N.S.S." = Not Statistically Significant.

Table B.2: Peak width data extracted from XIA LLC Si-PIN diode spectrometer prototype radioxenon and calibration source spectra, continued.

Radioisotope and Decay Mode	Decay Mode Energy				Peak Width (Standard Deviation)			
	[keV]		[keV]	[%]	[keV]		[keV]	[%]
^{133}Xe Kα X-Rays	30.850	±	N/R	N/R	0.9038	±	0.0252	2.8
^{133}Xe $K\beta_3$ and $K\beta_1$ X-Rays	34.964	±	N/R	N/R	0.5840	±	0.0580	9.9
^{133}Xe $K\beta_2$ X-Ray	35.818	±	N/R	N/R	D.N.E.	±	D.N.E.	D.N.E.
^{133}Xe 45.0133 keV K CE	45.0133	±	0.0012	0.0027	1.2630	±	0.0091	0.72
^{133}Xe 75.2836 keV L CE	75.2836	±	0.0012	0.0016	1.4002	±	0.0297	2.1
^{133}Xe M, N, O, and M CE	79.7632	±	0.0067	0.0084	0.8435	±	0.1011	12
^{133}Xe 79.6142 keV γ-Ray	79.6142	±	0.0012	0.0015	D.N.E.	±	D.N.E.	D.N.E.
^{133}Xe N and O CE	80.7928	±	0.0043	0.0054	0.7771	±	0.1318	17
^{133}Xe 80.9979 keV γ-Ray	80.9979	±	0.0011	0.0014	D.N.E.	±	D.N.E.	D.N.E.
^{135}Xe Kα X-Rays	30.850	±	N/R	N/R	0.7058	±	0.0862	12
^{135}Xe 213.809 keV K CE	213.809	±	0.015	0.0070	1.2290	±	0.0285	2.3
^{135}Xe 244.080 keV L CE	244.080	±	0.015	0.0061	1.3550	±	0.1868	14
^{135}Xe M, N, and O CEs	248.770	±	0.043	0.0173	D.N.E.	±	D.N.E.	D.N.E.
^{139}Ce Kα X-Rays	33.297	±	N/R	N/R	0.9906	±	0.0013	0.13
^{139}Ce $K\beta_3$ and $K\beta_1$ X-Rays	37.773	±	N/R	N/R	0.8478	±	0.0050	0.59
^{139}Ce $K\beta_2$ X-Ray	38.726	±	N/R	N/R	0.7518	±	0.0141	1.9
^{139}Ce 165.8575 keV γ-Ray	165.8575	±	0.0011	0.00066	1.0170	±	0.0097	0.96
^{203}Hg $K\alpha_2$ X-Ray	70.832	±	N/R	N/R	0.8510	±	0.0272	3.2
^{203}Hg $K\alpha_1$ X-Ray	72.873	±	N/R	N/R	0.8535	±	0.0188	2.2
^{203}Hg $K\beta_3$ and $K\beta_1$ X-Rays	82.416	±	N/R	N/R	1.0456	±	0.0949	9.1
^{203}Hg $K\beta_2$ X-Ray	84.865	±	N/R	N/R	0.5831	±	0.5291	91
^{203}Hg 279.1952 keV γ-Ray	279.1952	±	0.0010	0.00036	1.1880	±	0.1209	10
^{241}Am Lα X-Rays	13.9269	±	N/R	N/R	0.6616	±	0.0060	0.90
^{241}Am $L\beta_2$ and $L\beta_4$ X-Rays	16.91	±	N/R	N/R	0.6730	±	0.0087	1.3
^{241}Am $L\beta_5$ X-Ray	17.39	±	N/R	N/R	D.N.E.	±	D.N.E.	D.N.E.
^{241}Am $L\beta_1$ and $L\beta_3$ X-Rays	17.774	±	N/R	N/R	0.6420	±	0.0029	0.45
^{241}Am $L\gamma_1$ and $L\gamma_2$ X-Rays	20.83	±	N/R	N/R	D.N.E.	±	D.N.E.	D.N.E.
^{241}Am $L\gamma_3$, $L\gamma_6$, & $L\gamma_8$ X-Rays	21.38	±	N/R	N/R	D.N.E.	±	D.N.E.	D.N.E.
^{241}Am $L\gamma_4$ X-Ray	22.20	±	N/R	N/R	D.N.E.	±	D.N.E.	D.N.E.
^{241}Am 26.3446 keV γ-Ray	26.3446	±	0.0002	0.00076	0.6168	±	0.0031	0.50
^{241}Am 33.196 keV γ-Ray	33.196	±	0.001	0.0030	0.6686	±	0.0230	3.4
^{241}Am 59.5409 keV γ-Ray	59.5409	±	0.0001	0.00017	0.7027	±	0.0017	0.25
^{241}Am 98.97 keV γ-Ray	98.97	±	0.02	0.020	N.S.S.	±	N.S.S.	N.S.S.
^{241}Am 102.98 keV γ-Ray	102.98	±	0.02	0.019	N.S.S.	±	N.S.S.	N.S.S.

Notes: "N/R" = Not Reported; "D.N.E." = Did Not Evaluate; and "N.S.S." = Not Statistically Significant.

Table B.3: Peak area data extracted from XIA LLC Si-PIN diode spectrometer prototype radioxenon and calibration source spectra.

Radioisotope and Decay Mode	Decay Mode Energy				Peak Area			
	[keV]		[keV]	[%]	[unitless]		[unitless]	[%]
^{65}Zn Kα and Kβ X-Rays	8.133	±	N/R	N/R	789	±	191	24
^{109}Cd Kα X-Rays	22.103	±	N/R	N/R	2,460,314	±	1,718	0.070
^{109}Cd Kβ X-Rays	25.006	±	N/R	N/R	510,973	±	830	0.16
^{109}Cd 88.0336 keV γ-Ray	88.0336	±	0.0001	0.00011	5,745	±	79	1.4
^{113}Sn Kα X-Rays	24.137	±	N/R	N/R	1,477,343	±	1,294	0.088
^{113}Sn $K\beta_3$ and $K\beta_1$ X-Rays	27.263	±	N/R	N/R	211,508	±	15,754	7.4
^{113}Sn $K\beta_2$ X-Ray	27.863	±	N/R	N/R	38,594	±	15,882	41
^{113}Sn 255.134 keV γ-Ray	255.134	±	0.010	0.0039	N.S.S.	±	N.S.S.	N.S.S.
^{133}Ba Kα X-Rays	30.850	±	N/R	N/R	385,240	±	686	0.18
^{133}Ba $K\beta_3$ and $K\beta_1$ X-Rays	34.964	±	N/R	N/R	58,064	±	613	1.1
^{133}Ba $K\beta_2$ X-Ray	35.818	±	N/R	N/R	12,143	±	904	7.4
^{133}Ba 53.1622 keV γ-Ray	53.1622	±	0.0006	0.0011	2,676	±	161	6.0
^{133}Ba 79.6142 keV γ-Ray	79.6142	±	0.0012	0.0015	1,184	±	89	7.5
^{133}Ba 80.9979 keV γ-Ray	80.9979	±	0.0011	0.0014	12,300	±	132	1.1
^{137}Cs Kα X-Rays	32.061	±	N/R	N/R	68,239	±	318	0.47
^{137}Cs $K\beta_3$ and $K\beta_1$ X-Rays	36.353	±	N/R	N/R	10,081	±	188	1.9
^{137}Cs $K\beta_2$ X-Ray	37.255	±	N/R	N/R	2,303	±	155	6.7
^{131m}Xe Kα X-Rays	29.669	±	N/R	N/R	6,309	±	123	1.9
^{131m}Xe Kβ X-Rays	33.738	±	N/R	N/R	1,037	±	89	8.6
^{131m}Xe 129.369 keV K CE	129.369	±	0.008	0.0062	34,046	±	214	0.63
^{131m}Xe 158.477 keV L CE	158.477	±	0.008	0.0050	18,374	±	155	0.84
^{131m}Xe M and O CEs	162.813	±	0.008	0.0049	5,637	±	83	1.5
^{133m}Xe Kα X-Rays	29.669	±	N/R	N/R	3,200	±	352	11
^{133m}Xe $K\beta_3$ and $K\beta_1$ X-Rays	33.603	±	N/R	N/R	D.N.E.	±	D.N.E.	D.N.E.
^{133m}Xe $K\beta_2$ X-Ray	34.419	±	N/R	N/R	D.N.E.	±	D.N.E.	D.N.E.
^{133m}Xe 198.660 keV K CE	198.660	±	0.015	0.0076	17,327	±	167	0.97
^{133m}Xe 227.768 keV L CE	227.768	±	0.015	0.0066	6,031	±	121	2.0
^{133m}Xe M, N, and O CE	232.255	±	0.015	0.0065	1,863	±	92	4.9
^{133m}Xe 233.221 keV γ-Ray	233.221	±	0.015	0.0064	D.N.E.	±	D.N.E.	D.N.E.

Notes: "N/R" = Not Reported; "D.N.E." = Did Not Evaluate; and "N.S.S." = Not Statistically Significant.

Table B.3: Peak area data extracted from XIA LLC Si-PIN diode spectrometer prototype radioxenon and calibration source spectra, continued.

Radioisotope and Decay Mode	Decay Mode Energy				Peak Area			
	[keV]		[keV]	[%]	[unitless]		[unitless]	[%]
^{133}Xe Kα X-Rays	30.850	±	N/R	N/R	11,059	±	351	3.2
^{133}Xe $K\beta_3$ and $K\beta_1$ X-Rays	34.964	±	N/R	N/R	1,210	±	138	11
^{133}Xe $K\beta_2$ X-Ray	35.818	±	N/R	N/R	D.N.E.	±	D.N.E.	D.N.E.
^{133}Xe 45.0133 keV K CE	45.0133	±	0.0012	0.0027	58,461	±	362	0.62
^{133}Xe 75.2836 keV L CE	75.2836	±	0.0012	0.0016	10,626	±	231	2.2
^{133}Xe M, N, O, and M CE	79.7632	±	0.0067	0.0084	1,633	±	155	9.5
^{133}Xe 79.6142 keV γ-Ray	79.6142	±	0.0012	0.0015	D.N.E.	±	D.N.E.	D.N.E.
^{133}Xe N and O CE	80.7928	±	0.0043	0.0054	787	±	176	22
^{133}Xe 80.9979 keV γ-Ray	80.9979	±	0.0011	0.0014	D.N.E.	±	D.N.E.	D.N.E.
^{135}Xe Kα X-Rays	30.850	±	N/R	N/R	711	±	91	13
^{135}Xe 213.809 keV K CE	213.809	±	0.015	0.0070	5,192	±	118	2.3
^{135}Xe 244.080 keV L CE	244.080	±	0.015	0.0061	753	±	101	13
^{135}Xe M, N, and O CEs	248.770	±	0.043	0.0173	D.N.E.	±	D.N.E.	D.N.E.
^{139}Ce Kα X-Rays	33.297	±	N/R	N/R	826,574	±	1,068	0.13
^{139}Ce $K\beta_3$ and $K\beta_1$ X-Rays	37.773	±	N/R	N/R	122,630	±	684	0.56
^{139}Ce $K\beta_2$ X-Ray	38.726	±	N/R	N/R	24,645	±	557	2.3
^{139}Ce 165.8575 keV γ-Ray	165.8575	±	0.0011	0.00066	11,802	±	111	0.94
^{203}Hg $K\alpha_2$ X-Ray	70.832	±	N/R	N/R	3,145	±	116	3.7
^{203}Hg $K\alpha_1$ X-Ray	72.873	±	N/R	N/R	4,946	±	118	2.4
^{203}Hg $K\beta_3$ and $K\beta_1$ X-Rays	82.416	±	N/R	N/R	1,086	±	110	10
^{203}Hg $K\beta_2$ X-Ray	84.865	±	N/R	N/R	164	±	133	81
^{203}Hg 279.1952 keV γ-Ray	279.1952	±	0.0010	0.00036	264	±	37	14
^{241}Am Lα X-Rays	13.9269	±	N/R	N/R	26,678	±	243	0.91
^{241}Am $L\beta_2$ and $L\beta_4$ X-Rays	16.91	±	N/R	N/R	51,739	±	701	1.4
^{241}Am $L\beta_5$ X-Ray	17.39	±	N/R	N/R	D.N.E.	±	D.N.E.	D.N.E.
^{241}Am $L\beta_1$ and $L\beta_3$ X-Rays	17.774	±	N/R	N/R	177,817	±	762	0.43
^{241}Am $L\gamma_1$ and $L\gamma_2$ X-Rays	20.83	±	N/R	N/R	D.N.E.	±	D.N.E.	D.N.E.
^{241}Am $L\gamma_3$, $L\gamma_6$, & $L\gamma_8$ X-Rays	21.38	±	N/R	N/R	D.N.E.	±	D.N.E.	D.N.E.
^{241}Am $L\gamma_4$ X-Ray	22.20	±	N/R	N/R	D.N.E.	±	D.N.E.	D.N.E.
^{241}Am 26.3446 keV γ-Ray	26.3446	±	0.0002	0.00076	63,790	±	292	0.46
^{241}Am 33.196 keV γ-Ray	33.196	±	0.001	0.0030	2,647	±	96	3.6
^{241}Am 59.5409 keV γ-Ray	59.5409	±	0.0001	0.00017	208,662	±	478	0.23
^{241}Am 98.97 keV γ-Ray	98.97	±	0.02	0.020	N.S.S.	±	N.S.S.	N.S.S.
^{241}Am 102.98 keV γ-Ray	102.98	±	0.02	0.019	N.S.S.	±	N.S.S.	N.S.S.

Notes: "N/R" = Not Reported; "D.N.E." = Did Not Evaluate; and "N.S.S." = Not Statistically Significant.

Appendix C: XIA LLC Si-PIN Diode Spectrometer Prototype Geometric Efficiency Evaluation Method

The geometric efficiency of a radiation spectrometer is equivalent to the solid angle subtended by the spectrometer at the point, or points, associated with a radioactive source to be counted. When the source to be counted is a point source evaluating the solid angle subtended by the spectrometer is fairly straightforward. However, when the source to be counted is distributed over a volume evaluating the solid angle is somewhat more complicated because the contributions associated with each of the points in the volume must be considered separately and then consolidated. When evaluating the solid angles subtended by the points inside solid- and liquid-phase sources with substantial densities self-shielding effects may also need to be considered.

In the case of the XIA LLC Si-PIN diode spectrometer prototype [67, 68], there are two circular Si-PIN diodes attached to the front and back faces of the spectrometer chamber, which itself is a rectangular prism. The gaseous samples counted by the XIA LLC Si-PIN diode spectrometer prototype completely fill the inner volume of the spectrometer chamber. So, in order to evaluate the geometric efficiency associated with the XIA LLC Si-PIN diode spectrometer prototype the solid angle subtended by each of

the differential area elements associated with each of the two Si-PIN diodes at each of the differential volume elements inside the spectrometer chamber must be evaluated and consolidated. There are a number of ways the solid angle subtended by each of the different spectrometer chamber differential volume element–Si-PIN diode differential area element combinations could be evaluated. The method employed here involves discretizing the volume inside the spectrometer chamber and the area of a Si-PIN diode and approximating the solid angle subtended by each of the spectrometer chamber differential volume element–Si-PIN diode differential area element combinations as follows:

$$\Omega_{dV_{i_x,i_y,i_z}\to dA_{i_\varphi,i_r}} = \frac{dA_{i_\varphi,i_r}\cdot\cos\theta_{dV_{i_x,i_y,i_z}\to dA_{i_\varphi,i_r}}}{4\cdot\pi\cdot r^2_{dV_{i_x,i_y,i_z}\to dA_{i_\varphi,i_r}}}. \qquad \text{C.1}$$

Where: $\Omega_{dV_{i_x,i_y,i_z}\to dA_{i_\varphi,i_r}}$ is the solid angle subtended by Si-PIN diode differential area element dA_{i_φ,i_r} at spectrometer chamber differential volume element dV_{i_x,i_y,i_z}, $\cos\theta_{dV_{i_x,i_y,i_z}\to dA_{i_\varphi,i_r}}$ is the cosine of the angle between dV_{i_x,i_y,i_z} and dA_{i_φ,i_r}, and $r_{dV_{i_x,i_y,i_z}\to dA_{i_\varphi,i_r}}$ is the radial distance from dV_{i_x,i_y,i_z} to dA_{i_φ,i_r}.

The area of Si-PIN diode differential area element dA_{i_φ,i_r} may be calculated in terms of the differential azimuthal angle, the radius, and the differential radial thickness associated with dA_{i_φ,i_r} as follows:

$$dA_{i_\varphi,i_r} = d\varphi_{dA_{i_\varphi,i_r}}\cdot r_{dA_{i_\varphi,i_r}}\cdot dr_{dA_{i_\varphi,i_r}}. \qquad \text{C.2}$$

The cosine of the angle between dV_{i_x,i_y,i_z} and dA_{i_φ,i_r} may be calculated as follows:

$$\cos\theta_{dV_{i_x,i_y,i_z}\to dA_{i_\varphi,i_r}} = \frac{\left(x^2_{dV_{i_x,i_y,i_z}\to dA_{i_\varphi,i_r}} + y^2_{dV_{i_x,i_y,i_z}\to dA_{i_\varphi,i_r}}\right)^{1/2}}{r_{dV_{i_x,i_y,i_z}\to dA_{i_\varphi,i_r}}}. \quad \text{C.3}$$

Where: $x_{dV_{i_x,i_y,i_z}\to dA_{i_\varphi,i_r}}$ is the x-component of the distance from dV_{i_x,i_y,i_z} to dA_{i_φ,i_r} and

$y_{dV_{i_x,i_y,i_z}\to dA_{i_\varphi,i_r}}$ is the y-component of the distance from dV_{i_x,i_y,i_z} to dA_{i_φ,i_r}.

The radial distance from dV_{i_x,i_y,i_z} to dA_{i_φ,i_r} that appears in Equations C.1 and C.3 may be calculated in terms of $x_{dV_{i_x,i_y,i_z}\to dA_{i_\varphi,i_r}}$, $y_{dV_{i_x,i_y,i_z}\to dA_{i_\varphi,i_r}}$, and the the z-component of the distance from dV_{i_x,i_y,i_z} to dA_{i_φ,i_r}, $z_{dV_{i_x,i_y,i_z}\to dA_{i_\varphi,i_r}}$, as follows:

$$r_{dV_{i_x,i_y,i_z}\to dA_{i_\varphi,i_r}} = \left(x^2_{dV_{i_x,i_y,i_z}\to dA_{i_\varphi,i_r}} + y^2_{dV_{i_x,i_y,i_z}\to dA_{i_\varphi,i_r}} + z^2_{dV_{i_x,i_y,i_z}\to dA_{i_\varphi,i_r}}\right)^{1/2} \quad \text{C.4}$$

The x-component of the distance from dV_{i_x,i_y,i_z} to dA_{i_φ,i_r} may be calculated as follows:

$$x_{dV_{i_x,i_y,i_z}\to dA_{i_\varphi,i_r}} = \frac{l_{Chamber}}{2} - x_{dV_{i_x,i_y,i_z}}. \quad \text{C.5}$$

Where: $l_{Chamber}$ is the length of the interior of the spectrometer chamber in the x-dimension and

$x_{dV_{i_x,i_y,i_z}}$ is the x-coordinate associated with dV_{i_x,i_y,i_z}.

The y-component of the distance from dV_{i_x,i_y,i_z} to dA_{i_φ,i_r} may be calculated as follows:

$$y_{dV_{i_x,i_y,i_z}\to dA_{i_\varphi,i_r}} = y_0 - y_{dV_{i_x,i_y,i_z}} + r_{dA_{i_\varphi,i_r}} \cdot \cos\varphi_{dA_{i_\varphi,i_r}}. \quad \text{C.6}$$

Where: y_0 is the y-coordinate associated with the center of the Si-PIN diode,

$y_{dV_{i_x,i_y,i_z}}$ is the y-coordinate associated with dV_{i_x,i_y,i_z}, and

$\varphi_{dA_{i_\varphi,i_r}}$ is the azimuthal angle associated with dA_{i_φ,i_r} measured with respect to the positive y-axis in the y-z plane.

And finally, the z-component of the distance from dV_{i_x,i_y,i_z} to dA_{i_φ,i_r} may be calculated as follows:

$$z_{dV_{i_x,i_y,i_z}\to dA_{i_\varphi,i_r}} = z_0 - z_{dV_{i_x,i_y,i_z}} + r_{dA_{i_\varphi,i_r}} \cdot \sin\varphi_{dA_{i_\varphi,i_r}}. \quad \text{C.7}$$

Where: z_0 is the z-coordinate associated with the center of the Si-PIN diode and

$z_{dV_{i_x,i_y,i_z}}$ is the z-coordinate associated with dV_{i_x,i_y,i_z}.

Substituting Equations C.2 through C.7 into Equation C.1 produces an expression for the solid angle subtended by Si-PIN diode differential area element dA_{i_φ,i_r} at spectrometer chamber differential volume element dV_{i_x,i_y,i_z} in terms of only $d\varphi_{dA_{i_\varphi,i_r}}$, $r_{dA_{i_\varphi,i_r}}$, $dr_{dA_{i_\varphi,i_r}}$, $x_{dV_{i_x,i_y,i_z}}$, $dx_{dV_{i_x,i_y,i_z}}$, $y_{dV_{i_x,i_y,i_z}}$, $dy_{dV_{i_x,i_y,i_z}}$, $z_{dV_{i_x,i_y,i_z}}$, and $dz_{dV_{i_x,i_y,i_z}}$, all of which are known from the discretization scheme.

The total solid angle subtended by a Si-PIN diode at spectrometer chamber differential volume element dV_{i_x,i_y,i_z} may be evaluated by summing up the solid angles subtended by each of the Si-PIN diode differential area elements as follows:

$$\Omega_{dV_{i_x,i_y,i_z}} = \sum_{i_r=1}^{n_r}\sum_{i_\varphi=1}^{n_\varphi} \Omega_{dV_{i_x,i_y,i_z}\to dA_{i_\varphi,i_r}} \quad \text{C.8}$$

Note that the indices on the summations in Equation C.8 indicate that the summations are to be evaluated over all Si-PIN diode differential azimuthal angle element–differential radial thickness element combinations.

The total solid angle subtended by a Si-PIN diode may be evaluated as the summation of the solid angles subtended at each of the spectrometer chamber differential volume elements weighted by their respective contributions to the total spectrometer chamber volume as follows:

$$\Omega = \sum_{i_z=1}^{n_z} \sum_{i_y=1}^{n_y} \sum_{i_x=1}^{n_x} \Omega_{dV_{i_x,i_y,i_z}} \cdot \frac{dV_{i_x,i_y,i_z}}{V} \qquad \text{C.9}$$

Where: $\Omega_{dV_{i_x,i_y,i_z}}$ is the solid angle subtended by the Si-PIN diode at spectrometer chamber differential volume element dV_{i_x,i_y,i_z} and

V is the total internal spectrometer chamber volume.

In this case the indices on the summations in Equation C.9 indicate that the summations are to be evaluated over all spectrometer chamber differential volume element combinations.

Also note that the differential volume, dV_{i_x,i_y,i_z}, may be calculated as the simple product of $dx_{dV_{i_x,i_y,i_z}}$, $dy_{dV_{i_x,i_y,i_z}}$, and $dz_{dV_{i_x,i_y,i_z}}$. In the special case where the spectrometer chamber volume is divided into $n_x \cdot n_y \cdot n_z$ differential volume elements and all of the differential volume elements have the same dimensions and the same volume then the volume fraction that appears in Equation C.9 may be replaced by one over $n_x \cdot n_y \cdot n_z$, as follows:

$$\Omega = \sum_{i_z=1}^{n_z} \sum_{i_y=1}^{n_y} \sum_{i_x=1}^{n_x} \frac{\Omega_{dV_{i_x,i_y,i_z}}}{n_x \cdot n_y \cdot n_z} = \frac{1}{n_x \cdot n_y \cdot n_z} \cdot \sum_{i_z=1}^{n_z} \sum_{i_y=1}^{n_y} \sum_{i_x=1}^{n_x} \Omega_{dV_{i_x,i_y,i_z}} \qquad \text{C.10}$$

Figures C.1 and C.2 show the solid angles subtended by the Si-PIN diodes attached to the front and back faces of the XIA LLC Si-PIN diode spectrometer prototype at each of the spectrometer chamber differential volume elements, dV_{i_x,i_y,i_z}. Note that the solid angles subtended at spectrometer chamber differential volume elements near the surfaces of the Si-PIN diodes approach 50 %, as expected. Also note that the solid angles subtended by spectrometer chamber differential volume elements further from the surfaces of the Si-PIN diodes are very small. Photons and conversion electrons emitted in these spectrometer differential volume elements would be counted with very low efficiencies. The geometric efficiency of the XIA LLC Si-PIN diode spectrometer prototype was evaluated from the solid angle data presented in Figures C.1 and C.2 and was found to be 4.8 % for each Si-PIN diode and 9.6 % for the spectrometer as a whole.

Note that the XIA LLC Si-PIN diode spectrometer prototype geometric efficiency evaluation method described herein does not account for self-shielding effects in the gaseous samples in the interior of the spectrometer chamber because the pressures associated with the gaseous samples counted in support of the XIA LLC Si-PIN diode spectrometer prototype characterization efforts documented herein were all fairly small (on the order of about 50 Torr (6,700 Pa)) so that self-shielding effects are expected to be minimal.

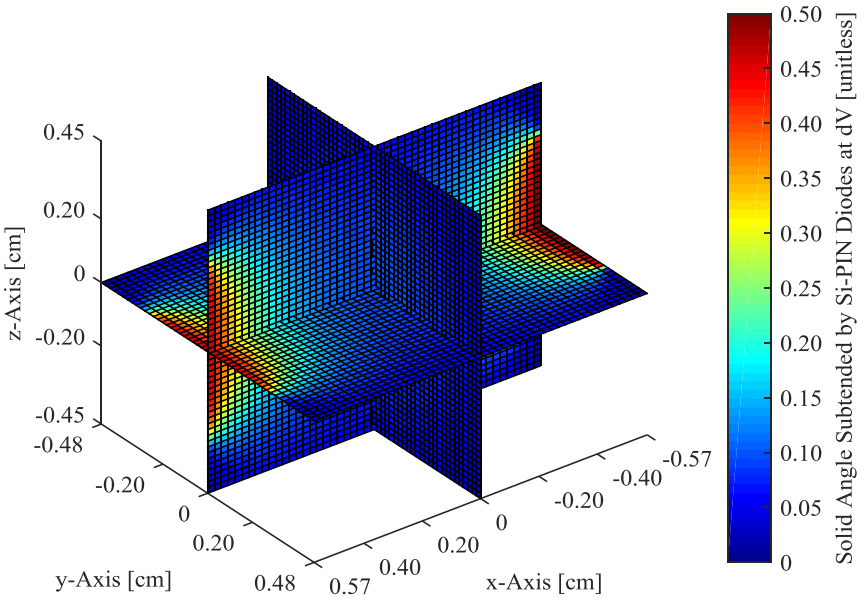

Figure C.1: Solid angles subtended by Si-PIN diodes (projection 1).

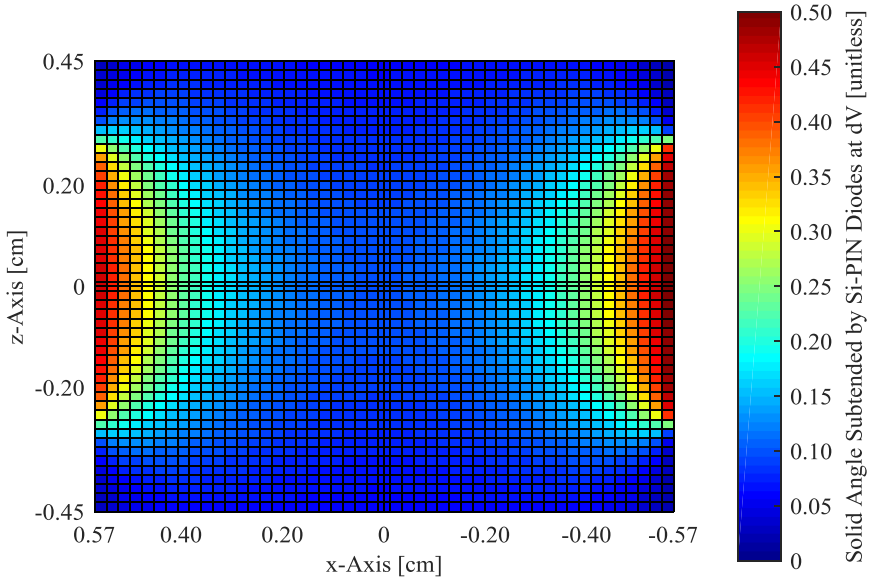

Figure C.2: Solid angles subtended by Si-PIN diodes (projection 2).

Appendix D: An MCNP Model of the XIA LLC Si-PIN Diode Spectrometer Prototype

This appendix presents a Monte Carlo N-Particle (MCNP) input deck associated with one of the MCNP models used to support the Si-PIN diode spectrometer prototype optimization studies documented in Section 2.3. The input deck was specifically developed to run in version 6.1.1beta of the MCNP code developed and maintained by Los Alamos National Laboratory [75]. Version 6.1.1beta was the most current version of MCNP available at the time the Si-PIN diode spectrometer optimization studies documented in Section 2.3 were initiated. This input deck has not been tested using any other versions of MCNP.

While the MCNP model defined by this input deck is one of only a few models used to support the Si-PIN diode spectrometer optimization studies documented in Section 2.3, it is representative of the models used to support the rectangular spectrometer chamber thickness studies documented in Section 2.3.3.1. This particular input deck models a Si-PIN diode spectrometer with a 1.06 cm thick spectrometer chamber. The Si-PIN diodes affixed to the front and back faces of the spectrometer chamber have surface areas equal to 0.25 mm^2. The input deck is heavily commented, so

additional information pertaining to specific aspects of the model can typically be found in the input deck itself.

An overview of the methods used to develop the MCNP model defined by this input deck is presented in Section 2.3.1. Sections 2.3.1.1 and 2.3.1.2 describe the methods used to define the geometric configurations of the Si-PIN diode spectrometers and the methods used to define the spectrometer material properties. Sections 2.3.1.3 and 2.3.1.4 describe the methods used to define the photon and conversion electron sources introduced to the models and the development of the tally cards used to extract simulated photon and conversion electron spectra from the MCNP models.

D.1 The MCNP Input Deck

```
The XIA LLC Two Si-PIN Diode Spectrometer Prototype
c ================================================
c
c Created by: William H. Wilson
c Created on: 30 October 2014
c Last updated on: 5 June 2016
c
c REFERENCES:
c ===========
c
c 1. W. Hennig, C. E. Cox, S.J. Asztalos, et al., "Radioxenon Measurements with
c    a Coincidence Silicon Detection System," in 2012 Monitoring Research
c    Review: Ground-Based Nuclear Explosion Monitoring Technologies,
c    Albuquerque, NM, USA, year, pp. 615-624.
c 2. W. Hennig, C. E. Cox, S. J. Asztalos, et al., "Study of silicon detectors
c    for high resolution radioxenon measurements," Journal of Radioanalytical
c    and Nuclear Chemistry, vol. 296, no. 2, pp. 675-681, April 2013.
c 3. National Institute of Standards and Technology. (14 April 2016). Physical
c    Reference Data [Online]. Available at: http://www.nist.gov/pml/...
c    data/index.cfm
c 4. R. J. McConn Jr, C. J. Gesh, R.T. Pagh, R. A. Rucker, et al., "Compendium
c    of Material Composition Data for Radiation Transport Modeling," Pacific
c    Northwest National Laboratory, Richland, WA, USA, Rep. PNNL-15870 Rev. 1,
c    4 March 2011.
c
c GENERAL MODEL INFORMATION:
c ==========================
c
c This MCNP input deck is used to model a two Si-PIN diode spectrometer
c prototype that was designed and assembled by Wolfgang Hennig and
c Christopher E. Cox of XIA LLC [1,2].
c
```

```
c ===========
c CELL CARDS:
c ===========
c
c Cell card modeling the copper spectrometer chamber:
c ================================================
c
c A single cell card, cell card 100, is used to model the copper spectrometer
c chamber in eight sections: (1) Section 1 represents the outer copper block on
c the left side of the copper spectrometer chamber. (2) Section 2 represents
c the outer copper block on the right side of the copper spectrometer chamber.
c (3) Section 3 represents the outer copper block on the bottom side of the
c copper spectrometer chamber. (4) Section 4 represents the outer copper block
c on the top side of the copper spectrometer chamber. (5) Section 5 represents
c the inner copper block on the left side of the copper spectrometer chamber.
c (6) Section 6 represents the inner copper block on the right side of the
c copper spectrometer chamber. (7) Section 7 represents the inner copper block
c on the bottom side of the copper spectrometer chamber. (8) Section 8
c represents the inner copper block on the top side of the copper spectrometer
c chamber. Note that sections 2 and 6 on the right side of the copper
c spectrometer chamber both have a cylindrical cutout in them. This cylindrical
c cutout allows the evacuate and fill tube that is used to evacuate and
c back-fill the gas volume trapped in the center of the copper spectrometer
c chamber.
c
c The mass density of the copper used to fabricate the copper spectrometer
c chamber is assumed to be consistent with the copper mass density reported by
c the National Institute of Standards and Technology (N.I.S.T.) [3].
c
c Photon and electron importances are both set equal to one in the copper
c spectrometer chamber.
c
100 1 -8.96000E+00
     ( 1000 -1003  1004 -1005  1010 -1015 ) : $ Section 1.
     ( 1000 -1003  1008 -1009  1010 -1015     $ Section 2.
       1016 ) :
     ( 1000 -1003  1005 -1008  1010 -1011 ) : $ Section 3.
     ( 1000 -1003  1005 -1008  1014 -1015 ) : $ Section 4.
     ( 1001 -1002  1005 -1006  1011 -1014 ) : $ Section 5.
     ( 1001 -1002  1007 -1008  1011 -1014     $ Section 6.
       1016 ) :
     ( 1001 -1002  1006 -1007  1011 -1012 ) : $ Section 7.
     ( 1001 -1002  1006 -1007  1013 -1014 )   $ Section 8.
     IMP:p,e=1
c
c Cell card modeling the SiO2 substrate mounted on the seating surface in
c the recessed area on the back face of the copper spectrometer chamber:
c ======================================================================
c
c A single cell card, cell card 101, is used to model the SiO2 substrate mounted
c on the seating surface in the recessed area on the back face of the copper
c spectrometer chamber.
c
c The SiO2 mass density is consistent with the SiO2 mass density quoted by John
c Pantazis, an Amptek sales representative, in an email dated 4 November 2014.
c
c Photon and electron importances are both set equal to one in the
c SiO2 substrate.
c
101 2 -2.30000E+00
     1017 -1001  1005 -1008  1011 -1014
     IMP:p,e=1
c
c Cell card modeling the SiO2 substrate mounted on the seating surface in
c the recessed area on the front face of the copper spectrometer chamber:
c ======================================================================
```

```
c
c A single cell card, cell card 102, is used to model the SiO2 substrate mounted
c on the seating surface in the recessed area on the front face of the copper
c spectrometer chamber.
c
c The SiO2 mass density is consistent with the SiO2 mass density quoted by John
c Pantazis, an Amptek sales representative, in an email dated 4 November 2014.
c
c Photon and electron importances are both set equal to one in the
c SiO2 substrate.
c
102 2 -2.30000E+00
     1002 -1018  1005 -1008  1011 -1014
     IMP:p,e=1
c
c Cell cards modeling the Si-PIN diode mounted on the SiO2
c substrate mounted on the seating surface in the recessed
c area on the back face of the copper spectrometer chamber:
c ========================================================
c
c Cell card modeling the sensitive volume
c associated with the back Si-PIN diode:
c --------------------------------------
c
c A single cell card, cell card 103, is used to model the sensitive volume
c associated with the Si-PIN diode mounted on the SiO2 substrate mounted on
c the seating surface in the recessed area on the back face of the copper
c spectrometer chamber.
c
c The mass density of the silicon used to fabricate the Si-PIN diodes is
c assumed to be consistent with the silicon mass density reported by
c the N.I.S.T. [3].
c
c Photon and electron importances are both set equal to one in the sensitive
c volume associated with the back Si-PIN diode.
c
103 3 -2.33000E+00
     1019 -1021 -1025
     IMP:p,e=1
c
c Cell card modeling the dead layer
c associated with the back Si-PIN diode:
c --------------------------------------
c
c A single cell card, cell card 104, is used to model the dead layer associated
c with the Si-PIN diode mounted on the SiO2 substrate mounted on the seating
c surface in the recessed area on the back face of the copper
c spectrometer chamber.
c
c The mass density of the silicon used to fabricate the Si-PIN diodes is
c assumed to be consistent with the silicon mass density reported by
c the N.I.S.T. [3].
c
c Photon and electron importances are both set equal to one in the dead layer
c associated with the back Si-PIN diode.
c
104 4 -2.33000E+00
     ( 1001 -1019 -1026 ) :
     ( 1019 -1021  1025 -1026 ) :
     ( 1021 -1023 -1026 )
     IMP:p,e=1
c
c Cell cards modeling the Si-PIN diode mounted on the SiO2
c substrate mounted on the seating surface in the recessed
c area on the front face of the copper spectrometer chamber:
c ========================================================
```

```
c
c Cell card modeling the sensitive volume
c associated with the front Si-PIN diode:
c -------------------------------------
c
c A single cell card, cell card 105, is used to model the sensitive volume
c associated with the Si-PIN diode mounted on the SiO2 substrate mounted on
c the seating surface in the recessed area on the front face of the copper
c spectrometer chamber.
c
c The mass density of the silicon used to fabricate the Si-PIN diodes is
c assumed to be consistent with the silicon mass density reported by
c the N.I.S.T. [3].
c
c Photon and electron importances are both set equal to one in the sensitive
c volume associated with the front Si-PIN diode.
c
105 3 -2.33000E+00
     1022 -1020 -1025
     IMP:p,e=1
c
c Cell card modeling the dead layer
c associated with the front Si-PIN diode:
c -------------------------------------
c
c A single cell card, cell card 106, is used to model the dead layer associated
c with the Si-PIN diode mounted on the SiO2 substrate mounted on the seating
c surface in the recessed area on the front face of the copper
c spectrometer chamber.
c
c The mass density of the silicon used to fabricate the Si-PIN diodes is
c assumed to be consistent with the silicon mass density reported by
c the N.I.S.T. [3].
c
c Photon and electron importances are both set equal to one in the dead layer
c associated with the front Si-PIN diode.
c
106 4 -2.33000E+00
     ( 1020 -1002 -1026 ) :
     ( 1022 -1020  1025 -1026 ) :
     ( 1024 -1022 -1026 )
     IMP:p,e=1
c
c Cell card modeling the stainless steel evacuate and fill tube:
c ============================================================
c
c A single cell card, cell card 107, is used to model the stainless steel
c evacuate and fill tube that is used to evacuate and back-fill the gas
c volume trapped in the center of the copper spectrometer chamber.
c
c The mass density of the stainless steel used to fabricate the stainless steel
c evacuate and fill tube is assumed to be consistent with the stainless steel
c alloy 304 mass density reported by P.N.N.L. [4].
c
c Photon and electron importances are both set equal to one in the
c stainless steel evacuate and fill tube.
c
107 5 -8.00000E+00
     1007 -1035 -1016  1027
        IMP:p,e=1
c
c Cell card modeling the gas volume trapped in the center
c of the copper spectrometer chamber, in the cylindrical
c cutout in the right side of the copper spectrometer
c chamber, and in the stainless steel evacuate and fill tube:
c ============================================================
```

```
c
c A single cell card, cell card 108, is used to model the gas volume trapped in
c the center of the copper spectrometer chamber, in the cylindrical cutout in
c the right side of the copper spectrometer chamber, and in the stainless steel
c evacuate and fill tube in two sections: (1) Section 1 represents the gas
c volume trapped in the center of the copper spectrometer chamber.
c (2) Section 2 represents the gas volume trapped in the cylindrical cutout
c in the right side of the copper spectrometer chamber and in the stainless
c steel evacuate and fill tube.
c
c The atom density of the gas volume trapped in the center of the copper
c spectrometer chamber, in the cylindrical cutout in the right side of the
c copper spectrometer chamber, and in the stainless steel evacuate and fill
c tube is consistent with a gas pressure of 50.0 Torr.
c
c Photon and electron importances are both set equal to one in the gas volume
c trapped in the center of the copper spectrometer chamber, in the cylindrical
c cutout in the right side of the copper spectrometer chamber, and in the
c stainless steel evacuate and fill tube.
c
108 6  1.64702E-06
     ( 1001 -1002  1006 -1007  1012 -1013 #103 #104 #105 #106 ) : $ Section 1.
     ( 1007 -1035 -1027 )                                        $ Section 2.
     IMP:p,e=1
c
c Cell card modeling the outer stainless steel box:
c ================================================
c
c A single cell card, cell card 109, is used to model the outer stainless steel
c box in six sections: (1) Section 1 represents the back side of the outer
c stainless steel box. (2) Section 2 represents the front side of the outer
c stainless steel box. (3) Section 3 represents the left side of the outer
c stainless steel box. (4) Section 4 represents the right side of the outer
c stainless steel box. (5) Section 5 represents the bottom side of the outer
c stainless steel box. (6) Section 6 represents the top side of the outer
c stainless steel box.
c
c The mass density of the stainless steel used to fabricate the outer stainless
c steel box is assumed to be consistent with the stainless steel alloy 304 mass
c density reported by P.N.N.L. [3].
c
c Photon and electron importances are both set equal to one in the outer
c stainless steel box.
c
109 5 -8.00000E+00
     (  1028 -1029  1032 -1035  1036 -1039 ) : $ Section 1.
     (  1030 -1031  1032 -1035  1036 -1039 ) : $ Section 2.
     (  1029 -1030  1032 -1033  1036 -1039 ) : $ Section 3.
     (  1029 -1030  1034 -1035  1036 -1039     $ Section 4.
        1016 ) :
     (  1029 -1030  1033 -1034  1036 -1037 ) : $ Section 5.
     (  1029 -1030  1033 -1034  1038 -1039 )   $ Section 6.
     IMP:p,e=1
c
c Cell card modeling the nitrogen gas trapped in the outer stainless steel box:
c ============================================================================
c
c A single cell card, cell card 110, is used to model the nitrogen gas trapped
c in the outer stainless steel box.
c
c The atom density of the nitrogen gas trapped in the outer stainless steel
c box is consistent with a gas pressure of 760 Torr.
c
c Photon and electron importances are both set equal to one in the nitrogen gas
c trapped in the outer stainless steel box.
c
```

```
c Note that when a calibration source is assumed to be inside the outer
c stainless steel box, the cell cards used to model the calibration source,
c cell cards 111 and 112, need to be active (i.e. not commented out) and
c included in the list of compliments associated with cell card 110, the cell
c card used to model the nitrogen gas trapped in the outer stainless steel box.
c When the calibration source is not assumed to be inside the outer stainless
c steel box, the cell cards used to model the calibration source need to be
c inactive (i.e. commented out) and should be removed from the list of
c compliments associated with the cell card used to model the nitrogen gas
c trapped in the outer stainless steel box. Changes also need to be made
c to the surface cards defining the boundaries of the calibration source and
c to the source definition card when assumptions pertaining to the placement
c of the calibration source are modified.
c
110 7  2.50348E-05
     1029 -1030  1033 -1034  1037 -1038
     #100 #101 #102 #103 #104 #105 #106 #107 #108 $ #111 #112
     IMP:p,e=1
c
c Cell cards modeling the calibration source:
c ==========================================
c
c Note that when a calibration source is assumed to be inside the outer
c stainless steel box, the cell cards used to model the calibration source,
c cell cards 111 and 112, need to be active (i.e. not commented out) and
c included in the list of compliments associated with cell card 110, the cell
c card used to model the nitrogen gas trapped in the outer stainless steel box.
c When the calibration source is not assumed to be inside the outer stainless
c steel box, the cell cards used to model the calibration source need to be
c inactive (i.e. commented out) and should be removed from the list of
c compliments associated with the cell card used to model the nitrogen gas
c trapped in the outer stainless steel box. Changes also need to be made
c to the surface cards defining the boundaries of the calibration source and
c to the source definition card when assumptions pertaining to the placement
c of the calibration source are modified. Additionally the acrylic plastic
c material data card needs to be active when the calibration source is
c assumed to be inside the outer stainless steel box. The acrylic plastic
c material data card needs to be inactive when the calibration source is
c not assumed to be inside the outer stainless steel box.
c
c Cell card modeling the acrylic plastic portion of the calibration source:
c ------------------------------------------------------------------------
c
c A single cell card, cell card 111, is used to model the
c calibration source inside the outer stainless steel box.
c
c The calibration sources are assumed to be composed of an acrylic plastic
c material. This assumption is based on an email from an Eckert and Ziegler
c customer service representative dated 4 April 2016. The acrylic density
c is assumed to be equal to the Lucite density reported by P.N.N.L. [4].
c
c Photon and electron importances are both set equal to one
c in the acrylic plastic portion of the calibration source.
c
c 111 8 -1.20000E+00
c      ( 1040 -1041 -1046 ) :
c      ( 1041 -1042  1044 -1046 ) :
c      ( 1042 -1043  1045 -1046 )
c      IMP:p,e=1
c
c Cell card modeling the epoxy plug in the calibration
c source inside the outer stainless steel box:
c ----------------------------------------------------
c
c A single cell card, cell card 112, is used to model the epoxy plug
c in the calibration source inside the outer stainless steel box.
```

```
c
c Not knowing what the composition of the epoxy really is, the epoxy plug in the
c calibration source inside the outer stainless steel box is also assumed to be
c composed of an acrylic material. The acrylic density is assumed to be equal
c to the Lucite density reported by P.N.N.L. [4].
c
c Photon and electron importances are both set equal
c to one in the epoxy plug in the calibration source.
c
c 112 8 -1.20000E+00
c      1041 -1042 -1044
c      IMP:p,e=1
c
c Cell card modeling the photon and particle graveyard:
c ====================================================
c
c A single cell card, cell card 999, is used to model the photon and
c particle graveyard.
c
c The photon and particle graveyard is filled with a void (MCNP material
c number 0).
c
c Photon and electron importances are both set equal to zero in the
c particle graveyard.
c
999 0
     -1028 : 1031 : -1032 :  1035 : -1036 : 1039
     IMP:p,e=0

c ==============
c SURFACE CARDS:
c ==============
c
c The following surface cards are used to define
c the boundaries of the copper spectrometer chamber:
c ==================================================
c
1000  PX -7.04850E-01 $ The back face of the copper spectrometer chamber.
c
1001  PX -5.82930E-01 $ The SiO2 substrate seating surface within the recessed
c                       area on the back face of the copper spectrometer
c                       chamber. This is also the back boundary of the gas
c                       volume trapped in the center of the copper
c                       spectrometer chamber.
c
1002  PX  5.82930E-01 $ The SiO2 substrate seating surface within the recessed
c                       area on the front face of the copper spectrometer
c                       chamber. This is also the front boundary of the gas
c                       volume trapped in the center of the copper
c                       spectrometer chamber.
c
1003  PX  7.04850E-01 $ The front face of the copper spectrometer chamber.
c
1004  PY -1.01473E+00 $ The left face of the copper spectrometer chamber.
c
1005  PY -5.95630E-01 $ The left side of the recessed area on the front face
c                       of the copper spectrometer chamber and the right side
c                       of the recessed area on the back face of the copper
c                       spectrometer chamber.
c
1006  PY -5.46100E-01 $ The inner, left boundary of the copper spectrometer
c                       chamber. This is also the left boundary of the gas
c                       volume trapped in the center of the copper
c                       spectrometer chamber.
c
1007  PY  4.24180E-01 $ The inner, right boundary of the copper spectrometer
```

```
c                       chamber. This is also the right boundary of the gas
c                       volume trapped in the center of the copper
c                       spectrometer chamber.
c
1008  PY  4.73710E-01 $ The right side of the recessed area on the front face
c                       of the copper spectrometer chamber and the left side
c                       of the recessed area on the back face of the copper
c                       spectrometer chamber.
c
1009  PY  1.01473E+00 $ The right face of the copper spectrometer chamber.
c
1010  PZ -7.04850E-01 $ The bottom face of the copper spectrometer chamber.
c
1011  PZ -5.34670E-01 $ The bottom side of the recessed areas on the front
c                       and back faces of the copper spectrometer chamber.
c
1012  PZ -4.54660E-01 $ The inner, bottom boundary of the copper spectrometer
c                       chamber. This is also the bottom boundary of the gas
c                       volume trapped in the center of the copper
c                       spectrometer chamber.
c
1013  PZ  4.54660E-01 $ The inner, top boundary of the copper spectrometer
c                       chamber. This is also the top boundary of the gas
c                       volume trapped in the center of the copper
c                       spectrometer chamber.
c
1014  PZ  5.34670E-01 $ The top side of the recessed areas on the front
c                       and back faces of the copper spectrometer chamber.
c
1015  PZ  7.04850E-01 $ The top face of the copper spectrometer chamber.
c
1016  CY  8.00100E-02 $ The cylindrical surface defining the cylindrical cutout
c                       in the right side of the copper spectrometer chamber
c                       through which the evacuate and fill tube that is used
c                       to evacuate and back-fill the gas volume trapped in the
c                       center of the copper spectrometer chamber passes.
c
c The following surface cards are used to define the boundaries
c of the SiO2 substrates that the Si-PIN diodes are mounted on:
c ============================================================
c
1017  PX -6.08330E-01 $ The outer surface of the SiO2 substrate mounted on the
c                       seating surface in the recessed area on the back face
c                       of the copper spectrometer chamber.
c
c                       Note that the inner surface of the SiO2 substrate
c                       mounted on the seating surface in the recessed area on
c                       the back face of the copper spectrometer chamber is
c                       defined by surface card 1001.
c
1018  PX  6.08330E-01 $ The outer surface of the SiO2 substrate mounted on the
c                       seating surface in the recessed area on the front face
c                       of the copper spectrometer chamber.
c
c                       Note that the inner surface of the SiO2 substrate
c                       mounted on the seating surface in the recessed area on
c                       the front face of the copper spectrometer chamber is
c                       defined by surface card 1002.
c
c The following surface cards are used to define the
c boundaries of the Si-PIN diodes and their dead layers:
c =====================================================
c
1019  PX -5.82915E-01 $ The outer surface of the sensitive volume of the
c                       Si-PIN diode mounted on the SiO2 substrate mounted on
c                       the seating surface in the recessed area on the back
```

```
c                       face of the copper spectrometer chamber.
c
1020  PX  5.82915E-01 $ The outer surface of the sensitive volume of the
c                       Si-PIN diode mounted on the SiO2 substrate mounted on
c                       the seating surface in the recessed area on the front
c                       face of the copper spectrometer chamber.
c
1021  PX -5.32945E-01 $ The inner surface of the sensitive volume of the
c                       Si-PIN diode mounted on the SiO2 substrate mounted on
c                       the seating surface in the recessed area on the back
c                       face of the copper spectrometer chamber.
c
1022  PX  5.32945E-01 $ The inner surface of the sensitive volume of the
c                       Si-PIN diode mounted on the SiO2 substrate mounted on
c                       the seating surface in the recessed area on the front
c                       face of the copper spectrometer chamber.
c
1023  PX -5.32930E-01 $ The inner surface of the dead layer that covers the
c                       inner face of the Si-PIN diode mounted on the
c                       SiO2 substrate mounted on the seating surface in the
c                       recessed area on the back face of the copper
c                       spectrometer chamber.
c
1024  PX  5.32930E-01 $ The inner surface of the dead layer that covers the
c                       inner face of the Si-PIN diode mounted on the
c                       SiO2 substrate mounted on the seating surface in the
c                       recessed area on the front face of the copper
c                       spectrometer chamber.
c
1025 C/X -6.09600E-02 $ The cylindrical surface defining the outer cylindrical
          0.00000E+00 $ surfaces of the sensitive volumes of each of the
          2.81985E-01 $ Si-PIN diodes. This is also the cylindrical surface
c                       that defines the inner cylindrical surfaces of the
c                       dead layers that wrap around the side faces of each
c                       of the Si-PIN diodes.
c
1026 C/X -6.09600E-02 $ The cylindrical surface defining the outer cylindrical
          0.00000E+00 $ surfaces of the dead layers that wrap around the side
          2.82000E-01 $ faces of each of the Si-PIN diodes.
c
c                       Note: (1) that the outer surfaces of the dead layers
c                       that cover the outer faces of the Si-PIN diodes are
c                       defined by surfaces 1001 and 1002, and (2) that the
c                       inner non-cylindrical surfaces of the sensitive volumes
c                       of the Si-PIN diodes are the outer non-cylindrical
c                       surfaces of the Si-PIN diode dead layers.
c
c The following surface card is used to define the inner
c boundary of the stainless steel evacuate and fill tube:
c ======================================================
c
1027  CY  2.79400E-02 $ The inner boundary of the stainless steel evacuate
c                       and fill tube.
c
c The following surface cards are used to define
c the boundaries of the nitrogen-filled outer chamber:
c ====================================================
c
1028  PX -4.00000E+00 $ The outer-back boundary of the nitrogen-
c                       filled outer stainless steel box.
c
1029  PX -3.60000E+00 $ The inner-back boundary of the nitrogen-
c                       filled outer stainless steel box.
c
1030  PX  3.60000E+00 $ The inner-front boundary of the nitrogen-
c                       filled outer stainless steel box.
```

```
c
1031  PX  4.00000E+00 $ The outer-front boundary of the nitrogen-
c                       filled outer stainless steel box.
c
1032  PY -8.10000E+00 $ The outer-left boundary of the nitrogen-
c                       filled outer stainless steel box.
c
1033  PY -7.70000E+00 $ The inner-left boundary of the nitrogen-
c                       filled outer stainless steel box.
c
1034  PY  3.50000E+00 $ The inner-right boundary of the nitrogen-
c                       filled outer stainless steel box.
c
1035  PY  3.90000E+00 $ The outer-right boundary of the nitrogen-
c                       filled outer stainless steel box.
c
1036  PZ -2.65000E+00 $ The outer-bottom boundary of the nitrogen-
c                       filled outer stainless steel box.
c
1037  PZ -2.25000E+00 $ The inner-bottom boundary of the nitrogen-
c                       filled outer stainless steel box.
c
1038  PZ  2.95000E+00 $ The inner-top boundary of the nitrogen-
c                       filled outer stainless steel box.
c
1039  PZ  3.35000E+00 $ The outer-top boundary of the nitrogen-
c                       filled outer stainless steel box.
c
c The following surface cards are used to define the boundaries
c of the calibration source in the nitrogen-filled outer chamber:
c ============================================================
c
c When the calibration source is assumed to be inside the outer stainless steel
c box, the surface cards below need to be active (i.e. not commented out).
c When the calibration source is not assumed to be inside the outer stainless
c steel box, the surface cards below need to be inactive (i.e. commented out).
c Changes also need to be made to several of the cell cards and to the source
c definition card when assumptions pertaining to the placement of the
c calibration source are modified. Additionally the acrylic plastic material
c data card needs to be active when the calibration source is assumed to be
c inside the outer stainless steel box. The acrylic plastic material
c data card needs to be inactive when the calibration source is not
c assumed to be inside the outer stainless steel box.
c
c 1040  PX  1.70485E+00 $ The back face of the calibration source. This is the
c                         red face, not the white face with the label on it.
c
c 1041  PX  1.98185E+00 $ The recessed surface within the calibration
c                         source on which the radioactive metallic
c                         source salts were deposited.
c
c 1042  PX  2.29985E+00 $ The recessed surface to which the white label is
c                         affixed on the front face of the calibration source.
c
c 1043  PX  2.33985E+00 $ The raised surface associated with the
c                         elevated lip that runs around the front
c                         face of the calibration source.
c
c 1044 C/X -3.10960E-01 $ The surface defining the cylindrical cavity
c          0.00000E+00 $ within which the radioactive metallic
c          2.50000E-01 $ source salts were deposited.
c
c 1045 C/X -3.10960E-01 $ The inner surface of the elevated lip that runs
c          0.00000E+00 $ around the front face of the calibration source.
c          1.07000E+00
c
```

```
c 1046 C/X -3.10960E-01 $ The outer cylindrical surface
c           0.00000E+00 $ of the calibration source.
c           1.27000E+00

c ===========
c DATA CARDS:
c ===========
c
c Material data for the copper spectrometer chamber:
c ==================================================
c
c The copper spectrometer chamber is assumed to be composed of natural copper,
c and the isotopic composition of natural copper is assumed to be consistent
c with the natural copper isotopic composition reported by the N.I.S.T. [3].
c
c Setting the "GAS" keyword equal to 0 specifies that an electron stopping power
c density-effect correction applicable to copper in the condensed state
c should be used.
c
c Setting the "COND" keyword equal to -1 specifies that the copper should be
c modeled as a non-conductor.
c
M1   029063  6.91500E-01 $ Cu-63
     029065  3.08500E-01 $ Cu-65
     GAS=0
     COND=-1
c
c Material data for the SiO2 substrate:
c =====================================
c
c The SiO2 substrate is assumed to be composed of SiO2, and the isotopic
c compositions of the Si and O that constitute the SiO2 are assumed to be
c consistent with the natural isotopic compositions of Si and O reported
c by the N.I.S.T. [3].
c
c Setting the "GAS" keyword equal to 0 specifies that an electron stopping power
c density-effect correction applicable to SiO2 in the condensed state
c should be used.
c
c Setting the "COND" keyword equal to -1 specifies that the SiO2 should be
c modeled as a non-conductor.
c
M2   008016  6.65047E-01 $ O-16
     008017  2.53333E-04 $ O-17
     008018  1.36667E-03 $ O-18
     014028  3.07410E-01 $ Si-28
     014029  1.56167E-02 $ Si-29
     014030  1.03067E-02 $ Si-30
     GAS=0
     COND=-1
c
c Material data for the sensitive volume of the Si-PIN diode:
c ===========================================================
c
c The sensitive volumes of the Si-PIN diodes are assumed to be composed of
c natural silicon, and the isotopic composition of the natural silicon is
c assumed to be consistent with the natural silicon isotopic composition
c reported by the N.I.S.T. [3].
c
c Setting the "GAS" keyword equal to 0 specifies that an electron stopping power
c density-effect correction applicable to silicon in the condensed state
c should be used.
c
c Setting the "COND" keyword equal to 1 specifies that the SiO2 should be
c modeled as a conductor.
c
```

```
M3   014028  9.22230E-01 $ Si-28
     014029  4.68500E-02 $ Si-29
     014030  3.09200E-02 $ Si-30
     GAS=0
     COND=1
c
c Material data for the dead layer of the Si-PIN diode:
c ======================================================
c
c The dead layers of the Si-PIN diodes are assumed to be composed of natural
c silicon, and the isotopic composition of the natural silicon is assumed to
c be consistent with the natural silicon isotopic composition reported by
c the N.I.S.T. [3].
c
c Setting the "GAS" keyword equal to 0 specifies that an electron stopping power
c density-effect correction applicable to silicon in the condensed state
c should be used.
c
c Setting the "COND" keyword equal to -1 specifies that the SiO2 should be
c modeled as a non-conductor.
c
M4   014028  9.22230E-01 $ Si-28
     014029  4.68500E-02 $ Si-29
     014030  3.09200E-02 $ Si-30
     GAS=0
     COND=-1
c
c Material data for the stainless steel outer box:
c ================================================
c
c The outer box is assumed to be composed of stainless steel, and the isotopic
c composition of the stainless steel is assumed to be consistent with the
c stainless steel alloy 304 isotopic composition reported by Pacific
c Northwest National Laboratory (P.N.N.L.) [4].
c
c Setting the "GAS" keyword equal to 0 specifies that an electron stopping power
c density-effect correction applicable to stainless steel in the condensed
c state should be used.
c
c Setting the "COND" keyword equal to -1 specifies that the stainless steel
c should be modeled as a non-conductor.
c
M5   006000  1.83000E-03 $ Natural C
     014000  9.78100E-03 $ Natural Si
     015031  4.08000E-04 $ P-31
     016000  2.57000E-04 $ Natural S
     024000  2.00762E-01 $ Natural Cr
     025055  1.00010E-02 $ Mn-55
     026000  6.90375E-01 $ Natural Fe
     028000  8.65870E-02 $ Natural Ni
        GAS=0
     COND=-1
c
c Material data for the gaseous mixture in the copper spectrometer chamber:
c =========================================================================
c
c For simplicity, the gaseous mixture in the copper spectrometer chamber is
c assumed to be composed purely of xenon gas. In reality the gaseous mixture is
c composed of a mixture of xenon and nitrogen.
c
c Setting the "GAS" keyword equal to 1 specifies that an electron stopping power
c density-effect correction applicable to the gaseous state should be used.
c
c Setting the "COND" keyword equal to -1 specifies that the gaseous mixture
c should be modeled as a non-conductor.
c
```

```
c Note that when the calibration source is assumed to be inside the outer
c stainless steel box the copper spectrometer chamber should be filled with
c nitrogen gas, defined by material data card M7, below as opposed to xenon gas.
c
M6   054132  1.00000E+00 $ Xe-132
     GAS=1
     COND=-1
c
c Material data for the nitrogen gas in the outer stainless steel box:
c ======================================================================
c
c The isotopic composition of the nitrogen gas in the outer stainless steel box
c is assumed to be consistent with the natural nitrogen isotopic composition
c reported by the N.I.S.T. [3].
c
c Setting the "GAS" keyword equal to 1 specifies that an electron stopping power
c density-effect correction applicable to the gaseous state should be used.
c
c Setting the "COND" keyword equal to -1 specifies that the nitrogen gas
c in the outer stainless steel box should be modeled as a non-conductor.
c
M7   007014  9.96360E-01 $ N-14
     007015  3.64000E-03 $ N-15
     GAS=1
     COND=-1
c
c Material data for the acrylic plastic portion of the calibration source:
c ========================================================================
c
c The calibration sources are assumed to be composed of an acrylic plastic
c material. This assumption is based on an email from an Eckert and Ziegler
c customer service representative dated 4 April 2016. The isotopic composition
c of the acrylic plastic is assumed to be consistent with the Lucite
c composition reported by the N.I.S.T. [3].
c
c Setting the "GAS" keyword equal to 1 specifies that an electron stopping power
c density-effect correction applicable to the gaseous state should be used.
c
c Setting the "COND" keyword equal to -1 specifies that the nitrogen gas
c in the outer stainless steel box should be modeled as a non-conductor.
c
c Note that the acrylic plastic material data card needs to be active when
c the calibration source is assumed to be inside the outer stainless steel
c box. The acrylic plastic material data card needs to be inactive when the
c calibration source is not assumed to be inside the outer stainless steel box.
c
c M8   001001  5.33320E-01 $ H-1
c      006000  3.33345E-01 $ Natural C
c      008016  1.33335E-01 $ O-16
c      GAS=0
c      COND=-1
c
c Data cards related to physics:
c ==============================
c
MODE p e $ Transport photons (p) and electrons (e).
c
MPHYS on $ Turn physics models on.
c
c Data cards related to source specification:
c ===========================================
c
c Data cards modeling radioxenon gas in the copper spectrometer chamber:
c ----------------------------------------------------------------------
c
c The following SDEF card specifies that:
```

```
c (1) the x-coordinate associated with the source position should
c     be determined in accordance with the sampling rules provided
c     on cards SI1 and SP1 (X=D1),
c (2) the y-coordinate associated with the source position should
c     be determined in accordance with the sampling rules provided
c     on cards SI2 and SP2 (Y=D2),
c (3) the z-coordinate associated with the source position should be
c     determined in accordance with the sampling rules provided on
c     cards SI3 and SP3 (Z=D3),
c (4) the source (x,y,z) positions determined using the x-, y-, and
c     z-coordinate sampling rules specified on the SI and SP cards associated
c     with the X, Y, and Z SDEF card keywords should be accepted only if they
c     lie within the specified cookie-cutter cell (CCC=108),
c (5) the rejection efficiency associated with the x-, y-, and z-coordinate
c     sampling must be greater than one percent (EFF=0.01),
c (6) the source should be either a photon source (p) or an electron source (e),
c     depending on the radioxenon decay mode of interest (PAR=p or PAR=e), and
c (7) the source kinetic energy, X, should be applicable to the radioxenon
c     decay mode of interest, where X is the energy of the radioxenon decay
c     mode in MeV (ERG=X).
c
SDEF X=D1 Y=D2 Z=D3 CCC=108 EFF=0.01 PAR=e ERG=0.150
c
c The following SI1 card specifies that the x-coordinate associated with the
c source position should be determined by sampling from a histogram with a
c single x-coordinate bin that covers the interval [-5.82930E-01 cm,
c 5.82930E-01 cm]. The SP1 card specifies that (1) the x-coordinate must take
c a value on this interval and (2) that all x-coordinates on this interval are
c equally probable.
c
SI1  H -5.82930E-01  5.82930E-01
SP1  D  0.00000E+00  1.00000E+00
c
c The following SI2 card specifies that the y-coordinate associated with the
c source position should be determined by sampling from a histogram with a
c single y-coordinate bin that covers the interval [-5.46100E-01 cm,
c 4.24180E-01 cm]. The SP2 card specifies that (1) the y-coordinate must take
c a value on this interval and (2) that all y-coordinates on this interval are
c equally probable.
c
SI2  H -5.46100E-01  4.24180E-01
SP2  D  0.00000E+00  1.00000E+00
c
c The following SI3 card specifies that the z-coordinate associated with the
c source position should be determined by sampling from a histogram with a
c single z-coordinate bin that covers the interval [-4.54660E-01 cm,
c 4.54660E-01 cm]. The SP3 card specifies that (1) the z-coordinate must take
c a value on this interval and (2) that all z-coordinates on this interval are
c equally probable.
c
SI3  H -4.54660E-01  4.54660E-01
SP3  D  0.00000E+00  1.00000E+00
c
c Data cards modeling the calibration source in the outer stainless steel box:
c --------------------------------------------------------------------------
c
c The radioactive metallic source salts deposited in the calibration sources
c were deposited on flat, circular surfaces at the bottom of shallow
c cylindrical cavities in the calibration sources. The source definition cards
c below are used to sample from the circular surface in the modeled calibration
c source and send out monoenergetic radiations isotropically from the surface.
c
c Note that when the calibration source is not assumed to be inside the outer
c stainless steel box the source definition card below and its associated
c source information and source probability cards need to be inactive
c (i.e. commented out).
```

```
c
c SDEF SUR=1041 POS=1.98185E+00 -3.10960E-01 0.00000E+00
c      RAD=D1 VEC=1 0 0 DIR=D2 PAR=p ERG=0.030850
c
c SI1   H  0.00000E+00  2.50000E-01
c
c SP1 -21  1.00000E+00
c
c SI2   H -1.00000E+00  1.00000E+00
c
c SP2   D  0.00000E+00  1.00000E+00
c
c Data cards related to tally specification:
c ==========================================
c
c Tally F101:
c -----------
c
c Tally F101 places a photon current tally on the flat, inner surface of
c the dead layer of the Si-PIN diode mounted on the SiO2 substrate mounted
c on the seating surface in the recessed area on the back face of the
c copper spectrometer chamber (MCNP surface 1023).
c
c Tally cosine card C101 establishes the angular bin structure to be used
c for the F101 photon current tally.
c
c Tally segment card FS101 subdivides MCNP surface 1023 into two segments
c for tallying purposes: (1) one segment with a negative sense with respect to
c MCNP surface 1026, and (2) a second segment with a positive sense with respect
c to MCNP surface 1026. We only care about segment (1), which represents the
c photon current through the flat, inner surface of the dead layer of the Si-PIN
c diode mounted on the SiO2 substrate mounted on the seating surface in the
c recessed area on the back face of the copper spectrometer chamber.
c
F101:p 1023
FC101 Photon current through flat, inner surf. of back Si-PIN diode dead lay.
C101 0 1
FS101 -1026
c
c Tally F111:
c -----------
c
c Tally F111 places a photon current tally on the outer cylindrical surface
c of the dead layer of the Si-PIN diode mounted on the SiO2 substrate mounted
c on the seating surface in the recessed area on the back face of the
c copper spectrometer chamber (MCNP surface 1026).
c
c Tally cosine card C111 establishes the angular bin structure to be used
c for the F111 photon current tally.
c
c Tally segment card FS111 subdivides MCNP surface 1026 into three segments
c for tallying purposes: (1) one segment with a negative sense with respect to
c MCNP surface 1001, (2) a second segment with a positive sense with respect
c to MCNP surface 1001 and a negative sense with respect to MCNP surface 1023,
c and (3) a third segment with a positive sense with respect to MCNP surfaces
c 1001 and 1023. We only care about segment (2), which represents the photon
c current through the outer cylindrical surface of the dead layer of the Si-PIN
c diode mounted on the SiO2 substrate mounted on the seating surface in the
c recessed area on the back face of the copper spectrometer chamber.
c
F111:p 1026
FC111 Photon current through cyl. surf. of back Si-PIN diode dead lay.
C111 0 1
FS111 -1001 -1023
c
c Tally F121:
```

```
c -----------
c
c Tally F121 places a photon current tally on the flat, outer surface of
c the dead layer of the Si-PIN diode mounted on the SiO2 substrate mounted
c on the seating surface in the recessed area on the back face of the
c copper spectrometer chamber (MCNP surface 1001).
c
c Tally cosine card C121 establishes the angular bin structure to be used
c for the F121 photon current tally.
c
c Tally segment card FS121 subdivides MCNP surface 1001 into three segments
c for tallying purposes: (1) one segment with a negative sense with respect to
c MCNP surface 1025, (2) a second segment with a positive sense with respect
c to MCNP surface 1025 and a negative sense with respect to MCNP surface 1026,
c and (3) a third segment with a positive sense with respect to MCNP surfaces
c 1025 and 1026. We only care about segment (2), which represents the photon
c current through the flat, outer surface of the dead layer of the Si-PIN
c diode mounted on the SiO2 substrate mounted on the seating surface in
c the recessed area on the back face of the copper spectrometer chamber.
c
F121:p 1001
FC121 Photon current through flat, outer surf. of back Si-PIN diode dead lay.
C121 0 1
FS121 -1025 -1026
c
c Tally F131:
c -----------
c
c Tally F131 places a photon current tally on the flat, inner surface of
c the sensitive volume of the Si-PIN diode mounted on the SiO2 substrate
c mounted on the seating surface in the recessed area on the back face
c of the copper spectrometer chamber (MCNP surface 1021).
c
c Tally cosine card C131 establishes the angular bin structure to be used
c for the F131 photon current tally.
c
c Tally segment card FS131 subdivides MCNP surface 1021 into two segments
c for tallying purposes: (1) one segment with a negative sense with respect to
c MCNP surface 1025, and (2) a second segment with a positive sense with respect
c to MCNP surface 1025. We only care about segment (1), which represents the
c photon current through the flat, inner surface of the sensitive volume of the
c Si-PIN diode mounted on the SiO2 substrate mounted on the seating surface
c in the recessed area on the back face of the copper spectrometer chamber.
c
F131:p 1021
FC131 Photon current through flat, inner surf. of back Si-PIN diode sens. vol.
C131 0 1
FS131 -1025
c
c Tally F141:
c -----------
c
c Tally F141 places a photon current tally on the outer cylindrical surface
c of the sensitive volume of the Si-PIN diode mounted on the SiO2 substrate
c mounted on the seating surface in the recessed area on the back face of
c the copper spectrometer chamber (MCNP surface 1025).
c
c Tally cosine card C141 establishes the angular bin structure to be used
c for the F141 photon current tally.
c
c Tally segment card FS141 subdivides MCNP surface 1025 into three segments
c for tallying purposes: (1) one segment with a negative sense with respect to
c MCNP surface 1001, (2) a second segment with a positive sense with respect
c to MCNP surface 1001 and a negative sense with respect to MCNP surface 1021,
c and (3) a third segment with a positive sense with respect to MCNP surfaces
c 1001 and 1021. We only care about segment (2), which represents the photon
```

```
c current through the outer cylindrical surface of the sensitive volume of the
c Si-PIN diode mounted on the SiO2 substrate mounted on the seating surface
c in the recessed area on the back face of the copper spectrometer chamber.
c
F141:p 1025
FC141 Photon current through cyl. surf. of back Si-PIN diode sens. vol.
C141 0 1
FS141 -1001 -1021
c
c Tally F151:
c -----------
c
c Tally F151 places a photon current tally on the flat, outer surface of
c the sensitive volume of the Si-PIN diode mounted on the SiO2 substrate
c mounted on the seating surface in the recessed area on the back face
c of the copper spectrometer chamber (MCNP surface 1001).
c
c Tally cosine card C151 establishes the angular bin structure to be used
c for the F151 photon current tally.
c
c Tally segment card FS151 subdivides MCNP surface 1001 into two segments
c for tallying purposes: (1) one segment with a negative sense with respect to
c MCNP surface 1025, and (2) a second segment with a positive sense with respect
c to MCNP surface 1025. We only care about segment (1), which represents the
c photon current through the flat, outer surface of the sensitive volume of the
c Si-PIN diode mounted on the SiO2 substrate mounted on the seating surface
c in the recessed area on the back face of the copper spectrometer chamber.
c
F151:p 1001
FC151 Photon current through flat, outer surf. of back Si-PIN diode sens. vol.
C151 0 1
FS151 -1025
c
c Tally F161:
c -----------
c
c Tally F161 places a photon current tally on the flat, inner surface of
c the dead layer of the Si-PIN diode mounted on the SiO2 substrate mounted
c on the seating surface in the recessed area on the front face of the
c copper spectrometer chamber (MCNP surface 1024).
c
c Tally cosine card C161 establishes the angular bin structure to be used
c for the F161 photon current tally.
c
c Tally segment card FS161 subdivides MCNP surface 1024 into two segments
c for tallying purposes: (1) one segment with a negative sense with respect to
c MCNP surface 1026, and (2) a second segment with a positive sense with respect
c to MCNP surface 1026. We only care about segment (1), which represents the
c photon current through the flat, inner surface of the dead layer of the Si-PIN
c diode mounted on the SiO2 substrate mounted on the seating surface in the
c recessed area on the front face of the copper spectrometer chamber.
c
F161:p 1024
FC161 Photon current through flat, inner surf. of front Si-PIN diode dead lay.
C161 0 1
FS161 -1026
c
c Tally F171:
c -----------
c
c Tally F171 places a photon current tally on the outer cylindrical surface
c of the dead layer of the Si-PIN diode mounted on the SiO2 substrate mounted
c on the seating surface in the recessed area on the front face of the
c copper spectrometer chamber (MCNP surface 1026).
c
c Tally cosine card C171 establishes the angular bin structure to be used
```

```
c for the F171 photon current tally.
c
c Tally segment card FS171 subdivides MCNP surface 1026 into three segments
c for tallying purposes: (1) one segment with a negative sense with respect to
c MCNP surface 1024, (2) a second segment with a positive sense with respect
c to MCNP surface 1024 and a negative sense with respect to MCNP surface 1002,
c and (3) a third segment with a positive sense with respect to MCNP surfaces
c 1024 and 1002. We only care about segment (2), which represents the photon
c current through the outer cylindrical surface of the dead layer of the Si-PIN
c diode mounted on the SiO2 substrate mounted on the seating surface in the
c recessed area on the front face of the copper spectrometer chamber.
c
F171:p 1026
FC171 Photon current through cyl. surf. of front Si-PIN diode dead lay.
C171 0 1
FS171 -1024 -1002
c
c Tally F181:
c -----------
c
c Tally F181 places a photon current tally on the flat, outer surface of
c the dead layer of the Si-PIN diode mounted on the SiO2 substrate mounted
c on the seating surface in the recessed area on the front face of the
c copper spectrometer chamber (MCNP surface 1002).
c
c Tally cosine card C181 establishes the angular bin structure to be used
c for the F181 photon current tally.
c
c Tally segment card FS181 subdivides MCNP surface 1002 into three segments
c for tallying purposes: (1) one segment with a negative sense with respect to
c MCNP surface 1025, (2) a second segment with a positive sense with respect
c to MCNP surface 1025 and a negative sense with respect to MCNP surface 1026,
c and (3) a third segment with a positive sense with respect to MCNP surfaces
c 1025 and 1026. We only care about segment (2), which represents the photon
c current through the flat, outer surface of the dead layer of the Si-PIN
c diode mounted on the SiO2 substrate mounted on the seating surface in
c the recessed area on the front face of the copper spectrometer chamber.
c
F181:p 1002
FC181 Photon current through flat, outer surf. of front Si-PIN diode dead lay.
C181 0 1
FS181 -1025 -1026
c
c Tally F191:
c -----------
c
c Tally F191 places a photon current tally on the flat, inner surface of
c the sensitive volume of the Si-PIN diode mounted on the SiO2 substrate
c mounted on the seating surface in the recessed area on the front face
c of the copper spectrometer chamber (MCNP surface 1022).
c
c Tally cosine card C191 establishes the angular bin structure to be used
c for the F191 photon current tally.
c
c Tally segment card FS191 subdivides MCNP surface 1022 into two segments
c for tallying purposes: (1) one segment with a negative sense with respect to
c MCNP surface 1025, and (2) a second segment with a positive sense with respect
c to MCNP surface 1025. We only care about segment (1), which represents the
c photon current through the flat, inner surface of the sensitive volume of the
c Si-PIN diode mounted on the SiO2 substrate mounted on the seating surface
c in the recessed area on the front face of the copper spectrometer chamber.
c
F191:p 1022
FC191 Photon current through flat, inner surf. of front Si-PIN diode sens. vol.
C191 0 1
FS191 -1025
```

```
c
c Tally F201:
c -----------
c
c Tally F201 places a photon current tally on the outer cylindrical surface
c of the sensitive volume of the Si-PIN diode mounted on the SiO2 substrate
c mounted on the seating surface in the recessed area on the front face of
c the copper spectrometer chamber (MCNP surface 1025).
c
c Tally cosine card C201 establishes the angular bin structure to be used
c for the F201 photon current tally.
c
c Tally segment card FS201 subdivides MCNP surface 1025 into three segments
c for tallying purposes: (1) one segment with a negative sense with respect to
c MCNP surface 1022, (2) a second segment with a positive sense with respect
c to MCNP surface 1022 and a negative sense with respect to MCNP surface 1002,
c and (3) a third segment with a positive sense with respect to MCNP surfaces
c 1022 and 1002. We only care about segment (2), which represents the photon
c current through the outer cylindrical surface of the sensitive volume of the
c Si-PIN diode mounted on the SiO2 substrate mounted on the seating surface
c in the recessed area on the front face of the copper spectrometer chamber.
c
F201:p 1025
FC201 Photon current through cyl. surf. of front Si-PIN diode sens. vol.
C201 0 1
FS201 -1022 -1002
c
c Tally F211:
c -----------
c
c Tally F211 places a photon current tally on the flat, outer surface of
c the sensitive volume of the Si-PIN diode mounted on the SiO2 substrate
c mounted on the seating surface in the recessed area on the front face
c of the copper spectrometer chamber (MCNP surface 1002).
c
c Tally cosine card C211 establishes the angular bin structure to be used
c for the F211 photon current tally.
c
c Tally segment card FS211 subdivides MCNP surface 1002 into two segments
c for tallying purposes: (1) one segment with a negative sense with respect to
c MCNP surface 1025, and (2) a second segment with a positive sense with respect
c to MCNP surface 1025. We only care about segment (1), which represents the
c photon current through the flat, outer surface of the sensitive volume of the
c Si-PIN diode mounted on the SiO2 substrate mounted on the seating surface
c in the recessed area on the front face of the copper spectrometer chamber.
c
F211:p 1002
FC211 Photon current through flat, outer surf. of front Si-PIN diode sens. vol.
C211 0 1
FS211 -1025
c
c Tally F221:
c -----------
c
c Tally F221 places an electron current tally on the flat, inner surface of
c the dead layer of the Si-PIN diode mounted on the SiO2 substrate mounted
c on the seating surface in the recessed area on the back face of the
c copper spectrometer chamber (MCNP surface 1023).
c
c Tally cosine card C221 establishes the angular bin structure to be used
c for the F221 electron current tally.
c
c Tally segment card FS221 subdivides MCNP surface 1023 into two segments
c for tallying purposes: (1) one segment with a negative sense with respect to
c MCNP surface 1026, and (2) a second segment with a positive sense with respect
c to MCNP surface 1026. We only care about segment (1), which represents the
```

```
c electron current through the flat, inner surface of the dead layer of the
c Si-PIN diode mounted on the SiO2 substrate mounted on the seating surface
c in the recessed area on the back face of the copper spectrometer chamber.
c
F221:e 1023
FC221 Elec. current through flat, inner surf. of back Si-PIN diode dead lay.
C221 0 1
FS221 -1026
c
c Tally F231:
c -----------
c
c Tally F231 places an electron current tally on the outer cylindrical surface
c of the dead layer of the Si-PIN diode mounted on the SiO2 substrate mounted
c on the seating surface in the recessed area on the back face of the copper
c spectrometer chamber (MCNP surface 1026).
c
c Tally cosine card C231 establishes the angular bin structure to be used
c for the F231 electron current tally.
c
c Tally segment card FS231 subdivides MCNP surface 1026 into three segments
c for tallying purposes: (1) one segment with a negative sense with respect to
c MCNP surface 1001, (2) a second segment with a positive sense with respect
c to MCNP surface 1001 and a negative sense with respect to MCNP surface 1023,
c and (3) a third segment with a positive sense with respect to MCNP surfaces
c 1001 and 1023. We only care about segment (2), which represents the electron
c current through the outer cylindrical surface of the dead layer of the Si-PIN
c diode mounted on the SiO2 substrate mounted on the seating surface in the
c recessed area on the back face of the copper spectrometer chamber.
c
F231:e 1026
FC231 Elec. current through cyl. surf. of back Si-PIN diode dead lay.
C231 0 1
FS231 -1001 -1023
c
c Tally F241:
c -----------
c
c Tally F241 places an electron current tally on the flat, outer surface of
c the dead layer of the Si-PIN diode mounted on the SiO2 substrate mounted
c on the seating surface in the recessed area on the back face of the
c copper spectrometer chamber (MCNP surface 1001).
c
c Tally cosine card C241 establishes the angular bin structure to be used
c for the F241 electron current tally.
c
c Tally segment card FS241 subdivides MCNP surface 1001 into three segments
c for tallying purposes: (1) one segment with a negative sense with respect to
c MCNP surface 1025, (2) a second segment with a positive sense with respect
c to MCNP surface 1025 and a negative sense with respect to MCNP surface 1026,
c and (3) a third segment with a positive sense with respect to MCNP surfaces
c 1025 and 1026. We only care about segment (2), which represents the electron
c current through the flat, outer surface of the dead layer of the Si-PIN
c diode mounted on the SiO2 substrate mounted on the seating surface in
c the recessed area on the back face of the copper spectrometer chamber.
c
F241:e 1001
FC241 Elec. current through flat, outer surf. of back Si-PIN diode dead lay.
C241 0 1
FS241 -1025 -1026
c
c Tally F251:
c -----------
c
c Tally F251 places an electron current tally on the flat, inner surface of
c the sensitive volume of the Si-PIN diode mounted on the SiO2 substrate
```

```
c mounted on the seating surface in the recessed area on the back face
c of the copper spectrometer chamber (MCNP surface 1021).
c
c Tally cosine card C251 establishes the angular bin structure to be used
c for the F251 electron current tally.
c
c Tally segment card FS251 subdivides MCNP surface 1021 into two segments
c for tallying purposes: (1) one segment with a negative sense with respect to
c MCNP surface 1025, and (2) a second segment with a positive sense with respect
c to MCNP surface 1025. We only care about segment (1), which represents the
c electron current through the flat, inner surface of the sensitive volume
c of the Si-PIN diode mounted on the SiO2 substrate mounted on the seating
c surface in the recessed area on the back face of the copper spectrometer
c chamber.
c
F251:e 1021
FC251 Elec. current through flat, inner surf. of back Si-PIN diode sens. vol.
C251 0 1
FS251 -1025
c
c Tally F261:
c -----------
c
c Tally F261 places an electron current tally on the outer cylindrical surface
c of the sensitive volume of the Si-PIN diode mounted on the SiO2 substrate
c mounted on the seating surface in the recessed area on the back face of
c the copper spectrometer chamber (MCNP surface 1025).
c
c Tally cosine card C261 establishes the angular bin structure to be used
c for the F261 electron current tally.
c
c Tally segment card FS261 subdivides MCNP surface 1025 into three segments
c for tallying purposes: (1) one segment with a negative sense with respect to
c MCNP surface 1001, (2) a second segment with a positive sense with respect
c to MCNP surface 1001 and a negative sense with respect to MCNP surface 1021,
c and (3) a third segment with a positive sense with respect to MCNP surfaces
c 1001 and 1021. We only care about segment (2), which represents the electron
c current through the outer cylindrical surface of the sensitive volume of the
c Si-PIN diode mounted on the SiO2 substrate mounted on the seating surface
c in the recessed area on the back face of the copper spectrometer chamber.
c
F261:e 1025
FC261 Elec. current through cyl. surf. of back Si-PIN diode sens. vol.
C261 0 1
FS261 -1001 -1021
c
c Tally F271:
c -----------
c
c Tally F271 places an electron current tally on the flat, outer surface of
c the sensitive volume of the Si-PIN diode mounted on the SiO2 substrate
c mounted on the seating surface in the recessed area on the back face
c of the copper spectrometer chamber (MCNP surface 1001).
c
c Tally cosine card C271 establishes the angular bin structure to be used
c for the F271 electron current tally.
c
c Tally segment card FS271 subdivides MCNP surface 1001 into two segments
c for tallying purposes: (1) one segment with a negative sense with respect to
c MCNP surface 1025, and (2) a second segment with a positive sense with respect
c to MCNP surface 1025. We only care about segment (1), which represents the
c electron current through the flat, outer surface of the sensitive volume of
c the Si-PIN diode mounted on the SiO2 substrate mounted on the seating surface
c in the recessed area on the back face of the copper spectrometer chamber.
c
F271:e 1001
```

```
FC271 Elec. current through flat, outer surf. of back Si-PIN diode sens. vol.
C271 0 1
FS271 -1025
c
c Tally F281:
c -----------
c
c Tally F281 places an electron current tally on the flat, inner surface of
c the dead layer of the Si-PIN diode mounted on the SiO2 substrate mounted
c on the seating surface in the recessed area on the front face of the
c copper spectrometer chamber (MCNP surface 1024).
c
c Tally cosine card C281 establishes the angular bin structure to be used
c for the F281 electron current tally.
c
c Tally segment card FS281 subdivides MCNP surface 1024 into two segments
c for tallying purposes: (1) one segment with a negative sense with respect to
c MCNP surface 1026, and (2) a second segment with a positive sense with respect
c to MCNP surface 1026. We only care about segment (1), which represents the
c electron current through the flat, inner surface of the dead layer of the
c Si-PIN diode mounted on the SiO2 substrate mounted on the seating surface
c in the recessed area on the front face of the copper spectrometer chamber.
c
F281:e 1024
FC281 Elec. current through flat, inner surf. of front Si-PIN diode dead lay.
C281 0 1
FS281 -1026
c
c Tally F291:
c -----------
c
c Tally F291 places an electron current tally on the outer cylindrical surface
c of the dead layer of the Si-PIN diode mounted on the SiO2 substrate mounted
c on the seating surface in the recessed area on the front face of the copper
c spectrometer chamber (MCNP surface 1026).
c
c Tally cosine card C291 establishes the angular bin structure to be used
c for the F291 electron current tally.
c
c Tally segment card FS291 subdivides MCNP surface 1026 into three segments
c for tallying purposes: (1) one segment with a negative sense with respect to
c MCNP surface 1024, (2) a second segment with a positive sense with respect
c to MCNP surface 1024 and a negative sense with respect to MCNP surface 1002,
c and (3) a third segment with a positive sense with respect to MCNP surfaces
c 1024 and 1002. We only care about segment (2), which represents the electron
c current through the outer cylindrical surface of the dead layer of the Si-PIN
c diode mounted on the SiO2 substrate mounted on the seating surface in the
c recessed area on the front face of the copper spectrometer chamber.
c
F291:e 1026
FC291 Elec. current through cyl. surf. of front Si-PIN diode dead lay.
C291 0 1
FS291 -1024 -1002
c
c Tally F301:
c -----------
c
c Tally F301 places an electron current tally on the flat, outer surface of
c the dead layer of the Si-PIN diode mounted on the SiO2 substrate mounted
c on the seating surface in the recessed area on the front face of the
c copper spectrometer chamber (MCNP surface 1002).
c
c Tally cosine card C301 establishes the angular bin structure to be used
c for the F301 electron current tally.
c
c Tally segment card FS301 subdivides MCNP surface 1002 into three segments
```

```
c for tallying purposes: (1) one segment with a negative sense with respect to
c MCNP surface 1025, (2) a second segment with a positive sense with respect
c to MCNP surface 1025 and a negative sense with respect to MCNP surface 1026,
c and (3) a third segment with a positive sense with respect to MCNP surfaces
c 1025 and 1026. We only care about segment (2), which represents the electron
c current through the flat, outer surface of the dead layer of the Si-PIN
c diode mounted on the SiO2 substrate mounted on the seating surface in
c the recessed area on the front face of the copper spectrometer chamber.
c
F301:e 1002
FC301 Elec. current through flat, outer surf. of front Si-PIN diode dead lay.
C301 0 1
FS301 -1025 -1026
c
c Tally F311:
c -----------
c
c Tally F311 places an electron current tally on the flat, inner surface of
c the sensitive volume of the Si-PIN diode mounted on the SiO2 substrate
c mounted on the seating surface in the recessed area on the front face
c of the copper spectrometer chamber (MCNP surface 1022).
c
c Tally cosine card C311 establishes the angular bin structure to be used
c for the F311 electron current tally.
c
c Tally segment card FS311 subdivides MCNP surface 1022 into two segments
c for tallying purposes: (1) one segment with a negative sense with respect to
c MCNP surface 1025, and (2) a second segment with a positive sense with respect
c to MCNP surface 1025. We only care about segment (1), which represents the
c electron current through the flat, inner surface of the sensitive volume
c of the Si-PIN diode mounted on the SiO2 substrate mounted on the seating
c surface in the recessed area on the front face of the copper spectrometer
c chamber.
c
F311:e 1022
FC311 Elec. current through flat, inner surf. of front Si-PIN diode sens. vol.
C311 0 1
FS311 -1025
c
c Tally F321:
c -----------
c
c Tally F321 places an electron current tally on the outer cylindrical surface
c of the sensitive volume of the Si-PIN diode mounted on the SiO2 substrate
c mounted on the seating surface in the recessed area on the front face of
c the copper spectrometer chamber (MCNP surface 1025).
c
c Tally cosine card C321 establishes the angular bin structure to be used
c for the F321 electron current tally.
c
c Tally segment card FS321 subdivides MCNP surface 1025 into three segments
c for tallying purposes: (1) one segment with a negative sense with respect to
c MCNP surface 1022, (2) a second segment with a positive sense with respect
c to MCNP surface 1022 and a negative sense with respect to MCNP surface 1002,
c and (3) a third segment with a positive sense with respect to MCNP surfaces
c 1022 and 1002. We only care about segment (2), which represents the electron
c current through the outer cylindrical surface of the sensitive volume of the
c Si-PIN diode mounted on the SiO2 substrate mounted on the seating surface
c in the recessed area on the front face of the copper spectrometer chamber.
c
F321:e 1025
FC321 Elec. current through cyl. surf. of front Si-PIN diode sens. vol.
C321 0 1
FS321 -1022 -1002
c
c Tally F331:
```

```
c -----------
c
c Tally F331 places an electron current tally on the flat, outer surface of
c the sensitive volume of the Si-PIN diode mounted on the SiO2 substrate
c mounted on the seating surface in the recessed area on the front face
c of the copper spectrometer chamber (MCNP surface 1002).
c
c Tally cosine card C331 establishes the angular bin structure to be used
c for the F331 electron current tally.
c
c Tally segment card FS331 subdivides MCNP surface 1002 into two segments
c for tallying purposes: (1) one segment with a negative sense with respect to
c MCNP surface 1025, and (2) a second segment with a positive sense with respect
c to MCNP surface 1025. We only care about segment (1), which represents the
c electron current through the flat, outer surface of the sensitive volume of
c the Si-PIN diode mounted on the SiO2 substrate mounted on the seating surface
c in the recessed area on the front face of the copper spectrometer chamber.
c
F331:e 1002
FC331 Elec. current through flat, outer surf. of front Si-PIN diode sens. vol.
C331 0 1
FS331 -1025
c
c Tally F348:
c -----------
c
c Tally F348 places a combined photon/electron pulse height tally in the
c sensitive volume of the Si-PIN diode mounted on the SiO2 substrate mounted
c on the seating surface in the recessed area on the back face of the
c copper spectrometer chamber (MCNP cell 103).
c
c Tally energy card E348 establishes the energy bin structure to be used
c for combined photon/electron pulse height tally F348. The energy bin
c structure consists of 8,192 bins spaced over an energy interval that
c extends from 0 keV to 311.296 keV.
c
c Note that the values associated with the Gaussian Energy Broadening (GEB)
c keyword used below on the special tally treatment card were developed from
c resolution calibration data associated with the Si-PIN diode spectrometer
c prototype data acquisitions.
c
F348:p,e 103
FC348 Combined photon/electron pulse height tally in the back Si-PIN diode.
E348 0.00000E+00 8190I 3.11296E-01 NT $ Energy bin structure for tally F348.
FT348 GEB 1.05556E-03 8.05653E-04 0.00000E+00
c
c Tally F358:
c -----------
c
c Tally F358 places a combined photon/electron pulse height tally in the
c sensitive volume of the Si-PIN diode mounted on the SiO2 substrate mounted
c on the seating surface in the recessed area on the front face of the
c copper spectrometer chamber (MCNP cell 105).
c
c Tally energy card E358 establishes the energy bin structure to be used
c for combined photon/electron pulse height tally F358. The energy bin
c structure consists of 8,192 bins spaced over an energy interval that
c extends from 0 keV to 311.296 keV.
c
c Note that the values associated with the Gaussian Energy Broadening (GEB)
c keyword used below on the special tally treatment card were developed from
c resolution calibration data associated with the Si-PIN diode spectrometer
c prototype data acquisitions.
c
F358:p,e 105
FC358 Combined photon/electron pulse height tally in the front Si-PIN diode.
```

```
E358 0.00000E+00 8190I 3.11296E-01 NT $ Energy bin structure for tally F358.
FT358 GEB 1.05556E-03 8.05653E-04 0.00000E+00
c
c Data cards related to problem termination:
c ==========================================
c
c Setting the "npp" keyword on the "NPS" card equal to 1E+09 specifies
c that the problem should be terminated after 1E+09 histories have
c been transported.
c
NPS 1E+09
c
PRDMP J J 1
```

Appendix E: The Terrestrial Xenon and Argon Simulator (TeXAS) Application

The Terrestrial Xenon and Argon Simulator

The Terrestrial Xenon and Argon Simulator (TeXAS) application is a set of MATLAB [140] code modules developed to support the generation of high-fidelity, site-specific background activity concentration estimates for 100 radioactive particulates and noble gases identified as relevant to the verification regime of the Comprehensive Nuclear-Test-Ban Treaty (CTBT) [116]. The background activity concentration estimates generated by the TeXAS application should be viewed as nominal upper limits; they account for production via three natural processes—(1) spontaneous fission, (2) cosmic neutron induced fission, and (3) cosmic neutron induced activation—and for loses via radioactive decay. Note that the TeXAS application does not make any attempt to account for the physical movement or loss of radioactive particulates or noble gases resulting from transport processes. Also note that the so-called "cosmic neutrons" are not,

strictly speaking, of cosmic origin, but rather they are produced via cosmic-ray induced spallation reactions in the Earth's atmosphere [128].

The TeXAS application supports the generation of the aforementioned CTBT-relevant radioactive particulate and noble gas background activity concentration estimates by: (1) automating and streamlining the process of developing high-fidelity material composition and temperature data, (2) incorporating the data into Monte Carlo N-Particle (MCNP) radiation transport code [74, 75, 76, 77] models, (3) collecting and processing the best-available nuclear data required to support the MCNP models, and (4) post-processing the outputs generated by the MCNP models and evaluating the radioactive particulate and noble gas background activity concentration estimates.

Perhaps most importantly, the TeXAS application was designed to do all of these things automatically. Users of the TeXAS application need to have working MATLAB, MCNP, and NJOY 2012 nuclear data processing system [141] installations, but they do not need have any experience working with any of the aforementioned codes. The TeXAS application was created to make it possible for anyone to develop high-fidelity, site-specific CTBT-relevant radioactive particulate and noble gas background activity concentration estimates by handling all the details associated with the material data processing, the development of the MCNP models, and the nuclear data processing so that TeXAS application users are not encumbered with the details of these processes, but rather are left free to focus on the basic inputs associated with the studies they wish to conduct.

E.1 Overview of the TeXAS Application

As mentioned previously, the TeXAS application supports the generation of high-fidelity, site-specific CTBT-relevant radioactive particulate and noble gas background activity concentration estimates by: (1) automating and streamlining the process of developing high-fidelity material composition and temperature data, (2) incorporating the data into Monte Carlo N-Particle (MCNP) radiation transport code [74, 75] models, (3) collecting and processing the best-available nuclear data required to support the MCNP models, and (4) post-processing the outputs generated by the MCNP models and evaluating the radioactive particulate and noble gas background activity concentration estimates. The first three of the aforementioned tasks are performed by one overarching code module (the `TeXASModDev` code module), while the fourth task is performed by a second overarching code module (the `TeXASPostProc` code module).

Figure E.1 presents an overview of the `TeXASModDev` code module. As illustrated by Figure E.1, the `TeXASModDev` code module consists of eight principal code modules itself. The first of these code modules reads principal and auxiliary formatted input files provided by the user and checks for errors in the formatted input files (see Sections E.5.1 and E.5.2 for more information regarding the purposes and formats of the principal and auxiliary formatted input files). The second, third, and fourth code modules process the atmospheric, geological, and seawater inputs provided in the principal and auxiliary formatted input files, as applicable. The functional details associated with code modules 2, 3, and 4 are described in Sections E.2.2, E.2.3,

and E.2.4, respectively. The fifth `TeXASModDev` code module supports the second, third, and fourth code modules by applying material composition perturbations requested by the user and generating isotopic vectors for each of the atmospheric, geological, and seawater layers, as applicable. The functional details associated with this module are described in Section E.2.5. The sixth `TeXASModDev` code module is responsible for creating the MCNP radiation transport code input decks. Various aspects of this module are described throughout Sections E.2.1 through E.2.10. The last two `TeXASModDev` code modules, code modules 7 and 8, collect relevant nuclear data files and generate NJOY 2012 nuclear data processing system [141] input decks to support the production of study-specific nuclear data libraries which are themselves required to support the

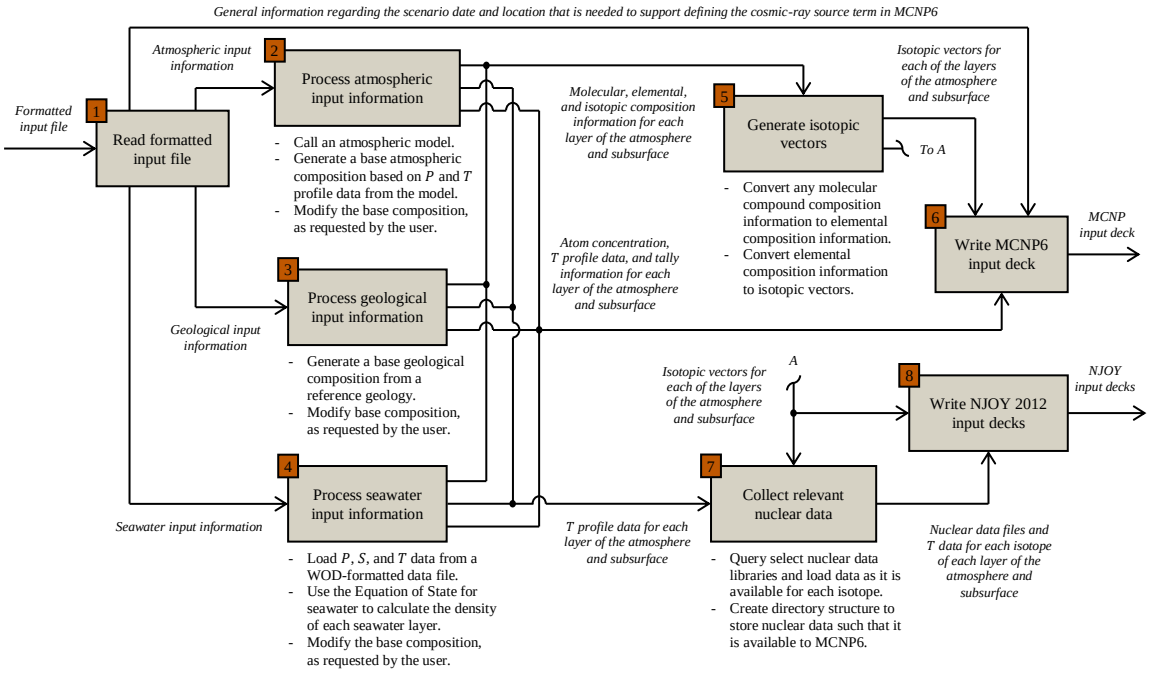

Figure E.1: Overview of the `TeXASModDev` code module of the TeXAS application.

MCNP models. The functional details associated with `TeXASModDev` code modules 7 and 8 are described throughout Section E.3.

The second overarching TeXAS application code module is referred to as the `TeXASPostProc` module. This code module post-processes the outputs generated by the MCNP models generated by the `TeXASModDev` code module and uses them to evaluate the CTBT-relevant radioactive particulate and noble gas background activity concentration estimates. The functional details associated with the `TeXASPostProc` code module are described in Section E.4.

E.2 MCNP Model Development

At the most basic level, developing a Monte Carlo N-Particle (MCNP) radiation transport code [74, 75] model involves simply defining the geometric and material properties of a system through which radiation is to be transported. All of the MCNP models created by the TeXAS application have the same basic geometric configuration—a vertical cylinder with an outer radius of 1 km, vertically segmented as requested by the user. Additional information regarding the geometric aspects of the MCNP models created by the TeXAS application is presented in Section E.2.1.

In order for MCNP to properly model the transport of radiation through a particular system, various properties of the materials associated with the system must be defined. The most important material properties in the context of the CTBT-relevant radioactive particulate and noble gas background activity concentration studies supported

by the TeXAS application are the mean isotopic compositions and the temperatures associated with the atmospheric and subsurface layers of the MCNP models. The TeXAS application includes a number of modules and stand-alone tools that serve to automate and streamline the process of developing high-fidelity isotopic composition and temperature data for the atmospheric and subsurface layers specific to a given CTBT-relevant radioactive particulate and noble gas background activity concentration study. These modules and tools are described in Sections E.2.2.1, E.2.3.1, and E.2.3.2.

In addition to the geometric and material properties associated with the system through which the radiation is transported, the properties of the radiation source itself must also be defined. For the CTBT-relevant radioactive particulate and noble gas background activity concentration studies the TeXAS application is designed to support, the radiation source of interest is the cosmic-ray source incident upon the upper layers of the Earth's atmosphere. This cosmic-ray source term is composed primarily of protons and alpha particles originating in deep space [128]. The protons and alpha particles induce a cascade of "cosmic neutrons" as they participate in spallation reactions with various constituents of the Earth's atmosphere [128]. As discussed in Section E.2.6, the TeXAS application uses the cosmic-ray source term built into MCNP [74, 75] to model the cosmic-ray source incident upon the upper layers of the Earth's atmosphere.

MCNP users must request that MCNP return information pertaining to specific aspects of the radiation transport process that are of interest using what are referred to as MCNP tally cards [74, 75]. MCNP supports a variety of tally types, all of which are

useful in certain applications [74, 75]. The particle and photon tallies requested by the TeXAS application are all `F1` surface current, `F2` surface flux, and `F4` cell flux tallies [74, 75]. More information regarding the methods used to develop the MCNP tally cards utilized by MCNP models developed by the TeXAS application are presented in Section E.2.8.

The MCNP models created by the TeXAS application employ a somewhat sophisticated variance reduction scheme that allows MCNP to focus its computational efforts on the photons and particles moving through spatial regions that are most important in establishing the radioactive particulate and noble gas background activity concentrations of interest. The variance reduction scheme, which is discussed in more detail in Section E.2.9, utilizes the weight-window generator built into MCNP [74, 75] in an iterative fashion.

E.2.1 Geometric Configuration of the MCNP Models

The MCNP models created by the TeXAS application all have the same basic geometric configuration. The configuration, which is illustrated in Figure E.2, is a vertical cylinder with an outer radius of 1 km. The outer surfaces of the cylinder are specularly reflecting surfaces, which means that photons and particles that encounter the outer cylindrical surfaces are reflected back in at angles equal to their incident angles [74, 75]. The MCNP models are about 66 km tall, give or take a few meters depending on the

number and thickness of subsurface layers required to support a given CTBT-relevant radioactive particulate and noble gas background activity concentration study.

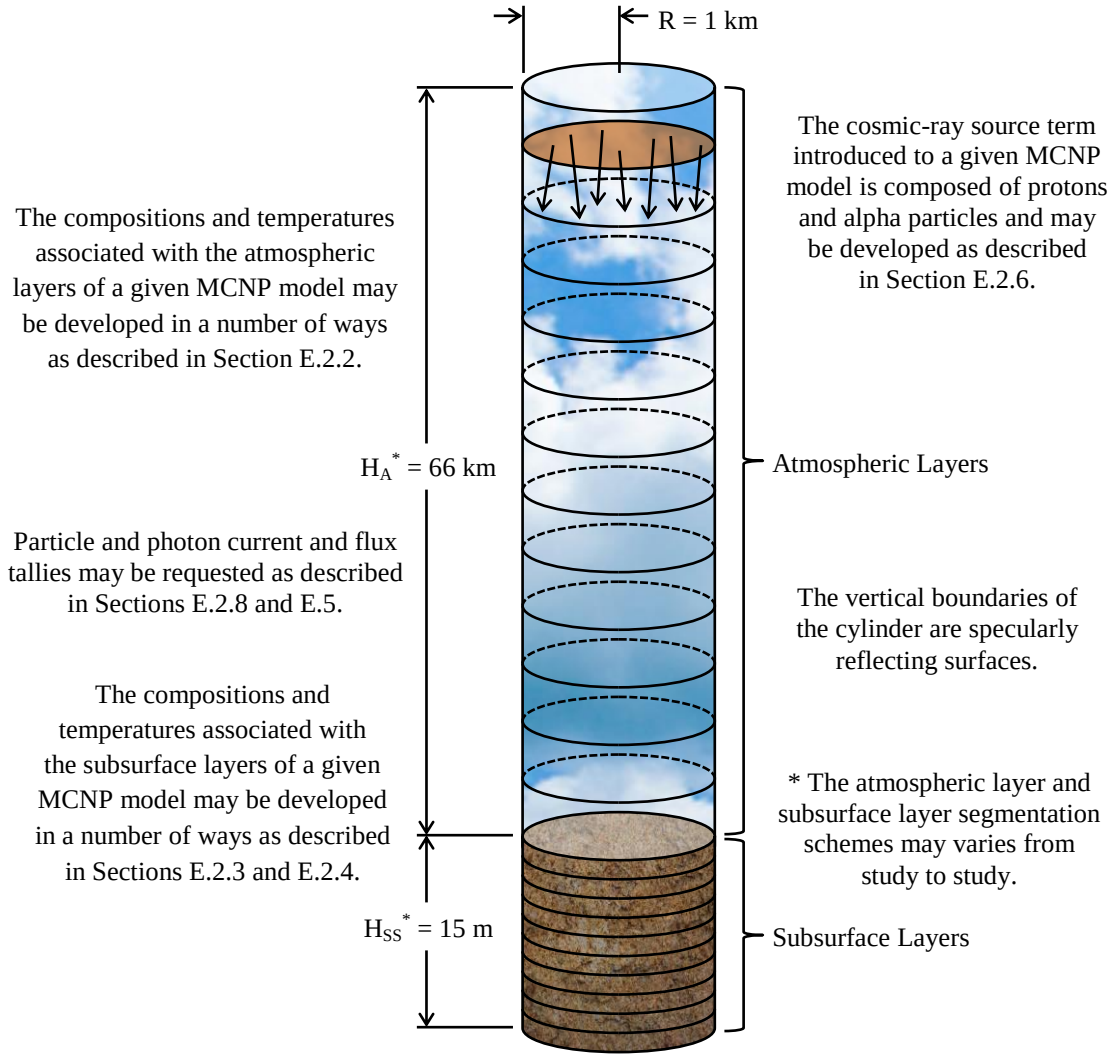

Figure E.2: The geometric configuration of the MCNP models created by the TeXAS application.

The vertical cylinder associated with a given MCNP model is segmented vertically as requested by the user. Each cylindrical segment represents a particular layer of the atmosphere or subsurface. TeXAS application users may define atmospheric and subsurface segmentation schemes using a principal formatted input file as described in Section E.5. Note that if study-specific nuclear data (*i.e.* temperature adjusted nuclear data) is to be used to support a given MCNP job, the format of the MCNP material ZAID identifiers generated by the TeXAS application places an upper limit on the number of atmospheric and subsurface layers that may be associated with a given MCNP model; the upper limit is 100 layers. More atmospheric and subsurface layers may be used if study-specific nuclear data is not required.

E.2.2 Development of MCNP Model Atmospheric Layers

This section describes the methods the second code module of the `TeXASModDev` code module of the TeXAS application uses to develop pressure and temperature data for the atmospheric layers of the MCNP models it creates in support of site-specific CTBT-relevant radioactive particulate and noble gas background activity concentration studies. Two different atmospheric pressure and temperature profile development methods are available to TeXAS application users: the first method allows users to manually define mean atmospheric pressure and temperature profiles, while the second method allows users to use the *U.S. Standard Atmosphere, 1976* [142] to develop mean atmospheric composition and temperature profiles. Both methods assume that the

Earth's atmosphere may be treated as a dry, ideal gas below a geometric height of about 86 km [142]. The equation of state for an ideal gas, also known as the ideal gas law, states that the pressure, volume, number of moles, and temperature of an ideal gas are related to one another as follows:

$$P \cdot V = n \cdot R \cdot T. \qquad \text{E.2.2.1}$$

Where: P, V, n, and T are the pressure, volume, number of moles, and Temperature, respectively, associated with the ideal gas, and

R is the molar gas constant.

The number of moles of an ideal gas may be related to the number density of the ideal gas (N), the volume of the ideal gas, and the Avogadro constant (N_A) as follows:

$$n = \frac{N \cdot V}{N_A}. \qquad \text{E.2.2.2}$$

Substituting Equation E.2.2.2 into Equation E.2.2.1 produces the following expression relating the number density of an ideal gas to the pressure and temperature of the ideal gas, via the Avogadro constant and the molar gas constant [142]:

$$N = \frac{P \cdot N_A}{R \cdot T}. \qquad \text{E.2.2.3}$$

When a TeXAS application user understands the mean pressure and temperature profiles associated with the atmospheric segmentation scheme they wish to use to develop the atmospheric layers of a given MCNP model they may input them directly (as described in Section E.5) and the TeXAS application simply plugs them into Equation E.2.2.3 to evaluate the mean number density associated with each layer.

However, in many cases TeXAS application users will lack a detailed understanding of the mean atmospheric pressure and temperature profiles. In these cases TeXAS application users needs only to provide an atmospheric segmentation scheme and the TeXAS application can develop the mean pressure, temperature, and number density profiles in accordance with the *U.S. Standard Atmosphere, 1976* [142]. According to the *U.S. Standard Atmosphere, 1976*, the Earth's atmosphere may be divided into seven different molecular scale temperature layers. The molecular scale temperature, T_m, is constant through two of these layers and a function of geopotential height through the other five as illustrated in Figure E.3. The molecular scale temperature gradients associated with atmospheric layers 1, 3, 4, 6, and 7 are reported in Table E.1.

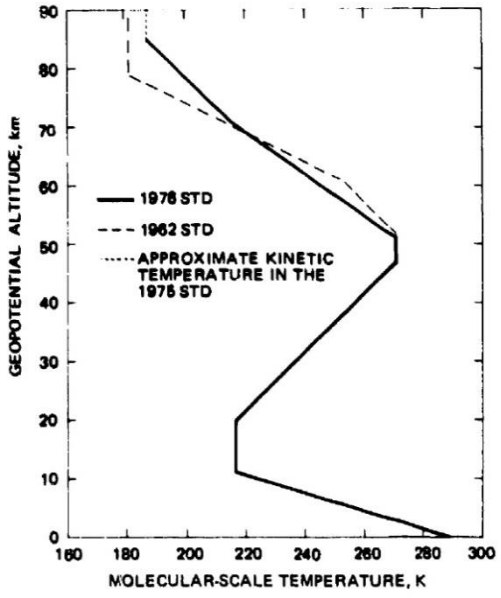

Figure E.3: Molecular scale temperature as a function of geopotential height, according to the *U.S. Standard Atmosphere, 1976* [142].

Table E.1: Atmospheric layer molecular-scale temperatures and molecular-scale temperature gradients, according to the *U.S. Standard Atmosphere, 1976* [142].

Atmospheric Layer	Subscript, b	Geopotential Height at the base of the Layer, H_b [m']	Molecular-Scale Temperature at the base of the Layer, $T_{m,b}$ [K]	Molecular-Scale Temperature Gradient, $L_{m,b}$ [K-m']
1	0	0	288.15	-0.0065
2	1	11,000	216.65	0
3	2	20,000	216.65	0.0010
4	3	32,000	228.65	0.0028
5	4	47,000	270.65	0
6	5	51,000	270.65	-0.0028
7 *	6	71,000	214.65	-0.0020

* Note that the seventh atmospheric layer extends from a geopotential height of 71,000 m' up to a maximum geopotential height of 84,852.0 m' [142].

The molecular scale temperature at any particular geopotential height, H, may be calculated using the data in Table E.1 and the following expression [142]:

$$T_m(H) = T_{m,b} + L_{m,b} \cdot (H - H_b). \qquad \text{E.2.2.4}$$

Where: $T_m(H)$ is the molecular-scale temperature at geopotential height H,

$T_{m,b}$ is the molecular scale temperature at the base of atmospheric layer b,

$L_{m,b}$ is the molecular scale temperature gradient in atmospheic layer b, and

H_b is the geopotential height at the base of atmospheric layer b.

While Equation E.2.2.4 provides an expression to calculate the molecular-scale temperature at any particular geopotential height, it is really the mean molecular-scale temperatures associated with the atmospheric layers that are of interest. The mean molecular-scale temperature associated with a given atmospheric layer may be evaluated

by applying the mean value theorem of integrals to Equation E.2.2.4 and evaluating the integral over the range of geopotential heights associated with an atmospheric layer of interest. The result is as follows:

$$\bar{T}_m|_{[h_L,h_U]} = \frac{T_{m,b} \cdot (h_U - h_L) + 1/2 \cdot L_{m,b} \cdot (h_U^2 - h_L^2) - L_{m,b} \cdot H_b \cdot (h_U - h_L)}{h_U - h_L}. \quad \text{E.2.2.5}$$

Where: $\bar{T}_m|_{[h_L,h_U]}$ is the mean molecular scale temperature associated with an atmospheric layer that extends from a lower geopotential height of h_L up through an upper geopotential height of h_U.

A similar method may be used to calculate the atmospheric pressure in each of the seven atmospheric layers associated with the *U.S. Standard Atmosphere, 1976* (see Table E.1). For atmospheric layers 1, 3, 4, 6, and 7 where the molecular-scale temperature gradient is not equal to zero the atmospheric pressure at any particular geopotential height may be calculated in accordance with the following expression [142]:

$$P(H) = P_b \cdot \left[\frac{T_{m,b}}{T_{m,b} + T_{m,b} \cdot (H - H_b)}\right]^{\frac{g_0' \cdot M_0}{R \cdot L_{m,b}}}. \quad \text{E.2.2.6}$$

Where: $P(H)$ is the atmospheric pressure at geopotential height H,

P_b is the atmospheric pressure at the base of atmospheric layer b,

g_0' is a dimensional constant selected to relate the standard geopotential meter (in units of m'), to the standard geometric meter (in units of m),

M_0 is the mean molecular weight of the atmosphere at sea level, and

R is the molar gas constant.

Applying the mean value theorem of integrals to Equation E.2.2.6 and evaluating the integral over the range of geopotential heights associated with an atmospheric layer of interest produces the following result describing the mean atmospheric pressure associated with the atmospheric layer (remember that the molecular scale temperature gradient in the atmospheric layer is assumed to be nonzero):

$$\bar{P}|_{[h_L,h_U]} = \frac{P_b \cdot T_{m,b}^{\frac{g_0' \cdot M_0}{R \cdot L_{m,b}}} \cdot R}{(h_U - h_L) \cdot \left(R \cdot L_{m,b} - g_0' \cdot M\right)} \cdots$$
$$\cdot \left[\left(T_{m,b} + L_{m,b} \cdot (h_U - H_b)\right)^{1-\frac{g_0' \cdot M_0}{R \cdot L_{m,b}}} - \left(T_{m,b} + L_{m,b} \cdot (h_L - H_b)\right)^{1-\frac{g_0' \cdot M_0}{R \cdot L_{m,b}}}\right]. \quad \text{E.2.2.7}$$

Where: $\bar{P}|_{[h_L,h_U]}$ is the mean atmospheric pressure associated with an atmospheric layer that extends from a lower geopotential height of h_L up through an upper geopotential height of h_U.

Note that the atmospheric pressures at the bases of each of the seven the atmospheric layers established by the *U.S. Standard Atmosphere, 1976* are reported in Table E.2.

For atmospheric layers 2 and 5 in which the molecular scale temperature gradient is zero the expression for the atmospheric pressure as a function of geopotential height is as follows:

$$P(H) = P_b \cdot e^{-\frac{g_0' \cdot M_0 \cdot (H - H_b)}{R \cdot T_{m,b}}}. \quad \text{E.2.2.8}$$

Table E.2: The atmospheric pressures at the bases of each of the seven the atmospheric layers established by the *U.S. Standard Atmosphere, 1976* [142].

Atmospheric Layer	Subscript, b	Geopotential Height, H_b [m']	Atmospheric Pressure at the base of the Layer, $T_{m,b}$ [Pa]
1	0	0	101,325
2	1	11,000	22,632
3	2	20,000	5,475
4	3	32,000	868
5	4	47,000	111
6	5	51,000	67
7	6	71,000	4

Applying the mean value theorem of integrals to Equation E.2.2.8 and evaluating the integral over the range of geopotential heights associated with an atmospheric layer of interest produces the following result describing the mean atmospheric pressure associated with the atmospheric layer (remember that the molecular scale temperature gradient in the atmospheric layer is assumed to be zero):

$$\bar{P}|_{[h_L,h_U]} = \frac{P_b \cdot R \cdot T_{m,b}}{g_0' \cdot M_0 \cdot (h_U - h_L)} \cdot \left[e^{-\frac{g_0' \cdot M_0 \cdot (h_L - H_b)}{R \cdot T_{m,b}}} - e^{-\frac{g_0' \cdot M_0 \cdot (h_U - H_b)}{R \cdot T_{m,b}}} \right]. \qquad \text{E.2.2.9}$$

The mean atmospheric number density associated with an atmospheric layer that extends from a lower geopotential height of h_L up through an upper geopotential height of h_U and has a nonzero molecular scale temperature gradient may be calculated as follows:

$$\bar{N}|_{[h_L,h_U]} = \frac{N_A \cdot P_b}{g_0' \cdot M_0 \cdot (h_U - h_L)} T_{m,b}^{\frac{g_0' \cdot M_0}{R \cdot L_{m,b}}} \cdot \left[\left(T_{m,b} + L_{m,b} \cdot (h_L - H_b) \right)^{-\frac{g_0' \cdot M_0}{R \cdot L_{m,b}}} \ldots \right.$$

$$\left. - \left(T_{m,b} + L_{m,b} \cdot (h_U - H_b) \right)^{-\frac{g_0' \cdot M_0}{R \cdot L_{m,b}}} \right]. \qquad \text{E.2.2.10}$$

Where: $\bar{N}|_{[h_L,h_U]}$ is the mean atmospheric number density associated with an atmospheric layer that extends from a lower geopotential height of h_L up through an upper geopotential height of h_U.

Similarly, the mean atmospheric number density associated with an atmospheric layer that extends from a lower geopotential height h_L up through an upper geopotential height h_U and has a molecular scale temperature gradient equal to zero may be calculated as follows:

$$\bar{N}|_{[h_L,h_U]} = \frac{N_A \cdot P_b}{g_0' \cdot M_0 \cdot (h_U - h_L)} \cdot \left[e^{-\frac{g_0' \cdot M_0 \cdot (h_L - H_b)}{R \cdot T_{m,b}}} - e^{-\frac{g_0' \cdot M_0 \cdot (h_U - H_b)}{R \cdot T_{m,b}}} \right]. \qquad \text{E.2.2.11}$$

The atmospheric number densities calculated in accordance with Equations E.2.2.3, E.2.2.10, and E.2.2.11 are total atmospheric number densities. The number densities associated with each of the individual atmospheric constituents in a particular atmospheric layer may be evaluated by multiplying the total atmospheric number density associated with the atmospheric layer by the volume fraction associated with each of the atmospheric constituents, which are listed in Table E.3 [142]. Because the dry portion of the earth's atmosphere is assumed to be homogenously mixed up through a geometric height of about 86,000 m, the atmospheric constituent volume

fractions reported in Table E.3 are applicable to all atmospheric layers up through a maximum geometric height of 86,000 m [142].

Ultimately, the second code module of the `TeXASModDev` code module of the TeXAS application produces two outputs for each of the atmospheric layers associated with a given CTBT-relevant radioactive particulate and noble gas background activity concentration study: The first output is an atmospheric composition vector that specifies the number densities associated with each of the atmospheric constituents identified in Table E.3. The second output is a mean atmospheric temperature. These outputs are passed from the second code module to the fifth and seventh code modules of the overarching `TeXASModDev` code module (see Figure E.1).

Figure E.4 presents examples of total atmospheric number density and temperature profiles generated by the TeXAS application via the *U.S. Standard Atmosphere, 1976* method. These outputs were validated by comparing the total atmospheric number densities and temperatures generated by the TeXAS application with the total atmospheric number densities and temperatures reported in Tables I and II presented in Part 4 of the *U.S. Standard Atmosphere, 1976* [142]. The comparisons revealed that the total atmospheric number densities and temperatures generated by the TeXAS application were identical to the expected total atmospheric number densities and temperatures out through at least four significant digits, and in most cases through all five significant digits. In cases where the fifth significant digit deviated from the expected value, the deviation was assumed to result from differences in numerical precision.

Table E.3: Atmospheric constituent concentrations, according to the *U.S. Standard Atmosphere, 1976* [142].

Atmospheric Constituent	Major or Trace Constituent	Constituent Concentration [unitless volume fraction]
N_2	Major	7.8084×10^{-1}
O_2	Major	2.09476×10^{-1}
Ar	Major	9.34×10^{-3}
CO_2	Major	3.22×10^{-4}
Ne	Major	1.818×10^{-5}
He	Major	5.24×10^{-6}
CH_4	Major	1.5×10^{-6}
Kr	Major	1.14×10^{-6}
H_2	Major	5×10^{-7}
N_2O	Trace	2.7×10^{-7}
CO	Trace	1.9×10^{-7}
Xe	Major	8.7×10^{-8}
O_3	Trace	4×10^{-8}
NH_3	Trace	4×10^{-9}
NO_2	Trace	1×10^{-9}
SO_2	Trace	1×10^{-9}
NO	Trace	5×10^{-10}
H_2S	Trace	5×10^{-11}

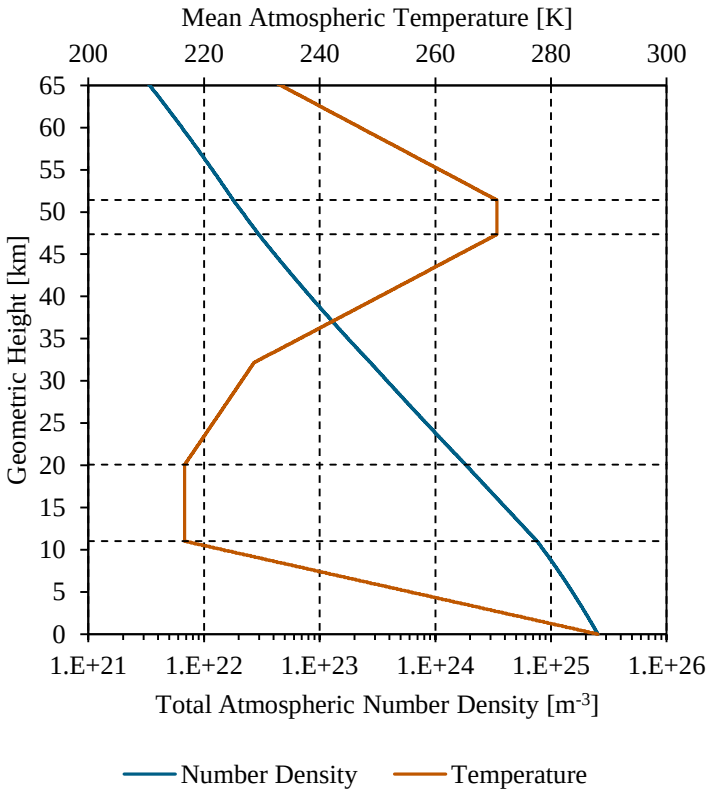

Figure E.4: Examples of total atmospheric number density and atmospheric temperature profiles generated by the TeXAS application via the *U.S. Standard Atmosphere, 1976* method.

E.2.2.1 A Tool to Develop Atmospheric Water Vapor Profiles

The previous section describes the methods the TeXAS application uses to develop composition information for the dry portion of the Earth's atmosphere. In some cases, TeXAS application users may also wish to account for the effects of atmospheric water vapor when using the Monte Carlo N-Particle (MCNP) radiation transport code [74, 75] to simulate the transport of cosmic neutrons down through the Earth's

atmosphere. This section describes a tool users of the TeXAS application may use to estimate the mean water vapor mixing ratio in any atmospheric layer up through a maximum geometric height of about 16,000 m.

The tool, which is implemented as a simple spreadsheet named `AtmH2OProfGen.xlsx`, was developed from atmospheric water vapor mixing ratio data extracted from the *U.S. Standard Atmosphere, 1976* [142]. The data is reproduced below in Figure E.5. As illustrated in Figure E.5, below a geometric height of about 4,000 m the atmospheric water vapor mixing ratio is basically a linear function of geometric height. Above a geometric height of about 4,000 m the atmospheric water vapor profile basically falls of exponentially as geometric height continues to increase. Therefore, two expressions, a linear expression and an exponential expression, were fit to the atmospheric water vapor mixing ratio data points applicable to geometric heights between 0 and 4,000 m, and between 4,000 and 16,000 m. The linear and exponential expressions are given by Equations E.2.2.1.1 and E.2.2.1.2 respectively.

$$\zeta_{H_2O}(z) = 4.60688 \times 10^{-3} - 8.47617 \times 10^{-7} \cdot z \qquad \text{E.2.2.1.1}$$

$$\zeta_{H_2O}(z) = 1.29503 \times 10^{-2} \cdot e^{-5.56242 \times 10^{-4} \cdot z} \qquad \text{E.2.2.1.2}$$

Where: $\zeta_{H_2O}(z)$ is the atmospheric water vapor mixing ratio at gemoetric height z.

Applying the mean value theorem of integrals to Equations E.2.2.1.1 and E.2.2.1.2 and integrating from a lower geometric height of z_L up through an upper geometric height of z_U produced the following expressions describing the mean water

vapor mixing ratios in atmospheric layers having geometric heights between 0 and 4,000 m, and between 4,000 and 16,000 m, respectively.

$$\bar{\zeta}_{H_2O}\big|_{[z_L,z_U]} = 4.60688 \times 10^{-3} - \frac{8.47617 \times 10^{-7} \cdot (z_U^2 - z_L^2)}{2 \cdot (z_U - z_L)} \qquad \text{E.2.2.1.3}$$

$$\bar{\zeta}_{H_2O}\big|_{[z_L,z_U]} = -\frac{1.29503 \times 10^{-2} \cdot \left(e^{-5.56242\times10^{-4}\cdot z_U} - e^{-5.56242\times10^{-4}\cdot z_L}\right)}{5.56242 \times 10^{-4} \cdot (z_U - z_L)} \qquad \text{E.2.2.1.4}$$

Where: $\bar{\zeta}_{H_2O}\big|_{[z_L,z_U]}$ is the mean atmospheric water vapor mixing ratio associated with an atmospheric layer that extends from a lower geometric height of z_L up through an upper geometric height of z_U.

Equations E.2.2.1.3 and E.2.2.1.4 are coded into the `AtmH2OProfGen.xlsx` spreadsheet packaged with the TeXAS application. The mean atmospheric water vapor mixing ratios generated by the spreadsheet may be incorporated into the appropriate layers of an MCNP model as perturbations (see Section E.2.5).

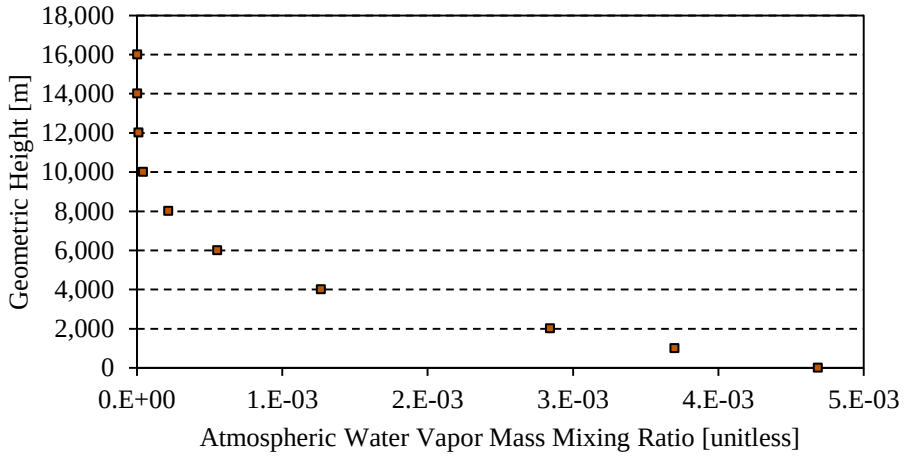

Figure E.5: Atmospheric water vapor mixing ratio data extracted from the *U.S. Standard Atmosphere, 1976* [142].

E.2.3 Development of MCNP Model Geological Layers

This section describes the methods the third code module of the `TeXASModDev` code module of the TeXAS application uses to develop composition data for the geological layers of the MCNP models it creates in support of site-specific CTBT-relevant radioactive particulate and noble gas background activity concentration studies.

The process of developing geological composition data applicable to a given geological layer may be divided into four stages: The first stage involves developing the composition of the base geology from density, porosity, and composition information specific to the geology of interest. For example, if the geology of interest is a granite geology, the true density of the granite, the porosity of the granite, and the composition of the granite (in terms of either number or mass fractions) would be provided by the user as described in Section E.5. Note that the TeXAS application is capable of accepting geological composition information in terms of molecular compounds, elements, isotopes, or a mixture of all three. The TeXAS application uses the density, porosity, and composition data provided as inputs to develop number densities for each of the constituents of the base geology. At the end of this stage of the geological composition data development process the constituent number densities are all still in the forms provided by the user. That is to say that constituent concentrations provided in terms of molecular compounds are still expressed in terms of molecular compounds, constituent concentrations provided in terms of elements are still expressed in terms of elements, and

constituent concentrations provided in terms of isotopes are still expressed in terms of isotopes.

The second stage of the geological composition development process involves applying perturbations to the base geological composition. For example, a TeXAS application user might want to increase the uranium concentration associated with the base geological composition by 5 % relative to the nominal uranium concentration associated with the geology of interest. Alternatively, a user might want to introduce one or more totally new constituents to the base geology. The TeXAS application is capable of accepting these types of composition perturbation requests from users, applying them as required, and then renormalizing the composition of the base geology.

The third stage of the geological composition development process involves developing composition data for the material, or materials, that are assumed to fill the geological porosity volumes. Porosity volumes may be filled with atmospheric air, a user defined material, or a mixture of atmospheric air and a user defined material. In situations where the porosity volumes are assumed to be filled with atmospheric air, the TeXAS application automatically uses the atmospheric air composition developed for the atmospheric layer closest to the surface. For user defined materials the TeXAS application accepts density and composition information from the user and develops number densities for each of the constituents automatically. In cases where the porosity volumes are assumed to be filled with a mixture of atmospheric air and a user defined

material, the composition of the mixture is evaluated in accordance with Equation E.2.3.1:

$$N_{i,Por} = N_{i,Atm} \cdot f_{Atm} + N_{i,User\ Def} \cdot (1 - f_{Atm}). \quad \text{E.2.3.1}$$

Where: $N_{i,Por}$ is the constituent i number density in the atmospheric air and user defined material mixture filling the porosity volumes,

$N_{i,Atm}$ and $N_{i,User\ Def}$ are the constituent i number densities in the atmospheric air and the user defined material, respectively, and

f_{Atm} is the fraction of the porosity volume that is assumed to be filled with atmospheric air (*i.e.* $f_{Atm} = V_{Atm}/V_{Pores}$).

The total number density of the mixture filling the porosity volumes may be calculated by summing the number densities associated with each of the constituents as follows:

$$N_{Por} = \sum_{i=1}^{n_{Por\ Cons}} N_{i,Por}. \quad \text{E.2.3.2}$$

The fourth stage of the geological composition development process involves combining the composition of the base geology with the composition of the atmospheric air and user-defined material in the porosity volumes. The compositions are combined in accordance with Equation E.2.3.3:

$$N_i = N_{i,Geo} \cdot (1 - f_{Por}) + N_{i,Por} \cdot f_{Por}. \quad \text{E.2.3.3}$$

Where: N_i is the total constituent i number density in the geological layer,

$N_{i,Geo}$ is the constituent i number density in the base geology, and

f_{Por} is the porosity volume associated with the geological layer expressed as a fraction of the total geological layer volume (*i.e.* $f_{Pores} = V_{Pores}/V_{Total}$).

The total number density of a given geological layer may be calculated by summing the number densities associated with each of the constituents as follows:

$$N = \sum_{i=1}^{n_{Cons}} N_i. \qquad \text{E.2.3.4}$$

At the end of the fourth and final stage of the geological composition development process the geological composition associated with each geological layer, accounting for the composition of the base geology and the composition of the material in the porosity volumes, is known, and the third code module of the `TeXASModDev` code module of the TeXAS application ultimately produces a single output for each geological layer—a geological composition vector that specifies the number densities associated with each of the geological constituents. Note that while the TeXAS application is capable of developing temperature profiles for the atmospheric layers of MCNP models, temperature profiles for the geological layers of MCNP models must be manually defined by TeXAS application users. A tool to support the development of subsurface temperature profiles is described in the next section. The geological composition vectors produced by the third code module of the overarching `TeXASModDev` code module and the geological temperature profile provided by the user are passed to the fifth and seventh code modules of the `TeXASModDev` code module (see Figure E.1).

E.2.3.1 A Tool to Develop Geological Subsurface Temperature Profiles

The previous section describes the methods the TeXAS application uses to develop composition information for the geological layers of Monte Carlo N-Particle (MCNP) radiation transport code [74, 75] models used to support CTBT-relevant radioactive particulate and noble gas background activity concentration studies. In some cases, particularly those where study-specific nuclear data is to be used, TeXAS application users may wish to account for the subsurface temperature profile associated with a given site as accurately as possible in their MCNP models. This section describes a tool users of the TeXAS application may use to develop subsurface temperature profile estimates from atmospheric temperature data, which is often more readily available than subsurface temperature profile data. The tool is implemented as a MATLAB script called `SubsurfTempProfGen.m` and is packaged with the TeXAS application.

The subsurface temperature profile estimates generated by the `SubsurfTempProfGen.m` MATLAB script utilize the equation Labs [157] developed to estimate the temperature at any subsurface depth and on any day of the year:

$$T(z,t) = T_m - A_S \cdot e^{-z\cdot\sqrt{\frac{\pi}{365\cdot\alpha}}} \cdot \cos\left[\frac{2\cdot\pi}{365}\cdot\left(t - t_0 - \frac{z}{2}\cdot\sqrt{\frac{365}{\pi\cdot\alpha}}\right)\right]. \qquad \text{E.2.3.1.1}$$

Where: $T(z,t)$ is the subsurface temperature at a depth of z meters on day t of the year,

T_m is the mean surface ground temperature (in units of °C),

A_S is the annual surface temperature amplitude (in units of °C),

α is the thermal diffusivity of the subsurface (in units of m^2-d^{-1}), and

t_0 is a phase constant equal to the day of the year on which the surface temperature attains its minimum value.

An expression for the mean subsurface temperature associated with some subsurface layer extending from a lower depth of z_L up to an upper depth of z_U may be evaluated by applying the Mean Value Theorem of Integrals to Equation E.2.3.1.1 and evaluating the integral from z_L to z_U. The result of the integration is as follows:

$$\bar{T}(t)|_{[z_L,z_U]} = T_m \cdot (z_U - z_L) + \frac{365.25 \cdot A_S}{2 \cdot \pi} \cdot \sqrt{\frac{\pi \cdot \alpha}{365.25}} \cdot e^{\sqrt{\frac{\pi}{365.25 \cdot \alpha}}} \ldots$$
$$\cdot \left[e^{-z_U} \cdot \left\{ \sin\left(\frac{2 \cdot \pi}{365.25} \cdot \left[t - t_0 - \frac{z_U}{2} \cdot \sqrt{\frac{365.25}{\pi \cdot \alpha}} \right] \right) + \cos\left(\frac{2 \cdot \pi}{365.25} \cdot \left[t - t_0 - \frac{z_U}{2} \cdot \sqrt{\frac{365.25}{\pi \cdot \alpha}} \right] \right) \right\} \ldots \quad \text{E.2.3.1.2}$$
$$- e^{-z_L} \cdot \left\{ \sin\left(\frac{2 \cdot \pi}{365.25} \cdot \left[t - t_0 - \frac{z_L}{2} \cdot \sqrt{\frac{365.25}{\pi \cdot \alpha}} \right] \right) + \cos\left(\frac{2 \cdot \pi}{365.25} \cdot \left[t - t_0 - \frac{z_L}{2} \cdot \sqrt{\frac{365.25}{\pi \cdot \alpha}} \right] \right) \right\} \Bigg].$$

Where:$\bar{T}(t)|_{[z_L,z_U]}$ is the mean temperature associated with a subsurface layer extending from a lower depth of z_L up to an upper depth of z_U on day t of the year.

In situations where the mean surface ground temperature and the annual surface temperature amplitude applicable to a given site are known, the temperatures may be substituted in Equation E.2.3.1.2 and used to evaluate the mean subsurface temperatures associated with the subsurface layers and the date of interest. In cases where the mean surface ground temperature and the annual surface temperature amplitude are not known, they may be estimated from atmospheric temperature data [157, 158]. The mean surface ground temperature applicable to a given site may be estimated by adding about 1.7 °C to the mean annual air temperature associated with the site [157, 158]. The annual surface temperature amplitude applicable to a given site may be estimated by adding 1.1 °C to

one-half of the difference between the July and January long-term monthly average air temperatures associated with the site [157, 158].

The `SubsurfTempProfGen.m` MATLAB script accepts the mean surface ground temperature and the annual surface temperature amplitude applicable to a given site as inputs. The only other input that must be provided is a subsurface segmentation scheme. TeXAS application users who use the `SubsurfTempProfGen.m` MATLAB script to develop subsurface temperature profiles should take care to ensure that the subsurface segmentation schemes they incorporate into the principal formatted input files they use to develop their MCNP models are equivalent to the subsurface segmentation schemes they use when they develop their subsurface temperature profiles.

Subsurface temperature profiles generated using the `SubsurfTemp-ProfGen.m` MATLAB script may be incorporated into MCNP models developed by the TeXAS application as described in Section E.5. Note that mean subsurface temperature profiles generated using Equation E.2.3.1.2 typically have units of °C, but the `SubsurfTempProfGen.m` MATLAB script reports the mean subsurface temperatures in units of both °C and K. TeXAS application users who utilize the `SubsurfTempProfGen.m` MATLAB script should take care to ensure that they incorporate the temperature data reported in units of K into their principal formatted input files (again, see Section E.5).

E.2.3.2 A Tool to Develop Subsurface Plutonium Contamination Concentration Profiles

This section describes a tool TeXAS application users may use to develop plutonium contamination concentration profiles from total subsurface plutonium contamination concentration data. The tool is implemented as a MATLAB script called `SubsurfPuProfGen.m` and is packaged with the TeXAS application.

Subsurface plutonium isotope fallout concentrations have been evaluated at many locations all over the world and the results of these evaluations are widely available in the literature. However, the concentrations are typically reported as total subsurface plutonium isotope concentrations applicable to subsurface depth intervals over which the samples supporting the evaluations were drawn. However, because the CTBT-relevant radioactive particulate and noble gas background activity concentration estiamtes generated by the TeXAS application are generated as functions of geometric height and subsurface depth, an expression describing the distribution of the subsurface plutonium isotope concentrations as a function of subsurface depth is needed. Subsurface plutonium isotope fallout concentration evaluations carried out at several locations led Beck *et al.* [159] to conclude that the total subsurface plutonium fallout concentration at a given location may be reasonably assumed to be distributed exponentially down through some maximum subsurface depth. Thus, a subsurface plutonium isotope fallout concentration profile applicable to a given location should be described reasonably well by the following expression:

$$C_x(z) = \frac{b_x \cdot C_{Tot} \cdot e^{-b_x \cdot z}}{1 - e^{-b_x \cdot z_{Max}}} \qquad \text{E.2.3.2.1}$$

Where: $C_x(z)$ is the concentration of plutonium isotope x, where x is typically 238, 239, or 240, at subsurface depth z,

b_x is the plutonium-isotope-x- and location-specific relaxation distance,

C_{Tot} is the total plutonium isotope concentration at the location of interest, and

z_{Max} is the maximum depth to which the plutonium isotopes are assumed to penetrate at the location of interest.

In order to incorporate subsurface plutonium isotope fallout concentration profiles into an MCNP model the subsurface plutonium isotope fallout concentrations applicable to each of the subsurface layers of the model are needed. The plutonium isotope fallout concentrations applicable to each of the subsurface cells of an MCNP model may be evaluated by applying the Mean Value Theorem for Integrals to Equation E.2.3.2.1. Applying the Mean Value Theorem for Integrals to Equation E.2.3.2.1 reveals that the plutonium isotope x concentration applicable over a subsurface depth interval extending downward from z_1 through z_2 is as follows:

$$\bar{C}_x|_{[z_1,z_2]} = \frac{C_{Tot} \cdot [e^{-b_x \cdot z_1} - e^{-b_x \cdot z_2}]}{1 - e^{-b_x \cdot z_{Max}}} \qquad \text{E.2.3.2.2}$$

An example of a subsurface ^{239}Pu fallout concentration profile generated for a hypothetical location where the ^{239}Pu relaxation distance is assumed to be 0.33 cm^{-1}, the total ^{239}Pu concentration is assumed to be 3.39×10^8 cm^{-3}, and the maximum depth to which the ^{239}Pu is assumed to penetrate is 10 cm is presented below in Figure E.6.

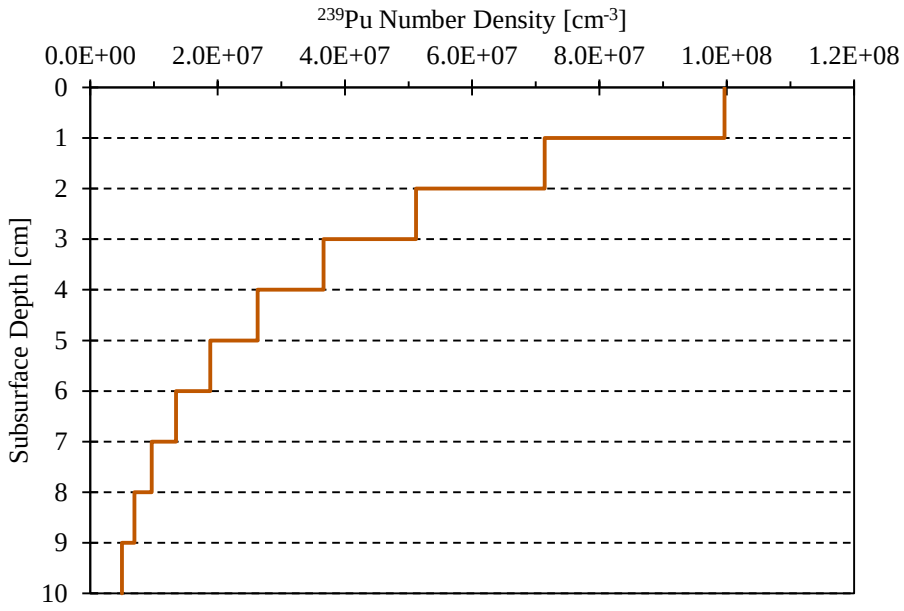

Figure E.6: An example of a ^{239}Pu fallout concentration profile.

E.2.4 Development of MCNP Model Seawater Layers

This section describes the methods the fourth code module of the `TeXASModDev` code module of the TeXAS application uses to develop composition and temperature data for the seawater layers of the MCNP models it generates in support of site-specific CTBT-relevant radioactive particulate and noble gas background activity concentration studies. Two different seawater composition and temperature development methods are available to TeXAS application users: The first method allows TeXAS application users to manually define mean seawater pressure, salinity, and temperature profiles, while the second method allows TeXAS application users to use pressure, salinity, and temperature data taken from the World Ocean Database (WOD) [148] to develop mean seawater

pressure, salinity, and temperature profiles. Both of the aforementioned methods use the Equation of State for Seawater [149, 150, 151, 152] to develop mean seawater mass density profiles from mean seawater pressure, salinity, and temperature profiles. The Equation of State for Seawater is as follows [149, 150, 151, 152]:

$$\rho(P,S,T) = \frac{\rho_{1\,atm}(S,T)}{1 - \frac{P}{K(P,S,T)}}. \qquad \text{E.2.4.1}$$

Where: $\rho(P,S,T)$ is the density of seawater (in units of kg-m^{-3}) having an applied pressure P (in units of bar), a salinity S (in units of ppt), and a temperature T (in units of °C);

$\rho_{1\,atm}(S,T)$ is the density of seawater having an applied pressure of 1 atm, a salinity S, and a temperature T; and

$K(P,S,T)$ is a second degree secant bulk modulus.

The expression for the density of seawater having an applied pressure of 1 atm, a salinity S, and a temperature T, is as follows:

$$\rho_{1\,atm}(S,T) = f_{\rho,1}(T) + f_{\rho,2}(S,T) + f_{\rho,3}(S,T) + f_{\rho,4}(S). \qquad \text{E.2.4.2}$$

The expression for the first function of temperature, $f_{\rho,1}(T)$, is:

$$f_{\rho,1}(T) = 9.99842594 \times 10^{2} + 6.793952 \times 10^{-2} \cdot T \ldots$$
$$-9.095290 \times 10^{-3} \cdot T^{2} + 1.001685 \times 10^{-4} \cdot T^{3} \ldots \qquad \text{E.2.4.3}$$
$$-1.120083 \times 10^{-6} \cdot T^{4} + 6.536336 \times 10^{-9} \cdot T^{5}.$$

The expression for the second function of both salinity and temperature, $f_{\rho,2}(S,T)$, is:

$$f_{\rho,2}(S,T) = (8.24493 \times 10^{-1} - 4.0899 \times 10^{-3} \cdot T \ldots$$
$$+7.6438 \times 10^{-5} \cdot T^2 - 8.2467 \times 10^{-7} \cdot T^3 \ldots \quad \text{E.2.4.4}$$
$$+5.3875 \times 10^{-9} \cdot T^4) \cdot S.$$

The expression for the third function of both salinity and temperature, $f_{\rho,3}(S,T)$, is:

$$f_{\rho,3}(S,T) = (-5.72466 \times 10^{-3} + 1.0227 \times 10^{-4} \cdot T \ldots$$
$$-1.6546 \times 10^{-6} \cdot T^2) \cdot S^{3/2}. \quad \text{E.2.4.5}$$

The final expression, $f_{\rho,4}(S)$, is a function of salinity:

$$f_{\rho,4}(S) = 4.8314 \times 10^{-4} \cdot S^2. \quad \text{E.2.4.6}$$

The expression for the second degree secant bulk modulus, $K(P,S,T)$, is as follows:

$$K(P,S,T) = f_{K,1}(T) + f_{K,2}(S,T) + f_{K,3}(S,T) + \left[f_{K,4}(T) + f_{K,5}(S,T) \ldots\right.$$
$$\left.+f_{K,6}(S)\right] \cdot P + \left[f_{K,7}(T) + f_{K,8}(S,T)\right] \cdot P^2. \quad \text{E.2.4.7}$$

The expression for the first function of temperature, $f_{K,1}(T)$, is:

$$f_{K,1}(T) = 1.965221 \times 10^4 + 1.484206 \times 10^2 \cdot T \ldots$$
$$-2.327105 \cdot T^2 + 1.360477 \times 10^{-2} \cdot T^3 \ldots \quad \text{E.2.4.8}$$
$$-5.155288 \times 10^{-5} \cdot T^4.$$

The expression for the second function of both salinity and temperature, $f_{K,2}(S,T)$, is:

$$f_{K,2}(S,T) = (5.46746 \times 10^1 - 6.03459 \times 10^{-1} \cdot T \ldots$$
$$+1.09987 \times 10^{-2} \cdot T^2 - 6.1670 \times 10^{-5} \cdot T^3) \cdot S. \quad \text{E.2.4.9}$$

The expression for the third function of both salinity and temperature, $f_{K,3}(S,T)$, is:

$$f_{K,3}(S,T) = (7.944 \times 10^{-2} + 1.6483 \times 10^{-2} \cdot T \ldots \\ -5.3009 \times 10^{-4} \cdot T^2) \cdot S^{3/2}. \quad \text{E.2.4.10}$$

The expression for the fourth function of temperature, $f_{K,4}(T)$, is:

$$f_{K,4}(T) = 3.239908 + 1.43713 \times 10^{-3} \cdot T \ldots \\ +1.16082 \times 10^{-4} \cdot T^2 - 5.77905 \times 10^{-7} \cdot T^3. \quad \text{E.2.4.11}$$

The expression for the fifth function of both salinity and temperature, $f_{K,5}(S,T)$, is:

$$f_{K,5}(S,T) = (2.2838 \times 10^{-3} - 1.0981 \times 10^{-5} \cdot T \ldots \\ -1.6078 \times 10^{-6} \cdot T^2) \cdot S. \quad \text{E.2.4.12}$$

The expression for the sixth function of salinity, $f_{K,6}(S)$, is:

$$f_{K,6}(S) = 1.91075 \times 10^{-4} \cdot S^{3/2}. \quad \text{E.2.4.13}$$

The expression for the seventh function of temperature, $f_{K,7}(T)$, is:

$$f_{K,7}(T) = 8.50935 \times 10^{-5} - 6.12293 \times 10^{-6} \cdot T \ldots \\ +5.2787 \times 10^{-8} \cdot T^2. \quad \text{E.2.4.14}$$

The expression for the eighth function of both salinity and temperature, $f_{K,8}(S,T)$, is:

$$f_{K,8}(S,T) = (-9.9348 \times 10^{-7} + 2.0816 \times 10^{-8} \cdot T \ldots. \\ +9.1697 \times 10^{-10} \cdot T^2) \cdot S. \quad \text{E.2.4.15}$$

Plugging Equations E.2.4.3 through E.2.4.6 into Equation E.2.4.2 produces a final expression for $\rho_{1\,atm}(S,T)$. Plugging Equations E.2.4.8 through E.2.4.15 into Equation E.2.4.7 produces a final expression for $K(P,S,T)$. And finally, plugging the

final expressions for $\rho_{1\ atm}(S,T)$ and $K(P,S,T)$ into Equation E.2.4.1 produces the final expression for $\rho(P,S,T)$. This expression may be used to evaluate the mass density (in units of kg-m^{-3}) of seawater having any pressure P (in units of bar), any salinity S (in units of ppt), and any temperature, T (in units of °C).

In situations where TeXAS application users understand the mean pressure, salinity, and temperature profiles associated with the seawater segmentation scheme they wish to use to develop the seawater layers of a given MCNP model they may input them directly (as described in Section E.5) and the TeXAS application simply plugs them into Equations E.2.4.1 through E.2.4.15 to evaluate the mean mass density associated with each seawater layer. Seawater composition information (also provided by TeXAS application users as described in Section E.5) is then used to develop the mean molar mass of the seawater. The mean molar mass of the seawater is then ultimately used to evaluate the total number density associated with the seawater as well as the number density associated with each of the seawater constituents.

In many cases, however, TeXAS application users will presumably lack a detailed understanding of the mean pressure, salinity, and temperature profiles needed to develop mean seawater mass density and number density profiles. In these cases TeXAS application users may provide a seawater pressure, salinity, and temperature dataset taken from the World Ocean Database (WOD) [148] as an input to the TeXAS application. The TeXAS application is capable of accepting WOD pressure, salinity, and temperature datasets—in the native WOD file format—and then parsing the individual pressure,

salinity, and temperature data associated with each of the datasets to produce mean pressure, salinity, and temperature data for each of the seawater layers requested by the user. The total number density associated with the seawater and the number densities associated with each of the seawater constituents are then evaluated in the manner described previously. After evaluating the mean pressure, salinity, temperature, and number density profiles associated with a given WOD dataset the TeXAS application selects the WOD datset that is most representative of the mean profiles and uses that dataset to support the remainder of the seawater composition development effort. Examples of seawater mass density, salinity, and temperature profiles developed using data taken from the WOD are shown below in Figure E.7. Note that the temperature data is reported in units of K in Figure E.7.

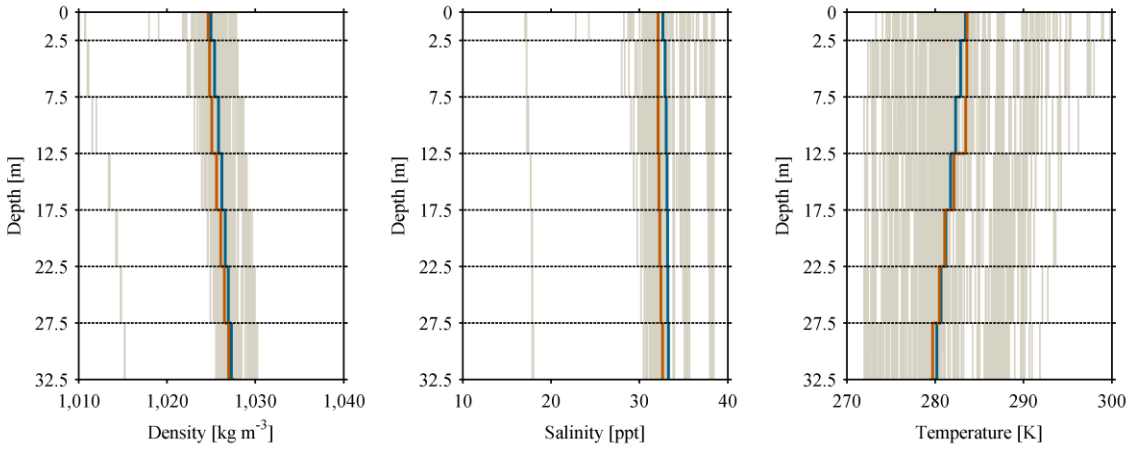

Legend:

Most-representative WOD seawater density, salinity, and temperature profiles.

Mean WOD seawater density, salinity, and temperature profiles.

All other seawater density, salinity, and temperature profiles returned by the WOD dataset query.

Figure E.7: Example seawater mass density, salinity, and temperature profiles.

E.2.5 Application of Material Composition Perturbations

The TeXAS application is capable of applying material composition perturbations as they are requested by TeXAS application users. Twelve different types of constituent concentration perturbations may be applied: (1) absolute number density perturbations, (2) relative number density perturbations, (3) absolute mass density perturbations, (4) relative mass density perturbations, (5) absolute number mixing ratio perturbations, (6) relative number mixing ratio perturbations, (7) absolute mass mixing ratio perturbations, (8) relative mass mixing ratio perturbations, (9) absolute number fraction perturbations (10) relative number fraction perturbations, (11) absolute mass fraction perturbations, and (12) relative mass fraction perturbations.

The algorithm the TeXAS application uses to apply material composition perturbations supports perturbing the concentrations associated with multiple material constituents simultaneously. Furthermore, different types of perturbations may be applied to each of the constituents to be perturbed. Additionally, each constituent concentration perturbation may be applied such that the total mass / number density of the material is either held constant or allowed to vary with the constituent concentration perturbation. Both types of constituent concentration perturbations may be useful in different scenarios.

TeXAS application users may request that material constituent concentration perturbations be applied using TeXAS application principal formatted input files as described in Sections E.5.1.3 through E.5.1.5. The details associated with the material

constituent concentration perturbations must be defined using auxiliary formatted input files as described in Section E.5.2.

The TeXAS application approaches the problem of applying material composition perturbations as a six step process: (1) The first step of the process involves converting all of the base material constituent concentrations not originally provided in terms of number densities to number densities. (2) Second, all of the requested material constituent concentration perturbations not requested in terms of number density perturbations are reframed as number density perturbations. After steps (1) and (2) all of the base material constituent concentrations and all of the material constituent concentration perturbations are expressed in terms of number densities.

(3) During the third step of the material composition perturbation process all material constituent concentration perturbations that specify a final material constituent concentration that is independent of the other material constituent concentration perturbations requested are evaluated. As an example, if a TeXAS application user requests that an absolute number density perturbation be applied to constituent x, then the final number density associated with constituent x is known immediately before any other material constituent perturbations have even been applied. Conversely, if a TeXAS application user requests that a relative mass mixing ratio perturbation be applied to constituent x, then the final number density associated with constituent x must be evaluated in parallel with the other material constituent concentration perturbations requested by the user.

(4) During the fourth step of the material composition perturbation process the effects of the material constituent concentration perturbations evaluated in Step (3) are applied to the total mass / number density of the material. (5) During the fifth step of the process a set of simultaneous equations is developed to mathematically describe each of the material constituent concentrations to be applied and their effects on the total mass / number density of the material. The set of simultaneous equations includes equations for the actively perturbed material constituents—these are the material constituents for which the TeXAS application user actually requests perturbations—as well as equations describing the final number densities of the material constituents that are not actively perturbed. Note that the number densities associated with the material constituents that are not actively perturbed may be passively perturbed depending on the active material constituent concentration perturbations.

(6) The sixth step of the material composition perturbation process involves reformulating the set of simultaneous equations developed during step (5) as a linear algebra problem and solving for the unknowns. In this case the unknowns are the final material constituent concentrations. This represents the last step in the material composition perturbation process.

Note that the coefficient matrices generated during step (6) of the material composition perturbation process sometimes have condition numbers that are quite small. The TeXAS application proceeds with the material composition perturbation process anyway, but it is possible that the results produced via this method may be in error when

the condition number associated with the coefficient matrix is very small. TeXAS application users should always verify that the final material constituent concentrations resulting from a requested material composition perturbation appear to be as expected. The TeXAS application reports the final material constituent concentrations in terms of several different bases so it should be relatively easy to verify that the requested perturbations were all applied properly.

E.2.6 Development of the MCNP Cosmic-Ray Source Term

The Monte Carlo N-Particle (MCNP) radiation transport code [74, 75] models generated by the TeXAS application utilize the cosmic-ray source term built into MCNP. The cosmic-ray source term was first incorporated into version 6 of the MCNP radiation transport code in 2012, and thus the cosmic-ray source term is still a relatively new feature of the MCNP radiation transport code [74, 75].

The MCNP cosmic-ray source term may be invoked by setting the `PAR` keyword of the MCNP `SDEF` card equal to `CR`, as illustrated in Figure E.8. Invoking the MCNP cosmic-ray source term forces MCNP to select an appropriate cosmic-ray type and energy for each source particle history it starts. As described in Section 3.3.4.1 of the MCNP User's Manual, MCNP determines the appropriate cosmic-ray type and energy using solar modulation and rigidity data built into MCNP [74, 75]. Yearly solar modulation values are available for dates between 1960 and 2005. A linear interpolation scheme is used to select the appropriate modulation for a particular date. The latitudinal

resolution of the rigidity data is about 5 ° and the longitudinal resolution is about 20 ° [74, 75]. A closest match procedure is used when selecting the rigidity grid point to use in support of a particular study.

Other MCNP SDEF card keywords used to define the cosmic-ray source term are the SUR, VEC, NRM, POS, RAD, DAT, and LOC keywords. The DAT and LOC keywords are used to specify the date and location of interest, respectively [74, 75]. The SUR, VEC, NRM, POS, and RAD keywords are used, in conjunction with the MCNP source information (SI) and Source Probability (SP) cards, to specify the initial position and direction of the cosmic-rays as they are introduced to the MCNP model. The values assigned to the MCNP SDEF, SI, and SP cards shown in Figure E.8 are used to create an isotropic cosmic-ray source term that is sampled uniformly over a circle centered at 44.908 ° N latitude, 122.995 ° E longitude, and 65,000 m above sea level.

```
      …  …
15,795   c The source definition card:
15,796   c ---------------------------
15,797   c
15,798   SDEF SUR=00000002 VEC=0 0 -1 NRM=1 POS=0 0 6500000 RAD=D1
15,799        PAR=CR DAT=11 1 2003 LOC=44.908 -122.995 65
15,800   c
15,801   c Source information cards:
15,802   c -------------------------
15,803   c
15,804   SI1 H 0 100000
15,805   c
15,806   c Source probability cards:
15,807   c -------------------------
15,808   c
15,809   SP1 -21 1
      …  …
```

Figure E.8: Example of an MCNP source definition (SDEF) card utilizing the built-in cosmic-ray source term, an MCNP SI card, and an MCNP SP card.

E.2.7 Specification of MCNP Physics Modelling and Other Options

The Monte Carlo N-Particle (MCNP) radiation transport code [74, 75] `SDEF` card used to define the cosmic ray source term as described in the previous section is one example of an MCNP data card. There are many other types of MCNP data cards, a number of which are utilized by the MCNP models created by the TeXAS application. In this section the MCNP data cards used to specify MCNP physics modelling, MCNP problem termination, and MCNP output control options in the MCNP models created by the TeXAS application are described. Six different MCNP physics modelling cards are described; they are (1) the MCNP `MODE` card, (2) the MCNP `PHYS` card, (3) the MCNP `CUT` card, (4) the MCNP `MPHYS` card, (5) the MCNP `LCA` card, and (6) the MCNP `LCB` card [74, 75]. Four different MCNP problem termination and output control cards are described; they are (1) the MCNP `NPS` card, (2) the MCNP `CTME` card, (3) the MCNP `PRINT` card, and (4) the MCNP `PRDMP` card [74, 75].

The MCNP `MODE` *Card:*

The MCNP `MODE` card is used to specify the particle and photon types that should be transported by MCNP [74, 75]. The `MODE` cards written to the MCNP input decks generated by the TeXAS application specify that neutrons, protons, antineutrons, antiprotons, positive pions, negative pions, neutral pions, positive kaons, negative kaons, deuterons, tritons, helions, alpha particles, heavy ions, negative muons, positive muons, and photons should all be transported by MCNP. This is a relatively exhaustive list

intended to ensure that all particle and photon types that could eventually result in the production of neutrons or muons are transported. For more information regarding the MCNP `MODE` card, refer to Section 3.3.3.1 of the MCNP User's Manual [75]. An example of an MCNP `MODE` card written to an MCNP input deck generated by the TeXAS application is presented in Figure E.9.

```
     …  …
15,698  c Specify which particles should be transported by MCNP:
15,699  c ------------------------------------------------------
15,700  c
15,701  c Use the MODE card to specify that the following
15,702  c particles and photons should be transported by MCNP:
15,703  c Nucleons: neutrons (N) and protons (H).
15,704  c Antinucleons: antineutrons (Q) and antiprotons (G).
15,705  c Pions: positive pions (/), negative pions (*), and neutral pions (Z).
15,706  c Kaons: positive kaons (K) and negative kaons (?).
15,707  c Light Ions: deuterons (D), tritons (T), helions (S),
15,708  c             and alpha particles (A).
15,709  c Heavy Ions: heavy ions (#) - a complete list of the heavy ions available
15,710  c             for transport in MCNP6.1.1 beta is provided in Table 16-1
15,711  c             of Appendix I of the MCNP6.1.1 beta User's Manual.
15,712  c Muons: negative muons (|) and positive muons (!).
15,713  c Photons: (P).
15,714  c
15,715  MODE N H Q G / * Z K ? D T S A # | ! P
     …  …
```

Figure E.9: An example of an MCNP `MODE` card written to an MCNP input deck generated by the TeXAS application.

The MCNP `PHYS` *Cards:*

The MCNP `PHYS` cards are used to set physics modelling options for specific particle and photon types [74, 75]. The MCNP input decks generated by the TeXAS application utilize five MCNP `PHYS` cards: one for neutrons (`PHYS:N`), one for photons (`PHYS:P`), one for protons (`PHYS:H`), one for muons (`PHYS:|`), and one for "other" particle types (`PHYS:<pl>`) [74, 75]. Full descriptions of the MCNP `PHYS:N`,

PHYS:P, PHYS:H, PHYS:|, and PHYS:<pl> cards and their respective keywords are presented in Sections 3.3.3.2.1, 3.3.3.2.2, 3.3.3.2.4, and 3.3.3.2.5 of the MCNP User's Manual [74, 75]. The majority, but not all, of the MCNP PHYS card keywords are assigned their default values. Examples of MCNP MODE cards written to an MCNP input deck generated by the TeXAS application are presented in Figure E.10.

Note that the MCNP User's Manual indicates that the PHYS:H, the PHYS:|, and the PHYS:<pl> cards should have a sixteenth keyword—a ckvnum keyword—that is not utilized in the MCNP input decks generated by the TeXAS application because attempting to utilized the keyword caused MCNP to return a fatal error. The ckvnum keyword appears to be relatively new to MCNP and the fatal error appears to be the result of a bug that will likely be corrected in the near future.

```
    …  …
15,717  c Set MCNP neutron physics options:
15,718  c --------------------------------
15,719  c
15,720  c Use the PHYS:N card to set the MCNP neutron physics options.
15,721  c The values assigned to the majority of the keywords associated with
15,722  c the PHYS:N card are the MCNP6.1.1 beta default values. Refer to
15,723  c Section 3.3.3.2.1 of the MCNP6.1.1 beta User's Manual for more
15,724  c information regarding the keywords associated with the PHYS:N card.
15,725  c
15,726  PHYS:N 1E+06 0 0 J J J 1 -1 1 J J 0 0
15,727  c
15,728  c Set MCNP photon physics options:
15,729  c --------------------------------
15,730  c
15,731  c Use the PHYS:P card to set the MCNP photon physics options.
15,732  c The values assigned to the majority of the keywords associated with
15,733  c the PHYS:P card are the MCNP6.1.1 beta default values. Refer to
15,734  c Section 3.3.3.2.2 of the MCNP6.1.1 beta User's Manual for more
15,735  c information regarding the keywords associated with the PHYS:P card.
15,736  c
15,737  PHYS:P 100 0 0 -1 0 J 1
    …  …
```

Figure E.10: Examples of MCNP PHYS cards written to an MCNP input deck generated by the TeXAS application.

```
…  …
15,739  c Set MCNP proton physics options:
15,740  c --------------------------------
15,741  c
15,742  c Use the PHYS:H card to set the MCNP proton physics options.
15,743  c The values assigned to the majority of the keywords associated with
15,744  c the PHYS:H card are the MCNP6.1.1 beta default values. Refer to
15,745  c Section 3.3.3.2.4 of the MCNP6.1.1 beta User's Manual for more
15,746  c information regarding the keywords associated with the PHYS:H card.
15,747  c
15,748  PHYS:H 1E+06 0 -1 J 0 J 1 J J J 0 0 0 0.917 J
15,749  c
15,750  c Set muon physics options:
15,751  c -------------------------
15,752  c
15,753  c Use the PHYS:| card to set the MCNP muon physics options.
15,754  c The values assigned to the majority of the keywords associated with
15,755  c the PHYS:| card are the MCNP6.1.1 beta default values. Refer to
15,756  c Section 3.3.3.2.5 of the MCNP6.1.1 beta User's Manual for more
15,757  c information regarding the keywords associated with the PHYS:| card.
15,758  c
15,759  PHYS:| 1E+06 J J J 0 J 1 0.65 J J 0 0 0 0.917 J
15,760  c
15,761  c Set "other particle" physics options:
15,762  c -------------------------------------
15,763  c
15,764  c Use the PHYS:<pl> card to set the MCNP “other particle” physics options.
15,765  c The values assigned to the majority of the keywords associated with
15,766  c the PHYS:<pl> card are the MCNP6.1.1 beta default values. Refer to
15,767  c Section 3.3.3.2.5 of the MCNP6.1.1 beta User's Manual for more
15,768  c information regarding the keywords associated with the PHYS:<pl> card.
15,769  c
15,770  PHYS:/,*,Z,K,?,D,T,S,A,# 1E+06 J J J 0 J J J J J 0 0 0 0.917 J
…  …
```

Figure E.10: Examples of MCNP `PHYS` cards written to an MCNP input deck generated by the TeXAS application, continued.

```
…  …
15,754  c Set physics cutoffs:
15,755  c --------------------
15,756  c
15,757  c Use the CUT card to set the energy cutoff associated with
15,758  c particle types N, H, Q, G, D, T, S, and A to 0 MeV. Refer to
15,759  c Section 3.3.3.4.1 of the MCNP6.1.1 beta User's Manual for more
15,760  c information regarding the keywords associated with the CUT card.
15,761  c
15,762  CUT:N,H,Q,G,D,T,S,A J 0 J J J
…  …
```

Figure E.11: An example of an MCNP `CUT` card written to an MCNP input deck generated by the TeXAS application.

The MCNP CUT *Card:*

The MCNP CUT card is used to set the time, energy, and weight cutoffs for each particle type [74, 75]. Neither time nor weight cutoffs are utilized by the MCNP input decks generated by the TeXAS application. Energy cutoffs are used, however, and the energy cutoffs associated with all particle types are all set equal to 0 MeV. For more information regarding the MCNP CUT card, refer to Section 3.3.3.4.1 of the MCNP User's Manual [74, 75]. An example of an MCNP CUT card written to an MCNP input deck generated by the TeXAS application is presented in Figure E.11.

The MCNP MPHYS *Card:*

The MCNP MPHYS card is used to toggle MCNP physics models on and off [74, 75]. In the MCNP input decks generated by the TeXAS application the MCNP physics models are toggled ON. Note that the physics models would have been toggled ON automatically by MCNP given the particles and photons being transported [74, 75]. For more information regarding the MCNP MPHYS card, refer to Section 3.3.3.7.1 of the MCNP User's Manual [74, 75]. An example of an MCNP MPHYS card written to an MCNP input deck generated by the TeXAS application is presented in Figure E.12.

The MCNP `LCA` and `LCB` *Cards:*

The MCNP `LCA` and `LCB` cards are used to specify intermediate-energy regime intra-nuclear cascade physics modelling options and high-energy physics modelling options [74, 75]. MCNP includes four intermediate-energy regime intra-nuclear cascade physics models [74, 75]; they are (1) the Bertini model, (2) the ISABEL model, (3) the INCL4 model, and (4) the CEM03.03 model [160, 161]. In MCNPX [74, 162], two high-energy physics models were available [74, 162]: they were (1) the FLUKA model and (2) the LAQGSM03.03 model [161]. Only one high-energy physics model, the LAQGSM03.03 model, is available in MCNP6 [74, 75, 161].

The MCNP models created by the TeXAS application utilize the CEM03.03 intra-nuclear cascade model in the intermediate-energy regime and the LAQGSM03.03 physics model in the high-energy physics regime. These physics modelling options are selected by setting the `icem` and the `ilaq` keywords on the MCNP `LCA` card equal to one [74, 75] as illustrated in Figure E.13. Note that these are not the default MCNP physics modelling options; they are the physics modelling options recommended for use with the MCNP cosmic-ray source term by McKinney *et al.* [163].

The model transition energies are also reduced relative to their default values. The nucleon transition energy is reduced from 3,500 MeV to 1,000 MeV. This means that nucleon physics modelling is handled by the CEM03.03 model at nucleon energies less than 1,000 MeV and by the LAQGSM03.03 model at nucleon energies greater than 1,000 MeV. The pion transition energy is reduced from 2,500 MeV to 1,000 MeV.

This means that pion physics modelling is handled by the CEM03.03 model at pion energies less than 1,000 MeV and by the LAQGSM03.03 model at pion energies greater than 1,000 MeV. These model transition energies are consistent with the transition energies recommended by McKinney *et al.* [163].

```
      …  …
15,780   c Turn physics models on:
15,781   c -----------------------
15,782   c
15,783   c Use the MPHYS card to turn physics models on. Refer to
15,784   c Section 3.3.3.7.1 of the MCNP6.1.1 beta User's Manual for more
15,785   c information regarding the keywords associated with the MPHYS card.
15,786
15,787   c
15,788   MPHYS ON
      …  …
```

Figure E.12: An example of an MCNP `MPHYS` card written to an MCNP input deck generated by the TeXAS application.

```
      …  …
15,785   c Select physics models and set certain model parameters:
15,786   c -----------------------------------------------------
15,787   c
15,788   c Use the LCA card to select the CEM03.03 and LAQGSM03.03 models as
15,789   c recommended by G. W. McKinney et al. (LA-UR-12-0196). Refer to
15,790   c Section 3.3.3.7.2 of the MCNP6.1.1 beta User's Manual for more
15,791   c information regarding the keywords associated with the LCA card.
15,792   c
15,793   LCA 2 1 1 0023 1 1 0 1 1 1
15,794   c
15,795   c Set particle-energy-dependent physics model controls:
15,796   c -----------------------------------------------------
15,797   c
15,798   c Use the LCB card to reduce the model transition energies from
15,799   c their default values to about 1,000 MeV. Refer to Section 3.3.3.7.3
15,800   c of the MCNP6.1.1 beta User's Manual for more information regarding
15,801   c the keywords associated with the LCB card.
15,802   c
15,803   LCB 1000 1000 1000 1000 800 800 -1 -1
      …  …
```

Figure E.13: Examples of MCNP `LCA` and `LCB` cards written to an MCNP input deck generated by the TeXAS application.

The MCNP NPS and CTME *Cards:*

The MCNP NPS and CTME cards are used to terminate MCNP runs after either (a) a certain number of source particle histories have been run (in the case of the NPS card), or (b) a certain amount of computation time has elapsed (in the case of the CTME card) [74, 75]. In the ideal case, the MCNP runs supporting CTBT-relevant radioactive particulate and noble gas background activity concentration studies terminate after the NPS criteria is satisfied. MCNP runs that terminate according to an NPS criteria run the desired number of source particle histories and tend to have smaller tally variances. However, the computation time criteria specified using the CTME card can also be important, particularly in the case of MCNP jobs run on shared clusters with job scheduling systems configured to automatically close sessions after predetermined time periods. See Sections E.2.9 and E.5 for more information regarding the assignment of values to the NPS and CTME card keywords. Examples of MCNP NPS and CTME cards written to an MCNP deck generated by the TeXAS application are presented in Figure E.14.

The MCNP PRINT *and* PRDMP *Cards:*

The MCNP PRINT and PRDMP cards are used to control the output generated by MCNP. In the MCNP input decks generated by the TeXAS application, the PRINT card is used to suppress the output of output tables 20, 30, 32, 35, 38, 44, 55, 62, 80, 86, 87, 90, 95, 115, 117, 118, 128, 150, 163, 170, 175, and 178. The PRDMP card is used to

control the intervals at which tallies are printed to the MCNP output file and the intervals at which information is dumped to the run tape file [74, 75]. Refer to Section 3.3.7.2.1 of the MCNP User's Manual [74, 75] for more information regarding the MCNP `PRINT` card and to Table 3-138 of the MCNP User's Manual [74, 75] for more information about each of the output tables suppressed by the `PRINT` card written to the MCNP input decks generated by the TeXAS application. Refer to Section 3.3.7.2.3 of the MCNP beta User's Manual [74, 75] for more information regarding the MCNP `PRDMP` card. Examples of MCNP `PRINT` and `PRDMP` cards written to an MCNP input deck generated by the TeXAS application are presented in Figure E.15.

```
…
c Problem termination cards:
c -------------------------
c
c Use the NPS card to terminate the MCNP run after a specified number
c of source particle histories have been run. Refer to Section 3.3.7.1.1
c of the MCNP6.1.1 beta User's Manual for more information regarding
c the keywords associated with the NPS card.
c
NPS 5000
c
c Use the CTME card to terminate the MCNP run after a specified amount of
c computation time (in minutes) has elapsed. Refer to Section 3.3.7.1.1
c of the MCNP6.1.1 beta User's Manual for more information regarding
c the keywords associated with the CTME card.
c
CTME 10800
…
```

Figure E.14: Examples of MCNP `NPS` and `CTME` cards written to an MCNP input deck generated by the TeXAS application.

```
     …  …
15,785  c Output control cards:
15,786  c ---------------------
15,787  c
15,788  c Use the PRINT card to suppress the output of output tables 20, 30,
15,789  c 32, 35, 38, 44, 55, 62, 80, 86, 87, 90, 95, 115, 117, 118, 128,
15,790  c 150, 163, 170, 175, and 178. Refer to Section 3.3.7.2.1 of the
15,791  c MCNP6.1.1 beta User's Manual for more information regarding
15,792  c the PRINT card and the suppressed output tables.
15,793  c
15,794  PRINT -20  -30  -32  -35  -38  -44  -55  -62  -80  -86  -87
15,795        -90  -95 -115 -117 -118 -128 -150 -163 -170 -175 -178
15,796  c
15,797  c Use the PRDMP card to specify the intervals at which tallies are printed
15,798  c to the MCNP output file and the intevals at which information is dumped
15,799  c to the MCNP run tape file. Refer to Section 3.3.7.2.3 of the MCNP6.1.1
15,800  c beta User's Manual for more information regarding the PRDMP card.
15,801  c
15,802  PRDMP -720 -720 1 100 5000
     …  …
```

Figure E.15: Examples of MCNP `PRINT` and `PRDMP` cards written to an MCNP input deck generated by the TeXAS application.

E.2.8 Development of MCNP Tally Cards

In order to extract useful information from an MCNP run, an MCNP user must specifically request that certain events or phases of the radiation transport process be recorded by MCNP. The events and phases of interest may be many different things in different MCNP runs, but in the MCNP runs supporting the TeXAS application the events and phases of interest involve neutrons resulting from cosmic-ray induced reactions moving through and interacting in specific spatial regions of the Earth's atmosphere and subsurface. An MCNP user must specifically request that these events and phases of the radiation transport process be recorded by MCNP using what are referred to as "tallies." Tallies are evaluated using MCNP tally cards.

The TeXAS application automatically incorporates cross-section weighted neutron flux tally cards into the MCNP input decks it generates to support evaluating incident-neutron induced fission and activation reaction rates. The fission and activation reactions of interest are the fission and activation reactions that lead to the production of the radioactive particulates and noble gases identified as relevant to the CTBT [116]. The fissionable targets for which tallies are evaluated are ^{232}Th, ^{234}U, ^{235}U, ^{238}U, ^{238}Pu, ^{239}Pu, and ^{240}Pu. The activation targets for which tallies are evaluated are the activation targets that produce the CTBT-relevant activation products via the (n,γ), (n,p), (n,α), and (n,2n) reactions identified in Table 3.2.

As mentioned previously, the TeXAS application automates the process of creating the MCNP tally cards required to support evaluating the CTBT-relevant radioactive particulate and noble gas background activity concentrations. Users of the TeXAS application are only required to specify the atmospheric and subsurface layers in which they wish to evaluate the CTBT-relevant radioactive particulate and noble gas background activity concentrations. The TeXAS application then determines which target materials are present in the atmospheric and subsurface layers identified by the user and writes tally cards to the MCNP input deck as appropriate. Figure E.16 provides an example of an MCNP tally card used to evaluate the ^{235}U neutron-induced fission cross-section weighted neutron flux in a 1 m thick subsurface layer centered at geometric height of 63 m above sea level (in this particular case 63 m above sea level is 1 m below the surface). Note that the comments included in Figure E.16 are also generated

automatically by the TeXAS application to aid in the evaluation and interpretation of tally results, as needed.

```
…
26,512  c Request that a fission cross-section weighted neutron cell flux tally
26,513  c (MCNP tally 00015484) specific to U-235 be evaluated in MCNP cell 00000091
26,514  c which is at a mean geometric height of 6.300000E+01 m:
26,515  c
26,516  F00015484:N 00000091
26,517  FM00015484 3.14159E+10 00003792 -6
…
```

Figure E.16: An example of an MCNP tally card used to evalaute a ^{235}U neutron-induced fission cross-section weighted neutron flux tally.

E.2.9 The Variance Reduction Scheme

The Monte Carlo N-Particle (MCNP) radiation transport code [74, 75] models created by the TeXAS application transport a large number of particle and photon types having a wide range of energies over considerable distances, especially by MCNP standards. In order to support developing the best possible results in the shortest amount of time possible, the MCNP models created by the TeXAS application employ a somewhat sophisticated variance reduction scheme that allows MCNP to focus its computational efforts on the photons and particles moving through spatial regions that are most important in establishing the radioactive particulate and noble gas background activity concentrations of interest. The variance reduction scheme utilizes the weight-window generator built into MCNP [74, 75] in an iterative fashion, as illustrated in Figure E.17.

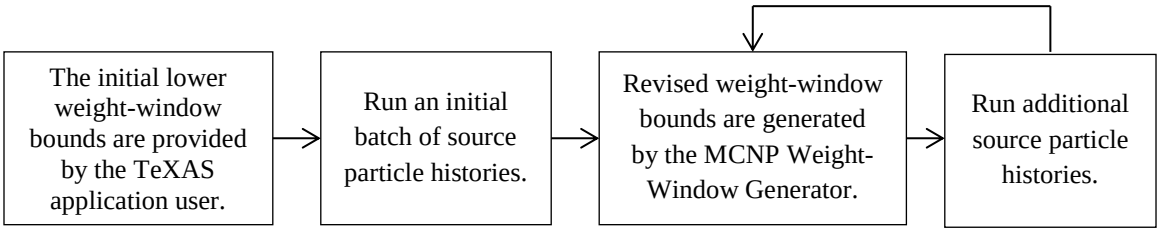

Figure E.17: The variance reduction scheme employed by MCNP models created by the TeXAS application.

The idea of the variance reduction scheme employed by the TeXAS application is to initially assume that all particle and photon types and all spatial regions are equally important in establishing the radioactive particulate and noble gas background activity concentrations of interest. The MCNP weight-window generator is then used to update the particle and photon importances as it sees fit as source particle histories are run. The particle and photon importances are updated in an iterative manner so that fewer source particle histories are run using the initial, poorly informed importances, and more source particle histories are run using the importances developed by the MCNP weight-window generator as more and more source particle histories are run.

This idea is implemented as follows. The lower weight-window bounds associated with all particle and photon types and all spatial regions are initially set equal to the same value (0.5). A small fraction of the total source particle histories are then run using these lower weight-window bounds. The number of source particle histories run using the initial lower weight-window bounds depends on the total number of source particle histories to be run, but for MCNP jobs for which a total of 10^6 source particle

histories are to be run the initial weight-window bounds would be used to run the first 5,000 source particle histories.

After the first round of source particle histories are run the MCNP weight-window generator is used to re-evaluate the lower weight-window bounds associated with all particle and photon types and all spatial regions. These weight-window bounds are then used to run additional source particle histories. The number of source particle histories run using the updated weight-window bounds again depends on the total number of source particle histories to be run, but for MCNP jobs for which a total of 10^6 source particle histories are to be run the updated weight-windows are used to run an additional 15,000 source particle histories.

This process of running source particle histories, running the MCNP weight-window generator to update the weight window lower bounds, and then running additional source particle histories may be repeated as many as six times depending on the number of source particle histories to be run. As mentioned previously, for MCNP jobs for which a total of 10^6 source particle histories are to be run the initial weight-window bounds would be used to run the first 5,000 source particle histories and the updated weight-window bounds would be used to run an additional 15,000 source particle histories. The weight windows for this MCNP job would be updated four more times and used to run an additional 30,000, 50,000, 100,000, and 800,000 source particle histories.

E.2.10 Development of Linux Bash Shell Scripts to Automate MCNP Job Execution

Because the TeXAS application was developed to allow researchers not specifically familiar with the details associated with the Monte Carlo N-Particle (MCNP) radiation transport code [74, 75] to use MCNP to develop study-specific reaction cross-section and neutron flux profiles required to support high-fidelity CTBT-relevant radionuclide background activity concentration estimates, the TeXAS application generates Linux Bash shell scripts and Windows batch files to simplify and automate the process of executing MCNP models created by the TeXAS application.

Generally speaking, executing an MCNP job involves first directing the system to the appropriate MCNP executable and nuclear data file directory. These steps are often handled in advance by modifying the `PATH` and `DATAPATH` system environment variables at the time of an MCNP installation. In order to verify that the `PATH` and `DATAPATH` environment variables are set properly, the Linux Bash shell script and Windows batch file generated by the TeXAS application set the `PATH` and `DATAPATH` environment variables each time a job is submitted for execution assuming an MCNP installation consistent with the default Linux and Windows MCNP installations described in the `ABOUT_MCNP611.html` file packaged with the MCNP version 6.1.1beta. For MCNP jobs executed on Linux systems, the `PATH` and `DATAPATH` environment variables are set as follows:

PATH

DATAPATH

For MCNP jobs executed on WINDOWS systems, the PATH and DATAPATH environment variables are set as follows:

```
@ set PATH=%PATH%;C:\my_mcnp\MCNP_CODE\bin
@ set DATAPATHC:\my_mcnp\MCNP_DATA
```

After directing the system to the appropriate MCNP executable and nuclear data file directory, an MCNP job may be executed by setting the relevant execution line keywords and calling the MCNP executable. The MCNP models created by the TeXAS application require that six keywords be set each time an MCNP job is submitted for execution. The first keyword that must be set is the `INP` keyword. The `INP` keyword directs the MCNP executable to an MCNP input file generated by the TeXAS application. The string assigned to the `INP` keyword is created by combining the study, scenario, and perturbation ID strings provided by the user in a principle formatted input file with a `.inp0#` file extension. The `#` character in the file extension is replaced by a "1," a "2," a "3," *etc.* as appropriate based on the status of a given MCNP job as an initiate run or a continue run. Six examples of `INP` keyword assignments are shown in Figure E.18.

```
# TeXASMCNPExec.sh
#
# Set environment variables:
#
@ PATH C:\MCNP\MCNP_CODE\bin;%PATH%
@ set DATAPATH=C:\MCNP\MCNP_DATA
@ set DISPLAY=localhost:0
#
# Run the MCNP initiate run:
#
mpirun -np 61 mcnp611.mpi INP=0005-0031-1984.inp01 \
   WWINP=0005-0031-1984.wwinp01 \
   OUTP=0005-0031-1984.outp01 \
   WWOUT=0005-0031-1984.wwout01 \
   MCTAL=0005-0031-1984.mctal01 \
   RUNTPE=0005-0031-1984.runtpe
#
sleep 600
#
# Run the first MCNP continue run:
#
mpirun -np 61 mcnp611.mpi C INP=0005-0031-1984.inp02 \
   WWINP=0005-0031-1984.wwout01 \
   OUTP=0005-0031-1984.outp02 \
   WWOUT=0005-0031-1984.wwout02 \
   MCTAL=0005-0031-1984.mctal02 \
   RUNTPE=0005-0031-1984.runtpe
#
sleep 600
#
# Run the second MCNP continue run:
#
mpirun -np 61 mcnp611.mpi C INP=0005-0031-1984.inp03 \
   WWINP=0005-0031-1984.wwout02 \
   OUTP=0005-0031-1984.outp03 \
   WWOUT=0005-0031-1984.wwout03 \
   MCTAL=0005-0031-1984.mctal03 \
   RUNTPE=0005-0031-1984.runtpe
#
sleep 600
#
# Run the third MCNP continue run:
#
mpirun -np 61 mcnp611.mpi C INP=0005-0031-1984.inp04 \
   WWINP=0005-0031-1984.wwout03 \
   OUTP=0005-0031-1984.outp04 \
   WWOUT=0005-0031-1984.wwout04 \
   MCTAL=0005-0031-1984.mctal04 \
   RUNTPE=0005-0031-1984.runtpe
#
sleep 600
…
```

Figure E.18: An example of a Linux Bash shell script used to simplify and automate the process of executing MCNP models generated by the TeXAS application.

```
…  …
53  # Run the fourth MCNP continue run:
54  #
55  mpirun -np 61 mcnp611.mpi C INP=0005-0031-1984.inp05 \
56     WWINP=0005-0031-1984.wwout04 \
57     OUTP=0005-0031-1984.outp05 \
58     WWOUT=0005-0031-1984.wwout05 \
59     MCTAL=0005-0031-1984.mctal05 \
60     RUNTPE=0005-0031-1984.runtpe
61  #
62  sleep 600
63  #
64  # Run the fifth MCNP continue run:
65  #
66  mpirun -np 61 mcnp611.mpi C INP=0005-0031-1984.inp06 \
67     WWINP=0005-0031-1984.wwout05 \
68     OUTP=0005-0031-1984.outp06 \
69     WWOUT=0005-0031-1984.wwout06 \
70     MCTAL=0005-0031-1984.mctal06 \
71     RUNTPE=0005-0031-1984.runtpe
72  #
73  sleep 600
```

Figure E.18: An example of a Linux Bash shell script used to simplify and automate the process of executing MCNP models generated by the TeXAS application, continued.

The second keyword that must be set is the `WWINP` keyword. The `WWINP` keyword is used to specify the name of the weight-window generator input file required to support the MCNP variance reduction scheme utilized by the TeXAS application. See Section E.2.9 for more information regarding the variance reduction scheme utilized by the TeXAS application. For an MCNP initiate run, the string assigned to the `WWINP` keyword is created by combining the study, scenario, and perturbation ID strings provided by the user in a principle formatted input file with a `.wwinp01` file extension. For a continue run, the `WWINP` keyword is set equal to the `WWOUTP` keyword associated with the weight-window generator output file generated by the preceding MCNP job.

The third keyword that must be set is the OUTP keyword. The OUTP keyword specifies the name of the file to which MCNP outputs generated by a given MCNP job should be written. The string assigned to the OUTP keyword is created by combining the study, scenario, and perturbation ID strings provided by the user in a principle formatted input file with a .outp0# file extension. The # character in the file extension is replaced by a "1," a "2," a "3," *etc.* as appropriate based on the status of a given MCNP job as an initiate run or a continue run. Six examples of OUTP keyword assignments are shown in Figure E.18.

The fourth keyword that must be set is the WWOUT keyword. The WWOUT keyword is used to specify the name of the file to which lower weight window bounds generated by the MCNP weight-window generator should be written. The string assigned to the WWOUT keyword is created in the same way the INP and OUTP keyword strings are created.

Additionally, an MCTAL keyword must be set each time an MCNP job is submitted for execution. The MCTAL keyword is used to specify the name of the file to which tallies generated by the MCNP job should be written. The string assigned to the MCTAL keyword is created in the same way the INP, OUTP, and WWOUT keyword strings are created.

Finally, a RUNTPE keyword must also be set each time an MCNP job is submitted for execution. The RUNTPE keyword is used to specify the name of the run tape to which binary start and restart data should be written by the MCNP job. A single

run tape is created by an MCNP initiate run and then the same run tape is read and amended by any subsequent MCNP continue runs. The string assigned to the `RUNTPE` keyword is created by combining the study, scenario, and perturbation ID strings provided by the user in a principle formatted input file with a `.runtpe` file extension.

After setting the relevant execution line keywords as described above, an MCNP job may be executed by calling the MCNP executable. MCNP models developed by the TeXAS application are designed to be executed using MCNP version 6.1.1beta, and thus the Linux Bash script and Windows batch file created by the TeXAS application call either the serial `MCNP611.exe` executable if only a single processor is to be used to execute the MCNP job, or an MPI enabled `MCNP611.mpi` executable if multiple processors are to be used to execute the MCNP job (see Section E.5). These executables may be modified manually, of course, as required to run MCNP on a given system.

The file name associated with the Linux Bash shell scripts generated by the TeXAS application is `TeXASMCNPExec.sh`. An example of a Linux Bash script used to automate the execution of MCNP models created by the TeXAS application is presented in Figure E.18. In order to execute the commands in a Linux Bash shell script generated the TeXAS application, open a terminal window, navigate to the directory containing the Linux Bash shell script, and type `./BashMCNPExec.sh`. Note that on some systems it may be necessary to modify the permissions associated with the Linux Bash script before attempting to run it as an executable.

The file name associated with the Windows batch files created by the TeXAS application is `TeXASBatchSubmit.bat`. The contents of Windows batch files created by the TeXAS application are comparable to the contents of the example Linux Bash shell script presented in Figure E.18, with the principle difference being the lines used to set the `PATH` and `DATAPATH` environment variables. The Windows batch files created by the TeXAS application may be executed by simply double-clicking them.

E.3 Nuclear Data Library Development

The TeXAS application is capable of developing nuclear data libraries specific to each of the CTBT-relevant radionuclide background activity concentration studies for which it generates Monte Carlo N-Particle (MCNP) radiation transport code [74, 75] input decks. The principal reason for developing study-specific nuclear data libraries is to make as much study-specific nuclear data as possible available to MCNP. As discussed in Sections E.2.3 through E.2.5, the TeXAS application supports the development of high-fidelity material composition and temperature data specific to individual CTBT-relevant radionuclide background activity concentration studies. MCNP is only able to take full advantage of the high-fidelity material composition and temperature data if temperature-adjusted nuclear data associated with each isotopic constituent of each material is also made available. Making more temperature-adjusted nuclear data available to MCNP allows MCNP to better model the transport of radiation through the atmosphere and

subsurface layers of a given MCNP model and, ultimately, allows for the production of better, more study-specific results.

The TeXAS application generates Nuclear data libraries specific to individual CTBT-relevant radionuclide background activity concentration studies via the basic process illustrated in pseudocode form in Figure E.19. The process essentially involves stepping through each of the atmospheric and subsurface layers of a given MCNP model, collecting isotope-specific nuclear data as it is available, processing the nuclear data using the NJOY 2012 nuclear data processing code [141], and then post-processing and consolidating the processed nuclear data. The process of collecting the isotope-specific nuclear data is described in more detail in the next section (Section E.3.1). The nuclear data is processed using the NJOY 2012 nuclear data processing code as described in Section E.3.2. Section E.3.3 describes the post-processing and consolidation of the processed nuclear data.

E.3.1 Collection of Relevant ENDF-Formatted Nuclear Data Files

The first step of the nuclear data library development process involves collecting the relevant ENDF-formatted nuclear data. The highest level of the nuclear data collection process involves stepping through the Atmospheric block and each of the subsurface blocks associated with a given MCNP model. Within a given block, the TeXAS application then steps through each of the layers of the block, one at a time. Each layer has a temperature and a material associated with it. Each material has an isotopic

composition. The TeXAS application steps through each of the isotopes associated with each material and looks to see if ENDF-formatted nuclear data is available for each isotope.

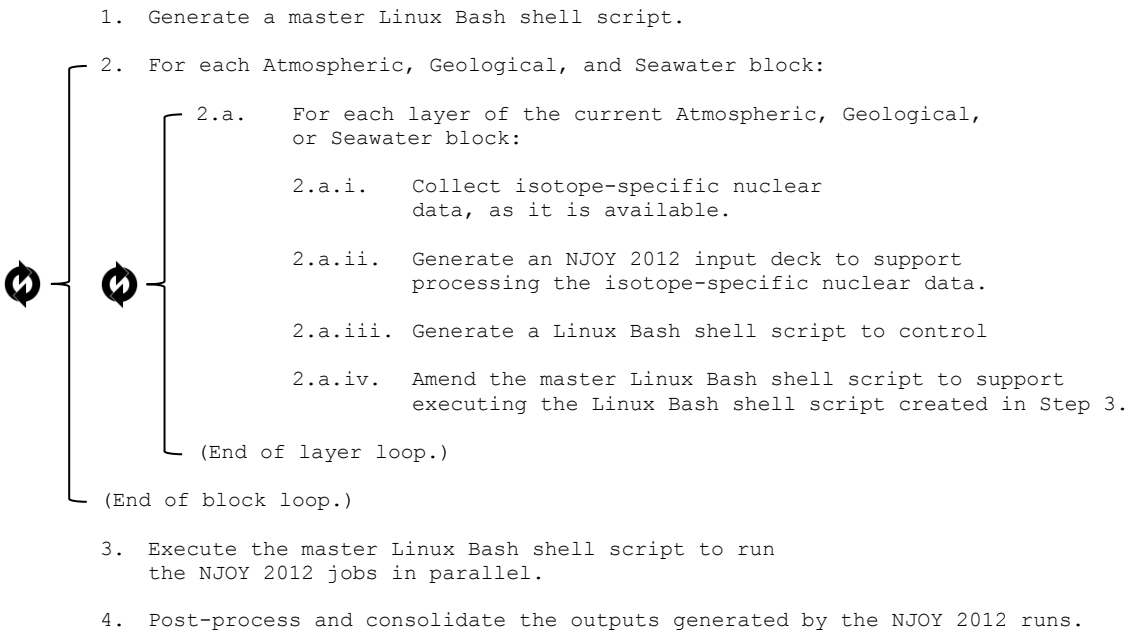

Figure E.19: The basic nuclear data library generation process utilized by the TeXAS application.

The TeXAS application has access to six nuclear data libraries in which it may search for ENDF-formatted nuclear data files: (1) The BROND library maintained by the Russian Nuclear Data Center [117, 164]; (2) the CENDL library maintained by the China Nuclear Data Center [117, 165]; (3) the ENDF-B library maintained by the Cross Section Evaluation Working Group [117, 118]; (4) the JEFF library maintained by Nuclear Energy Agency (NEA) data bank member countries [117, 166, 167, 168]; (5) the JENDL library maintained by the Japan Atomic Energy Agency [117, 169]; and (6) the TENDL library maintained by Koning and Rochman at the Paul Scherrer Institut [170]. The TeXAS application actually has access to multiple version of some of the aforementioned nuclear data libraries as illustrated in Table E.4. For example, the TeXAS application has access to versions VII.0 and VII.1 of the ENDF-B nuclear data library.

Table E.4: Nuclear data libraries to which the TeXAS application has access.

Library	Version	Nuclear Data Classes Available									
		A	C	E	H	O	P	R	S	T	U
BROND	2.2		✓								
CENDL	2		✓								
	3.1		✓								
ENDF-B	VII.0		✓	✓	✓	✓	✓	✓	✓	✓	✓
	VII.1		✓	✓	✓	✓	✓	✓	✓	✓	✓
JEFF	3.1.1		✓		✓					✓	
	3.1.2		✓								
	3.2		✓								
JENDL	4.0		✓	✓			✓			✓	
	4.0u		✓	✓			✓			✓	
	4.0u2		✓	✓			✓			✓	
TENDL	2015	✓	✓		✓	✓		✓	✓		✓

Additionally, within each version of each nuclear data library the TeXAS application may have access to up to nine classes of nuclear data. The data classes available within each version of each nuclear data library are summarized in Table E.4. Class A, C, E, H, O, R, and S nuclear data is continuous-energy data for incident alpha particles, neutrons, electrons, protons, deuterons, tritons, and helions, respectively. Class P nuclear data is photoatomic nuclear data. Class T nuclear data is thermal neutron scattering data. And finally, Class U nuclear data is photonuclear data. While in some cases the TeXAS application may have access to data for all of the aforementioned nuclear data classes, it does not always access and utilize data from all of the data classes; it only accesses and utilizes data for the data classes requested by the user. Note that utilizing nuclear data from multiple data classes often results in the generation of very large study-specific nuclear data libraries and that MCNP sometimes has trouble loading and accessing the data even if it is made available.

As the TeXAS application finds isotope-specific ENDF-formatted nuclear data files relevant to a particular CTBT-relevant radionuclide background activity concentration study it copies them to directories that are created as required in a `NuclearData` directory specific to the study. For example, if the TeXAS application finds Class C nuclear data for ^{235}U while conducting CTBT-relevant radionuclide background activity concentration study 0005-0031-1984 it stores the data in the following directory: `/0005-0031-1984/NuclearData/092235.15c`. The `/0005-0031-1984` directory is created in the directory in which the TeXAS

application is installed. The lowest level of the directory hierarchy denotes (1) that the nuclear data stored in the directory is for ^{235}U which has an atomic number of 92 and a mass number of 235, (2) that the ^{235}U nuclear data stored in the directory is adjusted to the fifteenth temperature at which ^{235}U appears in the study, and (3) that the ^{235}U nuclear data stored in the directory is Class C nuclear data. ENDF-formatted nuclear data files are renamed `tape20` as they are copied to their respective directories. The reason for renaming the ENDF-formatted files `tape20` is discussed in Section E.3.2. Copying all of the ENDF-formatted nuclear data files relevant to a particular CTBT-relevant radionuclide background activity concentration study in the manner described here makes it such that all the raw nuclear data supporting a given study is archived for later reference, as it may be required for quality assurance and quality control purposes.

In addition to the ENDF-formatted nuclear data file, two additional files are written to each of the nuclear data file directories. The first is an NJOY 2012 [141] input file, and the second is a Linux Bash shell script used to execute the NJOY 2012 input file, modify certain aspects of the output generated by the NJOY 2012 run, and redirect the standard output and standard error messages generated by the NJOY 2012 run. The NJOY 2012 input files are discussed in the next section (Section E.3.2).

An example of a Linux Bash shell script used to support the execution of an NJOY 2012 run is presented in Figure E.20. The commands on lines 12 and 13 of the Bash shell script support executing the NJOY 2012 input file, while lines 15 and 16 support copying the outputs generated by the NJOY 2012 run, `tape25` and `tape26`, to

two new directories called `AllACEFormattedFiles` and `AllCrossSec-DirLines`, respectively. Lines 18 through 20 support modifying the contents of the second output file generated by the NJOY 2012 run. The significance of these changes is discussed in Section E.3.2. Line 22 supports redirecting the standard output and standard error messages output by the NJOY 2012 run. The remainder of the lines of the Linux Bash shell script support organizing and formatting the standard output and standard error messages generated by the NJOY 2012 run.

```
 1  #!/bin/bash
 2
 3  (
 4
 5  echo "stdout Redirected from BASHShellScript-092235.75c.sh" >&1
 6  echo "==================================================" >&1
 7
 8  echo "stderr Redirected from BASHShellScript-092235.75c.sh" >&2
 9  echo "==================================================" >&2
10  echo -e "\n" >&2
11
12  cd ./092235.75c
13  xnjoy < NJOY2012InpDeck-092235.75c
14
15  cp -i tape25 ../AllACEFormattedFiles/092235.75c
16  cp -i tape26 ../AllCrossSecDirLines/092235.75c
17
18  cd ../AllCrossSecDirLines
19  sed -i 's/filename/092235.75c/g' 092235.75c
20  sed -i 's/route/0*/g' 092235.75c
21
22  ) 1> ./AllstdoutRedirects/092235.75c 2> ./AllstderrRedirects/092235.75c
23
24  cd ./AllstdoutRedirects
25  echo -e "\n" >> 092235.75c
26
27  cd ../AllstderrRedirects
28  echo -e "\n" >> 092235.75c
```

Figure E.20: An example of a Linux Bash shell script used to simplify and automate the process of executing MCNP models created by the TeXAS application.

As ENDF-Formatted files, NJOY 2012 input files, and Linux Bash shell scripts are written to the nuclear data file directory specific to a given CTBT-relevant radionuclide background activity concentration study, lines are written to a master Linux Bash shell script created in the `/0005-0031-1984/NuclearData` directory. These lines support executing each of the individual Linux Bash scripts described above in parallel using the GNU parallel shell tool [171].

E.3.2 Processing Nuclear Data Using NJOY 2012

The second step of the nuclear data library development process involves processing the ENDF-formated nuclear data files collected as described in the previous section using the NJOY 2012 nuclear data processing code [141]. NJOY 2012 is used to load fundamental nuclear data from ENDF-formatted files, modify the data in various ways, and then produce pointwise nuclear data in forms that are suitable for other applications. The NJOY 2012 nuclear data processing code consists of a set of modules [141]. Each module performs a well-defined task and is linked to the other NJOY 2012 modules by input and output files [141]. The TeXAS application utilizes the following NJOY 2012 modules: (1) MODER, (2) RECONR, (3) BROADR, (4) PURR, (5) THERMR, and (6) ACER [141]. The tasks performed by each of these NJOY 2012 modules are described below.

The NJOY 2012 MODER Module:

The MODER module of the NJOY 2012 nuclear data processing code is used to convert ENDF-formatted tapes back and forth between the ASCII-formatted mode and the NJOY 2012 blocked binary mode [141]. ENDF-formatted tapes in the ASCII-formatted mode are eye readable while ENDF-formatted tapes in the NJOY 2012 blocked binary mode are not. However, the NJOY 2012 nuclear data processing code is able to process data in tapes in the blocked-binary mode more efficiently than data in tapes in the ASCII-formatted mode [141]. In order to make the nuclear data processing as efficient as possible, ENDF-formatted tapes are typically converted to the blocked binary mode at the beginning of each NJOY 2012 input deck.

As illustrated in Figure E.21, there are only two inputs to the NJOY 2012 MODER module. The first is the input tape number (20) and the second is the output tape number (-21). Note that the fact that the input tape number is positive indicates that the input tape is in the ASCII-formatted mode and the fact that the output tape is negative indicates that the output tape is in the NJOY 2012 blocked binary mode.

```
…  …
 8  -- Call the NJOY 2012 MODER module:
 9  -- --------------------------------
10  --
11  moder
12  20 -21
…   …
```

Figure E.21: An excerpt from an NJOY 2012 input deck generated by the TeXAS application showing the format of the NJOY 2012 MODER module.

The NJOY 2012 RECONR Module:

The NJOY 2012 RECONR module is used (1) to reconstruct pointwise cross-sections from cross-section data provided using non-linear interpolation schemes in ENDF-formatted files and (2) to reconstruct resonance cross-sections defined using resonance parameters in ENDF-formatted files [141]. The pointwise cross-sections must be reconstructed because the cross-sections stored in ENDF-formatted files effectively have data points missing. The missing data points are removed from the ENDF-formatted files and replaced with interpolation scheme information so that the sizes of the ENDF-formatted files may be kept relatively small. However, NJOY 2012 performs all of its cross-section modifications using a linear-linear interpolation scheme, and thus the RECONR module must be used to reconstruct pointwise cross-sections from the data provided in ENDF-formatted files [141].

There are six input cards associated with the NJOY 2012 RECONR module [141]. Four of them are utilized by the TeXAS application. The first card is used to specify the input and output tape numbers [141]. The input and ouput tape numbers associated with the first card of the RECONR module in the example shown in Figure E.22 are -21 and -22. These tapes numbers indicate that the input and output tapes associated with the RECONR module are both in the NJOY 2012 blocked binary mode.

The second card allows the user to write a character string to the output tape generated by the RECONR module [141]. The TeXAS application creates a character string to specify the isotope the nuclear data corresponds to, the nuclear data library from

which the original ENDF-formatted file was taken, and that the data in the output tape has been processed using the NJOY 2012 nuclear data processing code.

The third RECONR module card is used to specify (1) the material for which pointwise cross-sections are to be reconstructed, (2) the number of descriptive data cards included in the NJOY 2012 input deck, and (3) the number of energy grid points added manually by the user [141]. In the example shown in Figure E.22, the material to be processed is ^{235}U. The second and third inputs on the third card of the RECONR module are assigned their default values (zeros) [141].

The fourth card associated with the RECONR module is used to specify (1) the fractional reconstruction tolerance to be used when the resonance-integral critereon is not satisfied, (2) the reconstruction temperature (in K), (3) the fractional reconstruction tolerance to be used when the resonance-integral critereon is satisfied, and (4) the maximum resonance-integral error per grid point [141]. The reconstruction temperature is passed to the NJOY 2012 input deck from the TeXAS application on an MCNP model block- and layer-specific basis. The reconstruction tolerances and the maximum resonance-integral error are assigned their default values [141].Execution of the RECONR module is terminated by the `0/` character string assinged to the last card associated with the RECONR module.

```
 …  …
14  -- Call the NJOY 2012 RECONR module:
15  -- ---------------------------------
16  --
17  reconr
18  -21 -22
19  'NJOY 2012 processed ENDF/B-VII.1 U-235 cross-section data'/
20  9228 0 0
21  1.00000E-03 0.00000E+00 1.00000E-02 5.00000E-08
22  0/
 …  …
```

Figure E.22: An excerpt from an NJOY 2012 input deck generated by the TeXAS application showing the format of the NJOY 2012 RECONR module.

The NJOY 2012 BROADR Module:

The BROADR module of the NJOY 2012 nuclear data processing code is used to add temperature dependence to pointwise cross-sections generated by the NJOY 2012 RECONR module by Doppler-broadening or thinning the pointwise cross-sections, as appropriate, based on the relationship between the desired cross-section temperature and the temperature associated with the cross-section data provided in the original ENDF-formatted file [141]. This temperature dependence must be accounted for because in a material at temperature T, the target nuclei in the material move around randomly with a distribution of velocities given by the Maxwell-Boltzman distribution [141]. As neutrons move through the material it is the velocity of the neutrons relative to the target nuclei that dictates the cross-sections that should be used to calculate reaction rates involving the target nuclei. While the details associated with the broadening and thinning procedures employed by NJOY 2012 are not disucssed here, it should be noted that NJOY 2012 uses the "kernel broadening" method originally utilized by the SIGMA1

code [141]. Figure E.23 presents an example of ^{240}Pu radiative capture cross-sections Doppler broadened from 0 K to 30,000 K and 300,000 K.

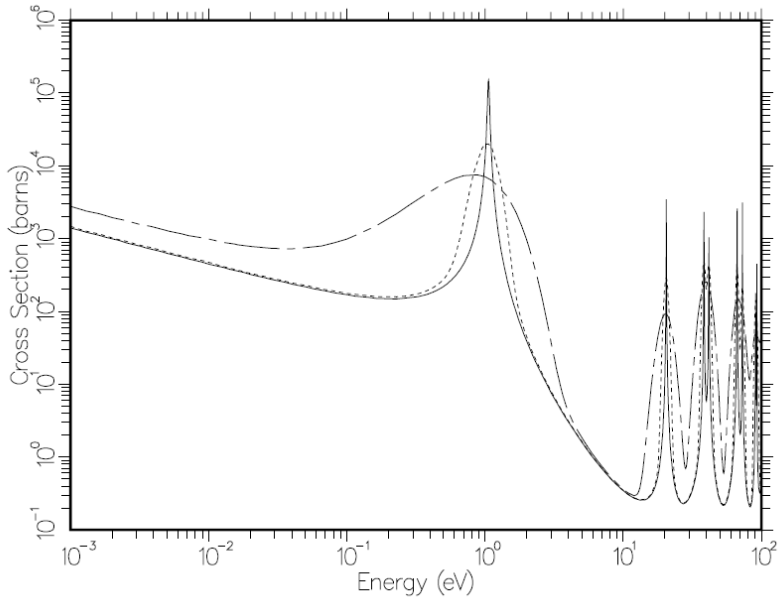

Figure E.23: ^{240}Pu radiative capture cross-sections Doppler broadened from 0 K to 30,000 K and 300,000 K [141].

There are five input cards associated with the NJOY 2012 BROADR module [141]. Four of them are utilized by the TeXAS application. The first card is used to specify the input and output tape numbers [141]. The input tape numbers associated with the first card of the BROADR module in the example shown in Figure E.24 are -21 and -22 and the output tape number is -23. Again, these input and ouput tape numbers indicate that the BROADR module input and output tapes are all in the NJOY 2012 blocked binary mode.

The second card of the BROADR module is used to specify (1) the material to be broadened or thinned, (2) the number of final temperatures, (3) whether or not the broadening operation is a continuation of a previous broadening operation, (4) whether or not the broadening operation is to be bootstraped, and (5) the starting temperature (in K) [141]. The starting temperature associated with the cross-section data processed in the example shown in Figure E.24 is 0 K. Non of the NJOY 2012 input decks generated by the TeXAS application utilize restarts or bootstrapping.

The third card of the NJOY 2012 BROADR module is used to specify (1) the fractional tolerance for broadening and thinning, (2) the maximum energy for broadening and thinning (in eV), (3) the fractional tolerance to be used when the resonance integral critereon is satisfied, and (4) a parameter to control integral thinning [141]. The TeXAS application assigns the default values to all of these parameters. The fourth card of the NJOY 2012 BROADR module specifies the temperatures to which the corss-sections are to be broadened or thinned (in K) [141]. In the example shown in Figure E.24, the ^{235}U cross-section is Doppler broadened to a final temperature of 293.3 K. Execution of the BROADR module is terminated by the `0/` character string assinged to the last card associated with the BROADR module.

```
…  …
24  -- Call the NJOY 2012 BROADR module:
25  -- ---------------------------------
26  --
27  broadr
28  -21 -22 -23
29  9228 1 0 0 0.00000E+00
30  1.00000E-03 1.00000E+06 1.00000E-02 5.00000E-08
31  2.933E+02
32  0/
…  …
```

Figure E.24: An excerpt from an NJOY 2012 input deck generated by the TeXAS application showing the format of the NJOY 2012 BROADR module.

The NJOY 2012 PURR Module:

There are two NJOY 2012 modules that may be used to produce effective self-shielded cross-sections in the unresolved energy range. The first is the RECONR module and the second is the PURR module. The effective self-shielded cross-sections produced by the RECONR module are suitable for use in multigroup calculations after being processed by the GROUPR NJOY 2012 module, but are not very useful to continuous energy Monte Carlo codes like the Monte Carlo N-Particle (MCNP) radiation transport code [141]. The more natural approach to deal with unresolved resonance region self-shielding effects in Monte Carlo calculations is the so-called probability table method. This method allows complications resulting from geometric and mixing effects to resolve themselves naturally during the Monte Carlo calculation [141]. The probability table generation method employed by the NJOY 2012 nuclear data processing system are discussed in detail in the NJOY 2012 manual [141].

There are four input cards associated with the NJOY 2012 PURR module, and all four of them are utilized by NJOY 2012 input decks generated by the TeXAS application [141]. The first card is used to specify the input and output tape numbers [141]. The input tape numbers associated with the first card of the PURR module in the example shown in Figure E.25 are -21 and -22 and the output tape number is -24. These input and ouput tape numbers indicate that the PURR module input and output tapes are all in the NJOY 2012 blocked binary mode.

The second card of the NJOY 2012 PURR module is used to specify (1) the material to be processed, (2) the number of temperatures for which unresolved energy range effective self-shielded cross-sections are to be generated, (3) the number of background crosss-sections for which unresolved energy range effective self-shielded cross-sections are to be generated, (4) the number of probability bins to be used, (5) the number of resonane ladders to be used, (6) a print option, and (7) the number of energy points desired [141]. In the example shown in Figure E.25 the material to be processed is ^{235}U, unresolved energy range effective self-shielded cross-sections are to be generated for one temperature and one background cross-section, and 20 probability bins and 64 resonance ladders are to be used. The default values are assigned to the remainder of the entries on the fourth card of the NJOY 2012 PURR module.

Note that the number of probability bins and resonance ladders to be used in a given NJOY 2012 input deck are typically established on a case basis at the user's discretion. The number of probability bins and resonance ladders used in NJOY 2012

input decks created by the TeXAS application are always the same and are as illustrated in the example shown in Figure E.25. These values were selected based on discussion with subject matter experts [172].

```
 …  …
34  -- Call the NJOY 2012 PURR module:
35  -- -------------------------------
36  --
37  purr
38  -21 -23 -24
39  9228 1 1 20 64 1 0
40  2.933E+02
41  1.00000E+10
42  0/
 …  …
```

Figure E.25: An excerpt from an NJOY 2012 input deck generated by the TeXAS application showing the format of the NJOY 2012 PURR module.

The NJOY 2012 THERMR Module:

The THERMR module is used to produce cross-section and energy-to-energy matrices for ^{1}H bound in water (H_2O) in the thermal energy range [141]. There are four input cards associated with the NJOY 2012 THERMR module, and all four of them are utilized by NJOY 2012 input decks generated by the TeXAS application [141].

The first card is used to specify the input and output tape numbers [141]. The input tape numbers associated with the first card of the THERMR module in the example shown in Figure E.26 are -21 and -25 and the output tape number is -26. These input and ouput tape numbers indicate that the THERMR module input and output tapes are all in the NJOY 2012 blocked binary mode.

There are ten entries associated with the second card of the NJOY 2012 THERMR module [141]. The first two entries specify the materials of interest in the original ENDF-formatted file and the PENDF-formatted file generated by the NJOY 2012 PURR module [141]. The fourth entry specifies the number of temperatures for which cross-section and energy-to-energy matrices should be generated [141]. The fifth and sixth entries are used to specify inelastic and elastic scattering options, respectively [141]. The eighth entry is used to specify the number of principal atoms associated with the scatter (for H_2O this entry should be set equal to two) [141]. The remainder of the entries assocaited with the NJOY 2012 THERMR card are described in Section 7.6 of the NJOY 2012 manual [141].

The third card of the NJOY 2012 THERMR module is used to specify the temperature of the material in units of K [141]. In the example shown in Figure E.26 the temperature is shown to be `2.936E+02` K (293.6 K).

The fourth, and final, card associated with the THERMR module is used to specify the tolerance and the maximum energy at which the thermal treatment should be applied [141]. In the example shown in Figure E.26, the tolerance is shown to be `1.00000E-03` (unitless) (0.1 %) and the maximum energy at which the thermal treatment should be applied is `5.00000E+00` MeV (5 MeV).

```
 …  …
44  -- Call the NJOY 2012 THERMR module:
45  -- ---------------------------------
46  --
47  thermr
38  21 -25 -26
49  0001 0125 8 1 2 0 0 2 222 0
50  2.936E+02
51  1.00000E-03 5.00000E+00
 …  …
```

Figure E.26: An excerpt from an NJOY 2012 input deck generated by the TeXAS application showing the format of the NJOY 2012 THERMR module.

The NJOY 2012 ACER Module:

The NJOY 2012 ACER module is used to prepare ACE-formatted nuclear data files that can be read and utilized by the MCNP radiation transport code [141]. The ACE file format attempts to capture all the details of an ENDF-formatted nuclear data file but it represents the data in a different way [141]. The primary difference between ACE-formatted files and ENDF-formatted files is ACE-formatted files utilize pointers while ENDF-formatted files do not [141]. The pointers in ACE-formatted files allow MCNP to randomly acces various parts of the data in the ACE-formatted files, and thus they increase the speed at which MCNP can access and use the data it needs in a given ACE-formmated file [141].

In addition to an ACE-formatted file, each ACER module run also generates a line to be incorporated into a Monte Carlo N-Particle (MCNP) radiation transport code `xsdir` file or written to an MCNP input deck `XS` card. The TeXAS application collects, modifies, and consolidates the lines generated by all the NJOY 2012 runs supporting a

given CTBT-relevant radionuclide background activity concentration study and consolidates them as described in the next section (Section E.3.3).

For NJOY 2012 runs processing fast cross-section data, five ACER module input cards are utilized. They are the first, second, third, fifth, and sixth ACER module input cards. The first ACER module input card is used to specify the input and output tape numbers [141]. The input tape numbers associated with the first card of the ACER module in the example shown in Figure E.27 are -21, -24, and 0, and the output tape numbers are 25 and 26. The first output tape (25) is the ACE-formatted file and the second (26) is the MCNP input deck XS card line.

```
…  …
44 -- Call the NJOY 2012 ACER module:
45 -- -------------------------------
46 --
47 acer
48 -21 -24 0 25 26
49 1 1 1 .75 0
50 'NJOY 2012 processed ENDF/B-VII.1 U-235 cross-section data'/
51 9228 2.933E+02
52 1 1
53 /
…  …
```

Figure E.27: An excerpt from an NJOY 2012 input deck generated by the TeXAS application showing the format of an NJOY 2012 ACER module supporting a fast data run.

The first, third, and fourth entries on the second card of the ACER module are used to specify the type of ACER run, the ACE-formatted file ouptut type (type 1 or type 2), and the suffix to be assigned to the material ZAID [141]. In the example shown in Figure E.27, the ACER run is a fast data run (type 1), the ACE-formatted file is set to type 1, and the suffix to be assigned to the material ZAID is `75`. The third ACER module card is used to write a character sting to the output tape generated by the ACER run [141].

The fourth ACER module card specifies the material and the temperature of the cross-section data to be written to the ACE-formatted file. In the example shown in Figure E.27 the material is ^{235}U and the temperature is 293.3 K. The fifth ACER module card specifies the cumulative angle distribution and photon treatment to be used during the NJOY 2012 run. As illustrated in Figure E.27, the NJOY 2012 input decks generated by the TeXAS application utilize the new "LAW=61" cumulative angle distributions (the first entry on the fifth ACER module card is `1`) and the detailed photon treatment (the second entry on the fifth ACER module card is `1`).

For NJOY 2012 runs processing thermal cross-secion data, five ACER module input cards are utilized. They are the first, second, third, eighth (8 and 8a), and ninth ACER module input cards. The first, second, and third ACER module cards supporting NJOY 2012 thermal cross-section data processing runs are the same as the first, second, and third ACER module cards supporting NJOY 2012 fast cross-section data processing runs.

For thermal cross-section data runs, the eighth ACER module card specifies the material, the temperature, and the thermal ZAID name associated with the data to be written to the ACE-formatted file [141]. In the example shown in Figure E.28 the material is ^{1}H, the temperature is 293.6 K, and the thermal ZAID name is `HinH2O`. The next card in the example shown in Figure E.28 is card 8a, and it is used to specify the moderator component za value [141].

```
 …  …
53  -- Call the NJOY 2012 ACER module:
54  -- -------------------------------
55  --
56  acer
57  -22 -26 0 27 28
58  2 1 1 .00 0
59  'NJOY 2012 processed ENDF/B-VII.1 H-1 cross-section data'/
60  0125 2.936E+02 HinH2O
61  1001 0 0
62  222 64 0 0 1 5.00000E+00 2
63  /
 …  …
```

Figure E.28: An excerpt from an NJOY 2012 input deck generated by the TeXAS application showing the format of an NJOY 2012 ACER module supporting a thermal data run.

The first three entries on the ninth card associated with the NJOY 2012 ACER module are used to specify (1) the MT number associated with the thermal incoherent data, (2) the number of bins for incoherent scattering, and (3) the thermal elastic scattering data MT number. The values assigned to the first and third entries on the ninth ACER module card shown in the example in Figure E.28 were established based on the guidance provided in Secton 17.17 and Table 25 of the NJOY 2012 manual [141].

The ACER modules in NJOY 2012 input decks supporting thermal data runs generated by the TeXAS application use 64 incoherent scattering. The number of bins requested is larger than the default (16), consistent with the guidance provided in Section 17.17 of the NJOY 2012 manual [141].

The fourth entry on the ninth card of NJOY 2012 input decks supporting thermal data runs specify whether elastic scattering is coherent or incoherent. The elastic scattering data for ^{1}H in water is coherent scattering data [141]. The fifth, sixth, and seventh entries on the ninth card of ACER modules supporting NJOY 2012 thermal data runs specify the number of atom types in a mixed moderator, the maximum energy for the thermal treatment, and a weighting option, respectively [141]. In the example shown in Figure E.28, the fifth, sixth, and seventh entries are set equal to 1, 5 eV, and 2, respectively, for consistency with the guidance provided in Section 17.17 of the NJOY 2012 manual [141].

E.3.3 Post-Processing NJOY 2012 Outputs

The third and final step of the nuclear data library development process involves post-processing and consolidating the outputs generated by the NJOY 2012 nuclear data processing code [141]. As discussed in the previous section, each of the NJOY 2012 jobs run in support of a given CTBT)-relevant radionuclide background activity concentration study produces two outputs. The first is an ACE-formatted file and the second is a line to be incorporated into a Monte Carlo N-Particle (MCNP) radiation transport code `xsdir`

file or written to an MCNP input deck `XS` card. The first steps of the NJOY 2012 output post-processing and consolidation process involve copying the ACE-formatted files from their individual nuclear data file directories to a single `/AllACEFormattedFiles` directory and modifying the MCNP `XS` card lines as described in Section E.3.1.

The remainder of the NJOY 2012 output post-processing and consolidation process involves making additional changes to the MCNP input deck XS card lines, consolidating all of the XS card lines into a single text file, and consolidating the standard output and standard error messages generated by each of the NJOY 2012 runs into two large standard output and standard error message text files. The XS card lines are actually consolidated into a single text file first, and then modified in a single pass. The modifications serve (1) to add an XS card number to the beginning of each of the XS card lines, (2) to replace the `0*` character string on each XS card line with a character string denoting the directory in which the nuclear data file called by the XS card line is stored and a line feed character, and (3) to format certain aspects of the XS card lines for consistency across all XS card lines. The standard output and standard error messages generated by the NJOY 2012 runs are consolidated into two large standard output and standard error message text files to make the messages easier to review.

The final products of the NJOY 2012 outputs post-processing and consolidation process are (1) an `/AllACEFormattedFiles` directory containing all the ACE-formatted files required to support the MCNP job associated with a particular CTBT-relevant radionuclide background activity concentration study, (2) an `AllXSCard-`

`Lines.txt` file that contains all of the MCNP input deck XS cards required to direct MCNP to each of the ACE-formatted files, (3) an `AllstdoutMessages.txt` file containing all of the standard output messages generated by the NJOY 2012 runs, and (4) an `AllstderrMessages.txt` file containing all of the standard error messages generated by the NJOY 2012 runs.

E.4 Post-Processing MCNP Outputs and Generating CTBT-Relevant Radionuclide Background Activity Concentration Estimates

The Monte Carlo N-Particle (MCNP) radiation transport code [74, 75] outputs produced by the MCNP jobs created by the first overarching TeXAS application code module—the `TeXASModDev` code module—are post-processed and used to develop the radioactive particulate and noble gas background activity concentration estimates required to complete a given CTBT-relevant radioactive particulate and noble gas background activity concentration study by a second overarching TeXAS application code module called the `TeXASPostProc` code module.

The `TeXASPostProc` code module is capable of developing radioactive particulate and noble gas background activity concentration estimates resulting from three types of natural processes, as supporting data is made available: (1) spontaneous fission, (2) cosmic neutron-induced fission, and (3) cosmic neutron-induced activation. Background activity concentration estimates associated with each of the aforementioned processes account for multiple reactions, when appropriate. For example, if the

composition associated with a geological layer is defined such that it contains ^{232}Th, ^{234}U, ^{235}U, and ^{238}U, and if all four parent radionuclides produce ^{133}Xe via spontaneous fission, then the ^{133}Xe background activity concentration estimate generated by the TeXAS application accounts for contributions from all four parent radionuclides.

The basic equation describing the rate at which the CTBT-relevant radionuclide $CTBT_i$ number density changes with time at time t is as follows:

$$\frac{dN_{CTBT_i}(t)}{dt} = \begin{matrix} CTBT_i\ Production\ Rate \\ via\ Spontaneous \\ Fission\ at\ Time\ t \end{matrix} + \begin{matrix} CTBT_i\ Production\ Rate \\ via\ n-Induced \\ Fission\ at\ Time\ t \end{matrix} \ldots$$
$$+ \begin{matrix} CTBT_i\ Production\ Rate \\ via\ n-Induced \\ Activation\ at\ Time\ t \end{matrix} - \begin{matrix} CTBT_i\ Loss\ Rate \\ via\ Radioactive \\ Decay\ at\ Time\ t \end{matrix}. \quad \text{E.4.1}$$

Note that Equation E.4.1 does not account for account losses resulting from physical transport processes. Equation E.4.1 may be expanded by plugging expressions describing each of the production and loss mechanisms into Equation E.4.1. The expression describing the production of CTBT-relevant radionuclide $CTBT_i$ via spontaneous fission at time t is as follows:

$$\begin{matrix} CTBT_i\ Production\ Rate \\ via\ Spontaneous \\ Fission\ at\ Time\ t \end{matrix} = \sum_{j=1}^{n_{SFP}} N_{SFP_j}(t) \cdot \lambda_{SFP_j} \cdot \beta_{SF,SFP_j} \cdot \chi_{CTBT_i,SFP_j}. \quad \text{E.4.2}$$

Where: $N_{SFP_j}(t)$ is the parent radionuclide SFP_j number density at time t,

λ_{SFP_j} is the decay constant associated with parent radionuclide SFP_j,

β_{SF,SFP_j} is the spontaneous fission branching ratio associated with parent radionuclide SFP_j, and

χ_{CTBT_i,SFP_j} is the CTBT-relevant radionuclide $CTBT_i$ yield resulting from the spontaneous fission of parent radionuclide SFP_j.

Note that in Equation E.4.2 the summation over all parent radionuclides $j = 1$ through n_{SFP} indicates that the total CTBT-relevant radionuclide $CTBT_i$ background activity concentration estimate generated by Equation E.4.2 accounts for contributions from all spontaneously fissioning parent radionuclides in a given atmospheric, geological, or seawater layer of interest.

The expression describing the production of CTBT-relevant radionuclide $CTBT_i$ via neutron-induced fission at time t is as follows:

$$\begin{matrix} CTBT_i\ Production\ Rate \\ via\ n-Induced \\ Fission\ at\ Time\ t \end{matrix} = \sum_{k=1}^{n_{FT}} \sum_{E=1}^{n_E} N_{FT_k}(t) \cdot \sigma_{Fiss,FT_k,E} \cdot \Phi_E(t) \cdot \chi_{CTBT_i,FT_k}. \quad \text{E.4.3}$$

Where: $N_{FT_k}(t)$ is the fissionable target FT_k number density at time t,

$\sigma_{Fiss,FT_k,E}$ is the neutron-induced fission cross-section associated with fissionable target FT_k and energy bin E,

$\Phi_E(t)$ is the neutron-flux associated with energy bin E at time t, and

χ_{CTBT_i,FT_j} is the CTBT-relevant radionuclide $CTBT_i$ yield resulting from neutron-induced fissions of fissionable target FT_k.

Note that in Equation E.4.3 the summation over energy bins $E = 1$ through n_E indicates that the total CTBT-relevant radionuclide $CTBT_i$ background activity concentration estimate generated by Equation E.4.3 accounts for contributions from all incident neutron energies. Similarly, the summation over all fissionable targets $k = 1$ through n_{FT}

indicates that the total fission product $CTBT_i$ background activity concentration estimate generated by Equation E.4.3 accounts for contributions from all fissionable targets in a given atmospheric, geological, or seawater layer of interest.

The expression describing the production of CTBT-relevant radionuclide $CTBT_i$ via neutron-induced activation at time t is as follows:

$$\begin{matrix} CTBT_i\ Production\ Rate \\ via\ n-Induced \\ Activation\ at\ Time\ t \end{matrix} = \sum_{l=1}^{n_{AT}} \sum_{E=1}^{n_E} N_{AT_l}(t) \cdot \sigma_{Act,AT_l,E} \cdot \Phi_E(t) \cdot m_{CTBT_i,AT_l}. \quad \text{E.4.4}$$

Where: $N_{AT_l}(t)$ is the activation target AT_l number density at time t,

$\sigma_{Act,AT_l,E}$ is the neutron-induced activation cross-section associated with activation target AT_l and energy bin E,

$\Phi_E(t)$ is the neutron-flux associated with energy bin E at time t, and

m_{CTBT_i} is the multiplicity by which CTBT-relevant radionuclide $CTBT_i$ is produced via neutron induced activation of activation target AT_l.

Note that in Equation E.4.4 the summation over energy bins $E = 1$ through n_E indicates that the total CTBT-relevant radionuclide $CTBT_i$ background activity concentration estimate generated by Equation E.4.4 accounts for contributions from all incident neutron energies. Similarly, the summation over all activation targets $l = 1$ through n_{AT} indicates that the total fission product $CTBT_i$ background activity concentration estimate generated by Equation E.4.4 accounts for contributions from all activation targets in a given atmospheric, geological, or seawater layer of interest.

And finally, the expression describing the loss of CTBT-relevant radionuclide $CTBT_i$ via radioactive decay is as follows:

$$\begin{matrix} CTBT_i\ Loss\ Rate \\ via\ Radioactive \\ Decay\ at\ Time\ t \end{matrix} = N_{CTBT_i}(t) \cdot \lambda_{CTBT_i}. \qquad \text{E.4.5}$$

Where: $N_{CTBT_i}(t)$ is the CTBT-relevant radionuclide $CTBT_i$ number density at time t and

λ_{CTBT_i} is the radioactive decay constant associated with CTBT-relevant radionuclide $CTBT_i$.

Substituting Equations E.4.2 through E.4.5 into Equation E.4.1 produces the following expression describing the rate at which the CTBT-relevant radionuclide $CTBT_i$ number density changes with time at time t:

$$\begin{aligned} \frac{dN_{CTBT_i}(t)}{dt} = & \sum_{j=1}^{n_{SFP}} N_{SFP_j}(t) \cdot \lambda_{SFP_j} \cdot \beta_{SF,SFP_j} \cdot \chi_{CTBT_i,SFP_j} \cdots \\ & + \sum_{k=1}^{n_{FT}} \sum_{E=1}^{n_E} N_{FT_k}(t) \cdot \sigma_{Fiss,FT_k,E} \cdot \Phi_E(t) \cdot \chi_{CTBT_i} \cdots \\ & + \sum_{l=1}^{n_{AT}} \sum_{E=1}^{n_E} N_{AT_l}(t) \cdot \sigma_{Act,AT_l,E} \cdot \Phi_E(t) \cdot m_{CTBT_i,AT_l} - N_{FP_i}(t) \cdot \lambda_{FP_i}. \end{aligned} \qquad \text{E.4.6}$$

The TeXAS application assumes that the number densities associated with the spontaneously fissioning parent radionuclides, the fissionable targets, and the activation targets of interest are all invariant with time. The neutron flux is also assumed to be invariant with time so that the CTBT-relevant radionuclide $CTBT_i$ number density also

ends up being invariant with time. Given these assumptions, Equation E.4.6 may be rewritten in the following form:

$$0 = \sum_{j=1}^{n_{SFP}} N_{SFP_j} \cdot \lambda_{SFP_j} \cdot \beta_{SF,SFP_j} \cdot \chi_{CTBT_i,SFP_j} \cdots$$

$$+ \sum_{k=1}^{n_{FT}} \sum_{E=1}^{n_E} N_{FT_k} \cdot \sigma_{Fiss,FT_k,E} \cdot \Phi_E(t) \cdot \chi_{CTBT_i} \cdots \qquad \text{E.4.7}$$

$$+ \sum_{l=1}^{n_{AT}} \sum_{E=1}^{n_E} N_{AT_l} \cdot \sigma_{Act,AT_l,E} \cdot \Phi_E \cdot m_{CTBT_i,AT_l} - N_{CTBT_i} \cdot \lambda_{CTBT_i}.$$

Adding $N_{CTBT_i} \cdot \lambda_{CTBT_i}$ to both sides of Equation E.4.7 and recognizing that the product $N_{CTBT_i} \cdot \lambda_{CTBT_i}$ is equal to the CTBT-relevant radionuclide $CTBT_i$ activity concentration produces the following expression for A_{CTBT_i}:

$$A_{CTBT_i} = \sum_{j=1}^{n_{SFP}} N_{SFP_j} \cdot \lambda_{SFP_j} \cdot \beta_{SF,SFP_j} \cdot \chi_{CTBT_i,SFP_j} \cdots$$

$$+ \sum_{k=1}^{n_{FT}} \sum_{E=1}^{n_E} N_{FT_k} \cdot \sigma_{Fiss,FT_k,E} \cdot \Phi_E(t) \cdot \chi_{CTBT_i} \cdots \qquad \text{E.4.8}$$

$$+ \sum_{l=1}^{n_{AT}} \sum_{E=1}^{n_E} N_{AT_l} \cdot \sigma_{Act,AT_l,E} \cdot \Phi_E \cdot m_{CTBT_i,AT_l}.$$

The TeXAS application uses Equation E.4.8 to generate background activity concentration estimates for each of the 100 radioactive particulates and noble gases identified as relevant to the verification regime of the CTBT. Note that, because Equation E.4.8 does not account for losses resulting from physical transport processes, the

background activity concentration estimates generated by the TeXAS application should be viewed as nominal upper limits.

Several different inputs are obviously required to evaluate Equation E.4.8. The number densities associated with the spontaneously fissioning parent radionuclides, the fissionable targets, and the activation targets of interest are evalauted by code modules 2 through 5 of the the `TeXASModDev` code module as described in Sections E.2.2 through E.2.5. The neutron fluxes and the fission and activation cross-sections required to evaluate Eqution E.4.8 must be extracted from `.mctal` files generated by the MCNP jobs created by the `TeXASModDev` code module. The neutron fluxes and the fission and activation cross-sections are extracted from the `.mctal` files by a module of the second overarching code module of the TeXAS application—the `TeXASPostProc` code module.

The remainder of the inputs required to evaluate Equation E.4.8 were developed in advance using nuclear data taken from the ENDF-B/VII.1 nucear data library [117, 118] and the TENDL 2015 nuclear library [170]. The decay constant data, branching ratio data, fission yield data, and multiplicity data required to evaluate Equation E.4.8 was developed using data taken from the ENDF-B/VII.1 nucear data library as it was available; data that was not available in the ENDF-B/VII.1 nucear data library was taken from the TENDL 2015 nuclear library.

E.5 Using the TeXAS Application

TeXAS application users provide inputs to the TeXAS application using so-called principal formatted input files (text files) and auxiliary formatted input files (also text files). Every CTBT-relevant radionuclide background activity concentration study conducted using the TeXAS application must be supported by one, and only one, principal formatted input file. An auxiliary formatted input file may or may not be needed to support a given study. Some studies may utilize multiple auxiliary formatted input files. The sections that follow describe the contents and formats associated with the principal and auxiliary formatted input files used to provide inputs to the TeXAS application.

Note that TeXAS application users only need to provide the TeXAS application with the name of a principal formatted input file in order to conduct a study; the names of any auxiliary formatted input files that might be required to support the study are provided in the principal formatted input file. Also note that all principal and auxiliary formatted input files are assumed to be stored in subdirectories of the `/TeXAS` directory called `/PriFormInpFiles` and `/AuxFormInpFiles`, respectively.

E.5.1 TeXAS Application Principal Formatted Input Files

An overview of a TeXAS application principal formatted input file is presented in Figure E.29. As illustrated by the figure, the principal formatted input file begins with four header lines. These header lines, which serve as comment lines that TeXAS

application users may use to make notes regarding the contents of the principal formatted input file, are ignored by the TeXAS application. The TeXAS application assumes that the contents of the principal formatted input file begin on the fifth line of the principal formatted input file.

Every TeXAS application principal formatted input file is broken into a number of sections, referred to as blocks, which must be separated by blank lines. A given principal formatted input file may contain as many as five types of blocks. The five principal formatted input file block types are: (1) a General (`Gen`) block type, (2) a Source (`Src`) block type, (3) an Atmospheric (`Atm`) block type, (4) a Geological (`Geo`) block type, and (5) a Seawater (`Sea`) block type. Every principal formatted input file must contain one, and only one, General block; one, and only one, Source block; and one, and only one, Atmospheric block. One or more Geological blocks may be included as required to support a given CTBT-relevant radionuclide background activity concentration study. Similarly, one or more Seawater blocks may be included as required to support a given CTBT-relevant radionuclide background activity concentration study. The first block in every principal formatted input file must be a General block. The other blocks may appear in any order.

E.5.1.1 The General Block of a Principal Formatted Input File

As the name suggests, the General (`Gen`) block of a principal formatted input file is used to pass general information specific to a given CTBT-relevant radionuclide

background activity concentration study to the TeXAS application. A principal formatted input file must contain one, and only one, General block. An example of a TeXAS application principal formatted input file General block is presented in Figure E.30. The first line of the General block has only one entry: a `Gen` flag, which serves to identify the block as a General block. Nine General block cards follow the `Gen` flag.

```
  1  0002-0000-0000
  2  Created by: William H. Wilson and Ashleigh M. Wilson
  3  Created on: 7 September 2011
  4
  5  Gen
  …  …
 15
 16  Src
  …  …
 19
 20  Atm
  …  …
 98
 99  Geo
  …  …
124
125  EOF
```

Figure E.29: Overview of a TeXAS application principal formatted input file.

```
  …  …
  5  Gen
  6  BlockEles 4
  7  FundPhysConsts FundPhysConsts.txt
  8  IsoComps NISTIsoCompData.txt
  9  MagField NoMag
 10  nCPUs 1
 11  nHist 5000000
 12  RelAtomicMasses NISTRelAtomicMassData.txt
 13  StudyID 0002 0000 0000
 14  tLim 20160
  …  …
```

Figure E.30: An example of a TeXAS application principal formatted input file General block.

The first card in the TeXAS application principal formatted input file General block shown in the example in Figure E.30 is a `BlockEles` card. The `BlockEles` card tells the TeXAS application how many blocks the principal formatted input file contains, including the General block itself. In the example shown in Figure E.30, the value assigned to the `BlockEles` card entry is `4`, indicating that the principal formatted input file contains four block elements. In this particular case the block elements are: (1) a General block, (2) a Source block, (3) an Atmospheric block, and (4) a Geological block, as illustrated in Figure E.29.

The second card associated with the General block is a `FundPhysConsts` card. The `FundPhysConsts` card has one entry which is used to direct the TeXAS application to a formatted text file containing values for each of the fundamental physical constants the TeXAS application needs to perform its calculations. In the example shown in Figure E.30 the formatted text file containing the fundamental physical constants is named `FundPhysConsts.txt`. This file comes packaged with the TeXAS application. Users of the TeXAS application are encouraged to avoid modifying this particular formatted text file; instead, TeXAS application users are encouraged to use the `FundPhysConsts` card described here to direct the TeXAS application to a different formatted text file if an alternative set of fundamental physical constants is to be used. Note that the formatted text file containing the fundamental physical constants is assumed to be stored in a subdirectory of the `/TeXAS` directory called `/FundPhys-ConstsLoader`.

The third card in the TeXAS application principal formatted input file General block is an `IsoComps` card. The `IsoComps` card has one entry which is used to direct the TeXAS application to a formatted text file containing isotopic composition data for all of the known elements. In the example shown in Figure E.30 the formatted text file containing the isotopic composition data is named `NISTIsoCompData.txt`. This file, which contains the isotopic composition data reported by the National Institute of Standards and Technology [173], comes packaged with the TeXAS application. Again, users of the TeXAS application are encouraged to avoid modifying this particular formatted text file; instead, TeXAS application users are encouraged to use the `IsoComps` card described here to direct the TeXAS application to a different formatted text file if different isotopic composition data is to be used. Note that the formatted text file containing the isotopic composition data is assumed to be stored in a subdirectory of the `/TeXAS` directory called `/IsoCompDataLoader`.

The fourth card associated with the General block is a `MagField` card. This card has one entry that may be used to specify whether or not information pertaining to the Earth's magnetic field should be incorporated into the Monte Carlo N-Particle (MCNP) radiation transport code [74, 75] input deck generated by the TeXAS application. The `MagField` entry should be set equal to `Yes` if magnetic field information should be incorporated into the MCNP input deck, or `No` if magnetic field information should not be incorporated into the MCNP input deck. If information pertaining to the Earth's magnetic field is to be incorporated into a given MCNP model, it is developed on a layer

by layer basis in accordance with the World Magnetic Model [174]. In the example shown in Figure E.30, the `MagField` card entry is set equal to `No`, indicating that information pertaining to the Earth's magnetic field was not incorporated into the MCNP model generated by this particular TeXAS application run.

The fifth card in the General block is an `nCPUs` card. This card may be used to specify the number of CPUs on which the MCNP job generated by the TeXAS application is to be run. In the example shown in Figure E.30, the `nCPUs` card entry is set equal to `1`, indicating that the MCNP job generated by the TeXAS application was to be run on a single CPU.

The sixth card in the General block is an `nHist` card. This card may be used to specify the total number of source particle histories to be run by the MCNP job generated by the TeXAS application. In the example shown in Figure E.30, the `nHist` card entry is set equal to `5000000`, indicating that the MCNP job was to run a total of five million source particle histories. Note that in this case the total number of source particle histories would have been run by six different MCNP jobs to support the variance reduction scheme described in Section E.2.9.

The seventh card associated with the General block of the principal formatted input file is a `RelAtomicMasses` card. This card has one entry which may be used to direct the TeXAS application to a formatted text file containing relative atomic mass data for all of the known elements. In the example shown in Figure E.30 the formatted text file containing the relative atomic mass data is named `NISTRelAtomic-`

MassData.txt. This file, which contains the relative atomic mass data reported by the National Institute of Standards and Technology [173], comes packaged with the TeXAS application. Users of the TeXAS application are encouraged to avoid modifying this particular formatted text file; instead, TeXAS application users are encouraged to use the RelAtomicMasses card described here to direct the TeXAS application to a different formatted text file if different relative atomic mass data is to be used. Note that the formatted text file containing the relative atomic mass data is assumed to be stored in a subdirectory of the /TeXAS directory called /RelAtomicMassDataLoader.

The eighth card in the General block is a StudyID card. This card has three entries that may be used to define a unique identifier specific to the CTBT-relevant radionuclide background activity concentration study supported by the principal formatted input file. The first entry of the StudyID card is used to define the study ID, the second entry is used to define the scenario ID, and the third entry is used to define the perturbation ID. In the example shown in Figure E.30, the entry defining the study ID is set equal to 0002, and the entries defining the scenario and perturbation IDs are both set equal to 0000.

The ninth card associated with the General block is a tLim card. The value assigned to the entry on the tLim card, which is used to specify the maximum amount of computation time to be allocated to a given MCNP job in units of minutes, is passed to the CTME card(s) of the MCNP input deck(s) generated by the TeXAS application. The value assigned to the entry on the tLim card is also used to determine the values that

should be assigned to the ndp, ndm, mct, ndmp, and dmmp keywords associated with the PRDMP card(s) of the MCNP input deck(s) generated by the TeXAS application. TeXAS application users who plan to run their MCNP jobs on shared clusters with job scheduling systems configured to automatically close sessions after predetermined time periods should carefully consider the values they assign to their tLim cards to ensure their MCNP jobs terminate gracefully before their sessions are closed automatically by their cluster job schedulers. In the example shown in Figure E.30, the tLim card entry is set equal to 20160 minutes (14 days).

E.5.1.2 The Source Block of a Principal Formatted Input File

The Source (Src) block of a principal formatted input file is used to pass information required to develop a Monte Carlo N-Particle (MCNP) radiation transport code [74, 75] cosmic-ray source term applicable to a given CTBT-relevant radionuclide background activity concentration study to the TeXAS application. A principal formatted input file must contain one, and only one, Source block. An example of a TeXAS application principal formatted input file Source block is presented in Figure E.31. The first line of the Source block has only one entry: an Src flag, which serves to identify the block as a Source block. Two Source block cards follow the Src flag.

```
 …  …
16  Src
17  Date 2003 11 1
18  Loc 44.908 -122.995 65000
 …  …
```

Figure E.31: An example of a TeXAS application principal formatted input file Source block.

The first card in the TeXAS application principal formatted input file Source block example shown in Figure E.31 is a `Date` card. The Source block `Date` card has three entries that may be used to specify the date associated with the CTBT-relevant radionuclide background activity concentration study supported by the principal formatted input file. The first entry on the `Date` card is used to specify the year associated with the study, the second entry is used to specify the month, and the third entry is used to specify the day. The values assigned to the `Date` card entries in TeXAS application principal formatted input files are passed to the appropriate `SDEF` card `DAT` keyword entries in the MCNP input decks generated by the TeXAS application. In the example shown in Figure E.31, the values assigned to the `Date` card entries specify that the date associated with the CTBT-relevant radionuclide background activity concentration study should be 1 November 2003.

The second card associated with the Source block of TeXAS application principal formatted inputs is a `Loc` card. This card has three entries that may be used to specify the location associated with the CTBT-relevant radionuclide background activity concentration study supported by the principal formatted input file. The first entry on the

`Loc` card is used to specify the latitude associated with the study (in degrees relative to the equator), the second entry is used to specify the longitude (in degrees relative to Greenwich, UK), and the third entry is used to specify the altitude (in units of m). The values assigned to the `Loc` card entries in TeXAS application principal formatted input files are passed to the appropriate `SDEF` card `LOC` keyword entries in the MCNP input decks generated by the TeXAS application. In the example shown in Figure E.31, the values assigned to the first two entries on the `Loc` card specify that the latitude and longitude associated with the CTBT-relevant radionuclide background activity concentration study should be 44.908° N latitude and 122.995° E longitude. The third entry on the `Loc` card specifies that the altitude associated with the study should be 65,000 m above sea level.

E.5.1.3 The Atmospheric Block of a Principal Formatted Input File

The Atmospheric (`Atm`) block of a principal formatted input file is used to pass atmospheric properties specific to the atmospheric layers of a given CTBT-relevant radionuclide background activity conc-entration study to the TeXAS application. A principal formatted input file must contain one, and only one, Atmospheric block. An example of a TeXAS application principal formatted input file Atmospheric block is presented in Figure E.32. The first line of the Atmospheric block has only one entry: an `Atm` flag, which serves to identify the block as an Atmospheric block. Three Atmospheric block cards follow the `Atm` flag.

```
…  …
20   Atm
21   AtmPT USSA76
22   AtmComp FiUSSA76.txt
23   AtmLayInfo 74
24   Atm1 6.600000E+04 6.500000E+04 NoPerts NoTal
25   Atm2 6.500000E+04 6.400000E+04 NoPerts NoTal
26   Atm3 6.400000E+04 6.300000E+04 NoPerts NoTal
…  …
72   Atm49 1.900000E+04 1.800000E+04 NoPerts NoTal
73   Atm50 1.800000E+04 1.700000E+04 NoPerts NoTal
74   Atm51 1.700000E+04 1.595983E+04 NoPerts NoTal
75   Atm52 1.595983E+04 1.500050E+04 0002-0000-0000_H2O_Atm52.txt NoTal
76   Atm53 1.500050E+04 1.499950E+04 0002-0000-0000_H2O_Atm53.txt Tally
77   Atm54 1.499950E+04 1.396923E+04 0002-0000-0000_H2O_Atm54.txt NoTal
78   Atm55 1.396923E+04 1.300000E+04 0002-0000-0000_H2O_Atm55.txt NoTal
79   Atm56 1.300000E+04 1.197739E+04 0002-0000-0000_H2O_Atm56.txt NoTal
80   Atm57 1.197739E+04 1.100000E+04 0002-0000-0000_H2O_Atm57.txt NoTal
81   Atm58 1.100000E+04 9.984293E+03 0002-0000-0000_H2O_Atm58.txt NoTal
82   Atm59 9.984293E+03 9.000000E+03 0002-0000-0000_H2O_Atm59.txt NoTal
83   Atm60 9.000000E+03 7.989945E+03 0002-0000-0000_H2O_Atm60.txt NoTal
84   Atm61 7.989945E+03 7.000000E+03 0002-0000-0000_H2O_Atm61.txt NoTal
85   Atm62 7.000000E+03 5.994342E+03 0002-0000-0000_H2O_Atm62.txt NoTal
86   Atm63 5.994342E+03 5.000000E+03 0002-0000-0000_H2O_Atm63.txt NoTal
87   Atm64 5.000000E+03 3.997485E+03 0002-0000-0000_H2O_Atm64.txt NoTal
88   Atm65 3.997485E+03 3.000000E+03 0002-0000-0000_H2O_Atm65.txt NoTal
89   Atm66 3.000000E+03 1.999371E+03 0002-0000-0000_H2O_Atm66.txt NoTal
90   Atm67 1.999371E+03 9.998427E+02 0002-0000-0000_H2O_Atm67.txt NoTal
91   Atm68 9.998427E+02 6.950000E+01 0002-0000-0000_H2O_Atm68.txt NoTal
92   Atm69 6.950000E+01 6.850000E+01 0002-0000-0000_H2O_Atm69.txt Tally
93   Atm70 6.850000E+01 6.750000E+01 0002-0000-0000_H2O_Atm70.txt Tally
94   Atm71 6.750000E+01 6.650000E+01 0002-0000-0000_H2O_Atm71.txt Tally
95   Atm72 6.650000E+01 6.550000E+01 0002-0000-0000_H2O_Atm72.txt Tally
96   Atm73 6.550000E+01 6.450000E+01 0002-0000-0000_H2O_Atm73.txt Tally
97   Atm74 6.450000E+01 6.400000E+01 0002-0000-0000_H2O_Atm74.txt NoTal
…  …
```

Figure E.32: An example of a TeXAS application principal formatted input file Atmospheric block.

The first card in the TeXAS application principal formatted input file Atmospheric block example shown in Figure E.32 is an `AtmPT` card. The `AtmPT` card is used to specify the method the TeXAS application should use to develop mean atmospheric pressure, temperature, and number densities for each of the atmospheric layers of the Monte Carlo N-Particle (MCNP) radiation transport code [74, 75] model to be generated by the TeXAS application. Two different character strings may be assigned to the `AtmPT` card entry. The first option is a `Man` character string. This character string

should be assigned to the `AtmPT` card entry when the TeXAS application user intends to manually specify the mean pressure (in units of Pa) and the mean temperature (in units of K) associated with each atmospheric layer. When this option is utilized the mean number densities associated with each of the atmospheric layers are calculated using the ideal gas law (see Equation E.2.2.1) and the mean atmospheric pressures and temperatures provided by the TeXAS application user.

Alternatively, a `USSA76` character string may be assigned to the first entry on the `AtmPT` card. This character string should be assigned to the first entry on the `AtmPT` card when the TeXAS application user intends to allow the TeXAS application to use the *U.S. Standard Atmosphere, 1976* [142] to develop mean atmospheric pressures, temperatures, and number densities for each of the atmospheric layers. When this option is utilized the mean atmospheric pressures, temperatures, and number densities associated with each of the atmospheric layers are calculated in accordance with Equations E.2.2.5, E.2.2.7, E.2.2.9, E.2.2.10, and E.2.2.11, as applicable to each of the atmospheric layers. In the example shown in Figure E.32 the character string assigned to the `AtmPT` card entry indicates that the user wants to use the atmospheric model defined by the *U.S. Standard Atmosphere, 1976* [142] to develop mean atmospheric pressures, temperatures, and number densities for each of the atmospheric layers of the MCNP model to be generated by the TeXAS application.

The second card associated with the Atmospheric block is an `AtmComp` card. The `AtmComp` card has one entry which is used to direct the TeXAS application to a

formatted text file containing composition information for the dry portion of the Earth's atmosphere. In the example shown in Figure E.32 the formatted text file containing the atmospheric composition information is named `FiUSSA76.txt`. This formatted text file, which contains the atmospheric composition information associated with the *U.S. Standard Atmosphere, 1976* [142], comes packaged with the TeXAS application. Users of the TeXAS application are encouraged to avoid modifying this particular formatted text file; instead, use the `AtmComp` card described here to direct the TeXAS application to a different formatted text file if different atmospheric composition information is to be used. Note that the formatted text file containing the atmospheric composition information is assumed to be stored in a subdirectory of the `/TeXAS` directory called `/AtmDataProc/AtmModelParams`.

The third card in the TeXAS application principal formatted input file Atmospheric block example shown in Figure E.32 is an `AtmLayInfo` card. The `AtmLayInfo` card is used to specify the number of layers the Atmospheric block of the MCNP model should be composed of and also to provide input information specific to each of the atmospheric layers. In the example shown in Figure E.32 the value assigned to the first entry on the `AtmLayInfo` card specifies that the Atmospheric block of the MCNP model should be composed of 74 atmospheric layers.

The entries on the 74 lines that follow the `AtmLayInfo` card are used to provide input information specific to each of the atmospheric layers. In the example shown in Figure E.32 the character string assigned to the entry on the `AtmPT` card indicates that

the user wants to use the *U.S. Standard Atmosphere, 1976* [142] to develop mean atmospheric pressures, temperatures, and number densities for each of the atmospheric layers of the MCNP model to be generated by the TeXAS application. When this is the case, the format of the lines that follow the `AtmLayInfo` card is as follows: The first entry on each line is a user-specified atmospheric layer ID. The second and third entries specify the upper and lower bounds, respectively, associated with each of the atmospheric layers in units of m.

The fourth entry is used to specify whether or not the user wants to apply perturbations to the base material composition associated with a given atmospheric layer. If material composition perturbations are to be applied, the fourth entry is set equal to the name of the auxiliary formatted input file containing the perturbation information. If no perturbations are to be applied the fourth entry is simply set equal to `NoPerts`. Note that the auxiliary formatted input file containing the perturbation information is assumed to be stored in a subdirectory of the `/TeXAS` directory called `/AuxFormInpFiles`. Also note that the auxiliary formatted input files containing perturbation information are formatted as described in Section E.5.2.

The fifth entry, which is the last entry, is used to specify whether or not the user wants to evaluate tallies, and, by extension, CTBT-relevant radionuclide background activity concentrations, in a given atmospheric layer. The fifth entry is set equal to `NoTal` if no tallies are to be evaluated in the atmospheric layer; it is set equal to `Tally` if tallies are to be evaluated in the atmospheric layer; and it is set equal to `Opt` if the

MCNP weight window generator is to be configured to optimize tallies evaluated in the atmospheric layer (see Section E.2.9 for more information regarding weight windows and the variance reduction scheme).

In the example shown in Figure E.32 the first entry on line 25 of the principal formatted input file specifies that the user-defined layer ID associated with the second atmospheric layer is `Atm2`. The second and third entries on line 25 of the principal formatted input file specify that the upper and lower bounds associated with the second atmospheric layer are `6.500000E+04` (65,000) and `6.400000E+04` (64,000) m, respectively. The fourth entry (`NoPerts`) specifies that no perturbations are to be applied to the base composition of the atmospheric layer, and the fifth entry (`NoTal`) specifies that no tallies are to be evaluated in the atmospheric layer.

In the example shown in Figure E.32 the first entry on line 76 of the principal formatted input file specifies that the user-defined layer ID associated with the 53rd atmospheric layer is `Atm53`. The second and third entries on line 76 of the principal formatted input file specify that the upper and lower bounds associated with the 53rd atmospheric layer are `1.500050E+04` and `1.499950E+04` m, respectively. The fourth entry specifies that perturbations are to be applied to the base composition of the atmospheric layer, and that the perturbation information is stored in a formatted text file named `0002-0000-0000_H2O_Atm53.txt`. Note that the formatted text file containing the perturbation information is assumed to be formatted as described in Section E.5.2, and to be stored in a subdirectory of the `/TeXAS` directory called

/AuxFormInpFiles. The fifth entry (Tally) specifies that tallies are to be evaluated in the 53rd atmospheric layer.

If the user choses to manually specify the mean pressure and temperature associated with each atmospheric layer the format of the lines that follow the AtmLayInfo card varies somewhat from the format described above. The first through third entries remain the same as described previously and specify the layer ID, the upper bound, and the lower bound, respectively, associated with each of the atmospheric layers. The fourth and fifth entries described previously, the entries used to apply material composition perturbations and request tallies, repsectively, become the sixth and seventh entries in the new format. The fourth and fifth entries in the new format are used to specify the mean pressure and the mean temperature associated with each atmospheric layer in units of Pa and K, respectively.

E.5.1.4 The Geological Blocks of a Principal Formatted Input File

The Geological (Geo) blocks of a principal formatted input file are used to pass geological properties specific to each of the geological layers of a given CTBT-relevant radionuclide background activity concentration study to the TeXAS application. An example of a TeXAS application principal formatted input file Geological block is provided in Figure E.33. The first line of a given geological block has only one entry: a Geo flag, which serves to identify the block as a Geological block. Five Geological block cards follow the Geo flag.

```
…  …
 99  Geo
100  PorFill Atm
101  GeoComp Granite.txt
102  GeoDens Rho 2.63
103  GeoPor 0.01
104  GeoLayInfo 19
105  Geo1 6.400000E+01 6.399000E+01 2.934865E+02 NoPerts Tally
106  Geo2 6.399000E+01 6.398000E+01 2.934562E+02 NoPerts Tally
107  Geo3 6.398000E+01 6.397000E+01 2.934260E+02 NoPerts Tally
108  Geo4 6.397000E+01 6.396000E+01 2.933959E+02 NoPerts Tally
109  Geo5 6.396000E+01 6.395000E+01 2.933658E+02 NoPerts Tally
110  Geo6 6.395000E+01 6.394000E+01 2.933358E+02 NoPerts Tally
111  Geo7 6.394000E+01 6.393000E+01 2.933058E+02 NoPerts Tally
112  Geo8 6.393000E+01 6.392000E+01 2.932759E+02 NoPerts Tally
113  Geo9 6.392000E+01 6.391000E+01 2.932461E+02 NoPerts Tally
114  Geo10 6.391000E+01 6.390000E+01 2.932163E+02 NoPerts Tally
115  Geo11 6.390000E+01 6.350000E+01 2.926244E+02 NoPerts NoTal
116  Geo12 6.350000E+01 6.250000E+01 2.908157E+02 NoPerts Tally
117  Geo13 6.250000E+01 6.150000E+01 2.887395E+02 NoPerts Tally
118  Geo14 6.150000E+01 6.050000E+01 2.872509E+02 NoPerts Tally
119  Geo15 6.050000E+01 5.950000E+01 2.862634E+02 NoPerts Tally
120  Geo16 5.950000E+01 5.850000E+01 2.856759E+02 NoPerts Opt
121  Geo17 5.850000E+01 5.750000E+01 2.853882E+02 NoPerts NoTal
122  Geo18 5.750000E+01 5.650000E+01 2.853105E+02 NoPerts NoTal
123  Geo19 5.650000E+01 5.550000E+01 2.853679E+02 NoPerts NoTal
…  …
```

Figure E.33: An example of a TeXAS application principal formatted input file Geological block.

The first card in the TeXAS application principal formatted input file Geological block example shown in Figure E.33 is a `PorFill` card. The `PorFill` card is used to specify what the porosity voids in a given Geological block should be filled with. There are three options: (1) atmospheric air (`Atm`), (2) a user defined material (`UserDef`), and (3) a mixture of atmospheric air and a user-defined material (`Mix`). When the entry on the `PorFill` card is set equal to `Atm` the porosity voids are filled with atmospheric air having the same composition as the atmospheric air in the closest atmospheric layer. When the entry on the `PorFill` card is set equal to `UserDef` the porosity voids are filled with a material having a composition that may be defined by the

user in a separate formatted text file. When the entry on the `PorFill` card is set equal to `Mix` the porosity voids are filled with a mixture of atmospheric air and a user-defined material. In the example shown in Figure E.33 value assigned to the entry on the `PorFill` card is set equal `Atm`.

When the first entry on the `PorFill` card is set equal to `UserDef`, two additional Geological block cards not shown in Figure E.33 are required to define the properties of the user-defined material in the geological porosity voids. The first of these additional cards is a `FillDens` card. The `FillDens` card is used to specify the units and the magnitude of the density of the user-defined material filling the geological porosity voids. The first entry on the `FillDens` card is currently required to be a `Rho` character string. When the first entry on the `FillDens` card is set equal to `Rho` the density of the user-defined material filling the geological porosity voids is assumed to be provided in unis of $g\text{-}cm^{-3}$. In the future, the TeXAS application may be extended to accept user-defined material densities in number density units. The second entry on the `FillDens` card is used to specify the magnitude of the density of the user-defined material filling the geological porosity voids.

The second additional Geological block card required when the first entry on the `PorFill` card is set equal to `UserDef` is a `FillComp` card. The `FillComp` card has one entry which is used to direct the TeXAS application to a formatted text file containing composition information specific to the user-defined material filling the geological porosity voids. Note that the formatted text file containing the material

composition information is assumed to be formatted as described in Section 5.3, and to be stored in a subdirectory of the /TeXAS directory called /AuxFormInpFiles.

When the first entry on the PorFill card is set equal to Mix, a third additional Geological block card not shown in Figure E.33 is also required in addition to the FillDens and FillComp cards described above. The third additional card is a FillAtmFrac card. The FillAtmFrac card is used to specify the fraction of the geological porosity voids occupied by atmospheric air. The remainder of the geological porosity voids are assumed to be filled by the user-specified material.

An example of a TeXAS application principal formatted input file Geological block where the entry on the PorFill card is set equal to Mix is provided in Figure E.34. Note the presence of the FillAtmFrac, FillDens, and FillComp cards on lines 101, 102, and 103, respectively, of the principal formatted input file.

```
 …  …
 99  Geo
100  PorFill Mix
101  FillAtmFrac 0.5
102  FillDens Rho 1.0
103  FillComp FillPoresWithH2O.txt
104  GeoComp Granite.txt
105  GeoDens Rho 2.63
106  GeoPor 0.01
107  GeoLayInfo 19
108  Geo1 6.400000E+01 6.399000E+01 2.934865E+02 NoPerts Tally
109  Geo2 6.399000E+01 6.398000E+01 2.934562E+02 NoPerts Tally
110  Geo3 6.398000E+01 6.397000E+01 2.934260E+02 NoPerts Tally
 …  …
```

Figure E.34: An example of a TeXAS application principal formatted input file Geological block (with the PorFill card entry set equal to Mix).

Returning now to the example shown in Figure E.33, the second card in the TeXAS application principal formatted input file Geological block example shown in Figure E.33 is a `GeoComp` card. The `GeoComp` card has one entry which is used to direct the TeXAS application to a formatted text file containing composition information specific to the geology of interest. Note that the formatted text file containing the composition information is assumed to be formatted as described in Section 5.3, and to be stored in a subdirectory of the `/TeXAS` directory called `/AuxFormInpFiles`. In the example shown in Figure E.33 the formatted text file containing composition information specific to the geology of interest is named `Granite.txt`.

The third card associated with each Geological block is a `GeoDens` card. The `GeoDens` card is used to specify the units and the magnitude of the density of the geology of interest. As with the `FillDens` card, described previously, the first entry on the `GeoDens` card is currently required to be a `Rho` character string. When the first entry on the `GeoDens` card is set equal to `Rho` the density of the geology is assumed to be provided in units of g-cm^{-3}. In the future, the TeXAS application may be extended to accept geological densities in number density units. The second entry on the `GeoDens` card is used to specify the magnitude of the density of the geology. In the example shown in Figure E.33 the density of the granite geology of interest is apparently 2.63 g-cm^{-3}.

The fourth card associated with each Geological block is a `GeoPor` card. The `GeoPor` card has one entry that is used to specify the porosity of the geology of

interest as a unitless volume fraction. In the example shown in Figure E.33 the entry on the `GeoPor` card is set equal to `0.01`, or 1 %.

The fifth card in the TeXAS application principal formatted input file Geological block example shown in Figure E.33 is a `GeoLayInfo` card. The `GeoLayInfo` card is used to specify the number of layers the Geological block of the MCNP model should be composed of and also to provide input information specific to each of the geological layers. In the example shown in Figure E.33 the value assigned to the first entry on the `GeoLayInfo` card specifies that the Geological block of the MCNP model should be composed of 19 layers.

The entries on the 19 lines that follow the `GeoLayInfo` card are used to provide input information specific to each of the geological layers. The format of these lines is as follows: The first entry on each line is a user-specified geological layer ID. The second and third entries specify the upper and lower bounds, respectively, associated with each of the geological layers in units of m. The fourth entry on each line is used to specify the temperature of the geological layer in units of K.

The fifth entry is used to specify whether or not the user wants to apply perturbations to the base material composition associated with a given geological layer. If material composition perturbations are to be applied, the fifth entry is set equal to the name of the formatted text file containing the perturbation information. If no perturbations are to be applied the fifth entry is simply set equal to `NoPerts`. Note that the formatted text file containing the perturbation information is assumed to be stored in a

subdirectory of the /TeXAS directory called /AuxFormInpFiles. Also note that the formatted text files containing perturbation information are formatted as described in Section E.5.2.

The sixth entry, which is the last entry, is used to specify whether or not the user wants to evaluate tallies, and, by extension, CTBT-relevant radionuclide background activity concentrations, in a given geological layer. The sixth entry is set equal to NoTal if no tallies are to be evaluated in the geological layer; it is set equal to Tally if tallies are to be evaluated in the atmospheric layer; and it is set equal to Opt if the MCNP weight window generator is to be configured to optimize tallies evaluated in the geological layer (see Section E.2.9 for more information regarding weight windows and the variance reduction scheme).

In the example shown in Figure E.33 the first entry on line 106 of the principal formatted input file specifies that the user-defined layer ID associated with the second geological layer is Geo2. The second and third entries on line 106 of the principal formatted input file specify that the upper and lower bounds associated with the atmospheric layer are 6.399000E+01 (63.99) and 6.398000E+01 (63.98) m, respectively. The fourth entry specifies that the temperature associated with the geological layer is 2.934865E+02 K (about 20.3 °C). The fifth entry (NoPerts) specifies that no perturbations are to be applied to the base composition of the geological layer, and the sixth entry (Tally) specifies that tallies are to be evaluated in the geological layer.

In the example shown in Figure E.33 the first entry on line 120 of the principal formatted input file specifies that the user-defined layer ID associated with the 16th geological layer is `Geo16`. The second and third entries on line 120 of the principal formatted input file specify that the upper and lower bounds associated with the atmospheric layer are `5.950000E+01` (59.5) and `5.850000E+01` (58.5) m, respectively. The fourth entry specifies that the temperature associated with the 16th geological layer is `2.856759E+02` K (about 12.5 °C). The fifth entry (`NoPerts`) specifies that no perturbations are to be applied to the base composition of the geological layer, and the sixth entry (`Opt`) specifies that the MCNP weight window generator is to be configured to optimize tallies evaluated in the 16th geological layer.

E.5.1.5 The Seawater Blocks of a Principal Formatted Input File

The Seawater blocks of a principal formatted input file are used to pass seawater properties specific to each of the seawater layers of a given CTBT-relevant radionuclide background activity concentration study to the TeXAS application. An example of a TeXAS application principal formatted input file Seawater block is provided in Figure E.35. The first line of the Seawater block has only one entry: a `Sea` flag, which serves to identify the block as a Seawater block. Three Seawater block cards follow the `Sea` flag.

```
…  …
 99  Sea
100  SeaPST WOD WODDataQuery0000.txt
101  SeaComp SeaCompSVERDRUPele.txt
102  SeaLayInfo 11
103  Sea1 0.0 -0.5 NoPerts NoTal
104  Sea2 -0.5 -1.5 NoPerts Tally
105  Sea3 -1.5 -2.5 NoPerts Tally
106  Sea4 -2.5 -3.5 NoPerts Tally
107  Sea5 -3.5 -4.5 NoPerts Tally
108  Sea6 -4.5 -5.5 NoPerts Tally
109  Sea7 -5.5 -6.5 NoPerts NoTal
110  Sea8 -6.5 -7.5 NoPerts NoTal
111  Sea9 -7.5 -8.5 NoPerts NoTal
112  Sea10 -8.5 -9.5 NoPerts NoTal
113  Sea11 -9.5 -10.5 NoPerts NoTal
…  …
```

Figure E.35: An example of a TeXAS application principal formatted input file Seawater block.

The first card in the TeXAS application principal formatted input file Seawater block example shown in Figure E.35 is a `SeaPST` card. The `SeaPST` card is used to specify the method the TeXAS application should use to develop mean pressure, salinity, and temperature profiles for each of the seawater layers of the MCNP model to be generated by the TeXAS application. Two different character strings may be assigned to the first entry on the `SeaPST` card. The first option is a `Man` character string. This character string should be assigned to the first entry on the `SeaPST` card when the TeXAS application user intends to manually specify the mean pressure (in units of Pa), salinity (in units of ppt), and temperature (in units of K) associated with each of the seawater layers. If the first entry on the `SeaPST` card is a `Man` character string there are no other entries on the `SeaPST` card.

Alternatively, a WOD character string may be assigned to the first entry on the SeaPST card. This character string should be assigned to the first entry on the SeaPST card when the TeXAS application user intends to use seawater, pressure, salinity, and temperature data taken from the World Ocean Database (WOD) [148] to develop mean seawater pressure, salinity, and temperature profiles. When the first entry on the SeaPST card is set equal to WOD to indicate that WOD data is to be used, the SeaPST card has a second entry that may be used to specify the name of the formatted text file containing the WOD data. In the example shown in Figure E.35 the first entry on the SeaPST card is set equal to WOD and the second entry is set equal to WODDataQuery-0000.txt. This indicates that the TeXAS application user intended to use WOD seawater pressure, salinity, and temperature data stored in a formatted text file named WODDataQuery0000.txt.

The second card in the TeXAS application principal formatted input file Seawater block example shown in Figure E.35 is a SeaComp card. The SeaComp card has one entry which is used to direct the TeXAS application to a formatted text file containing seawater composition information. Note that the formatted text file containing the seawater composition information is assumed to be formatted as described in Section 5.3, and to be stored in a subdirectory of the /TeXAS directory called /AuxFormInpFiles. In the example shown in Figure E.35 the formatted text file containing the seawater composition information is named SeaCompSVERDRUP-ele.txt.

The third card in the TeXAS application principal formatted input file Seawater Block example shown in Figure E.35 is a `SeaLayInfo` card. The `SeaLayInfo` card is used to specify the number of layers the Seawater Block of the MCNP model should be composed of and also to provide input information specific to each of the seawater layers. In the example shown in Figure E.35 the value assigned to the first entry on the `SeaLayInfo` card specifies that the Seawater block of the MCNP model should be composed of 11 layers.

The entries on the 11 lines that follow the `SeaLayInfo` card are used to provide input information specific to each of the seawater layers. In the example shown in Figure E.35 the character string assigned to the `SeaPST` card indicates that the user wants to use pressure, salinity, and temperature data taken from the WOD to develop mean seawater pressure, salinity, and temperature profiles for each of the seawater layers of the MCNP model to be generated by the TeXAS application. When this is the case, the format of the lines that follow the `SeaLayInfo` card is as follows: The first entry on each line is a user-specified seawater layer ID. The second and third entries specify the upper and lower bounds, respectively, associated with each of the seawater layer in units of m.

The fourth entry is used to specify whether or not the user wants to apply perturbations to the base seawater material composition associated with a given seawater layer. If perturbations are to be applied, the fourth entry is set equal to the name of the auxiliary formatted text file containing the composition perturbation information. If no

perturbations are to be applied the fourth entry is simply set equal to `NoPerts`. Note that the auxiliary formatted text file containing the perturbation information is assumed to be stored in a subdirectory of the `/TeXAS` directory called `/AuxFormInpFiles`. Also note that the auxiliary formatted text files containing the composition perturbation information are formatted as described in Section E.5.2.

The fifth entry, which is the last entry, is used to specify whether or not the user wants to evaluate tallies, and, by extension, CTBT-relevant radionuclide background activity concentrations, in the seawater layer. The fifth entry is set equal to `NoTal` if no tallies are to be evaluated in the seawater layer; it is set equal to `Tally` if tallies are to be evaluated in the atmospheric layer; and it is set equal to `Opt` if the MCNP weight window generator is to be configured to optimize tallies evaluated in the seawater layer (see Section E.2.9 for more information regarding weight windows and the variance reduction scheme).

In the example shown in Figure E.35 the first entry on line 104 of the principal formatted input file specifies that the user-defined layer ID associated with the second seawater layer is `Sea2`. The second and third entries on line 104 of the principal formatted input file specify that the upper and lower bounds associated with the seawater layer are `-0.5` and `-1.5` m, respectively. The fourth entry (`NoPerts`) specifies that no perturbations are to be applied to the base composition of the seawater layer, and the fifth entry (`NoTal`) specifies that no tallies are to be evaluated in the seawater layer.

If the user choses to manually specify the mean pressure, the mean salinity, and the mean temperature associated with each seawater layer the format of the lines that follow the `SeaLayInfo` card varies somewhat from the format described above. The first through third entries remain the same as described previously and specify the layer ID, the upper bound, and the lower bound, respectively, associated with each of the seawater layers. The fourth and fifth entries described previously, the entries used to apply material composition perturbations and request tallies, respectively, become the seventh and eighth entries in the new format. The fourth, fifth, and sixth entries in the new format are used to specify the mean pressure (in units of Pa), the mean salinity (in units of ppt), and the mean temperature (in units of K) associated with each seawater layer, respectively.

E.5.2 TeXAS Application Auxiliary Formatted Input Files

As mentioned previously in Section E.2.5 and a number of other sections, atmospheric, geological, and seawater material composition perturbations may be applied to any atmospheric, geological, and/or seawater layers of a given Monte Carlo N-Particle (MCNP) radiation transport code [74, 75] model using so-called auxiliary formatted input files. Each material composition perturbation must be defined in its own auxiliary formatted input file. That said, multiple material constituent concentrations may be perturbed in a given auxiliary formatted input file. Additionally, note that the same material composition perturbation may be applied to multiple atmospheric, geological, or

seawater layers. All auxiliary formatted input files are assumed to be stored in a subdirectory of the `/TeXAS` directory called `/AuxFormInpFiles`.

TeXAS application auxiliary formatted input files begin with four comment lines that TeXAS application users may use to make notes regarding the contents of the auxiliary formatted input files. The TeXAS application assumes that the contents of each auxiliary formatted input file begin on the fifth line of the auxiliay formatted input file. Each line of each auxiliary formatted input file has six entries, all of which are required. The first entry is used to specify whether the perturbation is to be applied to a molecular compound (`Comp`), an element (`Ele`), or an isotope (`Iso`).

The second entry is used to specify the identity of the molecular compound, element, or isotope to which the perturbation is to be applied. The identities of molecular compounds to which perturbations are to be applied should be specified using the standard molecular compound notation. The identities of elements to which perturbations are to be applied should be specified using the standard elemental symbols. The identities of isotopes to which perturbations are to be applied should be specified using the standard *Symbol-A* notation, where *Symbol* is the standard elemental symbol of the isotope and *A* is the mass number of the isotope.

The third entry on a given auxiliary formatted input file line is a flag used to indicate that a given perturbation is either an absolute materical constituent concentration perturbation or a relative material constituent concentration perturbation. Absolute material constituent concentration perturbations are used to override material

constituent concentrations on an absolute basis while relative material constituent concentration perurbations are used to perturb material constituent concentrations relative to their concentrations in a base material composition. an `Abs` flag is used to specify a perturbation is an absolute material constituent concentration perturbation while a `Rel` flag is used to specify that a perturbation is a relative material constituent concentration perturbation.

The fourth entry on a given auxiliary formatted input file line is a character string used to specify the basis for the perturbation. Six different perturbation bases may be used: (1) a number density basis (`N`), (2) a number fraction basis (`fN`), (3) a number mixing ratio basis (`r`), (4) a mass density basis (`Rho`), (5) a mass fraction basis (`fM`), and (6) a mass mixing ratio basis (`Omega`). A given auxiliary formatted input file may be used to apply multiple material consituent concentrations using different bases (*i.e.* not all perturbations have to be applied using the same basis).

The fifth entry on a given auxiliary formatted input file line is used to specify the magnitude of the material constituent concentration perturbation. This entry is a numerical entry. It may be most convenient to specify the magnitudes of very small and very large material composition perturbations using a scientific notation. For very small pertubrations the scientific notation format is as follows: $Base$E-Exp, where $Base$ is the base of the numerical value, and Exp is the base-10 exponent associated with the number. For very large pertubrations the scientific notation format is as follows: $Base$E+Exp,

where again $Base$ is the base of the numerical value, and Exp is the base-10 exponent associated with the number.

The sixth entry on a given auxiliary formatted input file line is used to specify whether or not the given material constituent concentration perturbation is allowed to perturb the overall material number/mass density. If the material constituent concentration perturbation is allowed to perturb the overall material number/mass density the sixth entry is set equal to `TotPert` and the perturbed material number/mass density is evaluated as described in Section E.2.5. If the material constituent concentration perturbation is not allowed to perturb the overall material number/mass density the entry is set equal to `NoPerts` and the concentrations of the unperturbed constituents are renormalized as described in Section E.2.5.

Three examples of auxiliary formatted input files are presented in Figures E.36 through E.37. The auxiliary formatted input file presented in Figure E.36 is used to increase the elemental uranium concentration by ten percent, on a mass fraction basis, relative to the uranium concentration in some base material composition. The `TotPert` character string assigned to the sixth entry specifies that the uranium concentration perturbation is allowed to perturb the overall material number/mass density so that the perturbation essentially serves to add new, additional uranium to the base material.

The auxiliary formatted input file presented in Figure E.37 is used to modify the absolute H_2O concentration associated with some base material. The `Omega` character string assigned to the fourth entry specifies that the perturbation is applied as a mass

mixing ratio, the magnitude of which is 4.552422×10^{-3} (unitless). The `TotPert` character string assigned to the sixth entry specifies that the H_2O concentration perturbation is allowed to perturb the overall material number/mass density.

The auxiliary formatted input file presented in Figure E.38 is used to modify the ^{239}Pu and ^{240}Pu absolute number densities associated with some base material. The new ^{239}Pu number density is set to 9.979363×10^{7} cm^{-3} and the new ^{240}Pu number density is set to 4.422718×10^{6} cm^{-3}. Both the ^{239}Pu and the ^{240}Pu number density perturbations are allowed to perturb the overall material mass / number density.

```
1  Uranium Perturbation (10 % Increase)
2  Created by: William H. Wilson
3  Created on: 7 September 2011
4
5  Ele U Rel fM 1.10 TotPert
```

Figure E.36: An example of a TeXAS application auxiliary formatted input file used to modify the uranium concentration associated with some base material.

```
1  An Atmospheric H2O Mass Mixing Ratio Perturbation
2  Created by: William H. Wilson
3  Created on: 17 December 2013
4
5  Comp H2O Abs Omega 4.552422E-03 TotPert
```

Figure E.37: An example of a TeXAS application auxiliary formatted input file used to modify the H_2O concentration associated with some base material.

```
1  Plutonium Contamination Concentration representative of Global Fallout.
2  Created by: William H. Wilson
3  Created on: 28 September 2015
4
5  Iso Pu-239 Abs N 9.979363E+07 TotPert
6  Iso Pu-240 Abs N 4.422718E+06 TotPert
```

Figure E.38: An example of a TeXAS application auxiliary formatted input file used to modify the ^{239}Pu and ^{240}Pu concentrations associated with some base material.

E.5.3 Formatted Text Files used to Input Material Composition Information

TeXAS application users must input material composition information specific to the geological and seawater layers required to support their CTBT-relevant radioactive particulate and noble gas background activity concentration studies. The material composition inputs may be supplied to the TeXAS application using a third type of formatted input file. The TeXAS application assumes that these formatted input files are stored in a subdirectory of the `/TeXAS` directory called `/AuxFormInpFiles`.

An example of a formatted input file used to input material composition information specific to a granite geology is presented in Figure 39. Note that each of the lines of the formatted text file provides information specific to a given material constituent and that each of the lines has four keywords. The first keyword on a given line is used to specify whether the constituent described on that line is a molecular compound (`Comp`), an elemental constituent (`Ele`), or an isotopic constituent (`Iso`). The second keyword on a given line is used to specify the identity of the molecular compound, the element, or the isotope, as applicable. Note that molecular compounds

may be defined using either empirical formulas or molecular formulas and should be formatted as shown in Figure E.39. The identities of elemental constituents should be specified using their elemental symbols, and the identities of isotopic constituents should be specified using the standard `Z-A` notation, where `Z` denotes the symbol of the elemental symbol and `A` denotes the mass number of the isotope.

The third keyword on a given line is used to specify whether the concentration of the constituent described on that line is provided as an atom fraction (`fN`) or a mass fraction (`fM`). All material constituent concentrations provided in a given formatted input file must be specified as either number fractions or mass fractions; they may not be provided as a mixture of number fractions and mass fractions. And finally, the fourth keyword on a given line is used to specify the concentration of the constituent described on that line as either an atom fraction or a mass fraction.

```
 1  Comp SiO2 fM 7.180724E-01
 2  Comp Al2O3 fM 1.429214E-01
 3  Comp K2O fM 4.475723E-02
 4  Comp Na2O fM 3.829281E-02
 5  Comp CaO fM 1.641251E-02
 6  Comp FeO fM 1.146590E-02
 7  Comp Fe2O3 fM 9.234894E-03
 8  Comp MgO fM 6.165435E-03
 9  Comp H2O fM 5.769523E-03
10  Comp TiO2 fM 2.800093E-03
11  Comp P2O5 fM 2.134083E-03
12  Comp CO2 fM 1.421168E-03
13  Comp MnO fM 4.992329E-04
14  Ele Th fM 3.714988E-05
15  Ele U fM 9.622577E-06
16  Ele Gd fM 6.487284E-06
```

Figure E.39: An example of a formatted text file used to input material composition information specific to a granite geology.

E.6 Concluding Remarks Regarding the TeXAS Application

This appendix describes the TeXAS application, a set of MATLAB [140] code modules developed to support the generation of high-fidelity, site-specific background activity concentration estimates for 100 radioactive particulates and noble gases identified as relevant to the verification regime of the CTBT [116]. As discussed in Section E.4, the background activity concentration estimates generated by the TeXAS application account for production via three natural processes—(1) spontaneous fission, (2) cosmic neutron induced fission, and (3) cosmic neutron induced activation—and for loses via radioactive decay. Loses resulting from transport processes are not accounted for by the TeXAS application.

The principal objectives of the TeXAS application was to make it possible for anyone to develop high-fidelity, site-specific CTBT-relevant radioactive particulate and noble gas background activity concentration estimates. The TeXAS application was therefore developed to do the following: First, the TeXAS application automates and streamlines the process of developing high-fidelity material composition and temperature data. Additionally, the TeXAS application incorporates the data into Monte Carlo N-Particle (MCNP) radiation transport code [74, 75] models. The TeXAS application then collects and processes the best-available nuclear data required to support the MCNP models. And, finally, the TeXAS application post-processes the outputs generated by the MCNP models and evaluates the radioactive particulate and noble gas background activity concentration estimates of interest. The details associated with each of these

process are described in detail in Sections E.2.2 through E.2.5, in Sections E.2.1 through E.2.10, in Section E.3, and in Section E.4, respectively.

Perhaps most importantly, the TeXAS application was designed to do all of these things automatically. Users of the TeXAS application need to have working MATLAB, MCNP, and NJOY 2012 nuclear data processing system [141] installations, but they do not need have any experience working with any of the aforementioned codes. Again, the principal objective of the TeXAS application was to make it possible for anyone to develop high-fidelity, site-specific CTBT-relevant radioactive particulate and noble gas background activity concentration estimates by handling all the details associated with the material data processing, the development of the MCNP models, and the nuclear data processing so that TeXAS application users are not encumbered with the details of these processes, but rather are left free to focus on the basic inputs associated with the studies they wish to conduct.

Appendix F: Isotopic Compositions Supporting CTBT-Relevant Radionuclide Background Activity Concentrations Studies

This appendix documents the isotopic compositions incorporated into a number of the atmospheric, geological, and seawater layers associated with several of the Monte Carlo N-Particle (MCNP) input decks used to conduct the Comprehensive Nuclear-Test-Ban Treaty (CTBT)-relevant radionuclide background activity concentration studies documented in Chapter 3.

In Table F.1, isotopic compositions are provided for six atmospheric layers at six different geometric heights: (1) 50,000 m, (2) 15,000 m, (3) 5,000m, (4) 3,000 m, (5) 1,000 m, and (6) 1 m. The atmospheric layers are each assumed to be one meter thick and centered at the aforementioned geometric heights. The isotopic compositions were developed using the TeXAS application (see Appendix E). As discussed in Section E.2.2, the dry portions of the atmospheric compositions developed by the TeXAS application are developed using the methodology prescribed by the *U.S. Standard Atmosphere, 1976* [142]. According the *U.S. Standard Atmosphere, 1976* [142], the Earth's atmosphere is dry above geometric heights of about 15,960 m, and thus the isotopic composition reported here for the atmospheric layer assumed to be centered at 50,000 m

should be applicable to all atmospheric layers ranging from about 15,960 m up through a maximum geometric height of about 86,000 m, where the Earth's atmosphere can no longer be assumed to be well mixed [142].

The isotopic compositions given for the atmospheric layers centered at 15,000 m, 5,000 m, 3,000 m, 1,000 m, and 1 m account for water vapor present in the atmosphere at those geometric heights. The water vapor contents applied to each of these atmospheric layers was evaluated using mixing ratio data provided by the *U.S. Standard Atmosphere, 1976* [142] and applied to the dry atmospheric compositions as perturbations (see Section E.2.5 of Appendix E). Note that addition of the water vapor to these atmospheric layers causes the hydrogen number fractions, and, to a lesser extent, the oxygen number fractions to increase as the geometric height decreases. Also note that 58.5 %, 99.7 %, 99.8 %, 99.9 %, and 99.9 % of the ^{1}H present in the atmospheric layers centered at 15,000 m, 5,000 m, 3,000 m, 1,000 m, and 1 m, respectively, is present in the form of water vapor present in those atmospheric layers.

To convert the isotopic number fractions reported in Table F.1 to number densities, multiply the number fractions by the total atmospheric number density applicable to the appropriate atmospheric layer. For the atmospheric layers centered at 50,000 m, 15,000 m, 5,000 m, 3,000 m, 1,000 m, and 1 m, the total atmospheric number densities should be 2.14×10^{22} m^{-3}, 4.05×10^{24} m^{-3}, 1.53×10^{25} m^{-3}, 1.89×10^{25} m^{-3}, 2.31×10^{25} m^{-3}, and 2.53×10^{25} m^{-3}, respectively.

Table F.1: Isotopic compositions specific to six atmospheric layers centered at six different geometric heights.

Isotopic Constituent			Isotopic number fractions [unitless] applicable to atmospheric layers at six geometric heights					
Z	Symbol	A	50,000 m	15,000 m	5,000 m	3,000 m	1,000 m	1 m
1	H	1	3.52E-06	8.50E-06	1.30E-03	3.31E-03	6.00E-03	7.24E-03
1	H	2	4.05E-10	9.77E-10	1.49E-07	3.81E-07	6.90E-07	8.33E-07
2	He	3	3.53E-12	3.53E-12	3.52E-12	3.51E-12	3.50E-12	3.49E-12
2	He	4	2.63E-06	2.63E-06	2.63E-06	2.62E-06	2.61E-06	2.60E-06
6	C	12	1.61E-04	1.61E-04	1.61E-04	1.60E-04	1.59E-04	1.59E-04
6	C	13	1.74E-06	1.74E-06	1.74E-06	1.73E-06	1.72E-06	1.72E-06
7	N	14	7.82E-01	7.82E-01	7.80E-01	7.78E-01	7.74E-01	7.73E-01
7	N	15	2.86E-03	2.86E-03	2.85E-03	2.84E-03	2.83E-03	2.82E-03
8	O	16	2.10E-01	2.10E-01	2.10E-01	2.11E-01	2.11E-01	2.12E-01
8	O	17	8.01E-05	8.01E-05	8.02E-05	8.03E-05	8.05E-05	8.06E-05
8	O	18	4.32E-04	4.32E-04	4.33E-04	4.33E-04	4.34E-04	4.35E-04
10	Ne	20	8.26E-06	8.26E-06	8.25E-06	8.22E-06	8.19E-06	8.17E-06
10	Ne	21	2.47E-08	2.47E-08	2.46E-08	2.45E-08	2.44E-08	2.44E-08
10	Ne	22	8.45E-07	8.45E-07	8.43E-07	8.40E-07	8.37E-07	8.35E-07
16	S	32	5.01E-10	5.01E-10	5.00E-10	4.98E-10	4.96E-10	4.96E-10
16	S	33	3.96E-12	3.96E-12	3.95E-12	3.94E-12	3.92E-12	3.91E-12
16	S	34	2.24E-11	2.24E-11	2.24E-11	2.23E-11	2.22E-11	2.22E-11
16	S	36	5.27E-14	5.27E-14	5.26E-14	5.25E-14	5.23E-14	5.22E-14
18	Ar	36	1.58E-05	1.58E-05	1.58E-05	1.57E-05	1.56E-05	1.56E-05
18	Ar	38	2.96E-06	2.96E-06	2.96E-06	2.95E-06	2.94E-06	2.93E-06
18	Ar	40	4.67E-03	4.67E-03	4.66E-03	4.65E-03	4.63E-03	4.62E-03
36	Kr	78	2.03E-09	2.03E-09	2.03E-09	2.02E-09	2.01E-09	2.01E-09
36	Kr	80	1.31E-08	1.31E-08	1.31E-08	1.30E-08	1.30E-08	1.29E-08
36	Kr	82	6.64E-08	6.64E-08	6.63E-08	6.61E-08	6.58E-08	6.57E-08
36	Kr	83	6.58E-08	6.58E-08	6.57E-08	6.55E-08	6.53E-08	6.51E-08
36	Kr	84	3.26E-07	3.26E-07	3.26E-07	3.25E-07	3.23E-07	3.23E-07
36	Kr	86	9.89E-08	9.89E-08	9.87E-08	9.84E-08	9.80E-08	9.79E-08
54	Xe	124	4.16E-11	4.16E-11	4.15E-11	4.14E-11	4.12E-11	4.11E-11
54	Xe	126	3.89E-11	3.89E-11	3.88E-11	3.87E-11	3.85E-11	3.85E-11
54	Xe	128	8.35E-10	8.35E-10	8.33E-10	8.31E-10	8.27E-10	8.26E-10
54	Xe	129	1.15E-08	1.15E-08	1.15E-08	1.15E-08	1.14E-08	1.14E-08
54	Xe	130	1.78E-09	1.78E-09	1.78E-09	1.77E-09	1.76E-09	1.76E-09
54	Xe	131	9.28E-09	9.28E-09	9.26E-09	9.23E-09	9.19E-09	9.18E-09
54	Xe	132	1.18E-08	1.18E-08	1.17E-08	1.17E-08	1.17E-08	1.16E-08
54	Xe	134	4.56E-09	4.56E-09	4.55E-09	4.54E-09	4.52E-09	4.51E-09
54	Xe	136	3.87E-09	3.87E-09	3.86E-09	3.85E-09	3.84E-09	3.83E-09

Table F.2 presents isotopic compositions for each of the six geologies for which CTBT-relevant radionuclide background activity concentrations are presented in Section 3.5.2. Isotopic compositions are given for three igneous geologies—a granite geology, a basalt geology, and a granodiorite geology—and three sedimentary geologies—a shale geology, a sandstone geology, and a limestone geology. The TeXAS application was used to develop the isotopic compositions presented in Table F.2 from the granite, basalt, granodiorite, shale, sandstone, and limestone compositions developed as described in Section 3.5.2. Note that all six geological compositions account for atmospheric air assumed to be present to various extents in the geological porosity voids.

To convert the isotopic number fractions reported in Table F.2 to number densities, multiply the number fractions by the total geological number density applicable to the given geology. For the granite, basalt, granodiorite, shale, sandstone, and limestone geologies of interest here, the number densities should be $7.75 \times 10^{28}\ m^{-3}$, $6.65 \times 10^{28}\ m^{-3}$, $6.74 \times 10^{28}\ m^{-3}$, $7.56 \times 10^{28}\ m^{-3}$, $7.13 \times 10^{28}\ m^{-3}$, and $6.65 \times 10^{28}\ m^{-3}$, respectively.

Table F.3 presents the isotopic composition of seawater used to conduct the CTBT-relevant radionuclide background activity concentrations presented in Section 3.5.3. The seawater composition was evaluated using seawater temperature, pressure, and salinity data taken from the World Ocean Database [148] and the seawater salt mass concentrations reported by Castro and Huber [153] as described in Section 3.5.3.1.

Table F.2: Isotopic compositions associated with granite, basalt, granodiorite, shale, sandstone, and limestone geologies.

Isotopic Constituent			Isotopic Number Fractions [unitless] applicable to six Geologies					
Z	Symbol	A	Granite	Basalt	Granodiorite	Shale	Sandstone	Limestone
1	H	1	1.31E-02	4.05E-02	6.15E-02	2.26E-01	1.82E-02	4.05E-02
1	H	2	1.51E-06	4.66E-06	7.07E-06	2.60E-05	2.09E-06	4.66E-06
2	He	3	2.29E-17	2.94E-16	1.69E-14	4.09E-16	9.05E-15	2.94E-16
2	He	4	1.71E-11	2.19E-10	1.26E-08	3.05E-10	6.76E-09	2.19E-10
6	C	12	6.53E-04	2.18E-03	2.26E-03	1.40E-02	1.82E-01	2.18E-03
6	C	13	7.06E-06	2.36E-05	2.45E-05	1.52E-04	1.97E-03	2.36E-05
7	N	14	5.08E-06	6.51E-05	3.74E-03	9.07E-05	2.01E-03	6.51E-05
7	N	15	1.86E-08	2.38E-07	1.37E-05	3.31E-07	7.33E-06	2.38E-07
8	O	16	6.22E-01	5.85E-01	6.15E-01	5.28E-01	5.92E-01	5.85E-01
8	O	17	2.37E-04	2.23E-04	2.34E-04	2.01E-04	2.25E-04	2.23E-04
8	O	18	1.28E-03	1.20E-03	1.26E-03	1.08E-03	1.22E-03	1.20E-03
10	Ne	20	5.37E-11	6.88E-10	3.95E-08	9.59E-10	2.12E-08	6.88E-10
10	Ne	21	1.60E-13	2.05E-12	1.18E-10	2.86E-12	6.33E-11	2.05E-12
10	Ne	22	5.49E-12	7.04E-11	4.04E-09	9.80E-11	2.17E-09	7.04E-11
11	Na	23	2.53E-02	2.11E-02	1.66E-03	6.15E-03	3.59E-04	2.11E-02
12	Mg	24	2.47E-03	3.69E-02	4.43E-03	8.66E-03	4.00E-03	3.69E-02
12	Mg	25	3.13E-04	4.67E-03	5.61E-04	1.10E-03	5.06E-04	4.67E-03
12	Mg	26	3.44E-04	5.14E-03	6.18E-04	1.21E-03	5.57E-04	5.14E-03
13	Al	27	5.73E-02	5.54E-02	4.19E-02	4.15E-02	3.30E-03	5.54E-02
14	Si	28	2.25E-01	1.50E-01	2.24E-01	1.26E-01	1.02E-02	1.50E-01
14	Si	29	1.14E-02	7.62E-03	1.14E-02	6.42E-03	5.19E-04	7.62E-03
14	Si	30	7.55E-03	5.03E-03	7.50E-03	4.24E-03	3.43E-04	5.03E-03
15	P	31	6.15E-04	1.63E-03	2.87E-04	4.67E-04	1.46E-04	1.63E-03
16	S	32	3.26E-15	4.17E-14	2.40E-12	5.81E-14	1.29E-12	4.17E-14
16	S	33	2.57E-17	3.30E-16	1.89E-14	4.59E-16	1.02E-14	3.30E-16
16	S	34	1.46E-16	1.87E-15	1.07E-13	2.60E-15	5.75E-14	1.87E-15
16	S	36	3.43E-19	4.39E-18	2.52E-16	6.12E-18	1.35E-16	4.39E-18
18	Ar	36	1.03E-10	1.32E-09	7.56E-08	1.83E-09	4.05E-08	1.32E-09
18	Ar	38	1.93E-11	2.47E-10	1.42E-08	3.44E-10	7.61E-09	2.47E-10
18	Ar	40	3.04E-08	3.89E-07	2.24E-05	5.42E-07	1.20E-05	3.89E-07
19	K	39	1.81E-02	4.53E-03	8.90E-03	9.75E-03	6.15E-04	4.53E-03
19	K	40	2.27E-06	5.68E-07	1.12E-06	1.22E-06	7.71E-08	5.68E-07
19	K	41	1.31E-03	3.27E-04	6.43E-04	7.04E-04	4.44E-05	3.27E-04
20	Ca	40	5.80E-03	3.91E-02	1.93E-03	9.02E-03	1.75E-01	3.91E-02
20	Ca	42	3.87E-05	2.61E-04	1.29E-05	6.02E-05	1.17E-03	2.61E-04
20	Ca	43	8.08E-06	5.44E-05	2.69E-06	1.26E-05	2.44E-04	5.44E-05
20	Ca	44	1.25E-04	8.40E-04	4.15E-05	1.94E-04	3.77E-03	8.40E-04
20	Ca	46	2.39E-07	1.61E-06	7.97E-08	3.72E-07	7.23E-06	1.61E-06

Table F.2: Isotopic compositions associated with granite, basalt, granodiorite, shale, sandstone, and limestone geologies, continued.

Isotopic Constituent			Isotopic Number Fractions [unitless] applicable to six Geologies					
Z	Symbol	A	Granite	Basalt	Granodiorite	Shale	Sandstone	Limestone
20	Ca	48	1.12E-05	7.53E-05	3.72E-06	1.74E-05	3.38E-04	7.53E-05
22	Ti	46	5.91E-05	4.58E-04	9.63E-05	9.62E-05	1.21E-05	4.58E-04
22	Ti	47	5.33E-05	4.13E-04	8.69E-05	8.68E-05	1.09E-05	4.13E-04
22	Ti	48	5.28E-04	4.09E-03	8.61E-04	8.60E-04	1.08E-04	4.09E-03
22	Ti	49	3.88E-05	3.00E-04	6.32E-05	6.31E-05	7.92E-06	3.00E-04
22	Ti	50	3.71E-05	2.87E-04	6.05E-05	6.04E-05	7.58E-06	2.87E-04
25	Mn	55	1.44E-04	5.25E-04	1.64E-04	8.66E-05	1.29E-04	5.25E-04
26	Fe	54	3.29E-04	1.90E-03	6.70E-04	8.01E-04	8.61E-05	1.90E-03
26	Fe	56	5.16E-03	2.99E-02	1.05E-02	1.26E-02	1.35E-03	2.99E-02
26	Fe	57	1.19E-04	6.90E-04	2.43E-04	2.90E-04	3.12E-05	6.90E-04
26	Fe	58	1.59E-05	9.19E-05	3.23E-05	3.87E-05	4.15E-06	9.19E-05
36	Kr	78	1.32E-14	1.69E-13	9.73E-12	2.36E-13	5.22E-12	1.69E-13
36	Kr	80	8.51E-14	1.09E-12	6.27E-11	1.52E-12	3.36E-11	1.09E-12
36	Kr	82	4.32E-13	5.53E-12	3.18E-10	7.70E-12	1.70E-10	5.53E-12
36	Kr	83	4.28E-13	5.49E-12	3.15E-10	7.64E-12	1.69E-10	5.49E-12
36	Kr	84	2.12E-12	2.72E-11	1.56E-09	3.79E-11	8.38E-10	2.72E-11
36	Kr	86	6.43E-13	8.24E-12	4.74E-10	1.15E-11	2.54E-10	8.24E-12
54	Xe	124	2.71E-16	3.47E-15	1.99E-13	4.83E-15	1.07E-13	3.47E-15
54	Xe	126	2.53E-16	3.24E-15	1.86E-13	4.51E-15	9.98E-14	3.24E-15
54	Xe	128	5.43E-15	6.96E-14	4.00E-12	9.69E-14	2.14E-12	6.96E-14
54	Xe	129	7.50E-14	9.61E-13	5.52E-11	1.34E-12	2.96E-11	9.61E-13
54	Xe	130	1.16E-14	1.48E-13	8.52E-12	2.06E-13	4.57E-12	1.48E-13
54	Xe	131	6.03E-14	7.73E-13	4.44E-11	1.08E-12	2.38E-11	7.73E-13
54	Xe	132	7.65E-14	9.80E-13	5.63E-11	1.36E-12	3.02E-11	9.80E-13
54	Xe	134	2.97E-14	3.80E-13	2.18E-11	5.29E-13	1.17E-11	3.80E-13
54	Xe	136	2.52E-14	3.23E-13	1.85E-11	4.49E-13	9.94E-12	3.23E-13
64	Gd	152	1.69E-09	1.84E-09	1.66E-09	1.09E-09	-	1.84E-09
64	Gd	154	1.84E-08	2.01E-08	1.80E-08	1.18E-08	-	2.01E-08
64	Gd	155	1.25E-07	1.36E-07	1.22E-07	8.04E-08	-	1.36E-07
64	Gd	156	1.73E-07	1.88E-07	1.69E-07	1.11E-07	-	1.88E-07
64	Gd	157	1.32E-07	1.44E-07	1.30E-07	8.50E-08	-	1.44E-07
64	Gd	158	2.09E-07	2.29E-07	2.06E-07	1.35E-07	-	2.29E-07
64	Gd	160	1.84E-07	2.01E-07	1.81E-07	1.19E-07	-	2.01E-07
90	Th	232	3.27E-06	4.97E-07	1.07E-06	6.72E-07	8.15E-08	4.97E-07
92	U	234	4.46E-11	6.59E-12	6.61E-12	5.49E-11	6.73E-12	6.59E-12
92	U	235	5.95E-09	8.79E-10	8.82E-10	7.33E-09	8.98E-10	8.79E-10
92	U	238	8.20E-07	1.21E-07	1.22E-07	1.01E-06	1.24E-07	1.21E-07

Table F.3: Isotopic composition of seawater

Isotopic Constituent			Isotopic Fraction [unitless]
Z	Symbol	A	
1	H	1	6.62E-01
1	H	2	7.61E-05
5	B	10	5.58E-07
5	B	11	2.25E-06
6	C	12	1.37E-05
6	C	13	1.48E-07
8	O	16	3.31E-01
8	O	17	1.26E-04
8	O	18	6.80E-04
9	F	19	3.26E-07
11	Na	23	2.74E-03
12	Mg	24	2.47E-04
12	Mg	25	3.12E-05
12	Mg	26	3.44E-05
16	S	32	1.57E-04
16	S	33	1.24E-06
16	S	34	7.01E-06
16	S	36	1.65E-08
17	Cl	35	2.43E-03
17	Cl	37	7.76E-04
19	K	39	5.46E-05
19	K	40	6.85E-09
19	K	41	3.94E-06
20	Ca	40	5.89E-05
20	Ca	42	3.93E-07
20	Ca	43	8.20E-08
20	Ca	44	1.27E-06
20	Ca	46	2.43E-09
20	Ca	48	1.14E-07
35	Br	79	2.49E-06
35	Br	81	2.42E-06
38	Sr	84	5.27E-09
38	Sr	86	9.28E-08
38	Sr	87	6.59E-08
38	Sr	88	7.78E-07
90	Th	232	1.32E-15
92	U	234	4.59E-15
92	U	235	6.12E-13
92	U	238	8.44E-11

References

1. "United States Nuclear Tests July 1945 through September 1992," United States Department of Energy, National Nuclear Security Administration Nevada Field Office, Las Vegas, NV, USA, Rep. DOE/NV--209-REV 16, September 2015.

2. Preparatory Commission for the Comprehensive Nuclear-Test-Ban Treaty Organization. (2016 June 15). *Nuclear Testing 1945 – Today* [Online]. Available: https://www.ctbto.org/nuclear-testing/history-of-nuclear-testing/nuclear-testing-1945-today/

3. F. M. SZASZ, *The Day the Sun Rose Twice: The Story of the Trinity Site Nuclear Explosion, July 16, 1945*, Albuquerque, NM, USA: University of New Mexico Press, 1984.

4. Wikipedia: The Free Encyclopedia. (2016 June 25). *Trinity (nuclear test)* [Online]. Available: https://en.wikipedia.org/wiki/Trinity_(nuclear_test)

5. K. T. BAINBRIDGE, "Trinity," Los Alamos Scientific Laboratory of the University of California, Los Alamos, NM, USA, Rep. LA-6300-H, May 1976.

6. V. FEDCHENKO and R. F. HELLGREN, "Appendix 12B. Nuclear explosions, 1945-2006," in *SIPRI Yearbook 2007: Armaments, Disarmament, and International Security*, Stockholm, Sweden: Stockholm International Peace Research Institute, 2007, app. 12B, pp. 552-557.

7. Preparatory Commission for the Comprehensive Nuclear-Test-Ban Treaty Organization. (2016 June 15). *6 January 2016 North Korea Announced Nuclear Test* [Online]. Available: https://www.ctbto.org/the-treaty/developments-after-1996/2016-dprk-announced-nuclear-test/

8. Preparatory Commission for the Comprehensive Nuclear-Test-Ban Treaty Organization. (2016 June 15). *6 and 9 August 1945: Hiroshima / Nagasaki* [Online]. Available: https://www.ctbto.org/specials/testing-times/6-and-9-august-1945hiroshima-nagasaki

9. F. BARNABY and J. ROTBLAT, "The Effects of Nuclear Weapons," *Ambio*, vol. 11, no. 2/3, pp. 84-93, 1982.

10. Radiation Effects Research Foundation. (2016 June 25). *Frequently Asked Questions* [Online]. Available: http://www.rerf.jp/general/qa_e/qa1.html

11. Radiation Effects Research Foundation. (2016 June 25). *Late effects on survivors* [Online]. Available: http://www.rerf.jp/radefx/late_e/late.html

12. S. L. SIMON, A. BOUVILLE, and C. E. LAND, "Fallout from Nuclear Weapons Tests and Cancer Risks," *American Scientist*, vol. 94, no. 1, pp. 48-57, Jan/Feb 2006.

13. Preparatory Commission for the Comprehensive Nuclear-Test-Ban Treaty Organization. (2016 June 25). *The United States' Nuclear Testing Programme* [Online]. Available: https://www.ctbto.org/nuclear-testing/the-effects-of-nuclear-testing/the-united-states-nuclear-testing-programme/

14. Wikipedia: The Free Encyclopedia. (2016 June 25). *Daigo Fukuryū Maru* [Online]. Available: https://en.wikipedia.org/wiki/Daigo_Fukury ū Maru

15. S. SALAFF and B. SHAHN, "The Lucky Dragon," *Bulletin of the Atomic Scientists*, vol. 34, no. 5, pp. 21-23, May 1978.

16. United States Department of Health and Human Services (USDHHS), National Institutes of Health (NIH), National Cancer Institute (NCI), *Estimation of the Baseline Number of Cancers Among Marshallese and the Number of Cancers Attributable to Exposure to Fallout from Nuclear Weapons Testing Conducted in the Marshall Islands*. Bethesda, MD, USA:USDHHS, NIH, NCI, Sept 2004.

17. Preparatory Commission for the Comprehensive Nuclear-Test-Ban Treaty Organization. (2016 June 15). *1945 – 54: Early Efforts to Restrain Nuclear Testing* [Online]. Available: https://www.ctbto.org/the-treaty/history-1945-1993/1945-54-early-efforts-to-restrain-nuclear-testing/

18. United Nations. (2016 June 15). *Resolutions Adopted on the Reports of the First Committee* [Online]. Available: http://www.un.org/en/ga/search/view_doc.asp?symbol=A/RES/1(I)

19. United States Department of State, Office of the Historian. (2016 June 15). *The Acheson-Lilienthal & Baruch Plans, 1946* [Online]. Available: https://history.state.gov/milestones/1945-1952/baruch-plans

20. United Nations. (2016 June 16). *General Assembly Resolutions* [Online]. Available: http://www.un.org/en/sections/documents/general-assembly-resolutions/index.html

21. Preparatory Commission for the Comprehensive Nuclear-Test-Ban Treaty Organization. (2016 June 25). *29 August 1949 – First Soviet Nuclear Test* [Online]. Available: https://www.ctbto.org/specials/testing-times/29-august-1949-first-soviet-nuclear-test

22. International Atomic Energy Agency. (2016 June 16). *Then & Now* [Online]. Available: https://www.iaea.org/publications/magazines/bulletin/39-3

23. Preparatory Commission for the Comprehensive Nuclear-Test-Ban Treaty Organization. (2016 June 16). *1963 – 77: Limits on Nuclear Testing* [Online]. Available: https://www.ctbto.org/the-treaty/history-1945-1993/1963-77-limits-on-nuclear-testing/

24. International Atomic Energy Agency (IAEA). (16 June 2016). *Treaty on the Non-Proliferation of Nuclear Weapons* [Online]. Available: https://www.iaea.org/sites/default/files/publications/documents/infcircs/1970/infcirc140.pdf

25. Preparatory Commission for the Comprehensive Nuclear-Test-Ban Treaty Organization. (2016 June 16). *1977 – 94: Renewed Test-Ban Commitments* [Online]. Available: https://www.ctbto.org/the-treaty/history-1945-1993/1977-94-renewed-test-ban-commitments/

26. Preparatory Commission for the Comprehensive Nuclear-Test-Ban Treaty Organization. (2016 June 16). *1993 – 95: Prelude and Formal Negotiations* [Online].Available: https://www.ctbto.org/the-treaty/1993-1996-treaty-negotiations/1993-95-prelude-and-formal-negotiations/

27. Preparatory Commission for the Comprehensive Nuclear-Test-Ban Treaty Organization. (2016 June 16). *1994 – 96: Debating the Basic Issues* [Online]. Available: https://www.ctbto.org/the-treaty/1993-1996-treaty-negotiations/1994-96-debating-the-basic-issues/

28. Preparatory Commission for the Comprehensive Nuclear-Test-Ban Treaty Organization. (2016 June 16). *1994 – 96: Creating the Organization* [Online].Available: https://www.ctbto.org/the-treaty/1993-1996-treaty-negotiations/1994-96-creating-the-organization/

29. Preparatory Commission for the Comprehensive Nuclear-Test-Ban Treaty Organization. (2016 June 16). *The Executive Council* [Online]. Available: https://www.ctbto.org/the-organization/ctbto-after-entry-into-force/the-executive-council/

30. Preparatory Commission for the Comprehensive Nuclear-Test-Ban Treaty Organization. (2016 June 16). *1994 – 96: Monitoring and Inspection* [Online]. Available: https://www.ctbto.org/the-treaty/1993-1996-treaty-negotiations/1994-96-monitoring-and-inspection/

31. Preparatory Commission for the Comprehensive Nuclear-Test-Ban Treaty Organization. (2016 June 16). *1994 – 96: Entry into Force Formula* [Online]. Available: https://www.ctbto.org/the-treaty/1993-1996-treaty-negotiations/1994-96-entry-into-force-formula/

32. Preparatory Commission for the Comprehensive Nuclear-Test-Ban Treaty Organization. (2016 June 16). *1996: CTBT: A Long-Sought Success* [Online]. Available: https://www.ctbto.org/the-treaty/1993-1996-treaty-negotiations/1996-ctbt-a-long-sought-success/

33. Preparatory Commission for the Comprehensive Nuclear-Test-Ban TreatyOrganization. (2016 June 25). *Overview of the Verification Regime* [Online]. Available: https://www.ctbto.org/verification-regime/background/overview-of-the-verification-regime/

34. Preparatory Commission for the Comprehensive Nuclear-Test-Ban Treaty Organization. (2016 June 25). *International Monitoring System* [Online]. Available: https://www.ctbto.org/map/

35. Preparatory Commission for the Comprehensive Nuclear-Test-Ban Treaty Organization. (2016 June 25). *Seismic Monitoring* [Online]. Available: https://www.ctbto.org/verification-regime/monitoring-technologies-how-they-work/seismic-monitoring/

36. Preparatory Commission for the Comprehensive Nuclear-Test-Ban Treaty Organization. (2016 June 25). *Hydroacoustic Monitoring* [Online]. Available: https://www.ctbto.org/verification-regime/monitoring-technologies-how-they-work/hydroacoustic-monitoring/

37. Preparatory Commission for the Comprehensive Nuclear-Test-Ban Treaty Organization. (2016 June 25). *Infrasound Monitoring* [Online]. Available: https://www.ctbto.org/verification-regime/monitoring-technologies-how-they-work/infrasound-monitoring/

38. Preparatory Commission for the Comprehensive Nuclear-Test-Ban Treaty Organization. (2016 June 25). *Radionuclide Monitoring* [Online]. Available: https://www.ctbto.org/verification-regime/monitoring-technologies-how-they-work/radionuclide-monitoring/

39. Preparatory Commission for the Comprehensive Nuclear-Test-Ban Treaty Organization. (2016 June 25). *The Final Verification Measure* [Online]. Available: https://www.ctbto.org/verification-regime/on-site-inspection/the-final-verification-measure/

40. Preparatory Commission for the Comprehensive Nuclear-Test-Ban Treaty Organization. (2016 June 25). *Techniques* [Online]. Available: https://www.ctbto.org/verification-regime/on-site-inspection/techniques/

41. J. R. LAMARSH and A. J. BARATTA, *Introduction to Nuclear Engineering*, 3rd ed. Upper Saddle River, NJ, USA: Prentice Hall, 2001.

42. Nuclear Power. (2016 June 16). *Nuclear Fission* [Online]. Available: http://www.nuclear-power.net/nuclear-power/fission/#prettyPhoto/0/

43. K.M. MATTHEWS, "The CTBT verification significance of particulate radionuclides detected by the International Monitoring System," Ministry of Health, National Radiation Laboratory, Christchurch, New Zealand, Rep. 2005/1, 2005.

44. Japan Atomic Energy Agency. (2016 June 16). *Graph of Fission Product Yields*[Online]. Available: http://wwwndc.jaea.go.jp/cgi-bin/FPYfig?lib=11&mode=s&iso=nU235&sub=Draw&typ=g1&ynuc=Zr-90&yld=c&zlog=set&ylow=12&xpar=a&eng=e1

45. H. CEMBER, *Introduction to Health Physics*, 3rd ed. New York, NY, USA: McGraw-Hill, 1996.

46. L.-E. DE GEER, "Comprehensive Nuclear-Test-Ban Treaty: relevant radionuclides," *Kerntechnik*, vol. 66, no. 3, pp. 113–120, May 2001.

47. C. R. CARRIGAN and Y. SUN, "Detection of Noble Gas Radionuclides from an Underground Nuclear Explosion During a CTBT On-Site Inspection," *Pure and Applied Geophysics*, vol. 171, no. 3, pp. 717–734, March 2014.

48. Y. V. DUBASOV, "Underground Nuclear Explosions and Release of Radioactive Noble Gases," *Pure and Applied Geophysics*, vol. 167, no. 4, pp 455–461, May 2010.

49. S. M. BOWYER *et al.*, "Automated Particulate Sampler For Comprehensive Test Ban Treaty Verification (The DOE Radionuclide Aerosol Sampler/Analyzer)," *IEEE Transactions on Nuclear Science*, vol. 44, no. 3, pp. 551–556, June 1997.

50. S. M. BOWYER *et al.*, "Radiochemistry of the 3M SBMF-40VF filter media used by the DOE CTBT Radionuclide Aerosol Sampler/Analyzer (RASA)," *Journal of Radioanalytical and Nuclear Chemistry*, vol. 235, no. 1–2, pp. 121–124, September 1998.

51. H. S. MILEY *et al.*, "Automated Aerosol Sampling and Analysis for the Comprehensive Nuclear Test Ban Treaty," *IEEE Transactions on Nuclear Science*, vol. 45, no. 3, pp. 1034–1039, June 1997.

52. Yu. V. DUBASOV *et al.*, "The АРИКС-01 Automatic Facility for Measuring Concentrations of Radioactive Xenon Isotopes in the Atmosphere," *Instruments and Experimental Techniques*, vol. 48, no. 3, pp. 373–379, May 2005.

53. Y. S. POPOV *et al.*, "Measuring Low Activities of Fission-Product Xenon Isotopes Using the β–γ Coincidence Method," *Instruments and Experimental Techniques*, vol. 48, no. 3, pp. 380–386, May 2005.

54. T. W. BOWYER *et al.*, "Automatic Radioxenon Analyzer for CTBT Monitoring," Pacific Northwest National Laboratory, Richland, WA, USA, Rep. PNNL-11424, Nov 1996.

55. T. W. BOWYER *et al.*, "Detection and analysis of xenon isotopes for the comprehensive nuclear-test-ban treaty international monitoring system," *Journal of Environmental Radioactivity*, vol. 59, no. 2, pp 139–151, 2002.

56. B. D. MILBRATH *et al.*, "Atmospheric Radioxenon Measurements in North Las Vegas, NV," Pacific Northwest National Laboratory, Richland, WA, USA, Rep. PNNL-15976, July 2006.

57. A. RINGBOM *et al.*, "SAUNA—a system for automatic sampling, processing, and analysis of radioactive xenon," *Nuclear Instruments and Methods in Physics Research Section A*, vol. 508, no. 3, pp. 542 553, August 2003.

58. J.-P. FONTAINE *et al.*, "Atmospheric xenon radioactive isotope monitoring," *Journal of Environmental Radioactivity*, vol. 72, no. 1-2, pp. 129-135, 2004.

59. B. WERNSPERGER and C. SCHLOSSER, “Noble gas monitoring within the international monitoring system of the comprehensive nuclear test-ban treaty,” *Radiation Physics and Chemistry*, vol. 71, no. 3–4, pp. 775–779, Oct–Nov 2004.

60. National Nuclear Data Center. (2016 June 16). *Chart of Nuclides* [Online]. Available: http://www.nndc.bnl.gov/chart/

61. M. KALINOWSKI *et al.*, “Discrimination of Nuclear Explosions against Civilian Sources Based on Atmospheric Xenon Isotopic Activity Ratios,” *Pure and Applied Geophysics*, vol. 167, no. 4–5, pp. 517–539, May 2010.

62. M. AUER *et al.*, “Intercomparison of systems for the measurement of xenon radionuclides in the atmosphere,” *Applied Radiation and Isotopes*, vol. 60, no. 6, pp. 863–877, June 2004.

63. T. RAUF. (2016 June 16). *Another nuclear test announced by North Korea: Searching for a plan of action?* [Online]. Available: https://www.sipri.org/commentary/expert-comment/2016/another-nuclear-test-announced-north-korea-searching-plan-action

64. Preparatory Commission for the Comprehensive Nuclear-Test-Ban Treaty Organization. (2016 June 16). *The CTBT Verification Regime put to the Test – The Event in the DPRK on 9 October 2006* [Online]. Available: https://www.ctbto.org/press-centre/highlights/2007/the-ctbt-verification-regime-put-to-the-test-the-event-in-the-dprk-on-9-october-2006/

65. Preparatory Commission for the Comprehensive Nuclear-Test-Ban Treaty Organization. (2016 June 16). *CTBTO Detects Radioactivity Consistent with 12 February Announced North Korean Nuclear Test* [Online]. Available: https://www.ctbto.org/press-centre/press-releases/2013/ctbto-detects-radioactivity-consistent-with-12-february-announced-north-korean-nuclear-test/

66. XIA LLC. (25 June 2016). *XIA: Instruments that Advance the Art* [Online]. Available: http://www.xia.com/

67. W. HENNIG *et al.*, “Radioxenon Measurements with a Coincidence Silicon Detector System,” in *Proceedings of the 2012 Monitoring Research Review: Ground-Based Nuclear Explosion Monitoring Technologies*, Albuquerque, New Mexico, USA, 18-20 September 2012, pp. 615-624.

68. W. HENNIG *et al.*, “Study of silicon detectors for high resolution radioxenon measurements,” *Journal of Radioanalytical and Nuclear Chemistry*, vol. 296, no. 2, pp. 675-681, May, 2013.

69. G. GILMORE and J. D. HEMINGWAY, *Practical Gamma-Ray Spectrometery*. Chichester, NY, USA: Wiley and Sons, 1995.

70. L. A. CURRIE, "Limits for Qualitative Detection and Quantitative Determination: Application to Radiochemistry," *Analytical Chemistry*, vol. 40, no. 3, pp. 586-593, March 1968.

71. J. I. McINTYRE *et al.*, "Calculation of Minimum Detectable Concentration Levels of Radioxenon Isotopes Using the PNNL ARSA System," Pacific Northwest National Laboratory, Richland, WA, USA, Rep. PNNL-13102, March 2006.

72. N. TSOULFANIDIS and S. LANDSBERGER, *Measurement & Detection of Radiation*, 4th ed. Boca Raton, FL, USA: CRC Press, 2015.

73. A. J. HAYTER, *Probability and Statistics for Engineers and Scientists*, 2nd ed. Pacific Grove, CA, USA: Duxbury, 2002.

74. Los Alamos National Laboratory. (25 June 2016). *A General Monte Carlo N-Particle (MCNP) Transport Code* [Online]. Available: https://mcnp.lanl.gov

75. D. B. PELOWITZ *et al.*, Ed., "MCNP6™ USER'S MANUAL: Code Version 6.1.1beta," Los Alamos National Laboratory, Los Alamos, NM, USA, Rep. LA-CP-14-00745, Rev. 0, June 2014.

76. Los Alamos National Laboratory (staff of the X-5 Monte Carlo Team), "MCNP—A General Monte Carlo N-Particle Transport Code, Version 5: Volume I: Overview and Theory," Los Alamos National Laboratory, Los Alamos, NM, USA, Rep. LA-UR-03-1987, 1 Feb 2008.

77. Los Alamos National Laboratory (staff of the X-5 Monte Carlo Team), "MCNP—A General Monte Carlo N-Particle Transport Code, Version 5: Volume II: User's Guide," Los Alamos National Laboratory, Los Alamos, NM, USA, Rep. LA-CP-03-0245, 1 Feb 2008.

78. J. C. HAYES *et al.*, "Requirements for Xenon International: Revision 1," Pacific Northwest National Laboratory, Richland, WA, USA, Rep. PNNL-22227 (Rev 1), 30 December 2015.

79. A. R. HAMBLEY, *Electrical Engineering: Principles and Applications*, 3rd ed. Upper Saddle River, NJ, USA: Pearson / Prentice Hall, 2005.

80. E. LIPIANSKY, *Electrical, Electronics, and Digital hardware Essentials for Scientists and Engineers*. Hoboken, NJ, USA: Wiley and Sons, 2013.

81. Wikipedia: The Free Encyclopedia. (25 June 2016). *p-n junction* [Online]. Available: https://en.wikipedia.org/wiki/P-n_junction

82. Wikipedia: The Free Encyclopedia. (25 June 2016). *Diode* [Online]. Available: https://en.wikipedia.org/wiki/Diode

83. Wikipedia: The Free Encyclopedia. (25 June 2016). *p-n diode* [Online]. Available: https://en.wikipedia.org/wiki/P-n_diode

84. Microsemi Corp.-Waterown, *The PIN Diode Circuit Designers' Handbook*. Watertown, MA, USA: Microsemi Corp.-Watertown, 1998.

85. Wikipedia: The Free Encyclopedia. (25 June 2016). *PIN diode* [Online]. Available: https://en.wikipedia.org/wiki/PIN_diode

86. Amptek, Inc. (25 June 2016). *XR-100CR Si-PIN X-Ray Detector* [Online]. Available: http://amptek.com/products/xr-100cr-si-pin-x-ray-detector/

87. The University of Texas at Austin. (25 June 2016). *Nuclear and Radiation Engineering Program* [Online]. Available: https://nuclear.engr.utexas.edu/

88. Ortec. (25 June 2016). *High Purity Germanium (HPGe) and Silicon Lithium [Si(Li)] Radation Detectors* [Online]. Available: http://www.ortec-online.com/Products-Solutions/RadiationDetectors/Type.aspx

89. M. AL-TURNAY *et al.*, "PIXE analysis with the XR-100CR Si-PIN detector," *Nuclear Instruments and Methods in Physics Research B*, vol. 155, no. 1–2, pp. 137–142, July 1999.

90. M. GUERRA *et al.*, "Performance of three different Si X-ray detectors for portable XRF spectrometers in cultural heritage applications," *Journal of Instrumentation*, vol. 7, no. C10004, pp. 1–9, Oct 2012.

91. J. PANTAZIS, private communication, 6 Nov 2014.

92. J. PANTAZIS, private communication, 4 Nov 2014.

93. S. COLEMAN, "MECH-PRT-XEDD-CUBE_UT," XIA LLC, Hayward, CA, USA, Rep. MECH-PRT-XEDD-CUBE_UT, 6 Nov 2014.

94. Amptek Inc., (25 June 2016). *Amptek: Products for your imagination* [Online]. Available: http://amptek.com/

95. C. COX, "XIA LLC Si-PIN Diode Prototype Operation Manual," XIA LLC, Hayward, CA, USA.

96. XIA LLC. (25 June 2016). *DXP-XMAP* [Online]. Available: http://www.xia.com/DXP-XMAP_Software.html#xManager

97. D.A. HAAS, S. R. BIEGALSKI, and K. M. FOLTZ BIEGALSKI, "Radioxenon production through neutron irradiation of stable xenon gas," *Journal of Radioanalytical and Nuclear Chemistry*, vol. 282, no. 3, pp. 677–680, December 2009.

98. W. HENNIG, private communication, 3 Feb 2016.

99. G. F. KNOLL, *Radiation Detection and Measurement*. New York, NY, USA: Wiley and Sons, 2000.

100. S. AGHARA and W. CHARLTON, "Characterization and quantification of an in-core neutron irradiation facility at a TRIGA II research reactor," *Nuclear Instruments and Methods in Physics Research B*, vol. 248, no. 1, pp. 181–190, July 2006.

101. Swageolk. (25 June 2016). *PFA Plug Valves, 43 Series* [Online]. Available: http://www.swagelok.com/downloads/webcatalogs/EN/MS-01-56.pdf

102. T. H. TEO, "Certificate of Analysis [Xe-130]," Isoflex USA, San Francisco, CA, USA, Rep. 54-01-130-4008, 3 August 2010.

103. T. H. TEO, "Certificate of Analysis [Xe-132]," Isoflex USA, San Francisco, CA, USA, Rep. 5085, 12 August 2013.

104. T. H. TEO, "Certificate of Analysis [Xe-134]," Isoflex USA, San Francisco, CA, USA, Rep. 5086, 12 August 2013.

105. Ortec. (25 June 2016). *GammaVision Gamma-Ray Spectrum Analysis and MCA Emulator for Microsoft Windows 7 and XP Professional SP3* [Online]. Available: http://www.ortec-online.com/Service-Support/Library/Manuals.aspx

106. S. COLEMAN, "MECH-PRT-XEDD-CUBE_UT," XIA LLC, Hayward, CA, USA, Rep. MECH-PRT-XEDD-CUBE_UT, 6 Nov 2014.

107. Eckert and Ziegler. (25 June 2016). *Isotope Products* [Online]. Available: http://www.ezag.com/home/products/isotope_products/

108. MakerBot. (25 June 2016). *MakerBot 3D Printing Solutions* [Online]. Available: https://www.makerbot.com/products/3d-printers/

109. M. ALI, "Development and Characterization of a High Resolution Portable Gamma Spectrometer," M.A.S. thesis, Faculty of Energy Systems and Nuclear Science, University of Ontario Institute of Technology, Oshawa, Ontario, CA, April 2012.

110. S. J. NOVOTNY and D. TO, "Characterization of a high-purity germanium (HPGe) detector through Monte Carlo simulation and nonlinear least squares estimation," *Journal of Radioanalytical and Nuclear Chemistry*, vol. 304, no. 2, pp. 751–761, May 2015.

111. F. TZIKA *et al.*, "Application of the Monte Carlo method for the calibration of an in situ gamma spectrometer," *Applied Radiation and Isotopes*, vol. 68, no. 7–8, pp. 1441–1444, July–August 2010.

112. National Institutue of Standards and Technology. (25 June 2016). *Atomic Weights and Isotopic Compositions for All Elements* [Online]. Available: http://physics.nist.gov/cgi-bin/Compositions/stand_alone.pl?ele=

113. R. J. McCONN Jr *et al.*, "Compendium of Material Composition Data for Radiation Transport Modeling," Pacific Northwest National Laboratory, Richland, WA, USA, Rep. PNNL-15870 Rev. 1, 4 March 2011.

114. International Commission on Radiation Protection, "Nuclear Decay Data for Dosimetric Calculations," *Annals of the ICRP*, vol. 38, no. 3, pp. 1–96 and e1–e26, June 2008.

115. P. GOLDHAGEN, et al., "The energy spectrum of Cosmic-Ray Induced Neutrons Measured on an Airplane over a wide range of altitude and latitude," *Radiation Protection Dosimetry*, vol. 110, no. 1–4, pp. 387–392, 2004.

116. L.-E. DeGEER, "Comprehensive Nuclear-Test-Ban Treaty: Relevant Radionuclides," *Kerntechnik*, vol. 66, no. 3, pp. 113–120, May 2001.

117. International Atomic Energy Agency (IAEA). (4 August 2014). *Evaluated Nuclear Data File (ENDF) Database Version of March 14, 2004* [online]. Available: https://www-nds.iaea.org/exfor/endf.htm

118. A. TRKOV, M. HERMAN, and D. A. BROWN, Eds., "ENDF 6 Formats Manual: Data Formats and Procedures for the Evaluated Nuclear Data Files ENDF/B-VI and ENDF/B-VII," Brookhaven National Laboratory, Upton, NY, USA, Rep. BNL 90365 2009 Rev. 2, December 2011.

119. K. M. Matthews, “The CTBT verification significance of particulate radionuclides detected by the International Monitoring System,” National Radiation Laboratory, Christchurch, New Zealand, Rep. 2001/5, 2005.

120. M. B. KALINOWSKI and M. P. TUMA, “Global radioxenon emission inventory based on nuclear power reactor reports,” *Journal of Environmental Radioactivity*, vol. 100, no. 1, pp. 58–70, January 2009.

121. P. R. J. SAEY, T. W. BOWYER, and A. RINGBOM, “Isotopic noble gas signatures released from medical isotope production facilities—Simulations and measurements,” *Applied Radiation and Isotopes*, vol. 68, no. 9, pp. 1846–1854, September 2010.

122. P. R. J. SAEY *et al.*, “Worldwide measurements of radioxenon background near isotope production facilities, a nuclear power plant and at remote sites: the ‘‘EU/JA-II’’ Project,” *Journal of Radioanalytical and Nuclear Chemistry*, vol. 296, no. 2, pp. 1133–1142, May 2013.

123. K. H. WEDEPOHL, “The composition of the continental crust,” *Geochimica et Cosmochimica Acta*, vol. 59, no. 7, pp. 1217–1232, April 1995.

124. S. R. TAYLOR and S. M. McLENNAN, "The Geochemical Evolution of the Continental Crust," *Reviews of Geophysics*, vol. 33, no. 2, pp. 241–265, May 1995.

125. R. L. RUDNICK and S. GAO, “Composition of the Continental Crust,” in *Treatise on Geochemistry, Volume 3: The Crust.*” San Diego, CA, USA: Elsevier, Inc., 2005, ch. 3.01, pp. 1–64.

126. D. W. EFURD *et al.*, “Determination of the $^{240}Pu/^{239}Pu$ atom ratio in global fallout at two locations in the Northern Hemisphere,” *Journal of Environmental Radioactivity*, vol. 100, no. 1, pp. 58–70, January 2009.

127. D. H. HATHAWAY, “The Solar Cycle,” *Living Reviews in Solar Physics*, vol. 7, no. 1, December 2010.

128. J. F. ZIEGLER, “Terrestrial cosmic rays,” *IBM Journal of Research and Development*, vol. 40, no. 1, pp. 19-39, January 1996.

129. World Data Center (WDC), Royal Observatory of Belgium, Brussels. (20 April 2016). *Sunspot Number* [Online]. Available at: http://sidc.oma.be/silso/home

130. S. HEBEL, “Lithospheric Radioxenon and its influence on the interpretation of on-site inspection measurements verifying the Comprehensive Nuclear Test Ban Treaty,” Ph.D. dissertation, Department of Physics, University of Hamburg, Hamburg, Germany, 21 July 2008.

131. S. HEBEL, “Genesis and Equilibrium of Natural Lithospheric Radioxenon and its Influence on Subsurface Noble Gas Samples for CTBT On-site Inspections,” *Pure and Applied Geophysics*, vol. 167, no. 4–5, pp. 463–470, May 2010.

132. J. T. FABRYKA-MARTIN, “Production of Radionuclides in the Earth and their Hydrogeologic Significance, with Emphasis on Chlorine-36 and Iodine-129,” Ph.D. Dissertation, Department of Hydrology and Water Resources, The University of Arizona, Tucson, AZ, USA, 1988.

133. R. A. RIEDMANN and R. T. PURTSCHERT, "Natural ^{37}Ar Concentrations in Soil Air: Implications for Monitoring Underground Nuclear Explosions," *Environmental Science and Technology*, vol. 45, no. 20, pp. 8656–8664, 31 August 2011.

134. J. D. LOWREY, “Subsurface Radioactive Gas Transport and Release Studies using the UTEX Model,” Ph.D. Dissertation, Department of Mechanical Engineering, The University of Texas at Austin, Austin, TX, USA, August 2013.

135. C. M. JOHNSON, “Examination of Natural Background Sources of Radioactive Noble Gases with CTBT Signicance,” Master’s Thesis, Department of Mechanical Engineering, The University of Texas at Austin, Austin, TX, USA, December 2013.

136. C. JOHNSON, H. ARMSTRONG, W. H. WILSON, and S. R. BIEGLAKSI, “Examination of radioargon production by cosmic neutron interactions,” *Journal of Environmental Radioactivity*, vol. 140, pp. 123–129, February 2015.

137. W. LI, J. GONG, and Z. BIAN, “Final on Demonstration of Movable Argon-37 Rapid Detection System (In Chinese),” Chinese Academy of Engineering Physics, Institute of Nuclear Physics and Chemistry, Mianyang, China, Rep. CAEP-0167.

138. P. R.J. SAEY, “Ultra-Low-Level Measurements of Argon, Krypton and Radioxenon for Treaty Verification Purposes,” *ESARDA Bulletin*, vol. 36, pp. 42–56, June 2007.

139. D. A. HAAS *et al*., “The Science Case for ^{37}Ar as a Monitor for Underground Nuclear Explosions,” Pacific Northwest National Laboratory, Richland, WA, USA, Rep. PNNL-19458, June 2010.

140. MathWorks. (1 April 2017). *MATLAB: The Language of Technical Computing* [Online]. Available: https://www.mathworks.com/products/matlab.html

141. A. C. KAHLER, Ed., "The NJOY Nuclear Data Processing System, Version 2012," Los Alamos National Laboratory, Los Alamos, NM, USA, Rep. LA-UR-12-27079, 20 December 2012.

142. "U.S. Standard Atmosphere, 1976," National Oceanic and Atmospheric Administration, National Aeronautics and Space Administration, and United States Air Force, Washington, D.C., USA, Rep. NOAA-S/T 76-1562, October 1976.

143. R. L. PARKER, "Composition of the earth's crust," in *Data of Geochemistry*, 6th ed. Washington, D.C., USA: United States Government Printing Office, 1967, ch. D, pp. D1–D19.

144. W. B. WILSON *et al.*, "A Manual for CINDER'90 Version 07.4 Codes and Data," Los Alamos National Laboratory, Los Alamos, NM, USA, Rep. LA-UR-07-8412, December 2007.

145. W. R. RUDD and A. SHAKOOR, "Density," in *Physical Properties of Rocks and Minerals*, Y. S. TOULOUKIAN and C. Y. HO, Ed. New York, NY, USA: McGraw-Hill, 1981, ch. 3.

146. R. G. WOLFF , "Porosity, Permeability, Distribution Coefficients, and Dispersity," in *Physical Properties of Rocks and Minerals*, Y. S. TOULOUKIAN and C. Y. HO, Ed. New York, NY, USA: McGraw-Hill, 1981, ch. 4.

147. P. J. POTTS, A. G. TINDLE, and P. C. WEBB, "Geochemical Reference Material Compositions." Boca Raton, FL, USA: CRC Press, Inc., 1992.

148. National Oceanographic Data Center. (1 April 2017). "World Ocean Database" [Online]. Available: http://www.oecd-nea.org/dbforms/data/eva/evatapes/jeff_32/

149. F. J. MILLERO, C.-T. CHEN, A. BRADSHAW, and K. SCHLEICHER, "A new high pressure equation of state for seawater," *Deep Sea Research Part A*, vol. 27, no. 3–4, pp. 255-264, April 1980.

150. F. J. MILLERO and A. POISSON, "International one-atmosphere equation of state of seawater," *Deep Sea Research Part A*, vol. 28, no. 6, pp. 625–629, June 1981.

151. United Nations Educational, Scientific and Cultural Organization (Unesco), "Tenth report of the joint panel on oceanographic tables and standards," *Unesco technical papers in marine science*, no. 36, 1981.

152. United Nations Educational, Scientific and Cultural Organization (Unesco), "Background Papers and Supporting Data on the International Equation of State of Seawater 1980," *Unesco technical papers in marine science*, no. 38, 1981.

153. P. CASTRO and M. E. HUBER, "Marine Biology, 8th Ed.," New York, NY, USA: McGraw-Hill, 2010.

154. R. R. GREENBERG and H. M. KINGSTON, "Trace Element Analysis of Natural Water Samples by Neutron Activation Analysis with Chelating Resin," *Analytical Chemistry*, vol. 55, no. 7, pp. 1160–1165, June 1983.

155. T.-L. KU, K. G. KNAUSS, and G. G. MATHIEU, "Uranium in open ocean: concentration and isotopic composition," *Deep-Sea Research*, vol. 24, no. 11, pp. 1005–1017, November 1977.

156. J. A. SNYMAN, *Practical Mathematical Optimization: An Introduction to Basic Optimization Theory and Classical and New Gradient-Based Algorithms*. New York, NY, USA: Springer, 2005.

157. K. LABS, "Underground Building Climate," *Solar Age*, vol. 4, no. 10, pp. 44–50 (1979).

158. A.A. AL-TEMEEMI and D. J. HARRIS, "The generation of subsurface temperature profiles for Kuwait," *Energy and Buildings*, vol. 33, no. 8, pp. 837–841, October 2001.

159. H. L. Beck, "Environmental Gamma Radiation from Deposited Fission Products, 1960-1964," *Health Physics*, vol. 12, pp. 313–322, 1966.

160. S. MASHNIK and A. SIERK, "CEM03.03 User Manual," Los Alamos National Laboratory, Los Alamos, NM, USA, Rep. LA-UR-12-01364, 2012.

161. S. G. MASHNIK, K. K. GUDIMA, R. E. PRAEL, A. J. SIERK, M. I. BAZNAT, and N. V. MOKHOV, "CEM03.03 and LAQGSM03.03 Event Generators for the MCNP6, MCNPX, and MARS15 Transport Codes," presented at the *Joint ICTP-IAEA Advanced Workshop on Model Codes for Spallation Reactions*, Trieste, Italy, February 2008.

162. D. B. PELOWITZ *et al.*, Ed., "MCNPX^{TM} USER'S MANUAL: Version 2.7.0," Los Alamos National Laboratory, Los Alamos, NM, USA, Rep. LA-CP-11-00438, April 2011.

163. G. W. McKINNEY, H. J. ARMSTRONG, M. R. JAMES, J. M. CLEM, and P. GOLDHAGEN, "MCNP6 Cosmic-Source Option," Los Alamos National Laboratory, Los Alamos, NM, USA, Rep. LA-UR-12-0196, 2012.

164. Center Jadernykh Dannykh. (1 April 2017). "DATA" [Online]. Available: http://www.ippe.obninsk.ru/podr/cjd/page4_cjd.html

165. Nuclear Energy Agency. (1 April 2017). "CENDL-3.1 - The Chinese Evaluated Nuclear Data Library" [Online]. Available: https://www.oecd-nea.org/dbforms/data/eva/evatapes/cendl_31/

166. Nuclear Energy Agency. (1 April 2017). "JEFF-3.1.1 evaluated data library" [Online]. Available: https://www.oecd-nea.org/dbforms/data/eva/evatapes/jeff_31/index-JEFF3.1.1.html

167. Nuclear Energy Agency. (1 April 2017). "JEFF-3.1.2 - Neutron Data" [Online]. Available: https://www.oecd-nea.org/dbforms/data/eva/evatapes/jeff_31/JEFF312/

168. Nuclear Energy Agency. (1 April 2017). "JEFF-3.2 evaluated data library - Neutron data" [Online]. Available: https://www.oecd-nea.org/dbforms/data/eva/evatapes/jeff_32/

169. Japan Atomic Energy Agency, Nuclear Data Center. (1 April 2017). "JENDL: Japanese Evaluated Nuclear Data File" [Online]. Available: http://wwwndc.jaea.go.jp/jendl/jendl.html

170. A. J. KONING, D. ROCHMAN, *et al.* (1 April 2017). "TENDL-2015: TALYS-based evaluated nuclear data library" [Online]. Available: https://tendl.web.psi.ch/tendl_2015/tendl2015.html

171. Free Software Foundation, Inc. (1 April 2017). *GNU Parallel* [Online]. Available: https://www.gnu.org/software/parallel/

172. A. C. KAHLER, private communication, 14 May 2015 and 8 September 2015.

173. National Institute of Standards and Technology. (1 April 2017). *Atomic Weights and Isotopic Compositions with Relative Atomic Masses* [Online]. Available: https://www.nist.gov/pml/atomic-weights-and-isotopic-compositions-relative-atomic-masses

174. A. CHULLIAT *et al.*, "The US/UK World Magnetic Model for 2015-2020," National Geophysical Data Center, Boulder, CO, USA, 2015.

Vita

William Hamill Wilson is the son of Warren Hamill Wilson and Elba Wilson. He graduated from Dr. Ralph Poteet High School in Mesquite, Texas in May of 2002. In the fall of 2002 William entered The University of Texas at Austin as a freshman. In December of 2006 the university conferred on him a Bachelor of Science in Mechanical Engineering degree. Upon completion of his bachelor's degree, William entered the Graduate School at The University of Texas at Austin. In March of 2008 he married Ashleigh Marie Wilson. In August of 2008 he graduated from The University of Texas at Austin with a Master of Science in Engineering degree. Later that month William went to work at Knolls Atomic Power Laboratory in Schenectady, New York. William worked in the Reactor Safety Engineering unit at Knolls Atomic Power Laboratory for two years before transferring to Bremerton, Washington to serve as one of the laboratory's representatives at Puget Sound Naval Shipyard and Intermediate Maintenance Facility, where he worked for two years. In the fall of 2012 William re-entered the Graduate School at The University of Texas at Austin to begin his doctoral program.

Email Address: whwilson15@utexas.edu

This dissertation was typed by the author.